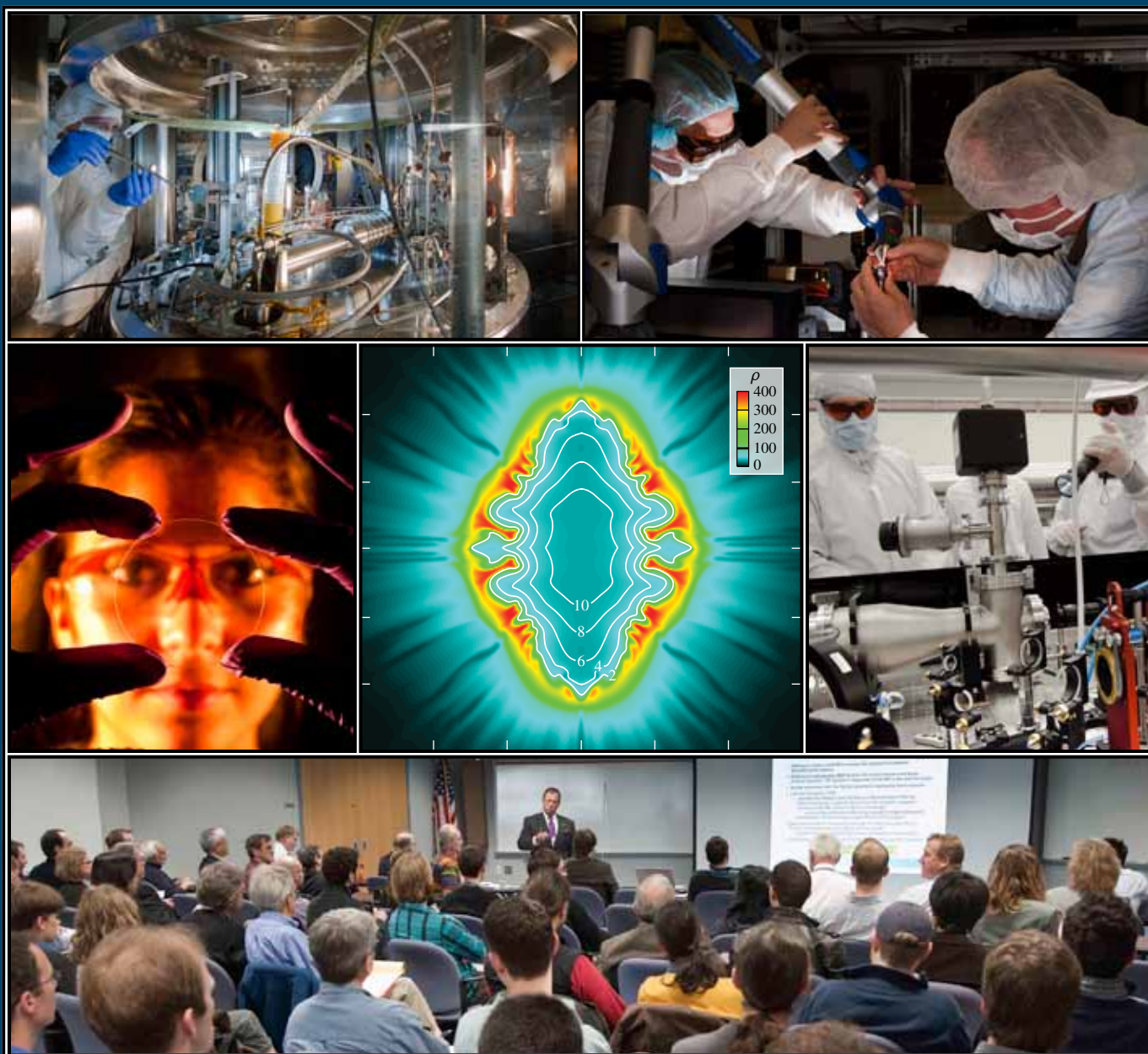


LLE 2011 Annual Report



October 2010 – September 2011



Cover Photos

Top left: LLE continues to make strides in pursuit of the perfectly formed target. A shroud cooler has been installed in the Fill/Transfer Station 1 (FTS-1). Accessing the chamber in which targets are filled with hydrogen isotopes occurs infrequently and is complicated to carry out. Mark Romanofsky, seen here under the dome, is fine-tuning the installation of the shroud cooler and guide-rail plates.

Top right: The pulse stretcher for the ultra-broadband front-end project, partially visible in the lower-left corner of this photo, uses gratings and cylindrical Öffner mirrors to stretch 200-nm pulses to 750 ps before they are amplified. Matt Millecchia and Jake Bromage are shown here using the Faro arm to position the stretcher optics before finely aligning the front end of the laser.

Middle left: The High School Summer Research Program completed its 23rd year at LLE with 16 high school students investigating real-world problems while being supervised by scientists and engineers at the Laboratory. In this photo Madeline Rutan of Penfield High School is shown examining a glass sample coated with a layer of abrasion-resistant sol-gel.

Center: LLE is exploring several advanced ignition concepts that can be tested at the National Ignition Facility in the coming decade. A calculated isodensity plot of the core of a polar-drive-ignition target as modeled by the code *DRACO* is shown here.

Middle right: Although periodic safety inspections are carried out at the Omega Laser Facility, special attention is paid to any major upgrades within the systems. Here, Matt Moore (left) is shown describing the upgrade of OMEGA EP's infrared alignment table to Doug Jacobs-Perkins, LLE's Chief Safety Officer.

Bottom: The third annual Omega Laser Facility Users Group (OLUG) Workshop was held at LLE in May 2011. Here, LLE Director Dr. Robert L. McCrory, a strong supporter of OLUG since its inception, welcomes the Users and talks about the evolving capabilities of the Omega Laser Facility that keep it at the cutting edge of research.

Prepared for
U.S. Department of Energy
Albuquerque Service Center
DOE/NA/28302-1036

Distribution Category
October 2010–September 2011

Printed in the United States of America
Available from
National Technical Information Services
U.S. Department of Commerce
5285 Port Royal Road
Springfield, VA 22161
www.ntis.gov

This report was prepared as an account of work conducted by the Laboratory for Laser Energetics and sponsored by New York State Energy Research and Development Authority, the University of Rochester, the U.S. Department of Energy, and other agencies. Neither the above named sponsors, nor any of their employees, makes any warranty, expressed or implied, or assumes any legal liability or responsibility for the accuracy, completeness, or usefulness of any information, apparatus, product, or process disclosed, or represents that its use would not infringe privately owned rights. Reference herein to any specific commercial product, process, or service by trade name, mark, manufacturer, or otherwise, does not necessarily constitute or imply its endorsement, recommendation, or favoring by the United States Government or any agency thereof or any other sponsor. Results reported in the LLE Review should not be taken as necessarily final results as they represent active research. The views and opinions of authors expressed herein do not necessarily state or reflect those of any of the above sponsoring entities.

The work described in this volume includes current research at the Laboratory for Laser Energetics, which is supported by New York State Energy Research and Development Authority, the University of Rochester, the U.S. Department of Energy Office of Inertial Confinement Fusion under Cooperative Agreement No. DE-FC52-08NA28302, and other agencies.

For questions or comments, Laboratory for Laser Energetics,
250 East River Road, Rochester, NY 14623-1299, (585) 275-5286.
www.lle.rochester.edu

LLE 2011 Annual Report

October 2010 – September 2011



Inertial Fusion Program and
National Laser Users' Facility Program

Contents

Executive Summary	v
The Velocity and Timing of Multiple Spherically Converging Shock Waves in Liquid Deuterium	1
Impeding Hohlraum Plasma Stagnation in Inertial Confinement Fusion	7
Initial Cone-in-Shell, Fast-Ignition Experiments on OMEGA	13
Submicrometer-Resolution Mapping of Ultraweak 355-nm Absorption in HfO ₂ Monolayers Using Photothermal Heterodyne Imaging	25
Large Tunable, THz Electro-Optic Response in Cadmium Manganese Telluride (Cd,Mn)Te Single Crystals	33
Improvements to Long-Pulse–System Performance and Operational Efficiency on OMEGA EP	37
Precision Equation-of-State Measurements on NIF Ablator Materials from 1 to 12 Mbar Using Laser-Driven Shock Waves	47
Refractive Index of Lithium Fluoride Ramp Compressed to 800 GPa	59
Hot-Electron Heating Caused by Two-Plasmon-Decay Instability	66
Fusion Yield Enhancement in Laser-Driven Magnetized Implosions	80
Amplifying Nanosecond Optical Pulses at 1053 nm with an All-Fiber Regenerative Amplifier	85
Analysis and Suppression of Parasitic Processes in Noncollinear Optical Parametric Amplifiers	90
Stress Compensation in Hafnia/Silica Optical Coatings by Inclusion of Alumina Layers	100
Langmuir Turbulence and Suprathermal Electron Production from the Two-Plasmon-Decay Instability Driven by Crossed Laser Beams in an Inhomogeneous Plasma	109
Demonstration of a Closed-Loop Beam-Shaping System Based on the Phase-Only Carrier Method in High-Power Lasers	113
Temporal Contrast Degradation at the Focus of Ultrafast Pulses from High-Frequency Spectral Phase Modulation	117
Highly Accurate Wavefront Reconstruction Algorithms Over Broad Spatial-Frequency Bandwidth	130
Time-Resolved Optical Response of All-Oxide, YBa ₂ Cu ₃ O ₇ /La _{0.7} Sr _{0.3} MnO ₃ Proximitized Bilayers	141

Hot-Spot Mix in Ignition-Scale Inertial Confinement Fusion Targets	145
Measurements of the Differential Cross Section for the Elastic $n\text{-}^3\text{H}$ and $n\text{-}^2\text{H}$ Scattering at 14.1 MeV by Using an Inertial Confinement Fusion Facility	151
Study of Rayleigh–Taylor Growth in Directly Driven Cryogenic-Deuterium Targets	157
Highly Efficient Room-Temperature Yb:YAG Ceramic Laser and Regenerative Amplifier	163
LLE’s Summer High School Research Program	166
FY11 Laser Facility Report	168
National Laser Users’ Facility and External Users’ Programs	171
The Third Omega Laser Facility Users’ Group Workshop	250
Publications and Conference Presentations	259

Executive Summary

The fiscal year ending September 2011 (FY11) concluded the fourth year of the third five-year renewal of Cooperative Agreement DE-FC52-08NA28302 with the U.S. Department of Energy (DOE). This annual report summarizes progress in inertial fusion research at the Laboratory for Laser Energetics (LLE) during the past fiscal year including work on the National Ignition Campaign (NIC). It also reports on LLE's progress on laboratory basic science research; laser, optical materials, and advanced technology development; operation of OMEGA and OMEGA EP for the NIC and high-energy-density (HED) campaigns, the National Laser Users' Facility (NLUF), and other external users; and programs focusing on the education of high school, undergraduate, and graduate students during the year.

Progress in Inertial Confinement Fusion (ICF) Research

One of LLE's principal missions is to conduct research in inertial confinement fusion (ICF) with particular emphasis on supporting the goal of achieving ignition on the National Ignition Facility (NIF). This program relies on the full use of the OMEGA 60-beam UV laser as well as the OMEGA EP high-energy, short-pulse laser system. During FY11, a total of 1805 target shots were taken at the Omega Laser Facility. The OMEGA Laser System operated reliably and returned publishable scientific data for numerous campaigns. The largest fraction of experiments, more than 40% of all the shots, were conducted for the NIC. OMEGA operated with Availability and Experimental Effectiveness averages for FY11 of 93% and 96%, respectively.

Within the NIC, LLE plays a lead role in the validation of the performance of cryogenic target implosions, essential to all forms of ICF ignition. LLE is responsible for a number of critical elements within the Integrated Experimental Teams (IET's) supporting the demonstration of indirect-drive ignition on the NIF and is the lead laboratory for the validation of the polar-drive approach to ignition on the NIF. LLE has also developed, tested, and constructed a number of diagnostics that are being used on the NIF for the NIC. During this past year, progress in the inertial fusion research program continued in three principal areas: NIC experiments; development of diag-

nostics for experiments on OMEGA, OMEGA EP, and the NIF; and theoretical analysis and design efforts aimed at improving direct-drive-ignition capsule designs and advanced ignition concepts such as fast ignition and shock ignition.

1. National Ignition Campaign Experiments in FY11

In this volume, we report on experiments that were conducted on OMEGA to measure the velocity and timing of multiple converging shock waves inside spherical targets filled with liquid (cryogenic) deuterium (p. 1). The results show that shock timing can be measured to better than the ± 50 -ps timing precision required for ignition targets. The technique was applied to full-scale experiments to tune hohlraum-driven ignition targets on the NIF.

Pioneering experiments conducted on OMEGA by a collaborative team led by scientists from MIT's Plasma Science and Fusion Center (PSFC) and comprised of LLE, LLNL, and General Atomics (GA) scientists obtained proton radiographic images of gas-filled hohlraum-driven implosions showing the dynamics of the interior of the hohlraums including inhibition of plasma-jet formation and the mitigation of plasma stagnation on the hohlraum axis (p. 7). The results demonstrated the important roles of spontaneously created magnetic and electric fields in the hohlraum dynamics and capsule implosions and provided insight into the effects of the fill gas on x-ray-driven implosions.

In a collaborative experiment led by scientists from LLE along with scientists from LLNL, GA, Sandia National Laboratories (SNL), Los Alamos National Laboratory (LANL), and the University of Nevada, Reno, the hydrodynamic-instability-induced mixing of ablator material into the hot spot of ignition-scale ICF implosions was measured with x-ray spectroscopy on NIF implosion experiments (p. 145). The experimentally inferred values of hot-spot-mix mass, based on the absolute spectral brightness of the emergent Ge K-shell emission, ranged from 2 to 400 ng. Most implosions were measured to have less than 75 ng of hot-spot mix, consistent with the requirements for ignition.

Measurements of hot-electron generation by the two-plasmon–decay instability (TPD) are reported in an article beginning on p. 151. The OMEGA EP ultraviolet laser beams provide the high energy (9 kJ) necessary to produce overlapped laser intensities of 7×10^{14} W/cm² in large, 1-mm-diam laser spots. These laser conditions produced 2.5-keV coronal electron temperatures with density scale lengths at $n_{cr}/4$ of ~ 400 μ m in CH plasmas. The total number of hot electrons was measured to increase exponentially over nearly four orders of magnitude and the hot-electron temperature increased from 30 keV to 110 keV. These results compare well with a new TPD model designed to provide a physics-based predictive capability for TPD at ignition conditions.

In this volume, we report on an OMEGA experiment carried out by a collaborative team led by MIT-PSFC, LLE, and LLNL that for the first time measured the differential cross section for the elastic neutron–triton (n –³H) and neutron–deuteron (n –²H) scattering at 14.1 MeV using an inertial confinement facility (p. 151). In these experiments, carried out by simultaneously measuring elastically scattered ³H and ²H ions from a deuterium–tritium gas-filled ICF capsule implosion, the differential cross section for the elastic n –³H scattering was obtained with significantly higher accuracy than achieved in previous accelerator experiments. The results compare well with calculations that combine the resonating group method with an *ab initio* no-core model, which demonstrates that recent advances in *ab initio* theory can provide an accurate description of light-ion reactions.

The results of direct-drive, Rayleigh–Taylor (RT) growth experiments conducted in planar cryogenic, liquid deuterium (D₂) targets on the OMEGA laser are reported (p. 157). These are the first RT measurements in deuterium at conditions relevant to ICF using a mass-preimposed initial modulation. The measured modulation optical depths are in agreement with the 2-D hydrodynamic code *DRACO* using flux-limited local thermal transport, providing an important step in the experimental validation of simulations for direct-drive ignition.

2. Theoretical Design and Analysis

A report co-authored by scientists from LLE, Lodestar Research Corp., and the University of California, San Diego, describes the dynamics of hot-electron heating in direct-drive–implosion experiments caused by TPD instability (p. 66). TPD instability was identified as a potential source of target preheat in direct-drive experiments on OMEGA, and a physical model of electron heating has been developed that relies on extended Zakharov simulations to predict the nonlinearly saturated

Langmuir wave spectrum. Because of the relatively low areal density of the targets during the time of TPD instability, hot-electron recirculation and reheating are potentially important effects. These effects were modeled by using a particular form of boundary conditions on the test-particle trajectories. Adoption of these boundary conditions was shown to lead to an increase in the computed hot-electron temperature by a factor of 3.

An article beginning on p. 109 describes how a fully kinetic reduced particle-in-cell method, utilizing novel diagnostics, has been applied to simulations of TPD instability in inhomogeneous plasma for parameters consistent with recent direct-drive experiments. This work is the result of a collaboration among scientists from LLE, Lodestar Research Corp., the University of California, San Diego, and LANL. The nonlinear saturated state of TPD is one of Langmuir turbulence involving the coexistence of the Langmuir cavitation and collapse, the Langmuir decay instability, and ponderomotive density-profile modification. The saturated state is characterized by very spiky electric fields, and Langmuir cavitation occurs preferentially inside density channels produced by the ponderomotive beating of the crossed laser beams. Statistical analyses show that cavitons follow Gaussian statistics. At times exceeding 10 ps, the excited Langmuir turbulence moves away from the quarter-critical surface to lower densities. The heated electron-distribution function is, in all cases, bi-Maxwellian, with hot-electron temperatures in the range of 60 keV to 100 keV. In all cases considered, Langmuir cavitation and collapse provide dissipation by producing suprathermal electrons that stabilize the system in saturation and drive the Langmuir wave spectrum to the small dissipation scales at the Landau cutoff. The net hot-electron energy flux out of the system is a small fraction (+0.5% to 2%) of the input laser power in these simulations.

Lasers, Optical Materials, and Advanced Technology

Improvements to optimize the long-pulse, on-target energy of the OMEGA EP laser are reported (p. 37). The improvements included the procurement of higher-UV-damage-threshold beam-transport optics, improvements in the quality of the beam near field profiles, and the development of simulation tools to provide rapid prediction of the laser performance during shot operations. The beam’s near-field quality was improved by introducing new apodizer designs in two laser stages: (1) angular detuning of the frequency-conversion crystals to reduce UV beam-intensity modulations and (2) the installation of a programmable spatial-light modulator in the laser front end to provide closed-loop correction of the near-field beam amplitude.

The use of photothermal heterodyne imaging (PHI) to evaluate the spatial distribution of absorbers in hafnia nonlayers is reported (p. 25). The metal-oxide layer is the weakest part of the thin-film coating and typically where damage is initiated. Insight into the nature and distribution of damage precursors is valuable to further improve the material's damage resistance. Gold nanoparticles embedded in a silica film were used to determine the system's resolution of ~ 5 -nm particle size and an ~ 0.5 - μm particle separation. PHI images of hafnia films prior to laser irradiation are structureless, pointing to absorber separations much smaller than the spatial resolution of this method. Using PHI data and atomic force microscopy mapping of damage-initiation sites, an upper limit for absorber separation was calculated to be ~ 0.1 μm . By comparing heterodyne signals for different film thicknesses, it was determined that hafnia/silica interfacial absorption is not a major factor in damage initiation, but the main contribution comes from absorption inside the hafnia film.

The large tunable, terahertz electro-optic (EO) response in cadmium manganese telluride (Cd,Mn)Te single crystals is reported (p. 33). This crystal, known as CMT, is a well-studied semiconductor material because of its stable zinc-blend structure for high-Mn concentrations that provides a wide tuning range of the energy band gap. It exhibits a large magneto-optic Faraday effect and has a very high stopping power making it a great potential for x - and γ -ray detection. The measurements demonstrated CMT's exceptionally large EO Pockels effect and showed that the EO sensitivity can be magnified for a particular probe wavelength using band-gap engineering.

In FY11 we demonstrated a highly efficient pulsed-diode-pumped, room-temperature Yb:YAG ceramic laser with a slope efficiency of 78% and an optical-to-optical efficiency of 51% (p. 168). This is the highest slope efficiency for a room-temperature Yb:YAG ceramic laser reported to date. A regenerative amplifier with +15-mJ output energy and fourth-order super-Gaussian beam profile based on this laser has been demonstrated.

The amplification of nanosecond, 1053-nm optical pulses from 15 pJ to 240 nJ by a Yb-doped all-fiber regenerative amplifier (AFRA) has achieved an overall gain of 42 dB (p. 85). This is believed to be the highest AFRA output-pulse energy ever reported. The AFRA is an attractive candidate as a chirped-pulse-amplification (CPA) seed source because of its high output-pulse energy in comparison to seed pulses commonly used in existing CPA systems.

Our work on the suppression of parasitic processes in non-collinear optical parametric amplifiers (NOPA) for walk-off and non-walk-off compensating configurations is reviewed beginning on p. 90. Modeling shows that the second-harmonic generation of the signal can reduce the NOPA output energy by 10%. Quantitative measurements on an ultra-broadband, few-cycle NOPA support these findings in the walk-off compensating case, and the effect is reduced by an order of magnitude in the non-walk-off compensating case. A detailed phase-matching analysis for the most common nonlinear crystals is presented as a guide for designing NOPA system.

Stress compensation in hafnia/silica optical coatings by the inclusion of alumina layers is discussed (p. 100). Hafnia/silica films deposited using electron-beam evaporation tend to exhibit high tensile stresses when used in vacuum or low-relative-humidity environments, resulting in film cracking or crazing. The inclusion of alumina layers within the film stack leads to a compressive overall film stress negating this failure mode in the dry-use environments. A film-stress model incorporating the stress of the individual materials and material thicknesses along with the interfacial film effects was developed to calculate the overall film stress when designing multilayer coatings using alumina since this film stress (compressive) was measured to be very different than the alumina monolayer film stress (tensile). While the slow diffusion of water in alumina films presents some manufacturing and operational challenges, a large-aperture hafnia/silica/alumina polarizer coating was fabricated and installed in the OMEGA EP short-pulse cavity location, eliminating the crazing issue observed with the previous films.

A closed-loop, high-resolution beam-shaping system based on a liquid-crystal-on-silicon (LCOS) spatial-light modulator (SLM) in a multiterawatt laser system and in the OMEGA EP long-pulse front end was demonstrated (p. 113). The closed-loop algorithm is based on the linearity of image transformation between the control device and the measured image, where miscalibration of the linear parameters or blurring of the image affects the stability of the algorithm. One of the main causes of blurring is ascribed to the presence of tilted plates and wedges in the imaging system. These are common elements in complex laser systems. Such effects can be either compensated for or avoided by careful design. The procedure and results of damage-threshold measurement for LCOS-SLM are presented to help determine a safe operation regime for this device in high-power laser systems.

The impact of high-frequency spectral phase modulation on the temporal contrast of ultrafast pulses was investigated (p. 117). Expressions were derived for the low-intensity pedestal produced by optical component surface roughness within pulse stretchers and compressors. Phase noise, added across the near field of a spectrally dispersed beam, produces space-time coupling in the far field or focal plane. The pedestal is swept across an area in the focal plane many times the size of the diffraction-limited spot. Simulations were performed for generic stretchers and compressors that showed fundamentally different forms of temporal contrast degradation at focus.

New wavefront reconstruction algorithms for high-spatial-resolution applications were developed (p. 130). Analyzing wavefront reconstructors in the frequency domain lends new insight into ways to improve frequency response and to understand noise propagation. The mathematical tools required to analyze the frequency domain are first developed for discrete band-limited signals. These tools are shown to improve frequency response in either spatial- or frequency-domain reconstruction algorithms. A new spatial-domain iterative reconstruction algorithm based on the Simpson rule is presented. The previously developed rectangular-geometry band-limited algorithm in frequency domain is adapted to hexagonal geometry, which adds flexibility when applying frequency-domain algorithms. Finally, a generalized analytic error propagation formula is found for different types of reconstructors and compared with numerical simulations.

Femtosecond pump-probe spectroscopy studies of time-resolved optical reflectivity of all-oxide, $\text{YBa}_2\text{Cu}_3\text{O}_7/\text{La}_{0.7}\text{Sr}_{0.3}\text{MnO}_3$ superconductor/ferromagnet nano-bilayers are presented (p. 141). The temperature dependence of the nonequilibrium carrier dynamics is investigated down to 4 K. The photoresponse of bilayers has two characteristic relaxation times that are shorter than that of the $\text{YBa}_2\text{Cu}_3\text{O}_7$ film, and their superconducting properties are revealed in sharp peaks near the superconducting transition. The bilayer dynamics cannot be interpreted as an incoherent sum of contributions from the two layers; instead, the results point to an active role of an interface layer, where the electronic charge transfer from $\text{La}_{0.7}\text{Sr}_{0.3}\text{MnO}_3$ to $\text{YBa}_2\text{Cu}_3\text{O}_7$ takes place.

National Laser Users' Facility and External Users' Programs

Under the facility governance plan that was implemented in FY08 to formalize the scheduling of the Omega Laser Facility as a National Nuclear Security Agency (NNSA) facility,

Omega Facility shots are allocated by campaign. The majority (65.1%) of the FY11 target shots were allocated to the NIC conducted by integrated teams from the national laboratories and LLE and to the high-energy-density campaigns (HED) conducted by teams led by scientists from the national laboratories.

In FY11 29% of the facility shots were allocated to basic science experiments. Nearly half of these were conducted for university basic science under the NLUF Program and the remaining shots were allotted to the Laboratory Basic Science (LBS) Program comprising peer-reviewed basic science experiments conducted by the national laboratories and LLE/Fusion Science Center (FSC).

The Omega Laser Facility is also being used for several campaigns by teams from the Commissariat à l'Énergie Atomique et aux Énergies Alternatives (CEA) of France and Atomic Weapons Establishment (AWE) of the United Kingdom. These programs are conducted on the facility on the basis of special agreements put in place by the DOE/NNSA and the participating institutions.

The facility users during this year included 11 collaborative teams participating in the NLUF Program; 15 teams led by LLNL and LLE scientists participating in the LBS Program; many collaborative teams from the national laboratories conducting experiments for the NIC; investigators from LLNL and LANL conducting experiments for HED physics programs; scientists and engineers from the CEA and AWE; and scientists, engineers, and students from the Center for Radiative Shock Hydrodynamics of the University of Michigan.

1. NLUF Program

FY11 was the first of a two-year period of performance for the NLUF projects approved for the FY11–FY12 funding and OMEGA shots. Eleven NLUF projects were allotted Omega Facility shot time and conducted a total of 260 target shots on the facility. Brief summaries of this work may be found beginning on p. 172. Table I lists the approved FY11 and FY12 NLUF proposals.

2. Laboratory Basic Science Programs

In FY11, LLE issued a solicitation for LBS proposals to be conducted in FY12. A record 41 proposals were submitted. An independent review committee reviewed and rank-ordered the proposals; the top-ranked 15 proposals were allotted 28 shot days on the Omega Laser Facility in FY12. Table II lists the successful FY12 LBS proposals.

Table I: Approved FY11 and FY12 NLUF proposals.

Principal Investigator	Institution	Project Title
F. N. Beg	University of California, Berkeley	Systematic Study of Fast-Electron Transport in Imploded Plasmas
R. P. Drake	University of Michigan	Experimental Astrophysics on the OMEGA Laser
T. Duffy	Princeton University	Ramp Compression for Studying Equations of State, Phase Transitions, and Kinetics on OMEGA
R. Falcone	University of California, Berkeley	Detailed <i>In-Situ</i> Diagnostics of High-Z Shocks
P. Hartigan	Rice University	Clumpy Environments and Interacting Shock Waves: Realistic Laboratory Analogs of Astrophysical Flows
R. Jeanloz	University of California, Berkeley	Recreating Planetary Core Conditions on OMEGA
K. Krushelnick	University of Michigan	Intense Laser Interactions with Low-Density Plasma Using OMEGA EP
R. Mancini	University of Nevada, Reno	Investigation of Hydrodynamic Stability and Shock Dynamics in OMEGA Direct-Drive Implosions Using Spectrally Resolved Imaging
R. D. Petrasso	Massachusetts Institute of Technology	Charged-Particle Probing of Inertial Confinement Fusion Implosions and High-Energy-Density Plasmas
A. Spitkovsky	Princeton University	Collisionless Shocks in Laboratory High-Energy-Density Plasmas
R. Stephens	General Atomics	Investigation of Laser to Electron Energy Coupling Dependence on Laser Pulse Duration and Material Composition

FY11 LBS Experiments

Fifteen LBS projects were allotted Omega Facility shot time and conducted a total of 303 target shots on the facility in FY11. Brief summaries of the FY11 LBS work may be found beginning on p. 184 of the report.

3. FY11 LLNL Omega Facility Programs

In FY11, LLNL conducted several campaigns on the OMEGA and OMEGA EP Laser Systems, as well as campaigns that used the OMEGA and OMEGA EP beams jointly. Overall, LLNL led 301 target shots involving OMEGA and 81 target shots involving OMEGA EP (not including LLNL-led shots under the LBS Program). Approximately 35% of the shots (126 OMEGA shots, 10 OMEGA EP shots) supported the NIC. The remainder were dedicated to experiments for HED physics (168 OMEGA shots, 72 OMEGA EP shots). Objectives of the LLNL-led NIC campaigns at OMEGA included the following:

- *Characterization of long-pulse, high-resolution, laser-produced backlighters*
- *4 ω Thomson scattering*
- *Neutron-induced backgrounds for ARIANE*

- *Thermal-conductivity measurements at a heated CH/Be interface by refraction-enhanced x-ray radiography*
- *18-keV x-ray Thomson scattering of shock-compressed beryllium and aluminum*
- *High-resolution measurements of velocity nonuniformities created by microscopic perturbations in NIF ablator materials*
- *X-ray Thomson scattering of shock-compressed beryllium on OMEGA EP*
- *Pb Hohlraums*
- *Surrogate mix targets with dual backlighting*

The LLNL-led HED campaigns covered four main areas of research:

1. *Material dynamics and equation of state*
 - a. *Kr Hugoniot measurements to 730 GPa*
 - b. *Ramped compression of different materials*
 - c. *Tin melt*
 - d. *Powder x-ray-diffraction measurements of solid Fe and Ta to 570 GPa*
 - e. *Hohlraum diffraction*

Table II: Approved FY12 LBS proposals.

Principal Investigator	Affiliation	Project Title
P. M. Celliers	LLNL	Measurement of the Viscosity of Shock-Compressed Fluids: Studies of Water and Silica
H. Chen	LLNL	Exploring Pair Plasma and Its Applications Using OMEGA EP and OMEGA Lasers
G. Fiksel	LLE	Magnetic Field Compression in Spherical Implosions on OMEGA
G. Fiksel	LLE	Magnetic Reconnection in High Energy Density Plasmas in the Presence of an External Magnetic Field
O. A. Hurricane	LLNL	Measurements of Linear, Nonlinear, and Turbulent-Mixing Regimes in Kelvin–Helmholtz Instability in the Subsonic Regime
A. L. Kritcher	LLNL	Nuclear-Atomic-Plasma Interactions in Laser-Produced Plasmas
B. R. Maddox	LLNL	Dislocations and Twinning at High Pressure and Strain Rate on BCC Metals
D. P. McNabb	LLNL	Thermonuclear Reactions in Stellar Plasmas and High Resolution Measurements of Three-Body Breakup in Isobaric Analogue Reactions
H.-S. Park	LLNL	Astrophysical Collisionless Shock Generation by Laser-Driven Laboratory Experiments on OMEGA and OMEGA EP
P. K. Patel	LLNL	Compton Radiography of Cone-in-Shell Implosions for Fast Ignition
S. P. Regan	LLE	Probing Shocked Liquid H, H/He, CH ₄ , N ₂ , and NH ₃ with Inelastic X-Ray Scattering and Shock Velocity Measurements: Toward the Equation-of-State of Planetary Interiors
J. R. Rygg	LLNL	Extreme Chemistry: Molecular Fluids at Mbar Pressure
V. A. Smalyuk	LLNL	Measurements of Ablative Richtmyer–Meshkov Instability in Nonlinear Regime
C. Stoeckl	LLE	Spectroscopy of Neutrons Generated Through Nuclear Reactions with Light Ions in Short-Pulse Laser Interaction Experiments
W. Theobald	LLE	Integrated Fast-Ignition Experiments

- f. Equation of state for foams
g. Gigabar equation of state
h. Double pulse
i. Dynamic and lattice diffraction
j. Tantalum Rayleigh–Taylor experiments
k. CEDrive-11A/ICEHohl-11A
l. Strength diffraction
2. High-temperature plasma opacity
a. High-temperature plasma opacity experiments on OMEGA and OMEGA EP
3. Hydrodynamics
a. Short-pulse, UV backlighting development for the NIF
b. Backlighting experiments on OMEGA
4. X-ray source development and application
a. Iron K-shell x-ray source development
b. Solar-cell electrostatic discharge
4. FY11 LANL Omega Facility Programs
In FY11, LANL executed 223 total shots: 195 on the OMEGA Laser System and 28 on the OMEGA EP Laser System. LANL experiments contributed to the NIC in the following ways:

- Measured the x-ray ablative Richtmyer–Meshkov growth of isolated defects on plastic ablators
- Studied branching ratios in DT-fusion plasmas
- Measured the shape of the DT-fusion gamma-ray spectrum
- Continued neutron-imaging development for the NIF

HED campaigns included

- Study of shear and reshock-driven turbulent mixing
- Backlit defect implosion experiments to study the effect of trench defect
- Measuring the effect of capsule asymmetries on neutron yield and ion temperature
- Platform development for dense plasmas and warm, dense matter's equation of state
- Measurement of a supersonic radiation wave
- Energetic ion generation for dynamic defect studies

The LANL-led experiments are summarized beginning on p. 203.

5. FY11 AWE Omega Facility Experiments

In FY11, AWE led six shot days on the OMEGA and OMEGA EP lasers. This work encompassed the development of MeV x-ray sources (one day in jointly funded collaboration with CEA) and 22- to 52-keV x-ray backlighters (three days in collaboration with LLNL, of which one was LLNL funded), a Laue x-ray diffraction asymmetrically driven hohlraums (one day). The AWE work is reviewed beginning on p. 238.

6. FY11 CEA Omega Facility Experiments

CEA-led teams conducted 56 target shots on OMEGA during FY11. The experiments included vulnerability diagnostics development, neutron-imaging diagnostics development, implosion dynamics, and rugby hohlraum characterization. Summaries of some of the CEA work may be found beginning on p. 242.

FY11 Facility Report

During FY11, the Omega Laser Facility conducted 1348 target shots on OMEGA and 457 target shots on OMEGA EP for a total of 1805 target shots (see Tables 128.V and 128.VI). OMEGA averaged 10.3 target shots per operating day with availability and experimental effectiveness averages for FY11 of 93.3% and 96.1%, respectively. OMEGA EP was operated extensively in FY11 for a variety of internal and external users. Of the 457 target shots, 401 were shot in the OMEGA EP target chamber and 56 were joint shots in the OMEGA target chamber. OMEGA EP averaged 5.5 target shots per operating day with availability and experimental effectiveness averages for FY11 of 85.6% and 95.2%, respectively.

OMEGA EP Improved Energy Capabilities

Short-pulse (IR) and long-pulse (UV) energy on target has been increased. The UV energy was increased after the acquisition of improved optics. Lithographic-quality fused-silica substrates were finished using LLNL-developed protocols, LLNL-supported production controls, and the latest LLNL post-processing techniques for enhanced damage threshold (Acid Mitigation Process II). The extended UV energy operational envelope was made available after completion of a damage-testing laser shot campaign with the previous optics. UV energy on target was increased from 2.3 kJ per beam to 6.6 kJ at 10 ns, exceeding the 6.5-kJ system design goal. Short-pulse IR energy was increased following the installation of improved damage-threshold gratings in the grating-compressor vessel. Additionally, a comprehensive short-pulse small-beam damage-testing program was conducted on multilayer dielectric coatings. The combination of new gratings and coating performance analysis resulted in an increase to the IR energy

operational envelope for the short-pulse laser beams. IR energy on target for beamline 2 at 10 ps was increased from 1.0 kJ to 1.6 kJ, 60% of the 2.6-kJ design goal. Up-to-date limits to the energy on target are now summarized and available to all users through the Operations Website.

OMEGA EP 100-ps UV Temporal Pulse Shapes

At the request of users, the shortest UV pulse durations have been extended from the previous limit of 1 ns to 100 ps. Users are now able to request pulse shapes between 100 ps and 10 ns. The 100-ps pulse shapes have been utilized to produce short-duration x-ray pulses useful for a variety of target-physics campaigns, including backlighter platform development for the NIF. With this new functionality, the temporal co-timing of all four beamlines has been calibrated to <50 ps.

OMEGA EP Short-Pulse Focal-Spot Improvement

Using a static wavefront corrector, wavefront correction has been developed for OMEGA EP to correct high-order residual wavefront that is beyond the spatial resolution of the existing adaptive optics. A small-aperture phase corrector, manufactured by QED Technologies, using the magnetorheological finishing (MRF) process, has been added to the injection system to precompensate for repeatable high-order wavefront errors that arise in the beamlines. Following successful proof-of-principle demonstrations, these optics were implemented on both of the OMEGA EP short-pulse beamlines, providing an $\sim 2\times$ reduction in focal-spot extent at the output of the beamline during active wavefront correction. On amplified shots, target-plane focal spots have met the specification of 80% of the energy in less than a 20- μm radius ($R_{80} < 20 \mu\text{m}$). An $\sim 25\%$ improvement is realized on the first shots, although thermal distortion of the amplifier disks has led to focal-spot degradation after multiple shots have been taken in a day. Future revisions of the phase-corrector design will partially compensate for this effect. This work follows on the successful implementation of advanced phase-retrieval techniques developed in FY10 that allow for accurate characterization of the focal spot.

OMEGA EP Infrared Alignment Table and Beamline Injection Table Enhancement

The daily operation of the OMEGA EP laser has been improved with enhancements to the OMEGA EP infrared alignment table (IRAT). This work improved the imaging accuracy from the laser source apodizer plane to the beamline input image plane. This improvement reduces modulation on critical optics in the OMEGA EP Laser System. Additional diagnostics were added to improve the injection energy mea-

surements and centering of beams. All of these improvements have increased system operability.

Improved OMEGA UV On-Target Predictions

Target experiments have been shown to slowly degrade the UV transmission, primarily of the final debris shield, causing a decrease in on-target energy relative to the diagnostic prediction. During FY11, the study of UV transmission has resulted in a better understanding of the loss mechanisms. The study found that the losses are dependent on target type, target composition, target quantity, number of beams used for each shot, and beam location in the tank. The results of this study and daily measurements of transmission on representative UV optics have been incorporated into a new on-target energy prediction that is reported to the principal investigator. The system's average loss is predicted within ~1% accuracy and the rms error is <2%.

Experimental Diagnostics

Diagnostic capabilities continue to evolve with the commissioning of 24 new diagnostic instruments on OMEGA and 9 new diagnostic instruments on OMEGA EP. These include a new spherical crystal x-ray imager, upgraded hard x-ray diode arrays, *B*-dot magnetic-field probes, an electron spectrometer, and a new test platform for chemical vapor deposition-diamond neutron detectors. Many of these new instruments were developed by or in cooperation with other laboratories (including LLNL, LANL, CEA, Oxford University, Osaka University, and SNL). Improvements to the online information systems available to our scientific users include availability of specification sheets and operating procedures for diagnostic instruments, as well as target chamber port assignment tables. Other facility improvements include commissioning of an additional image plate scanner and electromagnetic interference hardening of the target positioners on both OMEGA and OMEGA EP.

A number of safety improvements were implemented in the experimental area. These include the commissioning of filtered air flow hoods for servicing equipment that contains or is contaminated with beryllium, higher-resolution beryllium-monitoring capability, and review and certification of heavy equipment lift procedures. Additionally, tracking beryllium survey data and radioactive material inventory has improved visibility to the operators and other stakeholders.

Education

As the only major university participant in the National ICF Program, education continues to be an important mission for

the Laboratory. Laboratory education programs span the range of high school (p. 166) to graduate education.

1. High School Student Program

During the summer of 2011, 16 students from Rochester-area high schools participated in the Laboratory for Laser Energetics' Summer High School Research Program. The goal of this program is to excite a group of high school students about careers in the areas of science and technology by exposing them to research in a state-of-the-art environment. Too often, students are exposed to "research" only through classroom laboratories, which have prescribed procedures and predictable results. In LLE's summer program, the students experience many of the trials, tribulations, and rewards of scientific research. By participating in research in a real environment, the students often become more excited about careers in science and technology. In addition, LLE gains from the contributions of the many highly talented students who are attracted to the program.

The students spent most of their time working on their individual research projects with members of LLE's technical staff. The projects were related to current research activities at LLE and covered a broad range of areas of interest including experimental systems and diagnostic development, computational modeling of implosion physics, chemistry, materials science, laser system development and diagnostics, and database development (see Table III).

The program culminated on 24 August with the "High School Student Summer Research Symposium," at which the 16 students presented the results of their research to an audience including parents, teachers, and LLE staff. The students' written reports will be made available on the LLE Website.

Two hundred and eighty-one high school students have now participated in the program since it began in 1989. Thirty of the participating students have gone on to gain semi-finalist status in the Intel Science Talent Search national competition and four of the students have gained finalist status at this competition.

At the symposium LLE presented its 15th annual William D. Ryan Inspirational Teacher Award to Mrs. Deborah Reynolds, chemistry teacher at Brighton High School. This award is presented to a teacher who motivated one of the participants in LLE's Summer High School Research Program to study science, mathematics, or technology and includes a \$1000 cash prize.

Table III: High School Students and Projects—Summer 2011.

Name	High School	Supervisor	Project Title
Brandon Avila	Allendale Columbia	R. W. Kidder	Optimizing LLE Information Operations Through Natural Language Processing
Andrew Boyce	McQuaid	W. T. Shmayda	Water-Stimulated Tritium Release from Metals
Matthew DeCross	Pittsford Sutherland	L. D. Lund	Automation of Vibration Measurement and Characterization of Cryogenic Deuterium–Tritium Target Motion
Avery Gnolek	Webster Thomas	K. L. Marshall	Photoaligned Liquid Crystal Wave Plate
Dana Gretton	Honeoye Falls Lima	R. G. Peck, E. Druszkiewicz	Design of a New Master-Timing Generator
Sean Hamlin	Fairport	R. Epstein	X-Ray Fluorescence as an Imploded-Shell Diagnostic
Felix Jin	Brighton	G. Fiksel	Characterization of Magnetic Coils for the Magneto-inertial Fusion Energy Delivery System
Jefferson Lee	Canandaigua Academy	W. T. Shmayda	Modeling Tritium Removal from Metal Surfaces
Kevin Mizes	Pittsford Sutherland	R. Boni, D. H. Froula, S. Ivancic	Two Techniques for Array Generation with Applications in Grid-Imaging Refractometry
Patricia Olson	Brighton	R. S. Craxton	Optimization of Beam Configurations for Shock-Ignition Experiments on the NIF and OMEGA
Sean Reid	Fairport	M. Burke, R. Boni, S. D. Jacobs	Surface Grinding and Polishing to Remove Etch-Induced Noise Pitting in CR-39 Samples
Madeline Rutan	Penfield	K. L. Marshall	Abrasion-Resistant Antireflection Sol-Gel Coatings
Michael Statt	School of the Arts	K. L. Marshall, C. Dorrer	Generation of Radially Polarized Beams Using Optically Patterned Liquid Crystals
Troy Thomas	Webster Thomas	B. E. Kruschwitz	Optical Time-Domain Reflectometry for the Transport Spatial Filter on the OMEGA Extended Performance Laser
Harrison Xiao	Pittsford Sutherland	P. A. Jaanimagi	Dynamic Defocusing in Streak Tubes
Andrew Zhao	Webster Thomas	R. Boni, D. H. Froula, S. Ivancic	Image Processing and Analysis of 4ω Grid-Image Refractometry Data

Teachers are nominated by alumni of the summer program. Mrs. Reynolds was nominated by Nicholas Andrew Chun and Connie Chiang, participants in the 2010 Summer Program.

2. Undergraduate Student Programs

Approximately 41 undergraduate students participated in work or research projects at LLE this past year. Student projects include operational maintenance of the OMEGA Laser Facility; work in laser development, materials, and optical-thin-film-coating laboratories; computer programming; image processing; and diagnostics development. This is a unique opportunity for students, many of whom will go on to pursue a higher degree in the area in which they gained experience at the Laboratory.

3. Graduate Student Programs

Graduate students are using the OMEGA Facility as well as other LLE facilities for fusion and HED physics research and technology development activities. These students are making significant contributions to LLE's research program. Twenty-five faculty from the five University academic departments collaborate with LLE scientists and engineers. Presently, 77 graduate students are involved in research projects at LLE, and LLE directly sponsors 38 students pursuing Ph.D. degrees via the NNSA-supported Frank Horton Fellowship Program in Laser Energetics. Their research includes theoretical and experimental plasma physics, HED physics, x-ray and atomic physics, nuclear fusion, ultrafast optoelectronics,

high-power-laser development and applications, nonlinear optics, optical materials and optical fabrication technology, and target fabrication.

In addition, LLE directly funds research programs within the MIT Plasma Science and Fusion Center, the State Univer-

sity of New York (SUNY) at Geneseo, and the University of Wisconsin. These programs involve a total of approximately 6 graduate students, 25 to 30 undergraduate students, and 10 faculty members.

Robert L. McCrory

Director, Laboratory for Laser Energetics
Vice President, University of Rochester

The Velocity and Timing of Multiple Spherically Converging Shock Waves in Liquid Deuterium

Inertial confinement fusion (ICF) target designs use a sequence of shocks to compress the shell and fuel assembly before they implode.¹ The fuel entropy can be controlled by optimizing the strength and timing of these shocks, thereby minimizing the required driver energy. The goal is to maintain the internal pressure of the fuel to ~ 1 to 2 times its Fermi-degenerate pressure. To achieve these optimal conditions, the four shocks must merge in a precise sequence at the inner surface of the fuel layer.^{2,3} The National Ignition Campaign⁴ for ICF ignition at the National Ignition Facility (NIF)⁵ includes tuning experiments to verify shock timing as a method to set the laser to optimal drive conditions for hohlraum-driven ignition targets.³ Similarly, the fusion program at LLE requires validation of the hydrodynamic codes used in direct-drive ICF implosions. In this article, we report on results of direct-drive experiments that mimic and exceed the conditions for the first three shocks in an ignition target. These experiments develop a shock-timing technique for ignition targets and validate simulations of direct-drive ICF targets.⁶ The development was successful and this technique was applied to full-scale experiments to tune hohlraum-driven ignition targets on the NIF.⁷ To model these experiments, the simulations incorporated a nonlocal model⁶ to treat heat conduction in the coronal plasma. These simulations model shock velocity and timing quite well, providing confidence in the hydrodynamic codes used to design direct-drive ICF targets for OMEGA and the NIF.

In direct-drive ICF, the initial shocks are produced by short (~ 100 -ps) laser pulses preceding the main pulse that drives the implosion.⁸ Short individual pulses are desirable for direct-drive ICF because they are impulsive on hydrodynamic time scales. As a result, only the energy contained in the pulse matters, not the temporal shape. The simple temporal Gaussian pulses that high-power lasers readily produce are ideal for this purpose. Moreover, individual laser pulses provide discrete drive events that can be easily tuned to optimize shock-wave timing. The strength of those shocks depends on the energy in the pulses and on the details of the laser-target-coupling mechanisms. The strength (velocity) of those shocks is a very good measure of the efficiency of that coupling and, therefore,

a sound metric for validating the hydrodynamic codes used to design ICF targets.

These experiments measured the velocity and timing of multiple converging shock waves *inside* spherical targets filled with liquid (cryogenic) deuterium. The drive laser produced a sequence of up to four shocks, whose strength and timing were designed so that later stronger shocks overtake earlier weaker ones to produce multiply shocked deuterium. These shocks ultimately coalesce about $200\ \mu\text{m}$ into the deuterium, forming a single strong shock that converges toward the center of the targets. The shock velocities and the times of these mergers are measured with high precision using time-resolved velocity interferometry⁹ and streaked optical pyrometry.¹⁰ Shock velocity and timing are measured to better than the $\sim 1\%$ and ± 50 -ps precision required for ignition targets. This technique was used on full-scale NIF experiments to tune hohlraum-driven ignition targets.

The OMEGA results are best simulated when the hydrodynamic code uses a nonlocal model⁶ to transport the absorbed laser energy from the coronal plasma to the ablation surface. The simulations replicate the measured shock velocities and shock merger times with high fidelity.

These experiments are the first to time multiple, spherically converging shock waves in liquid deuterium. They produced the highest-reported shock velocities in liquid deuterium and the first observation of an increase in shock strength (velocity) caused by spherical convergence.

These experiments were performed on OMEGA—a 60-beam, 351-nm laser designed to directly drive spherical-target implosions with high-irradiation uniformity.¹¹ The velocity interferometry system for any reflector (VISAR)⁹ detects the Doppler shift of an optical (532-nm) probe beam that reflects off the shock front. To provide diagnostic access to the shock waves, spherical targets were fitted with a diagnostic cone similar to that used in the fast-ignition concept.¹² The targets are described in Ref. 7 and are shown in Fig. 125.1.

The spherical shell and cone were filled with liquid deuterium; VISAR observed the shocks on the inside of the shell through an aperture in the end of the cone.

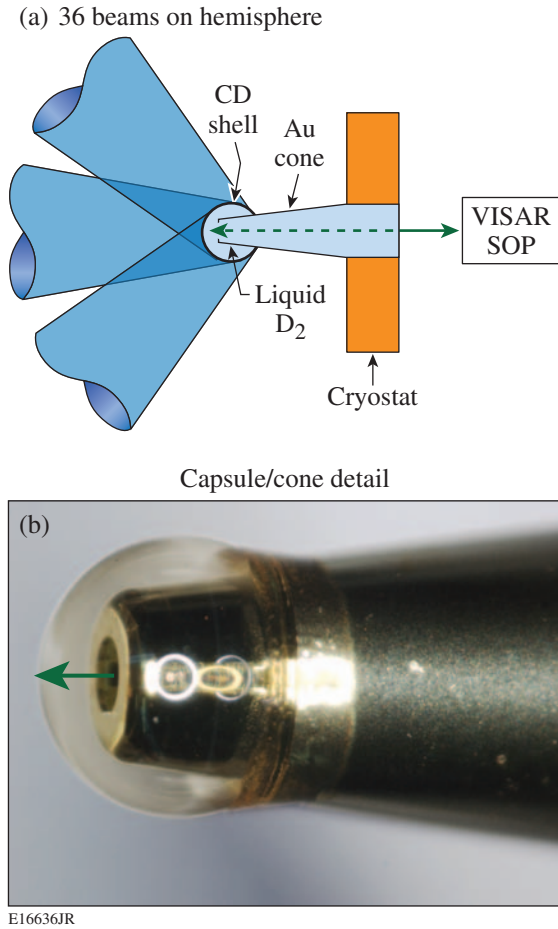


Figure 125.1
 (a) Schematic of target and beam irradiation showing the 900- μm -diam CD sphere with a re-entrant cone [Fig. 125.1(b)], which is irradiated with 36 OMEGA beams. The target and cone are filled with cryogenic liquid deuterium.

The sphere was irradiated by 36 OMEGA beams on its hemisphere opposite the line of sight of VISAR. The beams were fitted with the same SG4-distributed phase plates¹³ used for the 60-beam ICF implosion experiments. Two-dimensional simulations of the irradiation uniformity indicate that this configuration produces a uniform intensity distribution pattern that replicates the 60-beam irradiation uniformity in a region of $\sim\pm 20^\circ$ about the VISAR axis. (VISAR has an $f/3$ collection lens.) These experiments, therefore, produce an accurate surrogate for the shock-transit portion of a spherically symmetric ICF implosion. The liquid deuterium is surrogate for the deuterium–tritium ice layer in an ICF target; it provides an extended, uniform medium for the shocks to propagate. In

addition to VISAR, a streaked optical pyrometer (SOP)¹⁰ was used to observe the optical self-emission from the shocks in the deuterium.

Figure 125.2(a) shows VISAR data for a three-shock experiment (shot 59533) driven by three 100-ps laser pulses (at 0, 1, and 2 ns), which are depicted in the graph overlay in Fig. 125.2(a). The VISAR record is a 1-D image (vertical axis) of the target that is streaked in time (horizontal axis). Imposed on that image is a series of fringes whose vertical position (fringe phase) is proportional to the shock velocity. The image in Fig. 125.2(a) is a view of the shocks in the liquid deuterium

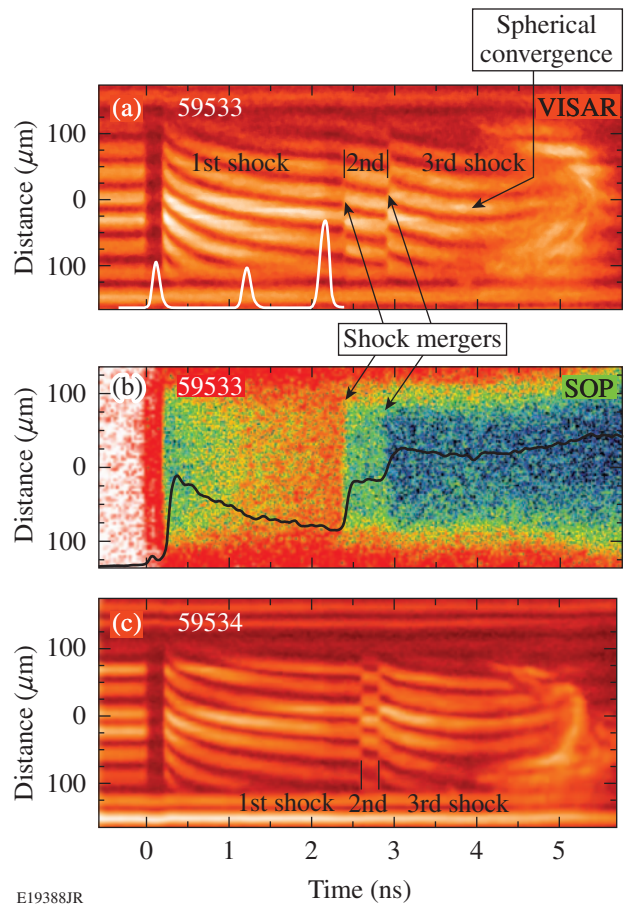


Figure 125.2
 (a) VISAR data record (space versus time) with fringes that represent the velocity of the shocks produced by the laser pulse shown in the figure. The three shocks are observed as well as the jump in fringe position that occurs when the second and third shocks merge at 2.4 and 2.9 ns, respectively. (b) Streaked optical pyrometer (SOP) data showing the self-emission intensity (lineout in figure) follows the shock velocity and shock mergers, providing corroboration of shock timing. (c) VISAR data for shot with lower second pulse and higher third pulse; these delay the first merger and advance the second, illustrating the technique to time shock in a tight sequence.

contained in the shell as observed through the aperture in the re-entrant cone. The experiment was arranged so these shock waves spherically converged along the VISAR axis. VISAR was able to track this convergence until the shock impacted the front of the cone, which was $200\ \mu\text{m}$ from the inside of the sphere.

Before $T = 0$, the fringes in Fig. 125.2(a) are horizontal because there was no shock or movement in the target. At $T = 0$ the signal disappears because the VISAR probe was absorbed by the $10\text{-}\mu\text{m}$ CD shell, which was photoionized by x rays from the laser-produced plasma. After the shock transited the CD and reached the deuterium (which remains transparent), the VISAR signal returns and the fringes abruptly shift in response to the shock velocity in the deuterium. At that time, the shock produced by the short pulse is unsupported and decelerating; the resulting VISAR fringes, therefore, exhibit curvature in time.

At $2.4\ \text{ns}$, the shock produced by the second laser pulse (at $\sim 1\ \text{ns}$) overtakes the first shock. [VISAR did not detect the second shock until it overtook the first because the first shock was reflective (and opaque).] At that point, the coalesced shock (first and second shocks) was stronger and had a higher velocity; VISAR detected this sudden increase in velocity as a jump in fringe position. This is a shock-timing measurement. Since this shock was also unsupported, it decelerated as it traveled through the deuterium and the fringes are seen to slope downward. (The decay rate of this second shock is different than that of the first because the rarefaction wave that produces it now encounters double-shocked deuterium.) At $2.9\ \text{ns}$, the shock from the third pulse (at $2\ \text{ns}$) overtakes that coalesced shock and another jump in velocity occurs. This final shock is also unsupported and begins to decay, producing a downward motion of the fringes in time. At about $4\ \text{ns}$, the fringes curve upward, indicating acceleration. This increase in velocity is a result of spherical convergence. As this final shock (three coalesced shocks) spherically converges, its specific volume decreases and the shock strength increases, producing higher velocities. Lastly, at $\sim 5\ \text{ns}$, the shock impinges on the face of the cone, producing a disturbance that propagates into the cone aperture and the VISAR line of sight. This produced the brighter signal at $5\ \text{ns}$ that moves toward the center of the image as it fills the aperture at $\sim 5.5\ \text{ns}$.

Figure 125.2(b) shows the SOP data acquired simultaneously with the VISAR data in Fig. 125.2(a). This is a color-scaled image (vertical axis) of the self-emission intensity streaked in time (horizontal axis). The solid black line through the image is a plot of the intensity (horizontal lineout) that represents the

temporal profile of shock brightness (temperature), which is proportional to velocity. Note that in response to the various shocks, the SOP intensity decays and jumps in a fashion similar to the VISAR data. SOP provides an independent measure of shock strength and timing.

Figure 125.2(c) shows a VISAR image of a similar experiment (shot 59534) with a slightly modified drive pulse. The second shock was a bit weaker and the third stronger. Compared to Fig. 125.2(a), the first merger in these data occurs later (at $2.6\ \text{ns}$) and the second earlier (at $2.8\ \text{ns}$); this demonstrates a technique to produce a tight sequence of shock arrivals for an ICF target design.

On the NIF, shocks must merge in a tight sequence with a precision of $\pm 50\ \text{ps}$. In the VISAR data, the shock mergers cause a fringe jump that occurs over, at most, two of the 10.6-ps pixels (i.e., $\sim 22\ \text{ps}$). Calibration techniques and the temporal optical fiducials on these data allow one to calibrate the streak cameras to better than 1% precision. Together, they provide the necessary precision to time shock waves on OMEGA and the NIF to the $\pm 50\ \text{ps}$ required for ignition targets.

For direct-drive ICF target designs, radiation–hydrodynamic codes have long used a heuristic *flux-limiter* model to simulate the reduced flux of energy from the corona, where laser energy is deposited, to the ablation surface where pressure is applied to the target. To simulate many experimental results, the heat flux in some regions had to be limited to $\sim 6\%$ of that predicted by the Spitzer–Härm free-streaming limit. Recent direct-drive experiments with laser intensities $\geq 3 \times 10^{14}\ \text{W/cm}^2$ were not well modeled using that flux limiter.^{14,15} We find this is also true for the shock-velocity measurements.

Figure 125.3 shows the velocity profiles measured by VISAR (solid) recorded from a two-shock experiment where the two drive pulses had irradiation intensities of $3 \times 10^{14}\ \text{W/cm}^2$ on a CD sphere filled with deuterium. The dotted curve in Fig. 125.3 shows the shock-velocity profile predicted by LILAC¹⁶ using the flux-limiter model with $f = 0.06$. This flux-limiter value was previously constrained by simulations of various experimental observables. Note in Fig. 125.3 that it underestimates the strength of the first shock. This type of disagreement was also true for recent absorption, acceleration, and scattered-light measurements on OMEGA.¹⁷ The dashed curve in Fig. 125.3 shows the velocities predicted when a nonlocal transport model is used.⁶ This model better simulates the shock velocity produced by the first pulse and the merger time of the two shocks. Early in time, when the first pulse interacts with the solid target,

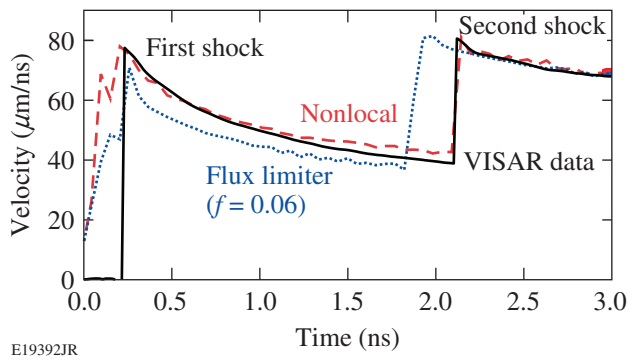


Figure 125.3

The shock-velocity profile (solid) for a two-shock experiment. The profile predicted by *LILAC* using the flux-limiter model with $f=0.06$ (dotted) and using a nonlocal transport model (dashed). The latter better simulates the experiments, particularly the initial interaction with the target and the first shock.

the density scale is very short near the critical density, where the majority of laser light is absorbed. In the flux-limiter model, the classical Spitzer flux is replaced with 6% of the free-stream limit in a narrow region near this surface, where this limit is applied. This produces a nonphysical jump in the electron density near the critical surface, which leads to reduced absorption of laser light. The nonlocal treatment eliminates this jump, resulting in higher laser coupling and a stronger first shock, in better agreement with experimental data. Figure 125.3 shows that proper treatment of this electron transport is essential to correctly model these plasmas and predict shock timing.

Figure 125.4 shows the measured (solid)-velocity profile from an experiment (shot 59667) that used a 900- μm -diam, 5- μm -thick CH shell filled with liquid deuterium. The triple-pulse drive is shown in the figure. The dotted curve in Fig. 125.4 is the simulated velocity that matches the experiment to better than the ± 50 ps required for ignition targets. Also shown is a lineout (dashed) of the SOP self-emission intensity versus time; it also provides a corroborative measure of shock velocities and shock mergers. These data also show the acceleration caused by convergence effects, as predicted by the simulations. In 5- μm -shell targets, the laser fully ablates the CH shell and begins to interact with the deuterium. The ability to model this phase is critical to the performance of direct-drive-ignition targets, which are expected to have very thin CH shells.

That the simulations accurately predict the first shock velocity indicates that the codes adequately treat the plasma-initiation problem. Similarly, the good agreement with the subsequent shock velocities indicates the expansion of the coronal plasma, and the interaction of later pulses with that preformed plasma is also well modeled. Lastly, the agreement

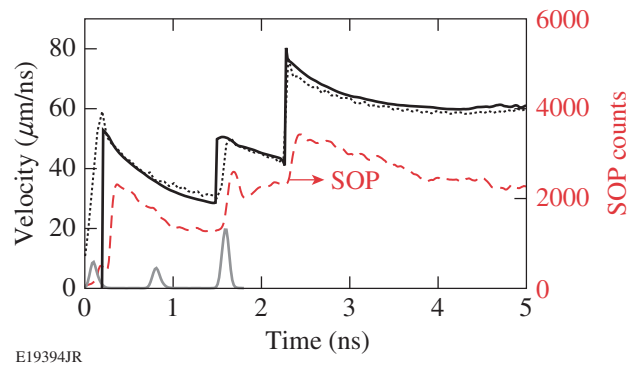


Figure 125.4

Measured-velocity profile (solid) and self-emission intensity (dashed) for a three-shock experiment. The simulated-velocity profiles (dotted) predict the velocities of each shock and their merger times with good accuracy including the effect of convergence.

of the predicted velocities and merger times with experiments indicates that the material properties (equations of state for CH and deuterium) used in the codes are also adequate. Obtaining good simulation of these data depended greatly on locating the target to within ~ 30 μm of the desired position. This ensured that the irradiation uniformity and intensity were as designed and expected.

A direct-drive ICF implosion on OMEGA has a longer (~ 1 -ns) fourth pulse that drives the target implosion. This pulse is more intense and has significantly higher energy than the individual ~ 100 -ps pulses preceding it. For shock-timing experiments, x rays from that drive pulse can be sufficiently intense to photoionize the quartz window at the end of the VISAR cone; this could prevent VISAR measurements. Figure 125.5 shows the VISAR signal from a four-pulse experiment where a reduction in the drive-pulse intensity made it possible to measure all four shocks using VISAR. The features of the data are similar to those in Figs. 125.2(a) and 125.2(c): the merger of the second shock with the first is evident at 1.9 ns; then at 2.4 ns the third shock merges with the first two. At 3.1 ns, the fourth shock from the main drive pulse (which started at 2 ns) overtakes the three merged shocks; soon after, the VISAR signal disappears. It is likely that, at these high pressures, the shock was sufficiently hot to photoionize the unshocked deuterium ahead of it and this material absorbed the VISAR probe beam.

In Fig. 125.6, the solid line is the velocity profile deduced from the VISAR data, showing shock velocities of 50, 56, 73, and 130 km/s for each of the four shocks. The latter velocity corresponds to a pressure of 2500 GPa in the deuterium. Ignition targets on the NIF will have the first three shock velocities in the range of 20, 40, and 70 km/s. These results

show that spherical shocks of those strengths in deuterium can readily be observed and timed using this technique. Note in Fig. 125.6 that the SOP (dashed) signal decreases (but does not disappear) at ~ 2.4 ns. This could be the result of initial blanking of the quartz window; the main pulse reaches its peak at this time. SOP detects light in the 590- to 850-nm range; photons in this range are better absorbed than those of the VISAR probe.

The velocity and timing of multiple, spherically converging shock waves have been measured in cryogenic-deuterium targets directly irradiated with laser pulses. A shock velocity of 135-km/s was observed in cryogenic deuterium. This is the highest shock velocity ever reported in deuterium and corresponds to a pressure of ~ 2500 GPa (25 Mb). This is also the first measurement of shock velocities that exhibited the effects

of spherical convergence, i.e., the increase in shock strength produced by that convergence.

To properly simulate these results, the hydrodynamic code used a nonlocal model to properly simulate heat transport in the coronal plasma. At high intensities, the initial plasmas produced by short (100-ps) pulses have steep density and temperature gradients, which the standard flux-limiter models do not properly treat. When a nonlocal thermal transport model is used instead, the shock velocities and timing are better modeled by the simulations. The ability to simulate these experimental results provides confidence in the hydrodynamic codes used to design direct-drive ICF targets for OMEGA and the NIF.

These experiments are the first to time multiple, spherically converging shock waves in liquid deuterium. The observed deuterium shock velocities were similar to and greater than those required for the initial phase of an ignition target on the NIF. They demonstrate the ability to time and control shock waves to the precision needed for ignition experiments. This technique was applied to full-scale experiments to tune hohlraum-driven ignition targets on the NIF.

ACKNOWLEDGMENT

This work was supported by the U.S. Department of Energy Office of Inertial Confinement Fusion under Cooperative Agreement No. DE-FC52-08NA28302, the University of Rochester, and the New York State Energy Research and Development Authority. The support of DOE does not constitute an endorsement by DOE of the views expressed in this article.

REFERENCES

1. J. D. Lindl, *Inertial Confinement Fusion: The Quest for Ignition and Energy Gain Using Indirect Drive* (Springer-Verlag, New York, 1998), Chap. 6, pp. 61–82.
2. D. H. Munro *et al.*, Phys. Plasmas **8**, 2245 (2001).
3. D. H. Munro, H. F. Robey, B. K. Spears, and T. R. Boehly, Bull. Am. Phys. Soc. **51**, 105 (2006).
4. B. A. Hammel and the National Ignition Campaign Team, Plasma Phys. Control. Fusion **48**, B497 (2006).
5. E. I. Moses, Fusion Sci. Technol. **54**, 361 (2008).
6. V. N. Goncharov, T. C. Sangster, P. B. Radha, R. Betti, T. R. Boehly, T. J. B. Collins, R. S. Craxton, J. A. Delettrez, R. Epstein, V. Yu. Glebov, S. X. Hu, I. V. Igumenshchev, J. P. Knauer, S. J. Loucks, J. A. Marozas, F. J. Marshall, R. L. McCrory, P. W. McKenty, D. D. Meyerhofer, S. P. Regan, W. Seka, S. Skupsky, V. A. Smalyuk, J. M. Soures, C. Stoeckl, D. Shvarts, J. A. Frenje, R. D. Petrasso, C. K. Li, F. Séguin, W. Manheimer, and D. G. Colombant, Phys. Plasmas **15**, 056310 (2008).

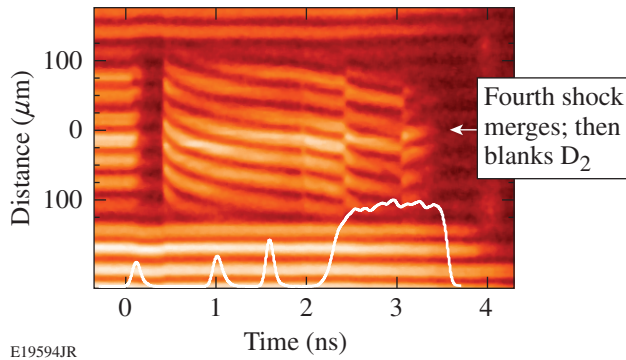


Figure 125.5
VISAR image for a four-shock experiment using an ICF drive pulse shown in the figure. Three shocks are visible as in Fig. 125.2(a) with mergers at 1.6 and 2.3 ns. At 3.1 ns, the fourth shock (produced by the main pulse) overtakes them, and soon after the x-ray flux from that pulse blanks the VISAR window.

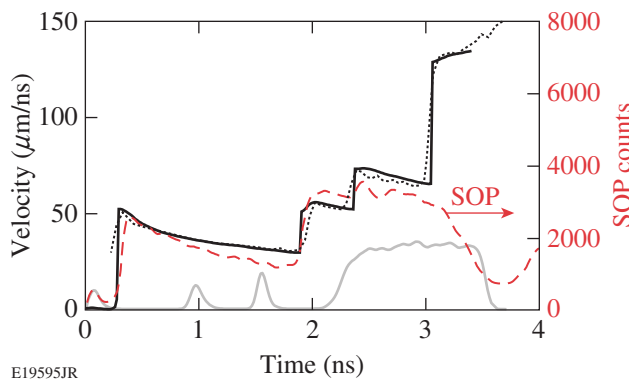


Figure 125.6
The velocity profile (solid) showing velocities of 42, 64, 83, and 135 km/s for each of the four shocks and the simulation (dotted). The latter velocity corresponds to a pressure of 2500 GPa. The SOP signal (dashed) follows VISAR during the first three shocks but then decreases at ~ 2.4 ns. Laser pulses are shown at the bottom of the graph.

7. T. R. Boehly, D. H. Munro, P. M. Celliers, R. E. Olson, D. G. Hicks, V. N. Goncharov, G. W. Collins, H. F. Robey, S. X. Hu, J. A. Marozas, T. C. Sangster, O. L. Landen, and D. D. Meyerhofer, *Phys. Plasmas* **16**, 056302 (2009).
8. V. N. Goncharov, in *Laser-Plasma Interactions*, edited by D. A. Jaroszynski, R. Bingham, and R. A. Cairns, Scottish Graduate Series (CRC Press, Boca Raton, FL, 2009), pp. 409–418.
9. P. M. Celliers, D. K. Bradley, G. W. Collins, D. G. Hicks, T. R. Boehly, and W. J. Armstrong, *Rev. Sci. Instrum.* **75**, 4916 (2004).
10. J. E. Miller, T. R. Boehly, A. Melchior, D. D. Meyerhofer, P. M. Celliers, J. H. Eggert, D. G. Hicks, C. M. Sorce, J. A. Oertel, and P. M. Emmel, *Rev. Sci. Instrum.* **78**, 034903 (2007).
11. T. R. Boehly, D. L. Brown, R. S. Craxton, R. L. Keck, J. P. Knauer, J. H. Kelly, T. J. Kessler, S. A. Kumpan, S. J. Loucks, S. A. Letzring, F. J. Marshall, R. L. McCrory, S. F. B. Morse, W. Seka, J. M. Soures, and C. P. Verdon, *Opt. Commun.* **133**, 495 (1997).
12. R. Kodama *et al.*, *Nature* **412**, 798 (2001).
13. Y. Lin, T. J. Kessler, and G. N. Lawrence, *Opt. Lett.* **20**, 764 (1995).
14. W. Seka, V. N. Goncharov, J. A. Delettrez, D. H. Edgell, I. V. Igumenshchev, R. W. Short, A. V. Maximov, J. Myatt, and R. S. Craxton, *Bull. Am. Phys. Soc.* **51**, 340 (2006).
15. W. Seka, D. H. Edgell, J. F. Myatt, A. V. Maximov, R. W. Short, V. N. Goncharov, and H. A. Baldis, *Phys. Plasmas* **16**, 052701 (2009).
16. J. Delettrez, R. Epstein, M. C. Richardson, P. A. Jaanimagi, and B. L. Henke, *Phys. Rev. A* **36**, 3926 (1987).
17. W. Seka, D. H. Edgell, J. P. Knauer, J. F. Myatt, A. V. Maximov, R. W. Short, T. C. Sangster, C. Stoeckl, R. E. Bahr, R. S. Craxton, J. A. Delettrez, V. N. Goncharov, I. V. Igumenshchev, and D. Shvarts, *Phys. Plasmas* **15**, 056312 (2008).

Impeding Hohlraum Plasma Stagnation in Inertial Confinement Fusion

The symmetry requirements for achieving ignition are fundamental and impose strict constraints on inertial confinement fusion (ICF).^{1–7} The tolerable drive asymmetry of an implosion, in a time-integrated sense, is less than 1% to 2% and depends on the ignition margin.^{3,4} In the indirect-drive approach to ICF, low-mode-number implosion asymmetries are a major concern because the quasi-uniform hohlraum radiation field provides drive with minimal high-mode-number nonuniformities.^{3–8} An example of such an asymmetry would be a time-integrated P2 (second-order Legendre polynomial) nonuniformity that could lead to different radial velocities and densities at pole and equator, converting less kinetic energy into internal energy and resulting in a higher drive energy required for ignition.

The high-Z plasma from the wall blowoff, usually gold (Au) or uranium (U), which causes motion in the laser-absorption region and alters the spatial distributions of x-ray energy sources and sinks, has been shown to cause low-mode-number implosion asymmetries.^{3–8} The blowoff quickly fills the interior of an initially empty (optically thin) hohlraum, leading to early on-axis plasma stagnation.^{3–8} The stagnated plasma has high pressure and can asymmetrically compress the capsule.

To achieve the required drive symmetry, the motion of the laser-deposition (x-ray emission) region must be minimized. Two proposed approaches are to overcoat a hohlraum wall surface with a low-Z liner and to fill a hohlraum interior with low-Z gas.⁴ Neither the liner nor the fill gas stops the wall blowoff; however, they displace the low-density plasmas. In the first approach, plasma jets form because of the interaction of pairs of adjacent, expanding plumes of low-Z liner blowoff.^{4,9} The radially moving jets are supersonic and quickly stagnate at the hohlraum interior, resulting in asymmetries in both the drive and the capsule implosion. The ignition campaign at the National Ignition Facility (NIF) currently adopts the second approach.^{3–7} Hohlräume are filled with helium-4 gas⁶ at a pressure ~ 0.4 atm (when fully ionized, $n_e \sim 0.04 n_{\text{crit}}$, the critical electron density for 0.35- μm laser light). The gas is

contained with thin polyimide windows over the laser entrance holes (LEH's).

This article presents the first proton radiography observations of the effects of gas fill on impeding the hohlraum plasma stagnation. The experiments, illustrated schematically in Fig. 125.7(a), were performed at the Omega Laser Facility.¹⁰ Radiographic images were made with 15-MeV protons at various implosion times through the LEH.^{9,11} Figure 125.7 shows two different types of images: proton fluence versus position [Fig. 125.7(b)] and proton mean energy versus position [Fig. 125.7(c)]. The proton fluence piles up in the gaps between the two expanding plasma plumes and in the region between the imploding capsule and the expanding plasmas, forming a five-prong, asterisk-like pattern—a consequence of OMEGA's laser-beam distribution.^{9,11} Contrary to earlier experiments that showed a deficit in proton fluence in these regions for vacuum hohlräume,^{9,11} this fluence surplus suggests that no high-density plasma jets were formed. The fill gas along the laser beam's path is fully ionized. The interfaces between the gas plasma and the Au wall blowoff are constrained near the wall's surface [Fig. 125.7(b), indicated by the open arrows]. Figure 125.8 shows the measured Au-wall plasma-fill gas interface radius as a function of time compared with the sound speed $\left[C_s \propto (ZT_e m_i^{-1})^{1/2} \right]$ that sets the scale for hydrodynamic rarefaction expansion in vacuum.^{11,12} The expansion speed of the Au blowoff is estimated to be $\sim (2.1 \pm 0.3) \times 10^7 \text{ cm s}^{-1}$, which is slower than $C_s \sim 2.5 \times 10^7 \text{ cm s}^{-1}$, indicating that the wall blowoff's expansion has been compressed by the fill gas.¹³ These measurements show that the fill gas impedes the wall plasma expansion.

An additional interface appears in the region around the imploding capsule [1.65 ns, Fig. 125.7(b)]. It is identified as the interface between the capsule's CH ablation and the fill-gas plasma. Because the implosion is nearing the deceleration phase, with the typical implosion velocity, $v_{\text{imp}} \left[\propto I_{15}^{1/8} \ln(m_0/m) \right] \sim 2$ to $3 \times 10^7 \text{ cm s}^{-1}$ and velocity of outward-moving ablated cap-

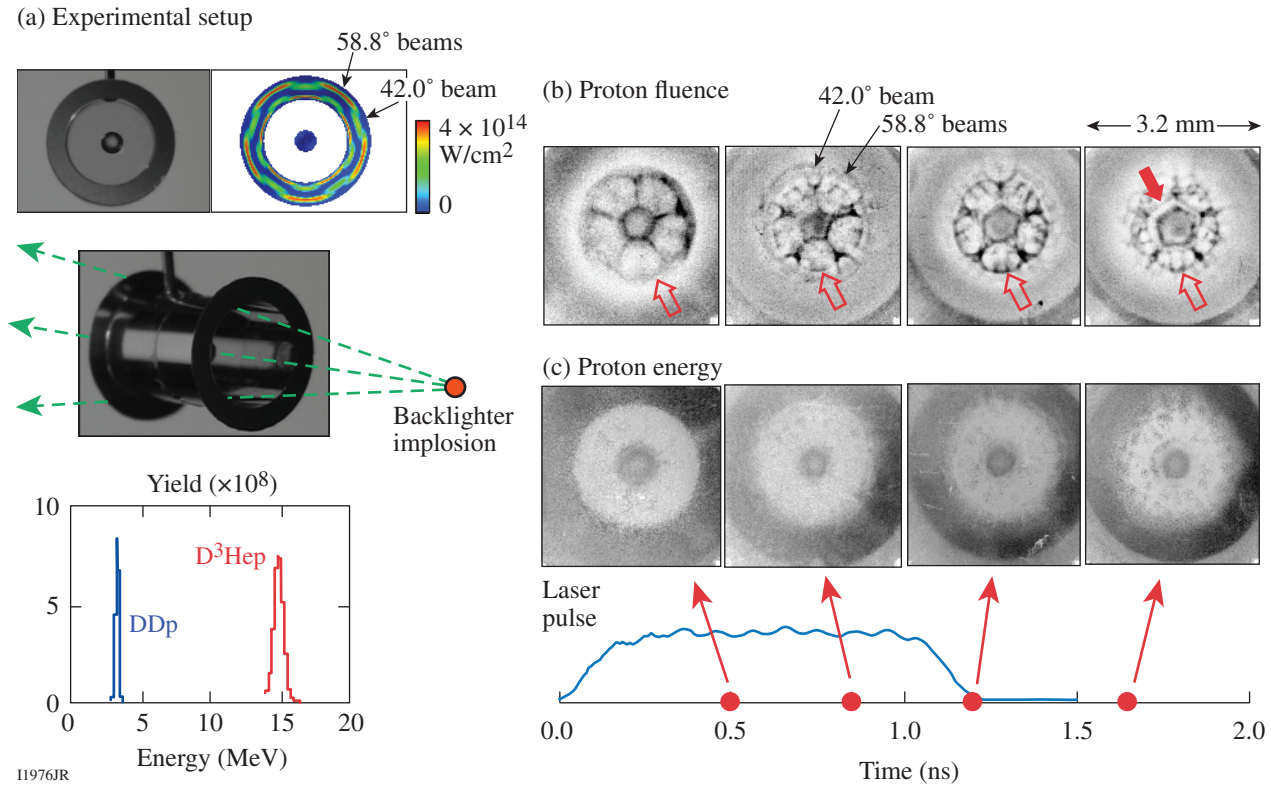


Figure 125.7

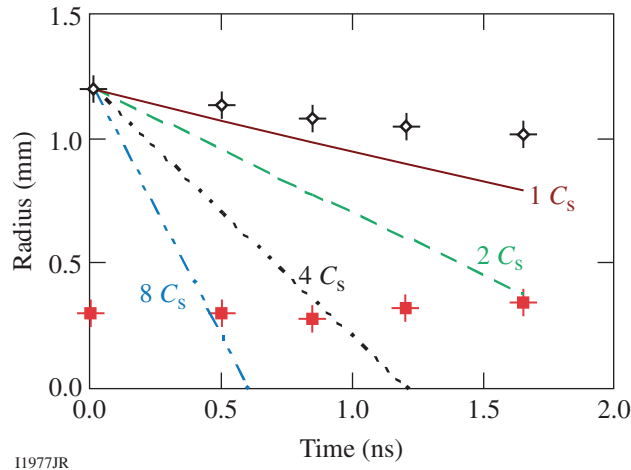
(a) Experimental setup. The two photos show an Au hohlraum filled with ~ 0.4 atm of neopentane gas (C_5H_{12}) and containing a CH capsule (30- μ m-thick, 550- μ m-diam plastic shell either empty or filled with 50 atm of H_2 gas). A proton backlighter (imploded, D^3He -filled, thin-glass-shell capsule driven by 30 OMEGA laser beams¹⁵) is typically 1 cm from the hohlraum center and has the illustrated monoenergetic spectra from the reactions $D+^3He \rightarrow \alpha + p$ (14.7 MeV) and $D + D \rightarrow T + p$ (3.0 MeV), recorded with a CR39 detector. The hohlraums had 30- μ m-thick gold walls, 100% laser entrance hole (LEH), 2.4-mm diameter, and 3.8-mm length. The hohlraum was driven by 30 laser beams with a wavelength of 0.351 μ m and total laser energy ~ 11 kJ in a 1-ns square pulse. The laser beams had full spatial and temporal smoothing.¹⁶ Radiographic images of (b) proton fluence and (c) proton energy taken with 15-MeV D^3He protons (the particle energy was slightly upshifted from its birth energy because of the capsule's positive charging) at various implosion times. Within each image, darker means (b) higher proton fluence or (c) lower proton energy. The open arrows in (b) point to the interfaces between the Au wall blowoff and gas plasmas. For the image at 1.65 ns, the solid arrow points to the interface between the capsule ablator and gas plasma.

sule material $v_{abl} \propto I_{15}^{9/40} \sim C_s$, the capsule is expected to be essentially unaffected by the pressure generated in this region.⁴

While the proton fluence shows large variations [Fig. 125.7(b)], the proton energy shows less variation [Fig. 125.7(c)] until later times (1.65 ns). This suggests that the trajectories of these backlighting protons have been largely affected by fields around the capsule and not by proton scattering in the plasma because Coulomb interactions are always accompanied by energy loss.^{9,14}

To explore the mechanism for forming such a unique spatial (fluence) structure and its effects on impeding the hohlraum wall's plasma expansion and drive dynamics, experiments were performed with solid, spherical CH targets driven in both gas-filled Au hohlraums and CH-lined vacuum Au hohlraums (Fig. 125.9). The two images show related asterisk-like

structures (with spokes in the gaps between pairs of expanding plasma plumes) but with opposite proton fluence distributions: protons were focused into the gaps (high-fluence spokes) for the gas-filled hohlraum [Figs. 125.9(a) and 125.9(c)] but were deflected away from the spokes in the CH-lined vacuum hohlraum [Figs. 125.9(b) and 125.9(d)]. The role of a spontaneously generated magnetic (B) field in these interactions can be excluded by symmetry since the toroidal B -field topology around the laser spots^{15,17} cannot result in such azimuthal proton deflections.⁹ Lateral electric (E) fields^{18,19} associated with azimuthally oriented electron pressure gradients (∇P_e) in the plasma plumes and in the radial plasma jets, $E = -\nabla P_e / en_e$, may be the source of these deflections. Another physical mechanism that could explain the deflection near the capsule before 0.5 ns is the E field associated with a supersonic heat front generated by the laser-heated gas channels that are in close



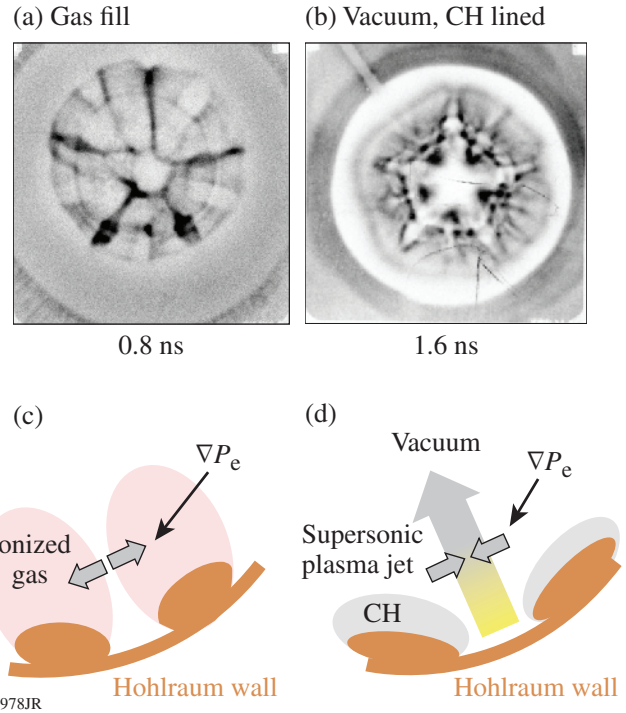
I1977JR

Figure 125.8

Measured interfaces between the Au wall blowoff and the gas plasma (open black diamonds), and between the capsule and the gas plasma (solid red squares), are compared to motion at multiples of the sound speed. The boundary position shown at ~ 0.5 ns suggests that the hot regions of the gas plasma have reached the surface of an imploding capsule at a fast speed ($\sim 8 C_s$). The uncertainties for sampling times were ~ 90 ps (the backlighter burn duration), while for the radius they were $\sim 10\%$ (the variation in image circularity). The linear fit yields the expansion speed $v \approx (2.1 \pm 0.3) \times 10^7$ cm s $^{-1}$ (reduced $\chi^2 = 0.662$).

proximity to the capsule. Work is in progress to quantitatively assess the relative importance of this mechanism in the generation of such a field. Since Figs. 125.9(a) and 125.9(b) show opposite deflections, E must have pointed in opposite directions.

As illustrated in the cartoon in Fig. 125.9(c) for the gas-filled hohlraum, the high plasma pressure should have resulted from an increase of temperature inside the plasma plume and ionized gas.²⁰ The steep ∇P_e results in strong E fields that point laterally away from the plumes, deflecting the backlighting protons into the gaps between pairs of approaching plasma plumes. For these underdense gas plasmas ($\sim 0.04 n_{\text{crit}}$), the rapidly rising plasma temperature in the region through which the laser passes does not result from continuous laser heating but is a consequence of the inhibition of heat flow caused by the self-generated megaGauss B field^{8,9,11} because the electron thermal transport is reduced by a factor of $(1 + \omega_{ce}^2 \tau^2)^{-1}$, where ω_{ce} is the electron gyro frequency and τ is the collision time.¹⁸ Including the contribution from magnetized window plasma, the Hall parameter $\omega_{ce} \tau$ is ~ 10 (Ref. 8). Eventually, the combination of inverse bremsstrahlung absorption in the Au wall and electron conduction establishes a near-equilibrium plasma conditions in the laser propagation channel, and the quasi pressure balance leads to continuous plasma heating and temperature increase.⁴



I1978JR

Figure 125.9

The proton fluence distributions show a surplus in the regions between the pairs of expanding plasma plumes in a gas-filled Au hohlraum (a) but show a deficit in a CH-lined, vacuum Au hohlraum (b), indicating opposing directions of the self-generated electric fields as illustrated schematically by the corresponding cartoons, in (c) and (d), respectively.

The spontaneous B field is generated initially at the hohlraum wall because of nonparallel density and temperature gradients ($\nabla n_e \times \nabla T_e$). Based on the proton deflection feature, the data [Fig. 125.7(b)] show that the plasma temperatures were high²⁰ even at the earlier time (~ 0.5 ns) for the fully ionized, low- Z gas plasma whose front boundary had already reached the surface of the imploding capsule within the region of the laser beam's propagation channel, indicating that inhibition of heat flow by fields must have taken place at an earlier time. This suggests that the transport of the field was much faster than the plasma's expansion speed that carried the "frozen in" field with $[\nabla \times (\mathbf{v} \times \mathbf{B})]$. The fluid velocity v ($< C_s$) is too slow to explain the rapid increase in gas plasma temperature at the earlier times (Figs. 125.7–125.9). Such a nonlocal field transport must have resulted from the convection of the B field with the heat flux associated with "faster" electrons because of the Nernst effect ($\propto \beta_\lambda \mathbf{b} \times \nabla T_e$, i.e., the current flow is driven perpendicular to a B field and ∇T_e , where $\mathbf{b} \equiv \mathbf{B}B^{-1}$ and β_λ is the thermoelectric coefficient perpendicular to the B field and temperature gradient).^{19,21} The velocity of convection of the B field in this

transport mechanism is approximately $v_N \approx 2q_e(5n_e T_e)^{-1}$, where $q_e = \kappa_\perp \nabla T_e$ is the electron heat flux and κ_\perp is the thermal conductivity. Using the data from Figs. 125.7(b) and 125.8 (the position of the boundary of the gas plasma that reached the surface of an imploding capsule), a rough estimate indicates that the lower limit for the B-field convection speed is $v_N \sim 8C_s$, suggesting that the field transport (convection) by heat flux is about one order of magnitude faster than the plasma expansion ($v_N \sim 10v$). The physical process of the B-field generation, evolution, and dissipation [$\nabla \times (D_m \nabla \times \mathbf{B})$] is described by Faraday's law in a plasma as^{18,19}

$$\frac{\partial \mathbf{B}}{\partial t} \approx -\frac{\nabla n_e \times \nabla T_e}{en_e} + \nabla \times (\mathbf{v} \times \mathbf{B}) - \nabla \times (D_m \nabla \times \mathbf{B}) - \frac{\nabla \times \mathbf{R}}{en_e}, \quad (1)$$

where D_m is the magnetic diffusion coefficient and

$$\mathbf{R} = \frac{(\alpha_\perp \mathbf{J}_\perp + \alpha_\parallel \mathbf{J} \times \mathbf{b})}{en_e} + \beta_\perp \nabla_\perp T_e - \beta_\parallel \mathbf{b} \times \nabla T_e \quad (2)$$

is the contribution of electron thermal and friction forces.^{18,19,21} The data suggest that the Nernst effect is responsible for the rapid B-field transport, which is shown to play an important role in observed rapid increase in the gas plasma temperature.

The behavior and dynamics are different in the laser-irradiated, CH-lined, Au vacuum hohlraum [Fig. 125.9(b)]. Although the ablated CH wall helps to compress the Au blowoff, radially moving CH plasma jets are generated with the Au blowoff trailing.⁹ This process is initiated by the CH liner ablating from the wall, which subsequently expands with the continual arrival of wall blowoff into the region between the two adjacent expanding plumes. These plasmas collide with one another, leading to the formation of the dense plasma spokes that are redirected radially and move toward the hohlraum interior. The steep ∇P_e around the jets results in radial E fields that deflect the imaging protons away from the jets and lead to the asterisk-like spoke structure in the fluence images [Fig. 125.9(d)]. The inward jets travel with supersonic speed ($\sim 4C_s$) generating an early-time stagnation pressure that affects capsule implosion symmetry and dynamics,⁹ a phenomenon also observed in the pure vacuum Au hohlraum-driven experiments.¹¹

The widths of the spokes in the images can be used with the imaging geometry to estimate the field $\int \mathbf{E} \times d\ell \sim 3 \times 10^5 \text{ V}$

(where $d\ell$ is the differential path length along the proton trajectory through the field area).⁹ A scale length of $\sim 0.1 \text{ cm}$ (\sim laser spot width) for the field in a jet spoke implies $E \sim 3 \times 10^6 \text{ V cm}^{-1}$.

To further study the dynamics of the interface and its effect on impeding the plasma stagnation, capsule implosions were performed with a denser hohlraum gas fill ($\sim 1 \text{ atm}$, C_5H_{12}) at two sampling times (Fig. 125.10). A relatively smooth interface appears between the expanding wall blowoff and the ionized fill gas at 0.8 ns, while chaotic spatial structure and interface interpenetration are evident at 1.6 ns. This interpenetration is caused by hydrodynamic instabilities. The surface perturbations that are seeded at the plume front can be amplified by the classical Rayleigh–Taylor (RT) instability occurring at the interface of the lighter, decelerating ionized gas plasma and the heavier, expanding Au blowoff.⁴ This instability has a growth rate⁴ $\gamma_{\text{RT}} \approx (2\pi A_t a k)^{1/2}$, where a is the acceleration, $\sim 10^{16} \text{ cm s}^{-2}$ is estimated from Fig. 125.7(b); $k = m(2\pi r)^{-1}$ is the perturbation wave number. As an example, for a mode number $m \sim 50$ at half the hohlraum radius $r \sim 0.5 \times 0.12 \text{ cm}$, $k \sim 130 \text{ cm}^{-1}$, and $A_t = (\rho_2 - \rho_1)/(\rho_2 + \rho_1)$ is the Atwood number at the interface. For $\sim 0.1 n_{\text{crit}}$ the gas-fill plasma has a $\rho_1 \approx 3 \text{ mg cm}^{-3}$ while the Au plasma has a $\rho_2 \approx 10 \text{ mg cm}^{-3}$; therefore $A_t \approx 0.54$. A rough estimate gives $\gamma_{\text{RT}} \sim 2.7 \times 10^9 \text{ s}^{-1}$ and a perturbation grows by a factor of ~ 15 in 1 ns. A similar interaction process occurred between the ablated capsule plasma and the gas plasma. The consequence is a reduced benefit of the gas fill because the enhanced interpenetration (or mixing) between the Au blowoff and the gas plasma leads to high-Z material stagnating earlier in the hohlraum interior. This effect does not appear to be

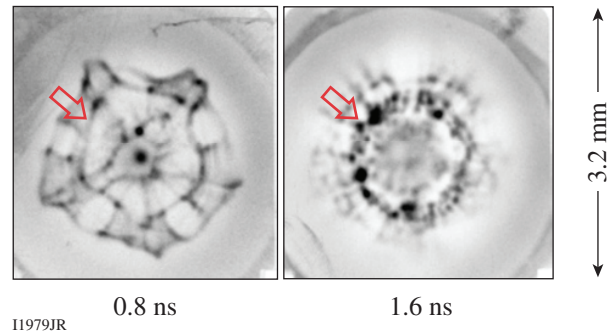


Figure 125.10

Proton fluence images of capsule implosions driven by gas-filled hohlraums. The open arrows point to interfaces between the Au wall blowoff and gas plasma. A relatively smooth interface appears between the expanding wall blowoff and the ionized fill gas at time 0.8 ns, while chaotic spatial structure and interface interpenetration are evident at time 1.6 ns. The fluence surplus inside the imploding capsule (0.8 ns) resulted from self-generated radial E fields.^{22,23}

severe because it happens during the coasting phase when the capsule implosion moves at a speed v_{imp} that is comparable to, or even faster than, the outward ablation speed ($\sim C_s$). At this time, the high- Z blowoff should be sonically decoupled from the imploding capsule.

To explore the role that CH windows play in impeding the plasma stagnation, we performed capsule implosions driven by vacuum hohlraums with a CH window on both LEH's. This is an important issue because when laser beams pass through the LEH's, the CH windows are immediately evaporated, ionized, and magnetized. The high-pressure, low- Z window plasma will rapidly flow into the hohlraum interior, filling it and altering the wall blowoff dynamics and impeding the plasma stagnation, like the gas fill does. The spontaneous B fields will convect with the flowing window plasma and inhibit electron thermal conduction, further increasing the plasma temperature^{18,19,21} and impeding the motion of the wall blowoff. Figure 125.11 shows radiographic images taken while the drive laser was on. Because of the inflow of CH window plasma, no plasma jets formed and the wall blowoff was contained radially. More protons deflected in the radial direction than in the lateral directions of the radial expanding plume. This is because $|L_T| > |L_n|$, where $L_T = T_e(\nabla T_e)^{-1}$ and $L_n = n_e(\nabla n_e)^{-1}$ are the temperature and density scale lengths, respectively, and $E \approx |E_r + E_\theta| \propto n_e^{-1} \nabla P_e \sim T_e |L_n^{-1} + L_T^{-1}|$, leading to $|E_r| > |E_\theta|$.

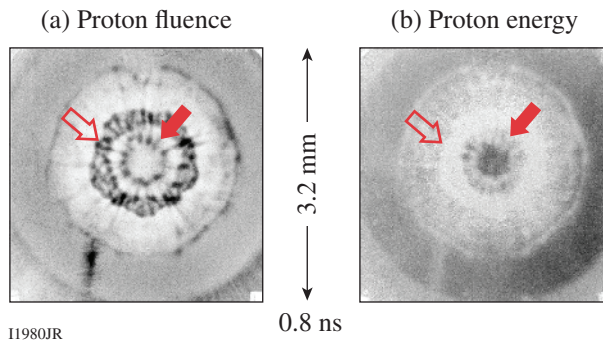


Figure 125.11

Images of (a) proton fluence and (b) proton energy from a solid CH sphere driven by a vacuum Au hohlraum with polyimide windows. The open (solid) arrows point to the interfaces between the Au wall blowoff and gas plasma (between the capsule ablation and gas plasma).

In summary, we have performed the first time-gated proton radiography of the spatial structure and temporal evolution of how the fill gas compresses the wall blowoff, inhibits plasma jet formation, and impedes plasma stagnation in the hohlraum interior. We have shown that the plasma interpenetrate

caused by the classical Rayleigh–Taylor instabilities occurs as the lighter, decelerating ionized fill gas pushes against the heavier, expanding gold wall blowoff. We have demonstrated the important roles of spontaneously generated E and B fields in the hohlraum dynamics and capsule implosion. The heat flux is shown to rapidly convect the B field because of the Nernst effect. This experiment provides novel physics insight into the effects of fill gas on x-ray–driven implosions and will have an important impact on the ignition experiments at the NIF.

ACKNOWLEDGMENT

This work was supported in part by the U.S. Department of Energy and LLE National Laser User's Facility (DE-FG52-07NA28059 and DE-FG03-03SF22691), LLNL (B543881 and LDRD-08-ER-062), LLE (414090-G), FSC (412761-G), and General Atomics (DE-AC52-06NA 27279). A. B. Zylstra is supported by the Stewardship Science Graduate Fellowship (DE-FC52-08NA28752).

REFERENCES

1. J. Nuckolls *et al.*, *Nature* **239**, 139 (1972).
2. R. L. McCrory, J. M. Soures, C. P. Verdon, F. J. Marshall, S. A. Letzring, S. Skupsky, T. J. Kessler, R. L. Kremens, J. P. Knauer, H. Kim, J. Delettrez, R. L. Keck, and D. K. Bradley, *Nature* **335**, 225 (1988).
3. S. W. Haan *et al.*, *Phys. Plasmas* **2**, 2480 (1995).
4. J. D. Lindl, *Inertial Confinement Fusion: The Quest for Ignition and Energy Gain Using Indirect Drive* (Springer-Verlag, New York, 1998).
5. S. Atzeni and J. Meyer-ter-Vehn, *The Physics of Inertial Fusion: Beam Plasma Interaction, Hydrodynamics, Hot Dense Matter*, International Series of Monographs on Physics (Clarendon Press, Oxford, 2004).
6. S. H. Glenzer *et al.*, *Science* **327**, 1228 (2010).
7. O. L. Landen, T. R. Boehly, D. K. Bradley, D. G. Braun, D. A. Callahan, P. M. Celliers, G. W. Collins, E. L. Dewald, L. Divol, S. H. Glenzer, A. Hamza, D. G. Hicks, N. Hoffman, N. Izumi, O. S. Jones, R. K. Kirkwood, G. A. Kyrala, P. Michel, J. Milovich, D. H. Munro, A. Nikroo, R. E. Olson, H. F. Robey, B. K. Spears, C. A. Thomas, S. V. Weber, D. C. Wilson, M. M. Marinak, L. J. Suter, B. A. Hammel, D. D. Meyerhofer, J. Atherton, J. Edwards, S. W. Haan, J. D. Lindl, B. J. MacGowan, and E. I. Moses, *Phys. Plasmas* **17**, 056301 (2010).
8. S. H. Glenzer *et al.*, *Phys. Plasmas* **6**, 2117 (1999).
9. C. K. Li, F. H. Séguin, J. A. Frenje, M. Rosenberg, R. D. Petrasso, P. A. Amendt, J. A. Koch, O. L. Landen, H. S. Park, H. F. Robey, R. P. J. Town, A. Casner, F. Philippe, R. Betti, J. P. Knauer, D. D. Meyerhofer, C. A. Back, J. D. Kilkenny, and A. Nikroo, *Science* **327**, 1231 (2010).
10. J. M. Soures, R. L. McCrory, C. P. Verdon, A. Babushkin, R. E. Bahr, T. R. Boehly, R. Boni, D. K. Bradley, D. L. Brown, R. S. Craxton, J. A. Delettrez, W. R. Donaldson, R. Epstein, P. A. Jaanimagi, S. D. Jacobs, K. Kearney, R. L. Keck, J. H. Kelly, T. J. Kessler, R. L. Kremens, J. P. Knauer, S. A. Kumpan, S. A. Letzring, D. J. Lonobile, S. J. Loucks,

- L. D. Lund, F. J. Marshall, P. W. McKenty, D. D. Meyerhofer, S. F. B. Morse, A. Okishev, S. Papernov, G. Pien, W. Seka, R. Short, M. J. Shoup III, M. Skeldon, S. Skupsky, A. W. Schmid, D. J. Smith, S. Swales, M. Wittman, and B. Yaakobi, *Phys. Plasmas* **3**, 2108 (1996).
11. C. K. Li, F. H. Séguin, J. A. Frenje, R. D. Petrasso, P. A. Amendt, R. P. J. Town, O. L. Landen, J. R. Rygg, R. Betti, J. P. Knauer, D. D. Meyerhofer, J. M. Soures, C. A. Back, J. D. Kilkenny, and A. Nikroo, *Phys. Rev. Lett.* **102**, 205001 (2009).
 12. R. P. Drake, *High-Energy-Density Physics: Fundamentals, Inertial Fusion, and Experimental Astrophysics*, Shock Wave and High Pressure Phenomena (Springer, Berlin, 2006).
 13. For an adiabatic rarefaction expansion of an ideal gas, the expansion speed is $3 C_s$ in vacuum, while the hot electrons advancing ahead of the rarefaction expansion because of their high mobility may further boost the motion of leading edge CH and Au ions ablating off the hohlraum wall by an additional C_s factor.⁹
 14. C. K. Li and R. D. Petrasso, *Phys. Rev. Lett.* **70**, 3059 (1993).
 15. C. K. Li, F. H. Séguin, J. A. Frenje, J. R. Rygg, R. D. Petrasso, R. P. J. Town, P. A. Amendt, S. P. Hatchett, O. L. Landen, A. J. MacKinnon, P. K. Patel, V. A. Smalyuk, T. C. Sangster, and J. P. Knauer, *Phys. Rev. Lett.* **97**, 135003 (2006).
 16. D. D. Meyerhofer, J. A. Delettrez, R. Epstein, V. Yu. Glebov, V. N. Goncharov, R. L. Keck, R. L. McCrory, P. W. McKenty, F. J. Marshall, P. B. Radha, S. P. Regan, S. Roberts, W. Seka, S. Skupsky, V. A. Smalyuk, C. Sorce, C. Stoeckl, J. M. Soures, R. P. J. Town, B. Yaakobi, J. D. Zuegel, J. Frenje, C. K. Li, R. D. Petrasso, D. G. Hicks, F. H. Séguin, K. Fletcher, S. Padalino, C. Freeman, N. Izumi, R. Lerche, T. W. Phillips, and T. C. Sangster, *Phys. Plasmas* **8**, 2251 (2001).
 17. R. D. Petrasso, C. K. Li, F. H. Séguin, J. R. Rygg, J. A. Frenje, R. Betti, J. P. Knauer, D. D. Meyerhofer, P. A. Amendt, D. H. Froula, O. L. Landen, P. K. Patel, J. S. Ross, and R. P. J. Town, *Phys. Rev. Lett.* **103**, 085001 (2009).
 18. S. I. Braginskii, in *Reviews of Plasma Physics*, edited by Acad. M. A. Leontovich (Consultants Bureau, New York, 1965), Vol. 1.
 19. M. G. Haines, *Phys. Rev. Lett.* **78**, 254 (1997).
 20. Such a temperature rise has been seen with Thomson scattering in Nova experiments, where an electron temperature ~ 2 keV was measured on the axis of a gas-filled hohlraum at early times during a 1-ns laser pulse ($I \approx 10^{15}$ W/cm²), and in LASNEX simulations of the development of hot regions along the laser-pass channel.⁸
 21. A. Nishiguchi *et al.*, *Phys. Rev. Lett.* **53**, 262 (1984).
 22. C. K. Li, F. H. Séguin, J. R. Rygg, J. A. Frenje, M. Manuel, R. D. Petrasso, R. Betti, J. Delettrez, J. P. Knauer, F. Marshall, D. D. Meyerhofer, D. Shvarts, V. A. Smalyuk, C. Stoeckl, O. L. Landen, R. P. J. Town, C. A. Back, and J. D. Kilkenny, *Phys. Rev. Lett.* **100**, 225001 (2008).
 23. P. A. Amendt *et al.*, *Plasma Phys. Control. Fusion* **51**, 124048 (2009).

Initial Cone-in-Shell, Fast-Ignition Experiments on OMEGA

Introduction

Fast ignition^{1,2} is an attractive option for inertial confinement fusion because the target compression and ignition stages are separated, relaxing the requirements on the symmetry of the implosion and the compression energy. Massive fuel shells can be imploded with low velocity, providing the potential of higher gains at lower total driver energy than in conventional central hot-spot ignition schemes.³ In fast ignition, the dense core is ignited by particles (electrons, protons, or ions) generated by a short, ultra-intense, high-energy laser pulse. Fast ignition relies on the localized deposition of the particle energy in the core. Design studies have been performed for electrons with integrated simulations coupling a hydrodynamic code with a hybrid particle-in-cell (PIC) code.⁴ The simulations estimate that electron-beam energies ranging from ~ 40 to 100 kJ are required for ignition, assuming a Gaussian-shaped fast-electron beam with an $\sim 30\text{-}\mu\text{m}$ spot size, a 10-ps duration, and a relativistic Maxwellian distribution with $\sim 2\text{-MeV}$ mean energy. The beam is injected 125 μm from the target center into a compressed DT core with $\rho \sim 500\text{-g/cm}^3$ peak density and $\rho R \sim 1\text{-g/cm}^2$ areal density.⁴ The ignition threshold depends on the initial beam's full-divergence angle, which was varied from 40° to 80° in the simulation. Similar ignition electron-beam energies have been obtained in other design studies.^{5,6} These design studies are still lacking a detailed description of the laser-plasma interaction, which is complex and will require massive, large-scale, three-dimensional (3-D) PIC simulations.⁷

Maximizing the coupling efficiency of the short-pulse energy into core heating remains a challenge for full-scale fast ignition. The conversion efficiency of fast electrons with the appropriate energy (1 to 2 MeV) needs to be maximized, and the particles must be transported efficiently from their source location to the compressed fuel, where they must be stopped in a sufficiently small volume that matches the optimal size of the ignition spark. Self-generated resistive magnetic fields are predicted to significantly affect the transport of hot electrons.^{8,9} A self-generated magnetic field may collimate the beam as a whole while it propagates into the dense core and, therefore, may increase the coupling efficiency.¹⁰

It is important to bring the fast-electron source as close as possible to the fuel assembly. A very promising approach is the cone-in-shell concept¹¹ with encouraging initial integrated experiments at the GEKKO Laser Facility, which reported significant heating by a 0.6-ps, 300-J short-pulse laser.¹² The re-entrant cone makes it possible for a high-energy petawatt laser pulse to propagate as close as possible to the dense core, avoiding the need to channel the laser beam through a large region of plasma material.

Figure 125.12 shows a schematic of the integrated cone-in-shell, fast-ignitor experiments reported here, which were conducted at the Omega Laser Facility,¹³ including the short-pulse OMEGA EP laser.¹⁴ The coupling efficiency will depend on the separation of the cone tip from the dense plasma. A shorter distance will increase the hydrodynamic forces on the cone tip, which result from a jet formed by imploded plasma impacting the cone tip and launching a shock wave through the tip. This shock wave must not break out from the inner cone surface before the short pulse is fired; otherwise, plasma will quickly fill the cone, significantly increasing the electron-propagation distance and lowering the transport efficiency.

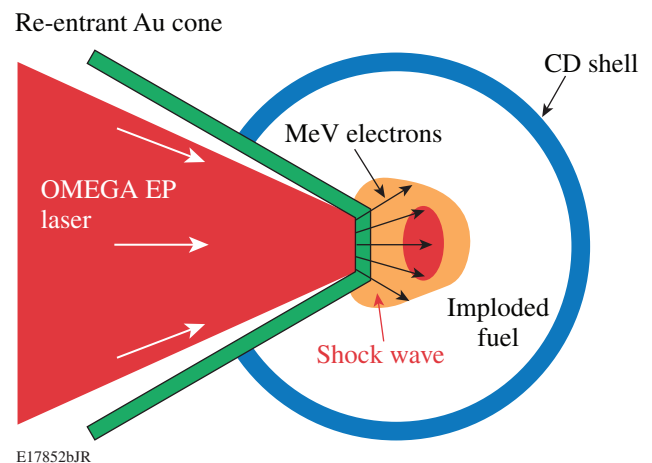


Figure 125.12
Schematic of the integrated cone-in-shell, fast-ignition experiment.

Design studies and experiments are needed to determine the optimum separation distance, tip thickness, and cone wall material. The shell mass and implosion velocity will have a significant effect on the force that the plasma jet exerts on the cone tip. It has been shown that low-velocity implosions of massive shells on a low adiabat lead to a cold and dense fuel assembly that is ideal for fast ignition.³ The resulting dense core has a relatively low pressure and large size, reducing the hydrodynamic forces and creating a smaller distance between the tip and the dense core edge. Spherical symmetric low-adiabat implosions of cryogenic targets in direct-drive geometry have been demonstrated on OMEGA with triple-picket laser pulses, achieving a neutron-rate-averaged areal density (ρR) of up to 300 mg/cm^2 (Ref. 15).

This article describes initial integrated fast-ignition experiments at the Omega Laser Facility, which uses low-adiabat implosions and demonstrates core heating with a 1-kJ, 10-ps, short-pulse laser. Companion experiments demonstrate that the cone tip is intact at the time when the short-pulse laser is fired into the cone. The integrated experiments produced up to $\sim 1.4 \times 10^7$ additional neutrons.

The following sections describe the targets and the laser setup; discuss shock-breakout measurements, the integrated fast-electron heating experiment, and the integrated simulations; and conclude with a summary.

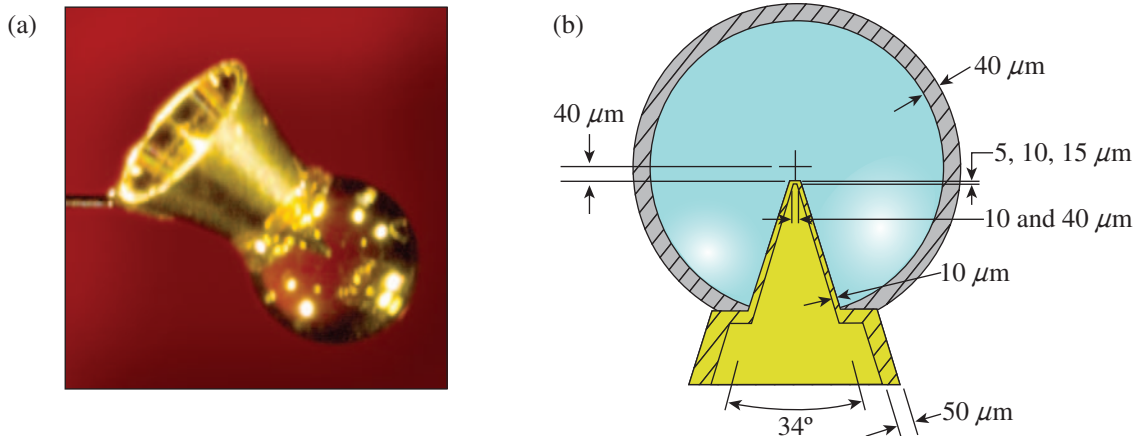
Targets and Laser Setup

The targets were relatively thick walled ($40\text{-}\mu\text{m}$), $\sim 870\text{-}\mu\text{m}$ -outer-diam deuterated-plastic (CD) shells with an inserted hollow gold cone; they were fabricated and characterized by

General Atomics.¹⁶ Figure 125.13(a) is a photograph of a target mounted on a support stalk; Fig. 125.13(b) shows a target cross section with target dimensions. A shelf is machined into the gold cone to attach the shell. This serves as a reference for placing the tip precisely in the desired location, $40 \pm 10 \mu\text{m}$ away from the center of the shell along the cone axis. The shell was not filled with gas for these experiments. An x-ray radiograph of such a target can be found in Ref. 17. The cone has an inner full opening angle of $34 \pm 1^\circ$, a side-wall thickness of $10 \mu\text{m}$, and a small circular flat tip. The cone wall is $50 \mu\text{m}$ thick outside the shell. The tip diameter was either 10 or $40 \mu\text{m}$. The tip thickness was 5 , 10 , or $15 \mu\text{m}$ in the shock-breakout experiment described in **Shock-Breakout Measurements**, p. 15 and 10 or $15 \mu\text{m}$ in the integrated shots discussed in **Integrated Fast-Electron-Heating Experiments**, p. 17.

The shells were imploded on an adiabat of $\alpha_{\text{in}} \approx 1.5$ (Ref. 18), where α_{in} is defined as the ratio of plasma pressure in the inner portion of the shell to the Fermi pressure of a fully degenerate electron gas. Figure 125.14 shows the $\sim 2.7\text{-ns}$ drive pulse, consisting of a 90-ps full-width-at-half-maximum (FWHM) Gaussian prepulse with $\sim 6.5 \text{ TW}$ of peak power attached to a shaped main pulse with a foot power of $\sim 0.8 \text{ TW}$ and a peak power of $\sim 12 \text{ TW}$. The shell was imploded using 54 out of the 60 UV OMEGA beams with a total energy of $\sim 20 \text{ kJ}$. The laser light was smoothed with polarization rotators and distributed phase plates.^{19,20}

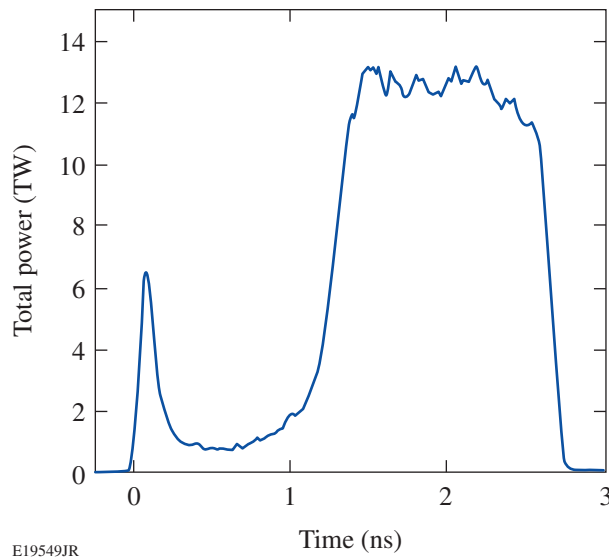
The fuel assembly was optimized in previous work,^{18,21} with a predicted peak ρR of $\sim 0.4 \text{ g/cm}^2$ and ρ_{max} of $\sim 150 \text{ g/cm}^3$ for an empty-shell target. Secondary proton measurements with symmetrically irradiated $40\text{-}\mu\text{m}$ spherical plastic shells filled



E19548JR

Figure 125.13

(a) Photograph of a gold re-entrant cone target; (b) cross-sectional drawing through the shell and cone tip with target dimensions.



E19549JR

Figure 125.14
Drive-laser pulse shape (shot 55154).

with 25 atm of D_2 gas demonstrated a fuel assembly close to the 1-D prediction, a measured neutron-averaged ρR of 0.15 g/cm^2 , and a peak ρR of 0.26 g/cm^2 (Ref. 18).

The 1053-nm-wavelength short pulse from the OMEGA EP laser had an energy of $\sim 1 \text{ kJ}$ and a 10-ps duration and was focused to a spot with a radius of $R_{80} = (26 \pm 2) \mu\text{m}$ and containing 80% of the laser energy. A high-resolution wavefront sensor measured the on-shot fluence distribution in the focal plane of the OMEGA EP pulse at full energy.²² More than 30% of the laser energy had an intensity $> 1 \times 10^{19} \text{ W/cm}^2$, while the average intensity within R_{80} was $(6 \pm 2) \times 10^{18} \text{ W/cm}^2$. The focal pattern and R_{80} varied slightly from shot to shot. A picture of the focal spot can be found in Ref. 23.

A high laser contrast, defined as the ratio of the peak power to the power of the pedestal before the main pulse, is critical for cone-in-shell fast ignition,²⁴ requiring careful characterization of the prepulse. A nanosecond prepulse caused by front-end parametric fluorescence preceded the OMEGA EP pulse, which was spatially and temporally resolved.²⁵ The on-shot temporal contrast was measured with a set of calibrated fast photodiodes. The measured power and energy contrast were $(3.1 \pm 0.5) \times 10^6$ and $(4.6 \pm 0.9) \times 10^4$, respectively, leading to a prepulse energy of $\sim 22 \text{ mJ}$ for a 1-kJ main-pulse energy. The prepulse is described by a Gaussian with FWHM of 0.9 ns and a peak 1 ns before the main pulse. [See Fig. 1(b) in Ref. 23.] The focal spot of the prepulse was measured to have a diameter of $39 \pm 3.5 \mu\text{m}$ FWHM, resulting in a prepulse intensity of $(1.7 \pm 0.4) \times 10^{12} \text{ W/cm}^2$.

Shock-Breakout Measurements

The compressing shell pushes a jet of plasma material toward the cone tip,¹⁷ heating the plasma to a temperature $> 1 \text{ keV}$ and creating a shock wave through the cone wall. Shock-breakout measurements²⁶ were performed by imploding the shell without a short-pulse beam, using targets with a $40\text{-}\mu\text{m}$ -diam flat tip and thicknesses between 5 and $15 \mu\text{m}$ (Fig. 125.15). When the shock wave reached the inner cone surface, it generated optical emission inside the hollow cone, which was measured and temporally resolved with a streaked optical pyrometer (SOP)²⁷ in the wavelength range ~ 600 to $\sim 750 \text{ nm}$ and a velocity interferometer system for any reflector (VISAR)²⁸ at a wavelength of 532 nm . Figure 125.15(b) shows the measured SOP signal as a function of time for a $14\text{-}\mu\text{m}$ -thick tip. The optical emission suddenly rises when the shock breaks out at 3.72 ns . SOP integrates over a time period of 150 ps , determined by the slit width and the sweep speed of the streak camera. The signal is differentiated with respect to time and the first peak determines shock breakout with an accuracy of $\pm 30 \text{ ps}$.²⁷ VISAR achieves a higher precision of $\pm 10 \text{ ps}$ in measuring shock breakout because of a faster streak camera.²⁸ Figure 125.15(c) shows the time of shock breakout as a function of tip thickness. The red circles are the VISAR and the blue squares the SOP measurements. Except for one shot at $10 \mu\text{m}$, there is good agreement between both diagnostics within their error bars. With increasing tip thickness, the breakout is delayed. For thicknesses of 10 and $15 \mu\text{m}$, the shock-breakout time was $3.70 \pm 0.03 \text{ ns}$ and $3.76 \pm 0.03 \text{ ns}$, respectively. The red line is a weighted fit through all the data points.

The implosion of the cone-in-shell target and the shock propagation through the cone wall were simulated with the 2-D hydrodynamics code *SAGE*²⁹ in cylindrical geometry. Figure 125.16 shows a sequence of frames with zoomed images of the cone tip at times around peak compression. The first frame at 3.46 ns shows an intact cone tip when the shock wave just starts to enter the cone wall. At 3.50 ns the shock has propagated about halfway through the cone wall, pushing the outside cone wall back by $\sim 5 \mu\text{m}$, but has not broken out at the inner wall. In the simulation, the shock breaks through at 3.54 ns , $\sim 0.2 \text{ ns}$ before the experimentally measured breakout time of 3.76 ns . After shock breakout, the cone is predicted to very rapidly fill up with plasma below solid density but above the critical density of the short-pulse laser. A run with a $10\text{-}\mu\text{m}$ flat tip shows very similar shock behavior and a slightly earlier (40 ps) breakout time. No breakout measurements are available for the $10\text{-}\mu\text{m}$ flat tip. Using the relative timing from the simulations and the absolute timing from the measurements, the breakout time for $10\text{-}\mu\text{m}$ flat and

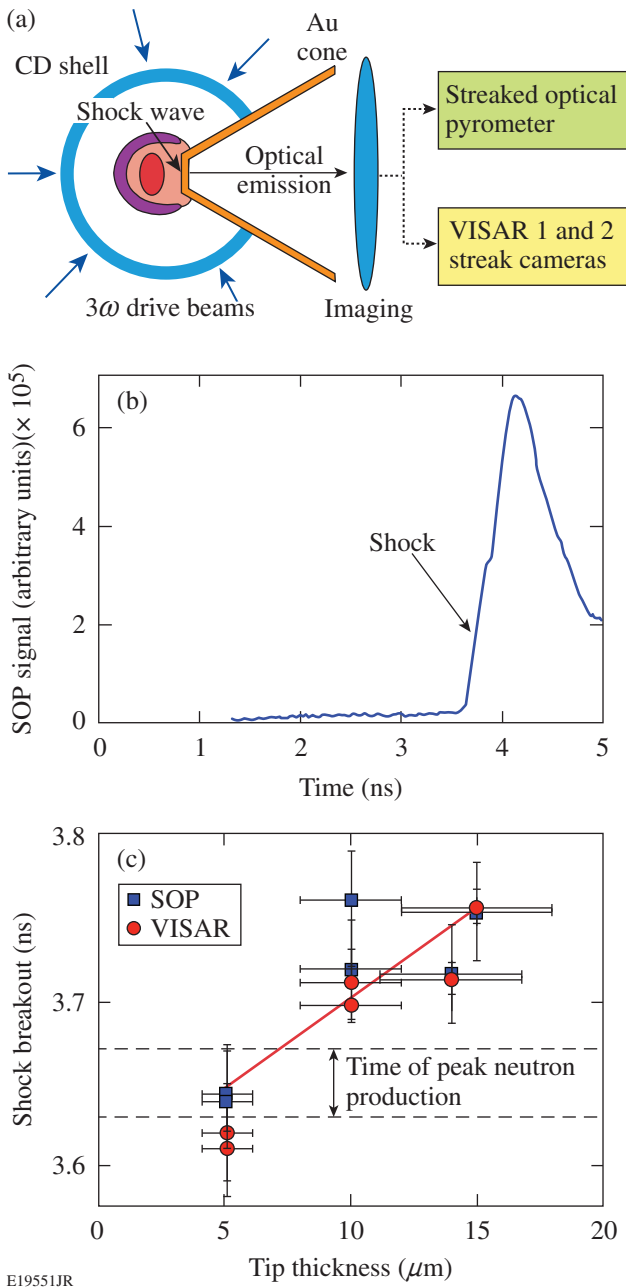


Figure 125.15

(a) Schematic of the shock-breakout experiment. The CD shell was imploded using just the long-pulse, 351-nm drive beams, resulting in shock propagation through the tip of the cone. Emergence of the shock at the inside of the tip was diagnosed using a streaked optical pyrometer (SOP) and VISAR. (b) SOP trace for a typical shot and (c) measured breakout time inside the cone for various tip thicknesses. The breakout is later for thicker cone tips.

15- μm -thick tip is extrapolated to 3.72 ± 0.03 ns. This number is compared to the measured time of peak neutron production [see **Integrated Fast-Electron-Heating Experiments**, p. 17], which results in 3.65 ± 0.02 ns for 10- μm flat, 15- μm -thick tips.

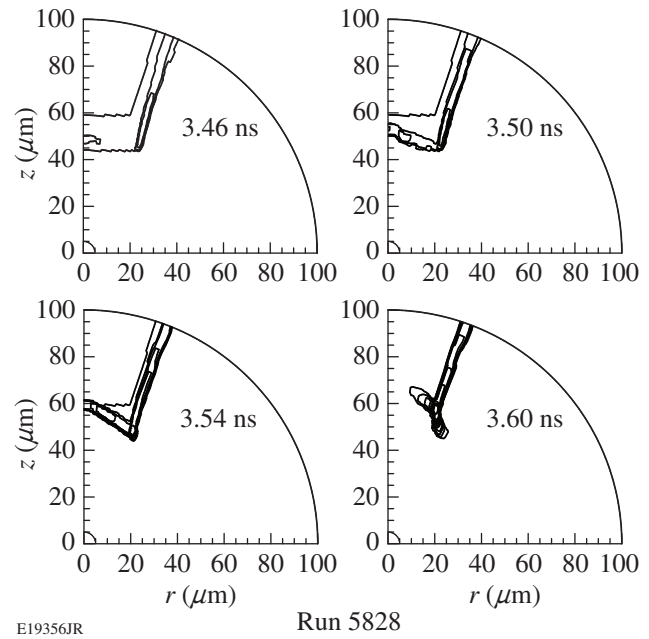
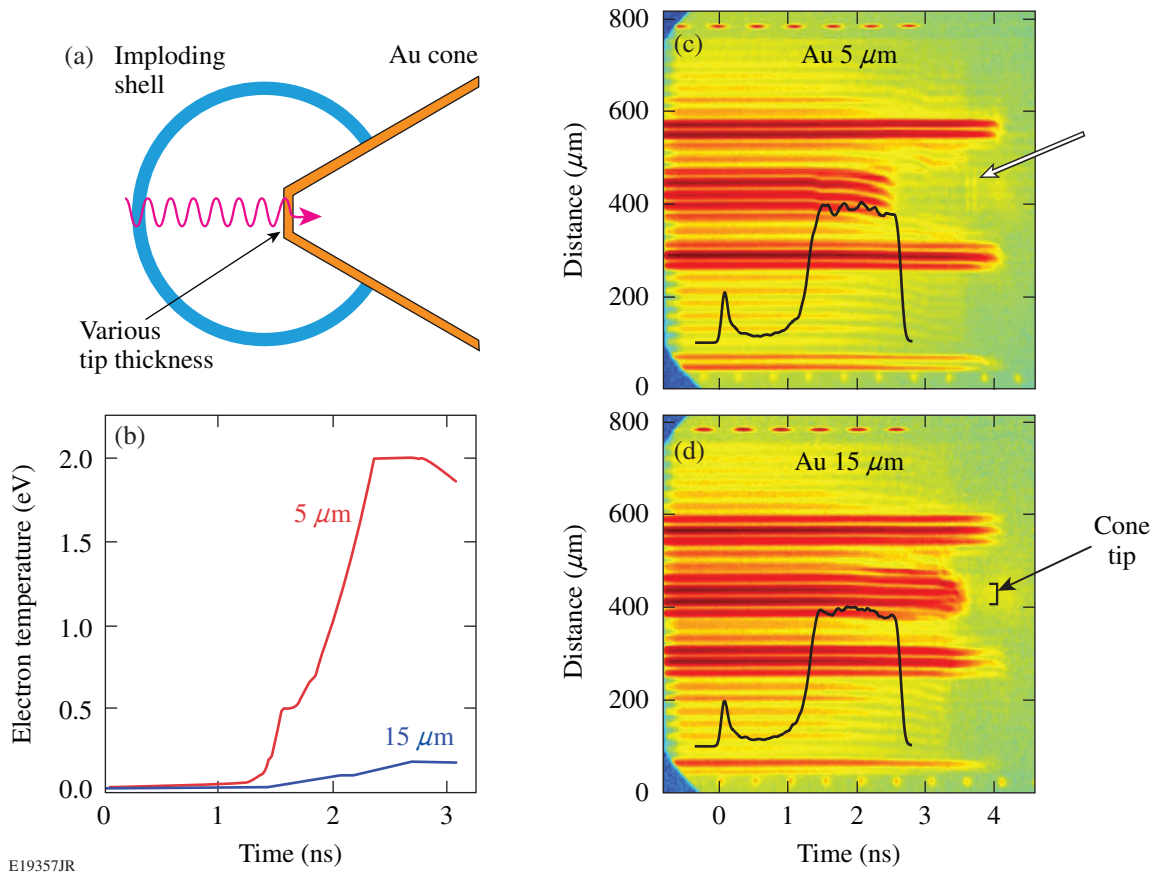


Figure 125.16

Sequence of density contours above 10 g/cm^3 in the tip of a Au cone from a 2-D *SAGE* simulation, showing the rapid propagation of a strong shock wave through a 15- μm cone tip. The fuel assembly from a cone-in-shell target (not shown) generates the shock. The shock propagates faster through the cone tip than through the wall.

Shock breakout appeared 70 ± 36 ps after the peak of neutron production, confirming that the cone tip was intact at optimum OMEGA EP timing.

The VISAR measurements indicate that preheat can lead to a premature release of material inside the hollow cone if the cone wall is not thick enough. X-ray radiation in the ~ 5 - to 10-keV photon range from the shell plasma can preheat the cone tip, as shown in Fig. 125.17(a). The temperature at the inside of the gold wall depends on the thickness of the tip. Figure 125.17(b) shows the electron temperature as a function of time for 5- μm and 15- μm thicknesses, calculated using the radiation hydrodynamic code *LILAC*.³⁰ *LILAC* modeled the x-ray production in the corona of the imploding shell during the drive pulse and its transport to the cone tip. At 1.5 ns, when the main-pulse intensity reaches its plateau, the temperature reaches ~ 0.5 eV or ~ 6000 K in the 5- μm case, while it is much lower for 15 μm . The temperature in the 5- μm tip is higher than the melting and boiling temperatures of gold, which are 1377 K and 3129 K (Ref. 31), respectively. Temperatures as high as ~ 2 eV or $\sim 24,000$ K are calculated at the end of the drive pulse are certainly sufficient to generate a gold plasma with a low degree of ionization. This effect is clearly observed in the VISAR measurement of Fig. 125.17(c).



E19357JR

Figure 125.17

(a) Schematic for simulations of radiation preheat of the cone tip. Coronal x-ray radiation from the shell driven by the strong UV pulse can penetrate through the cone wall, preheating the gold material. (b) Calculated electron temperature at the inside of the cone tip for 5- μm and 15- μm thicknesses. (c) VISAR trace for a 5- μm thickness; the disappearance of the fringes at ~ 2.5 ns indicate preheat. The white arrow marks the optical emission at the shock-breakout time. (d) VISAR trace for a 15- μm thickness, showing no attenuation before shock breakout at 3.75 ns. The brace indicates the spatial range of the flat tip. In (c) and (d) the black curve indicates the laser's temporal shape.

The fringes are formed by a probe laser reflecting from the inside of the cone tip back into an interferometer. The VISAR diagnostic is a high-resolution optical imager that projects a magnified image ($25.5\times$) of the inside of the cone onto the slits of a pair of streak camera detectors.²⁸ The system was aligned such that it imaged sharply the flat tip portion. The brace in Fig. 125.17(d) marks the spatial range, where fringes are formed through back reflection from that region. The two to three upper and lower fringes that remain up to 4 ns are due to reflection from the shelf in the cone. [See Fig. 125.13(b).] A fringe shift indicates a change in the optical path length with time, i.e., through a movement of the reflecting surface or through an increase in plasma density along the probe path. In Fig. 125.17(c) the fringes start to shift downward after the onset of the main pulse (black curve), indicating plasma formation within the cone. The velocity of the boundary of the gold plasma is predicted to steadily increase to $\sim 5 \times 10^5$ cm/s at

3 ns, consistent with the observed fringe shift. With increasing ionization, a density gradient develops in front of the reflecting surface so that eventually the probe laser is completely absorbed, explaining the disappearance of the fringes at ~ 2.5 ns. For a 5- μm thickness, breakout is measured at 3.60 ns, based on two short vertical lines [marked by the white arrow in Fig. 125.17(c)] that are created by optical self-emission from the emerging shock wave at a wavelength of 532 nm. The two lines are exactly separated by the expected etalon delay³² in the interferometer and provide a precise measurement of the breakout time. In contrast, the inner cone wall is well preserved for the 15- μm tip thickness, which is seen in Fig. 125.17(d), by the almost straight fringes up to the time of breakout.

Integrated Fast-Electron-Heating Experiments

In preparation for each integrated fast-ignition experiment, the short-pulse laser is precisely timed with respect to the drive

laser and pointed into the cone tip. The accuracy of pointing for the short-pulse laser is $\sim 15 \mu\text{m}$ as measured by x-ray pinhole images.²¹ The timing is measured *in situ* with ± 30 -ps precision at full energy by measuring the temporally resolved hard x-ray emission produced by the short-pulse laser interaction.²¹ The main diagnostic for inferring the coupling efficiency of short-pulse laser energy into the compressed core is the yield of thermonuclear neutrons that are produced by $\text{d}(\text{d},\text{n})^3\text{He}$ reactions. A new liquid-scintillator time-of-flight detector was developed to measure the neutron yield in the presence of a strong hard x-ray background from the short-pulse laser.³³ This was required because standard plastic scintillator detectors were overwhelmed by the hard x-ray radiation and did not provide a useful measurement in integrated shots.³³ The liquid scintillator detector completely suppresses the background at the time when the 2.45-MeV neutrons arrive and provides reliable neutron-yield data. The details of the new detector and background mitigation techniques in fast-ignition integrated experiments are discussed in Ref. 33. Examples of the measured neutron spectra are shown in Fig. 125.18 for different timings and two target types. The spectrum for an early arrival (3.52 ns) of the short-pulse laser is very similar to spectra obtained without the short-pulse laser. The spectrum at a later time (3.62 ns) for a 10- μm flat tip shows a significant enhanced neutron signal, while the increase is not as pronounced for the 40- μm flat tip (3.65 ns). No attempt was made to extract an ion temperature from the noisy and broadened spectra. This is because of (i) limited number of detected neutrons (~ 10 to 40 particles), (ii) neutron scattering by a 2.5-cm-thick lead plate that shielded x rays and was located in the line of sight and by other structures adjacent to the detector, and (iii) broadening effects from a relatively large (~ 3 liter) detector volume. The

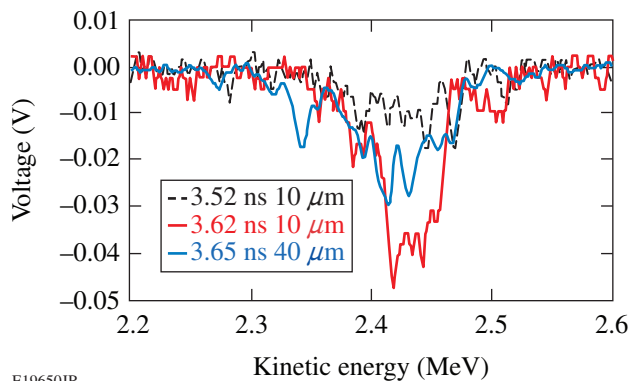


Figure 125.18 Time-of-flight spectra of 2.45-MeV neutrons from thermonuclear $\text{d}(\text{d},\text{n})^3\text{He}$ reactions in integrated fast-ignition experiments. Spectra with various timings of the OMEGA EP beam are shown for two target types.

neutron time-of-flight spectra are integrated to provide a total yield. The neutron detector was cross calibrated against another absolutely calibrated neutron detector³⁴ using a series of shots without the short-pulse laser.

The implosion produces thermonuclear neutrons in the hot, dense core surrounded by the cold shell; but neutrons are also generated in the corona of the plasma. The whole shell was deuterated and the drive laser heated the region between the critical and the ablation surface to temperatures > 1 keV, which generated a significant amount of neutrons outside the dense shell. The corona yield ($0.73 \pm 0.08 \times 10^7$) was measured in a series of shots with cone-in-shell targets without the short-pulse laser, where the inside of the shell was coated with a CH plastic layer (1 to 5 μm) to quench the yield from the target center. The neutron yield was $\sim 35\%$ lower compared to pure CD shells and did not depend on the thickness of the CH layer. Previous experiments³⁵ showed that an inner 1- μm CH layer is sufficient to quench the fusion yield from the central region. Simulations show that fast-electron heating is insignificant in the region of the corona neutrons. The amount of fast-electron energy deposited in this region is negligible compared to the fast-electron energy coupled in the central plasma region. This justifies that the corona yield is treated as an offset and is subtracted from the measured yield.

Figure 125.19 shows the measured neutron yield as a function of the arrival time of the OMEGA EP pulse in the cone. Two types of targets were used. The red circles show the results for a 10- μm tip diameter and the blue triangles for a

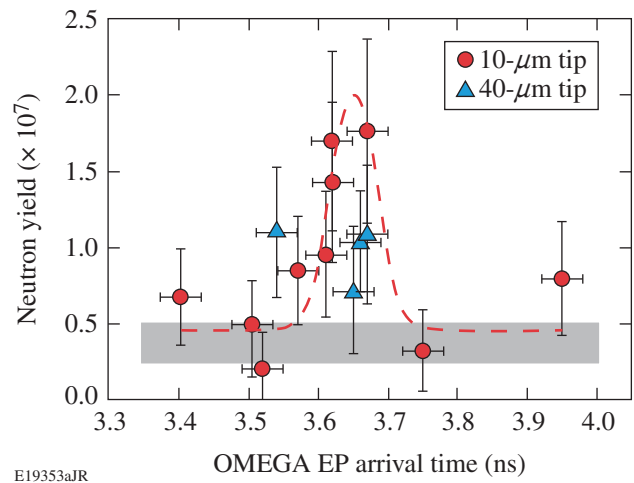


Figure 125.19 Measured neutron yield as a function of the arrival time of the short-pulse laser for two types of cone targets: 10- μm (circles) and 40- μm (triangles) tip diameter. The gray area represents data without the short-pulse laser.

larger tip ($40\ \mu\text{m}$). The $10\text{-}\mu\text{m}$ data show a peak in neutron yield at a delay time of $3.65\pm 0.02\ \text{ns}$. Most of the tips were $15\ \mu\text{m}$ thick. The dashed curve is a fit of a Gaussian profile to the red circles. The gray bar shows the yield from several shots without the short-pulse beam, measured with a different detector that had smaller yield error. Most of the null shots were taken with the $10\text{-}\mu\text{m}$ -flat-tip cone target, but some null shots were also taken with the $40\text{-}\mu\text{m}$ flat tip. The same implosion yield was measured within the measurement uncertainty. The error bars include the error caused by neutron statistics and the cross-calibration error. The uncertainty in yield without the OMEGA EP pulse, indicated by the width of the gray bar, is lower because it represents an average over many shots using the more-accurate detector. The $10\text{-}\mu\text{m}$ data show an enhancement in neutron yield by more than a factor of 4 for the smaller-tip targets and a properly timed short-pulse beam. The experiments measured $(1.4\pm 0.6)\times 10^7$ additional neutrons resulting from heating by the short-pulse laser in a narrow time window of less than 100 ps. This corresponds to a coupling efficiency of $3.5\pm 1.0\%$ of the short-pulse energy into the core.³⁶

It is expected that most of the OMEGA EP beam energy interacted with the side walls of the cone in the smaller-tip target, while a significant portion of laser energy interacted under normal incidence with the circular flat in the larger tip. It is surprising that the data from the larger tip may indicate a lower coupling efficiency. However, only four shots have been taken with this target type to date and more experiments are required covering a larger time range of OMEGA EP arrival times. The neutron peak might be shifted for the $40\text{-}\mu\text{m}$ tip. Hydrodynamic simulations are very similar for both targets and timing shifts of more than 50 ps are not expected. Possible causes for the difference in neutron yield are higher fast-electron conversion efficiency in the smaller tip and better electron transport. Intense laser-plasma interaction with cone-like structures might lead to a higher conversion efficiency into fast electrons³⁷ and enhanced surface acceleration of fast electrons.³⁸ It is expected that the density scale length plays an important role in the conversion efficiency and the directionality of the fast electrons.³⁹ A better understanding requires characterization of the preplasma (see below) and PIC simulations of the laser-plasma interaction.

Fast electrons that escaped the target were measured in two different directions with two absolutely calibrated electron spectrometers based on permanent magnets and image plates.⁴⁰ The spectrometers covered the energy range from 0.1 to 100 MeV. Figure 125.20 shows measured spectra in the laser's forward direction and sideways (at an angle of 79° to

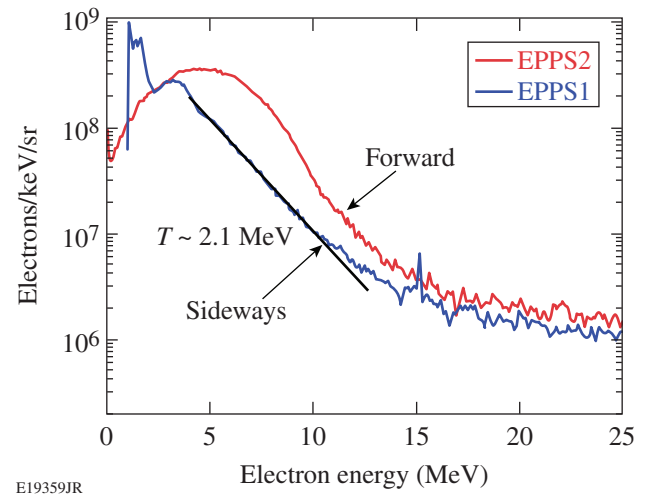


Figure 125.20

Fast-electron spectra measured in the laser's forward direction (red curve) and perpendicular to the laser direction (blue curve) (shot 59124).

the laser axis). The spectra were measured simultaneously. Significant numbers of electrons were measured with kinetic energies up to several tens of MeV in both directions. The total number of escaped electrons was $\sim 40\%$ higher in the forward direction. The mean energy averaged over the whole range was $\sim 5.1\ \text{MeV}$ in the forward direction and $\sim 3.7\ \text{MeV}$ sideways. The slope temperature of the sideways curve is about 2 MeV in the 5- to 10-MeV range and is significantly higher than that expected based on ponderomotive scaling of the average laser intensity in vacuum. It is interesting to note that in the range up to 2 MeV, $\sim 10\times$ more fast electrons are measured sideways. This might be caused by the forward-generated electrons as they are stopped in the dense fuel assembly. Another possible explanation is that strong self-generated electric and magnetic fields affect the directionality of the emitted electrons.^{41,42}

The energy spectrum of the escaped electrons is only indirectly related to that of the generated electrons.⁴² A few percent of the electrons are able to escape the target through the large Debye sheath fields that are formed at the plasma boundary. Escaping electrons lose energy to the sheath potential, which is a function of time, and therefore the spectrum of the escaping electrons is modified. Assuming that the forward-electron component is emitted into a cone with a 45° half-angle and that the colder distribution is emitted sideways from 90° to 45° with respect to the laser direction, it is estimated that the total energy carried away by the fast electrons is $\sim 7.3\ \text{J}$, which corresponds to $\sim 0.8\%$ of the OMEGA EP pulse energy. Assuming a conversion efficiency of $\sim 20\%$ to 30% of laser energy into fast electrons,^{23,43} a few percent of the fast electrons escaped

the target as expected. The estimate is not very sensitive on the half-angle of the forward-going component. For example, a total energy of ~ 5.8 J is estimated for a 10° half-angle.

The higher electron energies may be caused by cone filling by a preplasma. Self-focusing and beam filamentation in this preplasma seeded by the OMEGA EP beam nonuniformities may explain the observed hard electron spectrum.²⁴ Filamentary structures in an under-dense plasma with periodicity orthogonal to the laser beam direction can be driven by thermal,⁴⁴ ponderomotive,⁴⁵ and relativistic effects.⁴⁶ The last two are probably the dominant effects for the present experiment. An incident light beam that is slightly more intense in one region results in a lateral force, pushing the plasma electrons sideways from the region of highest laser intensity and leaving behind a region of lower electron density, n_e . This results in a transversal modulation of the index of refraction, $n = \sqrt{1 - n_e/n_c}$, where n_c is the critical density. The slightly increased index of refraction in the depleted region causes the wave front to curve in such a way that light is focused into the region of high intensity, which is counteracted by diffraction. The process leads to a positive feedback and results into what is known as the filamentation instability. Filamentation and self-focusing can therefore lead to much higher laser intensities than in vacuum and produce a hotter electron population, which was observed in this experiment. Some portion of the laser light may be transported in these filaments, at higher intensities, deeper into the preplasma. This effect was observed in 2-D PIC simulations for similar experimental conditions.²⁴

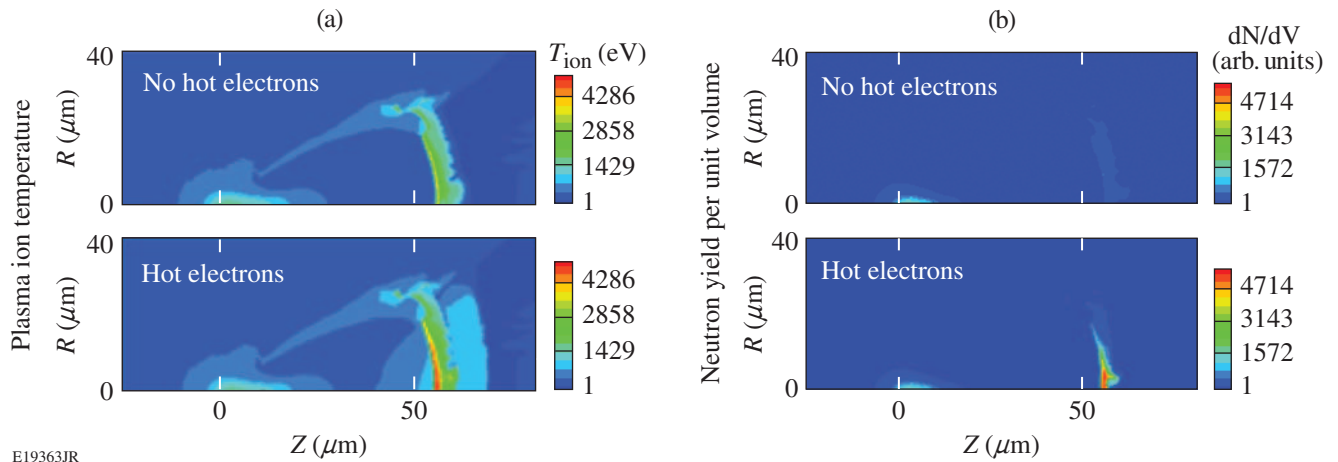
Integrated Simulations and Discussion

*DRACO*⁴⁷ + *LSP*⁴⁸ simulations were performed to estimate the coupling of fast electrons to the compressed CD.³⁶ *DRACO* simulated the fuel assembly in cylindrical geometry and was coupled with the implicit hybrid PIC code *LSP* to calculate the fast-electron propagation and energy deposition in the target.^{4,10} In the simulation, the Au cone tip had an inner diameter of $40 \mu\text{m}$, a wall thickness of $15 \mu\text{m}$, and a cone half-angle of 37° . The cone tip was $55 \mu\text{m}$ away from the center of the shell. The laser–plasma interaction was not modeled. The simulation assumed a fast-electron beam that was promoted from thermal electrons at the inside of the cone wall with an initial full-angle spread of 110° . Various experimental^{49,50} and theoretical work⁵¹ indicates that a full angle of about 100° for the MeV electrons is a reasonable number for the initial divergence angle. The electron-transport calculation through the gold cone included scattering. Similar to the experimental observation, the injection time of the fast electrons was chosen ~ 50 ps before shock breakout at a time when the shock wave

was transiting through the cone wall. An exponential energy distribution was assumed for the fast electrons with a mean energy given by the maximum of the ponderomotive⁵² and Beg⁵³ scalings. The total energy of the fast electrons generated at the inside cone wall contained 16% of the OMEGA EP beam energy with a fast-electron temperature of ~ 0.3 MeV.

Initial *DRACO* runs without the OMEGA EP beam yielded higher neutron numbers than measured, indicating higher density and temperature in the simulation. The fusion-reaction rate is highly sensitive to the density and temperature distribution in the assembled fuel. Beside an over-predicted density, mainly the higher temperature leads to a higher yield because the fusion reactivity roughly varies with the fourth power of the ion temperature in the range of interest. A number of effects contribute to the over-prediction. Radiation transport was not included and a uniform drive over the shell was assumed that is too optimistic. Low-adiabat implosions with plastic shells and high-convergence ratio are strongly RT unstable during the deceleration phase, giving rise to mixing of cold-shell material into hotter parts of the plasma, which quenches the fusion reaction and leads to lower temperatures than predicted.¹⁸ The presence of the cone also leads to a reduction in ion temperature. Neutron and proton measurements from D^3He -filled cone-in-shell targets have shown that measured ion temperatures are a factor of 2 lower than predicted, while ρR is reduced by only 30%.²⁶ This shows that the cone affects the ion temperature much more than ρR . The ion temperature was, therefore, reduced in the simulation to obtain a neutron yield consistent with the experiment. To match the neutron yield when the OMEGA EP beam is not fired, the temperature had to be reduced by a factor of 2.1 in the shell and a factor of 1.4 in the plasma region in front of the cone tip, which was heated by a shock that bounced back from the cone tip.

Figure 125.21(a) shows the ion temperature of the target without and with hot-electron heating. The simulation shows that the imploded shell material was pushed against the cone tip and was heated strongly up to ~ 2 keV. Fast electrons deposited more than 50% of their energy in the cone wall, which was strongly heated. Radiation cooling was not included in the simulation, and the temperature in gold was artificially clamped to 1 keV. Most of the fast electrons that were transmitted through the cone wall deposited their energy in the lower-density plasma ($> 2 \text{ g/cm}^3$) close to the tip of the cone between the tip and the core. From Fig. 125.21(b), the peak neutron-production density occurred at the core in the absence of hot electrons. With hot electrons, the neutron-production density is largest just to the left of the tip of the cone ($Z \approx 60 \mu\text{m}$). The simulation obtained



E19363JR

Figure 125.21

DRACO + LSP simulation for a 10-ps, 1.0-kJ, $R_{80} = 27\text{-}\mu\text{m}$ OMEGA EP pulse, showing contours of (a) plasma ion temperature and (b) neutron yield per unit volume, with and without hot electrons produced by the OMEGA EP pulse.

a neutron-yield enhancement of 1.4×10^7 , which required that $3.5 \pm 1.0\%$ of the OMEGA EP energy was coupled into the CD by fast electrons. Some fraction of fast electrons left the target without significant heating. According to the simulation, only about 0.4% of the OMEGA EP energy coupled to densities above 100 g/cm^3 .

The current results are now compared to previous integrated experiments. An integrated experiment performed on Rutherford Appleton Laboratory's VULCAN Laser studied the flux of high-intensity laser-generated electrons via a hollow cone into a laser-imploded plasma.⁴² The shell was imploded by six 900-J, 1-ns laser beams at $1.05\text{-}\mu\text{m}$ wavelength, and a 10-ps, 70-J laser pulse was focused into a hollow Au cone with a peak intensity of $\sim 3 \times 10^{18}\text{ W/cm}^2$ in vacuum. The compressed densities and areal densities were more than an order of magnitude lower than in the present case. The cone had similar dimensions with a tip thickness of $10\text{ }\mu\text{m}$. The flux of high-energy electrons traversing the imploded CD was determined from comparing the measured K_α fluorescence yield from a Cu dopant in the shell to Monte Carlo simulations that modeled the fast-electron transport in the CD and calculations of the K_α yield. It was estimated that $\sim 7\%$ to 22% of the short-pulse laser energy was converted into fast electrons in the CD, depending on the assumed hot-electron temperature.⁴² This number seems higher than what is reported here, but electron-transport modeling indicates that only a small fraction of the fast-electron energy ($\sim 9\%$) was actually deposited into the CD in the VULCAN experiment. The model in Ref. 42 did not include the physics of electron transport in the cone wall, which might affect the inferred coupling efficiency. Our modeling shows that fast-

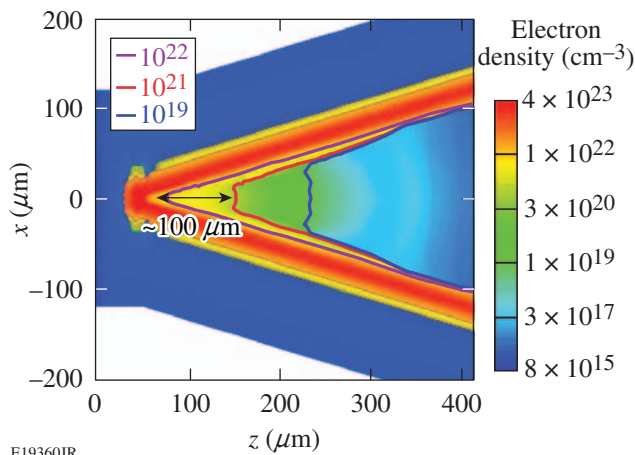
electron transport is very sensitive to scattering in the high-Z material and is influenced by resistive magnetic fields at the high-Z cone walls.³⁶

Integrated experiments were performed about a decade ago on the GEKKO XII Laser System in Japan.¹² A $500\text{-}\mu\text{m}$ -diam, $7\text{-}\mu\text{m}$ -thick CD shell was imploded by nine beams at a wavelength of $0.53\text{ }\mu\text{m}$ and with an energy of 2.5 kJ with 1.2-ns, flat-top pulses. The compressed density was estimated with 50 to 100 g/cm^3 . Similar peak densities were obtained in our experiment but with significantly higher drive energy and a shaped UV drive pulse. No shock-breakout measurements were reported in Ref. 12. With a 300-J, 0.6-ps (0.5-PW) heating beam, $\sim 2 \times 10^7$ neutrons were reported compared to 2 to 5×10^4 with no heating beam. The time window in which the enhancement was observed was ~ 80 ps, which is very similar to our measurement. Simple predictions of the neutron yield normalized to the yield without heating were used to derive a coupling of 15% to 30% of laser energy to core heating.¹² These numbers are considerably higher than the number reported here. The coupling efficiency here is based on comparing the measured heating neutron yield to more sophisticated integrated simulations that include the hydrodynamics and the fast-electron transport through the cone wall and into the fuel assembly. Possible explanation of the difference in coupling efficiency is a different level of preplasma formation.

Recent integrated experiments at GEKKO XII with the new LFEX short-pulse laser⁵⁴ were not able to reproduce the previous results and measured neutron yields are significantly lower.⁵⁵ This is attributed to the formation of a preplasma in the

cone by a laser prepulse or pedestal. Short-pulse experiments with cone-like structures on the TITAN Laser at LLNL and on the LULI 100 TW Laser in France revealed the presence of preplasma over $100\ \mu\text{m}$ away from the cone tip for very similar laser contrast.^{56,57} It was shown in Ref. 24 that a preformed plasma in a hollow cone strongly influences the ultra-intense laser–plasma interaction and the hot-electron generation. The laser beam filamented in the underdense plasma and the laser energy was diverted from the cone tip for large preplasmas. The laser beam propagation halted and energetic electrons were generated mostly transverse to the incoming beam.²⁴

Two-dimensional simulations were performed with the radiation–hydrodynamics code *HYDRA*⁵⁸ to study the preplasma formation for the present case using the measured prepulse. Figure 125.22 shows the simulated density contours for the smaller tip diameter. A preplasma fills the cone, and the nonrelativistic critical density shifts $\sim 100\ \mu\text{m}$ away from the original position of the inner cone wall at the time when the main pulse is incident. Results for the larger tip were similar but had slight differences in the shape of the density contours. An experimental characterization of the preplasma in the cone is important and will be performed in the future.



E19360JR

Figure 125.22

Electron-density contours from a 2-D *HYDRA* simulation at the time of the short-pulse interaction of the preplasma formation in a gold cone with inner tip diameter of $10\ \mu\text{m}$.

The integrated simulations were based on the assumption of a relatively low fast-electron temperature from the average intensity in vacuum. More heating of the dense portion of the core is expected with a hotter-electron distribution, which is expected from laser interactions with a preformed plasma. This requires large-scale PIC simulations that model the details of

the laser–preplasma interaction and couple these results to the integrated simulations. Such large-scale PIC simulations will be performed in the future.

Summary

The fast-ignitor, cone-in-shell target concept has been investigated at the OMEGA Laser Facility. Initial integrated fast-ignition experiments with room-temperature re-entrant cone targets were performed using a shaped laser pulse to implode the capsule with 20 kJ of UV energy on a low adiabat, followed by a 1-kJ, 10-ps, short-pulse IR beam interacting with a hollow gold cone at various times with respect to the driver laser.

Shock-breakout measurements have been performed with cone-in-shell targets under the same drive conditions, but without the short-pulse laser. The measurements confirm an intact cone tip at the time of peak neutron production in the integrated shots. VISAR measurements show that Au cones with a thin tip ($5\ \mu\text{m}$) are affected by x-ray preheat that is produced in the corona of the imploding shell. This leads to premature material release inside the hollow cone, which might affect the short-pulse laser interaction. The thicker cone walls ($15\ \mu\text{m}$ Au) that were used in the integrated shots are well shielded against the x rays and are not affected by preheat.

In the integrated shots, a fourfold increase in neutron yield was observed by short-pulse heating in a narrow (~ 100 -ps) time window close to peak compression. The additional $(1.4 \pm 0.6) \times 10^7$ neutrons produced by the short-pulse beam correspond to a coupling efficiency of $3.5 \pm 1.0\%$ of short-pulse energy into the CD, according to simulations with the integrated *DRACO* + *LSP* codes.

Electrons with energies higher than 20 MeV were measured in the direction of the short-pulse laser and perpendicular to it. More escaping electrons were measured in the forward direction, integrated over the whole energy range, but for energies below 2 MeV a significant depletion was observed in the spectrum through the dense plasma.

Integrated simulations show significant target heating in the lower-density CD plasma adjacent to the cone tip, which is where most of the additional neutrons are created. The simulations assumed a hot-electron temperature based on ponderomotive scaling of the laser intensity in vacuum and no preplasma. Additional two-dimensional hydrodynamic simulations using the measured laser prepulse indicate a significant production of preplasma in the cone. Laser interaction with and filamentation in a lower-density preplasma might consequently lead to much

higher laser intensities and produce a hotter-electron distribution. There is evidence for this from the measured spectra of escaped electrons showing significantly higher mean energy than expected.

This work addresses a number of important issues for fast ignition, which include cone survivability and the tradeoff of matching the cone thickness to the fast-electron energy. More work must be done to optimize the target geometry and materials. This also includes improvements in the short-pulse–laser contrast, a smaller focus, and a higher energy. It is expected that these improvements will increase the coupling efficiency and lead to a greater enhancement in the number of neutrons. Simulations were performed with a smaller focus ($R_{80} = 15 \mu\text{m}$) and higher laser energy (2.6 kJ) without contrast degradation, leading to a fourfold increase in coupling efficiency to densities above 100 g/cm^3 . Integrated experiments with improved laser parameters will be performed in the future.

ACKNOWLEDGMENT

This work was supported by the U.S. Department of Energy Office of Inertial Confinement Fusion under Cooperative Agreement No. DE-FC52-08NA28302, the OFES Fusion Science Center grant No. DE-FC02-04ER54789, the OFES ACE Fast Ignition grant No. DE-FG02-05ER54839, the DOE Laboratory Basic Science Program, the University of Rochester, and the New York State Energy Research and Development Authority. The support of DOE does not constitute an endorsement by DOE of the views expressed in this article.

REFERENCES

- N. G. Basov, S. Yu. Gus'kov, and L. P. Feokistov, *J. Sov. Laser Res.* **13**, 396 (1992).
- M. Tabak *et al.*, *Phys. Plasmas* **1**, 1626 (1994).
- R. Betti and C. Zhou, *Phys. Plasmas* **12**, 110702 (2005).
- A. A. Solodov, K. S. Anderson, R. Betti, V. Gotcheva, J. Myatt, J. A. Delettrez, S. Skupsky, W. Theobald, and C. Stoeckl, *Phys. Plasmas* **15**, 112702 (2008).
- S. Atzeni *et al.*, *Phys. Plasmas* **15**, 056311 (2008).
- J. J. Honrubia and J. Meyer-ter-Vehn, *Plasma Phys. Control. Fusion* **51**, 014008 (2009).
- A. J. Kemp, Y. Sentoku, and M. Tabak, *Phys. Rev. Lett.* **101**, 075004 (2008).
- J. R. Davies *et al.*, *Phys. Rev. E* **56**, 7193 (1997).
- A. R. Bell and R. J. Kingham, *Phys. Rev. Lett.* **91**, 035003 (2003).
- A. A. Solodov, K. S. Anderson, R. Betti, V. Gotcheva, J. F. Myatt, J. A. Delettrez, S. Skupsky, W. Theobald, and C. Stoeckl, *Phys. Plasmas* **16**, 056309 (2009).
- P. A. Norreys *et al.*, *Phys. Plasmas* **7**, 3721 (2000).
- R. Kodama *et al.*, *Nature* **412**, 798 (2001); R. Kodama *et al.*, *Nature* **418**, 933 (2002).
- T. R. Boehly, D. L. Brown, R. S. Craxton, R. L. Keck, J. P. Knauer, J. H. Kelly, T. J. Kessler, S. A. Kumpan, S. J. Loucks, S. A. Letzring, F. J. Marshall, R. L. McCrory, S. F. B. Morse, W. Seka, J. M. Soares, and C. P. Verdon, *Opt. Commun.* **133**, 495 (1997).
- L. J. Waxer, D. N. Maywar, J. H. Kelly, T. J. Kessler, B. E. Kruschwitz, S. J. Loucks, R. L. McCrory, D. D. Meyerhofer, S. F. B. Morse, C. Stoeckl, and J. D. Zuegel, *Opt. Photonics News* **16**, 30 (2005).
- V. N. Goncharov, T. C. Sangster, T. R. Boehly, S. X. Hu, I. V. Igumenshchev, F. J. Marshall, R. L. McCrory, D. D. Meyerhofer, P. B. Radha, W. Seka, S. Skupsky, C. Stoeckl, D. T. Casey, J. A. Frenje, and R. D. Petrasso, *Phys. Rev. Lett.* **104**, 165001 (2010).
- General Atomics, San Diego, CA, 92123.
- C. Stoeckl, T. R. Boehly, J. A. Delettrez, S. P. Hatchett, J. A. Frenje, V. Yu. Glebov, C. K. Li, J. E. Miller, R. D. Petrasso, F. H. Séguin, V. A. Smalyuk, R. B. Stephens, W. Theobald, B. Yaakobi, and T. C. Sangster, *Phys. Plasmas* **14**, 112702 (2007).
- C. D. Zhou, W. Theobald, R. Betti, P. B. Radha, V. A. Smalyuk, D. Shvarts, V. Yu. Glebov, C. Stoeckl, K. S. Anderson, D. D. Meyerhofer, T. C. Sangster, C. K. Li, R. D. Petrasso, J. A. Frenje, and F. H. Séguin, *Phys. Rev. Lett.* **98**, 025004 (2007).
- T. R. Boehly, V. A. Smalyuk, D. D. Meyerhofer, J. P. Knauer, D. K. Bradley, R. S. Craxton, M. J. Guardalben, S. Skupsky, and T. J. Kessler, *J. Appl. Phys.* **85**, 3444 (1999).
- Y. Lin, T. J. Kessler, and G. N. Lawrence, *Opt. Lett.* **21**, 1703 (1996).
- W. Theobald, K. S. Anderson, R. Betti, R. S. Craxton, J. A. Delettrez, J. A. Frenje, V. Yu. Glebov, O. V. Gotchev, J. H. Kelly, C. K. Li, A. J. MacKinnon, F. J. Marshall, R. L. McCrory, D. D. Meyerhofer, J. F. Myatt, P. A. Norreys, P. M. Nilson, P. K. Patel, R. D. Petrasso, P. B. Radha, C. Ren, T. C. Sangster, W. Seka, V. A. Smalyuk, A. A. Solodov, R. B. Stephens, C. Stoeckl, and B. Yaakobi, *Plasma Phys. Control. Fusion* **51**, 124052 (2009).
- J. Bromage, S.-W. Bahk, D. Irwin, J. Kwiatkowski, A. Pruyne, M. Millecchia, M. Moore, and J. D. Zuegel, *Opt. Express* **16**, 16561 (2008).
- P. M. Nilson, A. A. Solodov, J. F. Myatt, W. Theobald, P. A. Jaanimagi, L. Gao, C. Stoeckl, R. S. Craxton, J. A. Delettrez, B. Yaakobi, J. D. Zuegel, B. E. Kruschwitz, C. Dorrer, J. H. Kelly, K. U. Akli, P. K. Patel, A. J. MacKinnon, R. Betti, T. C. Sangster, and D. D. Meyerhofer, *Phys. Rev. Lett.* **105**, 235001 (2010).
- A. G. MacPhee *et al.*, *Phys. Rev. Lett.* **104**, 055002 (2010).
- C. Dorrer, D. Irwin, A. Consentino, and J. Qiao, presented at the ICUIL 2010 Conference, Watkins Glen, NY, 26 September–1 October 2010 (Paper ThO3).
- C. Stoeckl, T. R. Boehly, J. A. Delettrez, S. P. Hatchett, J. A. Frenje, V. Yu. Glebov, C. K. Li, J. E. Miller, R. D. Petrasso, F. H. Séguin, V. A.

- Smalyuk, R. B. Stephens, W. Theobald, B. Yaakobi, and T. C. Sangster, *Plasma Phys. Control. Fusion* **47**, B856 (2005).
27. J. E. Miller, T. R. Boehly, A. Melchior, D. D. Meyerhofer, P. M. Celliers, J. H. Eggert, D. G. Hicks, C. M. Sorce, J. A. Oertel, and P. M. Emmel, *Rev. Sci. Instrum.* **78**, 034903 (2007).
 28. P. M. Celliers, D. K. Bradley, G. W. Collins, D. G. Hicks, T. R. Boehly, and W. J. Armstrong, *Rev. Sci. Instrum.* **75**, 4916 (2004).
 29. R. S. Craxton and R. L. McCrory, *J. Appl. Phys.* **56**, 108 (1984).
 30. J. Delettrez, R. Epstein, M. C. Richardson, P. A. Jaanimagi, and B. L. Henke, *Phys. Rev. A* **36**, 3926 (1987); M. C. Richardson, P. W. McKenty, F. J. Marshall, C. P. Verdon, J. M. Soures, R. L. McCrory, O. Barnouin, R. S. Craxton, J. Delettrez, R. L. Hutchison, P. A. Jaanimagi, R. Keck, T. Kessler, H. Kim, S. A. Letzring, D. M. Roback, W. Seka, S. Skupsky, B. Yaakobi, S. M. Lane, and S. Prussin, in *Laser Interaction and Related Plasma Phenomena*, edited by H. Hora and G. H. Miley (Plenum Publishing, New York, 1986), Vol. 7, pp. 421–448.
 31. D. R. Lide, *CRC Handbook of Chemistry and Physics*, 82nd ed. (CRC Press, Boca Raton, FL, 2001), p. 4-132.
 32. W. Theobald, J. E. Miller, T. R. Boehly, E. Vianello, D. D. Meyerhofer, T. C. Sangster, J. Eggert, and P. M. Celliers, *Phys. Plasmas* **13**, 122702 (2006).
 33. C. Stoeckl, M. Cruz, V. Yu. Glebov, J. P. Knauer, R. Lauck, K. Marshall, C. Mileham, T. C. Sangster, and W. Theobald, *Rev. Sci. Instrum.* **81**, 10D302 (2010); R. Lauck *et al.*, *IEEE Trans. Nucl. Sci.* **56**, 989 (2009).
 34. V. Yu. Glebov, C. Stoeckl, T. C. Sangster, S. Roberts, G. J. Schmid, R. A. Lerche, and M. J. Moran, *Rev. Sci. Instrum.* **75**, 3559 (2004).
 35. F. J. Marshall, J. A. Delettrez, R. Epstein, V. Yu. Glebov, D. R. Harding, P. W. McKenty, D. D. Meyerhofer, P. B. Radha, W. Seka, S. Skupsky, V. A. Smalyuk, J. M. Soures, C. Stoeckl, R. P. Town, B. Yaakobi, C. K. Li, F. H. Séguin, D. G. Hicks, and R. D. Petrasso, *Phys. Plasmas* **7**, 2108 (2000).
 36. W. Theobald, A. A. Solodov, C. Stoeckl, K. S. Anderson, R. Betti, T. R. Boehly, R. S. Craxton, J. A. Delettrez, C. Dorrer, J. A. Frenje, V. Yu. Glebov, H. Habara, K. A. Tanaka, J. P. Knauer, R. Lauck, F. J. Marshall, K. L. Marshall, D. D. Meyerhofer, P. M. Nilson, P. K. Patel, T. C. Sangster, W. Seka, N. Sinenian, T. Ma, F. N. Beg, and R. B. Stephens, “Integrated Fast-Ignition Core-Heating Experiments on OMEGA,” submitted to *Physical Review Letters*.
 37. W. Theobald, V. Ovchinnikov, S. Ivancic, B. Eichman, P. M. Nilson, J. A. Delettrez, R. Yan, G. Li, F. J. Marshall, D. D. Meyerhofer, J. F. Myatt, C. Ren, T. C. Sangster, C. Stoeckl, J. D. Zuegel, L. Van Woerkom, R. R. Freeman, K. U. Akli, E. Giraldez, and R. B. Stephens, *Phys. Plasmas* **17**, 103101 (2010).
 38. H. Habara *et al.*, *Phys. Rev. Lett.* **97**, 095004 (2006).
 39. M. I. K. Santala *et al.*, *Phys. Rev. Lett.* **84**, 1459 (2000).
 40. H. Chen *et al.*, *Rev. Sci. Instrum.* **79**, 10E533 (2008).
 41. T. Yabuuchi *et al.*, *New J. Phys.* **11**, 093031 (2009).
 42. M. H. Key, J. C. Adam, K. U. Akli, M. Borghesi, M. H. Chen, R. G. Evans, R. R. Freeman, H. Habara, S. P. Hatchett, J. M. Hill, A. Heron, J. A. King, R. Kodama, K. L. Lancaster, A. J. MacKinnon, P. Patel, T. Phillips, L. Romagnani, R. A. Snavely, R. Stephens, C. Stoeckl, R. Town, Y. Toyama, B. Zhang, M. Zepf, and P. A. Norreys, *Phys. Plasmas* **15**, 022701 (2008).
 43. C. D. Chen *et al.*, *Phys. Plasmas* **16**, 082705 (2009).
 44. O. Willi and P. T. Rumsby, *Opt. Commun.* **37**, 45 (1981).
 45. B. I. Cohen and C. E. Max, *Phys. Fluids* **22**, 1115 (1979).
 46. C. Max, J. Arons, and A. B. Langdon, *Phys. Rev. Lett.* **33**, 209 (1974).
 47. P. B. Radha, T. J. B. Collins, J. A. Delettrez, Y. Elbaz, R. Epstein, V. Yu. Glebov, V. N. Goncharov, R. L. Keck, J. P. Knauer, J. A. Marozas, F. J. Marshall, R. L. McCrory, P. W. McKenty, D. D. Meyerhofer, S. P. Regan, T. C. Sangster, W. Seka, D. Shvarts, S. Skupsky, Y. Srebro, and C. Stoeckl, *Phys. Plasmas* **12**, 056307 (2005).
 48. D. R. Welch *et al.*, *Nucl. Instrum. Methods Phys. Res. A* **464**, 134 (2001).
 49. M. Storm, A. A. Solodov, J. F. Myatt, D. D. Meyerhofer, C. Stoeckl, C. Mileham, R. Betti, P. M. Nilson, T. C. Sangster, W. Theobald, and C. Guo, *Phys. Rev. Lett.* **102**, 235004 (2009).
 50. J. S. Green, V. M. Ovchinnikov, R. G. Evans, K. U. Akli, H. Azechi, F. N. Beg, C. Bellei, R. R. Freeman, H. Habara, R. Heathcote, M. H. Key, J. A. King, K. L. Lancaster, N. C. Lopes, T. Ma, A. J. MacKinnon, K. Markey, A. McPhee, Z. Najmudin, P. Nilson, R. Onofrei, R. Stephens, K. Takeda, K. A. Tanaka, W. Theobald, T. Tanimoto, J. Waugh, L. Van Woerkom, N. C. Woolsey, M. Zepf, J. R. Davies, and P. A. Norreys, *Phys. Rev. Lett.* **100**, 015003 (2008).
 51. C. Ren *et al.*, *Phys. Plasmas* **13**, 056308 (2006).
 52. S. C. Wilks and W. L. Kruer, *IEEE J. Quantum Electron.* **33**, 1954 (1997).
 53. F. N. Beg *et al.*, *Phys. Plasmas* **4**, 447 (1997).
 54. J. Kawanaka *et al.*, *J. Phys., Conf. Ser.* **112**, 032006 (2008).
 55. H. Azechi, *Bull. Am. Phys. Soc.* **55**, 291 (2010).
 56. L. Van Woerkom *et al.*, *Phys. Plasmas* **15**, 056304 (2008).
 57. S. D. Baton *et al.*, *Phys. Plasmas* **15**, 042706 (2008).
 58. M. M. Marinak *et al.*, *Phys. Plasmas* **3**, 2070 (1996).

Submicrometer-Resolution Mapping of Ultraweak 355-nm Absorption in HfO₂ Monolayers Using Photothermal Heterodyne Imaging

Introduction

Thin-film coatings for near-ultraviolet (UV), nanosecond (ns)-pulse-laser applications are usually comprised of metal oxide as the high-index component and silica oxide as the low-index material. High-resolution studies of laser-damage morphology¹ reveal two important facts about ns-pulsed-laser damage in these coatings: First, metal oxide is the weakest part and is where damage is initiated. Second, at close-to-threshold conditions, damage takes the form of submicrometer-sized craters. Such morphology indicates that the damage process starts at isolated sites and can be linked to localized absorbers, like few-nanometer-sized metal clusters,² or high-density electronic defect areas. Deposition of metal oxide using metal as a starting material provides the possibility for cluster formation. On the other hand, electronic defects are always present in metal-oxide dielectric materials, even in bulk form.³ In thin-film coatings, characterized by columnar structure and large internal surfaces, submicrometer-scale electronic defect density enhancements might be expected. Clarification of the exact nature and distribution of damage precursors is essential for further improvements in damage resistance of coating materials. In this work, we make an attempt to evaluate spatial distribution of absorbers in hafnia (HfO₂) monolayers by using photothermal heterodyne imaging (PHI).⁴ High sensitivity to absorption and true submicrometer resolution of this technique, developed specifically for nanoscale absorber detection and characterization, was demonstrated^{4,5} by imaging embedded gold nanoparticles with the smallest diameter of 1.4 nm. To gain insight into the damage mechanism, our present study of PHI mapping of hafnia monolayers before and after laser irradiation is complemented by atomic force microscopy (AFM) analysis of damage morphology. This article is organized as follows: first, we describe the PHI principle, setup for sample mapping, and system calibration; then sample preparation and characterization, followed by the results of PHI mapping of differently prepared HfO₂ monolayers prior to laser irradiation. Next, we present the results of damage-site mapping using PHI and AFM and discuss possible damage mechanisms and the nature of damage-initiating absorbers. Finally, the conclusions are presented.

Experimental

1. The PHI Principle and Setup

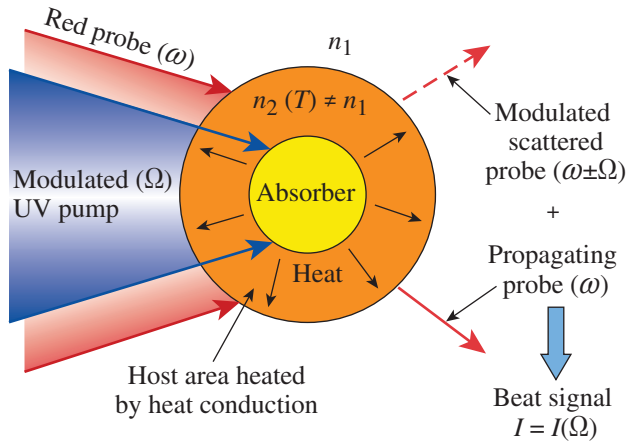
Like other versions of photothermal techniques, PHI relies on the presence of a modulated pump beam that causes local modulated heating of the material and of a probe beam that experiences modification (deflection, focusing, scattering, etc.) while passing through the heated volume. In the case of PHI (see Fig. 125.23), both the pump and probe beams are focused into an overlapping, very tight, preferably diffraction limited spot inside the material. A very small absorbing defect, being covered by such a spot, heats up and, by heat conduction, causes the temperature T to rise in the surrounding host material. This process leads to a variation in the host refractive index n according to $n = n(T)$ and, consequently, probe light scattering. Moreover, because of scatterer-size modulation, the probe laser's frequency ω is shifted by an amount equal to the modulation frequency Ω . Following the description in Ref. 5, the interference between scattered and propagating (or reflected, for back configuration) probe light in the far field creates a beat signal with intensity $I(\Omega)$:

$$I(\Omega) \sim I_{\text{pump}} I_{\text{probe}} n \partial n / \partial T \lambda^{-2} w^{-1} F(\Omega),$$

where I_{pump} and I_{probe} are the pump and probe intensities, λ and w are the probe wavelength and beam waist, respectively, and $F(\Omega)$ is a function describing heat conduction.

The experimental setup for PHI is shown in Fig. 125.24. A diode-pumped, continuous-wave (cw) semiconductor laser operating at 355-nm, 40-mW maximum output power (6 mW on sample) served as the pump laser, and a HeNe laser [633 nm, 10 mW (5 mW on sample)] was used as the probe. An acousto-optic modulator provided pump modulation in the frequency range of 100 kHz to 1 MHz, and only one beam diffracted into the first order was used as a pump. Pump and probe beams were combined at the entrance of the 40 \times , 0.95-N.A. (numerical aperture) microscope objective focusing both beams onto the sample mounted on the nanopositioning stage (Physik Instrumente). The stage had a minimum lateral step size of 10 nm, a maximum scan size of 200 μm , and an axial displacement of

20 μm . Probe light can be collected by either the same objective (back configuration) or an additional lens (forward configuration) and detected by a fast photodiode, lock-in amplifier (30-ms integration time), and a LabView-based data acquisition system. In the case of a back configuration, a quarter-wave plate and polarizing beam splitter were added to isolate the signal beam from the source. A detailed analysis of signals detected in either configuration can be found in Ref. 5. In this work, most measurements were performed using a forward configuration and 350-kHz modulation frequency.

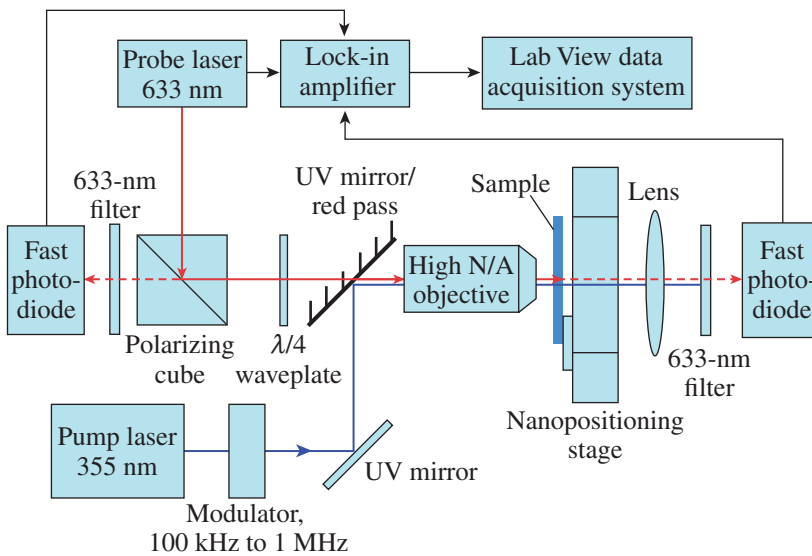


G9131JR

Figure 125.23
Schematic of photothermal heterodyne signal formation.

2. PHI-Setup Characterization and Calibration

Pump- and probe-beam focus spots were combined and characterized using a 1- μm pinhole in a metal foil. The pinhole was mounted on the nanopositioning stage using a sample holder and scanned across the beam. A corresponding image of the pump and probe beams' combined focal spot is shown in Fig. 125.25. A cross section through this image gives a full-width-at-half-maximum (FWHM) value of 0.79 μm , which should be considered an upper limit because of the transfer function of the pinhole. We estimated a real FWHM value $\sim 10\%$ to 15% smaller, or $\sim 0.7 \mu\text{m}$. Using this beam size and a maximum UV power on the sample of 6 mW, maximum power densities on the sample did not exceed $\sim 1.6 \text{ MW}/\text{cm}^2$. For the system's spatial resolution and sensitivity characterization, we used 5- to 14-nm-diam isolated gold nanoparticles embedded inside silica film.⁶ Figure 125.26 presents a 6- μm PHI scan and cross-sectional data for a sample with 14-nm particles, which show that a single particle is imaged as a feature with FWHM = 0.42 μm and that two particles separated by 0.55 μm can be clearly resolved. Also, particles as small as 5 nm were imaged using this setup. These calibration results proved both the true submicron spatial resolution and high sensitivity of the system. To characterize setup response in the case of homogeneous absorption, a TiO_2 film of $\sim 200\text{-nm}$ thickness and 49% transmission at 355 nm was deposited on a fused-silica substrate. Figure 125.27 shows PHI signal dependence as a function of the pump laser's output power. It should be



G9132JR

Figure 125.24
PHI setup for signal detection in a forward and backward configuration.

noted here that starting with powers of a few mW or higher, the signal declined as the exposure time was increased. Data shown in Fig. 125.27 were taken right after the beam shutter was opened. This effect can be attributed to some kind of sample bleaching during exposure. Consequently, it indicates that a strongly absorbing TiO₂ film is not the best solution to calibrate systems that rely on tightly focused beams. Still, with

a measured noise level of 0.5 μV and maximum PHI signal detected $\sim 6000 \mu\text{V}$, the signal-to-noise ratio was $>10^4$, which proves the high sensitivity of this PHI setup.

3. HfO₂ Sample

HfO₂ thin-film monolayer coatings, 179 nm thick (1-wave optical thickness at 355 nm), were deposited by electron-beam (e-beam) evaporation using either conventional or plasma-assisted (argon/oxygen mixture) deposition. The conventional e-beam deposition rate was 1.2 $\text{\AA}/\text{s}$ and the oxygen pressure was 8×10^{-5} Torr; in the case of the plasma-assisted deposition, the rate was $-0.8 \text{\AA}/\text{s}$ and the plasma source was operated at 180 V, 35 A. The latter was deliberately not optimized in order to produce samples with varying absorption for the same film thickness. In addition, 45-nm-thick (1/4-wave) HfO₂ film was prepared by conventional e-beam deposition to investigate PHI signal variation with film thickness. To create insulation from defects introduced by the polishing process, UV-grade

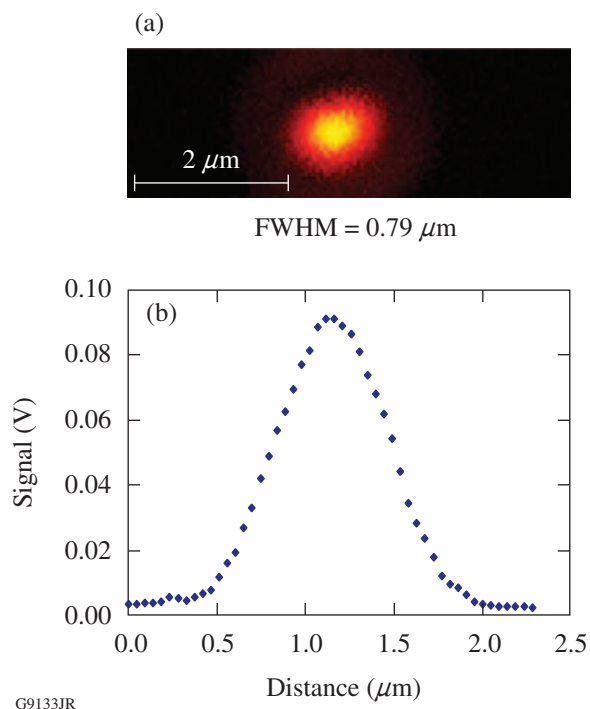


Figure 125.25
Characterization of the combined focal spot of 355-nm pump and 633-nm probe beams: (a) image of the focal spot obtained with a 1- μm pinhole; (b) cross-sectional profile.

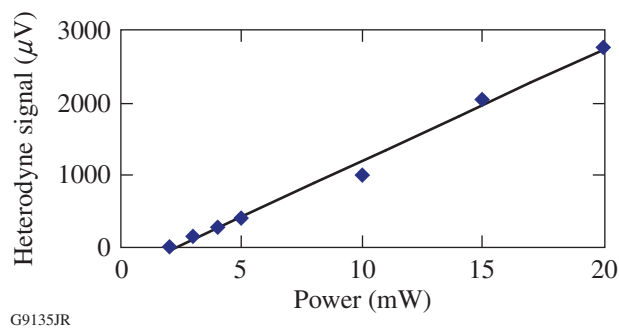


Figure 125.27
PHI signal from homogeneously absorbing TiO₂ thin-film sample as a function of 355-nm pump output power.

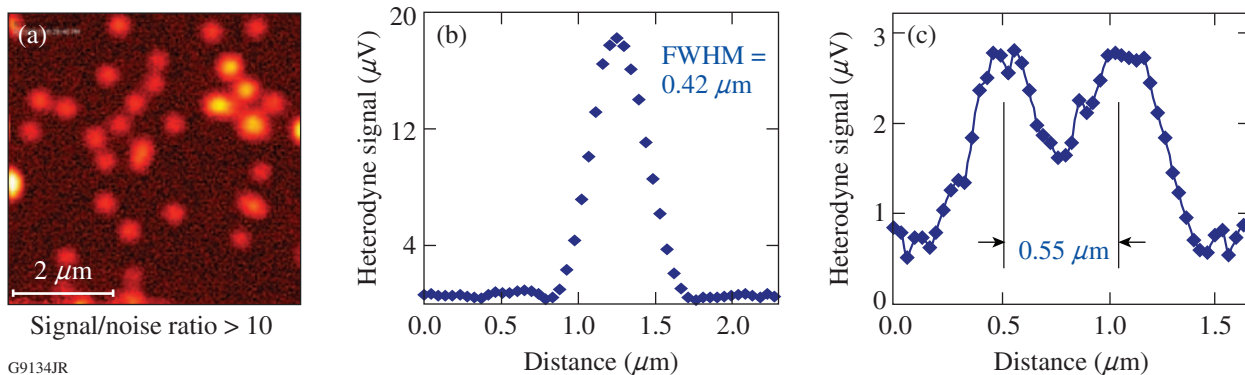


Figure 125.26
PHI calibration using embedded 14-nm gold nanoparticles: (a) $6 \times 6\text{-}\mu\text{m}$ PHI image, (b) single-particle signal profile, and (c) signal profile for two particles separated by 0.55 μm .

fused-silica substrates were coated first by a 1- μm -thick SiO_2 layer [see Fig. 125.28(a)]. Next, in the same coating run, HfO_2 films of appropriate thickness were deposited. The E-field intensity distribution peaked at both interfaces and in the bulk of the 1-wave-thick film [Fig. 125.28(b)] and had only one peak at the $\text{HfO}_2/\text{SiO}_2$ interface in the case of 1/4-wave film [Fig. 125.28(c)]. This information is important for the analysis of the PHI signal versus film-thickness variation.

4. Damage Testing and Damage Morphology

The PHI mapping of HfO_2 monolayers was complemented by damage-threshold and morphology studies using 351-nm, 0.5-ns pulses from a Nd-doped glass laser. Damage thresholds

(1-on-1 mode) were measured using 110 \times magnification, dark-field microscopy, and damage morphology was investigated by means of AFM. Note that the 355-nm wavelength of the pump laser for the PHI technique is very close to the 351-nm wavelength of the damage-test laser, which allows one to establish correlation between measured PHI signals and damage-threshold values.

Results and Discussion

1. PHI Imaging of HfO_2 Films Prior to Irradiation

Photothermal images of HfO_2 monolayer films (see Fig. 125.29) showed different absorption levels for different film thicknesses and deposition techniques but did not show

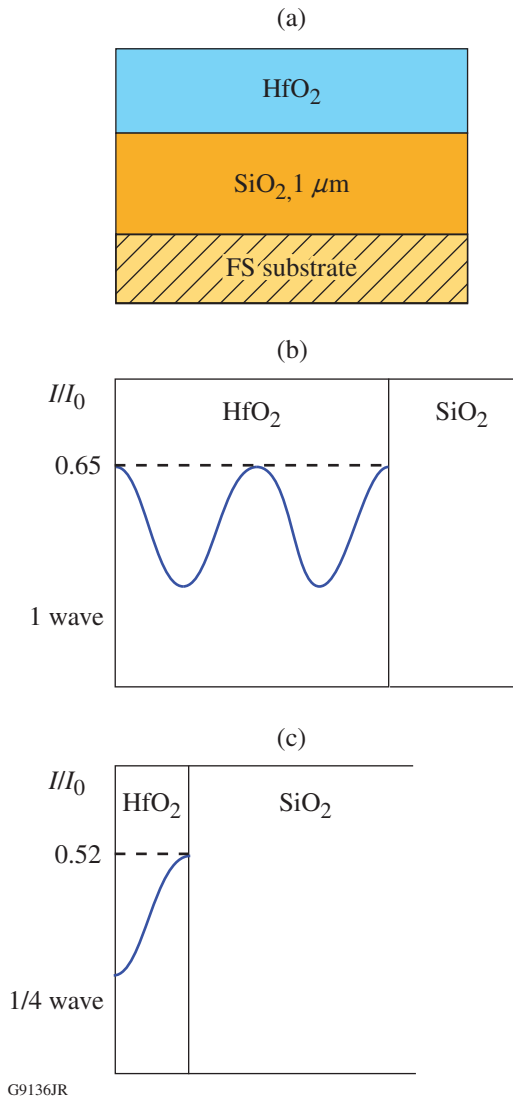


Figure 125.28 (a) Schematic of HfO_2 thin-film sample and E-field intensity distribution for (b) 1-wave-thick and (c) 1/4-wave-thick samples.

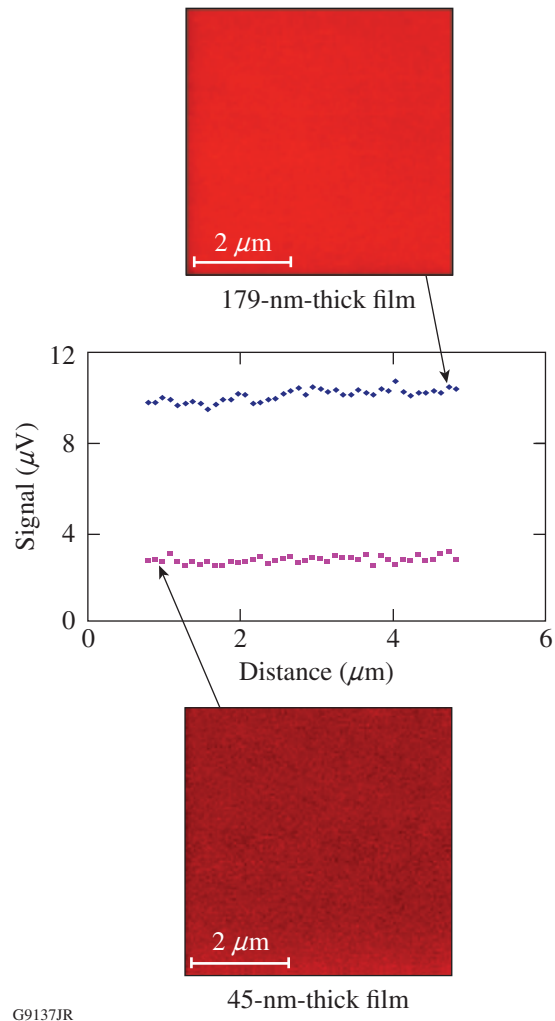


Figure 125.29 Heterodyne images and corresponding horizontal signal profiles of conventionally deposited 179-nm-thick and 45-nm-thick HfO_2 films prior to irradiation.

any structure attributable to the presence of isolated localized absorbers. This allows us to hypothesize that average distances between absorbing defects are much smaller than the laser beam's spot size and, moreover, than the $\sim 0.4\text{-}\mu\text{m}$ spatial resolution of the system. Comparison of PHI signals for two different HfO₂ film thicknesses, 1 wave and 1/4 wave, gave a ratio very close to 4:1 (Fig. 125.29), which renders a PHI signal proportional to the film thickness and also to the absorbing volume. This important result indicates that despite the presence of the intensity peak [Figs. 125.28(b) and 125.28(c)], absorption at the HfO₂/SiO₂ interface is not a dominating factor. Otherwise, the ratio of signals should be close to 1.25, in agreement with the intensity ratio at the interface position.

As expected, a 1-wave-thick sample deposited by a plasma-assisted technique, non-optimized for a laser-damage performance, generated an almost 3× higher PHI signal compared to a standard e-beam-deposited sample. This result correlates well with single-shot damage thresholds measured for these samples (see Table 125.I) and, if confirmed by the larger statistics for different coating materials, can point to the PHI technique as a preliminary indicator of ns-pulse laser damage performance.

Table 125.I: Damage thresholds (351 nm) and corresponding PHI signals for 1-wave-thick HfO₂ films.

HfO ₂ films	Damage thresholds (J/cm ²)	Heterodyne signal (μV)
Standard e-beam	3.57±0.23	9.8
Plasma assisted	2.03±0.13	27.6

2. PHI and AFM Mapping of HfO₂ Damage Morphology

PHI and AFM mapping of damaged sites revealed damage in the form of micrometer- and nanometer-scale craters. These craters appear as very dark (no signal) features on PHI images (Fig. 125.30). Taking into account that no signal was detected on silica samples without a hafnia layer, one can assume that the HfO₂ layer has been removed in the crater-formation process. Another observation is that scans performed in the central part of the damage site, and depicted in Fig. 125.30(c), show enhanced absorption in parts of the coating that survived laser irradiation. This indicates structural modification of HfO₂ film subjected to a fast heating and cooling cycle and allows one to forecast damage propagation under continuing pulse irradiation. PHI images of damage morphology also provided an opportunity to independently evaluate the method's spatial resolution, because of re-deposited nanoscale particles. A cross-sectional profile through one of these particulates, shown in Fig. 125.30(d), confirmed a true submicrometer resolution of $0.4\ \mu\text{m}$, in good agreement with the calibration value of $0.42\ \mu\text{m}$ obtained using gold nanoparticles. AFM imaging (Fig. 125.31) revealed further details about the damage process. Both isolated craters [Fig. 125.31(a)] imaged on the periphery of the damage site and merging craters from the heavier-damaged central part of the same site [Fig. 125.31(b)] are missing the granular structure of the surrounding coating material. Such morphology indicates that a melting point has been reached by the material at the bottom of the crater (SiO₂, as revealed by AFM analysis), and the observed smooth, glassy structure is a result of material flow and resolidification. Moreover, crater boundaries and narrow “bridges” between

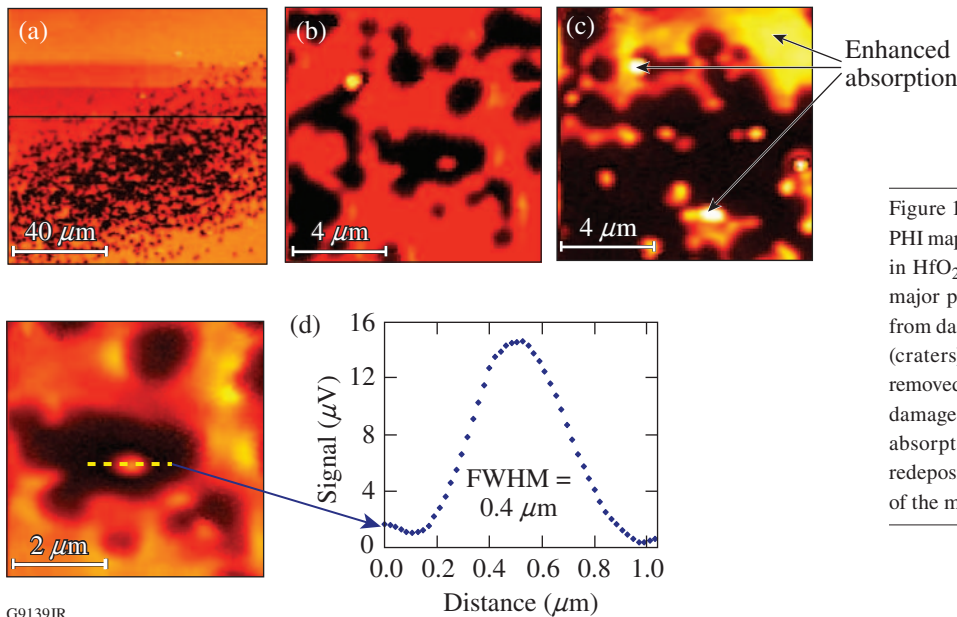


Figure 125.30
PHI mapping of 351-nm, 0.5-ns damage morphology in HfO₂ film samples: (a) 100- μm scan covering a major portion of the damage site; (b) 10- μm scan from damage site periphery [dark features are areas (craters) where hafnia film has been completely removed]; (c) 10- μm scan from the central part of the damage site; remaining hafnia film shows enhanced absorption; (d) cross-sectional profile through a redeposited particle, confirming $0.4\text{-}\mu\text{m}$ resolution of the method.

G9139JR

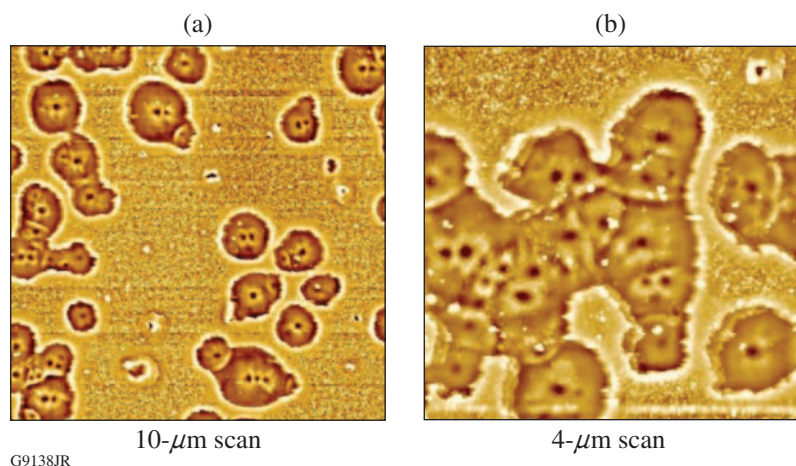
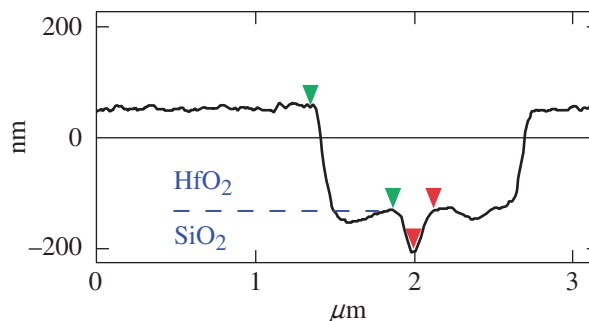
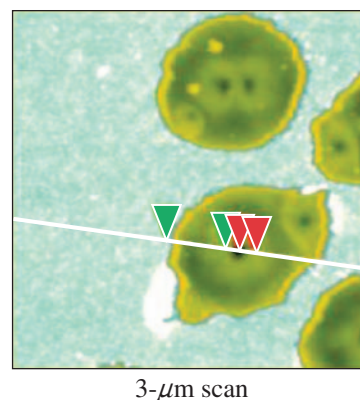


Figure 125.31

AFM images of damage morphology: (a) isolated craters formed on the damage-site periphery (10- μm scan); each crater has at least one damage origination point; (b) merging craters from the central part of the damage (4- μm scan); crater edges show smoothing of granular film structure, indicative of reaching the melting point.

craters [Fig. 125.31(b)] show HfO_2 film granularity that is much smoother than normal coating granularity, indicating the early stage of HfO_2 material melting. Small (100 nm or smaller) particles inside the area of heavier damage [presented in Fig. 125.31(b)] are attributed to material being redeposited onto the surface during crater formation. Another important observation here is that each crater [Fig. 125.31(a)] has in its central part at least one additional nanoscale protrusion—the point at which damage originates. Calculation of the average initiation-point separation using data from Fig. 125.31(b) gave a value of 272 ± 59 nm. Previous studies using artificial nanoscale absorbers⁷ demonstrated that damage initiation requires an effective energy transfer from absorber to the surrounding matrix; in porous thin-film material, only part of all absorbers can satisfy this condition. From this, we conclude that the actual distance between absorbing defects is smaller than the measured initiation-point separation. This conclusion is strongly supported by our previously derived estimate (see **PHI Imaging of HfO_2 Films Prior to Irradiation**, p. 28) that the separation would be much smaller than 0.4 μm . Consequently, we estimate the upper limit for the average absorber separation to be ~ 100 nm.

Cross-sectional profiles taken on AFM images (Fig. 125.32) through damage craters reveal further details of crater formation. An average crater depth of 186 nm appears to be very close to the 179-nm thickness of the HfO_2 layer, which strongly supports hafnia layer removal suggested by PHI mapping. A nanoscale protrusion located at the center of the main crater propagates 30 nm to 80 nm into the supporting SiO_2 layer, which also clearly points to localized absorption and material removal in the silica layer. Such observations suggest the following damage-process scenario: Energy from the laser pulse is initially absorbed at random locations within the HfO_2 layer, causing a local temperature rise. At selected locations, charac-



G9140JR

Figure 125.32

Damage crater cross-sectional profile (AFM). Crater-depth measurement points to removal of the hafnia layer within crater volume.

terized by good thermal contact between the HfO_2 and SiO_2 layers, heat conduction through the $\text{HfO}_2/\text{SiO}_2$ interface may raise the temperature in the SiO_2 material up to the melting point and higher. Recently, it was convincingly demonstrated⁸ that silica, upon reaching a temperature $T \approx 2200$ K (slightly above melting point), becomes absorbent enough at 355 nm to cause a dramatic drop in the nanosecond-pulse surface damage threshold. In our case, it means that once this temperature

is reached inside the SiO₂ layer within the laser-pulse-length interval, local temperature and pressure can grow dramatically by acquiring energy from the laser pulse. As a result, explosive removal of the HfO₂ material within the main crater volume and SiO₂ material within the central nanocrater takes place. Taking into account that the hafnia melting point $T_m(\text{HfO}_2) = 3085 \text{ K}$ is much higher than that of silica, $T_m(\text{SiO}_2) = 1986 \text{ K}$, HfO₂ material can be removed from the crater volume via a stress-driven mechanism, without full melting.⁹ This conclusion is supported by crater morphology (see Fig. 125.32) characterized by sharp edges that are missing an elevated smooth rim, typical for melted material flow.

3. Nature of Nanoscale Absorbers

As suggested in the **Introduction**, p. 25, there are two possible nanoscale absorber candidates in metal-oxide thin film: metal clusters and high-density areas of electronic defects. Figure 125.33 shows the spectral dependence of the absorption cross section for a 10-nm Hf cluster.¹⁰ Also on Fig. 125.33 are data for a 10-nm gold cluster calculated¹⁰ at 355-nm wavelength, which is just slightly larger than for Hf. In **Experimental**, p. 25, we reported on PHI imaging of gold clusters as small as 5 nm, making it realistic to assume that we could detect similarly sized Hf clusters using PHI, if the same were present in the HfO₂ film. Assuming $\sim 100\text{-nm}$ average separation between 5-nm clusters, lattice unit cell volumes³ of $2.23 \times 10^{-2} \text{ nm}^3$ for Hf, and $3.48 \times 10^{-2} \text{ nm}^3$ for HfO₂, the portion of Hf in a form of clusters inside HfO₂— 3.1×10^{-5} —is rather high. Another

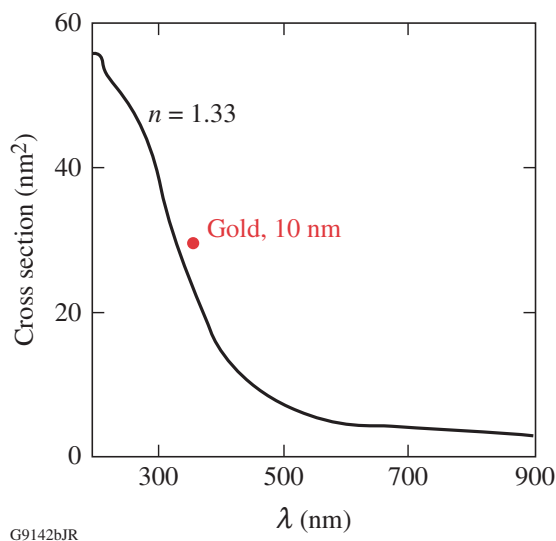


Figure 125.33
Absorption cross section for 10-nm-diam Hf cluster in a medium with refractive index = 1.33 as a function of wavelength. For comparison, 355-nm-wavelength data for a 10-nm Au cluster are also shown on the graph.

observation that questions the possible role of metal clusters is that HfO₂ films deposited from oxide, as a starting material, should have a lower probability of metal-cluster formation than films deposited from Hf metal. Nevertheless, films produced by oxide evaporation show higher absorption and lower UV–ns-pulse damage thresholds.¹¹ Thermodynamic modeling of cluster formation in an evaporation plume and also during film growth is needed to evaluate the realistic cluster fraction inside metal oxide film.

Absorption by electronic defects, enhanced at grain boundaries within columnar film structure, is another possible source of damage initiation. Photoluminescence excited by 266-nm, 4.66-eV photons revealed a rich spectrum attributable to absorption from electronic defect states.¹¹ Figure 125.34 shows an energy diagram for oxygen-ion vacancy defect states (V^+ and V^{2+}) inside a HfO₂ bandgap,³ where energy permits electron transition into the conduction band by absorption of 355-nm, 3.5-eV photons. Further heating of these electrons by a laser pulse ensures avalanche formation and damage. For obvious reasons, spatial density of the electronic defects must be much larger than cluster density in order to achieve a similar localized effect. That might explain the very small spatial signal variation on PHI images of HfO₂ films prior to irradiation as a result of averaging over a large number of absorbing defects. Further experiments and modeling are needed to clarify which type of absorbing defect plays a major role in the damage process.

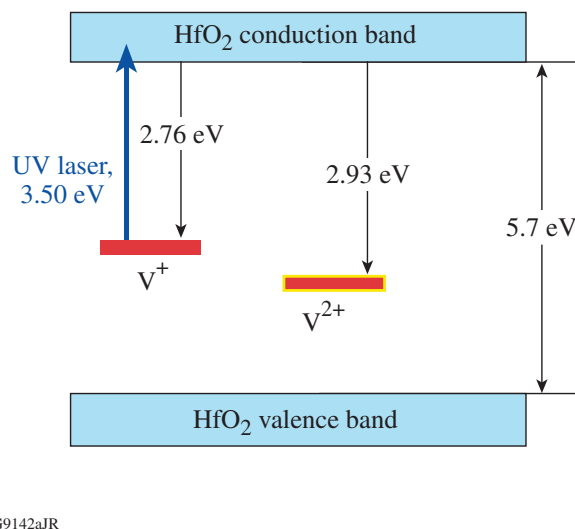


Figure 125.34
Energy-level diagram for defect states³ in monoclinic HfO₂ whose electron affinities permit electron excitation into the conduction band through absorption of a 355-nm photon.

Conclusions

Photothermal heterodyne imaging using near-UV light as a pump source can measure metal oxide's thin-film absorption properties with high sensitivity and submicron ($\sim 0.4\text{-}\mu\text{m}$) spatial resolution.

PHI images of HfO₂ films prior to irradiation are structureless, pointing to absorber separations much smaller than the $0.4\text{-}\mu\text{m}$ resolution of this method. Combining these data with damage initiation statistics allowed us to estimate an upper limit for an average absorber separation at ~ 100 nm. By comparing heterodyne signals for different film thicknesses, we found that HfO₂/SiO₂ interfacial absorption is not a major factor, but the main contribution comes from absorption inside HfO₂ film.

Observed correlation between PHI signals and measured nanosecond-pulse damage thresholds for HfO₂ monolayer films points to PHI as a useful technique for predicting laser-damage resistance of differently deposited thin films.

Using AFM and PHI to analyze the damage morphology allowed us to suggest a HfO₂ damage mechanism. The process starts with localized absorption and a temperature rise in the HfO₂ film and is followed by heat transfer to the supporting SiO₂ layer by means of heat conduction. At locations with good thermal contact, the temperature in SiO₂ can rise above the melting point and reach a critical temperature ~ 2200 K at which silica transforms into an effectively absorbing material. As a result, energy acquisition from the laser pulse leads to a quick temperature and pressure rise, explosive material removal, and damage.

Hafnium clusters and high-density areas of electronic defects still remain hypothetical candidates as damage initiators. Further experiments and modeling are required for unambiguous damage-driving absorber identification.

ACKNOWLEDGMENT

This work was supported by the U.S. Department of Energy Office of Inertial Confinement Fusion under Cooperative Agreement No. DE-FC52-08NA28302, the University of Rochester, and the New York State Energy Research and Development Authority. The support of DOE does not constitute an endorsement by DOE of the views expressed in this article.

REFERENCES

1. S. Papernov and A. W. Schmid, *J. Appl. Phys.* **82**, 5422 (1997).
2. S. Papernov, A. W. Schmid, A. L. Rigatti, J. B. Oliver, and J. D. Howe, in *Laser-Induced Damage in Optical Materials: 2005*, edited by G. J. Exarhos *et al.* (SPIE, Bellingham, WA, 2005), Vol. 5991, pp. 429–435.
3. A. S. Foster *et al.*, *Phys. Rev. B* **65**, 174117 (2002).
4. S. Berciaud *et al.*, *Phys. Rev. Lett.* **93**, 257402 (2004).
5. S. Berciaud *et al.*, *Phys. Rev. B* **73**, 045424 (2006).
6. S. Papernov and A. W. Schmid, *J. Appl. Phys.* **104**, 063101 (2008).
7. S. Papernov and A. W. Schmid, *J. Appl. Phys.* **92**, 5720 (2002).
8. J. Bude *et al.*, in *Laser-Induced Damage in Optical Materials: 2007*, edited by G. J. Exarhos *et al.* (SPIE, Bellingham, WA, 2007), Vol. 6720, p. 672009.
9. S. I. Kudryashov, S. D. Allen, S. Papernov, and A. W. Schmid, *Appl. Phys. B* **82**, 523 (2006).
10. J. A. Creighton and D. G. Eadon, *J. Chem. Soc. Faraday Trans.* **87**, 3881 (1991).
11. A. Ciapponi *et al.*, *J. Lumin.* **1029**, 1786 (2009).

Large Tunable, THz Electro-Optic Response in Cadmium Manganese Telluride (Cd,Mn)Te Single Crystals

Cadmium manganese telluride (Cd,Mn)Te (CMT) is a well-studied II–VI semiconductor because of its many desirable attributes and versatility. One such attribute is CMT’s stable zinc-blend structure for Mn concentrations, x , up to 0.70, providing a very wide tuning range of the energy bandgap E_g . CMT also exhibits a large magneto-optic Faraday effect and is commonly used for isolators. Finally, it has a very high stopping power, showing great potential for x - and γ -ray detection.^{1,2} In this article, we demonstrate CMT’s exceptionally large electro-optic (EO) Pockels effect, which has previously been underestimated because of screening of the applied electric field by free carriers. Furthermore, we discuss how the EO sensitivity can be magnified for a particular operating probe wavelength using bandgap engineering.

Electro-optic sampling (EOS) measurements were performed using a modified configuration of that described by Zheng *et al.*,³ in which the transmitted beam was collected. The subpicosecond pulses for all measurements were generated by a low-temperature-grown GaAs, freestanding photoconductive switch (PCS) integrated onto a coplanar strip (CS) transmission line.⁴ Our CMT samples were as-grown, millimeter-size single crystals obtained using a modified vertical Bridgman method.¹ The crystals were oriented in such a manner that the electric field was applied along the [110] direction, and the sampling beam, incident along the $[-110]$ direction, had parallel polarization with respect to the electric field. This configuration ensured maximum EO interaction.⁵

Since CMT is a semi-magnetic semiconductor, it was important to determine first whether the CMT optical response was a result of the EO Pockels effect or the magneto-optic Faraday effect. The PCS element was positioned at the center of the CS line, while the CMT transducer was placed on the transmission line, to one side of the PCS at first, and moved to the other side of the switch in a second measurement. This way the electric field of the signal generated by the PCS was constant on both ends of the CS line. However, the polarity of the magnetic field was flipped. The measurements showed no sign change of the

signal, establishing that the dominant mechanism in sampling an ultrafast signal is the EO effect.

EO transducers are able to resolve THz pulses by converting the electric field into a retardation Γ of the sampling beam’s polarization. For x -cut LiTaO₃, Γ is given by

$$\Gamma_{\text{LTO}} = \frac{2\pi(n_e - n_o)L_1}{\lambda} - \frac{\pi(n_e^3 r_{33} - n_o^3 r_{13})L_2}{\lambda d} V_{\text{LTO}}, \quad (1)$$

where the non-isotropic LiTaO₃ has two significant EO coefficients, r_{33} and r_{13} , and an extraordinary and ordinary refractive index, n_e and n_o , respectively. The gap between transmission lines is d , the crystal thickness is L_1 , the interaction length between crystal and electric field is L_2 , and V_{LTO} is the voltage transient propagating beneath the LiTaO₃ crystal. It is important to note that this transient is affected by the dielectric of the measuring transducer. The first term of the Γ_{LTO} equation is the intrinsic birefringence independent of the electric field and can be negated by a second perpendicular crystal of equal L_1 . The second term is the Pockels-induced birefringence.

Isotropic $\bar{4}3m$ crystals have no intrinsic birefringence, so Γ of the CMT transducer is⁶

$$\Gamma_{\text{CMT}} = \frac{2\pi(n_o^3 r_{41})L_2}{\lambda d} V_{\text{CMT}}, \quad (2)$$

where V_{CMT} is the CMT counterpart to V_{LTO} and the only nonzero components of the EO tensor are $r_{41} = r_{52} = r_{63}$. Literature⁶ for CdTe gives $r_{41} = 4.5$ pm/V, which is based on measurements taken at $\lambda = 1$ μm and for frequencies lower than 20 kHz. Assuming that the refractive indices and EO coefficients for LiTaO₃ (Ref. 7) are constant in the 633- to 800-nm wavelength range, calculations show that Γ_{CMT} is less than Γ_{LTO} . This is, however, in direct contradiction to our experimental results shown in Fig. 125.35, where we present the

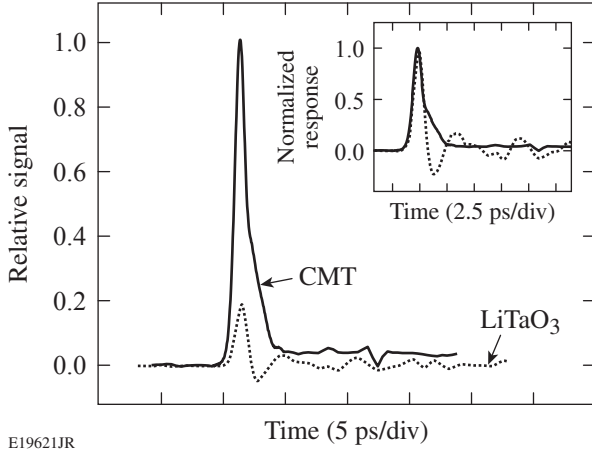


Figure 125.35
EOS response of a 1.45-V pulse detected by $\text{Cd}_{0.88}\text{Mn}_{0.12}\text{Te}$ (solid) and LiTaO_3 (dotted) transducers at a sampling beam wavelength of 800 nm. The inset compares the normalized responses of CMT (solid) and LiTaO_3 (dotted).

EO sampling responses of a $\text{Cd}_{0.88}\text{Mn}_{0.12}\text{Te}$ transducer (solid) and the widely used EO crystal LiTaO_3 (dotted). We see that CMT exhibits retardation five times greater than that of LiTaO_3 .

The differential transfer function for the EO modulator in our setup is

$$\frac{\Delta V}{V_0} = \frac{1}{2} \sin(\pi V/V_\pi) \approx \frac{\pi V}{2V_\pi}, \quad \text{for } V \ll V_\pi, \quad (3)$$

where V_π is the V_{LTO} required to retard the optical probe by π and the dc component (V_0) is 31.5 mV/ μW times the measured power of the transmitted probe. It is not possible, however, to determine the magnitude of r_{41} directly from the CMT EOS response because of the unknown variables L_2 and V_{CMT} . Therefore, we first determined the coupling between the transducer and transmission line using LiTaO_3 . Coupling measurements were easily accomplished by directly applying a 2-V peak-to-peak, low-frequency (MHz) sinusoid, bypassing the PCS entirely. Knowing the EO coefficients for LiTaO_3 (Ref. 6), V_{LTO} and L_2 were calculated from the EOS response and coupling measurements using Eqs. (1) and (3).

The L_2 was small ($1.18 \pm 0.26 \mu\text{m}$), which we assume was a result of the poor condition of the substrate. This was confirmed by calculating a large air gap of 24 μm between the transmission line and crystal. These calculations were determined by the impedance for our CS line in a multilayer substrate⁸ ($\text{LiTaO}_3/\text{air-gap}/\text{MgO}$) using the effective dielectric $\epsilon_{\text{eff}} = (c/v)^2 = 9.2$.

The velocity v was evaluated using the temporal delay of the EOS response measured for two spots with a known spatial separation. The ϵ_{eff} also established the reflection of the pulse at the crystal interface along the transmission line. The impedance mismatch in LiTaO_3 resulted in a 14% reflection of the generated pulse at the crystal interface, and the original signal of the PCS was then obtained (~ 1.45 V). Finally, the same air gap for CMT resulted in a smaller (3.5%) reflection, showing that V_{CMT} was $1.12 \times V_{\text{LTO}}$.

We strongly believe that the discrepancy between our ultrafast CMT retardation value and the low-frequency one given in the literature is caused by free carriers present in as-grown CMT crystals. These crystals are naturally p -type and holes are capable of screening slow oscillations of applied voltage, preventing any significant EO coupling at low frequencies. The free-carrier screening frequency can be estimated by dividing our CMT sample conductivity $\sigma \approx 10^{-3}$ S/cm (Ref. 1) by its permittivity, resulting in a value as high as 1.25 GHz. Measuring the EO response at 256 kHz, we calculated that the suppressed r_{41} for $\text{Cd}_{0.88}\text{Mn}_{0.12}\text{Te}$ was as low as 2.7 ± 0.8 pm/V. This result was in close approximation to CdTe [4.5 pm/V (Ref. 6)] and $\text{Cd}_{0.75}\text{Mn}_{0.25}\text{Te}$ [3.5 pm/V (Ref. 8)] coefficients found in literature.

The fact that our CMT transducer was able to render the ultrafast PCS signal precisely (Fig. 125.35) with the response 5 \times greater ($\Delta V = 504 \mu\text{V}$) than that of LiTaO_3 ($\Delta V = 95 \mu\text{V}$) is because the pulse generated by the switch contains frequency components far exceeding the carrier screening process.

Table 125.II provides the r coefficients and the V_π values for several CMT crystals, taking into account the previously calculated coupling factors and the wavelength-dependent n_0 , as well as the other EO transducers found in the literature. Comparative measurements in Table 125.II for $\text{Cd}_{0.82}\text{Mn}_{0.12}\text{Te}$ and $\text{Cd}_{0.91}\text{Mn}_{0.09}\text{Te}$ show that the kHz- and MHz-range measurements undervalue the EO coefficient by nearly an order of magnitude because of screening effects. Furthermore, our independent EO coupling measurements performed on $\text{Cd}_{0.91}\text{Mn}_{0.09}\text{Te}$ at 256 kHz but at 10 K, demonstrated that the EO response was 10 \times greater than that at 300 K. In the latter case, free carriers were immobilized by deep-level traps as the temperature was lowered.

EOS measurements for various wavelengths were performed using a $\text{Cd}_{0.91}\text{Mn}_{0.09}\text{Te}$ crystal (Fig. 125.36), showing a dramatic increase of the EO response when approaching E_g . Knowing that the signal is electro-optic in nature, we attributed

Table 125.II: Measurements (bold) and previously reported values of the optimum EO coefficients and V_{π} for several (Cd,Mn)Te crystals of x and for other popular EO transducers. Provided are the probe wavelength, tested signal frequency, and the probe wavelength appropriate n for the crystal.

Crystal	λ (nm)	f	n	r (pm/V)	$V_{\pi} \cdot d/L_2$ (V)
CdTe	855	THz	$n_o = 2.91$	$r_{41} = 30.2 \pm 2.9$	572
CdTe (Ref. 6)	1000	kHz	$n_o = 2.84$	$r_{41} = 4.5$	3880
Cd_{0.91}Mn_{0.09}Te	855	THz	$n_o = 2.76$	$r_{41} = 24.7 \pm 1.2$	821
Cd_{0.88}Mn_{0.12}Te	800	THz	$n_o = 2.79$	$r_{41} = 28.3 \pm 5.9$	651
Cd_{0.88}Mn_{0.12}Te	800	kHz	$n_o = 2.79$	$r_{41} = 2.7 \pm 0.8$	6825
Cd _{0.75} Mn _{0.25} Te (Ref. 8)	800	GHz	$n_o = 2.64$	$r_{41} = 3.5 \pm 0.5$	4735
Cd_{0.50}Mn_{0.50}Te	855	THz	$n_o = 2.52$	$r_{41} = 25.3 \pm 1.2$	1059
LiTaO ₃ (Ref. 6)	800	THz	$n_{e/o} = 2.18/2.176$	$r_{33/13} = 33/7.5$	3490
ZnTe (Ref. 12)	800	THz	$n_o = 3.24$	$r_{41} = 4.04$	2911
DAST (Ref. 3)	810	THz	$n_{a/b} = 2.46/1.68$	$r_{11/21} = 77/42$	790

this phenomenon to the wavelength dependence of n_o (Ref. 9). Our experimental EOS dependence on wavelength was fit (solid line in Fig. 125.36) using the $n(\lambda)$ dispersion model given by Schubert *et al.*¹⁰ Taking the asymptote as the crystal bandgap, the E_g (1.623 eV) was slightly smaller than the calculated value [1.646 eV (Ref. 11)], apparently, because of interstitial states broadening the bandgap. The EO dependence on λ can be easily exploited by either tuning the operating probe λ to near- E_g , as we have presented in Fig. 125.36. Alternatively, for tests using a fixed probe wavelength above 600 nm, crystals can be custom

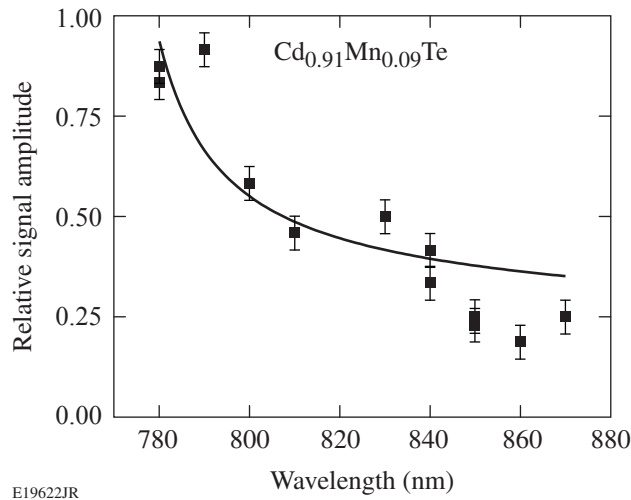


Figure 125.36 Wavelength dependence of Cd_{0.91}Mn_{0.09}Te EO effect. Fittings are based on $n(\lambda)$ dispersion (solid line).

grown to match for greatest signal quality. We finally note that Table 125.II shows that for an 855-nm probe, CdTe has twice the sensitivity as Cd_{0.50}Mn_{0.50}Te, but the CdTe bandgap limits its practical use to $\lambda > 812$ nm.

The calibration method used here allowed us to obtain absolute values of the EO coefficient for tested CMT crystals. We have demonstrated that, ultimately, CMT is significantly more sensitive at THz frequencies than previously expected¹² and more sensitive than the widely used indirect EO crystal LiTaO₃; the typical free-space THz EO transducer ZnTe;¹² and even when compared to DAST, an organic crystal exhibiting the largest EO coefficient of any material.^{3,13} Furthermore, CMT exhibits a low ϵ_r , so only a small percentage of the signal is lost because of reflections along the transmission line. The CMT EOS response shown in Fig. 125.35 also presents a much cleaner signal as compared to the LiTaO₃ response because of the absence of a significant dielectric loading. Carrier screening was verified as the source of an order-of-magnitude difference between the CMT EO effect response at very high (THz) and low (MHz) frequencies. Finally, the CMT EO wavelength dependence was exploited to garner the highest sensitivity.

ACKNOWLEDGMENT

The authors thank Drs. W. R. Donaldson and H. Irie for their many valuable discussions. A. S. C. acknowledges support from the Frank Horton Graduate Fellowship Program at the University of Rochester Laboratory for Laser Energetics. Work in Rochester was supported in part by NSF grant No. ECCS-0901701 and the U.S. Department of Energy Office of Inertial Confinement Fusion under Cooperative Agreement No. DE-FC 52-08NA28302, the University of Rochester, and the New York State Energy Research and

Development Authority. The support of DOE does not constitute an endorsement by DOE of the views expressed in this article. Work in Warsaw was supported by the Polish Ministry of Science and Higher Education through grant 3 T08A 046 30.

REFERENCES

1. A. Mycielski *et al.*, Phys. Stat. Sol. (C) **2**, 1578 (2005).
2. A. S. Cross, J. P. Knauer, A. Mycielski, D. Kochanowska, M. Wiktowska-Baran, R. Jakiela, J. Domagała, Y. Cui, R. B. James, and R. Sobolewski, Nucl. Instrum. Methods Phys. Res. A **624**, 649 (2010).
3. X. Zheng, S. Wu, R. Sobolewski, R. Adam, M. Mikulics, P. Kordoš, and M. Siegel, Appl. Phys. Lett. **82**, 2383 (2003).
4. R. Adam, M. Mikulics, A. Förster, J. Schelten, M. Siegel, P. Kordoš, X. Zheng, S. Wu, and R. Sobolewski, Appl. Phys. Lett. **81**, 3485 (2002).
5. S. Namba, J. Opt. Soc. Am. **51**, 76 (1961).
6. A. Yariv, *Optical Electronics in Modern Communications*, 5th ed., The Oxford Series in Electrical and Computer Engineering (Oxford University Press, New York, 1997).
7. Q. Wu and X.-C. Zhang, Appl. Phys. Lett. **68**, 1604 (1996).
8. E. Chen and S. Y. Chou, IEEE Trans. Microw. Theory Tech. **45**, 939 (1997).
9. A. S. Cross, D. Wang, G. Guarino, S. Wu, A. Mycielski, and R. Sobolewski, J. Phys., Conf. Ser. **92**, 012015 (2007).
10. D. W. Schubert *et al.*, Appl. Phys. Lett. **60**, 2192 (1992).
11. J. K. Furdyna, J. Appl. Phys. **64**, R29 (1988).
12. B. Pradarutti *et al.*, Opt. Commun. **281**, 5031 (2008).
13. F. Pan *et al.*, Appl. Phys. Lett. **69**, 13 (1996).

Improvements to Long-Pulse–System Performance and Operational Efficiency on OMEGA EP

Introduction

An important operational goal of the Omega EP Laser Facility is to provide principal investigators with maximum UV energy on target, while maintaining UV peak fluences within an acceptable margin for safe operation. To optimize the long-pulse, on-target energy of OMEGA EP, we have pursued a threefold effort: (1) improve the laser-induced damage threshold of beam-transport optics; (2) improve the near-field beam profile; and (3) develop simulation tools to use during shot operations that provide rapid prediction of laser-system performance. These simulation tools predict the UV near-field beam-fluence distribution and on-target energy based on measurements of the inputs to the main amplifiers and are regularly used during shot operations. They have streamlined daily system qualification, making it possible for UV energy to be maximized within current system constraints.

Each of the four OMEGA EP beamlines uses a folded architecture and type-I/type-II frequency-conversion crystal (FCC) design based at the National Ignition Facility (NIF), as shown in Figs. 125.37(a) and 125.37(b).¹ Beamlines 1 and 2 can be operated in either short-pulse or long-pulse mode, while Beamlines 3 and 4 are dedicated to long-pulse operation. All beams are amplified in two passes through a 7-disk booster amplifier and four passes through an 11-disk main amplifier. Depending on the required shot conditions, the main amplifier operates with a variable number of pumped disks. Each beamline has an independent front-end laser source that provides a seed pulse that is injected into the transport spatial filter. The seed originates in a single-frequency fiber laser and is amplified in a regenerative amplifier (regen) after temporal shaping to a level of ~5 mJ. Further preamplification is provided by Nd:glass amplifiers prior to injection into the beamline. Spatial beam shaping is accomplished by two different apodizing elements located in the laser sources' front end. The first apodizer is located immediately after the regen and shapes the edges of the beam from round to square. The second apodizer is located just prior to the glass amplification stage and provides pre-compensation for the roll-off in gain that occurs at the edges of the beamline disk amplifiers.² The spatial gain variation of

the front-end glass amplifiers is compensated by appropriately sizing the regen Gaussian output beam on the first apodizer.

Table 125.III shows the OMEGA EP individual beamline long-pulse–design energies, its current performance, and the total number of long-pulse target shots to date.

On-target 3ω energies have been limited by the laser-damage resistance of the installed 3ω transmissive optics.³ Effort is underway to achieve OMEGA EP's long-pulse–design capability by procuring 3ω optics with greater laser-damage resistance. The current 3ω transport optics have been preconditioned to mitigate 3ω laser-induced damage growth to a fluence of 4 J/cm^2 (3-ns Gaussian pulse),⁴ and it is anticipated that new processing methods⁵ applied to newly procured 3ω optics may provide up to a factor-of-2 increase in damage threshold.⁶

Owing to the current fluence limitation, OMEGA EP must operate in a regime where both the beamline amplifiers and the frequency-conversion crystals are not highly saturated, making the 3ω near-field beam structure very sensitive to small changes in the injected beam quality. Several methods to improve the near-field beam profile have been pursued and are described in the next section.

The sensitivity to laser front-end performance necessitates significant effort and care to avoid exceeding the established fluence limit. To maintain a high level of operational efficiency, simulation tools have been developed that predict the 3ω near-field beam-fluence distribution and on-target energy using the preamplified injected near-field beam that is measured during pre-shot qualification. During shot operations, these tools have

Table 125.III: OMEGA EP long-pulse beamline performance.

Design	Current	Total long-pulse shots through FY10
2.5 kJ ($t = 1 \text{ ns}$)	1.0 kJ ($t = 1 \text{ ns}$)	278
6.5 kJ ($t = 10 \text{ ns}$)	3.0 kJ ($t = 10 \text{ ns}$)	

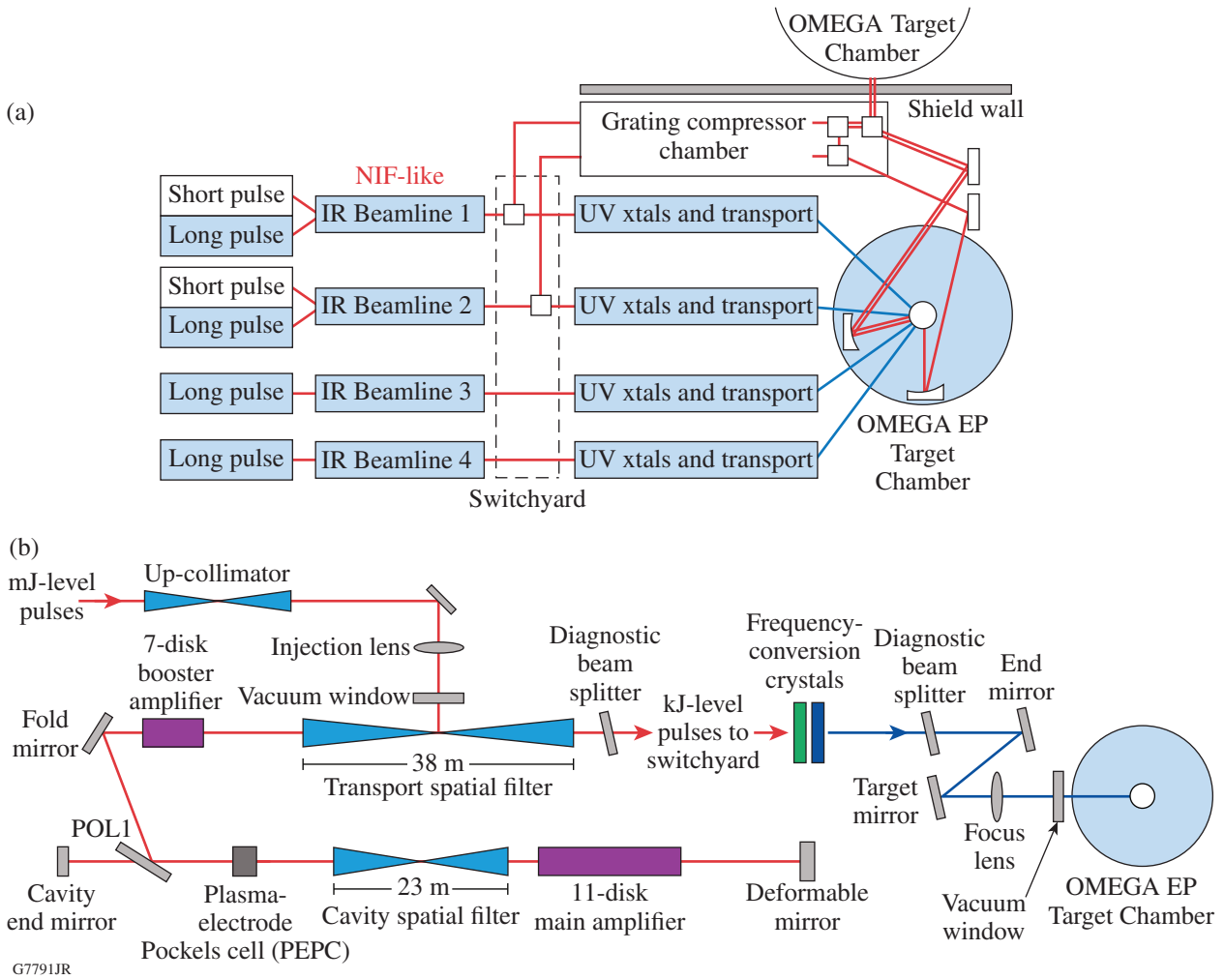


Figure 125.37 OMEGA EP Laser System configuration. (a) Beamlines 1 and 2 can be operated in either short-pulse or long-pulse mode, while Beamlines 3 and 4 are dedicated to long-pulse operation. (b) Each of the four beamlines uses a folded architecture and type-I/type-II frequency-conversion crystal design based on the NIF.

helped determine whether a user’s energy requirements will be met without exceeding the 3ω damage threshold using the current injected beam profile, or whether more time should be given to alignment and qualification activities. The rapid prediction capability that these tools provide has helped to ensure safe fluence levels while maintaining high operational efficiency. These simulation tools are described in **Simulation Tools for Operations**, p. 41.

Near-Field Beam Improvements

Improved beam-shaping methods in both stages of apodization in the long-pulse front end have enhanced the efficiency of shot operations by providing consistently better beam profiles, therefore reducing the time required for pre-shot qualification. The following subsections describe (1) new apodizers that have

been installed into both apodizing stages of Beamlines 3 and 4;^(a) (2) a proof-of-concept experiment to smooth the 3ω near-field beam by detuning the FCC’s; and (3) a programmable spatial light modulator (PSLIM), which will be installed into the front end of Beamlines 3 and 4 during FY11.

1. First-Stage Apodizer

Since there is only a small amount of saturation in the beamline, small changes in the regen output beam’s profile can produce large changes in the 3ω beam. In practice, using the shape of the laser sources’ regen output beam to precompensate for the approximately parabolic radial gain profile of the Nd:glass amplifiers has resulted in significant variations

^(a)These upgrades will be implemented in the long-pulse front end of Beamlines 1 and 2 during FY11.

in 3ω beam quality. The day-to-day variations in regen beam quality and pointing make it necessary to adjust the centering of the regen beam profile into both the first-stage apodizer and the gain profile of the rod amplifier on shot day to optimize the 3ω beam profile, resulting in costly alignment delays. A new approach has been implemented that has significantly reduced the time required to optimize alignment. The regen output beam has been expanded at the location of the first apodizer to an approximately flat intensity distribution, and a new apodizer has been installed that shapes the beam from round to square and provides precompensation of the measured preamplifier radial gain using a binary mask.⁷ The specified transmission profile combines a fourth-order polynomial fit to the measured small-signal radial gain with a square 40th-order super-Gaussian function. This has proven to be a much more robust design, providing better beam quality, greater ease of alignment, and greater reliability. Figure 125.38 shows that the measured transmission of the new apodizer matches the specified transmission within $\sim 1\%$.

2. Second-Stage Apodizer

The first realization of the apodizer designed to precompensate beamline disk gain roll-off was a one-dimensional design [see Fig. 125.39(d)]. Following small-signal–gain measurements in Beamlines 3 and 4, an improved beam shaper that takes into account the beamline disk gain variations in two dimensions was designed and installed. The specified and measured transmission profiles for the new apodizer are shown in Figs. 125.39(a)–125.39(c). Figure 125.40 shows that a more uniform beam has been achieved after replacement of both front-end apodizers. The contrast of the beam, defined as the standard deviation of the fluence normalized to the average, was reduced from 16.8% to 12.6% with the installation of the new apodizers. The contrast was calculated over the 31-cm-square region shown overlaid on the beams in Fig. 125.40. The greater uniformity achieved within the overlaid region in Fig. 125.40(b) is attributed primarily to the first-stage apodizer, whereas the qualitative improvement in fill factor seen near the corners of the beam is attributed primarily to the second-stage apodizer.

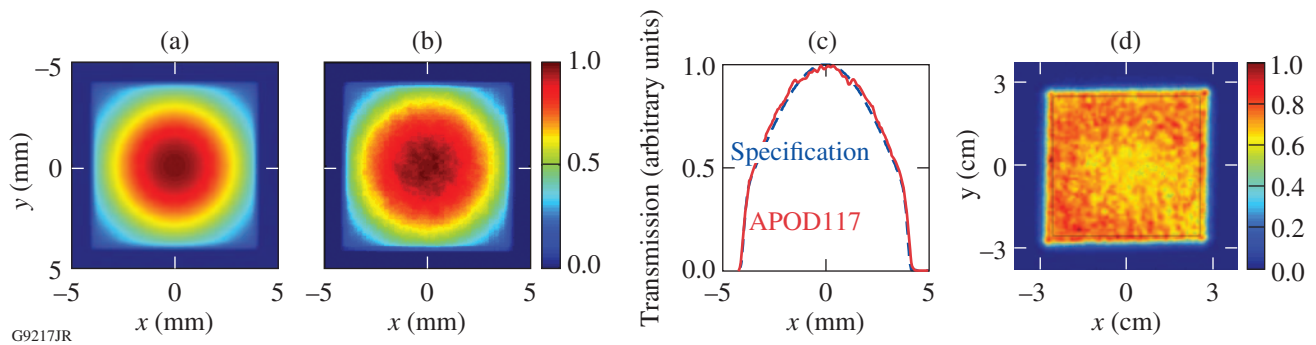


Figure 125.38

(a) Specified and (b) measured transmission of the new first-stage apodizer designed to precompensate the radial gain of the front-end Nd:glass amplifiers. Transmission lineouts are shown in (c) and the measured front-end output beam in (d).

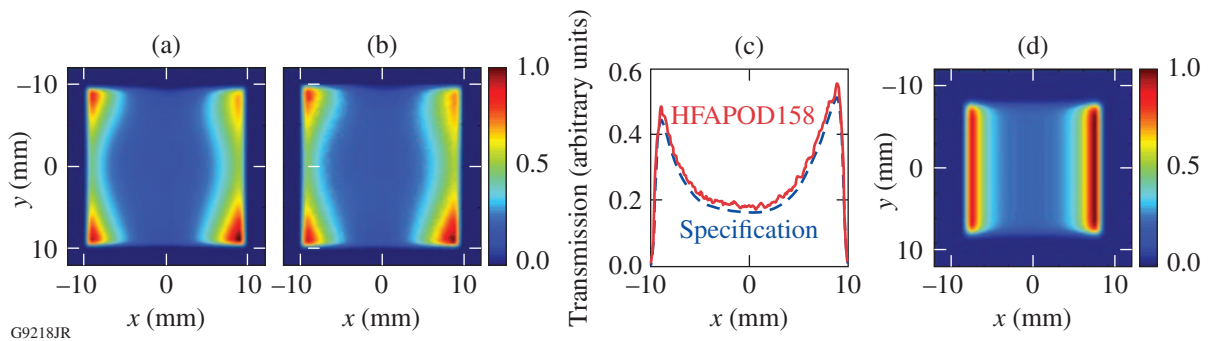


Figure 125.39

(a) Specified and (b) measured transmission of the new second-stage apodizer that precompensates the OMEGA EP beamline gain variation in two dimensions. Transmission lineouts are shown in (c). The previous one-dimensional apodizer design transmission is shown in (d).

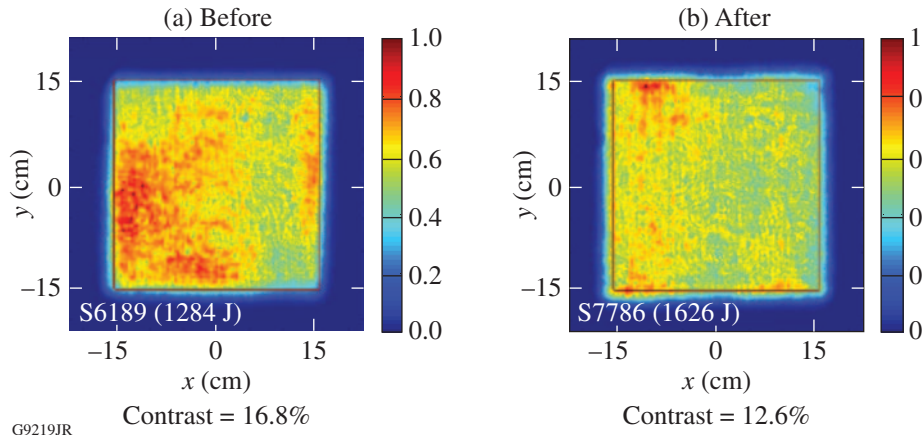
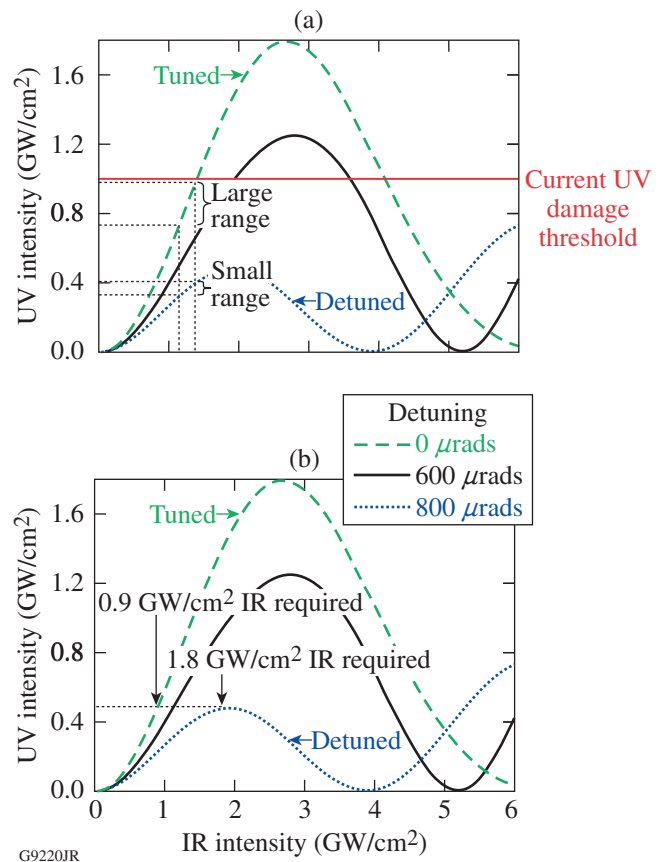


Figure 125.40
 Normalized fluence of Beamline 4's 1ω output beams (a) before and (b) after installation of the new front-end apodizers. The contrast of the beam, defined as the standard deviation of the fluence normalized to the average and computed within the 31-cm \times 31-cm area outlined in the figure, was reduced from 16.8% to 12.6% with the installation of the new apodizers.

G9219JR

3. UV Near-Field Beam Smoothing by FCC Detuning

Currently, the FCC's are angularly tuned to maximize the efficiency of the conversion process. When operated in this manner, the laser-damage thresholds of the current 3ω optics require that the 1ω laser intensity be maintained at a relatively low level ($\leq 1 \text{ GW/cm}^2$). In this regime, small 1ω intensity variations produce large 3ω intensity variations, as shown in Fig. 125.41(a), causing the 3ω beam to be highly modulated. It has been proposed⁸ that angularly detuning the FCC can reduce 3ω beam intensity modulations. Initial experiments on OMEGA EP have shown that by detuning the doubler crystal, the 3ω beam intensity modulation can be significantly reduced. The loss of conversion efficiency incurred by detuning the doubler is offset by increasing the 1ω energy into the FCC in order to maintain constant 3ω output energy [see Fig. 125.41(b)]. Measurements in Beamline 4 have shown a 13% reduction in peak 3ω fluence for the detuned FCC at nearly equivalent 3ω energy as the tuned FCC. Standard deviations of the 3ω beam fluence distributions were 21.2% and 14.7% for the tuned and detuned cases, respectively, indicating a significantly smoother beam for the detuned FCC, as shown in Fig. 125.42. This reduction in 3ω beam modulation should make it possible to deliver more energy to a target while maintaining peak 3ω intensities below the damage-threshold limit. To ensure that damage thresholds were not exceeded, this proof-of-concept experiment was performed at approximately half of the current 3ω energy limit for the 2-ns-square pulse shape used. The amount of increase in on-target energy that can be achieved will depend upon the reduction in peak fluence observed at energies approaching the 3ω damage threshold, which, in turn, will depend upon the level of saturation observed in the beamline. The utility of this beam-smoothing method on OMEGA EP will be explored in greater detail during FY11.



G9220JR

Figure 125.41
 Simulated 3ω output versus 1ω input for the 11-mm-doubler, 9-mm-tripler OMEGA EP FCC design showing that (a) within the current operating regime of OMEGA EP, a detuned doubler can produce a smaller range of UV intensities for the same range of IR intensities than a tuned doubler; and (b) a detuned doubler requires more IR intensity to achieve the same UV intensity (or UV energy) as a tuned doubler.

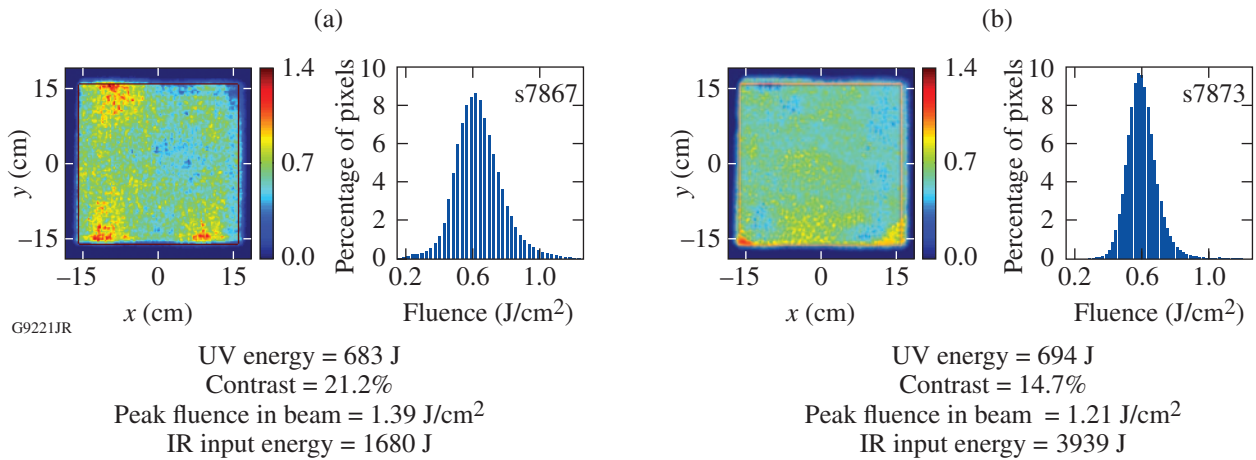


Figure 125.42
 3ω near-field beams with (a) tuned and (b) detuned doubler measured on OMEGA EP Beamline 4 showing a significantly smoother beam for the detuned case.

4. Programmable Spatial Light Modulator (PSLIM)

A programmable spatial light modulator (PSLIM) will be installed into the front end of Beamlines 3 and 4 during FY11 to provide closed-loop correction of near-field beam amplitude. The PSLIM system shapes the laser beam’s amplitude by using a liquid-crystal-on-silicon spatial light modulator that is based on an amplitude modulation carrier method.⁹ It will be used primarily to improve the fill factor of the beam by the dynamic tuning of gain precompensation and to reduce near-field modulation by smoothing beam hot spots and edges.¹⁰ Preliminary results for smoothing the beam at the location of the first apodizer in Beamline 3 are shown in Fig. 125.43.

Simulation Tools for Operations

The primary goal in the development of an operations simulation capability for OMEGA EP was to ensure UV system safety by predicting the 3ω peak fluence of an OMEGA EP beamline with high spatial resolution (1 k × 1 k) in a time

frame of 10 min or less using measured data from the daily injection qualification shot. A rapid prediction capability ensures that system operators will be prepared to shoot again within a qualification shot cycle if additional alignment corrections are required. Because of the combined time-critical and high-spatial-resolution requirements, a simplified model was chosen and its performance was characterized against actual measurements. The IR portion of the model incorporates the previously measured, spatially dependent small-signal gain of the beamline disk amplifiers, with gain saturation accounted for using the Frantz–Nodvik equations.¹¹ A one-dimensional version of the model is also available for high-resolution, temporal pulse-shaping simulations. Physical processes that are not included are free-space propagation, wavefront aberrations, and high-frequency spatial noise. As will be shown, by characterizing the model against measurements of current system performance, the model can be used as an efficient tool to determine the maximum-allowable 3ω energy during

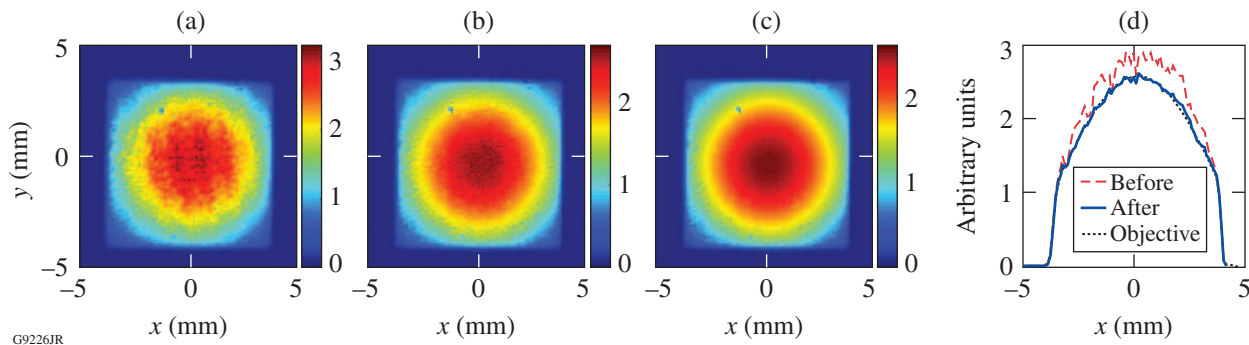


Figure 125.43
 Initial results for fine-tuning the shape of the radial gain-precompensated beam using a programmable spatial light modulator (PSLIM) in the front end of Beamline 3: (a) before correction, (b) after correction. The objective map for the device is shown in (c) and lineouts in (d).

shot operations. Convergence of the model to the measured IR beamline energy is achieved by adjusting the per-disk loss to account for current system performance. The 3ω beam and pulse are simulated using spline interpolation of data that have been generated from prior frequency-conversion simulations. A pc-based, MATLAB framework was used to provide a seamless interface to pre-shot alignment and analysis tools and to provide an intuitive environment for rapid development, testing, and deployment. A multiple-core, distributed computing capability can optionally be used. Model output predictions include 1ω and 3ω beamline output energies, near-field beam-fluence distributions, and pulse shapes. The model also has backward prediction capability, which is used to perform shot setup based on the requested 3ω energy and pulse shape, and to calculate the maximum-allowable 3ω energy and associated injection energy on a shot day.

Figure 125.44 compares simulated and measured square pulses for the 1ω beamline output using the one-dimensional model. The agreement between the pulse shapes for N points in time is characterized by their root-mean-square (rms) difference:

$$\text{rms difference} = \sqrt{\frac{1}{N} \sum_{i=1}^N [\text{sim}(i) - \text{meas}(i)]^2}, \quad (1)$$

which is equal to 4% for the pulses shown in Fig. 125.44(a). The simulations used the regen output pulse from an injection shot taken on the same day [see Fig. 125.44(b)]; therefore, the rms difference represents the model’s predictive capability and

the regen shot-to-shot pulse stability. The inset in Fig. 125.44(a) lists the simulated and measured beamline output energies, 3589 J and 3540 J, respectively. Figure 125.45 compares simulated and measured ramped pulse shapes for both the 1ω and 3ω beamline outputs. The rms difference in Fig. 125.45 is 3.6% for the 1ω pulse shape and 5.3% for the 3ω pulse shape. Table 125.IV shows that the measured and predicted beamline energies calculated using the pulse-shape prediction tool agree to within ~3%.

Simulated 1ω beamline output energies are compared with measurements in Fig. 125.46 for ~70 target shots taken during the third and fourth quarters of FY10. The simulations in Fig. 125.46 were performed using a $1\text{-k} \times 1\text{-k}$ grid and 22 temporal slices and required ~7 min each. To avoid the additional computing time required for the temporal integration in the IR section of the beamline, a continuous-wave (cw) amplification model is also available. Figure 125.47(a) compares simulated, 1ω beamline output energies with measured energies using the cw model; Fig. 125.47(b) shows the corresponding 3ω on-target

Table 125.IV: Simulated and measured beamline output energies for Beamline 3 (shot 7799) using the pulse-shape-prediction tool. The regen pulse shape for a qualification shot taken on the same day was used in the simulation.

	Simulation	Measurement
IR (J)	1375	1416
UV on-target (J)	442	454

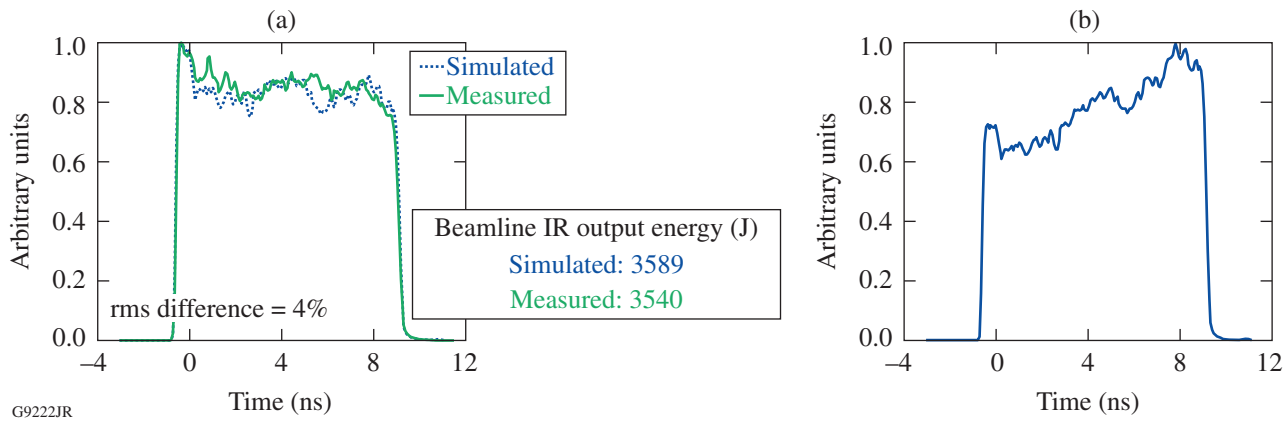
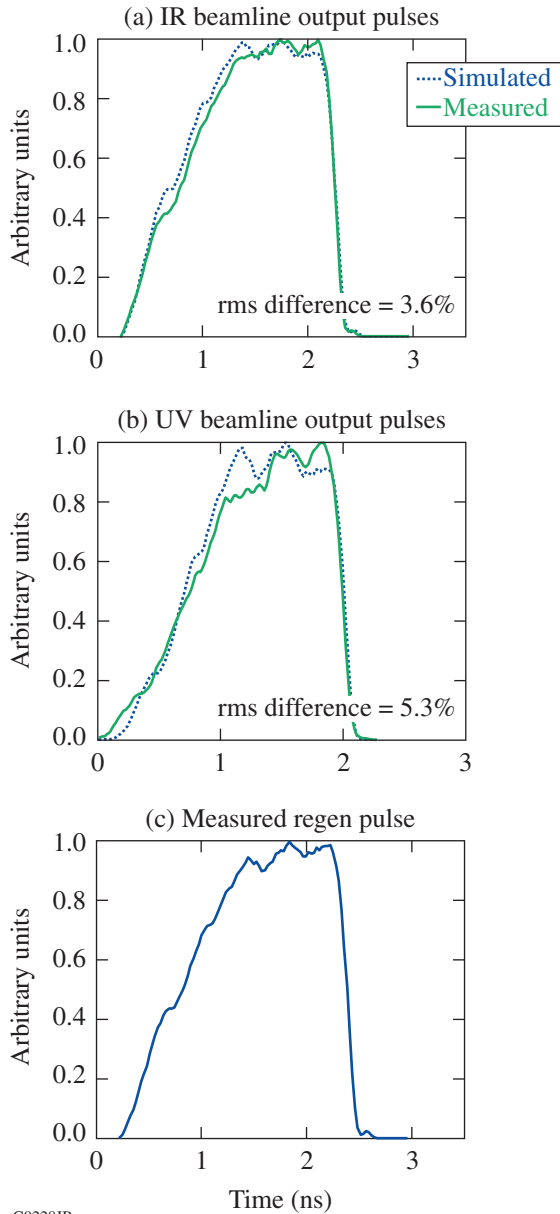


Figure 125.44 Simulated and measured ESG9901 square-pulse shapes are shown in (a) for the 1ω output of Beamline 4. Beamline energies and the rms difference between simulated and measured pulse shapes are given in the figure. Simulations used the regen output pulse shape shown in (b) for an injection shot taken on the same day.

energies. In this case, the 3ω simulations used measured IR beamline output-pulse shapes. The agreement between the simulations and measurements is within $\sim 5\%$, although an $\sim 5\%$ systematic offset is apparent in the region between 2 to 3 kJ in Figs. 125.46 and 125.47(a) and between 1 to 1.2 kJ in Fig. 125.47(b). This is suspected to be caused by a temporary

calibration drift in the energy diagnostic used for these shots. These results demonstrate the model's capability to accurately predict beamline energy and pulse shape using the measured qualification shot data.

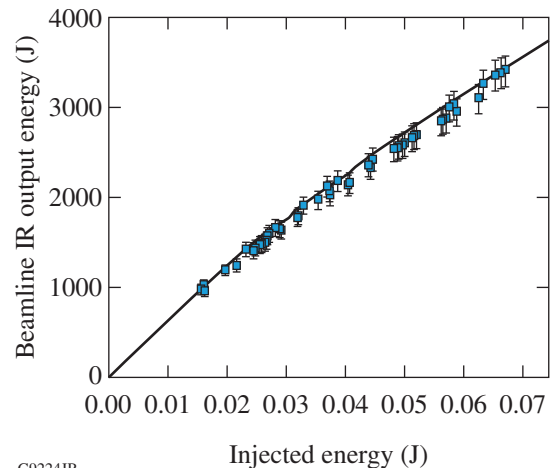
Simulated 3ω peak fluences for shots on OMEGA EP using a $1\text{-k} \times 1\text{-k}$ grid and 22 temporal slices are compared with their corresponding measured values in Fig. 125.48. The simulated values are, on average, $\sim 9\%$ below the measurements and are generally well within 20%. The difference between the 9% and 20% levels corresponds to the $2\text{-}\sigma$ distance for the fluence distribution formed by the difference between simulated and measured values. The systematic offset of the simulated peak fluence from the measured values suggests that allowable 3ω energies can be safely established using simulations that provide peak fluences less than or equal to 80% of the 3ω damage threshold. For OMEGA EP users requesting maximum 3ω energy on the first target shot of the day, the maximum-allowable energy is calculated in a two-step process: Prior to shot day, the 3ω energy limit is established based on the amount of modulation observed in the most recently measured 3ω near-field beam. This enables users to specify the entire laser configuration well in advance of the shot. On shot day, the maximum-allowable 3ω energy is calculated using the measured injected near-field beam to give a simulated peak fluence that is equal to 80% of the 3ω damage threshold. Simulations on shot day account for (1) changes in the injected near-field beam and (2) possible differences between the pre-shot-day and current-shot-day beamline configurations that may affect



G9228JR

Figure 125.45

Simulated and measured ERM2001 ramped-pulse shapes are shown in (a) and (b) for Beamline 3's 1ω and 3ω outputs, respectively. The rms differences between simulated and measured pulse shapes are given in the figure. Simulations used the regen output-pulse shape shown in (c) for an injection shot taken on the same day.



G9224JR

Figure 125.46

Simulated (line) and measured 1ω output energy versus injected energy of Beamline 4 with 16 laser slabs (9/7 main/booster amplifier configuration). Measurements represent the approximately 70 target shots taken during the third and fourth quarters of FY10.

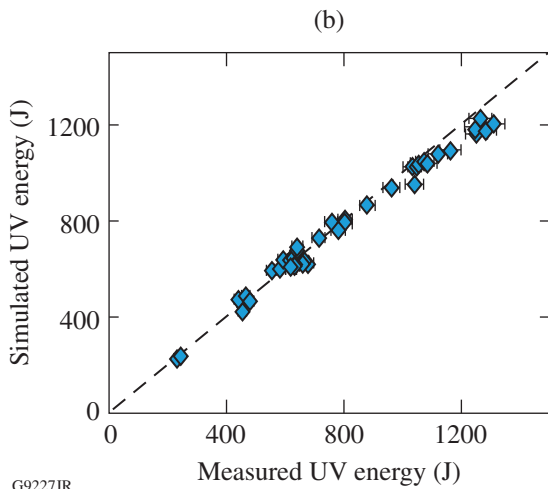
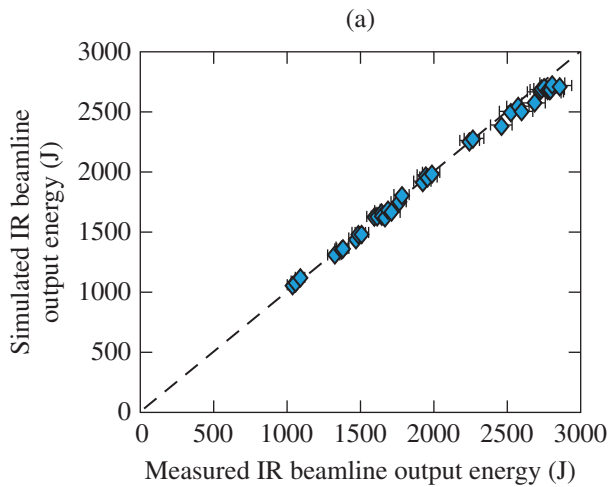


Figure 125.47
Simulated energies using the cw IR and UV beamline models versus measured energies: (a) 1ω Beamline 3 output and (b) corresponding 3ω on-target energy. The dashed line with slope of 1 is shown for reference.

UV near-field modulation. This two-step process provides a shot-ready laser configuration and ensures that 3ω damage thresholds are not exceeded. Typically, only small adjustments to the injection-energy throttle setting are required to achieve, on the first shot, measured 3ω peak fluences that are between 85% and 95% of the 3ω damage threshold. Notably, no significant damage has been observed to date in the long-pulse section of the OMEGA EP beamlines.

Summary

We have described several performance enhancements in the long-pulse section of OMEGA EP that have resulted in better beam quality, greater reliability, and improved efficiency

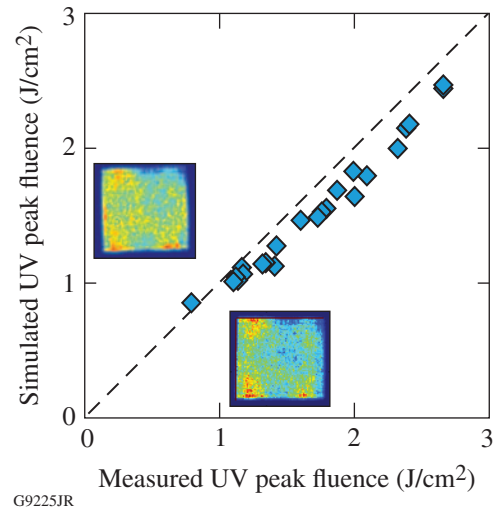


Figure 125.48

3ω peak fluence simulated by using the measured injected near-field beam is plotted against the corresponding measured peak fluence for several OMEGA EP target shots. A simulated and corresponding measured 3ω beam is also shown for one case. Simulated values were $\sim 9\%$ below measurements, on average (dashed line with slope of 1 is shown for reference). By characterizing the model's predictive capability, high-resolution, end-to-end beamline simulations were performed and facility direction provided to operators within a qualification shot cycle.

during shot operations. The sensitivity to front-end, near-field beam quality that results from operation in a regime of low saturation has been reduced using new apodizer designs. These designs have significantly improved the near-field beam profile and reduced the time required to qualify the injected beam. Other methods to reduce beam modulation, such as FCC detuning and the implementation of a PSLIM, are also being pursued. We have described simulation tools used during shot operations that have provided rapid and accurate predictions of beamline performance, ensuring that laser-damage thresholds are not exceeded and providing facility direction to operators within a qualification shot cycle. Higher-damage-threshold UV transport optics have also been procured. Higher energies will allow for greater saturation, greater levels of beam smoothing, and greater on-target energy for a given peak fluence.

ACKNOWLEDGMENT

The authors thank the OMEGA EP operations team for their contributions to the measurements reported here. This work was supported by the U.S. Department of Energy Office of Inertial Confinement Fusion under Cooperative Agreement No. DE-FC52-08NA28302, the University of Rochester, and the New York State Energy Research and Development Authority. The support of DOE does not constitute an endorsement by DOE of the views expressed in this article.

REFERENCES

1. J. H. Kelly, L. J. Waxer, V. Bagnoud, I. A. Begishev, J. Bromage, B. E. Kruschwitz, T. J. Kessler, S. J. Loucks, D. N. Maywar, R. L. McCrory, D. D. Meyerhofer, S. F. B. Morse, J. B. Oliver, A. L. Rigatti, A. W. Schmid, C. Stoeckl, S. Dalton, L. Folsbee, M. J. Guardalben, R. Jungquist, J. Puth, M. J. Shoup III, D. Weiner, and J. D. Zuegel, *J. Phys. IV France* **133**, 75 (2006).
2. T. Alger *et al.*, Lawrence Livermore National Laboratory, Livermore, CA, Report UCRL-ID-132680 (NIF-0014142), NTIS Order No. DE2002-791837 (1999). (Copies may be obtained from the National Technical Information Service, Springfield, VA 22161.)
3. Estimated to be 4 J/cm^2 with a 3-ns Gaussian pulse.
4. I. L. Bass *et al.*, in *High-Power Laser Ablation VI*, edited by C. R. Phipps (SPIE, Bellingham, WA, 2006), Vol. 6261, p. 62612A.
5. T. I. Suratwala *et al.*, “HF-Based Etching Processes for Improving Laser Damage Resistance of Fused Silica Optical Surfaces,” to be published in the *Journal of the American Ceramic Society*.
6. See Fig. 1 of Ref. 5.
7. C. Dorrer and J. D. Zuegel, *J. Opt. Soc. Am. B* **24**, 1268 (2007).
8. R. S. Craxton, *IEEE J. Quantum Electron.* **QE-17**, 1771 (1981).
9. V. Bagnoud and J. D. Zuegel, *Opt. Lett.* **29**, 295 (2004).
10. S.-W. Bahk, E. Fess, B. E. Kruschwitz, and J. D. Zuegel, *Opt. Express* **18**, 9151 (2010).
11. L. M. Frantz and J. S. Nodvik, *J. Appl. Phys.* **34**, 2346 (1963).

Precision Equation-of-State Measurements on NIF Ablator Materials from 1 to 12 Mbar Using Laser-Driven Shock Waves

Introduction

Hydrocarbons are often used as ablator materials for inertial confinement fusion (ICF) studies, satisfying low-surface-roughness constraints and enabling one to introduce dopant atoms that are chemically bonded to the hydrocarbon, preventing its migration through the capsule shell.¹ One of three target ablator designs for the National Ignition Facility (NIF)² calls for glow-discharge polymer ($\text{CH}_{1.3}\text{O}_{0.02}$) (GDP) ablators with various levels of germanium doping (Ge-GDP).^{1,3–5} Introducing a mid-Z dopant reduces preheating of the fuel by increasing the opacity to hard x rays generated close to the coronal plasma; it also lowers the Atwood number.^{1,5} This helps to optimize target performance and relaxes manufacturing constraints.

Ultimately, each proposed NIF target design has its strengths and weaknesses, and the choice of ablator relies on detailed hydrodynamic simulations to specify the shell dimensions, dopant levels, and laser pulse. The aim is to produce a sufficiently robust design such that ignition will be achieved despite experimental uncertainties and hydrodynamic instabilities. These simulations require knowledge of the ablator equation of state (EOS), setting constraints on tolerable capsule surface roughness, ablator thickness, and driver energy. Instability growth rates have been shown to strongly depend on the ablator compressibility and first shock strength as defined by its EOS.^{1,6}

Results presented here form part of a larger study that was aimed at better understanding the behavior of hydrocarbon ablators and to characterize the high-pressure behavior of germanium-doped GDP for NIF ignition targets. Initially there was concern that variation in material properties among GDP and Ge-GDP batches could compromise results. With this in mind, the EOS of CH (polystyrene) and CH_2 (polypropylene), two materials whose fabrication process is well known and reproducible, were measured to high precision.⁷ This resolved uncertainties in the high-pressure (≥ 1 -Mbar) behavior of CH and provided measurements on the high-pressure effect of changes in stoichiometry by varying the H-to-C ratio, through EOS measurements of CH_2 . This provided the basis for interim

tabular model development that described GDP and Ge-GDP for ignition target designs.

Until now, the EOS of CH has been used as a surrogate EOS to model GDP ablators. In comparison to CH, however, GDP has a higher H-to-C ratio and trace amounts of oxygen, absorbed by the films during the fabrication process. Material properties such as initial density and index of refraction also differ between CH and GDP/Ge-GDP films. Although the EOS of CH is known to high precision,⁷ it is not sufficient to accurately describe the behavior of GDP and Ge-GDP. It is still necessary to verify how differences in stoichiometry and material properties influence the EOS of such materials and compare with model predictions.

This study presents the first EOS measurements on GDP and Ge-GDP. These experiments used laser-driven shock waves to provide impedance-matching (IM) conditions with α -quartz as the standard material.^{8,9} Previous studies successfully used quartz as a standard, demonstrating a significant reduction in measurement uncertainties.^{7,9,10} By using velocity interferometry and transparent materials, $\sim 1\%$ precision was obtained in shock-velocity measurements.¹¹ GDP and Ge-GDP data are compared with available LEOS (Livermore equation of state) models, showing close agreement between measurements and model predictions. The IM technique, its associated error analysis, and optimization-enabling precision measurements are discussed in the next section. The sections that follow describe the experimental configuration, targets, and diagnostics, followed by the results and concluding remarks.

Impedance-Matching Technique

The impedance-matching technique allows one to determine a sample's particle velocity (U_p), pressure (P), and density (ρ) through shock-velocity measurements in a reference material, here z -cut α -quartz ($U_{s,Q}$), and the sample being tested, i.e., GDP ($U_{s,GDP}$) or Ge-GDP ($U_{s,Ge-GDP}$).^{12,13} Mass and momentum are conserved as the shock front transits the contact interface between standard and sample. The Rankine–Hugoniot equations¹² are valid at the contact interface, implying U_p and P must be continuous across this boundary. Measurement of the

shock velocity in the standard, at the contact interface, yields the initial shock state from where the standard releases (given the standard has higher impedance than the sample, as in this case). By measuring the shock velocity in the sample, at the contact interface, one can determine the conditions at which the standard and sample equilibrate, yielding the $P(U_p)$ state.

In this study the IM analysis was performed using quartz's experimentally determined Hugoniot^{8,14} and a constant Grüneisen parameter (Γ) to calculate off-Hugoniot states, as previously described.^{7,14,15} Using quartz ($\rho_0 = 2.65 \text{ g/cm}^3$, $n = 1.547$) as an IM standard provides higher precision than opaque standards by reducing errors associated with the standard's initial state, from which off-Hugoniot curves are launched. It also relaxes shock-stability constraints since changes in shock velocity are directly measured and can be accounted for in the analysis. By measuring *in-situ* shock velocities, one can measure observables ($U_{s,Q}$, $U_{s,GDP}$, and $U_{s,Ge-GDP}$) close to the contact interface, where the IM conditions are valid.

Data precision obtained through the IM technique is strictly correlated to the accuracy with which the states in the standard are known. Although not often accounted for, systematic uncertainties enter the IM analysis through calculation of the standard's Hugoniot and off-Hugoniot states. Quartz's shock EOS was previously measured in a large pressure range (~2 to 15 Mbar) through impedance matching with aluminum (Al) standard, using laser-driven shock waves.⁸ These experiments were in agreement with previous gas-gun and nuclear and chemical explosive studies, displaying linear behavior in the U_s-U_p plane, given by a piecewise linear function of general form $U_s = a_0 + a_1(U_p - \beta)$,

$$U_s = (6.914 \pm 0.028)(1.667 \pm 0.038)(U_p - 11.865),$$

for $U_p < 6.358 \text{ } \mu\text{m/ns}$, (1)

$$U_s = (19.501 \pm 0.068)(1.276 \pm 0.022)(U_p - 11.865),$$

for $U_p \geq 6.358 \text{ } \mu\text{m/ns}$, (2)

where an orthonormal basis is used such that resulting errors are uncorrelated.¹⁴ This fit was used in this study's analysis.

Quartz's release states were approximated via a Mie-Grüneisen EOS as described in McQueen *et al.*¹⁵ Based on solid and porous silica Hugoniot measurements,^{8,14,16,17} quartz's Grüneisen parameter was shown to be nearly constant with $\Gamma = 0.66 \pm 0.1$. Model predictions in a similar pressure range

estimate the value to be $\Gamma = 0.64 \pm 0.11$ (Ref. 9), in agreement with experimental results. This analysis uses the model-based value for Γ and corresponds to the only model-based parameter entering this IM analysis. By using quartz experimental principal Hugoniot and a Mie-Grüneisen formalism to approximate release states, one can propagate systematic uncertainties inherent in the IM technique.

Random uncertainties enter the IM analysis through calculation of the standard and sample Rayleigh lines, $P = \rho_0 U_s U_p$, describing the thermodynamic path taken during compression in the $P-U_p$ plane. These errors often involve only shock-velocity measurement uncertainties; in the case of GDP and Ge-GDP, uncertainties in their initial densities were also accounted for, translating to an increase in random errors in comparison to previous precision EOS measurements.⁷ The total error associated with the measured U_p , P , and ρ corresponds to the quadrature sum of both random and systematic uncertainties.

IM calculations are often performed in the $P-U_p$ plane since both of these quantities must be continuous across the contact interface between the standard and sample. In the previously described framework, the final $P(U_p)$ is a function of nine parameters: a_{0L} , a_{0H} , a_{1L} , a_{1H} , Γ , ρ_{0Q} , ρ_{0CH_x} , $U_{s,Q}$, and U_{s,CH_x} , and their corresponding uncertainties. The first four variables are fitting parameters for the quartz principal Hugoniot, where subscripts L and H refer to the low ($U_p < 6.358 \text{ } \mu\text{m/ns}$) and high ($U_p \geq 6.358 \text{ } \mu\text{m/ns}$) fits. The fifth parameter corresponds to the model-dependent Grüneisen parameter, and the last four correspond to the quartz and sample initial density and measured shock velocity. Because quartz's experimentally derived principal Hugoniot and Grüneisen-based release can be considered independent, error contributions from each parameter are found by calculating deviations from the nominal U_p , P , and ρ results. Note that this amounts to eight error contributions since no error is assumed for quartz's initial density.

Recent work on the Sandia Z Machine measured the EOS of quartz in the 1- to 16-Mbar pressure regime,¹⁸ observing curvature in the U_s-U_p plane not present in the EOS used herein. If real, this difference in EOS would cause systematic shifts in the derived sample EOS. Although these discrepancies in the principal Hugoniot of quartz have yet to be resolved, it is important to acknowledge them since they apply to the IM analysis. This subject is discussed in **Appendix A**, p. 56.

Experimental Method

Experiments were performed on the OMEGA laser,¹⁹ a frequency-tripled Nd:glass laser that produces 351-nm light.

Shock pressures were generated using ~250 to 2100 J delivered in a nominally 2-ns square pulse. Focal-spot profiles were smoothed using distributed phase plates,²⁰ leading to a uniform irradiation area with a 600- or 800- μm diameter. This resulted in average irradiances on target of 0.24 to 2.5×10^{14} W/cm².

Experiments were conducted using multilayered 3-mm \times 3-mm planar targets, which had a 20- μm CH ablator designed to prevent preheating of the target by minimizing x rays generated in the coronal plasma and a 90- μm -thick pusher made of z-cut α -quartz, used as the standard material for IM. On the rear side of the pusher were two samples: ~30 μm of Ge-GDP on the top half of the target and ~30 μm of GDP on the bottom half of the target. This allowed for simultaneous EOS measurements of both materials in a single shot to be conducted.

Ideally the probe beam used to diagnose shock velocities reflects off only the moving shock front; in practice, the system can register back-reflections and internal reflections from the target layers, referred to as “ghost fringes.” To mitigate these effects, the free surface of all targets, that opposite the drive beams, had an antireflection coating to minimize ghost reflections. Because IM measurements are performed at the contact interface between standard and sample, glue layers between these materials were kept at a minimum, estimated to be no more than 1 to 2 μm thick. For some shots, the GDP and Ge-GDP films were directly deposited onto the α -quartz, requiring no glue layer.

GDP and Ge-GDP films were made and characterized in small batches by General Atomics (GA).²¹ Material properties of these films, such as stoichiometry, initial density, and index

of refraction, varied slightly among batches (of the order of 1% to 3%). These differences were taken into account in the data analysis and are summarized in Table 126.I. Elemental compositional stoichiometry was based on x-ray fluorescence (XRF) chemical analysis and XRF calculations. Average initial densities were obtained by measuring the volume and weight of each film batch. The film length and width were measured within 0.1 mm, and thicknesses were measured by interferometry techniques to within 0.5 μm , resulting in initial density uncertainties between 1% and 2%. For each batch, a separate sample fabricated from the same batch material was used to measure index of refraction. This sample was submerged in various Cargille Laboratories²² series A index-matching fluids. White-light interferometry with a 532-nm filter was used to determine the best match among the various index-matching fluids. The index of refraction for the matching fluid was verified using an Abbé refractometer, finding agreement to ± 0.0005 . Both the Abbé refractometer and the index-matching fluids were referenced to the sodium D line at $\lambda = 589.3$ nm (at 25°C). The Cauchy equation, with coefficients provided by the vendor, were used to find the index of refraction at $\lambda = 532$ nm. Uncertainties associated with index-of-refraction measurements arise from estimated fringe offsets and wavelength correction.

Shock velocities were measured using a line-imaging velocity interferometer system for any reflector (VISAR),¹¹ with an 800- μm field of view. Two interferometers with different sensitivities were used to discern the 2π phase-shift ambiguity occurring at fringe jumps and breakout times. Uncorrelated velocity sensitivities of 2.732 and 6.906 $\mu\text{m}/\text{ns}/\text{fringe}$ were produced by using etalons with 18- and 7-mm thickness, respec-

Table 126.I: Material properties and associated errors at ambient conditions for ablator material films, as obtained for each batch. The shot numbers that used each of the batches are also indicated below.

Material	Formula	Ge (at. %)	ρ_0 (g/cm ³)	$n(\lambda = 532 \text{ nm})$
GDP*	CH _{1.36} O _{0.01}	—	1.06 \pm 0.02	1.571 \pm 0.005
GDP†	CH _{1.38} O _{0.02}	—	1.05 \pm 0.05	1.571 \pm 0.005
GDP‡	CH _{1.35} O _{0.01}	—	1.044 \pm 0.005	1.563 \pm 0.010
Ge-GDP§	CH _{1.42} O _{0.04}	0.7	1.13 \pm 0.05	1.572 \pm 0.005
Ge-GDP†	CH _{1.43} O _{0.05}	0.66	1.13 \pm 0.05	1.572 \pm 0.005
Ge-GDP	CH _{1.40} O _{n/a}	0.5	1.13 \pm 0.05	1.572 \pm 0.005
Ge-GDP‡	CH _{1.35} O _{0.01}	0.5	1.10 \pm 0.05	1.570 \pm 0.010

*Shots 54126, 54127, 54185, 54187, 52635

§Shots 54127, 54185, 54187, 52630

†Shots 55774, 55775, 55777–55785

||Shots 56115–56118

‡Shots 57162–57164

tively, where the velocity sensitivity in each material varied based on its index of refraction. The dielectric materials used were subject to drive pressures in the Mbar range, generating reflective shock fronts. The VISAR probe laser—a *Q*-switched, injection-seeded Nd:YAG laser operating at 532 nm with an ~50-ns full width at half maximum (FWHM)—reflected off the shock front. This signal was relayed to the set of interferometers and recorded on streak cameras with a 15- or 9-ns temporal window (one for each VISAR), providing streak images with temporal and 1-D spatial resolution. Since the shock fronts were highly reflective, the measured Doppler-shifted signal detected by VISAR is directly correlated to the velocity of the shock wave. Streak images were post-processed using a fast Fourier transform (FFT) method,^{11,23} resolving fringe jumps to ~5% of a fringe. This translates to ~1% precision in shock-velocity measurements, with typical measurements resulting in five fringe shifts. Although the streak cameras had temporal resolutions close to 10 ps, the diagnostic temporal response was dominated by etalon delay times of either 90 or 40 ps.

The experimental configuration is shown in Fig. 126.1(a); the OMEGA¹⁹ beams irradiate the front of the target, with VISAR aligned opposite the drive beams perpendicular to the rear surface of the target. Because targets were composed of only transparent materials, VISAR provided a continuous shock-velocity history as the shock wave transited each target layer. Figure 126.1(b) shows a section of the VISAR streak image, corresponding to the bottom half of the target (GDP). Here the quartz was driven to a shock pressure of 8.6 Mbar, corresponding to 4.90 Mbar in GDP and 5.08 Mbar in Ge-GDP. In Fig. 126.1(b) the laser drive starts at $t = 0$ and the shock enters the quartz at ~0.6 ns. By ~2 ns the shock in the quartz has equilibrated with the ablation pressure and its velocity stabilizes considerably. At ~4.5 ns, the shock reaches the GDP sample and reaches the sample's rear surface at ~6 ns. It is clear from Fig. 126.1(b) that the quartz:GDP contact interface has finite temporal width at 4.5 ns, owing to the glue layer and VISAR temporal resolution of 40 or 90 ps. (The same is true for the quartz:Ge-GDP interface, not shown.) Consequently, shock velocities are not measured at the “true” contact interface between reference and sample, but at an earlier and later time, respectively. This is accounted for by linearly fitting the velocity profile over ~300 ps and extrapolating to the time where the true contact interface would be, here defined to be the equidistant (temporal) location between the quartz and sample boundary, shown as t' in Fig. 126.1(c). This methodology also accounts for any deceleration observed in the measurements, such that the IM conditions are still matched despite shock-wave decay. Figure 126.1(c) shows the shock-velocity histories

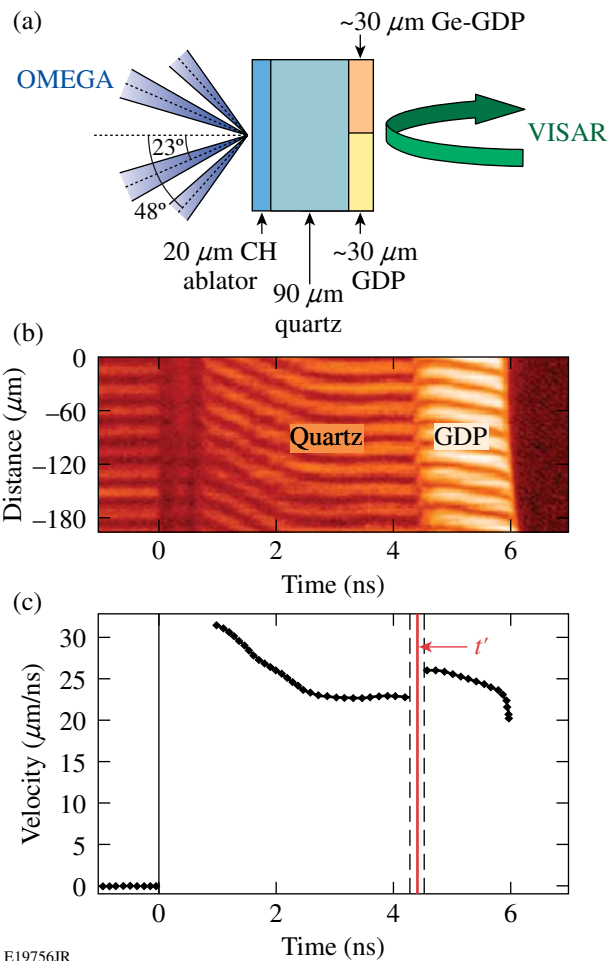


Figure 126.1

(a) Schematic of two material targets used in the experiments. Here the OMEGA beams irradiate the target at 23° and 48° to target normal, with VISAR aligned and focused to the rear surface of the target. Multilayer planar targets were composed of a CH ablator, quartz standard, and two different samples (GDP and Ge-GDP) to be tested. (b) VISAR streak image corresponding to the bottom half of the target, containing data for GDP, shows continuous tracking of the shock front within the standard and material being tested. (c) Final shock-velocity measurements in quartz and GDP after data extraction and analysis. For the IM analysis, shock velocities are evaluated at t' .

for quartz and GDP from the streak image data shown in Fig. 126.1(b), after applying the FFT and matching velocity solutions from both interferometers.

Results and Discussion

1. Glow-Discharge Polymer

Single-shock principal Hugoniot measurements for GDP were obtained from ~1 to 12 Mbar. Experimental observables and resulting kinematic properties for GDP are listed in Table 126.II. Results display a linear U_s-U_p relation, given by $U_s = (24.56 \pm 0.07) + (1.29 \pm 0.01)(U_p - 16.76)$. This fit was

obtained through a least-squares fit using an orthogonal polynomial basis, resulting in fitting parameters that are independent of each other, i.e., including higher-order terms does not affect the value of lower-order coefficients.²⁴ Because of this independence, the errors associated with such fitting parameters are independent. The initial density, compositional stoichiometry, and index of refraction of the samples varied between fabrication batches (Table 126.I); these variations were included in the analysis. Alterations of the high-pressure behavior caused by variations in initial parameters were not evident in the U_s-U_p plane; therefore, no distinction was made among the batches for the linear fit in this plane.

Recently an LEOS was developed for GDP (LEOS 5310). Current LEOS models are developed based on the quotidian equation of state (QEOS)²⁵-type construct, where an additive approach is taken to describe the Helmholtz free energy. The included components account for ion/nuclear and electron contributions, as well as semi-empirical bonding corrections, needed to obtain reasonable results for cold matter at or near solid density, or quantum or exchange corrections. Typically the electron contribution is calculated via a Thomas–Fermi model and the ion contribution via the Cowan EOS^{25,26} (an analytical model), combining ideal gas, fluid scaling laws, the Debye lattice theory, Grüneisen EOS, and the Lindenmann melt law.

Table 126.II: Principal Hugoniot results for glow-discharge polymer (GDP) using the IM technique with quartz reference. Measured shock velocity with error is given for both quartz ($U_{s,Q}$) and GDP ($U_{s,GDP}$). The resulting particle velocity ($U_{p,GDP}$), pressure (P_{GDP}), and density (ρ_{GDP}) of shocked GDP are listed, with given random and systematic uncertainties. Random uncertainties enter the IM analysis through errors in shock-velocity measurements and initial density variations, while systematic errors stem from uncertainties in quartz’s principal Hugoniot and release states.

Shot	$U_{s,Q}$ ($\mu\text{m/ns}$)	$U_{s,GDP}$ ($\mu\text{m/ns}$)	$U_{p,GDP}$ (ran,sys) ($\mu\text{m/ns}$)	P_{GDP} (ran,sys) (Mbar)	ρ_{GDP} (ran,sys) (g/cm^3)
55782	13.12±0.09	13.77±0.10	8.47(0.14,0.21)	1.22(0.02,0.03)	2.73(0.08,0.11)
55783	14.42±0.11	15.72±0.10	9.81(0.16,0.22)	1.62(0.03,0.03)	2.79(0.08,0.12)
55781	16.44±0.11	18.20±0.10	11.97(0.19,0.1)	2.29(0.04,0.02)	3.07(0.1,0.05)
55780	18.64±0.10	21.08±0.10	14.03(0.2,0.13)	3.11(0.04,0.03)	3.14(0.09,0.06)
55785	18.90±0.10	21.55±0.10	14.25(0.2,0.13)	3.22(0.05,0.03)	3.10(0.09,0.05)
55779	20.24±0.10	23.09±0.10	15.53(0.21,0.15)	3.77(0.05,0.04)	3.21(0.1,0.07)
55784	20.46±0.13	23.07±0.10	15.79(0.24,0.16)	3.82(0.06,0.04)	3.33(0.11,0.07)
55778	21.12±0.09	24.06±0.10	16.39(0.22,0.17)	4.14(0.06,0.04)	3.29(0.1,0.07)
55777	22.76±0.10	26.05±0.10	17.93(0.24,0.21)	4.90(0.07,0.06)	3.37(0.11,0.09)
52635	24.14±0.10	27.77±0.10	19.20(0.15,0.24)	5.65(0.05,0.07)	3.44(0.07,0.1)
55774	24.45±0.10	28.03±0.23	19.56(0.25,0.25)	5.76(0.08,0.07)	3.47(0.13,0.1)
55775	24.68±0.11	28.38±0.11	19.76(0.26,0.26)	5.89(0.08,0.08)	3.46(0.11,0.1)
54127	24.65±0.20	28.44±0.20	19.67(0.25,0.26)	5.93(0.08,0.08)	3.44(0.12,0.1)
54187	25.90±0.11	29.87±0.15	20.87(0.16,0.29)	6.61(0.06,0.09)	3.52(0.08,0.11)
57164	26.84±0.11	30.99±0.10	21.85(0.28,0.32)	7.07(0.09,0.1)	3.54(0.11,0.12)
54126	28.19±0.12	32.79±0.16	23.01(0.18,0.35)	8.00(0.07,0.12)	3.55(0.08,0.13)
54185	29.31±0.11	33.94±0.16	24.11(0.17,0.38)	8.67(0.07,0.14)	3.66(0.08,0.14)
57162	29.80±0.10	34.63±0.10	24.66(0.31,0.40)	8.91(0.11,0.14)	3.63(0.12,0.15)
57163	34.15±0.10	40.10±0.10	28.77(0.35,0.52)	12.04(0.15,0.22)	3.69(0.12,0.17)

These equations are parameterized such that limiting values (at solid density, as ρ approaches ∞ , etc.) yield reasonable results and available experimental data are recovered.²⁵ The LEOS models improve on this construct by providing alternate treatments for the ionic thermal contribution and melt matching to ensure positive heat capacities, break points for cold-curve modification, a differentiable density-dependent Grüneisen parameter, and a more adequate treatment for low-density states via a soft-sphere model.²⁷ Because experimental EOS measurements for GDP were unavailable at the time LEOS 5310 was constructed, this model was benchmarked¹ using precision EOS measurements for CH⁷ in the high-pressure regime and previous CH gas-gun data at lower pressures,²⁸ where density scaling based on the equilibrium densities of CH and GDP was used where applicable.²⁷ Modeled GDP behavior was further constrained by generating data from CHEETAH, a thermochemical model.²⁷ LEOS 5310 does not include dissociation. The assumed initial density and stoichiometry for LEOS 5310 are listed in Table 126.III.

The H-to-C ratio and initial density of LEOS 5310 were slightly different than the GDP samples used in these experiments; differences varied by $\sim 1\%$, on average, for both parameters. Oxygen levels measured in the GDP films were quite small (O-to-C ratios of 0.01 and 0.02) and had no detectable effect on the material's high-pressure behavior since batches with different oxygen levels compared well in both the U_s-U_p and $P-\rho$ planes (see Figs. 126.2 and 126.3). The oxygen doping in the LEOS 5310 model is comparable to that found in the films.

Figure 126.3 shows GDP results in the $P-\rho$ plane. Here, green (smaller) and gray (larger) error bars represent random and total errors, respectively. Material initial densities are distinguished by color shades as $\rho_0 = 1.06 \text{ g/cm}^3$, (dark green diamonds), 1.05 g/cm^3 (medium green diamonds), and 1.044 g/cm^3 (light green diamonds). Here the LEOS 5310 model was evaluated with initial density $\rho_0 = 1.05 \text{ g/cm}^3$, the average initial density between the GDP batches, for compari-

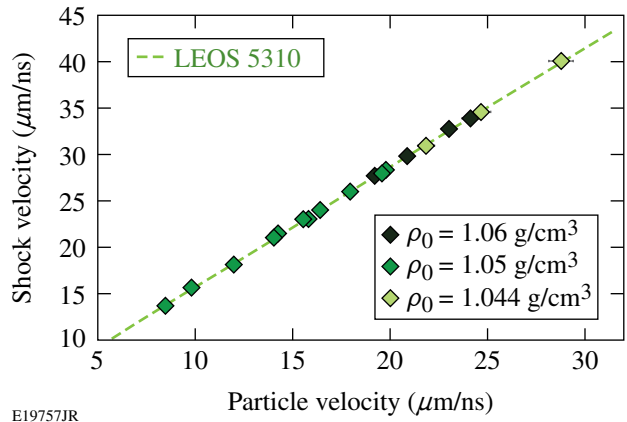


Figure 126.2
Principal Hugoniot measurements and models for GDP in the U_s-U_p plane. Data were obtained through the IM construct with quartz reference on GDP films with initial density $\rho_0 = 1.06$ (dark green diamonds), 1.05 (medium green diamonds), and 1.044 (light green diamonds) g/cm^3 .

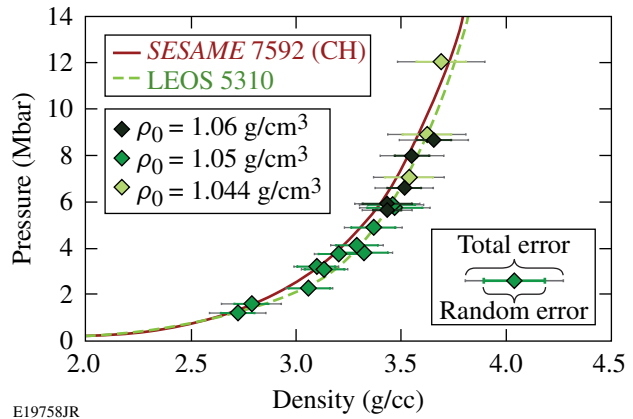


Figure 126.3
Principal Hugoniot data and models for GDP in the $P-\rho$ plane, with GDP film's initial densities as previously described. Data are compared with CH SESAME 7592 (Ref. 30) and the LEOS 5310 model, evaluated at initial density $\rho_0 = 1.05 \text{ g/cm}^3$. Random uncertainties are shown as green (smaller) error bars and total uncertainties (quadrature of random and systematic uncertainties) as the black (larger) error bars.

Table 126.III: Initial density and stoichiometry for available LEOS models for GDP and Ge-GDP.

Model	ρ_0 (g/cm^3)	Carbon (at. %)	Hydrogen (at. %)	Oxygen (at. %)	Germanium (at. %)
LEOS 5310	1.04	42.34	57.15	0.51	0
LEOS 5312	1.053	42.25	57.04	0.51	0.2
LEOS 5315	1.073	42.12	56.87	0.505	0.5

son. *SESAME 7592* (Ref. 29), the CH *SESAME* model that best fit the precision polystyrene data, is shown as a reference. Data are in close agreement with LEOS 5310 model predictions and are only slightly softer than *SESAME 7592*, showing that GDP behaves quite similarly to CH in the high-pressure fluid regime. In this plane, it is also evident that data precision is degraded in comparison to previous precision EOS studies, yielding 3.4% to 5.6% precision in density. This is due to the inclusion of initial density uncertainties, which accounted for anywhere between 5.2% to 44% of the total density error.

2. Germanium-Doped GDP

Germanium-doped GDP (Ge-GDP) was studied in the ~1- to 12-Mbar pressure range. Table 126.IV presents shock-velocity measurements and kinematic properties obtained through the IM technique using quartz standard. With the exception of one batch, the initial density and index of refraction of the Ge-GDP films were consistent (Table 126.I), although levels of Ge doping varied from 0.5% to 0.7%. The equation of state of Ge-GDP in the U_s-U_p plane (shown in Fig. 126.4) displays a linear relation given by $U_s = (23.39 \pm 0.07) + (1.31 \pm 0.01)(U_p - 15.92)$. Here

Table 126.IV: Principal Hugoniot results for germanium-doped glow-discharge polymer (Ge-GDP) using the IM technique with quartz reference. Measured shock velocities in quartz ($U_{s,Q}$) and GDP ($U_{s,Ge-GDP}$) are given with measured error. The resulting particle velocity ($U_{p,Ge-GDP}$), pressure (P_{Ge-GDP}), and density (ρ_{Ge-GDP}) of shocked Ge-GDP are listed with random and systematic uncertainties associated with each measurement. Random uncertainties enter the IM analysis through errors in shock-velocity measurements and initial density variations; systematic errors stem from uncertainties in quartz's principal Hugoniot and release states.

Shot	$U_{s,Q}$ ($\mu\text{m/ns}$)	$U_{s,Ge-GDP}$ ($\mu\text{m/ns}$)	$U_{p,Ge-GDP}$ (ran,sys) ($\mu\text{m/ns}$)	P_{Ge-GDP} (ran,sys) (Mbar)	ρ_{Ge-GDP} (ran,sys) (g/cm^3)
55782	12.98±0.11	13.56±0.09	8.20(0.15,0.21)	1.26(0.02,0.03)	2.86(0.09,0.11)
55783	14.50±0.09	15.21±0.11	9.83(0.14,0.22)	1.69(0.03,0.04)	3.20(0.1,0.14)
55781	15.97±0.10	17.28±0.12	11.37(0.17,0.11)	2.22(0.04,0.02)	3.3(0.11,0.06)
55780	18.64±0.10	20.76±0.11	13.83(0.19,0.12)	3.25(0.05,0.03)	3.38(0.1,0.06)
55785	18.84±0.10	20.87±0.27	14.04(0.19,0.12)	3.31(0.05,0.03)	3.45(0.15,0.06)
56118	19.24±0.11	21.18±0.09	14.44(0.2,0.13)	3.46(0.05,0.03)	3.55(0.11,0.07)
55779	20.29±0.10	22.5±0.11	15.41(0.2,0.15)	3.92(0.05,0.04)	3.59(0.11,0.08)
55784	20.44±0.12	22.81±0.10	15.53(0.22,0.15)	4.00(0.06,0.04)	3.54(0.11,0.07)
55778	20.91±0.10	23.53±0.19	15.94(0.21,0.16)	4.24(0.06,0.04)	3.5(0.12,0.07)
55777	22.66±0.10	25.53±0.16	17.59(0.23,0.2)	5.08(0.07,0.06)	3.64(0.12,0.09)
56117	23.37±0.09	26.53±0.11	18.23(0.23,0.21)	5.46(0.07,0.06)	3.61(0.11,0.09)
52630	24.18±0.10	27.35±0.10	19.02(0.24,0.24)	5.88(0.07,0.07)	3.71(0.11,0.10)
55774	24.34±0.10	27.87±0.11	19.11(0.24,0.24)	6.02(0.08,0.07)	3.59(0.11,0.10)
55775	24.5±0.12	27.76±0.12	19.31(0.25,0.24)	6.06(0.08,0.08)	3.71(0.12,0.11)
54127	24.7±0.10	28.02±0.18	19.49(0.24,0.25)	6.17(0.08,0.08)	3.71(0.13,0.11)
57164	27.04±0.10	31.14±0.11	21.78(0.27,0.31)	7.45(0.09,0.11)	3.65(0.11,0.12)
56116	26.82±0.10	30.75±0.20	21.45(0.26,0.30)	7.45(0.1,0.10)	3.73(0.12,0.12)
54185	29.22±0.09	33.72±0.09	23.67(0.28,0.36)	9.02(0.11,0.14)	3.79(0.11,0.14)
57162	29.90±0.10	34.57±0.15	24.47(0.29,0.39)	9.29(0.12,0.15)	3.76(0.12,0.15)
56115	31.80±0.10	36.65±0.10	26.12(0.31,0.44)	10.82(0.13,0.18)	3.93(0.12,0.16)
57163	33.89±0.10	39.64±0.14	28.20(0.33,0.50)	12.27(0.15,0.22)	3.80(0.12,0.17)

a least-squares fitting with an orthonormal basis was used. In this figure Ge-GDP data are compared to available models for Ge-doped GDP, LEOS 5312, and LEOS 5315 with assumed 0.2% and 0.5% Ge doping. These models display a similar behavior in this plane and are in agreement with measured data. LEOS 5312 and 5315 models for Ge-GDP were developed in a similar fashion as previously described for LEOS 5310. Because CHEETAH was not equipped to model Ge at the time, Si was used instead. LEOS 5315 and 5312 were developed independently; therefore the fit to the CHEETAH model is different for these models (LEOS 5310 and 5315 share the same fit). This is evident in the P - ρ plane (Fig. 126.5), where

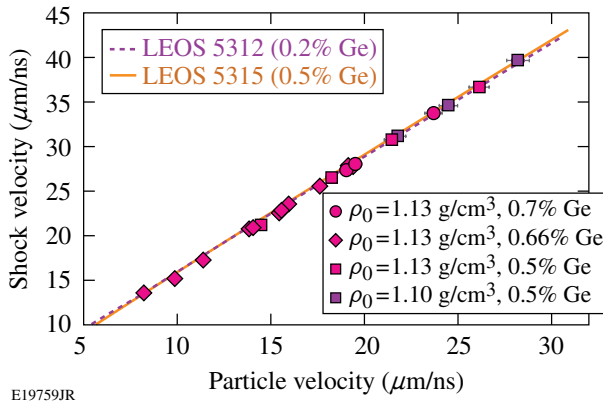


Figure 126.4
Principal Hugoniot measurements and models for Ge-GDP in the U_s-U_p plane. Data were obtained through the IM construct with quartz reference on Ge-GDP films with initial density $\rho_0 = 1.13 \text{ g/cm}^3$ (magenta circles, squares, and diamonds) and 1.10 g/cm^3 (purple squares), where circles, diamonds, and squares represent 0.7%, 0.66%, and 0.5% Ge doping.

the models cross at $\sim 2 \text{ Mbar}$. Like LEOS 5310, LEOS 5312 and 5315 do not include a dissociation model.²⁷ Development of LEOS models for GDP and Ge-GDP is an ongoing effort. Much of the difficulty in developing models that accurately describe material behavior over a wide range of states, in this case, is a lack of experimentally measured properties, which need to be inferred through codes such as CHEETAH or approximated using measured quantities of similar materials. Future LEOS table series, sharing the same fit to CHEETAH results, will include a dissociation model, have more stringent constraints to release states, and include new material response measurements as they become available, including this work. Material properties assumed by LEOS 5312 and 5315, such as initial density and compositional stoichiometry, are listed in Table 126.III.

The total uncertainty in density was between 3.5% and 5.4%, of which 7.2% to 40% was due to the Ge-GDP initial density error contribution, varying as a function of pressure. Figure 126.5 shows Ge-GDP EOS results in the P - ρ plane. Here samples with initial density of 1.13 g/cm^3 are shown as magenta circles (Ge at 0.7%), diamonds (Ge at 0.7%), and squares (Ge at 0.5%), while data taken on samples with initial density of 1.10 g/cm^3 are shown as purple squares (Ge at 0.5%). Random errors are shown as the colored error bars, which included shock velocity (in Ge-GDP and quartz) and initial density uncertainties. Total errors, representing the quadrature sum of random and systematic uncertainties, are shown as gray error bars. Data are compared with LEOS 5312 and LEOS 5315, both evaluated at an initial density of 1.13 g/cm^3 . LEOS 5310, evaluated at $\rho_0 = 1.05 \text{ g/cm}^3$, and *SESAME 7592* are plotted on this figure as a reference. On average, the percent differ-

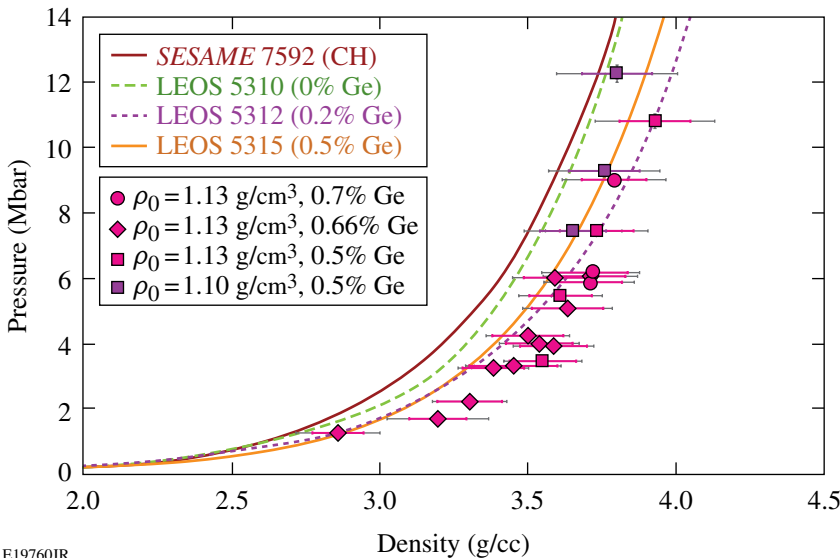


Figure 126.5
Principal Hugoniot data and models for Ge-GDP in the P - ρ plane, with Ge-GDP film initial densities and Ge doping as previously described. Data are compared with Ge-GDP available LEOS models, evaluated at an initial density $\rho_0 = 1.13 \text{ g/cm}^3$. Models used to compare with GDP data are included as reference. Random uncertainties are shown as the colored (shorter) error bars and total uncertainties (quadrature of random and systematic uncertainties) as the gray (longer) error bars.

ence between the model and sample H-to-C ratio was ~3.5%, although it varied up to 5.6%, and oxygen levels assumed in the models were smaller than those measured. Despite these differences, Fig. 126.5 shows that the data follow similar trends and agree with model predictions within experimental error. Between 2 and 4 Mbar, a slight softening of the data compared to model predictions is observed. Above these pressures, the Ge-GDP data begin to stiffen (becoming less compressible), approaching closer agreement with theoretical models. Although differences among models are amplified in the P - ρ plane, the data presented here are not able to discriminate between models because of random uncertainties.

Plotting the Ge-GDP results in the pressure-compression (P - ρ/ρ_0) plane (see Fig. 126.6) shows a smooth trend in close agreement with LEOS models for all pressures, i.e., no stiffening as observed in the P - ρ plane. The apparent stiffness at higher pressures observed in the P - ρ plane results from initial density variations. Ge-GDP was observed to undergo compression between $2.5\times$ and $3.4\times$, comparable to those reached by GDP, as shown in Fig. 126.7 (the composite results from both materials). Even with the fairly high precision of these measurements, the errors in the data make it difficult to favor any model behavior in this plane, even at the highest pressures, where models differ most.

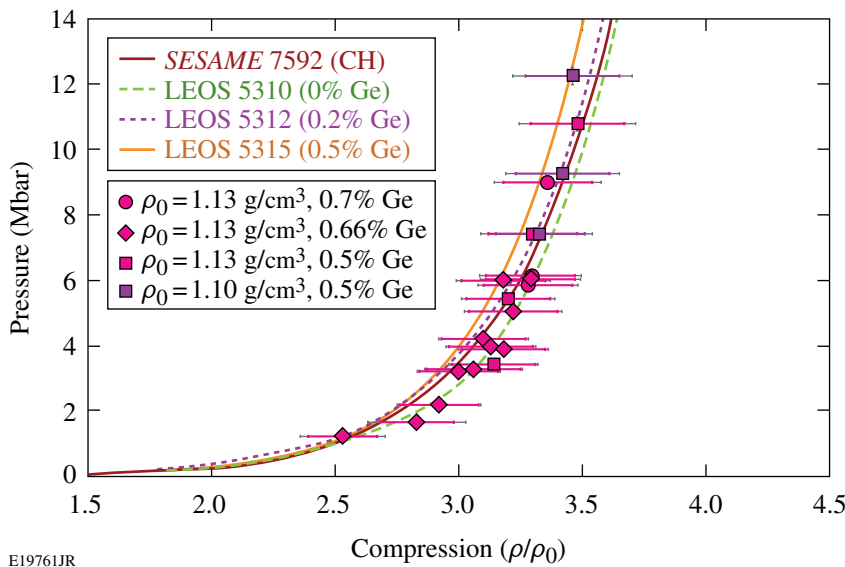


Figure 126.6
Ge-GDP results in the pressure-compression plane, with models and data as described in previous figures, showing structure observed in the P - ρ plane is likely due to initial density variations.

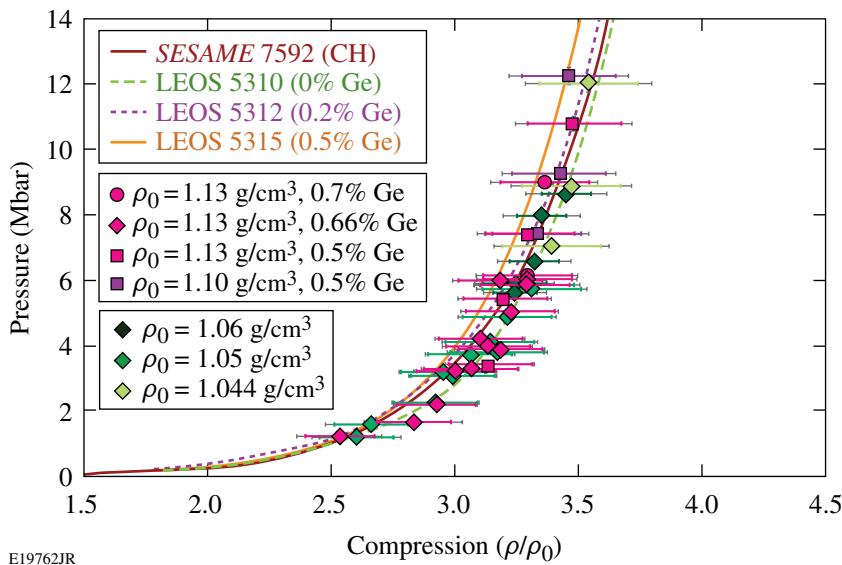


Figure 126.7
Results in the pressure-compression plane show that Ge-GDP and GDP reach similar compression states.

Conclusions

The high-pressure behavior of GDP and Ge-GDP was measured at shock pressures of ~ 1 to 12 Mbar. The use of quartz as the IM standard along with a time-resolved VISAR diagnostic facilitated the measurement of shock velocities to $\sim 1\%$ precision in transparent materials. This reduced the uncertainties in the initial shock state of quartz, in turn minimizing measurement errors in the GDP and Ge-GDP EOS results. Using quartz's experimentally derived principal Hugoniot and a Mie–Grüneisen EOS, systematic uncertainties inherent in the IM technique were accounted for in the analysis. Density uncertainties of 3.4% to 5.6% (GDP) and 3.5% to 5.4% (Ge-GDP) incorporate initial density variations in the samples. The initial density error contribution varies as a function of pressure and estimated error value, contributing up to 40% of the total error in the GDP and Ge-GDP density measurements.

GDP results are in close agreement with the LEOS 5310 model in both the U_s-U_p and $P-\rho$ planes, despite differences in stoichiometry of $\sim 1\%$. Likewise, data indicate that GDP behaves similarly to CH when shocked to greater than ~ 1 Mbar, displaying only a slight softness at higher pressures in comparison to this material. The effect of germanium doping on GDP samples is predicted reasonably well by available LEOS models, which are in agreement with measured Ge-GDP results, despite differences in assumed material. The compressibility of Ge-GDP on the Hugoniot is well predicted by both LEOS 5312 and LEOS 5315, although data are not able to discriminate between the two models.

ACKNOWLEDGMENT

The authors would like to thank the Omega Laser Facility personnel for their professionalism and outstanding work that enabled us to perform these experiments. This work was supported by the U.S. Department of Energy Office of Inertial Confinement Fusion under Cooperative Agreement No. DE-FC52-08NA28302, the University of Rochester, and the New York State Energy Research and Development Authority. The support of DOE does not constitute an endorsement by DOE of the views expressed in this article.

Appendix A: Influence of Quartz as a Standard

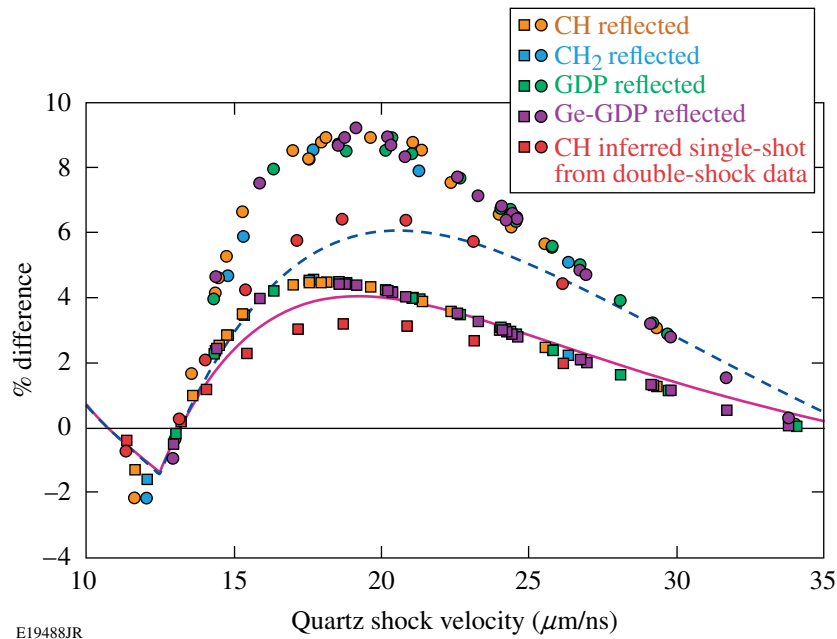
An uncertainty exists in the measured behavior of GDP and Ge-GDP as a result of discrepancies in the measured quartz EOS. Recent experiments performed on the Sandia Z Machine by Knudson *et al.*¹⁸ observed noticeable curvature in its $U_s(U_p)$ relation, previously observed to be linear in laser experiments.⁸ Since IM results are relative to the reference material, we present here an assessment of the effects of a different quartz EOS, were the Knudson result to be accurate.

The EOS of quartz enters the IM analysis through the principal Hugoniot and the off-Hugoniot (release) states. The

analysis presented in this study approximates release states using a Mie–Grüneisen EOS; this assumes Γ is independent of density such that Γ/V is constant. A curvature in the U_s-U_p plane could imply a non-constant Γ , having consequences in the methods used to calculate releases for IM calculations. Γ could also remain independent of density but would likely have a different value than that used in this study.

To compare both fits on an equal basis, the reflected-Hugoniot approximation was used to arrive at IM results for both cases, using measured quantities from CH, CH₂, GDP, and Ge-GDP experiments. Although the reflected Hugoniot is not a highly accurate approximation, for the pressures and material properties under consideration, the interest herein is in the *differences* among IM results, as a consequence of applying each quartz model. The percent differences in the CH, CH₂, GDP, and Ge-GDP density and pressure are shown in Fig. 126.8. Here a positive percent difference indicates the quartz fit obtained through laser data leads to larger pressure or density values, in comparison to the Z-machine quartz fit. The dashed blue and magenta curves represent the percent differences in density and pressure between the two quartz fits, peaking at $\sim 4\%$ and 6% in pressure and density. The orange, light blue, green, and purple circles and squares represent the percent differences in density and pressure for CH, CH₂, GDP, and Ge-GDP, respectively. This analysis groups together deviations in quartz's initial shock state and deviations between estimated release curves. Because these materials have similar impedances, the percent differences follow similar trends as a function of pressure (shock velocity), peaking at comparable quartz shock velocities. For these materials, maximum deviations in pressure and density were found to be $\sim 4.4\%$ and 8.8% at quartz shock velocities of 18 to 19 $\mu\text{m/ns}$, corresponding to hydrocarbon pressures of ~ 3.5 Mbar. On the other hand, percent differences in density and pressure were as low as 0.04% and 0.02%, respectively, and did not exceed more than 2% in both density and pressure (differences here arise from lowest and highest pressures accessed for each material). Considering precision EOS measurements presented have density precision between $\sim 3.5\%$ and 5.6%, Fig. 126.8 shows IM EOS states in hydrocarbons resulting from quartz states with $U_{s,Q}$ between 15 and 25 $\mu\text{m/ns}$, showing percent differences larger than 5.6%, would be most compromised.

Systematics between the two quartz fits can also be compared through inferred single-shock states from double-shock measurements. This inversion method was previously described by Hicks *et al.*³⁰ and was applied to double-shock measurements made on CH, yielding inferred single-shock states in



E19488JR

Figure 126.8

Percent differences between quartz model predictions in density and pressure, as a function of quartz shock velocity, are shown as the dashed blue and solid magenta curves. Circles and squares represent percent differences in density and pressure between IM results, assuming a reflected Hugoniot to calculate release states in quartz (orange, light blue, green, and purple circles and squares) and from inferred single-shock states using double-shock measurements (red circles and squares). Here a positive number means that a higher value is predicted using laser quartz fit in comparison to the Z-machine fit.

agreement with single-shock measurements.⁷ This method uses a model-averaged effective gamma to calculate off-Hugoniot states (in this case the CH re-shock), using the quartz fit only to establish the double-shock particle velocity and pressure. Percent differences resulting from using a different quartz model are shown in Fig. 126.8 as the red circles (density) and squares (pressure). This method yields more optimistic results, with percent differences in density and pressure peaking at 6.3% and 3.2%. In this case IM EOS states in hydrocarbons resulting from quartz shock states corresponding to $U_{s,Q}$ from 17.5 to 23 $\mu\text{m/ns}$ (with percent difference larger than 5.6%) would be most compromised. This corresponds to a smaller range than that predicted by the reflected Hugoniot analysis. Here quartz's influence enters only through the double-shocked pressure and particle velocity in CH.

The use of quartz as a standard in the IM technique has greatly improved the precision of EOS measurements, demonstrating the ability to provide EOS data that are able to more tightly constrain the high-pressure behavior of materials.^{7,9} A new equation of state of quartz could generate differences in the final EOS results but would not compromise the precision of these data.

REFERENCES

1. D. S. Clark *et al.*, *Phys. Plasmas* **17**, 052703 (2010).
2. G. H. Miller, E. I. Moses, and C. R. Wuest, *Nucl. Fusion* **44**, S228 (2004).
3. S. W. Haan *et al.*, *Phys. Plasmas* **2**, 2480 (1995).
4. T. R. Dittrich *et al.*, *Phys. Plasmas* **6**, 2164 (1999).
5. S. W. Haan *et al.*, *Phys. Plasmas* **12**, 056316 (2005).
6. B. A. Hammel *et al.*, *High Energy Density Phys.* **6**, 171 (2010).
7. M. A. Barrios, D. G. Hicks, T. R. Boehly, D. E. Fratanduono, J. H. Eggert, P. M. Celliers, G. W. Collins, and D. D. Meyerhofer, *Phys. Plasmas* **17**, 056307 (2010).
8. D. G. Hicks, T. R. Boehly, P. M. Celliers, J. H. Eggert, E. Vianello, D. D. Meyerhofer, and G. W. Collins, *Phys. Plasmas* **12**, 082702 (2005).
9. D. G. Hicks, T. R. Boehly, P. M. Celliers, D. K. Bradley, J. H. Eggert, R. S. McWilliams, R. Jeanloz, and G. W. Collins, *Phys. Rev. B* **78**, 174102 (2008).
10. N. Ozaki *et al.*, *Phys. Plasmas* **16**, 062702 (2009).
11. P. M. Celliers, D. K. Bradley, G. W. Collins, D. G. Hicks, T. R. Boehly, and W. J. Armstrong, *Rev. Sci. Instrum.* **75**, 4916 (2004).

12. Ya. B. Zel'dovich and Yu. P. Raizer, in *Physics of Shock Waves and High-Temperature Hydrodynamic Phenomena*, edited by W. D. Hayes and R. F. Probstein (Dover Publications, Mineola, NY, 2002), Vol. II, Chap. XI, pp. 685–784.
13. P. M. Celliers *et al.*, *J. Appl. Phys.* **98**, 113529 (2005).
14. D. G. Hicks S. Brygoo, P. Loubeyre, J. Eggert, R. S. McWilliams, P. M. Celliers, T. R. Boehly, and G. W. Collins (unpublished).
15. R. G. McQueen, Los Alamos National Laboratory, Los Alamos, NM, LA-UR-90-1996 (1989).
16. R. F. Trunin, *Shock Compression of Condensed Materials* (Cambridge University Press, Cambridge, England, 1998).
17. R. F. Trunin, *Phys.-Usp.* **37**, 1123 (1994).
18. M. D. Knudson and M. P. Desjarlais, *Phys. Rev. Lett.* **103**, 225501 (2009).
19. T. R. Boehly, R. S. Craxton, T. H. Hinterman, J. H. Kelly, T. J. Kessler, S. A. Kumpan, S. A. Letzring, R. L. McCrory, S. F. B. Morse, W. Seka, S. Skupsky, J. M. Soures, and C. P. Verdon, *Rev. Sci. Instrum.* **66**, 508 (1995).
20. Y. Lin, T. J. Kessler, and G. N. Lawrence, *Opt. Lett.* **20**, 764 (1995).
21. Project Staff, General Atomics, San Diego, CA, General Atomics Report GA-A26403 (2009).
22. Cargille Laboratories, Inc., Cedar Grove, NJ 07009 (<http://www.cargille.com/refractivestandards.shtml>).
23. M. Takeda, H. Ina, and S. Kobayashi, *J. Opt. Soc. Am.* **72**, 156 (1982).
24. P. R. Bevington and D. K. Robinson, *Data Reduction and Error Analysis for the Physical Sciences*, 3rd ed. (McGraw-Hill, Boston, 2003).
25. R. M. More *et al.*, *Phys. Fluids* **31**, 3059 (1988).
26. G. I. Kerley, Sandia National Laboratory, Albuquerque, NM, Report SAND-88-2291, NTIS Order No. DE91017717 (1991).
27. P. Sterne, Lawrence Livermore National Laboratory, private communication (2011).
28. S. P. Marsh, ed. *LASL Shock Hugoniot Data*, Los Alamos Series on Dynamic Material Properties (University of California Press, Berkeley, CA, 1980).
29. S. P. Lyon and J. D. Johnson, Los Alamos National Laboratory, Los Alamos, NM, Report LA-UR-92-3407, NTIS Order No. DE85014241 (1992).
30. D. G. Hicks, T. R. Boehly, P. M. Celliers, J. H. Eggert, S. J. Moon, D. D. Meyerhofer, and G. W. Collins, *Phys. Rev. B* **79**, 014112 (2009).

Refractive Index of Lithium Fluoride Ramp Compressed to 800 GPa

Introduction

The transition of an insulator to a metal (metallization) at high compression is generally the result of pressure-induced closure of the band gap.^{1–4} Lithium fluoride's (LiF's) large-band-gap and ionic crystalline structure produces its uniquely high ultraviolet transmissivity. Two rare-gas solids, He and Ne, have anomalously high metallization pressures because of the predicted intershell band overlap, which is unique among monatomic materials.⁵ LiF holds a rare position among binary compounds in that Li⁺ and F⁻ are isoelectronic with He and Ne, respectively. Therefore, LiF is expected to have a uniquely high metallization pressure among large-band-gap solid insulators.

Under strong shock compression, the insulating/conducting transition is enhanced by the thermal promotion of electrons across the band gap.⁶ This is a result of high temperatures produced by high-pressure (>100-GPa*) shock waves. A variety of materials has been shocked into conductive matter that is highly reflective at the shock front.^{6–10} LiF has been previously observed to be transparent when shocked to ~115 GPa (Refs. 8 and 11) and becomes reflective for shock pressures >500 GPa (Ref. 6).

Recently, ramp compression has been used to compress materials to pressures above 100 GPa, while keeping the temperature low compared to that of a shock wave.¹² This work shows that LiF remains transparent when ramp compressed to 800 GPa—the highest pressure under which a transparent insulator has ever been observed. We use a new technique to measure its refractive index at pressures of 30 to 800 GPa. Early dynamic-compression experiments have shown the refractive index of various insulators to increase linearly with density at low pressure (~100 GPa). The results presented here indicate that the linearity of the LiF refractive index increase over a larger density range than previously shown. This is expected since the electronic polarizabilities of large-band-gap insulators typically increase with compression. The results presented here are the highest-pressure refractive-index measurements to date.

Ramp-compressed LiF remains transparent at higher pressures than in shock compression because thermal excitation is insufficient to produce conduction electrons. As a result, at these high compressions we expect that only the effects of density are important and use this to infer the pressure-induced band-gap closure of LiF using a single-oscillator model.¹³ Extrapolation of those results, although crude, indicates that ramp-compressed LiF may remain transparent to greater than 4000 GPa, well above the Goldhammer–Herzfeld criterion for metallization (~2800 GPa) (Refs. 14–16). LiF will therefore continue to have technical utility as a diagnostic window for experiments at extreme pressures, and the predicted band-gap closure provides important estimates for band-structure calculations.

In the present work, the refractive index of LiF was measured using ramp compression to 800 GPa. Diamond pistons were ramp compressed using the OMEGA laser.¹⁷ Diamond targets consisted of two sections: a free surface and a LiF window mounted on half of the rear surface. VISAR measurements were made at both sections to determine the refractive index. The subsequent sections discuss the relevant theory regarding the measurement technique, followed by a discussion of the experimental method and the experimental results. In the final section, an effective-oscillator model is used to interpret the results, providing an estimation of the band-gap closure.

Theory

In many high-pressure experiments, the motion of a reflecting interface behind an optical window is detected by measuring Doppler shifts with a velocity interferometry system for any reflector (VISAR).¹⁸ The reflected probe beam passes through the compression wave in the window, so the observed Doppler shift depends on the refractive index of the compressed window material. LiF is frequently used as an optical window because its transparency at high pressure allows one to make *in-situ* measurements of samples confined by that window.^{8,11} Hayes¹⁹ showed that for unsteady compression waves in windows, the *true* (U_t) and *apparent* (U_a) interface velocities (viewed through the compressed window) are directly related to the density-dependent refractive index of the window as

*100 GPa = 1 Mbar

$$\left. \frac{dU_a}{dU_t} \right|_{U_t} = \left(n - \rho \frac{dn}{d\rho} \right) \bigg|_{U_t} = f(\rho), \quad (1)$$

where the density (ρ) and refractive index (n) are evaluated as functions of U_t . One can show that this gives $n(\rho)$ explicitly as

$$n(\rho) = \rho \left[\frac{n_0}{\rho_0} - \int_{\rho_0}^{\rho} \frac{f(\rho')}{\rho'^2} d\rho' \right]. \quad (2)$$

In this work, $U_a(U_t)$ was measured using diamond as an impedance-matching standard and the refractive index as a function of density was determined by solving Eq. (2).

Experimental Method

The targets consisted of a planar diamond piston with two sections: half a free surface and an LiF window attached to the second half [see inset of Fig. 126.9(a)]. Planar compression waves, driven by direct laser ablation, produced identical compression waves across the two sections (bare and LiF) of the piston. The free-surface (bare diamond) velocity (U_{fs}) and the *apparent* interface (diamond–LiF) velocity (U_a) were measured simultaneously using VISAR.¹⁸ The response of the free surface was used to infer the *true* velocity of the piston/window interface.

The method of characteristics²⁰ was used to determine the drive-pressure history applied to the target by propagating U_{fs} backward to the loading surface. The free-surface wave profile, shown in the inset of Fig. 126.9(a), displays a distinct plateau at 2 $\mu\text{m}/\text{ns}$ caused by the drop from the longitudinal to the bulk sound speed as the elastic limit of diamond was exceeded. In this experiment, as in previous experiments,¹² the plateau showed a very constant velocity and the elastic limit was treated as a straightforward drop in the sound speed. Using that assumption, the calculated drive pressure was determined and then forward propagated to the diamond/LiF boundary, where pressures were impedance matched, thereby determining U_t . The diamond-ramp wave response measured by Bradley *et al.*,¹² which includes diamond strength, and the *SESAME* Table 7271 (Ref. 21) for LiF were used. The LiF *SESAME* Table 7271 accounts for hydrostatic deformations while neglecting plastic deformations. The inclusion of a Steinberg–Guinan^{22,23} strength model in the LiF equation of state (EOS) influenced the calculated interface pressure by $\ll 1\%$ prior to peak compression. As Ao *et al.*²² have shown, plastic effects in the interface velocity are of consequence only after peak compression. Analysis is terminated when interface yielding or “pullback” is observed, corresponding to ~ 5.5 ns for the inset of Fig. 126.9(b). LiF strength effects were neglected since the error contribution was significantly less than other sources.

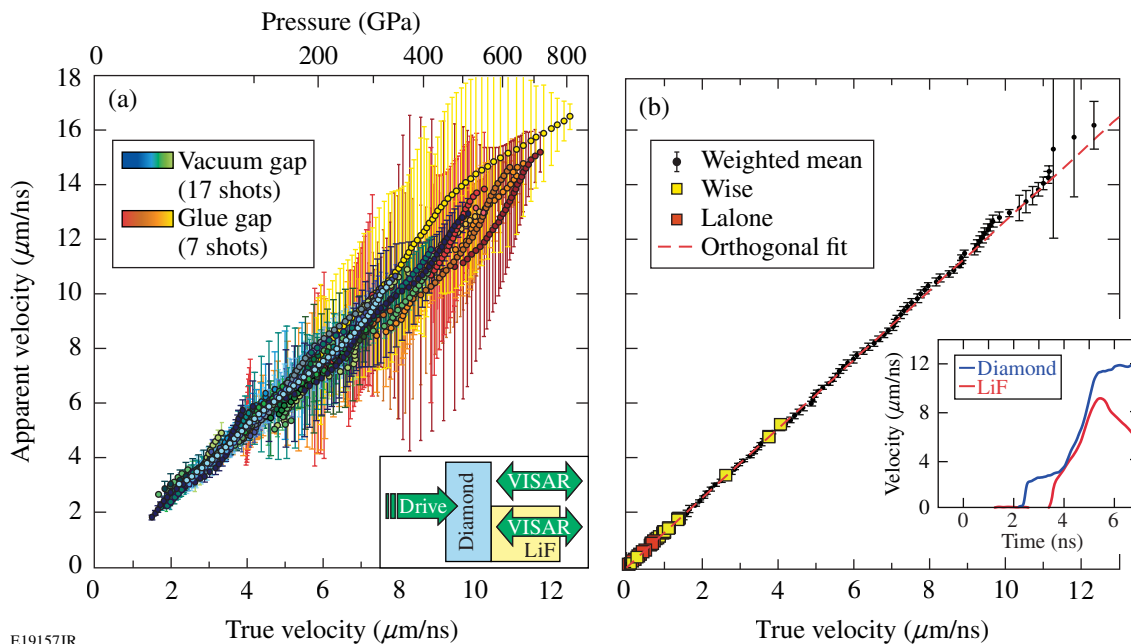


Figure 126.9

(a) *Apparent* and *true* velocity measurements for all experiments. Vacuum-gap and glue-gap experiments are distinguished by their corresponding colors. Inset shows the target diagram. (b) Weighted average of all shots. Orthogonal regression and previous shock data are included.^{8,11} Inset shows the VISAR measurements from a single experiment.

The experiments were performed on the OMEGA Laser System.¹⁷ The ablation pressure was controlled by temporal shaping the drive laser pulse to produce compressions in LiF from 30 to 800 GPa. These drive pulses compressed the targets without creating shock waves in either the chemical-vapor-deposition (CVD) diamond pusher or LiF samples over the duration of the experiment.

Laser intensity scaled as $\sim t^3$ for pulse-shape durations of 4 to 7 ns. The diamond thickness for those experiments was 46 μm ($\pm 1 \mu\text{m}$) and 100 μm ($\pm 3 \mu\text{m}$), respectively. A 500- μm -thick, high-purity LiF window was mounted over half of the rear of these diamond targets oriented with the $\langle 100 \rangle$ axis along the pressure-loading direction. Samples were glued at the edges such that the compressed diamond released directly into the LiF where there was no glue. A 1000- \AA titanium coating was applied to the diamond/LiF interface to increase the reflectivity for interferometer measurements. Three targets were constructed with gold layers (3 to 5 μm thick) placed 10 to 15 μm from the ablation surface to act as an x-ray shield to ensure there was no effect from high-energy x rays passing through the target. No difference was observed in the results from targets with and without these shields.

Experimental Result

1. Wave Profile Analysis

A total of 17 shots was performed to determine the *true* and *apparent* velocities as described above. Each of the 17 continuous measurements is shown as an ensemble of like-colored points in Fig. 126.9(a). The measured *apparent* velocities were observed to monotonically increase with pressure with no observed discontinuities, indicating a single phase of LiF existed to 800 GPa. This is consistent with recent *ab-initio* calculations performed by Smirnov.²⁴ The pressures corresponding to these velocities were determined from the LiF *SESAME* EOS²¹ as shown on the top axis. In those experiments, a weak shock was initiated in the LiF window; this was treated as an initial characteristic whose parameters were determined from impedance matching with the Hugoniot. The effect of shock formation in the LiF window is examined in **LASNEX Simulations** (p. 63).

Seven additional targets employed $\sim 2 \mu\text{m}$ of glue to fill the gap between the diamond and the LiF. At low pressures, the compressibility of the glue (and reverberations within it) caused the data to deviate from the targets with no glue between the LiF window and diamond. Once the glue “rang up” to higher pressure, the data followed the trend of targets with no glue-filled gap. Simulations indicated that after the glue rang up, corrections for the presence of $\sim 2\text{-}\mu\text{m}$ gaps caused a shift of the

true particle-velocity profiles after gap closure by ~ 3 ps, much less than the timing accuracy of these experiments.

The dominant errors in these calculations resulted from the precision of fringe-shift measurements (2.5% of a fringe) and uncertainty in the diamond isentrope cited by Bradley *et al.*¹² Measurements published by Hicks *et al.*,⁶ which were later re-examined by Celliers *et al.*,²⁵ are the only high-pressure measurements for LiF above 500 GPa published to date. Comparison of measurements made by Hicks *et al.*⁶ at ~ 1400 GPa with the *SESAME* Table 7271 indicates an $\sim 7\%$ error in pressure; therefore, a 10% error in pressure is assumed for the LiF isentrope.²² The errors in the timing correlation between U_a and U_t was of the order of 47 ps and 93 ps for cameras 1 and 2, respectively,¹⁸ corresponding to uncertainties added in quadrature of the etalon delay (37 ps and 78 ps) and nonuniformity in the drive planarity (5 pixels at sweep rates of 6 ps/pixel and 10 ps/pixel). Systematic uncertainties are attributed to camera shear (6 and 10 ps), gap correction ~ 1 ps (33% of the calculated temporal shift), and the neglect of LiF material strength ($\ll 1\%$ change in peak interface pressure). Systematic uncertainties are estimated to be 5% of the total uncertainty and therefore neglected. Random errors were propagated through the method of characteristics using a Monte Carlo procedure that propagates uncertainties randomly chosen from a normal distribution.²⁶

Steep gradients in the measured velocity profiles account for the large errors observed for single shots in Fig. 126.9(a). These were reduced by using a ramp compression that rose more gradually, albeit to lower pressures. Streaked optical pyrometer²⁷ measurements of LiF were dominated by thermal emission from the diamond anvil observed through the LiF. Comparison of the self-emission from the diamond-free surface and the diamond/LiF interface suggests that the LiF window temperature remained below 1000 K for all cases.

Figure 126.9(b) shows the weighted mean (black points) of the data from Fig. 126.9(a) using the associated errors discussed above. The large errors between 700 to 800 GPa occur because only a single experiment reached those pressures. The dashed line is the linear portion of a fit performed to that weighted mean (see below). Shock-wave data taken from Wise and Chhabildas⁸ and LaLone *et al.*¹¹ are shown up to 115 GPa as yellow and red squares, respectively.

A second-order orthogonal polynomial regression^{25,26} was to fit the U_t [km/s] and U_a [km/s] particle velocities: $U_a(U_t) = a_0 + a_1(U_t - \beta) + a_2(U_t - \gamma_1)(U_t - \gamma_2)$, where $\beta = 2.41$ km/s, $\gamma_1 = 0.713$ km/s, and $\gamma_2 = 9.53$ km/s were determined by the distribu-

tion of U_1 in the data being fit. Since these parameters depend on the independent variable, errors were not assigned. Coefficients (a_0 , a_1 , and a_2) were determined from a weighted χ^2 minimization. In the orthogonal fit, the value of each coefficient is independent of higher-order terms, diagonalizing the co-variance. U_1 is considered the independent variable and U_a the dependent one with a standard deviation $\sigma_{U_a}^2 = (\delta U_a)^2 + (1.28 \delta U_1)^2$. δU_a is the error associated with the measured interface velocity and δU_1 is the error determined by Monte Carlo simulations, which is weighted by 1.28 to account for the estimated slope. Errors determined in the orthogonal fitting coefficients underestimate deviations observed within the data. This was observed when shots were removed at random and orthogonal fitting was performed. Coefficient errors were determined by standard deviations calculated from 100 discrete shot groupings of the 24 experiments: $a_0 = 3.0634$ [km/s], $a_1 = 1.2751 \pm 0.0082$, and $a_2 = 0.0008 \pm 0.0015$ [s/km]. Errors were not assigned to a_0 since it represents the centroid of the data. The slope (a_1) dominates the determination of the refractive index [Eq. (1)], and contributions from the curvature (a_2) are assumed negligible because of their relative size and the bounding of zero.

Equation (2) was used to calculate $n(\rho)$ (Fig. 126.10) using the weighted mean (black line). The refractive index and density under standard conditions (1.3935 and 2.6380 g/cc) were used as the boundary. The refractive index determined from the orthogonal fitting parameters is

$$n = 1.275(\pm 0.008) + 0.045(\pm 0.003)\rho, \quad (3)$$

where the second-order term (a_2) has been neglected. The results obtained are in agreement with high-precision shock results up to 20 GPa (Ref. 11)

$$n = 1.277(\pm 0.002) + 0.0443(\pm 0.008)\rho, \quad (4)$$

and diamond-anvil experiments²⁸

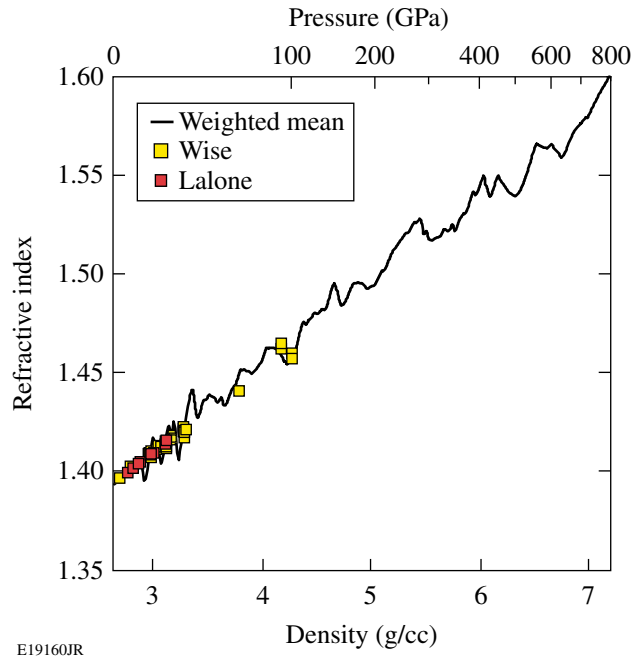
$$n = 1.25(\pm 0.03) + 0.05(\pm 0.01)\rho. \quad (5)$$

The effective polarizability (α) of LiF is calculated using the Clausius–Mossotti relation

$$\frac{1}{\rho} \frac{\varepsilon - 1}{\varepsilon + 2} = \frac{4\pi N_A}{3} \alpha, \quad (6)$$

where ε is the dielectric function and N_A is Avogadro's number. For these experiments, the LiF absorption was negligible, indicating that the imaginary part of the refractive index was small or $\varepsilon \approx n^2$. Using Eq. (6) and this approximation, the

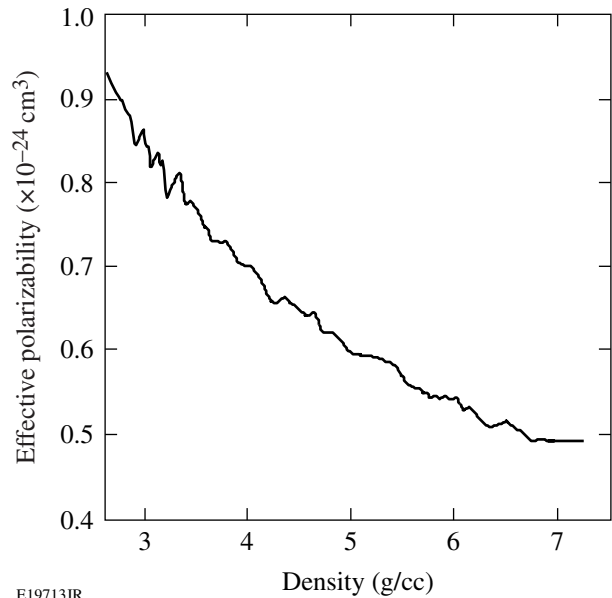
effective polarizability is calculated and plotted as a function of compression in Fig. 126.11. The effective polarizability is observed to decrease with increasing pressure.



E19160JR

Figure 126.10

Refractive index as a function of density determined using the weighted average and linear orthogonal fit. Previous data shock is included.^{8,11}



E19713JR

Figure 126.11

The effective polarizability determined from the Lorentz–Lorenz relation plotted as a function of density.

2. LASNEX Simulations

LASNEX²⁹ simulations were performed to address concerns regarding shock formation in the LiF window and LiF material strength. The arrival of the diamond elastic limit (EL) in the LiF window generates a weak shock. Compression waves in the LiF window may reflect off the shock front, and the arrival of those waves at the LiF would violate the conditions required in the derivation of Eq. (1) (Ref. 19). Since the method of characteristics does not account for the potential of shock formation, LASNEX simulations were performed to verify the characteristic calculations. LASNEX calculations used a diamond EOS with a Steinberg–Guinan–strength model to recover the EL²³ and LiF *SESAME* Table 7271 (Ref. 21). The pressure drive was applied 10 μm inside the front surface to account for the material ablated by the laser driver. This applied pressure is estimated to best match the measured diamond free-surface velocity.

LASNEX simulations were performed on shot 56113, and the results are shown in Figs. 126.12(a) and 126.12(b). Figure 126.12(a) contains a plot of the diamond free-surface velocity measured using VISAR (blue) and the estimated velocity determined from LASNEX (black) for an approximate applied laser intensity. Figure 126.12(a) shows that the LASNEX free-surface velocity correlates well with the measured free-surface velocity. The applied pressure drive that determines the free-surface velocity is then used to simulate the *true* interface velocity. The noticeable discrepancies between the LASNEX simulation and measure free-surface velocity at 3.9 ns and 4.2 ns is due to the limitations of Steinberg–Guinan–strength model. That model predicts a higher EL than observed in this study generating the noticeable two-wave structure. As observed by McWilliams *et al.* the diamond EL varies and these variations are the cause of the observed discrepancy.³⁰

Figure 126.12(b) compares interface velocities calculated using both methods. The LASNEX-predicted *true* interface velocity (black) and the *true* interface velocity calculated using the method of characteristics (red) infer nearly identical velocities prior to peak compression. The excellent agreement indicates that either (a) shock formation does not occur in the LiF window or (b) the effects of shock formation under these conditions do not significantly perturb the interface velocity prior to peak compression. This indicates that the requirements on Eq. (1) are met and Eq. (1) remains valid for these experiments. Furthermore, simulations performed with and without a Steinberg–Guinan–strength model differ $\ll 1\%$ in pressure.

Discussion

The temperatures achieved in this study are significantly lower than temperatures for identical pressures along the principal Hugoniot. *SESAME* Table 7271 predicts the principal isentrope temperature at 400 GPa and 800 GPa to be ~ 700 k and ~ 800 k, respectively. The temperature along the principal Hugoniot for those pressures are significantly higher (12,500 k and 31,500 k). Molecular dynamic simulations³¹ suggest that the Hugoniot approaches the melt line at ~ 150 GPa at ~ 3500 k. Quantum molecular dynamics simulations predict as LiF melts, it transitions from a large gap insulator into a reflective material and during this transition develops a nonlinear refractive index.³² The low temperatures achieved in this study prevent LiF from approaching melt, inhibiting the development of a nonlinear refractive index.

An effective-oscillator model¹³ was used to interpret the observed linear dependence of refractive index on density. The effective-oscillator model describes optical properties as a weighted average over the visible spectrum. It is a simplistic dielectric model that predicts the magnitude and dispersion of

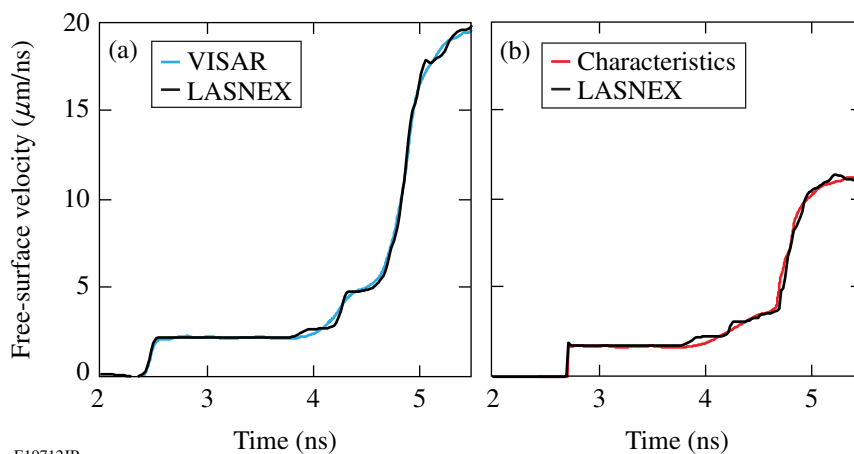


Figure 126.12
Comparison of hydrocode simulations and the method of characteristics for shot 56113. (a) LASNEX ablation pressure is determined by matching the LASNEX free-surface velocity (black) with VISAR measurement (blue). (b) The ablation pressure calculated using LASNEX is then used to determine the *true* interface velocity. Comparison of the LASNEX results (black) and the method of characteristics (red) is shown.

E19712JR

ionic and covalent substances. The refractive index is defined by two “average” parameters: the dispersion energy (E_d) and single-oscillator energy (E_0). E_0 is empirically related¹³ to the lowest direct optical transition E_t defined as the excitonic or band gap. The single-oscillator energy represents an average energy gap where the direct and indirect gaps may be smaller or exceed that energy.³³

Wemple and DiDomenico¹³ have shown that frequency-dependent refractive index for covalent and ionic materials can be fit to

$$n^2 - 1 = \frac{E_d E_0}{E_0^2 - \hbar^2 \omega^2}, \quad (7)$$

where E_d is the dispersion energy, E_0 is the single-oscillator energy, and $\hbar\omega$ is the photon energy. In a survey of over 100 solid and liquid insulators at ambient conditions, this model fits the frequency-dependent refractive index well.¹³

This model was applied to the pressure-induced closure of the H_2 band gap over a large density range^{34–36} and successfully predicted the emergence of excitonic absorption in the visible spectrum.⁴ Those studies show the H_2 exciton shifts from 14.5 eV to 2 eV with a slightly sublinear dependence on density over nearly 15-fold compression. The effective-oscillator model has been applied to H_2O ice, demonstrating a linear reduction in the band gap over 2.3-fold compression.³³ In that study, the dispersion was measured from 569 to 741 nm at pressures ranging from 0 to 120 GPa. At discrete pressures, the effective-oscillator parameters (E_d and E_0) were determined. Zha *et al.*³³ found that E_d was independent of density (remained constant) and that the effective gap closed monotonically with density. Wemple and DiDomenico¹³ have shown that the ratio of the band-gap energy to the lowest direct optical transition E_0/E_t is constant for constant dispersion energy (E_d).

The effective-oscillator model was applied to the data presented here, where the ambient values of E_d and E_0 were determined by fitting the refractive index to measured values in the range of 332 nm $< \lambda <$ 732 nm, i.e., the wavelength region near the probe laser.¹⁶ Fixing E_d to its ambient value, E_0 is calculated as a function of density using Eq. (7), as shown in Fig. 126.13. For the alkali halides of NaCl structure, the average ratio of single-oscillator energy to direct band gap is $E_0/E_t = 1.36$. This effective band gap begins at the intense exciton observed at ambient pressure³⁷ and then decreases with rising pressure.

Extrapolation of these results (a crude approximation) indicates that the band gap may close above >4000 GPa. This suggests that LiF will remain transparent well above the Goldhammer–Hertzfeld (G–H) criterion (~ 2800 GPa) (Refs. 14–16). This difference is consistent with the observed behavior of He and Ne, which exhibited abnormally high metallization at pressures $10\times$ greater than predicted by the G–H criterion.^{5,38}

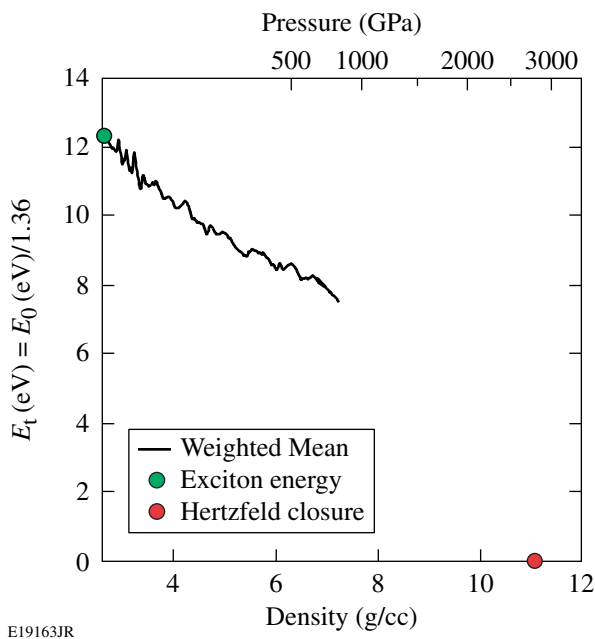


Figure 126.13 Density dependence of the single-oscillator model (E_t). Extrapolation suggests that LiF may remain transparent to pressure above 4000 GPa.

Conclusion

Direct laser ablation was used to ramp compress LiF from 30 to 800 GPa. LiF was observed to remain transparent over this pressure range; this is the highest-pressure insulator ever observed. The apparent and true particle velocities were measured over this range and were used to calculate the refractive index of compressed LiF, which was found to depend linearly on density. These are the highest pressure measurements of refractive index to date and are used to infer the pressure-induced band-gap closure of compressed LiF using an effective-oscillator model. These measurements provide a VISAR correction factor up to 800 GPa. Extrapolation of these results suggests that LiF remains transparent to pressures >4000 GPa as long as the temperature remains sufficiently low. If true, LiF will prove to be a valuable window for extremely high pressure ramp-compression experiments.

ACKNOWLEDGMENT

This work was supported by the U.S. Department of Energy Office of Inertial Confinement Fusion under Cooperative Agreement No. DE-FC52-08NA28302, the University of Rochester, and the New York State Energy Research and Development Authority.

REFERENCES

1. R. Reichlin *et al.*, Phys. Rev. Lett. **56**, 2858 (1986).
2. K. A. Goettel *et al.*, Phys. Rev. Lett. **62**, 665 (1989).
3. R. Reichlin *et al.*, Phys. Rev. Lett. **62**, 669 (1989).
4. P. Loubeyre, F. Occelli, and R. LeToullec, Nature **416**, 613 (2002).
5. J. C. Boettger, Phys. Rev. B **33**, 6788 (1986).
6. D. G. Hicks *et al.*, Phys. Rev. Lett. **91**, 035502 (2003).
7. S. B. Korner, Sov. Phys.-Usp. **11**, 229 (1968).
8. J. L. Wise and L. C. Chhabildas, Sandia National Laboratory, Albuquerque, NM, Report SAND-85-0310C, NTIS Order No. DE85015505 (1985).
9. D. K. Bradley *et al.*, Phys. Rev. Lett. **93**, 195506 (2004).
10. J. Eggert, S. Brygoo, P. Loubeyre, R. S. McWilliams, P. M. Celliers, D. G. Hicks, T. R. Boehly, R. Jeanloz, and G. W. Collins, Phys. Rev. Lett. **100**, 124503 (2008).
11. B. M. LaLone *et al.*, J. Appl. Phys. **103**, 093505 (2008).
12. D. K. Bradley *et al.*, Phys. Rev. Lett. **102**, 075503 (2009).
13. S. H. Wemple and M. DiDomenico, Jr., Phys. Rev. B **3**, 1338 (1971).
14. A. Goldhammer, in *Monatshefte für Mathematik* (Teubner, Leipzig, Berlin, 1913), Vol. 27.
15. K. F. Herzfeld, Phys. Rev. **29**, 701 (1927).
16. E. M. Bass, ed. *Handbook of Optics*, 2nd ed., Volume II: Devices, Measurements, and Properties (McGraw-Hill, New York, 1994).
17. T. R. Boehly, D. L. Brown, R. S. Craxton, R. L. Keck, J. P. Knauer, J. H. Kelly, T. J. Kessler, S. A. Kumpan, S. J. Loucks, S. A. Letzring, F. J. Marshall, R. L. McCrory, S. F. B. Morse, W. Seka, J. M. Soures, and C. P. Verdon, Opt. Commun. **133**, 495 (1997).
18. L. M. Barker and R. E. Hollenbach, J. Appl. Phys. **43**, 4669 (1972).
19. D. Hayes, J. Appl. Phys. **89**, 6484 (2001).
20. J. R. Maw, AIP Conf. Proc. **706**, 1217 (2004).
21. S. Crockett and S. Rudin, Los Alamos National Laboratory, Los Alamos, NM, LA-UR-06-8401 (2006).
22. T. Ao *et al.*, J. Appl. Phys. **106**, 103507 (2009).
23. D. J. Steinberg, S. G. Cochran, and M. W. Guinan, J. Appl. Phys. **51**, 1498 (1980).
24. A. Smirnov, Phys. Rev. B **83**, 014109 (2011).
25. P. M. Celliers *et al.*, J. Appl. Phys. **98**, 113529 (2005).
26. P. R. Bevington and D. K. Robinson, *Data Reduction and Error Analysis for the Physical Sciences*, 3rd ed. (McGraw-Hill, Boston, 2003).
27. J. E. Miller, T. R. Boehly, A. Melchior, D. D. Meyerhofer, P. M. Celliers, J. H. Eggert, D. G. Hicks, C. M. Sorce, J. A. Oertel, and P. M. Emmel, Rev. Sci. Instrum. **78**, 034903 (2007).
28. N. M. Balzaretti and J. A. H. Da Jornada, J. Phys. Chem. Solids **57**, 179 (1996).
29. G. B. Zimmerman and W. L. Kruer, Comments Plasma Phys. Control. Fusion **2**, 51 (1975).
30. R. S. McWilliams, J. H. Eggert, D. G. Hicks, D. K. Bradley, P. M. Celliers, D. K. Spaulding, T. R. Boehly, G. W. Collins, and R. Jeanloz, Phys. Rev. B **81**, 014111 (2010).
31. R. Boehler, M. Ross, and D. B. Boercker, Phys. Rev. Lett. **78**, 4589 (1997).
32. J. Clérouin *et al.*, Phys. Rev. B **72**, 155122 (2005).
33. C.-S. Zha *et al.*, J. Chem. Phys. **126**, 074506 (2007).
34. J. van Straaten and I. F. Silvera, Phys. Rev. B **37**, 6478 (1988).
35. A. García *et al.*, Phys. Rev. B **45**, 9709 (1992).
36. R. J. Hemley, M. Hanfland, and H. K. Mao, Nature **350**, 488 (1991).
37. D. J. Mickish, A. B. Kunz, and T. C. Collins, Phys. Rev. B **9**, 4461 (1974).
38. S. A. Kairallah and B. Militzer, Phys. Rev. Lett. **101**, 106407 (2008).

Hot-Electron Heating Caused by Two-Plasmon-Decay Instability

Introduction

High-energy electrons are detrimental to laser fusion because they can preheat the fuel, preventing the high compression necessary for central hot-spot ignition and high gain.¹ The direct-drive approach is particularly vulnerable as a result of the long scale length of plasma that exists at the quarter-critical density of the target, although it can also occur in indirect-drive geometry.²

Direct-drive-implosion experiments on OMEGA have observed hard x rays (a signature of hot electrons) that are coincident with the emission of half-integer harmonics and the predicted two-plasmon-decay (TPD) threshold.³ Four-channel x-ray spectroscopy ranging in energies from 20 to 500 keV indicates hot-electron temperatures of $T_{\text{hot}} \lesssim 100$ keV for irradiation intensities of $I_0 \sim 10^{15}$ W/cm² at $\lambda_0 = 351$ nm (Ref. 4). Since electrons in excess of 100 keV are inferred experimentally via the hard x rays that they produce, it is apparent that the possibility of preheating exists. This will lead to an increased fuel adiabat and diminished fuel compressibility. Estimates of target preheat based on measured x rays are difficult, but likely fall in the range of 40 to 50 J, where the impact on target performance might be measurable on OMEGA (Delettrez *et al.* estimate a 40% reduction in areal density for a worst-case scenario on the basis of one-dimensional hydrodynamic calculations⁵).

Definitive evidence of preheat-impaired performance [e.g., in reduced areal density (ρR)] on OMEGA is currently lacking,^{6,7} which complicates any extrapolation of preheat to ignition-scale designs. For example, in implosion experiments, close to 80% of maximum predicted areal density above 200 mg/cm² has been achieved using 10- μ m-thick deuterated plastic (CD) ablaters.⁸ The TPD instability is only weakly excited in these targets. It can be more strongly excited by using thinner shells since the TPD threshold is more easily attained in hydrogenic plasma. While a significant degradation of ρR is observed for thinner CD ablaters, it is not currently possible to rule out other competing mechanisms such as shock mistiming, hydrodynamic instability, radiation preheat, and preheat by nonlocal thermal electrons.

The need for a physical model of target preheat clearly exists. The self-consistent modeling, however, of hot-electron generation and the resulting preheating of the target is a very challenging problem. The purpose of this article is to present a model that represents an attempt in this direction. It includes aspects of the experimental conditions that are thought to be important. Namely, it assumes that all preheat is associated with TPD instability and the plasma inhomogeneities (density gradient) play an important role. The model contains nonlinearities that have been shown by detailed particle-in-cell calculations to play a dominant role in saturation.^{9,10} The possibility of multiple acceleration stages for hot electrons as they periodically pass through the quarter-critical surface is also investigated. It takes the trajectory of the heated electrons that lies outside of the simulation boundaries into account. It is shown that, for the parameters of current OMEGA direct-drive cryogenic implosions, recirculation (or reheating) of electrons is an important effect.

While several simplifications are made, we attempt to show how, in future work, these simplifications may be systematically relaxed. The most important of these is the development of a self-consistent quasilinear model for the evolution of the electron distribution function¹¹ that would replace the current test-particle treatment.

The sections that follow describe the model for electron heating, with subsections describing the extended Zakharov model for the saturated electric field spectrum and outlining the test-particle method; present the results of electron-heating calculations; and, finally, present a summary and conclusions.

Description of a Model for Hot-Electron Production

Based on experimental observations, there are reasons to believe that TPD is the sole instability active in producing hot electrons in current OMEGA experiments. Half-integer harmonic signatures of TPD are strongly correlated with hard x-ray production, with x-ray energies of the order of $E_{\text{x ray}} \sim 100$ keV (Refs. 3 and 4). The onset of TPD signatures is also well predicted by the simple linear threshold for the absolute TPD

instability of a plane electromagnetic wave in a density gradient when the intensity of the plane wave is equated with the average overlapped-beam intensity on OMEGA. Thresholds for TPD in a linear gradient have been computed by a number of authors.^{12–21} The “above-threshold parameter” $\eta = I_{14} L_{\mu\text{m}} / (320 T_{\text{keV}})$, which is based on the expression for absolute instability computed by Simon *et al.*,¹³ $(v_{\text{osc}}/v_e)^2 k_0 L > 4.134$ (i.e., the large β limit), has proven itself to be a very useful empirical tool for interpreting OMEGA experiments.^{3,5,8} While the onset is well predicted by the η parameter, which signals absolute instability, the measured spectrum of plasma waves is generally not consistent with the absolutely unstable eigenmode.³ Above threshold, the absolutely unstable wave corresponds to a forward-going plasmon of wave number close to k_0 , where k_0 is the laser vacuum wave number, and a plasmon with small perpendicular wave number given by

$$k_{\perp}/k_0 = 0.02 I_{14}^{1/4} (\lambda_0/0.351 \mu\text{m}) \times (T_e/2 \text{ keV})^{-1} (L/150 \mu\text{m})^{-1/2},$$

while experimentally, most Langmuir wave (LW) intensity is found to be located close to the Landau cutoff ($k \sim 0.25 k_{\text{De}}$, where k_{De} is the Debye wave number).³ This is not too surprising because convective growth can become important at similar intensities and can dominate the nonlinear state^{9,22} because it is not as easily saturated as the absolute mode (see **Zakharov Model for the Saturated LW Spectrum**, below).

Raman backscattering is neglected in the model because of the absence of an experimentally observed Raman backscattering signature. This is consistent with linear gain estimates: Raman scattering is expected to be convectively unstable below quarter-critical, with the Rosenbluth gain²³ $A_{\text{Ros}} = \pi \gamma_0^2 / |V_1 V_2 \kappa'|$ being negligible for the relevant experimental parameters

$$A_{\text{Ros}} \sim 0.04 I_{14} (1 - n_e/n_c)^{-1/2} (L_{\mu\text{m}}/150 \mu\text{m}).$$

The envelope approximation, upon which the previous expression relies, is not valid near the quarter-critical density. Drake *et al.* have demonstrated the potential for absolute instability of stimulated Raman scattering (SRS) near the quarter-critical density²⁴ with the threshold condition

$$v_{\text{osc}}/c > (1/2)(k_0 L)^{-2/3}.$$

The ratio of the TPD threshold to the above expression for absolute SRS is given approximately by

$$I_{\nabla}^{2\text{P}}/I_{\nabla}^{\text{R}} = 0.9 (T_{e,\text{keV}}/2 \text{ keV}) \times (0.351 \mu\text{m}/\lambda_0)(L/150 \mu\text{m})^{1/3}.$$

It appears that the effects of absolute Raman scattering near the quarter-critical density should be taken into account. The model currently omits this possibility (and achieves a worthwhile simplification by ignoring the equation for the envelope of the scattered transverse wave). This is based on the observations of the dominance of convective TPD over absolute TPD (see **Zakharov Model for the Saturated LW Spectrum**, below) and, by association, absolute Raman or high-frequency hybrid instability.^{18,19} The neglect of these terms also appears consistent with results reported for explicit particle-in-cell (PIC) calculations.⁹

The spectrum of LW's driven by TPD instability is assumed to be saturated by nonlinearities that are contained within the extended Zakharov approximation.^{25,26} Recent comparisons between the Zakharov model and reduced PIC calculations of TPD in homogeneous plasma indicate this to be a reasonable approximation.¹⁰ The model takes into account the density gradients and flow velocities at quarter-critical that are predicted to occur experimentally on the basis of 1-D radiation–hydrodynamic calculations using the *LILAC* code.²⁷

Electron heating in response to this spectrum of electrostatic waves is computed in a test-particle approximation, i.e., the electron distribution is heated by the LW's, but the modified electron-distribution function does not act back on the LW's, i.e., there is no kinetic modification of the LW dispersion relation. This is done in order to make contact with experimental observations, as well as to investigate the effects of recirculating electron trajectories, which have for a long time been thought to be important.^{11,28}

The test-particle approach to electron heating also allows for a systematic investigation of the validity of a self-consistent quasilinear model for TPD¹¹ along the lines of Sanbonmatsu *et al.*^{29,30} by explicitly computing the diffusion of electron velocities, $\langle (\Delta \vec{v})^2 / \Delta t \rangle$ (Refs. 31–33). This will be the subject of a future publication.

1. Zakharov Model for the Saturated LW Spectrum

The LW fields near the quarter-critical surface are modeled in the extended Zakharov approximation in two spatial dimensions taking into account a prescribed density gradient, as has been described previously,^{25,26} and now extended here to include a prescribed flow velocity

$$\begin{aligned}
& \nabla \cdot [2i\omega_{p0}(\partial_t + \vec{v}_0 \cdot \nabla + \nu_e^\circ) \\
& + 3v_e^2 \nabla^2 - \omega_{p0}^2(\delta n + \delta N)]\vec{E} \\
& = (e/4m_e) \nabla \cdot [\nabla(\vec{E}_0 \cdot \vec{E}^*) - \vec{E}_0 \nabla \cdot \vec{E}^*] + S_E. \quad (1)
\end{aligned}$$

In the above equation, \vec{E} is the slowly varying complex envelope of the longitudinal electric field $\vec{E}_l = 1/2\vec{E}\exp(i\omega_{p0}t) + \text{c.c.}$ (i.e., the electric field is decomposed into longitudinal and transverse components $\vec{E} = \vec{E}_l + \vec{E}_t$). The quantity \vec{E}_0 is the slowly varying (in time) complex envelope of the transverse, electromagnetic (EM) field,

$$\vec{E}_t = \sum_{j=1}^{N_j} \vec{E}_{0,j} \exp[i\vec{k}_{0,j} \cdot \vec{x} - i(\omega_0 - 2\omega_{p0})t + i\phi_j],$$

which consists of N_j beams of amplitude $\vec{E}_{0,j}$ and of wave number $\vec{k}_{0,j}$ that differs only in direction ($|\vec{k}_{0,i}| = |\vec{k}_{0,j}|$) and phase ϕ_j . The reference electron-plasma frequency is

$$\omega_{p0} = (4\pi n_0 e^2 / m_e)^{1/2},$$

and $v_e = (T_e / m_e)^{1/2}$ is the electron thermal velocity. For the slow density variation, $\delta n + \delta N$ represents the departure from the reference density $n_0 = 0.23 n_c$, where $n_c = m_e \omega_0^2 / (4\pi e^2)$ is the laser critical density. The static, i.e., non-evolving, component of the electron density corresponds to a linearly increasing density profile,

$$N(x) \equiv n_0 + \delta N = [0.23 + 0.04(2x/l_x - 1)]n_c,$$

which varies from $0.19 n_c$ to $0.27 n_c$ over the simulation length l_x , where $x \in [0, l_x]$ and has a density scale length of $L_n^{-1} \equiv d[\log N(x)]/dx = (8/23)l_x^{-1}$. The value of L_n is assumed to be constant in time during the integration period of the Zakharov model. The evolving component $\delta n(\vec{x}, t)$, a real quantity, satisfies the second Zakharov equation

$$\begin{aligned}
& [(\partial_t + \vec{v}_0 \cdot \nabla)^2 + 2\nu_i^\circ (\partial_t + \vec{v}_0 \cdot \nabla) - c_s^2 \nabla^2] \delta n \\
& = \frac{\nabla^2}{16\pi m_i} \left[|\vec{E}|^2 + \frac{1}{4} \left| \sum_j \vec{E}_{0,j} \exp i(\vec{k}_{0,j} \cdot \vec{x} + \phi_j) \right|^2 \right] \\
& + S_{\delta n}, \quad (2)
\end{aligned}$$

which takes into account the ponderomotive force of the light waves, each having the phase ϕ_j . The low-frequency (LF) fluctuations are also driven by the ponderomotive pressure of the LW's, which is quadratic in \vec{E} . The damping operators ν_e°

and ν_i° are local in k-space and contain the contribution of collisional and Landau-damping terms corresponding to a fixed Maxwellian ion- and electron-velocity distribution function of temperatures T_i and T_e , respectively. The terms S_E and $S_{\delta n}$ are noise terms that support a thermal level of LW and ion-acoustic-wave (IAW) fluctuations in the absence of other sources.²⁵

The numerical domain $\Omega = [0, l_x] \times [0, l_y]$ on which the extended Zakharov model is solved is typically arranged so that the linear electron-density profile spans the range $0.19 < n_e/n_c < 0.27$. This ensures that the electric field associated with the LW's vanishes on the longitudinal boundaries. The electrostatic waves are damped at low density (large $k_{\lambda D e}$) and reflected (turn) before encountering the boundary at the high-density side. Based on predicted scale lengths on OMEGA of $L_n \sim 150 \mu\text{m}$, this translates into a spatial dimension l_x of approximately $l_x \sim 50 \mu\text{m}$. The transverse dimensions are usually a few tens of microns. The transverse dimension should be as small as possible for computational efficiency, but no shorter than the correlation length for the LW fields. Typically, the transverse length l_y , where $y \in [0, l_y]$, is chosen to be $l_y \gtrsim 12.0 \mu\text{m}$.

a. Zakharov predictions for the saturated LW spectrum.

The nonlinear saturation of TPD based on the model presented in **Zakharov Model for Saturated LW Spectrum** (p. 67) is seen to involve a process of density-profile modification,^{25,34} the generation of ion-acoustic-wave turbulence as a result of the ponderomotive response to primary TPD LW's,^{9,25} LW cavitation and collapse, and Langmuir decay instability.²⁵ The development is quite similar to that observed in homogeneous reduced particle-in-cell calculations made recently by Vu *et al.*¹⁰ and is broadly consistent with earlier observations that saturation occurs as a result of ion-wave fluctuations³⁵ or profile steepening.^{34,36}

A series of two-dimensional calculations solving Eqs. (1) and (2) have been carried out with parameters motivated by conditions either currently or soon-to-be accessible on the OMEGA Laser System: the laser wavelength $\lambda_0 = 0.351 \mu\text{m}$, the electron temperature $T_e = 2.0 \text{ keV}$, the ion temperature $T_i = 1.0 \text{ keV}$, ion charge $Z = 3.5$ (effective charge state corresponding to CH plasma), IAW damping of $\nu_{i0} \equiv \nu_i/kc_s = 0.1$, and density-gradient scale lengths in the range $L_n = (100 \text{ to } 350) \mu\text{m}$. The simulation domain was chosen so as to include densities from $n_e = (0.19 \text{ to } 0.27) n_c$. In the case of $L_n = 150 \mu\text{m}$ (which we define as the ‘‘canonical’’ scale length on OMEGA), $l_x = 45.0 \mu\text{m}$, and $l_y = 12.0 \mu\text{m}$ (other cases were adjusted appropriately). The simulations were made with either a single-plane

electromagnetic (EM) wave ($N_j = 1$), normally incident along the direction of the density gradient ($\vec{k}_{0,1} \cdot \hat{e}_x/k_{0,1} = 1$), or with two overlapping plane waves ($N_j = 2$), each incident at an angle of $\theta_j = \cos^{-1}(\vec{k}_{0,j} \cdot \hat{e}_x/k_{0,j}) = \pm 0.23^\circ$ to the direction of the density gradient (the calculations with two crossed beams allow for the sharing of a common plasma wave¹⁰ that is thought to be an important experimental process on OMEGA.³⁷) The plane of simulation is chosen to be coincident with the plane of polarization, which also assumes that all N_j beams are similarly polarized. The laser intensities I_L (incoherent overlapped “intensity” $I_L \equiv c/(8\pi) \sum_{i=1}^{N_j} |\vec{E}_{0,i}|^2$ in the case of multiple beams) were varied in the range $I_L = (5 \times 10^{14} - 2 \times 10^{15})$ W/cm². The combination of laser intensity and density scale length was chosen to put the absolute TPD instability in either the weakly unstable ($\eta \sim 1.5$) or moderately unstable regime ($\eta \sim 2$ to 3) with respect to the threshold criterion as defined by Simon *et al.*¹³ Although there are differences between the single-beam and crossed-beam calculations, which will be described in a separate publication, the generic results described below are illustrative of both cases.

The calculations develop from the initial onset of absolute instability, which corresponds very well with the calculations of Simon *et al.*¹³ with regard to both the threshold intensity and unstable wave number (eigenmode), toward a broad spectrum of plasmons as shown in Fig. 126.14(a). [The onset of absolute

instability and the resulting growth rate were determined accurately by removing the nonlinear coupling between the Eqs. (1) and (2). The threshold intensity was therefore observed to coincide with the Simon *et al.* prediction to within 10% for the normally incident single-beam case].

The absolutely growing mode eventually reaches a sufficient amplitude where nonlinearities become important. The time required for strong nonlinearity to become important for canonical OMEGA parameters based on an initial noise level of $\langle |E|^2 \rangle / (8\pi n_0 T_e) = 6 \times 10^{-6}$ and a laser intensity of $I_L = 10^{15}$ W/cm² was found to be ~ 1.2 ps. Density-profile modification³⁴ was the saturating mechanism of the absolute modes in these calculations. This was determined by performing an estimate of the local steepening of the density gradient by taking a transverse (y direction) average of the density $\tilde{N}(x) \equiv \langle N(x) + \delta n(x, y) \rangle_y$ (as shown in Fig. 126.15) and estimating the modified gradient scale length in the neighborhood of the quarter-critical density $L_{\mu m}$. The observed scale length, when substituted into the threshold expression, was found to lead to marginal stability $\eta = I_{14} \tilde{L}_{\mu m} / (230 T_{\text{keV}}) \sim 1$. This situation was found to hold for all calculations that were performed. The collapse in growth of the initially unstable eigenmode is followed by an expanding region of large LW excitation at lower densities (corresponding to larger k_\perp LW’s in the single-beam case). This is seen in the Fourier spectrum

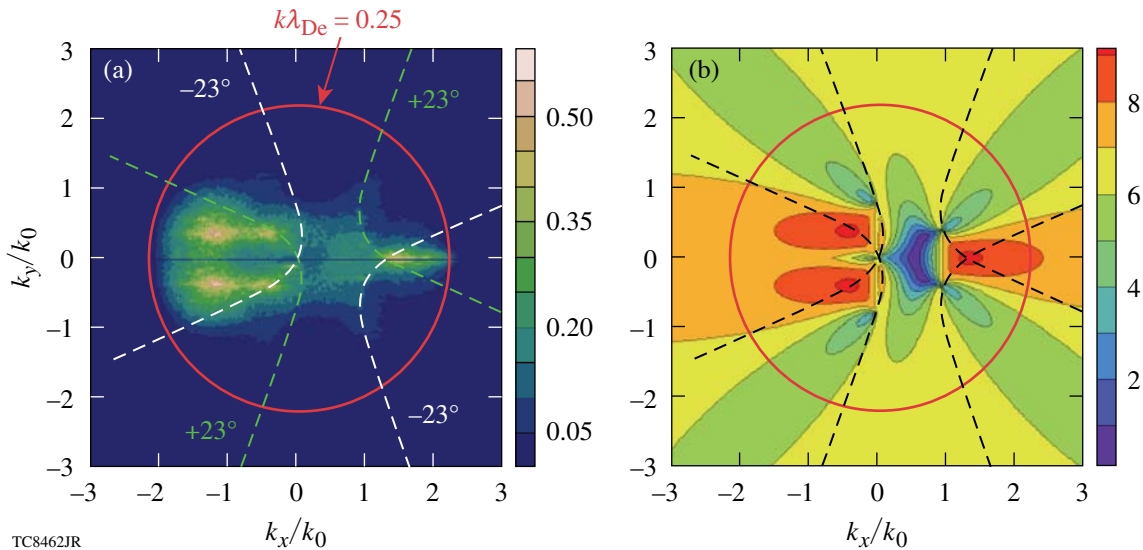
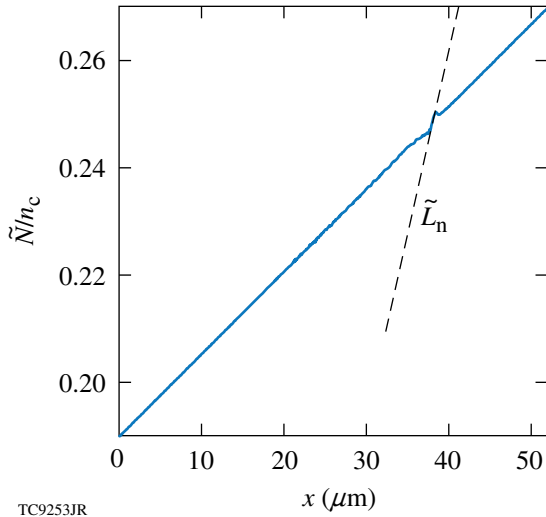


Figure 126.14

(a) The saturated Langmuir wave spectrum in Fourier space $|\vec{E}_k|^2$ corresponding to a crossed-beam irradiation geometry with an overlapped intensity of $I_L = 1 \times 10^{15}$ W/cm² (canonical OMEGA parameters). Two EM waves are incident at angles of $\pm 23^\circ$. For each beam, the single-beam maximum-growth-rate curves for TPD¹⁰ are shown as dashed lines, while the solid red line defines the Landau cutoff. (b) The TPD growth rate in arbitrary units from the theory of Short³⁷ for the same parameters as in (a).



TC9253JR

Figure 126.15

The solid line shows the modified 1-D density profile $\tilde{N}(x) \equiv \langle N(x) + \delta n(x, y) \rangle_y$ normalized to the critical density n_c , taken at the time of saturation of the absolutely unstable eigenmode ($t = 1.2$ ps) for the simulations described in **Zakharov Predictions for the Saturated LW Spectrum** (p. 68). The dashed line approximates the slope in the neighborhood of quarter critical and is used to define the modified density scale length \tilde{L}_n .

of the longitudinal electric-field intensity [Fig. 126.14(a)], where the active region of LW's extends as far as the Landau cutoff at wave numbers $k \sim 0.25 k_{De}$ (solid red line). These unstable modes, which are convective in nature, come to dominate the saturated LW spectrum at later times. The broad spectrum in Fig. 126.14(a), which corresponds to irradiation by two crossed beams, is dominated by the common LW and its associated daughter waves. This can be seen by comparing the spectral features in Fig. 126.14(a) with the expected growth rate based on a multiple-beam theory for identical parameters³⁷ [Fig. 126.14(b)]. The predicted maximum growth rate occurs at the intersection of the single-beam maximum growth rate curves (shown by the dashed lines) in Fig. 126.14. The growth rate has quite a broad peak, extending beyond the Landau cutoff (solid circle) for positive wave numbers—although the crossed-beam theory ignores wave damping. The absolute mode would appear to be relatively unimportant in the saturated state.

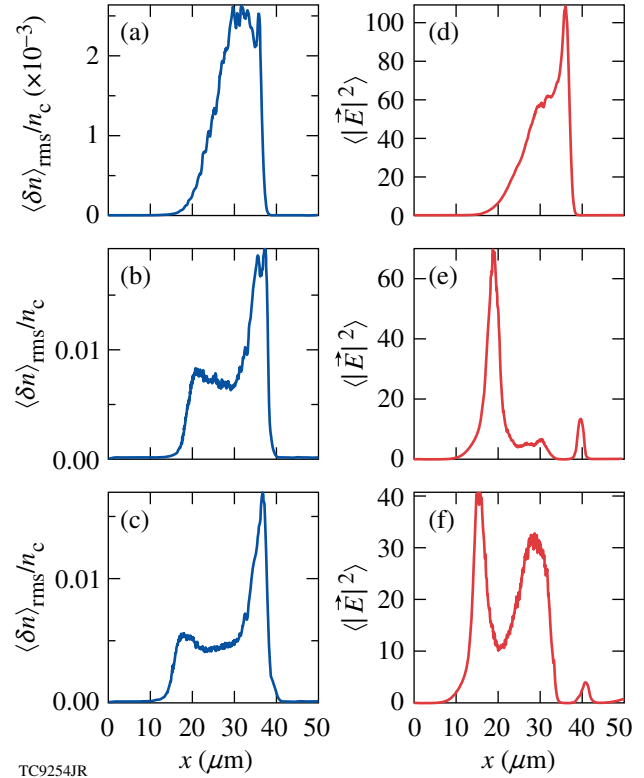
Yan *et al.*^{9,22} demonstrated that the convective Rosenbluth gain in amplitude [$g_R \sim \exp(\pi\Lambda)$] for the large k_\perp TPD modes can be simply written in terms of the Simon *et al.* threshold parameter for absolute instability

$$\pi\Lambda = 2.5 \left(1 - 0.0088 T_{\text{keV}} - 0.0047 T_{\text{keV}} \tilde{k}_\perp^2 \right) \eta,$$

where $\tilde{k} \equiv ck/\omega_0$. Convective gain in intensity is therefore several times larger than the threshold parameter and very weakly

dependent upon the transverse wave number for the parameters of current interest. Close to threshold, all transverse modes up to the Landau cutoff can saturate convectively without the need for nonlinear processes. As laser intensity increases, these convective modes are observed to saturate as a result of the excitation of large-amplitude ion-acoustic perturbations with relative-density perturbations on the few-percent level.

Features of the growth and nonlinear saturation of Fourier modes that come to dominate the spectrum at times $t \gtrsim 1.2$ ps in the case of single-beam illumination are illustrated in Fig. 126.16. The left-hand column [Figs. 126.16(a)–126.16(c)] shows a series of snapshots of the low-frequency density perturbations $\langle \delta n \rangle_{\text{rms}}(x)/n_c$ taken at different times (see figure caption). Note that the reference n_0 and linearly varying part of the density $\delta N(x)$ have been extracted and that a one-dimensional lineout has been obtained by taking the root-mean-square (rms) average over the transverse (y) coordinate,



TC9254JR

Figure 126.16

The left-hand column [(a)–(c)] shows a series of snapshots of the 1-D density perturbation $\langle \delta n \rangle_{\text{rms}}/n_c$, while the right-hand column [(d)–(f)] shows the transverse average of the LW excitation level $\langle |\vec{E}|^2 \rangle$, both plotted against the longitudinal coordinate x (in microns). From top to bottom, the rows correspond to times $t = 1.2$, $t = 2.0$, and $t = 2.4$ ps. The figure illustrates the correlation between LW amplitude and the region over which $\langle \delta n \rangle_{\text{rms}}/n_c \gtrsim 0.5\%$.

$$\langle \delta n \rangle_{\text{rms}}(x_i) \equiv \left[\left(1/n_y \right) \sum_{j=1}^{n_y} \delta n(x_i, x_j) \right]^2 \Bigg]^{1/2},$$

where n_y is the number of transverse grid points. The right-hand column [Figs. 126.16(d)–126.16(f)] shows the normalized LW excitation level $\langle |\tilde{E}|^2 \rangle$ averaged over the transverse direction.

Figure 126.16(a) shows the situation at $t = 1.2$ ps, where the convective LW growth is well described by the linear evolution. The excitation of the LF density perturbations is due to the nonlinear ponderomotive force [first term on the left side of Eq. (2)] of the unstable LW's and has a negligible effect on LW growth given by Eq. (1) (its contribution is negligible compared to the damping rate, for example). In Fig. 126.16(d), the LW's appear to grow more rapidly at higher density for reasons that are not fully understood. As time progresses [Fig. 126.16(b)], the density perturbation $\langle \delta n \rangle_{\text{rms}}(x)$ level has grown significantly and is at the few-percent level. A two-dimensional Fourier analysis of the density perturbations (not shown) reveals these perturbations to be IAW's driven in response to the ponderomotive beating of primary TPD LW's, a feature previously identified in the reduced PIC calculations of Vu *et al.*¹⁰ The absolute mode has saturated as described above. Notice that the maximum in the LW excitation level $\max \left[\langle |E|^2 \rangle(x) \right]$ occurs at roughly $x = 19 \mu\text{m}$, which is the point where $\langle \delta n \rangle_{\text{rms}}(x)/n_c$ falls below 0.5%. This peak in LW excitation moved to this location continuously from near $n_e = 0.25 n_c$, following the boundary of density excitations. For larger values of x , there is evidence of saturation of the LW amplitude. The saturation leads to a lower level of LW amplitudes and a weakening of the ponderomotive excitation of δn .

The onset of a new type of behavior is shown in Figs. 126.16(c)–126.16(f). The LF density perturbations have decreased to a value of $\langle \delta n \rangle_{\text{rms}}/n_c \lesssim 0.5\%$. This appears to permit some renewed growth of the LW's (i.e., at $x = 30 \mu\text{m}$) and leads to a new peak in LW excitation located close to the minimum in $\langle \delta n \rangle_{\text{rms}}/n_c$. This close correlation between the evolution of $|E|^2$ and δn is given as evidence of the detuning effect of LF density perturbations on the convective growth of TPD modes. We recall that this is the same mechanism proposed as the saturation mechanism for TPD in the *OSIRIS* PIC calculations of Yan *et al.*⁹ It would appear that density perturbations need to exceed the level $\langle \delta n \rangle_{\text{rms}}/n_c \approx 0.5\%$ in order to be effective. An alternate description of nonlinear saturation will be given in a paper by Vu *et al.*,³⁸ where evidence is presented from RPIC and Zakharov simulations that Langmuir collapse is the essential dissipative saturation mechanism in these relatively weakly driven regimes, with the Langmuir decay instability (LDI) playing a minor role.

In general, the evolution of the LW spectrum to a steady state is observed to take several tens of picoseconds. While oscillations of the kind described above persist, the spectrum becomes “steady” only after roughly one acoustic transit time across the density range Δn spanning from the Landau cutoff to quarter-critical. For canonical parameters, this time is $t_{\text{sat}} \sim \Delta x/c_s = (\Delta n/n_0) L_n \times 1/c_s \approx 100$ ps. This steady LW spectrum is used below to investigate the generation of hot electrons.

b. Estimate of the maximum energy gain for an electron in transit through the interaction region. The late-time (saturated) LW spectrum obtained from the Zakharov calculations on p. 68, although broad, is dominated by a shared common wave and the corresponding daughter waves whenever the irradiation consists of symmetrically arranged, overlapping plane waves (Fig. 126.14) (an effect that may explain the experimentally observed scaling of preheat on overlapped-beam intensities⁴). Since this is the usual experimental configuration on OMEGA, consider the simple case where the action on the plasma electrons is due to a single coherent LW wave. In this case, an estimate for the expected scale of electron heating can be obtained (although it should be noted that similar numbers can be obtained without invoking the common wave). Taking the wave numbers of the LW's at their point of origin to be $k\lambda_{\text{De}} = 0.16$ and 0.07 , respectively (see Fig. 126.14) (the common wave is only resonant at a particular density;¹⁰ here the density is $n_e/n_c = 0.241$), then the trapping width can be estimated from the formula

$$v_{\text{tr}} = 2(e\mathcal{E}_l/m_e k)^{1/2} = 2(v_{\text{osc}} v_{\phi})^{1/2},$$

where $v_{\text{osc}} = e\mathcal{E}_l/(m_e \omega)$ is the oscillatory velocity of an untrapped electron and $v_{\phi}/v_{\text{Te}} = 1/k\lambda_{\text{De}}(1 + 3k^2\lambda_{\text{De}}^2)^{1/2}$ is the LW phase velocity for a wave satisfying the Bohm–Gross dispersion relation $\omega^2 = \omega_p^2(1 + 3k^2\lambda_{\text{De}}^2)$. In practical units the trapping width becomes

$$\begin{aligned} \frac{v_{\text{tr}}}{v_{\text{Te}}} &= 0.37 \left(\frac{1}{k\lambda_{\text{De}}} \right)^{1/2} \left(\frac{\lambda_0}{0.351 \mu\text{m}} \right)^{1/2} \\ &\times \left(\frac{I_{14}}{T_{e,\text{keV}}} \right)^{1/4} \left(\frac{\mathcal{E}_l}{\mathcal{E}_i} \right)^{1/2}. \end{aligned} \quad (4)$$

Substituting the wave numbers for the common and daughter waves gives the values

$$v_{\text{tr}} = 1.38 v_{\text{Te}} (\mathcal{E}_l/\mathcal{E}_i)^{1/2}$$

and $2.1 v_{\text{Te}} (\mathcal{E}_l/\mathcal{E}_i)^{1/2}$, respectively. In both cases the trapping width is insufficient to trap thermal electrons because of the

high phase velocity of the waves ($v_\phi/v_{Te} = 6.49$ and 14.40 for the common and daughter LW's, respectively). As a result, wave breaking will not easily occur.³⁹

The presence of the density gradient modifies the propagation of the TPD-produced LW's from their point of origin. Theoretical treatments of wave-particle interaction that lead to particle trapping and acceleration most often consider unbounded homogeneous plasma.^{40,41} The present situation involves both a spatially localized region of LW excitation (excitation is restricted to densities in the range $0.2 \leq n_e/n_c \leq 0.25$) and plasma inhomogeneity. Of most importance is the inhomogeneity in the plasma density. For example, the common wave, which is blue shifted with respect to $\omega_0/2$, propagates up the density gradient. For a freely propagating LW of fixed frequency ω , the wave number will decrease in order to preserve the dispersion relation as the local density (and plasma frequency) increases. The phase velocity will likewise increase $v_\phi = v_{Te} \left\{ 3\omega^2 / [\omega^2 - \omega_p(x)^2] \right\}^{1/2}$, at some point becoming superluminal (the group velocity has the opposite dependence, $V_g = 3v_{Te}/v_\phi$). The density at which the LW will turn depends on its frequency. The daughter wave (red-shifted plasmon) propagates down the gradient. Its phase velocity decreases until it becomes a few times the thermal velocity and the wave is damped (the Landau cutoff).

The density gradient creates the potential for electron acceleration to higher energies than can be obtained in homogeneous plasma since the phase-velocity increase can keep pace with the electron as it is accelerated up the gradient.⁴² Given an arbitrary LW amplitude, it might be possible to accelerate electrons to arbitrarily high energies, but, practically, there will come a point at which the maximum acceleration in the LW field will be insufficient to match the acceleration of the LW phase velocity. Following Brooks *et al.*⁴² (with a trivial generalization to include relativistic velocities), the magnitude of the largest-attainable acceleration may be simply obtained from the relativistic momentum equation for electrons $|v'|_{\max} = e\mathcal{E}_l/(\gamma^3 m_e)$ by assuming the electron maintains constant phase with respect to the LW. In practical units the maximum-attainable acceleration is

$$|v'_{\text{ph}}|_{\max} = 1.5 \times 10^{24} I_{15}^{1/2} \gamma^{-3} (\mathcal{E}_l/\mathcal{E}_i) \text{ cm/s}^2,$$

where the prime denotes the time derivative. Equating this with the acceleration of the LW phase velocity up the density gradient $v'_\phi(x) = v_\phi^2(x) \omega_p(x)^2 [\omega^2 - \omega_p^2(x)]^{-1} / (2L_n)$ enables one to calculate the location x and phase velocity at which the electron can no longer remain in phase $(v_\phi)_{\max}$ —the above is solved iteratively since the relativistic gamma factor is dependent on the phase velocity $\gamma(v_\phi) = (1 - v_\phi^2/c^2)^{-1/2}$.

The energy gain is given by $\Delta E/(m_e c^2) = \gamma [(v_\phi)_{\max}] - \gamma [(v_\phi)_0]$, where $(v_\phi)_0$ is the initial (phase) velocity of the electron (LW). Substituting in values $I_{15} = 1$, $\mathcal{E}_l = \mathcal{E}_i$, and $(v_\phi)_0 = 6.49 v_{Te}$ from the Zakharov calculations presented in **Zakharov Predictions for the Saturated LW Spectrum** (p. 68) gives an estimate for the energy gain of $\Delta E \sim 110$ keV (or $\Delta E \sim 177$ keV for $\mathcal{E}_l = 2 \mathcal{E}_i$).

The actual situation does not involve a single coherent wave, but rather there are many waves whose resonances are expected to have significant overlap, leading to orbits that become diffusive. It might be possible to approximate the stochastic acceleration of electrons in the predicted LW fields with a self-consistent Fokker-Planck⁴³ or quasilinear model.^{11,29,30} To estimate the heating effect more accurately and to investigate the importance of reheating, test electron trajectories are directly integrated in the LW fields predicted by the Zakharov model of **Zakharov Predictions for the Saturated LW Spectrum** (p. 68). This will also form the basis for future work that will examine the applicability of quasilinear diffusion³²⁻⁴⁴ for the two-plasmon-decay instability.

2. Test-Particle Equations of Motion

Test-particle motion is governed by the relativistic Newton-Lorentz equations. For the i^{th} electron test particle, these are

$$\frac{d\vec{x}_i}{dt} = \vec{v}_i, \quad (5)$$

$$\frac{d\vec{p}_i}{dt} = -e \left[\vec{\mathcal{E}}_l(\vec{x}_i, t) + \vec{\mathcal{E}}_l(\vec{x}_i, t) + \vec{v}_i/c \times \vec{\mathcal{B}}(\vec{x}_i, t) \right], \quad (6)$$

where $\vec{p}_i = \gamma_i m_0 \vec{v}_i$ is the electron momentum. The longitudinal electric field $\vec{\mathcal{E}}_l$ is associated with the LW's resulting from the TPD instability and is obtained from the Zakharov field \vec{E} by restoring the carrier frequency ω_{p0} (which was explicitly removed in the Zakharov approximation)

$$\vec{\mathcal{E}}_l(\vec{x}, t) = 1/2 \vec{E}(\vec{x}, t) \exp(-i\omega_{p0}t) + \text{c.c.} \quad (7)$$

The transverse fields $\vec{\mathcal{E}}_t$ and $\vec{\mathcal{B}}$ are associated with the incident laser light and are currently ignored when computing test-particle trajectories (they are prescribed fields in the current extended Zakharov model). Although the transverse electric-field strength is quite large,

$$\mathcal{E}_t \sim 8.7 \times 10^8 \left(I_0 / 1 \times 10^{15} \text{ W/cm}^2 \right)^{1/2} \text{ V/cm},$$

it is not effective in accelerating electrons at nonrelativistic laser intensities ($I_0 \lesssim 10^{18} \text{ W/cm}^2$). The transverse fields result merely in a "quiver" imposed on the unperturbed motion. The

quantity $\vec{\mathcal{E}}_i$ is defined only at discrete spatial locations that are determined by the discretization (grid points) used in the numerical solution of Eqs. (1) and (2) and is interpolated onto the i^{th} test electron position \vec{x}_i using bilinear interpolation. The test-particle equations [Eqs. (5) and (6)] are integrated numerically using a fourth-order Runge–Kutta scheme.

Ensemble averages of test-particle quantities are obtained by averaging over test-particle initial conditions $\vec{x}_i(t=0)$ and $\vec{p}_i(t=0)$ since averaging over realizations of the electric-field spectrum is impractical. The initial position of a test particle $\vec{x}_0 \equiv \vec{x}(t=0)$ is a random variable defined on $\Omega = [0, l_x] \times [0, l_y]$ with a uniform probability distribution $f(\vec{x}_0)d\vec{x}_0 = d\vec{x}_0/(l_x l_y)$. The initial momentum $\vec{p}_0 \equiv \vec{p}(t=0)$ is given by

$$\vec{p}_0 = p_0 [\hat{e}_x \sin(\phi) + \hat{e}_y \cos(\phi)],$$

where the magnitude of the momentum p_0 is fixed according to a given kinetic energy

$$p_0 = m_0 c \left[\left(T_0 / m_0 c^2 + 1 \right)^2 - 1 \right]^{1/2},$$

while the angle ϕ is a uniform random variable on $[0, 2\pi]$ with the probability distribution $f(\phi)d\phi = d\phi/(2\pi)$. The effect of the finite boundary on the particle trajectories is addressed in the following section, while the boundary conditions on the longitudinal fields are periodic in the transverse direction $\vec{\mathcal{E}}_i(x, y + l_y) = \vec{\mathcal{E}}_i(x, y)$ and vanish at the longitudinal boundaries $\vec{\mathcal{E}}_i(x=0, y) = \vec{\mathcal{E}}_i(x=l_x, y) = 0$ (see Fig. 126.17).

3. Estimation of Global Particle Trajectories

For the numerical simulation of Eqs. (5) and (6), any potential for electrons to re-enter the TPD active region after their transit through the simulation domain must be manifested

through the boundary conditions because of limitations placed on the maximum size of the region over which Eqs. (5) and (6) can be realistically integrated. In general, the problem of boundary conditions in kinetic^{29,30} or PIC calculations⁹ is usually addressed by assuming that transverse boundaries are periodic, while longitudinal boundaries are thermalizing. The thermal boundary conditions have the effect of driving the electron-distribution function to a Maxwellian,³⁰ which may or may not be physically reasonable. It is clear that the choice of boundary condition has a significant impact on the properties of the hot-electron spectrum.^{11,28} Such a “thermalizing” scheme is easily implemented for test particles in Eqs. (5) and (6) above. Inspection of the target areal densities relevant to OMEGA implosions at the time of TPD instability ($\rho R \sim 10^{-2}$ g/cm²) shows, however, that they are unlikely to be completely stopped [the range $r_0 = 6.65 \times 10^{-2}$ g/cm² for an electron of energy of 100 keV in hydrogen in the continuous-slowing-down approximation—energies corresponding to those estimated in **Estimate of the Maximum Energy Gain for an Electron in Transit Through the Interaction Region** (p. 71) and observed experimentally^{41,45}]. As a result, an estimate of the effect of electron recirculation is needed.

The spherical nature of the quarter-critical surface means that hot electrons can pass through the center of the target and re-encounter it once more on the opposite side (as long as they are sufficiently energetic so as not to range out; i.e., trajectories of type A, shown in Fig. 126.18). Less obvious is the fact that electrons on outward-bound trajectories (heading away from the target) may also be reflected back by the presence of sheath fields^{11,46,47} (trajectory of type B, shown in Fig. 126.18). The possibility therefore exists for complex orbits where electrons can be accelerated multiple times by the TPD active region near the quarter-critical surface.

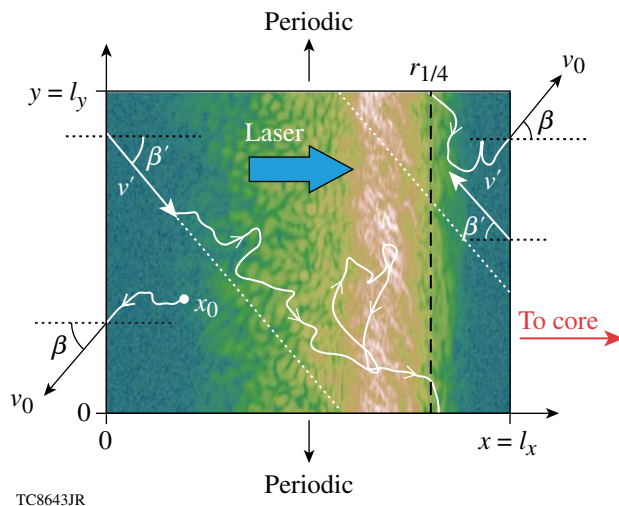


Figure 126.17

An illustration of how the boundary conditions for electron test particles are implemented. The region $\Omega = [0, l_x] \times [0, l_y]$ over which the LW fields are calculated is shown, where the colors correspond to the magnitude $|\vec{\mathcal{E}}(x, y)|^2$ from a particular run. Periodicity is assumed for trajectories crossing the transverse boundaries ($y=0$ or $y=l_y$), while a test particle reaching a longitudinal boundary ($x=0$ or $x=l_x$) at time t with angle β and energy E_0 is re-injected at the same boundary at the later time $t' = t + \Delta t$ with a reduced energy $E' = E_0 - \Delta E$. The position along the boundary at reinjection is randomized, while its angle is given by $\beta' = \beta$. The white curve illustrates this process for an imaginary trajectory.

TC8643JR

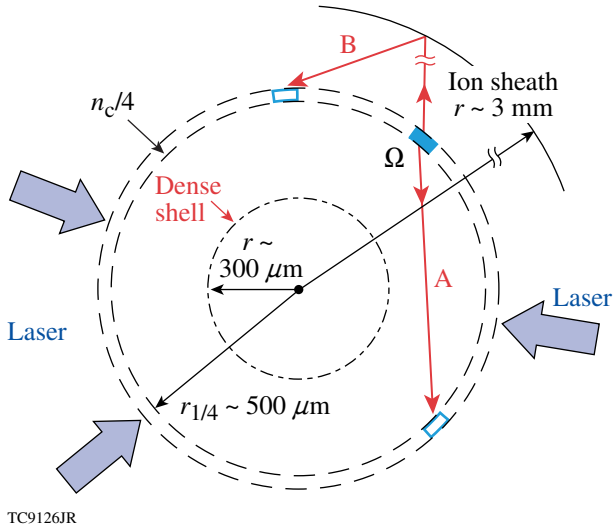


Figure 126.18

A schematic drawing showing a two-dimensional plane passing through the origin of a spherical implosion and containing the plane region Ω over which the extended Zakharov equations are simulated. The region Ω is illustrated by the blue shaded rectangle spanning the radius of the quarter-critical density surface, $r_{1/4}$. Periodicity (modulo l_y) is assumed in the tangential direction so that the whole annular region bounded by the dashed concentric circles is assumed to be modeled (mapped onto) Ω . Because of the spherical geometry, electrons that leave the region Ω in the direction of the origin (trajectory of type A as indicated) can re-intersect the quarter-critical surface and re-enter Ω . Outgoing trajectories (type B) can also return because of reflection from the ion sheath. Dimensions characteristic of OMEGA implosions are indicated.

The global radiation hydrodynamics of an imploding target at any given time during an implosion is calculated with the one-dimensional radiation–hydrodynamics code *LILAC*²⁷ without consideration of the effects of TPD (i.e., no increased absorption or effects of preheat). The parameters are taken to be those of current cryogenic implosion experiments on OMEGA at the time of peak TPD instability. These parameters place the quarter-critical surface at a radius of $r_{1/4} \sim 500 \mu\text{m}$, while the dense shell is at a radius of approximately $300 \mu\text{m}$ (see Fig. 126.18). The energy loss and time of flight associated with the electron trajectories beyond the quarter-critical surface are approximated below by “unperturbed” trajectories. That is, the energy loss and time of flight between an electron leaving the critical surface and returning (either by passing through the core or by reflection by sheath fields far out in the corona⁴⁶) are estimated assuming a straight-line trajectory with angle and energy given by the values on leaving the quarter-critical surface. The time of return will be delayed by an amount that is dependent on the particular boundary that has been crossed and the details of the trajectory. Periodicity in the transverse (y) direction is motivated by the fact that the radius of curvature of the quarter-critical surface is much larger (typically ten times

larger) than the lateral extent l_y of the simulation volume (and therefore the correlation length for \vec{E}).

a. Practical implementation of delay-type boundary conditions on test particles. At the boundary of the Zakharov calculation located at $x = l_x$ (see Fig. 126.17), which looks toward the target core, electrons crossing at time t with angle $\beta = \cos^{-1}(\vec{p} \cdot \hat{n}/p)$ with respect to the outward normal \hat{n} of the simulation volume ($\hat{n} = \hat{e}_x$) cut a chord of length $s_{\text{max}} = 2 r_{1/4} \cos(\beta)$ across the circle that describes the intersection of the quarter-critical surface with the plane defined by the laser polarization vector and the radius vector defined with respect to target origin (Fig. 126.18). Note that this angle (β) is, to an excellent approximation, the same as the angle between the negative radius vector and the electron momentum vector ($\hat{n} \approx -\hat{e}_r$). The radius $r(s)$ along this chord as a function of path length s is given by $r^2 = r_{1/4}^2 + s^2 - 2(r_{1/4}s)\cos(\beta)$, and inverting this function allows one to specify the hydrodynamic variables $n_e(r)$, $T_e(r)$ from the hydrocode *LILAC* along the trajectory, $n_e(s)$, $T_e(s)$. The time of flight for an electron to transit the path is estimated by

$$\Delta\tau = \frac{1}{c} \int_0^{s_{\text{max}}} \frac{ds}{\beta_e(s)}, \quad (8)$$

where the particle velocity is computed in terms of its energy $E(s)$ according to

$$\beta_e(s) = \left\{ \frac{2E(s)/m_e c^2 + [E(s)/m_e c^2]^2}{[1 + E(s)/m_e c^2]^2} \right\}^{1/2} \quad (9)$$

with

$$E(s) = E_0 - \int_0^s \left| \frac{dE}{ds} \right| ds \quad (10)$$

being the kinetic energy of the electron as a function of distance s along the path. The total energy loss along the path is simply $\Delta E = E_0 - E(s_{\text{max}})$. The stopping power $-dE/ds$ is given by $-dE/ds = e^2 \omega_p^2 / (c^2 \beta_e^2) \log[\beta_e^2 m_e c^2 / (\hbar \omega_p)]$. With the above assumptions, the energy loss ΔE and time delay Δt may be computed as a function of energy E_0 and angle β .

As mentioned previously, there is also a possibility that electrons leaving the outer simulation boundary ($x = 0$) (see Fig. 126.17) will return. This time, the effect is not geometrical but is instead related to the formation of a plasma sheath far out in the corona^{46,47} (see Fig. 126.18). In principle the structure and dynamics of the sheath formation are complicated and coupled to the hot-electron–generation mechanism itself, which

requires a level of knowledge that is currently unavailable. Here we take a practical approach and adopt a greatly simplified model that has been previously used by Delettrez *et al.*⁵ This has the advantage of facilitating comparisons between the current work and the phenomenological model of Delettrez *et al.* The model specularly reflects electrons when they reach the radius of the last Lagrangian cell of the *LILAC* calculation. The total path length is therefore given by $s_{\max} = 2 l_{\text{exc}}$, where $l_{\text{exc}} = r_{\text{sh}} \cos(\Theta) - r_{1/4} \cos(\beta)$ is the distance to the last Lagrangian cell of the *LILAC* calculation, r_{sh} is its radius, and $\Theta = \sin^{-1} [r_{1/4} / r_{\text{sh}} \sin(\beta)]$. The radius is now given in terms of the path length according to $r^2 + s^2 + r_{1/4}^2 + 2(r_{1/4}s) \cos(\beta)$ for $s \leq l_{\text{exc}}$, and by $r^2 = (2l_{\text{exc}} - s)^2 + r_{1/4}^2 + 2r_{1/4}(2l_{\text{exc}} - s) \cos \beta$ for $s > l_{\text{exc}}$.

The energy losses and time delays as a function of electron momentum (energy and angle) are precomputed and stored in look-up tables, one for each longitudinal boundary. Figures 126.19 and 126.20 show examples of look-up tables for the boundary at $x = l_x$ corresponding to a cryogenic implosion on OMEGA (shot 45009) at the time of experimental onset of two-plasmon-decay signatures (roughly 2.5 ns from the start

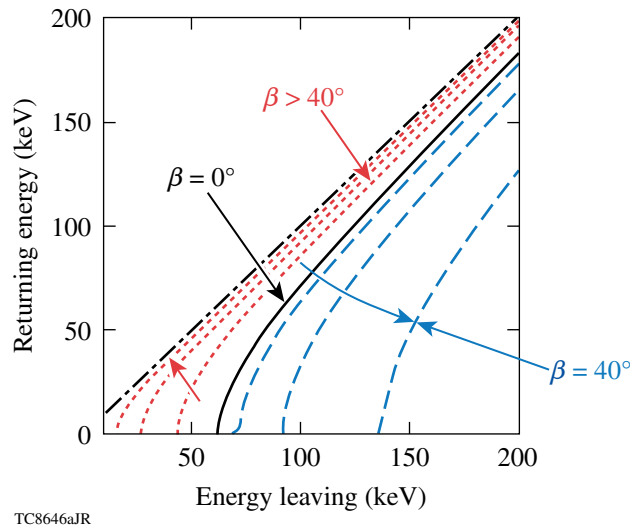


Figure 126.19

Look-up tables for energy loss at the $x = l_x$ boundary (i.e., type-A trajectories in Fig. 126.18) corresponding to OMEGA shot 45009 at time $t = 2.5$ ns. Angle β is the angle between the outward normal of the boundary ($\approx -\hat{e}_r$) and the direction of the electron-velocity vector (see Fig. 126.17). As β increases from 0° [radially inward trajectory (black solid curve)] to $\beta \leq 40^\circ$, the energy loss increases (i.e., the blue dashed curves move as indicated by the arrow). The effect is due to the increased path length in the dense compressed shell (see Fig. 126.18). Maximum energy loss occurs at $\beta \approx 40^\circ$. For angles greater than 40° (red dotted curves) the energy loss falls dramatically and vanishes at $\beta = 90^\circ$ since the trajectories no longer intersect the dense shell and the path length vanishes.

of the pulse). Test particles, upon reaching the boundary, are re-injected at the same boundary at a later time $t + \Delta t$ with the modified angle $\beta' = -\beta$ and energy $E_0 - \Delta E$. The transverse coordinate of the returning electron is randomized, taking the new position to be a uniform random variable on $[0, l_y]$. This is illustrated in Fig. 126.17. If a particular energy loss results in a re-injected energy of the electron falling below a threshold value (typically $E_{\text{cut}} = 200$ eV), the trajectory is terminated.

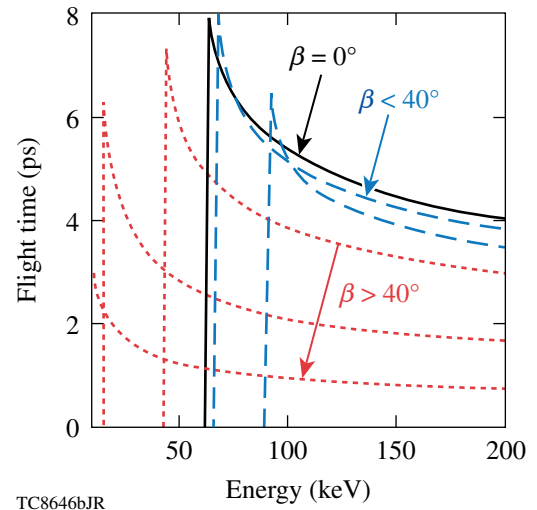


Figure 126.20

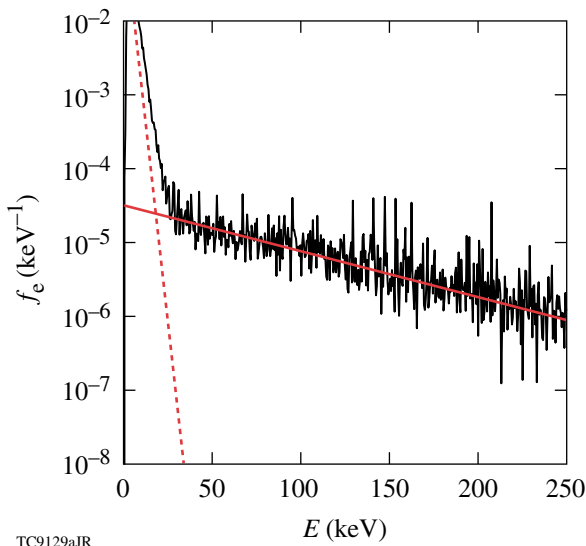
An example of the boundary look-up tables for time delay Δt at the $x = l_x$ simulation boundary corresponding to OMEGA shot 45009 at time $t = 2.5$ ps. The delay reaches a maximum value of $\Delta t \sim 8$ ps for trajectories that are nearly radial (inward) ($\beta \approx 0^\circ$), and it vanishes for tangential trajectories $\beta = 90^\circ$. The curves types/colors are the same as described in Fig. 126.19.

Results of Test-Particle Calculations

To quantify the contributions from separate processes, the effect of heating is first calculated with absorbing/thermal boundary conditions in the longitudinal direction, while periodicity is assumed in the transverse direction. This corresponds either to a massive target in which all hot electrons range out or alternatively to the usual boundary conditions that are applied in the kinetic modeling of TPD using PIC codes.^{9,10} The density scale length is varied within the range $L_n = (100 \text{ to } 350) \mu\text{m}$, while holding the electron temperature fixed at $T_e = 2$ keV. This addresses the range currently accessible on OMEGA and, for the longer scale lengths, the range accessible in the near future on OMEGA EP. The laser intensities are chosen to be between $I_L = (0.1 \text{ to } 2.0) \times 10^{15} \text{ W/cm}^2$. With this choice, the absolute TPD instability is found to be slightly above threshold to approximately three times above threshold [$\beta = (1.15 \text{ to } 3.1)$] according to the formula of Simon *et al.*¹³ Finally, the impact of reheating is addressed by taking as an example the hydro-

dynamic conditions of a cryogenic implosion that has been fielded on OMEGA (shot 45009) and computing the effects of reheating on the hot-electron temperature as the laser intensity is increased (within the above quoted range).

Figure 126.21 shows the energy distribution of test electrons as a function of electron energy for a typical case. The initial energies were chosen from a Maxwellian distribution of temperature $T_e = 2$ keV, chosen to be consistent with the electron temperature used in the Zakharov calculation. Note that the deviation from the initial Maxwellian occurs at an electron kinetic energy of roughly 20 keV. This is consistent with the smallest phase-velocity waves (largest wave number) observed in the LW spectrum (Fig. 126.14). The tail is well fit by an exponential, the slope of which is used to define an effective hot-electron temperature T_{hot} .

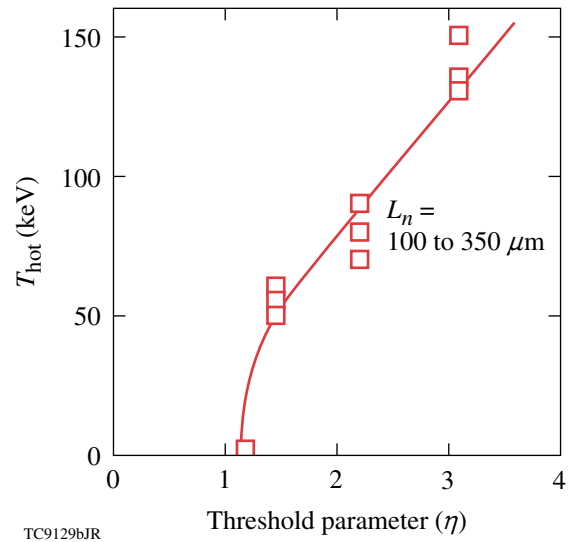


TC9129aJR

Figure 126.21

The electron test-particle distribution function $f_e(E)$ as a function of electron energy E constructed from an ensemble of 10^6 trajectories. The slope of the distribution function for energies $E \lesssim 30$ keV is close to the temperature of the sample distribution ($T_e = 2$ keV) as indicated by the steep dashed red line. For energies $E \gtrsim 30$ keV, a hot tail is observed. The slope of the hot tail is well fit by an exponential (solid red line), which is used to define an exponential slope temperature T_{hot} .

Figure 126.22 shows the hot-electron temperature T_{hot} inferred from a series of simulations, with the parameters as defined above, plotted against the threshold parameter η . Recall that density scale length and laser intensity are being varied, and while there is a small scatter in the inferred temperature for different combination of L_n and I giving the same η , the hot temperature is well predicted by the value of η alone. A hot component is generated once η has slightly exceeded unity



TC9129bJR

Figure 126.22

The hot-electron temperature T_{hot} as determined by the electron test-particle distribution function for a series of extended Zakharov realizations plotted against the threshold parameter $\eta [= I_{14} L_{\mu\text{m}} / (230 \text{ keV})]$. For a given η , the open squares show the effect of varying the density scale length in the range $L_n = (100 \text{ to } 350) \mu\text{m}$ while holding the initial electron temperature T_e fixed (intensities were adjusted appropriately). The red (solid) line indicates the general trend.

(which is also an experimental observation³) and increases from $T_{\text{hot}} \sim 50$ keV at $\eta = 2$ to a value of ~ 140 keV at $\eta = 3.0$.

The insensitivity of the hot-electron temperature to density scale length for a fixed value of the threshold parameter η is shown in Fig. 126.23. Once again, as the density scale length is increased, the laser intensity is decreased in order to keep the value of η constant. Solid lines connect simulation points having constant η , while the filled markers correspond to a laser intensity of $I_L = 4.8 \times 10^{14} \text{ W/cm}^2$. From the filled markers, the rapid increase in hot-electron temperature with density scale length can be visualized. The reason for this insensitivity can be determined upon an examination of the Zakharov predictions for the nonlinearly saturated LW spectrum in each case. Figure 126.24 shows the rms electric field taken over each Zakharov simulation volume (adjusted with L_n to span the density range of $0.19 < n_e/n_c < 0.27$). While the value of $\langle E \rangle_{\text{rms}}$ depends on the value of the threshold parameter for a given scale length and is of the order of $\langle E \rangle_{\text{rms}} = 10^6$ statvolts/cm for fixed η , it decreases with density scale length. It is therefore the laser intensity that determines the level of LW excitation. The acceleration of hot electrons, very crudely speaking, is given by the characteristic electric field multiplied by the acceleration length. In this way, the increasing acceleration length is offset by the reduction in electric field.

The above results have ignored the possibility of multiple transits of the hot electrons through the quarter-critical region

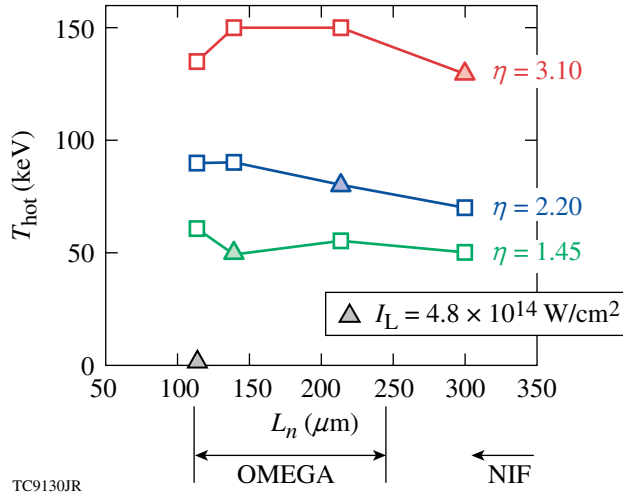


Figure 126.23

The hot-electron temperature T_{hot} in keV as determined by the electron test-particle distribution function for a series of extended Zakharov realizations plotted against density scale length L_n in microns. The upper (red), middle (blue), and lower (green) curves correspond to values of the threshold parameter of $\eta = 3.10$, 2.20, and 1.45, respectively. The filled triangles correspond to a laser intensity of $I_L = 4.8 \times 10^{14} \text{ W/cm}^2$. In all cases the initial electron temperature was $T_e = 2.0 \text{ keV}$.

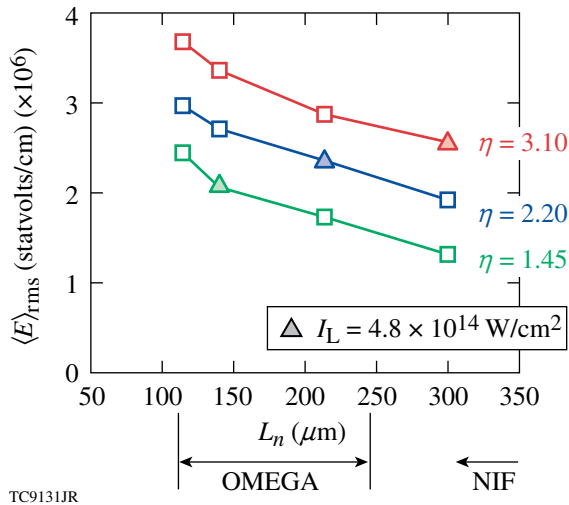


Figure 126.24

The root-mean-square electric field at saturation obtained from a series of extended Zakharov runs with an electron temperature $T_e = 2 \text{ keV}$ plotted against density scale length L_n in microns. The upper (red), middle (blue), and lower (green) curves correspond to values of the threshold parameter of $\eta = 3.10$, 2.20, and 1.45, respectively. It is evident that for a given value of η and for a fixed electron temperature, the rms electric field decreases with an increase (decrease) in density scale length L_n (laser intensity I_L). The filled markers correspond to a laser intensity of $I_L = 4.8 \times 10^{14} \text{ W/cm}^2$.

and therefore multiple stages of acceleration. The size of this effect has been demonstrated by implementing the boundary conditions exactly as described in **Practical Implementation of Delay-Type Boundary Conditions on Test Particles** (p. 74) (see Fig. 126.25). Look-up tables corresponding to shot 45009 at a time near the peak drive, when $\rho R \approx 1 \times 10^{-2} \text{ g/cm}^2$, have been used (Figs. 126.19 and 126.20). In Fig. 126.25 the square symbols show the hot-electron temperature as a function of the threshold parameter η with absorbing boundaries, while the circles show the hot-electron temperature when the “physical” boundary conditions are adopted. It can be seen that there is a significant effect; corresponding to an ($\sim 3\times$) increase in the hot-electron temperature. This demonstrates the futility of studying an isolated region of the target near the quarter-critical density when attempting to compute hot-electron temperature and, by extension, the expected hot-electron preheat. This is an extremely unfortunate result since the mixing of spatial scales is severe. On one hand, the LW wavelength must be resolved (which is submicron), while on the other, electron trajectories must be traced over millimeters. A similar mixing (four orders of magnitude) also holds for the temporal scale.

The size of the effect obviously increases in importance with higher one-pass temperatures since more-energetic electrons can more freely pass through the core. So as to not overstate

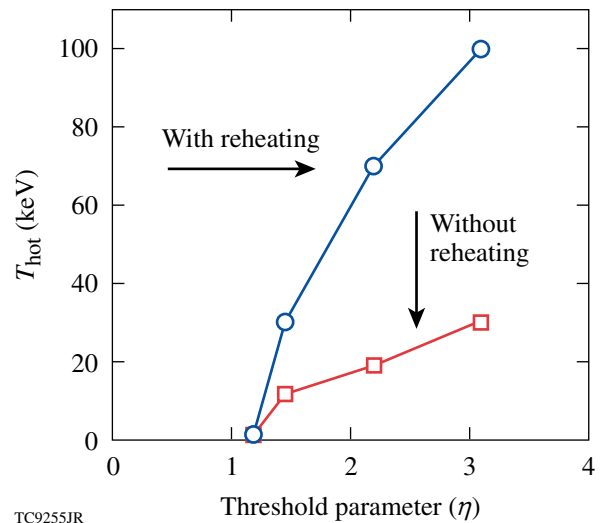


Figure 126.25

The hot-electron temperature T_{hot} in keV as a function of the threshold parameter η . The hot temperature was determined from the electron test-particle energy distribution for test-particle trajectories employing thermal boundary conditions (red curve) and delay-type boundary conditions as described on p. 74 (blue curve). The density scale length L_n and electron temperature T_e were held constant at $150 \mu\text{m}$ and 2 keV , respectively, while the intensity was varied.

the size of the effect, the one-pass temperatures were actually reduced from the pure Zakharov predictions in making these calculations (e.g., comparison of Fig. 126.25 with Fig. 126.22 shows a smaller one-pass temperature). In fact, when computing test-particle heating for Fig. 126.25, the predicted electric field \vec{E} has been reduced artificially (“renormalized”) in magnitude [only where it appears in Eq. (6)] so that the resulting hot-electron temperature, in the case of thermal boundaries, is computed to be no larger than the best current estimate based on reduced description particle-in-cell modeling.²⁸ It might be expected that the non-self-consistent test particle model would lead to exaggerated hot-electron temperatures because of the absence of any modification to the linear dispersion (damping) caused by the hot tail. It is hoped that a self-consistent treatment using a quasilinear model will remove the need for such renormalization.

Summary and Discussion

An extended Zakharov model of two-plasmon-decay instability has been presented and used to predict the saturated LW spectrum in the absence of electron kinetic effects (heating). The parameters were motivated by current OMEGA experiments, and the assumed electron temperature and density profiles were defined by 1-D radiation hydrodynamic (*LILAC*) calculations for a given time corresponding to peak TPD instability.

The LW spectrum has been observed to evolve as a consequence of the interaction between the unstable LW's and LF density fluctuations. It was argued that convectively unstable modes come to dominate the late-time spectrum, while the absolute TPD model is relatively unimportant after initial saturation by profile modification. The convective modes are either linearly saturated close to threshold or by ponderomotively driven ion-acoustic turbulence once threshold is exceeded significantly. It was noted that several tens of picoseconds are required for the LW spectrum to approach a statistical steady state.

Hot-electron production was first calculated by a non-self-consistent test particle approach using the Zakharov predictions for the electric fields at saturation and with the assumption of thermal boundary conditions. An exponential hot-electron tail was observed once the absolute threshold was exceeded ($\eta > 1$), and the characteristic temperature of this tail increased from approximately $T_{\text{hot}} = 50$ keV for $\eta \approx 1.5$ to a value of $T_{\text{hot}} = 140$ keV when $\eta = 3$. These temperatures were shown to be reasonable based on estimates of the maximum-allowable energy gain over the interaction region, and they are also broadly consistent with experimental measurements and RPIC simulations.

It was noted that electron heating also depends on the global details of the implosion because of the long-range nature of the hot electrons and the possibility of reheating [as has been described in **Practical Implementation of Delay-Type Boundary Conditions on Test Particles** (p. 74)]. This effect has been captured by using a particular form of boundary condition on the test-particle trajectories. A prescription for such boundary conditions has been constructed and described. Adoption of these boundary conditions was shown to lead to an increase in the computed hot-electron temperature by a factor of $\sim 3\times$. It was noted that any attempt to model the hot-electron temperature or preheat in such targets must account for this physical effect.

The model allows for systematic refinement. Future plans in this regard include the inclusion of a propagating scattered transverse EM envelope at a frequency $\omega_0/2$ so that absolute Raman and high-frequency hybrid instability¹⁸ may be included. The test-particle method developed here, together with reduced particle-in-cell calculations,¹⁰ will be used to guide the development of a self-consistent quasilinear model of electron heating. This will require the inclusion of the delay-type boundary conditions and an investigation into the effects of density inhomogeneity. The delay-type boundary condition model can also be improved. In particular, a self-consistent model for the sheath potential will be developed, and the effect of angular scattering will also be taken into account when computing electron trajectories.

Finally, diagnostics such as preheat, half-harmonic emission, and bremsstrahlung spectra^{26,48} will be added to the model to facilitate comparison with experiment.

ACKNOWLEDGMENT

This work was supported by the U.S. Department of Energy Office of Inertial Confinement Fusion under Cooperative Agreement No. DE-FC52-08NA28302 and by the National Nuclear Security Agency through its High-Energy Density Laboratory Plasmas Grant No. DE-FG52-09NA29545.

REFERENCES

1. J. D. Lindl *et al.*, *Phys. Plasmas* **11**, 339 (2004).
2. S. P. Regan, N. B. Meezan, L. J. Suter, D. J. Strozzi, W. L. Kruer, D. Meeker, S. H. Glenzer, W. Seka, C. Stoeckl, V. Yu. Glebov, T. C. Sangster, D. D. Meyerhofer, R. L. McCrory, E. A. Williams, O. S. Jones, D. A. Callahan, M. D. Rosen, O. L. Landen, C. Sorce, and B. J. MacGowan, *Phys. Plasmas* **17**, 020703 (2010).
3. W. Seka, D. H. Edgell, J. F. Myatt, A. V. Maximov, R. W. Short, V. N. Goncharov, and H. A. Baldis, *Phys. Plasmas* **16**, 052701 (2009).
4. C. Stoeckl, R. E. Bahr, B. Yaakobi, W. Seka, S. P. Regan, R. S. Craxton, J. A. Delettrez, R. W. Short, J. Myatt, A. V. Maximov, and H. Baldis, *Phys. Rev. Lett.* **90**, 235002 (2003).

5. J. A. Delettrez, V. N. Goncharov, P. B. Radha, C. Stoeckl, A. V. Maximov, T. C. Sangster, J. A. Frenje, and D. Shvarts, *Bull. Am. Phys. Soc.* **52**, 143 (2007).
6. D. Shvarts, V. A. Smalyuk, R. Betti, J. A. Delettrez, D. H. Edgell, V. Yu. Glebov, V. N. Goncharov, R. L. McCrory, P. W. McKenty, D. D. Meyerhofer, F. J. Marshall, P. B. Radha, T. C. Sangster, W. Seka, S. Skupsky, C. Stoeckl, B. Yaakobi, J. A. Frenje, C. K. Li, R. D. Petrasso, and F. H. Séguin, presented at the 37th Anomalous Absorption Conference, Maui, HI, 27–31 August 2007.
7. V. A. Smalyuk, D. Shvarts, R. Betti, J. A. Delettrez, D. H. Edgell, V. Yu. Glebov, S. X. Hu, F. J. Marshall, R. L. McCrory, P. W. McKenty, D. D. Meyerhofer, P. B. Radha, T. C. Sangster, W. Seka, S. Skupsky, C. Stoeckl, B. Yaakobi, J. A. Frenje, C. K. Li, R. D. Petrasso, and F. H. Séguin, presented at the 37th Anomalous Absorption Conference, Maui, HI, 27–31 August 2007.
8. V. N. Goncharov, T. C. Sangster, P. B. Radha, R. Betti, T. R. Boehly, T. J. B. Collins, R. S. Craxton, J. A. Delettrez, R. Epstein, V. Yu. Glebov, S. X. Hu, I. V. Igumenshchev, J. P. Knauer, S. J. Loucks, J. A. Marozas, F. J. Marshall, R. L. McCrory, P. W. McKenty, D. D. Meyerhofer, S. P. Regan, W. Seka, S. Skupsky, V. A. Smalyuk, J. M. Soures, C. Stoeckl, D. Shvarts, J. A. Frenje, R. D. Petrasso, C. K. Li, F. Séguin, W. Manheimer, and D. G. Colombant, *Phys. Plasmas* **15**, 056310 (2008).
9. R. Yan, A. V. Maximov, C. Ren, and F. S. Tsung, *Phys. Rev. Lett.* **103**, 175002 (2009).
10. H. X. Vu, D. F. DuBois, D. A. Russell, and J. F. Myatt, *Phys. Plasmas* **17**, 072701 (2010).
11. D. A. Russell, presented at the Workshop on Laser Plasma Instabilities, sponsored by Lawrence Livermore National Laboratory and the University of Rochester's Laboratory for Laser Energetics, Livermore, CA, 3–5 April 2002.
12. Y. C. Lee and P. K. Kaw, *Phys. Rev. Lett.* **32**, 135 (1974).
13. A. Simon, R. W. Short, E. A. Williams, and T. Dewandre, *Phys. Fluids* **26**, 3107 (1983).
14. L. V. Powers and R. L. Berger, *Phys. Fluids* **27**, 242 (1984).
15. L. V. Powers and R. L. Berger, *Phys. Fluids* **28**, 2419 (1985).
16. L. V. Powers and R. L. Berger, *Plasma Phys. Control. Fusion* **28**, 1575 (1986).
17. B. K. Sinha and G. P. Gupta, *Plasma Phys. Control. Fusion* **35**, 281 (1993).
18. B. B. Afeyan and E. A. Williams, *Phys. Rev. Lett.* **75**, 4218 (1995).
19. B. B. Afeyan and E. A. Williams, *Phys. Plasmas* **4**, 3845 (1997).
20. A. C. Machacek and J. S. Wark, *Phys. Plasmas* **8**, 4357 (2001).
21. A. C. Machacek and J. S. Wark, *Phys. Plasmas* **8**, 704 (2001).
22. R. Yan, A. V. Maximov, and C. Ren, *Phys. Plasmas* **17**, 052701 (2010).
23. M. N. Rosenbluth, *Phys. Rev. Lett.* **29**, 565 (1972).
24. J. F. Drake and Y. C. Lee, *Phys. Rev. Lett.* **31**, 1197 (1973).
25. D. A. Russell and D. F. DuBois, *Phys. Rev. Lett.* **86**, 428 (2001).
26. D. F. DuBois, D. A. Russell, and H. A. Rose, *Phys. Rev. Lett.* **74**, 3983 (1995).
27. J. Delettrez, R. Epstein, M. C. Richardson, P. A. Jaanimagi, and B. L. Henke, *Phys. Rev. A* **36**, 3926 (1987).
28. D. F. DuBois and H. X. Vu, Los Alamos National Laboratory and University of California—San Diego, private communication (2010).
29. K. Y. Sanbonmatsu *et al.*, *Phys. Rev. Lett.* **82**, 932 (1999).
30. K. Y. Sanbonmatsu *et al.*, *Phys. Plasmas* **7**, 2824 (2000).
31. J. J. Thomson, R. J. Faehl, and W. L. Kruer, *Phys. Rev. Lett.* **31**, 918 (1973).
32. J. I. Katz *et al.*, *Phys. Fluids* **16**, 1519 (1973).
33. K. Y. Sanbonmatsu *et al.*, *Geophys. Res. Lett.* **24**, 807 (1997).
34. A. B. Langdon, B. F. Lasinski, and W. L. Kruer, *Phys. Rev. Lett.* **43**, 133 (1979).
35. C. Ren, University of Rochester, private communication (2010).
36. H. A. Baldis and C. J. Walsh, *Phys. Fluids* **26**, 1364 (1983).
37. R. W. Short, *Bull. Am. Phys. Soc.* **55**, 115 (2010).
38. H. X. Vu, D. F. DuBois, J. F. Myatt, and D. A. Russell, “Langmuir Waves Collapse and Associated Suprathermal Electron Production by the Two-Plasmon Decay Instability in Inhomogeneous Plasmas,” submitted to *Physical Review Letters*.
39. W. L. Kruer, *The Physics of Laser-Plasma Interactions, Frontiers in Physics*, Vol. 73, edited by D. Pines (Addison-Wesley, Redwood City, CA, 1988).
40. Y. Elskens and D. Escande, *Microscopic Dynamics of Plasmas and Chaos*, Series in Plasma Physics (Institute of Physics Publishing, Bristol, England, 2003).
41. W. Rozmus and P. P. Goldstein, *Phys. Rev. A* **38**, 5745 (1988).
42. R. D. Brooks and Z. A. Pietrzyk, *Phys. Fluids* **30**, 3600 (1987).
43. D. Pesme, *Phys. Scr.* **T50**, 7 (1994).
44. J. J. Thomson *et al.*, *Phys. Fluids* **17**, 973 (1974).
45. H. O. Wyckoff, *ICRU Report*, International Commission on Radiation Units and Measurements, Inc., Bethesda, MD (1984).
46. J. S. Pearlman and G. H. Dahlbacka, *Appl. Phys. Lett.* **31**, 414 (1977).
47. D. M. Villeneuve, R. L. Keck, B. B. Afeyan, W. Seka, and E. A. Williams, *Phys. Fluids* **27**, 721 (1984).
48. J. Meyer and Y. Zhu, *Phys. Rev. Lett.* **71**, 2915 (1993).

Fusion Yield Enhancement in Laser-Driven Magnetized Implosions

Plasma confinement and the suppression of energy transport are fundamental to achieving the high-energy-density conditions necessary for fusion applications. In the magnetic fusion energy concept,¹ this is accomplished by applying strong magnetic fields of the order of ~ 0.1 MG, such that the magnetic pressure exceeds the total plasma energy density, i.e., $\beta = 2\mu_0 p/B^2 \ll 1$, with p being the total plasma pressure. Following the formalism developed by Braginskii,² the electron heat transport is governed by the magnetization parameter $\omega_{ce}\tau_e$, where ω_{ce} is the electron gyrofrequency and τ_e is the electron collision time. Electron confinement and suppression of electron heat conduction are achieved for $\omega_{ce}\tau_e > 1$. Heat-flux suppression is also the basis of magnetized target fusion, where a preformed magnetized plasma is compressed via a cylindrical liner implosion.³

Magnetizing the hot spot in an inertial confinement fusion (ICF) implosion can reduce conductive energy transport. This increases the plasma temperature and allows for more fuel to be compressed at lower implosion velocities while still reaching ignition conditions, leading to an improved energy gain.⁴ To achieve $\omega_{ce}\tau_e \sim 1$ in the hot spot of a typical direct-drive deuterium–tritium (DT) ignition target,⁵ fields of the order of tens of megagauss are required. Confining α particles generated in the nuclear burn stage, to further reduce energy losses from the hot spot, necessitates fields as high as hundreds of megagauss.⁶ Such strong fields are challenging to generate. Magnetic-flux compression, in which an initially lower B field is embedded into a conductor and then compressed, has been shown to be a viable path to tens of megagauss via implosions driven with high explosives and pulsed-power sources.⁷

Recently, laser-driven magnetic-flux compression has been demonstrated under ICF-relevant conditions, with an amplification factor (final field divided by seed field) of $\sim 10^3$, significantly exceeding that of “conventional” compression methods.^{6,8} In an ICF target, the shell does not, by itself, trap the enclosed magnetic flux. Instead, upon laser irradiation of the target, the ablation pressure drives a shock wave through the shell, which breaks out into the gas fill inside, therefore raising the gas temperature and fully ionizing it. The gas becomes a

conductor and traps the magnetic field. Provided that the field diffusion time is longer than the compression time scale, the laser-driven capsule compresses the embedded magnetic flux. For conditions relevant to ICF implosions, the diffusion time has been estimated to be ~ 200 ns, while the implosion time is ~ 4 ns, providing an efficient trapping of the magnetic field.⁸ Through simple flux conservation arguments, and taking into account that the diffusion of flux into the plasma shell is a result of the finite hot-spot resistivity, the compressed field strength can be expressed as $B_{\max} = B_0(R_0/R)^{2(1-1/R_m)}$. Here R is the hot-spot radius, $R_m \sim 50$ is the time-averaged magnetic Reynolds number, and B_0 and R_0 are the initial seed field and gas-fill radius, respectively.⁸

In previous laser-driven flux compression experiments using the OMEGA laser,⁹ a seed magnetic field of 50 kG was trapped and compressed to more than 30 MG in a cylindrical capsule filled with D_2 gas.^{6,8} Despite the hot-spot electrons being magnetized under these conditions, no evidence of fusion performance enhancement was observed compared to nonmagnetized implosions. In cylindrical implosions, the hot-spot density increases as $\rho \propto 1/R^2$ (as opposed to $1/R^3$ in spherical implosions), which limits the achievable plasma densities. Consequently, the hot ions most likely to undergo fusion reactions have a mean free path comparable to the hot-spot radius and undergo only a few collisions before leaving the hot spot. Additionally, large shot-to-shot fluctuations caused by target parameter variations (gas pressure, alignment) precluded an accurate assessment of the B-field effects on the target performance.^{6,8}

This article presents experimental results using spherical, magnetized targets that provide a higher hot-spot density and significantly improved shot-to-shot reproducibility. The field compression scales roughly as $1/R^2$, irrespective of a spherical or cylindrical implosion. The experimental results discussed represent the first observation of an enhancement in the ICF performance as a direct result of hot-spot magnetization. Because of the open field-line configuration, the hot-spot thermal losses are suppressed by only $\sim 50\%$. Despite the modest

improvement in thermal energy confinement, the enhancements in fusion yields and ion temperatures are clearly detectable. Future experiments will explore closed field-line configurations that are expected to greatly reduce the heat losses.

Figure 126.26 shows the setup at the center of the OMEGA target chamber. To assess the impact of a magnetized hot spot on an ICF capsule performance, a spherical implosion target was positioned in the center of a single Cu coil. The coil was attached to the MIFEDS device (magnetized inertial fusion energy delivery system),¹⁰ used to drive a 45-kA current with an ~ 350 -ns half-period. It had an inner radius of 3 mm and generated a seed field perpendicular to the coil plane in the \hat{z} direction of $B_0 = 80 \pm 10$ kG across the capsule. This was timed to coincide with the OMEGA laser beams compressing the target. In contrast to previous experiments using a Helmholtz-like coil assembly, the single-coil setup provides stronger magnetic seed fields and minimizes coil interference with laser beam paths. The capsules were CH shells with an outer radius of $430 \mu\text{m}$ filled with 10 atm of D_2 gas. The CH wall thickness, an important parameter for assessing the fuel assembly's performance,¹¹ varied between 23.1 and $24.5 \mu\text{m}$. The coil was in the equatorial plane of the OMEGA target chamber, blocking 20 OMEGA laser beams from illuminating the target. The remaining 40 beams were repointed using a platform developed for polar-drive (PD) applications.¹² This ensured a target implosion with a high degree of spherical symmetry, even with a nonspherical irradiation pattern.¹³ The target was

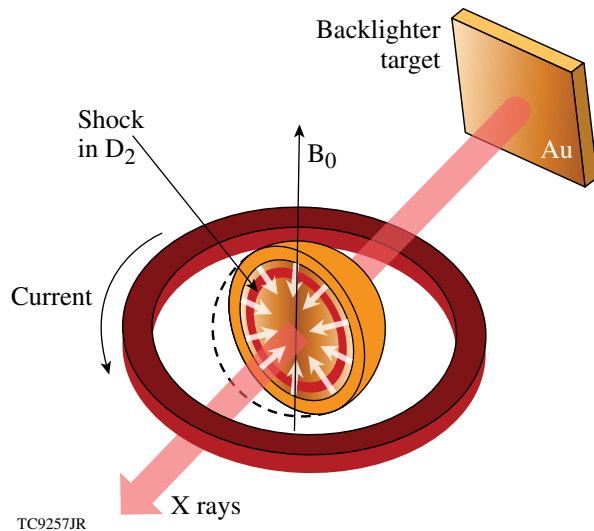


Figure 126.26

A spherical ICF target is placed inside a coil generating an 80-kG magnetic field. The target is imploded by the OMEGA laser, trapping and compressing the field inside. X-ray radiography is used to assess the implosion uniformity.

illuminated with 1-ns square laser pulses and a total on-target energy of 18 kJ with an average intensity of $\sim 7 \times 10^{14} \text{ W/cm}^2$. X-ray radiography assessed the implosion uniformity.¹⁴ The x rays were generated by illuminating a $25\text{-}\mu\text{m}$ Au foil mounted 5 mm away from the target at 52.6° off the equatorial plane (see Fig. 126.26) using four of the remaining OMEGA laser beams. The resulting x rays in the range of 2.5 to 4.5 keV were imaged onto a fast framing camera¹⁵ after passing through the imploding target. This technique has previously been applied successfully in polar-drive experiments, such as Ref. 13. To assess the target performance, the total neutron yield and the ion temperature were measured using a neutron time-of-flight (nTOF) diagnostic,¹⁶ situated 3 m from the target.

The 1-D hydrodynamic code *LILAC* was extended to solve the resistive magnetohydrodynamic (MHD) equations (*LILAC* MHD)^{17,18} to predict the compressed magnetic field and estimate its effect on the fuel assembly. Applying a 1-D simulation to the 3-D problem of a magnetic field in a spherically compressed target does not fully capture the nature of the experiment, and extending these calculations to the 3-D case will be the subject of future work. Nevertheless, it is possible to investigate characteristics of the B-field compression in a 1-D simulation by making the assumptions outlined below. The implosion can be treated as being spherically symmetric since the plasma pressure always exceeds the magnetic contribution ($\beta \gg 1$). Furthermore, the \hat{z} component of the B field was calculated at the target's equatorial plane via the induction equation and then extended over the entire target as a straight solenoidal field. The electron heat conduction is suppressed only perpendicular to the magnetic-field lines. In cylindrical geometry, this limitation was alleviated since the target length in the direction of the field significantly exceeded the target diameter, i.e., the field-normal heat loss suppression dominated the uninhibited lateral heat flow. In spherical geometry, the unmodified losses along the field lines must be included to treat the problem correctly. To do this, the total electron thermal conductivity κ_{tot} was treated as a superposition of the parallel and perpendicular contributions, κ_{\parallel} and κ_{\perp} , as $\kappa_{\text{tot}} = \kappa_{\parallel} A_{\parallel} / A_{\text{tot}} + \kappa_{\perp} A_{\perp} / A_{\text{tot}}$. A_{\parallel} and A_{\perp} are the parallel and perpendicular projections of the total hot-spot area A_{tot} . For a spherical hot spot, $A_{\parallel} / A_{\text{tot}} \approx 0.5$, such that even if all perpendicular heat losses are suppressed ($\kappa_{\perp} = 0$), the remaining total loss is reduced by 50% with respect to the unmagnetized case.

Simulation profiles for a spherical implosion using the experimental target and laser parameters and applying the approximations above are shown in Fig. 126.27. The compressed magnetic-field profile from a $B_0 = 80\text{-kG}$ seed field

(black), the ion temperature using the same seed (solid gray) and without an applied magnetic field (dashed gray) is shown. At this time, the hot-spot radius is $26 \mu\text{m}$ and the field has been amplified to $B_{\text{max}} \approx 80 \text{ MG}$, or a flux-averaged field across the hot spot of $B_{\text{avg}} = 15 \text{ MG}$. This compression is consistent with flux conservation and $R_m = 21$, with the theoretical limit in the case of no diffusion ($R_m \rightarrow \infty$) corresponding to a flux-averaged hot-spot field of $B_{\text{avg}} = 19.6 \text{ MG}$. The results in Fig. 126.27 are not at peak compression; therefore, the field is lower than the experimentally measured field in the cylindrical experiments.⁶ Based on these calculations, the expected experimental increase in ion temperature at the target center as a result of a magnetized hot spot is 8%, corresponding to a fusion yield enhancement of 13%. This calculated improvement of the target performance can be attributed solely to the magnetization of the hot spot and does not result from a change of the laser-coupling characteristics (e.g., via modification of the

heat transport at the ablation layer). This was confirmed by artificially removing any field effects in the simulation until after the laser had turned off. As expected, no discernable difference was observed compared to calculations with the B-field effects on for the full simulation interval. If the parallel heat losses are suppressed, e.g., by closing the magnetic-field lines, the simulations predict an increase of 42% in the ion temperature and a 73% neutron-yield enhancement. In this case, the target performance is primarily limited by radiative energy losses.

An experimental x-ray backlighter measurement is displayed in Fig. 126.28, showing an imploded target with and without an applied seed field and plotted using the same scale and color map. The MIFEDS coil was present around the target in both cases. The data were taken at $\sim 2 \text{ ns}$, a few 100 ps before peak compression. The bright area in the center is the location of the hot spot; the surrounding dark region results from x rays being absorbed in the dense shell and the coronal plasma. The center appears brighter than the background since the self-emission from the compressed core starts to become brighter than the backlighter emission at this time. The implosion is very uniform, despite using only 40 beams. This confirms the successful application of the PD platform to the magnetic-field compression experiments. No discernable difference is observed between the field and no-field cases, confirming that the magnetic field has no impact on implosion uniformity.

As shown in Ref. 11, the yield of an ICF implosion target decreases with increasing wall thickness. Figure 126.29 shows the measured neutron yield and ion temperatures from shots with an applied seed field of 80 kG (black dots) and without magnetic fields (blue squares) as a function of the target wall thickness. The magnetized target performance is visibly enhanced. To separate the effect of the magnetic field and the wall thickness on the neutron yield Y_n and the ion temperature

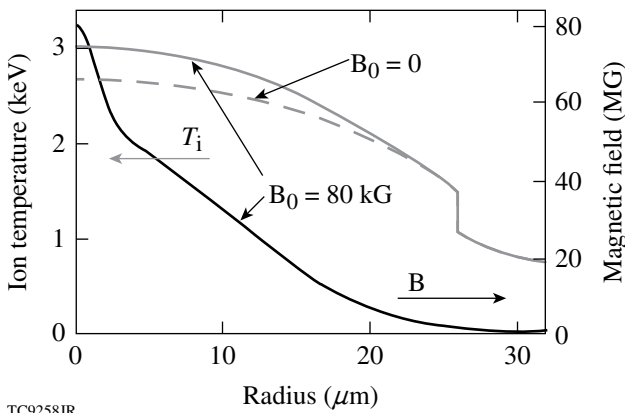


Figure 126.27
Compressed magnetic field (solid black) and ion temperature (solid gray) inside a spherical, magnetized hot spot simulated using *LILAC* MHD. The ion temperature is enhanced compared to the $B_0 = 0$ case (dashed gray).

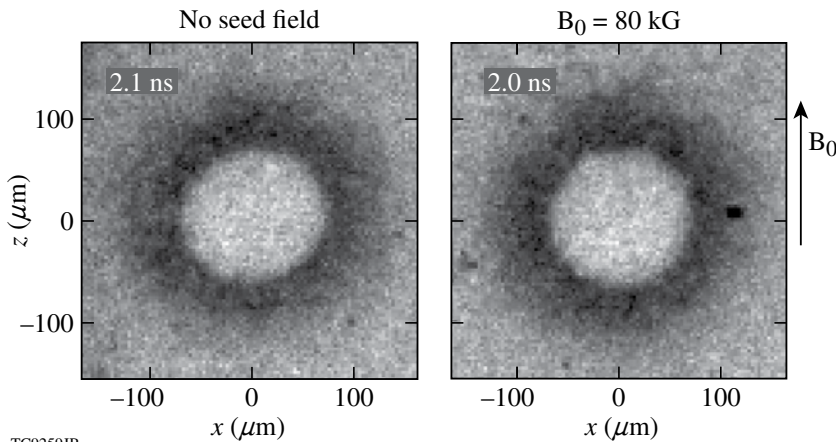
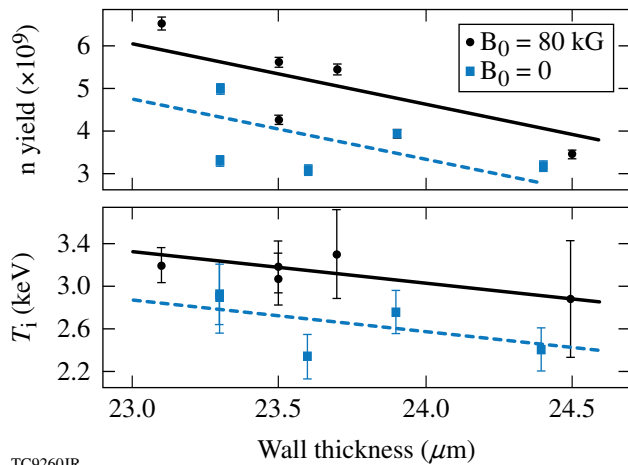


Figure 126.28
X-ray backlighter data show no impact by the magnetic seed field on the implosion uniformity.

T_i , a multiple linear regression method expressing these quantities as $Y_n = Y_{n0} + A_B B_0 + A_\Delta \Delta$ and $T_i = T_{i0} + C_B B_0 + C_\Delta \Delta$ is used. B_0 is the seed field (0 or 80 kG) and Δ denotes the shell thickness. A least squares fit to the data yields the fitting parameters listed in Table 126.V, giving the yield in units of 10^9 and the temperature in keV. The goodness of the fit is assessed through an F test that equates to a degree of confidence in the model of better than 94%. The result of the linear regression method is plotted as the lines in Fig. 126.29, showing a clear enhancement of both the neutron yield and the ion temperature. For shots where the magnetic seed field was applied, the yield was enhanced by 30% and the ion temperature by 15%. The overall scatter of data points for measurements with a magnetic field appears to be reduced compared to the no-field measurements. The data shown in Fig. 126.29 represent the first measurement of a fusion performance enhancement, resulting from embedding a strong magnetic field into an ICF capsule.

In previous experiments the compressed magnetic field was determined via proton deflectometry.^{6,8} The single coil

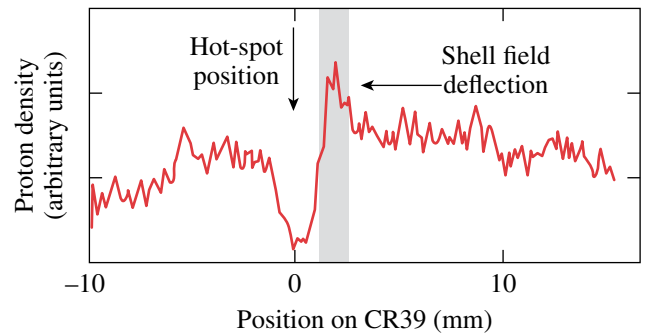


TC9260JR
 Figure 126.29
 Experimental neutron yield and ion temperature plotted against target wall thickness. A clear enhancement of the magnetized implosions (black dots) compared to the $B_0 = 0$ case (blue squares) is observed. The lines are fits to the data using the parameters listed in Table 126.V.

Table 126.V: Multiple linear regression coefficients for the fits to the experimental data in Fig. 126.29.

	Y_{n0}	$A_B (10^{-5}/G)$	$A_\Delta (1/\mu m)$
	T_{i0}	$C_B (10^{-6}/G)$	$C_\Delta (1/\mu m)$
$Y_n (\times 10^9)$	37.6	1.7 ± 0.6	-1.4 ± 0.6
T_i (keV)	8.57	4.8 ± 1.3	-0.25 ± 0.11

used here blocked the line of sight through the target perpendicular to the field, preventing the use of a proton probe. To confirm the flux amplification in spherical implosions, the single coil was exchanged with a Helmholtz coil, as used in Ref. 6, while a glass sphere filled with D^3He gas and imploded using 12 OMEGA beams was used as an ~ 15.2 -MeV proton source. The protons traversing the target were deflected by the magnetic field and recorded on a CR39 track detector with the deflection pattern giving information about field topology and magnitude. This has been shown to result in a characteristic two-peak structure.^{6,8} Protons traversing the compressed hot-spot field (~ 30 MG) provided a strongly deflected peak, while protons propagating through the target wall experienced a lower field (~ 1 MG) and were weakly deflected but produced a higher-amplitude peak. Given the hot-spot size, the number of protons interacting with a spherical hot spot was lower than in the cylindrical case, thus decreasing the signal-to-noise ratio. Indeed, so far it has been impossible to obtain an unambiguous spherical hot-spot field measurement by observing a strongly deflected peak. Figure 126.30 shows a proton density lineout across a CR39 detector for ~ 14.8 -MeV protons that have slowed down in the dense shell. A strong peak is visible to the right of the hot spot (positioned at zero) caused by deflection in the target shell. While this does not provide the hot-spot field amplitude as discussed above, it is a signature of the magnetic field being trapped and amplified in the target and confirms the presence of a strong magnetic field inside the capsule.



TC9261JR
 Figure 126.30
 The cross-core proton deflectometry lineout exhibits a one-sided peak from protons traversing the magnetized target shell—a signature of a compressed B field inside the capsule.

In summary, a seed magnetic field of about 80-kG strength was embedded into spherical ICF targets imploded by the OMEGA laser in a PD beam-pointing geometry. As a result of the high implosion velocities and ionization of the target gas fill, the magnetic field inside the capsule was trapped and amplified through magnetic-flux compression, with simula-

tions indicating a flux-averaged hot-spot field of 15 MG at peak neutron yield. The implosion was confirmed to be spherically uniform by using x-ray radiography, showing no discernable difference in core symmetry with or without an applied seed field. At the strong magnetic fields reached in these experiments, the hot spot inside a spherical target becomes strongly magnetized, suppressing the heat losses by about 50% through electron confinement. As a result, the experimentally measured ion temperature and fusion yield were improved by 15% and 30%, respectively. This is in qualitative agreement with results from 1-D *LILAC*-MHD calculations, giving 8% and 13%, respectively. The difference can be attributed to the limited applicability of a 1-D code to the inherently 3-D problem of the magnetic field in a spherically compressed target. Extending these calculations to three dimensions will be the subject of future work. The data discussed here represent the first experimental verification of ICF target performance being enhanced by magnetizing the hot spot.

ACKNOWLEDGMENT

This work was supported by the U.S. Department of Energy Office of Inertial Confinement Fusion under Cooperative Agreement Nos. DE-FC02-04ER54789 and DE-FC52-08NA28302, the University of Rochester, and the New York State Energy Research and Development Authority. The support of DOE does not constitute an endorsement by DOE of the views expressed in this article.

REFERENCES

1. J. A. Wesson, *Tokamaks*, 3rd ed. (Clarendon Press, Oxford, 2004).
2. S. I. Braginskii, in *Reviews of Plasma Physics*, edited by Acad. M. A. Leontovich (Consultants Bureau, New York, 1965).
3. R. C. Kirkpatrick, I. R. Lindemuth, and M. S. Ward, *Fusion Technol.* **27**, 201 (1995).
4. R. Betti and C. Zhou, *Phys. Plasmas* **12**, 110702 (2005).
5. P. W. McKenty, V. N. Goncharov, R. P. J. Town, S. Skupsky, R. Betti, and R. L. McCrory, *Phys. Plasmas* **8**, 2315 (2001).
6. O. V. Gotchev, P. Y. Chang, J. P. Knauer, D. D. Meyerhofer, O. Polomarov, J. Frenje, C. K. Li, M. J.-E. Manuel, R. D. Petrasso, J. R. Rygg, F. H. Séguin, and R. Betti, *Phys. Rev. Lett.* **103**, 215004 (2009).
7. A. D. Sakharov, *Sov. Phys. Usp.* **9**, 294 (1966); F. S. Felber *et al.*, *Phys. Fluids* **31**, 2053 (1988).
8. J. P. Knauer, O. V. Gotchev, P. Y. Chang, D. D. Meyerhofer, O. Polomarov, R. Betti, J. A. Frenje, C. K. Li, M. J.-E. Manuel, R. D. Petrasso, J. R. Rygg, and F. H. Séguin, *Phys. Plasmas* **17**, 056318 (2010).
9. T. R. Boehly, D. L. Brown, R. S. Craxton, R. L. Keck, J. P. Knauer, J. H. Kelly, T. J. Kessler, S. A. Kumpan, S. J. Loucks, S. A. Letzring, F. J. Marshall, R. L. McCrory, S. F. B. Morse, W. Seka, J. M. Soures, and C. P. Verdon, *Opt. Commun.* **133**, 495 (1997).
10. O. V. Gotchev, J. P. Knauer, P. Y. Chang, N. W. Jang, M. J. Shoup III, D. D. Meyerhofer, and R. Betti, *Rev. Sci. Instrum.* **80**, 043504 (2009).
11. F. J. Marshall, J. A. Delettrez, V. Yu. Glebov, R. P. J. Town, B. Yaakobi, R. L. Kremens, and M. Cable, *Phys. Plasmas* **7**, 1006 (2000).
12. F. J. Marshall, R. S. Craxton, M. J. Bonino, R. Epstein, V. Yu. Glebov, D. Jacobs-Perkins, J. P. Knauer, J. A. Marozas, P. W. McKenty, S. G. Noyes, P. B. Radha, W. Seka, S. Skupsky, and V. A. Smalyuk, *J. Phys. IV France* **133**, 153 (2006).
13. F. J. Marshall, P. W. McKenty, J. A. Delettrez, R. Epstein, J. P. Knauer, V. A. Smalyuk, J. A. Frenje, C. K. Li, R. D. Petrasso, F. H. Séguin, and R. C. Mancini, *Phys. Rev. Lett.* **102**, 185004 (2009).
14. O. L. Landen *et al.*, *Rev. Sci. Instrum.* **72**, 627 (2001).
15. D. K. Bradley *et al.*, *Rev. Sci. Instrum.* **66**, 716 (1995).
16. R. A. Lerche, D. W. Phillion, and G. L. Tietbohl, *Rev. Sci. Instrum.* **66**, 933 (1995).
17. J. Delettrez, R. Epstein, M. C. Richardson, P. A. Jaanimagi, and B. L. Henke, *Phys. Rev. A* **36**, 3926 (1987).
18. N. W. Jang, R. Betti, J. P. Knauer, O. Gotchev, and D. D. Meyerhofer, *Bull. Am. Phys. Soc.* **51**, 144 (2006).

Amplifying Nanosecond Optical Pulses at 1053 nm with an All-Fiber Regenerative Amplifier

Fiber optical amplifiers based on rare-earth-doped fibers have been investigated because of their advantages, including inherent compactness and stability, broadband gain, and good beam quality. The energy gain of conventional fiber amplifiers for low-duty-cycle pulse sources is limited by their single-pass design since broadband amplified spontaneous emission (ASE) competes for the gain and degrades the signal-to-noise ratio (SNR). This limitation can be overcome by implementing regenerative amplification in an all-fiber system. With a gain fiber in a fiber cavity, optical pulses circulate inside the cavity and gain energy in many round-trips. All-fiber regenerative amplifiers (AFRA's) greatly improve the energy gain and SNR, while preserving the advantages of an all-fiber architecture. A ring-cavity, Q -switched fiber regenerative amplifier based on Er-doped fiber demonstrated a gain of more than 40 dB for 10-ns, 3-pJ pulses at 1530 nm (Ref. 1). Another Yb-doped fiber regenerative amplifier operating at 1030 nm amplified 40-ps, 9-pJ pulses to 55 nJ (Ref. 2).

An important potential AFRA application is to produce chirped optical pulses to seed chirped-pulse-amplification (CPA) systems. An approximately quadratic temporal-phase profile (a linear frequency chirp) is required for CPA seed pulses to be amplified and then compressed by grating-pulse compressors.³ The conventional approach to producing such seed pulses uses a mode-locked laser and a grating-pulse stretcher. This combination can be replaced by an AFRA with an electro-optic phase modulator (EOM) integrated inside the ring cavity.⁴ The required temporal phase can be imposed onto the optical pulse during many round-trips inside the cavity. Compared with the conventional approach, such an all-fiber CPA seed source can provide precise and flexible control over the phase profile, higher seed pulse energy to increase the SNR and temporal contrast of the CPA output, single-mode and alignment-free operation, and increased cost effectiveness.

This article reports on an AFRA based on Yb-doped fiber to amplify nanosecond, 1053-nm optical pulses with a repetition rate of 10.5 kHz. The pulses are amplified from 15 pJ to 240 nJ in five passes through the gain fiber. To the best of our

knowledge, this is the highest AFRA output-pulse energy ever reported. The wavelength of the AFRA is required by existing high-energy CPA systems based on Nd-phosphate laser glass.⁵ This wavelength is 23 nm off the gain peak of a Yb-doped fiber at 1030 nm, so ASE suppression techniques to favor the signal gain have been employed.⁶ Cavity build-up dynamics evident from leakage-pulse measurements and numerical modeling shows that the AFRA is not saturated in five round-trips and higher pulse energy can be extracted in more round-trips.⁷ This is limited, however, by the onset of bifurcation instability previously identified for solid-state regenerative amplifiers operating at high repetition rates.⁸ This limitation can be lifted by reducing the repetition rate from 10.5 kHz to below 0.5 kHz. Numerical simulations show that operating the AFRA at saturation not only increases the output level but also improves the output stability.

The experimental AFRA setup is shown in Fig. 126.31. The amplifier is seeded by 10-ns square pulses at 1053 nm. A fiber ring cavity is built with a section of polarization-maintaining (PM) Yb-doped fiber (3.5-m, 6- μ m core, 30 \pm 10 dB/m absorption at 980 nm) as the gain medium. The gain fiber is counter-pumped by a 500-mW continuous-wave diode laser at 976 nm (JDSU 29-7552-500) through a 976/1053-nm wavelength division multiplexer (WDM1). An additional 976/1053-nm WDM (WDM2) protects the pump diode against amplified optical signals at 1053 nm from the cavity. It provides 20-dB isolation over 1053 nm at the 976-nm port. A 2 \times 2 acousto-optic modulator (AOM) switch is used to switch the pulse in and out of the ring and to Q -switch the cavity. The two transmission states of the AOM switch, shown in the inset of Fig. 126.31, alternate the cavity between low- Q and high- Q phases. In the low- Q phase, lasing is suppressed and the gain fiber accumulates stored energy from pumping. The fiber cavity is essentially a single-pass system in this state. The cavity is switched to the high- Q phase after a seed pulse is injected, which gains energy in multiple passes through the gain fiber before being switched out at the end of this phase. A delay generator synchronized to the seed pulses controls the duration of the "on" state of the AOM and therefore the number of round-trips in the cavity. To

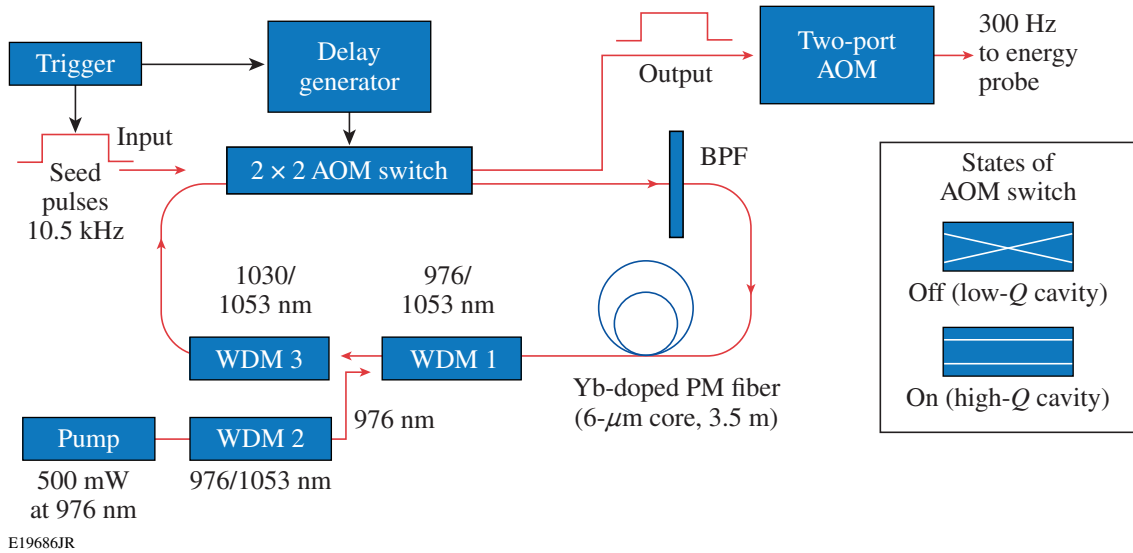


Figure 126.31 Experimental setup for the all-fiber regenerative amplifier (AFRA). In addition to the Yb-doped fiber as the gain medium, a 10-nm bandpass filter and a 1030/1053-nm WDM are built into the fiber cavity to suppress ASE and favor the signal gain. Optical pulses are switched in and out of the cavity by a 2 × 2 AOM switch. The two states of the switch are shown on the right.

favor the signal gain, a 1030/1053-nm WDM (WDM3) suppresses the 1030-nm gain peak, and a 10-nm bandpass filter (BPF) centered at 1055 nm further suppresses ASE at 1042 to 1046 nm. The output-pulse train’s repetition rate is reduced to 300 Hz by a two-port AOM to enable one to directly measure the output-pulse energy with an energy probe limited to a maximum 2-kHz rate.

The effects of the ASE suppression techniques are shown in Fig. 126.32. The solid curve shows the spectrum of a 10-nJ

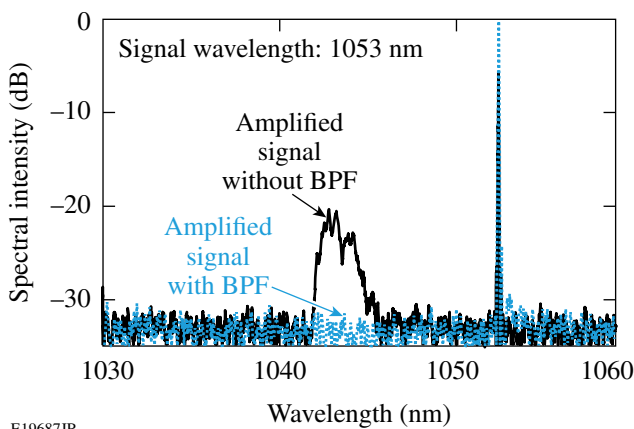
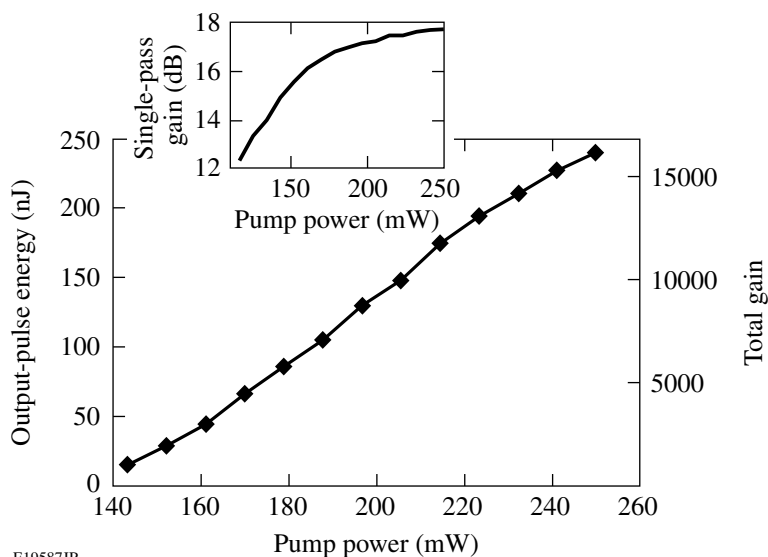


Figure 126.32 Spectra of 10-nJ output-pulse train from the fiber ring cavity without a BPF (dotted) and with a BPF (solid). The 1030-nm gain peak is suppressed by WDM3, and ASE at 1042 to 1046 nm is suppressed by the BPF.

output-pulse train without the bandpass filter in the cavity. WDM3 effectively suppresses ASE around 1030 nm, but ASE at 1042 to 1046 nm still develops. As the dotted curve shows, this ASE is completely suppressed by the bandpass filter. The bandpass filter also blocks any leakage pump beam from going back into the seed laser.

The 15-pJ seed pulses are amplified to 240 nJ in five round-trips in the cavity. Figure 126.33 shows the output-pulse energy and the total gain from five round-trips as the pump power is increased from 145 mW to 250 mW. The single-pass, small-signal gain of the Yb-doped fiber at pump levels up to 250 mW is plotted in the inset. Increasing the pump power beyond 250 mW does not increase the gain as the population inversion reaches maximum and additional pump is not absorbed, limiting the single-pass gain to about 18 dB and the total gain in five round-trips to 42 dB. At the highest output level, the pulse energy has a short-term (200 samples) fluctuation of 1.5% (rms) and a long-term drift of 6% (peak to valley).

Input and output pulses are measured using a 12-GHz photodiode (Discovery DSC50S) and single-shot oscilloscope (Tektronix DPO70604) to investigate the effect of the regenerative amplifier on the pulse shape. Normalized input and output waveforms are plotted in Fig. 126.34. The data are smoothed numerically to reduce instrumental noise. Compared to the input square pulse (solid), the output pulse (dashed) has a trailing edge 15% lower than the leading edge. This square-pulse



E19587JR

Figure 126.33

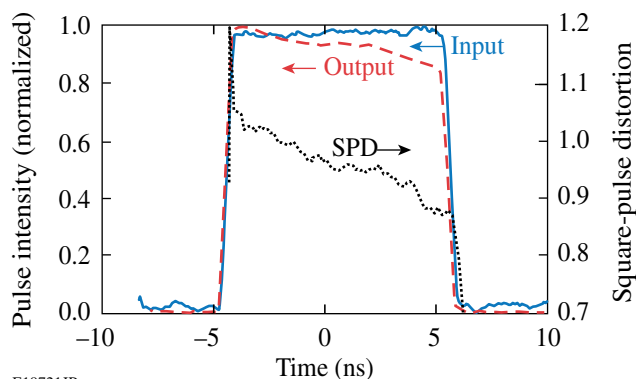
Measured pulse energy and total gain as pump power is increased. The pulse circulates in the ring cavity for five round-trips. Inset is the single-pass gain.

distortion (SPD), the ratio between the instantaneous intensities of the output pulse over the input pulse, originates from gain saturation of the regenerative amplifier and is also plotted (dotted) in Fig. 126.34.

Ideally for a regenerative amplifier, the pulse would circulate inside the cavity to accumulate energy until the stored energy is depleted and the gain is overcome by cavity loss (saturation). Maximum output-pulse energy is obtained when the pulse is ejected from the cavity at saturation. At the highest stable output level of the AFRA, the pulse energy increases exponentially (9 dB/RT) before cavity dump, which indicates that the amplifier does not saturate in five round-trips. This is further proved by numerical modeling.⁷ The laser pulse

amplification and population inversion in the gain medium are governed by rate equations that can be integrated to yield recurrence relations. The pulse fluence (proportional to pulse energy) and single-pass gain in the regenerative amplifier can be calculated for each pass using these recurrence relations. The solid curve in Fig. 126.35(a) shows the growth in pulse energy and the dashed curve shows the gain for each pass, calculated with this model. The gain is hardly depleted in five round-trips, and the AFRA has the potential to produce much higher pulse energy in more round-trips.

Producing higher pulse energy in the AFRA by increasing the number of round-trips is limited by the onset of period-doubling instability, where the output-pulse energy switches between different values.⁸ When the stored energy in the gain medium fully recovers through pumping between successive seed pulses, each pulse experiences the same gain and the output-pulse energy is stable. This may not be the case when the repetition rate of the regenerative amplifier is high enough that the time separation between seed pulses (cycle period) is comparable with or shorter than the upper-state lifetime of the gain medium. As the number of round-trips is increased and more energy is extracted in the high- Q phase, the population inversion will not have an opportunity to fully recover in the following low- Q phase because of its short duration. This reduces the gain for the next pulse and results in a lower pulse energy, which, in turn, leaves a larger amount of stored energy in the gain fiber to produce higher output in the cycle after the next. With the AFRA operating at 10.5 kHz, the cycle period ($\sim 95 \mu\text{s}$) is much shorter than the Yb upper-state lifetime ($\sim 840 \mu\text{s}$) and period-doubling instability is observed.



E19721JR

Figure 126.34

Input-pulse (solid) and output-pulse (dashed) shape and SPD (dotted) of the fiber amplifier. The output pulse has a 15%-lower trailing edge because of gain saturation.

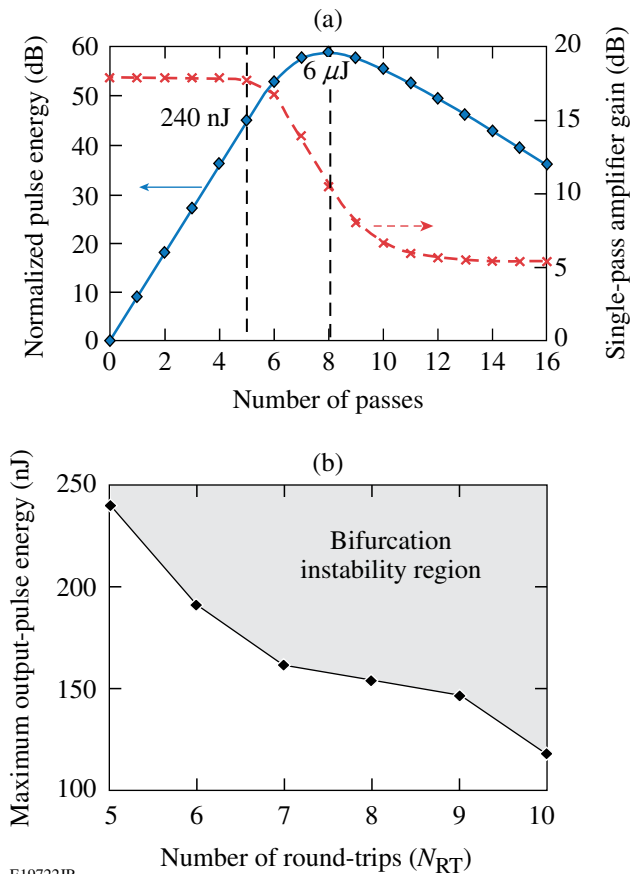


Figure 126.35

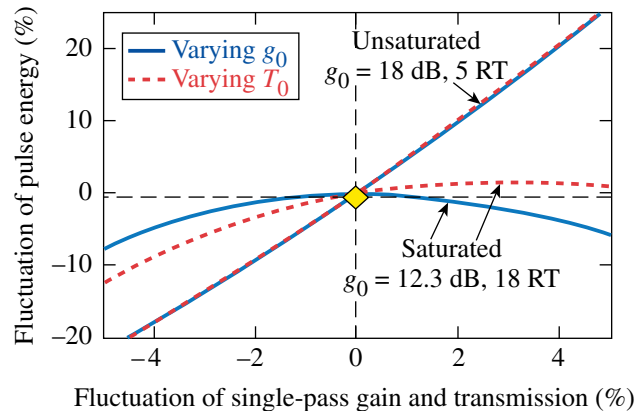
(a) Numerical simulation shows that the AFRA is not saturated after five round-trips and much higher pulse energy can be extracted from the amplifier in more round-trips. (b) The maximum stable output-pulse energy decreases when the number of round-trips is increased.

To avoid this, the pump level to the AFRA must be decreased as the number of round-trips increases. The maximum stable output-pulse energy decreases with more round-trips as shown in Fig. 126.35(b).

At repetition rates lower than 0.5 kHz, the cycle period will be long enough for the stored energy to fully recover.⁸ The pulse would circulate in the cavity for more round-trips and gain higher energy without causing period-doubling instability. Scaling the AFRA to higher pulse energies requires investigating detrimental nonlinear effects such as stimulated Brillouin scattering (SBS) and stimulated Raman scattering (SRS). For a 10-ns pulse, the estimated threshold pulse energy is 1.5 μ J for SBS⁹ and 5 μ J for SRS.¹⁰ With the single-pass gain reduced to

12.3 dB, the numerical model described above shows that the amplifier can produce 1.5- μ J pulse energy in 17 round-trips at saturation.

Operating the AFRA at saturation will not only increase the output level but also improve the output stability. As mentioned above, the AFRA output-pulse energy fluctuates because of variations in amplifier parameters like the single-pass small-signal gain (g_0) and loop transmission (T_0). The sensitivity of the output-pulse energy with respect to these parameters is determined by varying them in the numerical model described above. Figure 126.36 compares the output sensitivities of two operating points: five round-trips with a single-pass gain of 18 dB (unsaturated) and 18 round-trips with a single-pass gain of 12.3 dB (saturated). For the unsaturated case, the output fluctuation is 5 \times any variation of g_0 and T_0 . The output sensitivity is greatly reduced for the saturated case. Operating the amplifier for one round-trip after maximum pulse energy (reached in 17 round-trips) yields the best stability, with only 2% of energy penalty.



E19723JR

Figure 126.36

Variation of the amplifier output-pulse energy as small-signal gain (solid) and loop transmission (dashed) are varied. Comparing the output sensitivities of the saturated and unsaturated AFRA, it is found that operating the amplifier at saturation will greatly improve the output stability.

In conclusion, an all-fiber regenerative amplifier with Yb-doped fiber as the gain medium has been built. Nanosecond optical pulses at 1053 nm (23 nm off the gain peak of Yb-doped fiber) were amplified to as much as 240 nJ by the amplifier, achieving a total gain of 42 dB. The AFRA output level is limited by the onset of bifurcation instability previously iden-

tified for solid-state regenerative amplifiers operating at high repetition rates. Higher pulse energy may be expected from the AFRA at repetition rates lower than 0.5 kHz, limited by SBS. Sensitivity of the output-pulse energy with respect to amplifier parameters has been tested with numerical simulation, which suggests that operating the amplifier at saturation will greatly improve the output stability. The hundreds-of-nJ output-pulse energy makes the AFRA an attractive candidate as a CPA seed source (once a phase modulator is integrated into the cavity), compared to hundreds-of-pJ seed pulses commonly used in existing high-energy CPA systems.⁵

ACKNOWLEDGMENT

The authors are grateful for numerous conversations with and helpful support from J. R. Marciante, A. V. Okishev, and W. Bittle.

This work was supported by the U.S. Department of Energy Office of Inertial Confinement Fusion under Cooperative Agreement No. DE-FC52-08NA28302, the University of Rochester, and the New York State Energy Research and Development Authority. The support of DOE does not constitute an endorsement by DOE of the views expressed in this article.

REFERENCES

1. A. Yang, *Jpn. J. Appl. Phys.* **45**, L673 (2006).
2. S. Kanzelmeyer *et al.*, presented at Advanced Solid-State Photonics (ASSP), San Diego, CA, 31 January–3 February 2010 (Paper AWB15).
3. D. Strickland and G. Mourou, *Opt. Commun.* **56**, 219 (1985).
4. R. Xin and J. D. Zuegel, presented at Advanced Solid-State Photonics (ASSP), San Diego, CA, 31 January–3 February 2010 (Paper AMD3).
5. J. D. Zuegel, S. Borneis, C. Barty, B. LeGarrec, C. Danson, N. Miyanaga, P. K. Rambo, C. LeBlanc, T. J. Kessler, A. W. Schmid, L. J. Waxer, J. H. Kelly, B. Kruschwitz, R. Jungquist, E. Moses, J. Britten, I. Jovanovic, J. Dawson, and N. Blanchot, *Fusion Sci. Technol.* **49**, 453 (2006).
6. J. R. Marciante and J. D. Zuegel, *Appl. Opt.* **45**, 6798 (2006).
7. W. H. Lowdermilk and J. E. Murray, *J. Appl. Phys.* **51**, 2436 (1980).
8. J. Döring *et al.*, *Opt. Express* **12**, 1759 (2004).
9. H. Li and K. Ogusu, *Jpn. J. Appl. Phys.* **38**, 6309 (1999).
10. R. G. Smith, *Appl. Opt.* **11**, 2489 (1972).

Analysis and Suppression of Parasitic Processes in Noncollinear Optical Parametric Amplifiers

Introduction

Optical parametric amplifiers (OPA's) are widely used as sources of broadly tunable femtosecond pulses. Critically phase matched borate crystals, such as beta-barium borate (BBO), lithium borate (LBO), and bismuth borate (BiBO) have been employed to generate tunable ultrashort pulses from the visible to the near-infrared wavelength range.^{1–3} In particular, a noncollinear OPA (NOPA) allows for ultra-broad gain bandwidth that supports few-cycle pulse durations.^{4,5} Signal gain of 10^3 to 10^6 can be achieved within millimeter-long crystals as a result of perfect phase matching and large nonlinear coefficients. The lack of energy storage and low residual absorption in the crystals makes it possible to scale OPA's to several watts of average output power at pulse energies ranging from the sub- μJ level to $>100 \mu\text{J}$ (Refs. 6–8). Large-aperture crystals of deuterated potassium dihydrogen phosphate (DKDP) create the potential for ultra-intense optical parametric chirped-pulse-amplification (OPCPA) systems ($>10^{23} \text{ W/cm}^2$) using kilojoule Nd:glass lasers as pump sources.^{9,10}

Parasitic nonlinear processes can significantly degrade the performance of OPA's.^{2,11} For example, frequency doubling of one or more of the interacting waves can lead to spectral deformation and reduced efficiency. This article presents a detailed study of parasitic second-harmonic generation of signal and idler waves. The analysis focuses on critically phase matched NOPA's, but similar issues can occur in quasi-phase-matched materials.¹² Experimental observations are presented for two BBO-based NOPA systems. The first system is a MHz-rate NOPA that is seeded by white-light continuum generated in sapphire—a common choice for ultrafast time-dependent spectroscopy.¹³ The second system has been optimized for amplification of an ultra-broadband width ranging from 650 to 1050 nm to support few-cycle pulse durations. The experimental observations agree well with the results of a 2-D numerical model that was used to evaluate the influence of parasitic processes on the NOPA's overall efficiency.

To avoid unwanted parasitic processes, different crystals and noncollinear phase-matching configurations can be used. For

this purpose, calculations of the phase-matching properties for broadband BBO, LBO, BiBO, and DKDP NOPA's are presented. These results allow one to identify configurations that are free from phase-matched parasitic second-harmonic-generation (SHG) processes over the desired signal-wavelength range.

Noncollinear Phase-Matching Geometry

NOPA's achieve broadband gain by having a noncollinear angle α between the pump and signal to match the group velocity of the signal and idler.^{3,14} Figure 126.37 shows a common configuration for BBO, a crystal widely used for visible-wavelength NOPA's. The pump is extraordinary polarized (*e* wave) and its Poynting vector (S_p) and wave vector (k_p) are separated by an angle ρ . In BBO, the optimum α for the broadest gain is comparable to ρ . For example, $\rho = 3.3^\circ$ and $\alpha = 2.6^\circ$ when the wavelengths of the pump and signal are chosen to $\lambda_p = 523 \text{ nm}$ and $\lambda_s = 800 \text{ nm}$, respectively. Pump-signal birefringent walk-off is partially compensated by positioning the signal on the side to which the pump walks off, away from the crystal axis [see Fig. 126.37(b)]. In this case, the angle between the pump and signal Poynting vectors is $\rho - \alpha = 0.7^\circ$. The idler is angularly dispersed ($5 \times 10^{-3} \text{ deg/nm}$) and has an average angle relative to the signal of $\sim 7.4^\circ$.

Since the signal and idler are ordinary polarized (*o* waves), identical phase-matching conditions exist for any orientation of the signal *wave vector* around the pump wave vector, provided α is kept constant. This is shown in Fig. 126.37(a) as a circle around the pump wave vector. The largest pump-signal walk-off occurs when the angle between their Poynting vectors is $\rho + \alpha = 5.9^\circ$ [see Fig. 126.37(c)]. The two extremes are referred to as walk-off compensating (WC) and non-walk-off compensating (NWC), respectively.

Figure 126.38 shows the signal angles θ_s at which signal wavelengths are phase matched for a BBO NOPA pumped at 523 nm. Curves for several noncollinear angles α are shown (in red) for both the (a) WC and (b) NWC configurations. The NOPA phase matching has, to first order, the broadest bandwidth when the curves are horizontal,^{3,15} that is, a choice of

internal signal angle achieves perfect phase matching for the broadest range of signal wavelengths. Also shown (in blue) are the phase-matching curves for signal SHG. For the WC case, certain combinations of θ_S and α simultaneously phase match both the NOPA and signal SHG processes; therefore, parasitic SHG can occur.

Figure 126.39 shows a calculation of the phase-matching conditions for idler SHG. The internal angle of the idler wave to the crystal axis, θ_I , was calculated to compensate the pump

wave's vector component k_P , perpendicular to the signal wave vector k_S . Two values of α for both the WC and NWC configurations are shown (red curves). The phase-matching curves for idler SHG are shown in blue. In the WC configuration, phase matching is achieved at an idler wavelength of 1265 nm, and the angular deviations between the idler and the SHG phase-matching curve are small, in the wavelength range between 1100 nm and 1500 nm. In contrast, the NWC configuration avoids idler SHG since the phase-matched idler wavelengths (865 nm and 900 nm) are typically not present.

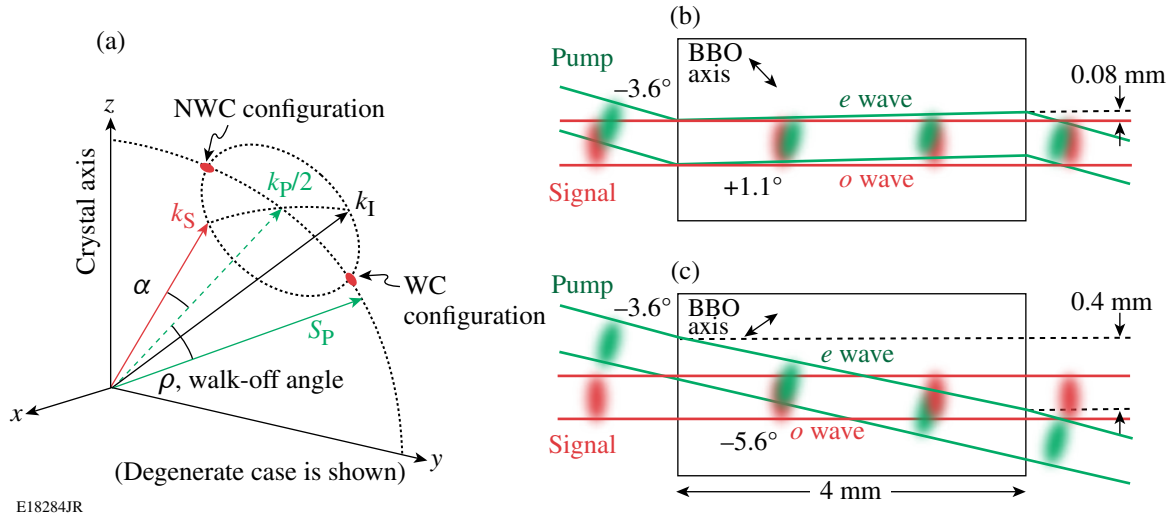


Figure 126.37 (a) Geometry for critical phase matching in a uniaxial crystal. The noncollinear angle between the pump and signal wave vectors is α . The walk-off angle between the pump Poynting vector (S_P) and signal wave vector is ρ . (b) Definition of the walk-off compensating (WC) configuration for negative uniaxial crystals. (c) Non-walk-off compensating (NWC) configuration. The idler wave vectors are angularly dispersed (not shown) and angles are exaggerated for clarity.

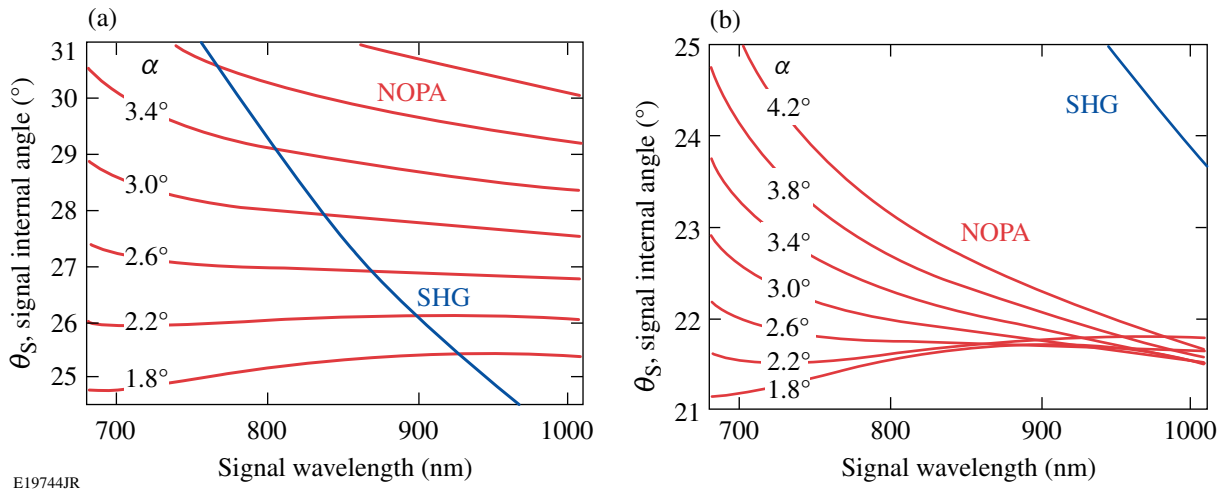
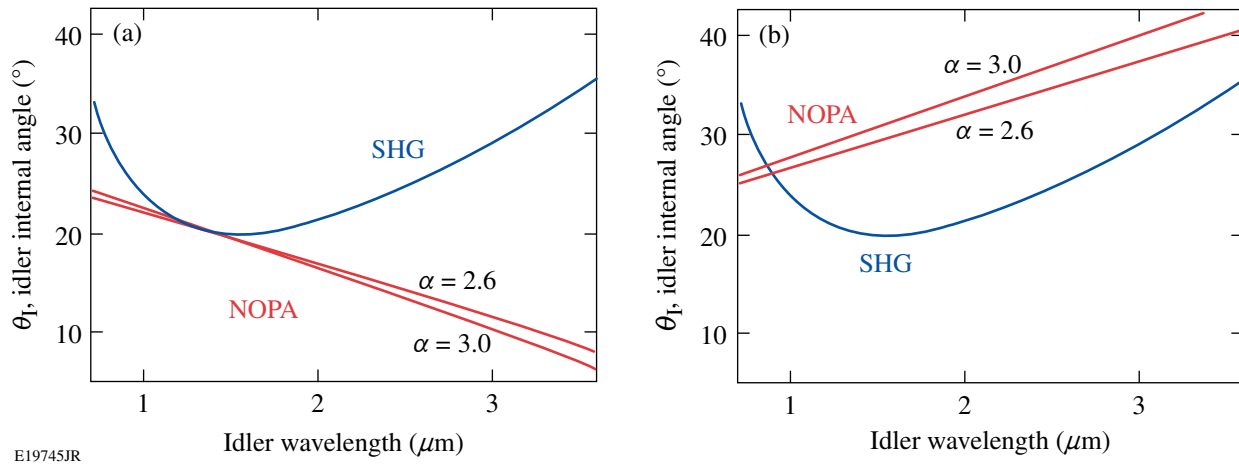


Figure 126.38 NOPA phase-matching curves (red) for BBO pumped at 523 nm for several noncollinear angles α : (a) the walk-off compensating (WC) and (b) the non-walk-off compensating (NWC) configurations. The phase-matching curves for signal SHG are shown in blue.



E19745JR

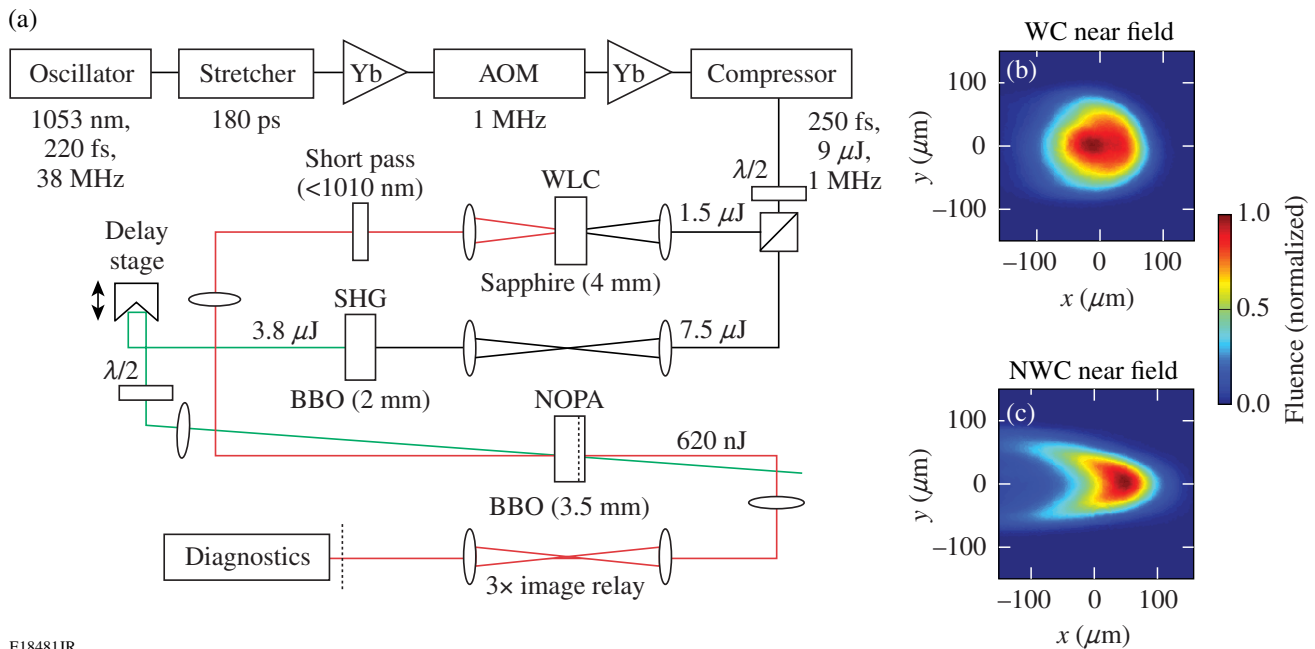
Figure 126.39

The idler wavelengths and internal angles for NOPA phase matching in BBO pumped at 523 nm for two values of α (in red): (a) the WC and (b) the NWC configurations. The phase-matching curves for idler SHG are shown in blue.

Experimental Observation of Parasitic Signal SHG

Parasitic processes were experimentally investigated using a BBO-based NOPA pumped at 1 MHz by a fiber chirped-pulse-amplifier (FCPA) system. A schematic of the system is shown in Fig. 126.40. Pulses from a mode-locked oscillator were stretched from 220 fs to 180 ps, down-selected from

38 MHz to 1 MHz, and amplified by a chain of four ytterbium-doped fiber amplifiers. A large-mode-area photonic-crystal fiber amplifier was used for the final stage, producing 12- μ J pulses centered at 1047 nm (Ref. 16). The compressor used two multilayer dielectric gratings (1740 lines/mm) to produce 9- μ J, 250-fs pulses. A portion of the energy (20%) was picked off and



E18481JR

Figure 126.40

(a) Experimental setup. Yb: ytterbium-doped fiber amplifiers; AOM: acousto-optic modulator; WLC: white-light continuum; SHG: second-harmonic generation; NOPA: noncollinear optical parametric amplifier. Near-field profiles of the amplified beams for (b) walk-off compensating (WC) and (c) non-walk-off compensating (NWC) configurations.

weakly focused into a static 4-mm sapphire plate to generate a chirped white-light continuum (WLC) seed.¹⁷ The rest was doubled in a 2-mm BBO crystal, producing 3.8- μ J pulses at 523 nm for pumping the NOPA.

The BBO crystal used in the NOPA was 4 mm long and was cut at an angle such that the seed beam was approximately perpendicular to the crystal face (27.1° and 21.6° for the WC and NWC geometries, respectively). The pump and seed were focused into the NOPA crystal with ~ 120 - μ m beam waists. The pump–signal walk-off lengths, defined as the distance required for a change in separation equal to their beam waists, were 8.2 mm for WC and 0.96 mm for NWC. The impact of pump–signal walk-off is clearly seen in the near-field beam profiles [Figs. 126.40(a) and 126.40(b)]. In the WC case, the near field is approximately Gaussian. In contrast, in the NWC case, there is a large asymmetry along the direction of walk-off (x - z plane). Despite this significant difference, the maximum signal power obtained for each configuration was roughly equal at ~ 850 nJ, when the seed delay and phase matching were optimized for 780 nm.

Amplified signal spectra for the two walk-off configurations are shown in Fig. 126.41. For the WC configuration, parasitic signal SHG was phase matched in the center of the gain band [Fig. 126.41(a)]. This resulted in a narrow spectral line at 412 nm (shown in blue), a large notch in the center of the signal spectrum at 824 nm, and smaller notches on either side at 788 nm and 865 nm. The side notches are due to non-degenerate sum–frequency generation: $(788 \text{ nm})^{-1} + (865 \text{ nm})^{-1} =$

$(412 \text{ nm})^{-1}$. No parasitic signal SHG was observed for the NWC configuration, and the signal spectrum had a smooth Gaussian-like shape [Fig. 126.41(b)].

Second-harmonic generation from the idler was also observed in the WC configuration. Figure 126.42 shows a measurement of its spectrum. Like the idler, which is angularly dispersed because of noncollinear phase matching, the idler second harmonic (SH) is angularly dispersed, producing a visible rainbow at the output of the amplifier that extends from

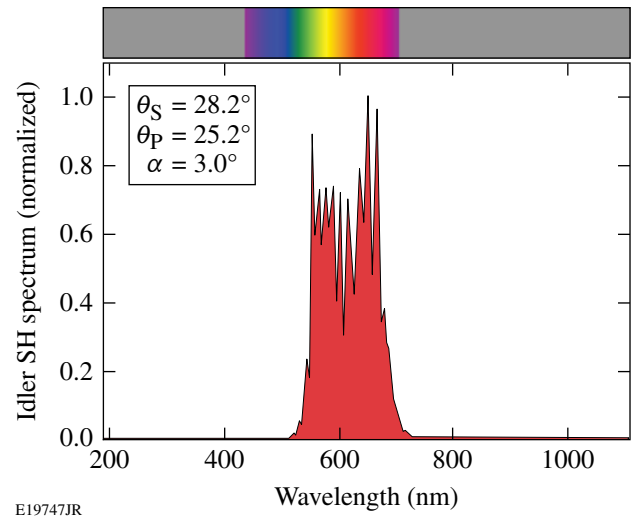


Figure 126.42 Spectra measured from idler SHG for the WC configuration. The spectrum spans much of the visible spectrum, as shown by the color bar above.

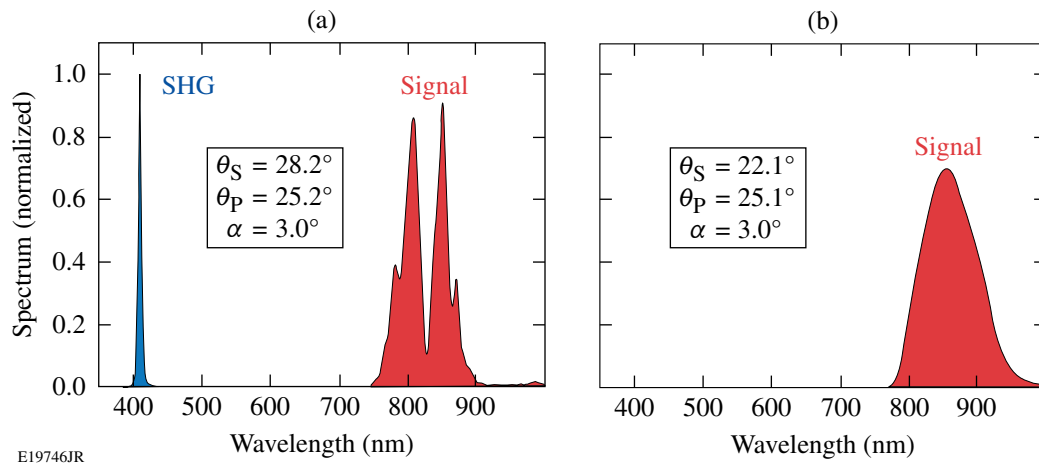


Figure 126.41 Signal spectra for (a) the WC and (b) the NWC configurations. The pump angle θ_p and noncollinear angle α were similar in both cases. In the WC configuration, the signal angle θ_s of 28.2° made it possible for parasitic second-harmonic generation to produce a narrow spectral line at 410 nm, leaving notches in the signal spectrum in the 780- to 870-nm range.

550 nm to 700 nm. This observation fits well to the phase-matching calculations shown in Fig. 126.39. A rough estimate of the idler SH energy is 0.1 to 0.4 nJ, which is less than 1% of the signal energy. Errors in this measurement result from calibration uncertainties for the broadband edge filter used to separate the idler and its second harmonic.

Numerical Model for Parasitic Signal and Idler SHG

The growth of parasitic signal and idler SHG was investigated using a 2-D numerical model. The equations of motion for the relevant optical fields were integrated using a split-step code that employed a fourth-order Runge–Kutta algorithm. The nonlinear propagation was modeled using Eqs. (1) for the field amplitudes in the time domain, $A_j(z, t)$, where $j = S, I, P, SSH, ISH$ for the signal, idler, pump, signal SH, and idler SH fields, respectively.

$$\begin{aligned} \frac{dA_S}{dz} &= i \frac{2\omega_S d_{\text{eff}}}{n_S c} (A_I^* A_P - A_S^* A_{SSH}), \\ \frac{dA_I}{dz} &= i \frac{2\omega_I d_{\text{eff}}}{n_I c} (A_S^* A_P - A_I^* A_{ISH}), \\ \frac{dA_P}{dz} &= i \frac{2\omega_P d_{\text{eff}}}{n_P c} A_S A_I, \\ \frac{dA_{SSH}}{dz} &= -i \frac{2\omega_{SSH} d_{\text{eff}}}{n_{SSH} c} A_S^2, \\ \frac{dA_{ISH}}{dz} &= -i \frac{2\omega_{ISH} d_{\text{eff}}}{n_{ISH} c} A_I^2. \end{aligned} \quad (1)$$

A constant nonlinear coefficient d_{eff} was assumed to be 2.16 pm/V (Ref. 18). Linear propagation effects such as dispersion and phase matching were included in the frequency domain using conjugate field amplitudes $a_j(z, \Omega)$, calculated from the time-domain amplitude using

$$a_j(z, \Omega) = \text{FFT}^{-1} [A_j(z, t), t \rightarrow \Omega]. \quad (2)$$

Ω is defined as the optical-frequency difference relative to the field's center frequency ω_j . The linear part of the split-step propagation, for step size h , was given by

$$a_j(z+h, \Omega) = a_j(z, \Omega) e^{in_j h(\omega_j + \Omega)/c - ih\Omega/v_S}, \quad (3)$$

where n_j is the frequency-dependent refractive index calculated using Sellmeier equations for BBO.¹⁹ The second term in the

exponent is added so that calculations are done in the frame of the signal pulse traveling with a group velocity v_S .

Figure 126.43 compares measured and simulated signal spectra for the WC configuration. Results are plotted for a range of signal angles θ_S . Similar features are seen in both, despite

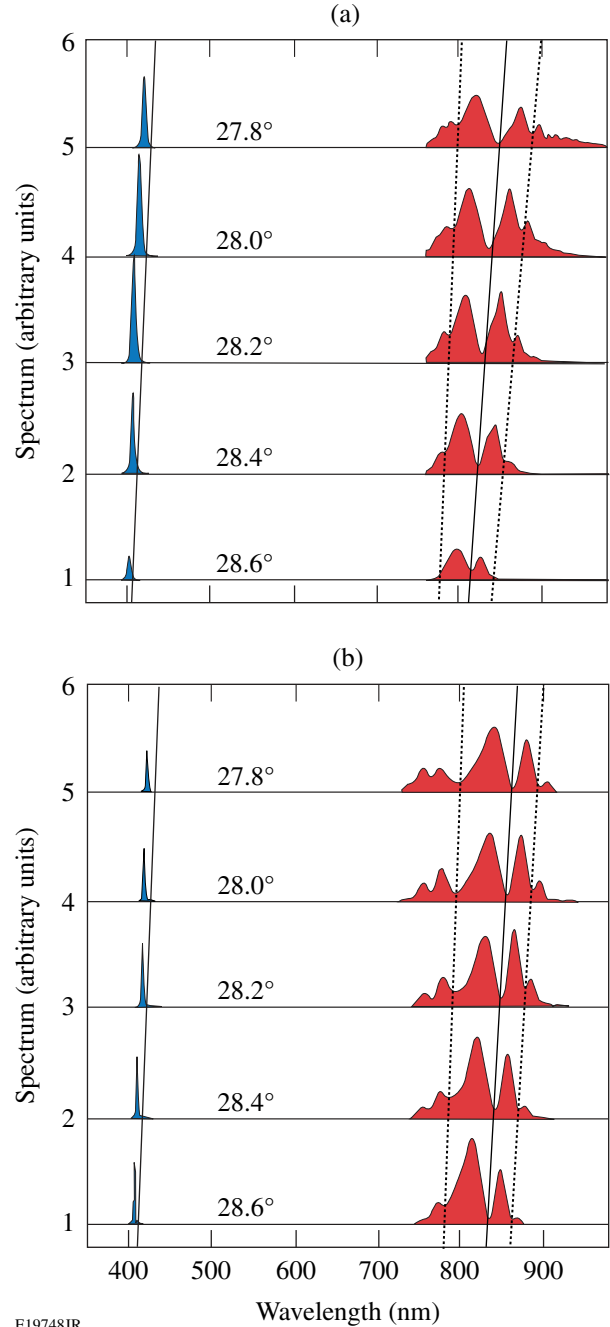


Figure 126.43

Comparison of (a) experimental measurements and (b) numerical simulations for a range of signal angles in the WC configuration.

the fact that the simulations use a simple 2-D model that does not include effects of spatial walk-off and intensity variation over the pump, signal, and idler beams. In both cases, notches are seen in the signal spectra corresponding to the generation of signal SHG, and the notches shift to longer signal wavelengths as the signal angle is reduced, consistent with the SHG phase-matching curves shown in Fig. 126.38. The calculated spectral features of parasitic signal SHG agree well with the experimental results.

Impact of Signal SHG on NOPA Efficiency

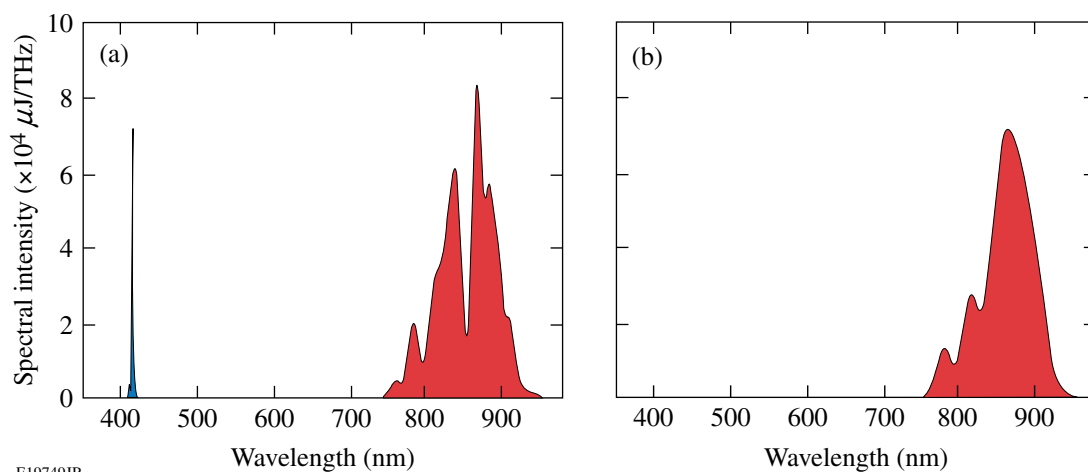
One benefit of an accurate model is the ability to evaluate the impact of parasitic processes by comparing results calculated either with or without the process. Furthermore, the axial evolution of each field within the crystal can be calculated to show the exchange of energy between the fields. The parameters shown in Table 126.VI were chosen for a case study of a BBO NOPA, corresponding approximately to the experimental configuration in Fig. 126.40.

Figure 126.44 shows amplified signal spectra for cases where the signal SHG was either included or suppressed in the model. The sharp notch and signal SH are evident in Fig. 126.44(a). Some spectral modulation is also seen in Fig. 126.44(b), even though SHG was suppressed in the simulation and the experimentally measured spectra were smooth [see Fig. 126.41(b)]. In this case the modulation is due to reconversion of the signal. The 2-D nature of the model, which considers only one value of peak temporal intensity for the pump and signal, means that averaging of reconversion effects over the Gaussian beam were not included and the spectral structure was not averaged away.

The impact of signal SHG on peak amplifier efficiency is shown in Fig. 126.45. Simulations predict that 10% of the signal pulse energy is lost to SHG at the optimum crystal length of 2.3 mm. In contrast, simulations of idler SHG show that a small *increase* in efficiency of a few percent can be expected when idler SHG is present. Similar effects have been observed in pulsed optical parametric oscillators (OPO's); absorption of

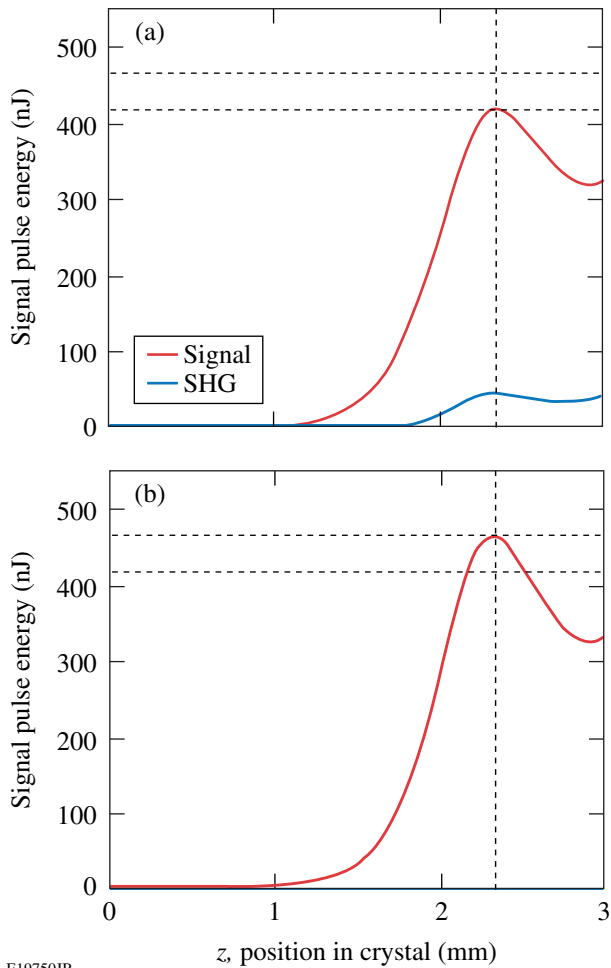
Table 126.VI: Input parameters for signal SHG case study.

Parameter	Value	Parameter	Value
Noncollinear angle (α)	3.1°	Signal spectral phase (ϕ_2)	200 fs ²
Signal angle (θ_S)	28.2°	Pump width (Gaussian) (τ)	250 fs
Pump angle (θ_P)	25.1°	Pump–signal delay at input	75 fs
Signal center wavelength (λ_S)	820 nm	Beam widths ($1/e^2$)	120 μm
Pump wavelength (λ_P)	523.5 nm	Signal input energy (E_S)	0.1 nJ
Input signal bandwidth ($\Delta\lambda_S$)	250 nm	Pump input energy (E_P)	2 μJ
Order of Gaussian signal spectrum	Tenth order	BBO crystal length (l_C)	3 mm



E19749JR

Figure 126.44
Spectra for simulation case study. Signal SHG (a) turned on and (b) turned off in the model.



E19750JR

Figure 126.45

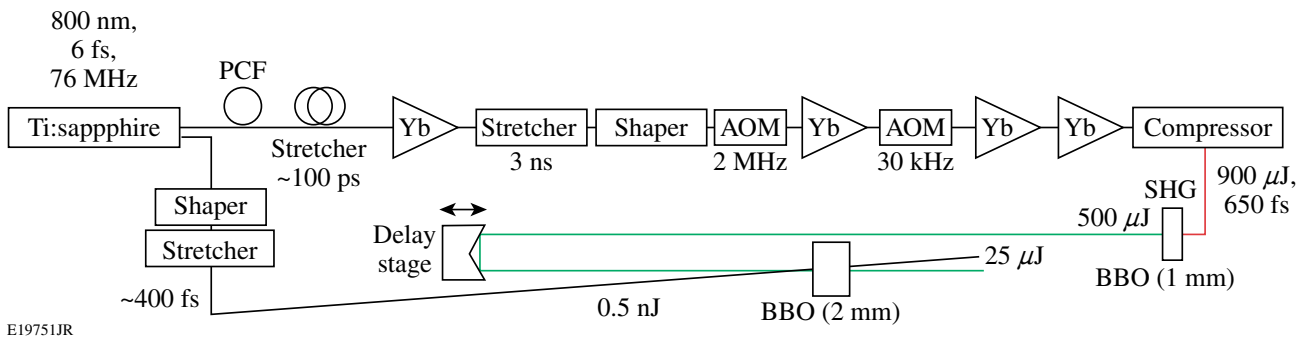
Simulated signal energy along the crystal, (a) with and (b) without signal SHG. In both cases signal reversion means that the length for optimum efficiency is 2.3 mm. When SHG is included in the simulations, 10% of the signal energy at this length is lost to the parasitic process.

the idler removes it from the three-wave interaction, increasing the threshold at which the signal is reconverted to the pump.²⁰

Parasitic Processes in Few-Cycle NOPA

NOPA's can support the extremely large optical bandwidth required by few-cycle pulses. Parasitic nonlinearities may occur over a significant wavelength range of the signal and idler. To investigate parasitic SHG effects over a larger spectral bandwidth, measurements with a few-cycle NOPA were performed. The experimental setup of the system is shown in Fig. 126.46 and is similar to the one presented in Refs. 5 and 7. A Ti:sapphire oscillator (Femtolasers Rainbow) delivering few-cycle pulses is used for seeding both the NOPA and a state-of-the-art FCPA system. The FCPA system delivers 900- μ J, 650-fs pump pulses that are frequency doubled in a 1-mm BBO crystal with an efficiency of 56%, resulting in 500- μ J pump pulses for the NOPA. Focusing to 100 GW/cm² provides a gain of 5×10^4 . The signal pulses traverse a pulse-shaping device and a prism stretcher before being imaged into the BBO crystal. The non-collinear angle is 2.5° to achieve broadband phase matching. This is slightly lower than the angle for group-velocity matching of signal and idler (2.6°). As a result, the phase matching is improved in the spectral wings, while a slight phase mismatch is generated in the center. This configuration leads to a larger effective gain bandwidth, therefore shorter pulses at the output of the system.¹⁵ Because of the high pump intensity, the 0.5-nJ oscillator pulses can be amplified to 25 μ J in a single stage in both the WC and NWC configurations.

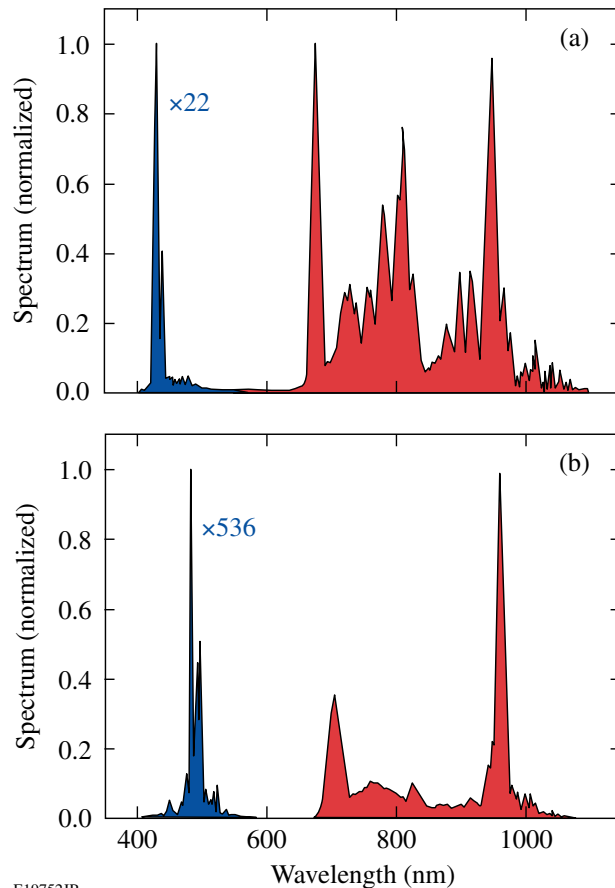
Quantitative measurements of the parasitic process were made using a bandpass filter (Newport BG.40) to separate the signal's fundamental and SH pulses. Their spectra for the WC and NWC configurations are shown in Figs. 126.47(a) and 126.47(b), respectively. The SH energy for the WC geometry measured after the filter is 1.1 μ J, corresponding to ~4% of the energy of the amplified signal. The measured spectra clearly show phase-matched SHG of 860-nm signal to 430 nm. This agrees with the phase-matching calculations for the NOPA configuration. The amplified signal spectrum shows modulation that may originate



E19751JR

Figure 126.46

A noncollinear OPCPA setup pumped by the second harmonic of a high-energy FCPA system.



E19752JR

Figure 126.47

Measured spectra for (a) the WC and (b) the NWC configurations containing the signal and its second harmonic. Note that both the fundamental and the second-harmonic spectra have been normalized to their peak value, independently.

not only from signal SHG, but also from sum-frequency generation (similar to the side notches shown in Fig. 126.41).

In contrast, the parasitic signal SHG is significantly reduced in the NWC configuration and the spectrum of the amplified

signal has less modulation. For the same amplified pulse energy, the signal SH power after the BG.40 filter is only 37 nJ, corresponding to $\sim 0.1\%$ of the amplified signal energy. Phase-matching calculations show that no signal wavelengths are perfectly phase matched in this configuration, resulting in inefficient signal SHG.

The idler SHG was also observed in the WC configuration and spanned from 550 nm to 750 nm. This is supported by the calculation of the phase-matching conditions shown in Fig. 126.39. As expected, no idler SHG was measured in the NWC configuration.

Parasitic Phase-Matching Curves for Other Common Nonlinear Crystals

Parasitic SHG processes are not limited to BBO-based NOPA's. The phase-matching curves for signal and idler SHG are shown in Fig. 126.48 for other common nonlinear crystals: LBO, BiBO, and DKDP. In all cases, the noncollinear angle was chosen for group-velocity matching of the signal and idler. The resulting signal angle within the crystal is plotted in dashed lines for both configurations, together with the corresponding SHG phase-matching curves, in Figs. 126.48(a), 126.48(c), and 126.48(e), respectively. The internal idler angles for idler SHG are plotted in Figs. 126.48(b), 126.48(d), and 126.48(f) (dashed lines). The SHG phase-matched signal and idler wavelengths for each crystal type and configuration are given in Table 126.VII.

The resulting idler wavelengths, which are phase matched for second-harmonic generation, and the corresponding signal wavelengths are displayed in Table 126.VII. The last row of Table 126.VII represents the usable parasitic SHG-free signal wavelength range around an 800-nm central wavelength. It has to be taken into account for the design of a broadband OPCPA system. In summary, the NWC configuration offers the largest parasitic-SHG-free bandwidth for all considered crystals. Furthermore, BBO in the NWC configuration seems

Table 126.VII: SHG phase-matched signal and idler wavelengths for BBO, LBO, BiBO, and DKDP in both WC and NWC configurations for NOPA's pumped by the second harmonic of Yb-based systems ($\lambda_p = 510$ to 525 nm). The corresponding signal wavelength for parasitic idler SHG is calculated from the energy conversion. The parasitic SHG free-wavelength range is summarized in the last row.

Crystal material	BBO		LBO		BiBO		DKDP	
	WC	NWC	WC	NWC	WC	NWC	WC	NWC
Signal SHG wavelength (nm)	860	1119	963	1012	889	1025	942	1090
Idler SHG wavelength (nm)	1265	864	1031/1067	983/1794	1102/2338	969	1110	951
Signal λ for idler SHG (nm)	869	1275	1029/758	1082/722	966/660	1099	961	1123
Parasitic SHG free λ range (nm)	<860	<1119	758...963	722...1012	660...889	<1025	<942	<1090

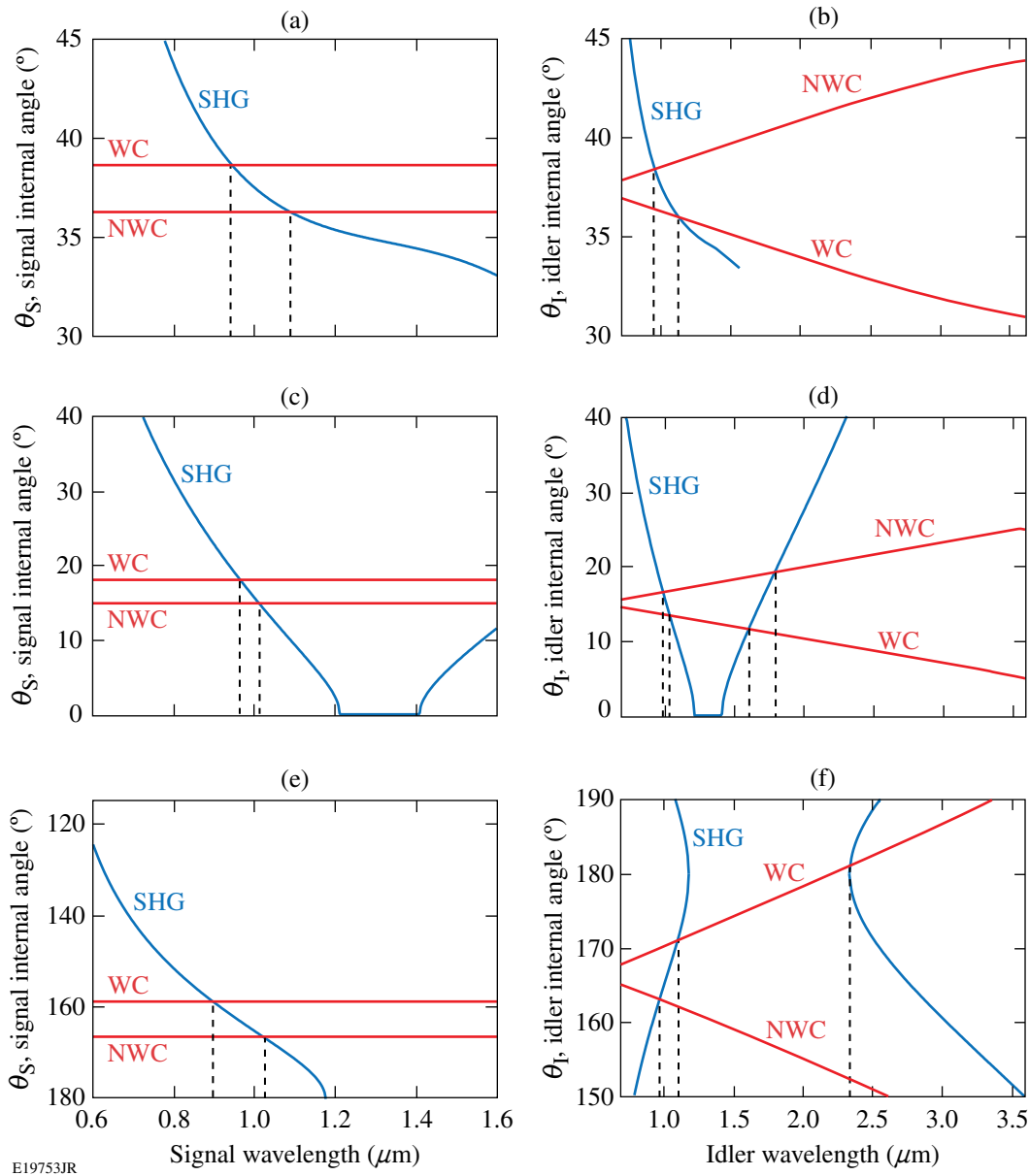


Figure 126.48

Phase-matching curves for signal (left column) and idler (right column) SHG for other common NOPA crystals: [(a),(b)] DKDP; [(c),(d)] LBO; and [(e),(f)] BiBO.

to be most suitable for ultra-broadband NOPA's since it is free of parasitic-SHG phase matching until 1129 nm. Deviations from the assumed noncollinear angles and pump wavelength will shift the SHG phase-matched wavelength slightly, although the general behavior remains the same.

Conclusions

A detailed analysis of parasitic nonlinear effects, namely second-harmonic generation of the signal and idler waves, on

broadband high-repetition-rate NOPA's has been presented. Results from an experimental study of a white-light-seeded NOPA agree well with 2-D numerical simulations. Modeling shows that second-harmonic generation of the signal can reduce the NOPA output energy by 10%.

A quantitative analysis was carried out for an ultra-broadband, few-cycle NOPA. For the WC configuration, a few percent of the output is converted into signal SH, while the

effect is reduced by at least an order of magnitude for the NWC configuration. Strong spectral modulation is observed in the WC configuration that originates from SHG and SFG of the spectral components of the signal and idler. Such modulation can significantly reduce the pulse quality of the output pulses and can be avoided by using the NWC configuration. A detailed phase-matching analysis for the most common nonlinear crystals is presented as a guide for designing NOPA systems.

The NOPA application dictates which configuration is best suited. For a laser front end, for example, a symmetric near-field profile and good spectral uniformity across the beam are required. In the case of low pump-pulse energy ($<10 \mu\text{J}$) and peak power ($\sim 10 \text{ MW}$), the WC geometry is the best choice, provided parasitic SHG can be avoided over the amplifier's wavelength range. For spectroscopic applications, where the bandwidth and tuning range of the signal are primary requirements, the NWC configuration is a better choice, provided that lower gain is acceptable or that the poor beam symmetry and spectral nonuniformity across the beam are tolerable. In the case of an ultra-broadband, few-cycle NOPA, the NWC configuration must be used to avoid power loss and spectral modulation on the ultra-broad spectrum. Distortions in the amplified beam can be avoided in this case by weakly focusing the high-peak-power pump laser.

ACKNOWLEDGMENT

This work has been supported by the U.S. Department of Energy Office of Inertial Confinement Fusion under Cooperative Agreement No. DE-FC52-08NA28302, the University of Rochester, and the New York State Energy Research and Development Authority. The support of DOE does not constitute an endorsement by DOE of the views expressed in this article.

This work was also supported by the German Federal Ministry of Education and Research (BMBF) with project 03ZIK455 "onCOOPtics," the Helmholtz Institute Jena, and the European Research Council under the European Union's Seventh Framework Programme (FP7/2007-2013)/ERC Grant agreement 240460. S. H. acknowledges financial support by the Carl Zeiss Stiftung Germany.

REFERENCES

1. C. Schriever *et al.*, *Opt. Lett.* **33**, 192 (2008).
2. J. Piel *et al.*, *Opt. Lett.* **31**, 1289 (2006).
3. G. Cerullo and S. De Silvestri, *Rev. Sci. Instrum.* **74**, 1 (2003).
4. A. Steinmann *et al.*, *Opt. Express* **14**, 10,627 (2006).
5. S. Hädrich *et al.*, *Opt. Lett.* **36**, 313 (2011).
6. J. Rothhardt *et al.*, *Opt. Express* **15**, 16,729 (2007).
7. J. Rothhardt *et al.*, *Opt. Express* **16**, 8981 (2008).
8. J. Rothhardt *et al.*, *Opt. Express* **18**, 12,719 (2010).
9. Y. Tang *et al.*, *Opt. Lett.* **33**, 2386 (2008).
10. V. V. Lozhkarev *et al.*, *Opt. Express* **14**, 446 (2006).
11. G. Arisholm *et al.*, *Opt. Express* **12**, 518 (2004).
12. J. Hellström *et al.*, *Opt. Lett.* **26**, 352 (2001).
13. E. Riedle *et al.*, *Appl. Phys. B* **71**, 457 (2000).
14. G. M. Gale *et al.*, *Opt. Lett.* **20**, 1562 (1995).
15. D. N. Schimpf *et al.*, *J. Opt. Soc. Am. B* **24**, 2837 (2007).
16. For more system details, see J. Bromage, J. M. Fini, C. Dorrer, and J. D. Zuegel, *Appl. Opt.* **50**, 2001 (2011).
17. R. R. Alfano, *The Supercontinuum Laser Source: Fundamentals with Updated References*, 2nd ed. (Springer, New York, 2006).
18. G. G. Gurzadian, V. G. Dmitriev, and D. N. Nikogosian, *Handbook of Nonlinear Optical Crystals*, 3rd rev. ed., Springer Series in Optical Sciences, Vol. 64 (Springer-Verlag, Berlin, 1999).
19. D. Eimerl *et al.*, *J. Appl. Phys.* **62**, 1968 (1987).
20. G. Rustad, O. Farsund, and G. Arisholm, presented at Advances in Optical Materials (AIOM), Istanbul, Turkey, 16–18 February 2011 (Paper AWA25).

Stress Compensation in Hafnia/Silica Optical Coatings by Inclusion of Alumina Layers

Introduction

Optical coatings are a critical technology for the successful construction and operation of high-peak-power laser systems. Optical coatings must provide appropriate spectral and photometric performance while maintaining high laser-damage resistance at the wavelength(s) and pulse duration(s) of interest. Additionally, the surface figure of the coated optics must be maintained to preserve the optical performance of the system. Thin-film stresses resulting from the optical coating process, both compressive and tensile, pose a risk to the performance and longevity of the coated components.

Electron-beam deposition of optical coatings has been the standard process for fabricating multilayer coatings for high-peak-power laser applications. The ability to scale the process to large substrates, flexibility in source materials and coating designs, and relatively low cost encourage the selection of this deposition process. Ultimately, however, the determination to date that such coatings produce the highest laser-damage thresholds has led to the use of electron-beam evaporation as the primary deposition process for large, high-peak-power laser components for systems such as OMEGA, OMEGA EP, the National Ignition Facility, Laser Megajoule, and others.

Multilayer coatings consisting of hafnium dioxide and silicon dioxide have been the standard choice for applications at both 1053 nm and 351 nm for these laser systems.¹⁻⁶ These materials provide good spectral and uniformity control while maintaining high laser-damage thresholds. Hafnia/silica multilayers, however, exhibit high tensile stresses, particularly on low-thermal-expansion substrates in low-relative-humidity environments, sufficient to provide significant substrate deformation and potentially cracking of the coated surface.^{2,7} Modification of the electron-beam deposition process for hafnia/silica coatings has been explored elsewhere, both through evaporation parameters and energetic assistance.⁷⁻⁹ In this work, the use of aluminum oxide is explored as a means of adjusting the stress in multilayer reflective coatings.

Aluminum oxide has a high bandgap with a corresponding high laser-damage resistance.^{10,11} Its relatively low refractive index makes it unattractive choice, however, for the high-index material in interference coating designs since such a refractive index leads to significantly thicker coatings with far greater numbers of layers. Alumina films deposited by electron-beam evaporation have been shown to exhibit tensile film stresses with a very slow diffusion of water, suggesting a relatively dense film structure without large, columnar pores in the coating.¹² The limited number of available coating materials with sufficiently high laser-damage resistance requires the exploration of all available choices. The diffusion behavior of alumina, coupled with its band gap and laser-damage resistance, suggests that further investigation of alumina performance could be beneficial to modifying the performance of hafnia/silica coatings.

Background

Tensile stresses pose significant challenges for implementation of optical components. First, any film stress leads to a deformation of the optic surface in accordance with the mechanical properties of the film and substrate, as described by Stoney's equation:¹³

$$\sigma = \frac{E_s t_s^2}{6(1 - \nu_s) t_f R}, \quad (1)$$

where σ is the film stress, R is the radius of curvature of the surface, E_s is Young's modulus of the substrate, ν_s is Poisson's ratio for the substrate, and t_f and t_s are the thickness of the film and substrate, respectively. This describes the impact of the stress on the radius of curvature of the optic surface, leading to changes in the flatness and corresponding optical performance of the component. While mechanically stiff substrate materials of sufficient thickness t_s will exhibit minimal bending from film stress, tensile stresses remain a problem if they lead to cracking, or crazing, of the coating.¹⁴

Fracture of a coating's surface results when tensile stresses exceed the fracture toughness of the film. Fracture will initiate at a defect in the coating, whether initiated by a scratch at the edge caused by coating tooling or optic mounting, or at a defect within the film such as shown in Fig. 126.49. Fracture also requires a sufficiently thick film in which the stress can be relieved through fracture at the surface, given the strain at that point. This relationship is given by Hutchinson and Suo:¹⁴

$$h_c = \frac{\Gamma E_f}{Z\sigma^2}, \quad (2)$$

where h_c is the critical coating thickness, Γ is the fracture resistance of the film, E_f is Young's modulus of the film, Z is a geometrical constant dependent on the fracture type (1.976 for film crazing), and σ is the tensile stress in the film. Compressive stresses will not lead to fracture of the coating surface; instead, excessive compressive stresses may lead to a buckling of the coating, potentially with delamination from the surface. This dependence on the thickness of the film relative to the film stress provides a means for understanding failure mechanisms in the coating.

Given the relationships in Eqs. (1) and (2), it is important to reduce the film stress such that optical performance of the component is preserved while fracture of the coating is avoided. Thicker substrates may aid in maintaining flatter optical surfaces and thinner coatings help to prevent cracking, but both of

these approaches result in a cost in substrate size and/or achievable coating performance. To provide optimal performance of the optical coating, the magnitude of the tensile film stress must be kept low or ideally moved to a compressive state. Compressive stress also must be kept low in order to maintain surface flatness of the optical component in accordance with Eq. (1).

Stresses in a multilayer coating are a function of the film thickness of each constituent material in the coating, as well as the stress in each material. Equation (1) may be modified to account for the individual stress in each layer by¹⁵

$$\sigma_1 t_1 + \sigma_2 t_2 + \dots + \sigma_n t_n = \frac{E_s t_s^2}{6(1-\nu_s)R}, \quad (3)$$

where σ_i and t_i are now the stress and thickness of each layer of the coating, respectively. Likewise, the total stress in the multilayer will be given by

$$\sigma_{\text{total}} = \frac{\sigma_1 t_1 + \sigma_2 t_2 + \dots + \sigma_n t_n}{\sum_i t_i} \quad (4)$$

since the individual stress contributions are simply weighted by the relative layer thicknesses of each. Modification of selected layers provides a means of adjusting the overall stress, with the use of three materials providing the ability to calculate the stress according to

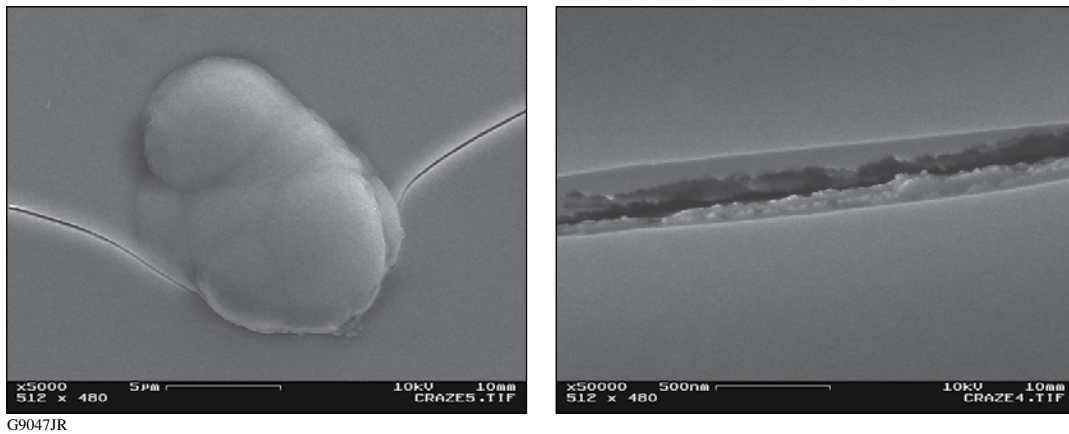


Figure 126.49

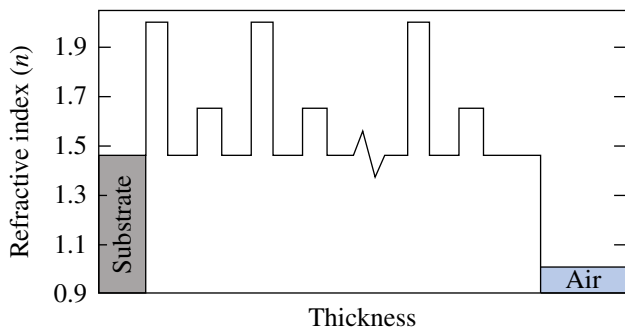
Scanning electron microscope imaging of the initiation site and crack that forms as a result of the high tensile stress in the film. A defect site in the coating provides an initiation site for tensile stress failure, while tearing of the film is evident within the crack that forms.

$$\sigma_{\text{total}} = \frac{\sigma_{\text{H}}T_{\text{H}} + \sigma_{\text{L}}T_{\text{L}} + \sigma_{\text{A}}T_{\text{A}}}{T_{\text{H}} + T_{\text{L}} + T_{\text{A}}}, \quad (5)$$

where T_i is now the total thickness of a given material in the entire multilayer since the stress is assumed to be constant for all layers of the same material deposited in the same manner. Subscripts H, L, and A denote hafnia (high refractive index), silica (low refractive index), and alumina, respectively. Given individual material stresses, coating designs may then be modified to yield the desired overall stress.

Experimental Procedure

Coating depositions were performed in a 54-in. coating chamber equipped with quartz heater lamps, dual electron-beam guns, and planetary substrate rotation. Granular silicon dioxide was evaporated from a continuously rotating pan while hafnium metal or aluminum oxide was deposited from a stationary six-pocket electron-beam gun. The baseline coating is a 32-layer hafnia/silica quarter-wave mirror centered at $\lambda_0 = 1053$ nm with a half-wave silica overcoat on fused-silica substrates. Alumina layers were substituted for selected hafnia layers, uniformly distributing the alumina layers throughout the coating. In addition, the first high-index layer on the incident side of the coating was always replaced by alumina to take advantage of its higher band gap in the region of highest electric-field intensity. In this manner, the coating has alumina/silica interfaces but no hafnia/alumina interfaces. The refractive-index profile of such a coating is shown in Fig. 126.50, with the outermost layers on the air side being a half-wave optical thickness of silica, with a quarter-wave optical thickness of alumina immediately beneath it.



G9050JR

Figure 126.50

Refractive index profile of a hafnia/silica/alumina high-reflector coating. Selected hafnia layers are replaced with alumina layers of equivalent optical thickness with the alumina layers being equally distributed throughout the overall thickness of the coating.

The primary means of altering the coating in this study was through the amount of alumina introduced in the coating design, relative to the overall thickness, as well as through the number of interfaces of each material. Depositions were performed with different overall coating thicknesses, relative numbers of layers and associated interfaces, and individual layer thicknesses. Deposition parameters such as oxygen backfill pressures, deposition rate, and substrate temperature remained constant throughout, in an effort to maintain a consistent film stress for each material between depositions.

Spectral measurements were performed on a Perkin-Elmer Lambda 900 spectrophotometer operating in transmission at normal incidence. The spectrophotometer environment was maintained at 0% relative humidity in order to eliminate optical thickness variations as a result of film water content. Photometric measurements were executed on a laser-based reflectometer system, again in a nitrogen-purged environment to achieve 0% relative humidity; measurements were performed at a constant wavelength while scanning the incident angle on the substrate. The measurement procedure incorporates a dual-beam configuration, using lock-in amplifiers and a chopped signal to minimize signal noise. Extended integration times at each point in the measurement scan further improve the quality of the measured result.

Surface flatness measurements of the 1-in.-diam substrates were performed on a Zygo New View white-light interferometer in a nitrogen-purged enclosure at approximately 0% relative humidity. Samples were purged for 15 h prior to measurement to stabilize the coating stress; measurement routines were automated to ensure consistent purge times. Samples measured after 6 h of purging exhibited irregular measurement results, with a significant decrease in correlation with deposition parameters. Measurements were corrected for cavity irregularity by referencing a $\lambda/50$ calibration flat, and all measurements subtracted the pre-coating flatness measurement of the individual substrate. Samples were supported on a three-point ball bearing mount, with each point positioned 120° apart at 65% of the radius of the substrate to minimize distortion caused by gravity in mounting. The uncoated surface of the samples was measured to avoid interferometric phase errors resulting from the coating. Film stresses based on these surface measurements were compared to those carried out on 310-mm-diam \times 14-mm-thick fused-silica substrates measured on an 18-in. Zygo interferometer, with calculated stresses agreeing to within ± 8 MPa. Film stresses were also compared to measurements taken in a custom vacuum cell on the Zygo New View; vacuum film stresses were measured to be approximately 8 MPa more tensile than those determined in a

nitrogen environment. Given the relative difficulty in making in-vacuum measurements, this shift in determined film stress was considered acceptable at this time.

Laser-damage testing was performed using 1-ns pulses at a wavelength of 1053 nm. The irradiation spot size, illuminated by a 2-m-focal-length lens, was 600 mm, making it possible to use fluences up to 100 J/cm². The sample was inspected under 110× magnification using dark-field microscopy, with an observable change in the surface being defined as damage. Testing may be targeted on defects present in the coating, as a means of identifying the weakest points in the film structure, or on sites that appear pristine, as a means of evaluating the maximum-possible damage threshold for a clean substrate and zero-particulate process. Modes of testing included 1-on-1, where each site on the substrate is illuminated only once, and N-on-1, where the fluence on a given site is gradually ramped through a series of shots until damage is observed.¹⁶

Results and Discussion

The goal of this work is to alter the tensile stress in the hafnia/silica multilayer coatings, shifting it to a low-magnitude compressive stress to eliminate the risk of cracking the coating while minimizing substrate deformation. Observations of current hafnia/silica coatings in vacuum have indicated that multilayers of greater-than-5-μm total film thickness consistently exhibit tensile stress failures in accordance with Eq. (2), providing the motivation for this effort. In addition, such coatings have tensile stresses of 80 MPa or greater, significantly deforming the substrate surface.^{4,9} Since polarizer coatings for use in the near-infrared cannot be realized with coatings of less than 5-μm thickness, the stress in the film must be shifted to a more compressive state.⁴

Evaporated alumina films have been reported in the literature as both tensile and compressive.^{11,17} The films being studied were found to have a tensile stress when deposited as a monolayer, with a stress of the order of 70±15 MPa. This would suggest alumina is not a viable material for compensation of tensile stresses in high-damage-threshold coatings since it would not offset the tensile stress generated in high-refractive-index hafnia layers. Composite film stresses in hafnia/silica multilayers, however, were tensile, but alumina/silica multilayers remained quite compressive. This could in part be a result of the magnitude of the tensile stress in alumina being less than that in hafnia, allowing it to be compensated by the compressive silica stress.

The film stresses as measured in the hafnia/silica multilayers, alumina/silica multilayers, and the hafnia/alumina/silica (hybrid)

multilayers indicate an unexpected interaction between the different layer materials. The hybrid three-material coating design is more compressive than either of the two-material designs; given the relative proportion of materials in each design, this should not be possible in order for Eq. (5) to be valid for all coatings using comparable stress values for the materials in each. This suggests that a modification to Eq. (5) is necessary, possibly to account for inhomogeneous layer stresses and/or interfacial effects.¹⁸ Either effect will be a function of the number of interfaces of the given material, so Eq. (5) is modified to a form

$$\sigma_{\text{total}} = \frac{\sigma_{\text{H}}T_{\text{H}} + \sigma_{\text{L}}T_{\text{L}} + \sigma_{\text{A}}T_{\text{A}}}{T_{\text{H}} + T_{\text{L}} + T_{\text{A}}} + \sigma_{\text{H/L}}I_{\text{H/L}} + \sigma_{\text{A/L}}I_{\text{A/L}}, \quad (6)$$

where $\sigma_{\text{H/L}}$ and $\sigma_{\text{A/L}}$ are the stresses resulting from interfacial and film-growth effects at each of the hafnia/silica ($I_{\text{H/L}}$) and alumina/silica ($I_{\text{A/L}}$) interfaces, respectively. The number of interfaces in the coating design is counted for each combination of materials, and since both hafnia and alumina have silica layers above and below each layer, the directional dependence is eliminated.

It is possible to determine values for each of the five stresses included in Eq. (6) by establishing a linear series of five equations for simultaneous solution. The six depositions provide a means of calculating the stresses six times, by eliminating one of the depositions from consideration for each calculation. The calculation is most readily constructed in matrix form, for five given depositions:

$$\begin{pmatrix} T_{\text{H1}} & T_{\text{L1}} & T_{\text{A1}} & I_{\text{H/L1}} & I_{\text{A/L1}} \\ T_{\text{H2}} & T_{\text{L2}} & T_{\text{A2}} & I_{\text{H/L2}} & I_{\text{A/L2}} \\ T_{\text{H3}} & T_{\text{L3}} & T_{\text{A3}} & I_{\text{H/L3}} & I_{\text{A/L3}} \\ T_{\text{H4}} & T_{\text{L4}} & T_{\text{A4}} & I_{\text{H/L4}} & I_{\text{A/L4}} \\ T_{\text{H5}} & T_{\text{L5}} & T_{\text{A5}} & I_{\text{H/L5}} & I_{\text{A/L5}} \end{pmatrix} \times \begin{pmatrix} \sigma_{\text{H}} \\ \sigma_{\text{L}} \\ \sigma_{\text{A}} \\ \sigma_{\text{H/L}} \\ \sigma_{\text{A/L}} \end{pmatrix} = \begin{pmatrix} \sigma_{\text{total1}} \\ \sigma_{\text{total2}} \\ \sigma_{\text{total3}} \\ \sigma_{\text{total4}} \\ \sigma_{\text{total5}} \end{pmatrix}, \quad (7)$$

where σ_{total_i} are the measured stress values of the multilayer coatings, after having stabilized with age. Rearranging this for solution yields

$$\begin{pmatrix} T_{\text{H1}} & T_{\text{L1}} & T_{\text{A1}} & I_{\text{H/L1}} & I_{\text{A/L1}} \\ T_{\text{H2}} & T_{\text{L2}} & T_{\text{A2}} & I_{\text{H/L2}} & I_{\text{A/L2}} \\ T_{\text{H3}} & T_{\text{L3}} & T_{\text{A3}} & I_{\text{H/L3}} & I_{\text{A/L3}} \\ T_{\text{H4}} & T_{\text{L4}} & T_{\text{A4}} & I_{\text{H/L4}} & I_{\text{A/L4}} \\ T_{\text{H5}} & T_{\text{L5}} & T_{\text{A5}} & I_{\text{H/L5}} & I_{\text{A/L5}} \end{pmatrix}^{-1} \times \begin{pmatrix} \sigma_{\text{total1}} \\ \sigma_{\text{total2}} \\ \sigma_{\text{total3}} \\ \sigma_{\text{total4}} \\ \sigma_{\text{total5}} \end{pmatrix} = \begin{pmatrix} \sigma_{\text{H}} \\ \sigma_{\text{L}} \\ \sigma_{\text{A}} \\ \sigma_{\text{H/L}} \\ \sigma_{\text{A/L}} \end{pmatrix}. \quad (8)$$

The six possible solutions, based on elimination of each of depositions 1–6, are summarized in Table 126.VIII.

Table 126.VIII. Solutions to the system of equations describing the individual stress contributions. Only solutions B and F fit the constraints of the problem.

	A	B	C	D	E	F
σ_H	-200.5	234.3	-5869.5	-252.3	NaN	246.1
σ_L	283.9	-92.8	4367.0	248.4	NaN	-81.0
σ_A	-1058.0	-622.9	-5024.7	1.2×10^{18}	NaN	-630.9
$\sigma_{H/L}$	-0.8	0.6	-8.9	0.1	NaN	0.1
$\sigma_{A/L}$	3.9	3.9	-0.8	-7.9×10^{15}	NaN	3.9

Analysis of the results shows a number of the mathematical solutions do not fit the parameters of the problem. Based on single-layer stress measurements, σ_H is expected to be of the order of 200 MPa and σ_L is of the order of -80 MPa. Only solutions B and F appear to fit the constraints of the problem. While the solutions are very similar, the calculated stress in the alumina films is excessively compressive; this may be due to inhomogeneous stresses that are poorly described by Eq. (6), errors in the stress measurements, or other effects. Given that the magnitude of the stress in the alumina layers is expected to be a maximum of ± 100 MPa, rather than the -600 MPa calculated, the modeled values fit the mathematical constraints of the system of equations without necessarily identifying the physical stress contributions accurately.¹¹ Using an average solution of B and F for coating designs containing different numbers of alumina layers, the determined stress is compared to measured values for selected coatings in Fig. 126.51. While the various stress contributions may not be appropriately distributed among the film materials, the model does provide an indication of the trends in expected film stress for a composite hafnia/silica/alumina coating.

The previous results were used to predict the stresses likely to be achieved for two additional coating depositions, with designs $\{(HL)^3 [AL(HL)^3]^3 A2L\}$ designated sample #7 and $\{[AL(HL)^2]^5 A2L\}$ designated #8, where A, L, and H represent quarter-wave optical thicknesses at 1053 nm of alumina, silica, and hafnia, respectively, coefficients indicate a multiple of quarter-wave thickness, and superscripts signify the repetition of that portion of the coating design. The key difference with these hybrid designs is the alteration of the alumina content and the number of alumina/silica interfaces. Calculation of the expected film stress upon aging, using an average of solutions B and F, yields stresses of -11 MPa for #7 and -49 MPa for #8. Calculated stresses based on the measured surface flatness of samples #7 and #8 resulted in -34.5 MPa and -77 MPa, respectively, in both instances understating the compressive stress in the film. While the inaccuracy in the model's predic-

tion is undesirable, the presence of additional compressive stress avoids the risk of tensile stress failure.

The developed model provided general trends for the stress in the film but yielded errors in the predicted stress of -23.5 MPa and -28 MPa in samples #7 and #8. While efforts have been taken to account for the stresses in each material and any differences in stresses attributed to the number of interfaces, no allowance has been made for the potential modification of the stress in one material resulting from the presence of a different material in the multilayer coating. In particular, alumina has been shown to inhibit diffusion of water; it is likely that the presence of alumina layers influences the hydrolysis of silica, with the aging of the film to a more-tensile state over time being largely avoided.^{4,6} Refining the model to include such effects would require that all samples contain similar materials, and that the stress in any given layer be a function of the layers above it. The complexity of the model would increase significantly, in order to provide a functional dependence of the stress in each layer to all layers to the incident side, as well as the relative porosity. It is currently expected that such complexity is necessary, however, to fully describe the influence of alumina on the stresses in a hafnia/silica film.

It is suggested by the observed stresses that the changes in coating stress caused by the inclusion of alumina layers are a result of the reduced diffusion of water through the coating

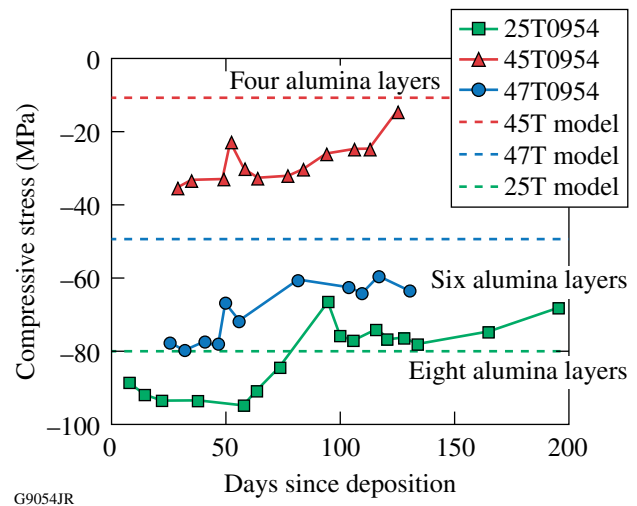
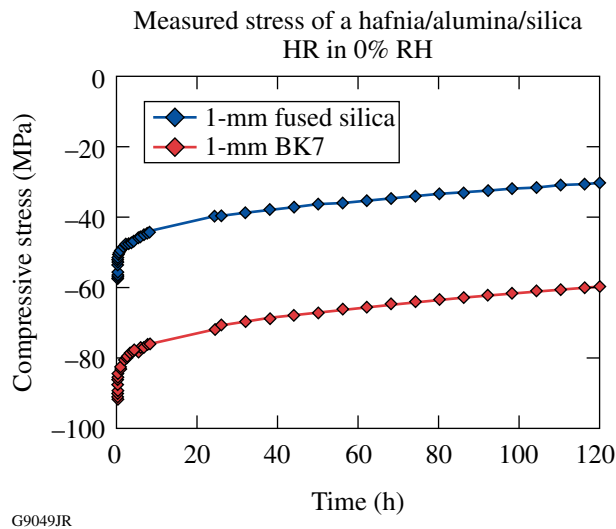


Figure 126.51

Influence of the number of alumina layers on the resulting stress in the multilayer coating. Use of a greater proportion of alumina instead of hafnia shifts the composite multilayer stress more compressively, making the coating suitable for use in a dry or vacuum environment.

structure. As shown in Fig. 126.52, the stress in an alumina/hafnia/silica coating exhibits a very slow drift as the coating is dried in a nitrogen-purged environment. This leads to a strong time dependence for all measured values of stress in order to stabilize the coating performance as much as possible. This uncertainty makes it very difficult to precisely determine the stress of coatings containing alumina since even after a week of drying time, the stress is not fully stabilized.



G9049JR

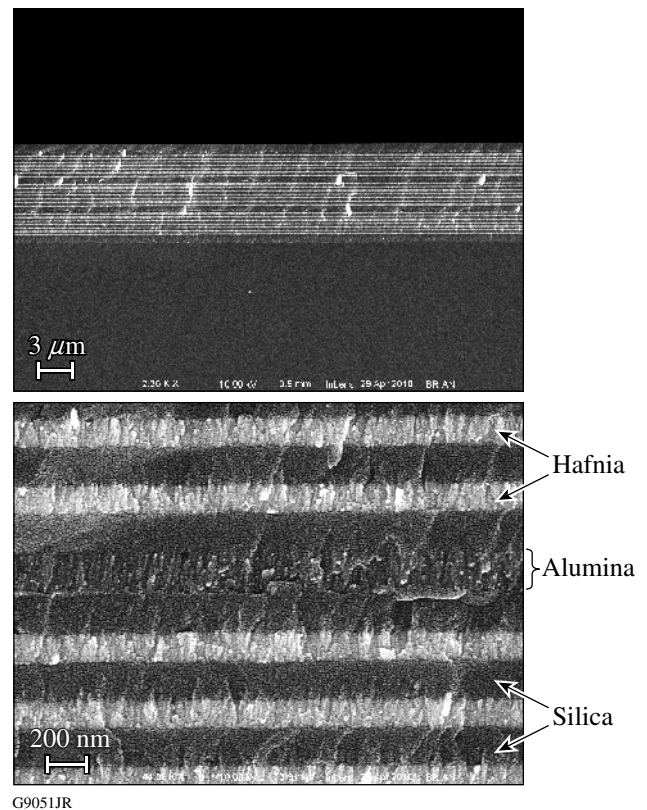
Figure 126.52

Change in stress in an alumina/silica coating as a function of time in dry nitrogen. Note that the stress changes quite slowly, leading to instability in the optical performance over an extended period of time since the surface flatness continues to change.

Implementation

A key advantage of this type of coating modification is that it can be readily performed in a standard evaporation system with minimal equipment changes required. This process was implemented in a 1.8-m coating chamber to alter the stress in a 0.9-m-aperture polarizer coating for use in vacuum on the OMEGA EP Laser System, as previously produced with evaporated hafnia/silica.⁴ To integrate this process, the standard six-pocket electron-beam gun used for hafnium metal evaporation was replaced with an EB Sources large-capacity, 12-pocket electron-beam gun, providing additional capacity for alumina evaporation. All deposition monitoring was performed with weighted averaging using an Inficon IC5 and three SensorsTech cartridge-type quartz crystal monitors mounted under stationary uniformity-correction masks, with the substrate mounted in a counter-rotating planetary rotation system.^{19,20} Silica was deposited using granular silica in a continuously rotating EB Sources large-capacity, pan-type electron-beam gun.

The original 48-layer polarizer coating design developed for this application was replaced with a 50-layer design containing four alumina layers, with all alumina layers adjoining only silica layers.⁴ The alumina layers are nominally one quarter-wave optical thickness, except the layer on the substrate, which is approximately three quarter-waves in optical thickness. The coating design was fully optimized with Optilayer refinement to maximize the photometric coating performance.²¹ The alumina layers were inserted every 16th layer, such that the layer on the substrate was alumina and the final high-index layer was alumina. The outermost layer of the coating remained a thick silica layer of greater than one half-wave optical thickness. The overall coating thickness was 9.1 μm , requiring approximately 10 h of deposition time. Cross-sectional scanning electron microscope images of the completed polarizer coating are shown in Fig. 126.53, with the alumina layers appearing very similar to the surrounding silica layers; only the film microstructure differentiates it from the adjoining layers.



G9051JR

Figure 126.53

Cross-sectional scanning electron micrographs of the polarizer coating modified with four alumina layers. The alumina layers appear to have a more columnar structure than the surrounding silica layers, which appear amorphous. The hafnia layers appear columnar and much brighter in the image.

Coating performance was measured using a laser-based photometer, providing a highly collimated source, a precise angle of incidence, and high polarization contrast. The performance of this polarizer is shown in Fig. 126.54, indicating p -polarized transmission of greater than 98% through the component over an angular range of nearly 9° incidence; polarizer contrast, defined as T_p/T_s , exceeds 200:1 over 8° of this range. In wavelength space, this component has a useful bandwidth of 30 nm after accounting for slight uniformity errors over the 0.9-m aperture and installation alignment tolerances.

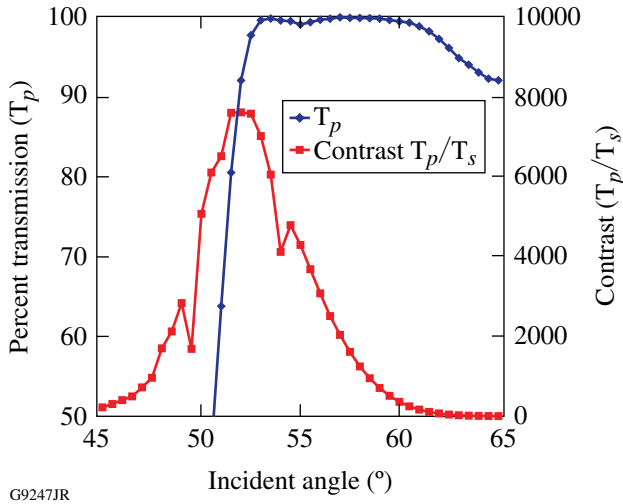


Figure 126.54

Photometric measurement of short-pulse polarizer Z011 installed on OMEGA EP, utilizing alumina for stress control in a dry environment. This polarizer coating provides high transmission and contrast over a wavelength range of 30 nm with incident 1053-nm light.

Laser-damage testing of this coating using a 1053-nm laser with s -polarized light in a 1:1 mode indicated damage thresholds of greater than 74 J/cm² when tested at 1 ns (clean sites, with no testing performed above this fluence) and 44 J/cm² when targeting defects visible using dark-field microscopic inspection.¹⁶ Transmitted laser-damage tests in p -polarization remained above 20 J/cm². Stress measurements indicate the coating on a BK7 substrate maintains a compressive stress of approximately -100 MPa when measured in an N₂-purged environment at 0% relative humidity. This controlled compressive stress provides a coating that will not fail in tension, even when used in a vacuum environment. As noted previously, the slow drift in film stress as a function of drying time makes it very difficult to accurately determine the stress, with an expected measurement uncertainty of ± 20 MPa.

While this coating effort was highly effective—far exceeding the performance requirements for this component—the use of alumina poses significant challenges to the successful implementation in the laser system. The diffusion-barrier properties of the coating significantly restrict the movement of water into and out of the film structure, leading to very slow changes in the coating stress and photometric performance as the relative humidity changes. This change in photometric performance was measured for the polarizer coating, initially stored in an ambient-humidity environment, over a period of multiple days in an N₂-purged, 0%-relative-humidity environment as shown in Fig. 126.55. The coating performance undergoes a substantial change in photometric performance, requiring days or even weeks of recovery time if the optic is stored for long periods in an ambient-humidity environment. Provided the water penetration is slow, short exposure times during installation and alignment can be overcome relatively quickly.

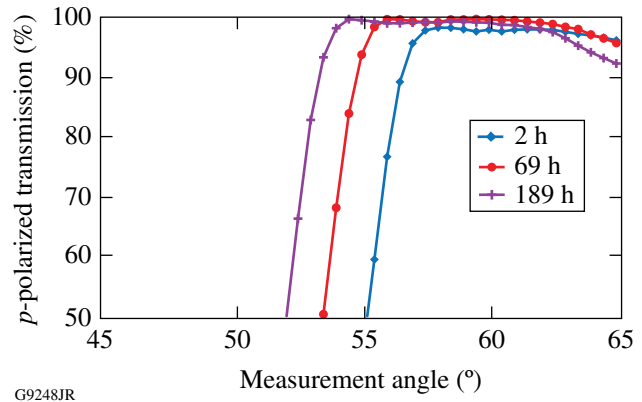
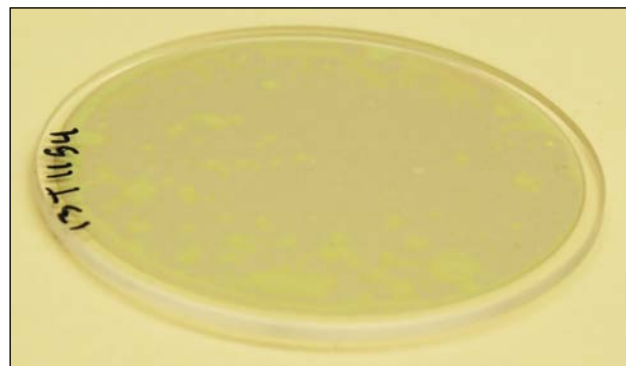


Figure 126.55

Change in photometric performance of a hafnia/silica polarizer coating containing alumina layers. Note that similar to the stress changes in Fig. 126.52, the optical performance of the coating changes significantly over an extended period of time in a dry nitrogen environment. In this case, measurements were performed over a period of approximately 8 days.

The slow drift in performance may be overcome by maintaining the storage and transport of such coatings in a dry atmosphere, while minimizing exposure to humid air during installation and use. Initial evaluation suggests the movement of water into the coating also takes place over a long time scale, as evidenced by the “mottled” appearance that develops as the coating is exposed to moist, ambient air. It is understood that moisture penetration through defect sites in the coating leads to the localized exchange of water for void in the coating, resulting in an increase in the optical thickness and a change

in the color of the coating as shown in Fig. 126.56. Over time, diffusion of the water within the coating structure will bring the water content in the coating to equilibrium, with the coating once again appearing to be a consistent color as the individual moisture-penetration sites through the diffusion barrier coalesce, eliminating the mottled appearance. Alumina is a highly effective diffusion barrier to water penetration and, as such, may require many days of exposure to moist air before the coating once again appears uniform. As shown in Fig. 126.56, a hafnia/silica coating containing alumina barrier layers continues to exhibit a mottled appearance 2 days after deposition. The alumina is quite dense, with isolated defects providing a path for the moisture through the layer, with the surrounding hafnia/silica layers in the multilayer remaining relatively porous.



G9249JR

Figure 126.56
Multilayer dielectric coating containing alumina layers 2 days after deposition. Note the “mottled” appearance of the coating color in reflection, indicating an irregular absorption of water into the coating structure.

Conclusions

The inclusion of alumina layers in standard hafnia/silica high-reflectance coatings leads to a significantly more compressive overall film stress, enabling one to use such coatings in vacuum environments on low-thermal-expansion substrates without the risk of tensile-stress failure causing cracking, or crazing, of the film. The use of multiple designs incorporating different numbers of layers, numbers of interfaces, and thicknesses of the constituent materials provides the opportunity to determine the individual contributions of hafnia, silica, and alumina to the overall stress in the multilayer optical coating—a contribution found to be very different than that expected by monolayer stresses. Additionally, interfacial

effects were incorporated to account for the inhomogeneous film stresses as each layer was formed. Such calculations, while likely not appropriately allocating the stress contributions of each material, have been demonstrated to provide a somewhat predictive ability for arbitrary multilayer coating designs. The stress in hafnia/silica coating designs, including alumina stress compensation layers, has been demonstrated to agree with theoretical predictions, and hafnia/silica/alumina films can be manufactured without degradation of spectral performance or laser-damage resistance. This process was used to produce large-aperture polarizer coatings for use in an N_2 -purged environment on OMEGA EP. It has been shown that such coating designs may be readily implemented using standard electron-beam evaporation systems, are easily scaled to large-aperture substrates, and provide a means of addressing the need for vacuum-use coatings in pulse-compressed laser systems. The slow diffusion of water in such coatings poses some difficulties in implementation, but this may be overcome by storage in a low-relative-humidity environment.

ACKNOWLEDGMENT

The authors wish to express their appreciation to Alex Maltsev for his efforts on the fabrication of extremely high quality, high-aspect-ratio substrates for this study.

This work was supported by the U.S. Department of Energy Office of Inertial Confinement Fusion under Cooperative Agreement No. DE-FC52-08NA28302, the University of Rochester, and the New York State Energy Research and Development Authority. The support of DOE does not constitute an endorsement by DOE of the views expressed in this article.

REFERENCES

1. R. Chow *et al.*, *Appl. Opt.* **32**, 5567 (1993).
2. J. F. Anzellotti, D. J. Smith, R. J. Sczupak, and Z. R. Chrzan, in *Laser-Induced Damage in Optical Materials: 1996*, edited by H. E. Bennett *et al.* (SPIE, Bellingham, WA, 1997), Vol. 2966, pp. 258–264.
3. J. B. Oliver, J. Howe, A. Rigatti, D. J. Smith, and C. Stolz, in *Optical Interference Coatings*, OSA Technical Digest (Optical Society of America, Washington, DC, 2001), Paper ThD2.
4. J. B. Oliver, A. L. Rigatti, J. D. Howe, J. Keck, J. Szczepanski, A. W. Schmid, S. Papernov, A. Kozlov, and T. Z. Kosc, in *Laser-Induced Damage in Optical Materials: 2005*, edited by G. J. Exarhos *et al.* (SPIE, Bellingham, WA, 2005), Vol. 5991, pp. 394–401.
5. J. B. Oliver, S. Papernov, A. W. Schmid, and J. C. Lambropoulos, in *Laser-Induced Damage in Optical Materials: 2008*, edited by G. J. Exarhos *et al.* (SPIE, Bellingham, WA, 2008), Vol. 7132, p. 71320J.
6. H. Leplan *et al.*, *J. Appl. Phys.* **78**, 962 (1995).

7. D. J. Smith, M. McCullough, C. Smith, T. Mikami, and T. Jitsuno, in *Laser-Induced Damage in Optical Materials: 2008*, edited by G. J. Exarhos *et al.* (SPIE, Bellingham, WA, 2008), Vol. 7132, p. 71320E.
8. E. Lavastre *et al.*, in *Optical Interference Coatings*, OSA Technical Digest (Optical Society of America, Washington, DC, 2004), Paper TuF3.
9. J. B. Oliver, P. Kupinski, A. L. Rigatti, A. W. Schmid, J. C. Lambropoulos, S. Papernov, A. Kozlov, and R. D. Hand, in *Optical Interference Coatings*, OSA Technical Digest (Optical Society of America, Washington, DC, 2010), Paper WD6.
10. M. Henyk, D. Wolframm, and J. Reif, *Appl. Surf. Sci.* **168**, 263 (2000).
11. M. Reichling, A. Bodemann, and N. Kaiser, *Thin Solid Films* **320**, 264 (1998).
12. R. Thielsch, A. Gatto, J. Herber, and N. Kaiser, *Thin Solid Films* **410**, 86 (2002).
13. G. G. Stoney, *Proc. R. Soc. Lond. A* **82**, 172 (1909).
14. J. W. Hutchison and T. Y. Wu, eds. *Advances in Applied Mechanics*, Vol. 29 (Academic Press, San Diego, CA, 1992).
15. M. Ohring, *Materials Science of Thin Films: Deposition and Structure*, 2nd ed. (Academic Press, San Diego, 2002), pp. 723–730.
16. S. Papernov and A. W. Schmid, *J. Appl. Phys.* **82**, 5422 (1997).
17. J. Proost and F. Spaepen, *J. Appl. Phys.* **91**, 204 (2002).
18. Y. Shen *et al.*, *Rare Met. Mater. Eng.* **36**, 412 (2007).
19. J. B. Oliver and D. Talbot, *Appl. Opt.* **45**, 3097 (2006).
20. D. J. Smith, A. Staley, R. Eriksson, and G. Algar, in *Proceedings of the 41st Annual Technical Conference of the Society of Vacuum Coaters* (Society of Vacuum Coaters, Albuquerque, NM, 1998), pp. 193–196.
21. A. V. Tikhonravov and M. K. Trubetskov, OptiLayer Thin Film Software, Optilayer Ltd., <http://www.optilayer.com> (9 June 2005).

Langmuir Turbulence and Suprathermal Electron Production from the Two-Plasmon-Decay Instability Driven by Crossed Laser Beams in an Inhomogeneous Plasma

It is currently a time of great anticipation for inertial confinement fusion (ICF) research. An attempt to demonstrate ignition will likely be made at the National Ignition Facility (NIF) within the year.¹ Ignition will be attempted first in indirect-drive geometry (where the laser energy is first converted to soft x rays that drive the target), with an attempt in direct-drive geometry (where the laser directly illuminates the target) likely to occur later. In both approaches, uncertainties with regard to laser-plasma instabilities remain a serious concern. This article presents new results regarding two-plasmon-decay (TPD) instability, which is perhaps the most-serious instability for direct-drive ICF targets. TPD instability is the decay of a laser photon into two Langmuir waves (plasmons). The plasma turbulence driven by TPD produces suprathermal electrons, which can preheat the target, reducing its compressibility and negatively impacting performance.^{2–4} While TPD instability has been unambiguously observed in recent direct-drive experiments (at LLE’s OMEGA Laser Facility), in which diagnostic evidence includes the simultaneous observation of odd half-harmonic radiation and hard x rays attributable to hot-electron generation,⁵ it is not currently possible to test at the NIF scale. This makes the calculation of hot-electron generation by TPD in relevant parameter regimes highly valuable.

In previous papers, we have studied two nonlinear models of TPD in regimes relevant to the LLE experiments: (1) the extended Zakharov model (ZAK)—a reduced fluid-like model with no nonlinear kinetic effects,^{6–8} and (2) the fully kinetic reduced-description particle-in-cell (RPIC) model.⁹ It is noted here that the ZAK model has been derived directly from the RPIC model as a limiting case, primarily for weak laser drives.⁹ The significant nonlinear processes, noted in Ref. 9, included Langmuir decay instability (LDI), wherein the TPD Langmuir waves (LW’s) parametrically decay into another LW and an ion-acoustic wave (IAW). The RPIC simulations in Ref. 9 showed significant kinetic effects, such as hot-electron generation by the excited Langmuir turbulence.

This article presents new results concerning TPD instability having three key novel components. First, TPD is excited by

overlapped (crossed) laser beams, which is a generic and important feature of directly driven ICF.^{9,10} Second, it includes the effects of plasma inhomogeneity. Finally, the TPD-generated flux of suprathermal electrons and their energy spectrum are explicitly computed (tolerable levels of preheat in direct-drive designs at the NIF scale are at a level of 400 J). Included in the results is a detailed description of the structure of the nonlinear state of LW turbulence that will facilitate the construction of further-reduced models. These results have been made possible by extending the RPIC model⁹ to include these effects. The Zakharov model applied to inhomogeneous plasmas^{7,11} predicted, in addition to nonlinear effects mentioned above,^{6–8} significant electron-density profile modification caused by the ponderomotive pressure of the LW’s; this modification moved the ensuing turbulent region from densities near $n_c/4$ [$n_c = m_e \omega_0^2 / (4\pi e^2)$ is the critical density] to densities that were sufficiently low enough to stabilize TPD by Landau damping (the so-called Landau cutoff). This profile modification occurs on an ion-acoustic time scale and requires integration times of several tens of picoseconds (ps). The identification of the primary TPD LW’s and secondary nonlinear fluctuations, such as those caused by LDI, involves the Fourier spectra of the LW envelope and low-frequency electron-density fields, similar to the procedure in Ref. 9, and will be demonstrated elsewhere.¹²

For all of the two-dimensional (2-D) simulations considered here, the plasma consisted of a linear gradient with electron density n_e/n_c varying from 0.19 to 0.27 over an axial (x) extent of 45 μm , resulting in a gradient scale length $L_n \approx 130 \mu\text{m}$. The transverse (y) extent of the plasma was 10 μm and the temperatures $T_{e0} = 2 \text{ keV}$ and $T_{i0} = 1 \text{ keV}$. The incident pump laser light consisted of spatially uniform plane waves propagating at angles $\pm 23^\circ$ with respect to the x axis, each with a fluence of I_0 and wavelength $\lambda_0 = 351 \text{ nm}$, with polarizations in the x - y plane. The linear density gradient under consideration was compatible with the frequency envelope representation of the LW fields because the electron-plasma frequency varied by $\sim \pm 4\%$ about the reference envelope frequency, chosen to be in the center of the simulation domain for which $n_e/n_c = 0.23$. The linear energy growth rate γ versus (beamlet) fluence I_0 was

obtained from a series of RPIC simulations in which only I_0 was varied. A very good fit to these data is given by the best-fit empirical expression $\gamma(I_0) = \gamma_0(I_0/I_{\text{thres}} - 1)$, where $I_{\text{thres}} \approx 1 \times 10^{15} \text{ W/cm}^2$ and $\gamma_0 \approx 5.8 \text{ ps}^{-1}$. A more-detailed discussion of the RPIC thresholds and the influence of discrete particle effects will be given elsewhere.¹² It is observed in all of our RPIC simulations that above threshold ($I_0/I_{\text{thres}} > 1$), Langmuir cavitation and collapse are observed at very early times (comparable to the e -folding time of the linear TPD growth), even for cases just above the TPD threshold, and appear to be primarily responsible for suprathermal electron production and nonlinear saturation of TPD.

A representative RPIC simulation with $I_0/I_{\text{thres}} = 2$ is analyzed in detail to illustrate our results. To quantify whether Langmuir cavitation actually occurs, we compute the ‘‘caviton correlator’’ (Ref. 13):

$$C(x,t) = \langle -\delta n |E_{\text{LW}}|^2 \rangle_y / \left[\langle (\delta n) \rangle_y^{1/2} \langle |E_{\text{LW}}|^2 \rangle_y \right],$$

where the operator $\langle \rangle_y$ denotes averaging in the transverse (y) direction, δn is the low-frequency electron-density perturbation, and E_{LW} is the LW field envelope. A *caviton* is essentially a local maximum of $|E_{\text{LW}}|^2$, spatially coincident with a local minimum of δn (i.e., $\delta n < 0$). Figure 127.1 plots $C(x,t)$, $E_{\text{LW}}(x,y)$, and $\delta n(x,y)$ at $t = 20 \text{ ps}$. The solid curve on the top panel represents the spatiotemporal evolution of the quarter-critical surface. The boxes in the middle and bottom panels mark regions where Langmuir cavitation and collapse will be examined in greater spatial detail (see Fig. 127.3). As indicated in the top panel of Fig. 127.1, Langmuir cavitation and collapse are observed within a short time ($t < 1 \text{ ps}$) and are observed to be accompanied by the production of suprathermal electrons after a short delay ($\tau < 2 \text{ ps}$), leading to nonlinear saturation of TPD, while throughout this process, the IAW’s

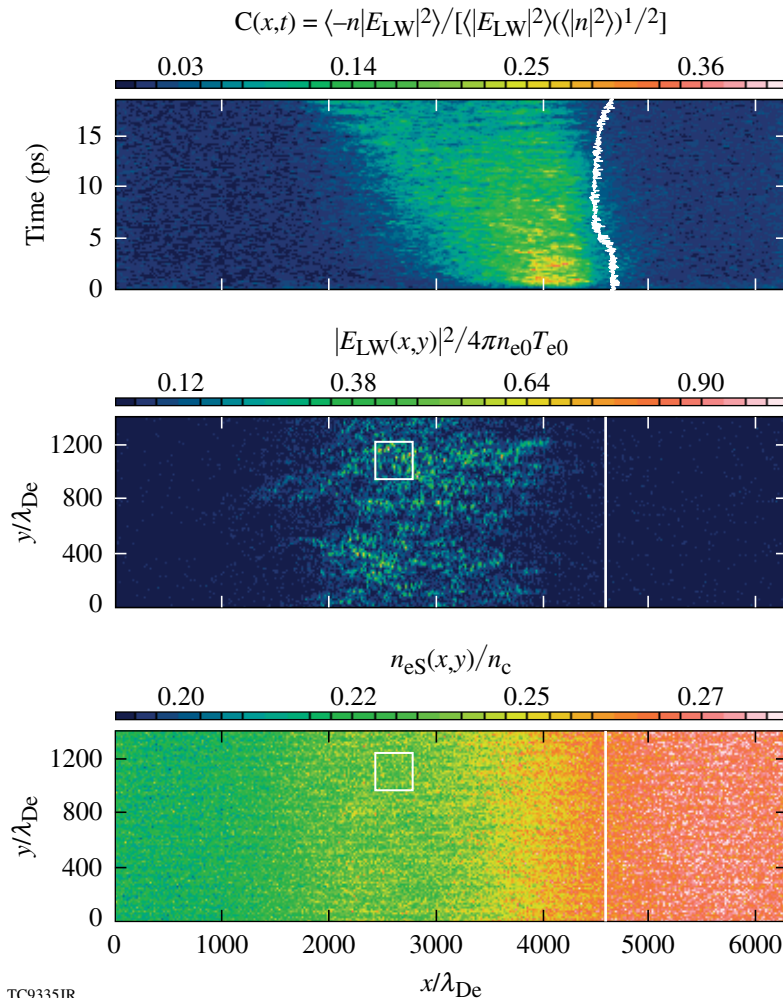


Figure 127.1

Plots of the caviton correlator $C(x,t)$, LW energy density, and the low-frequency density fluctuation at $t = 20 \text{ ps}$. The solid curve on the top panel represents the spatiotemporal evolution of the quarter-critical surface. The boxes in the middle and bottom panels mark regions where Langmuir cavitation and collapse will be examined in greater spatial detail (see Fig. 127.3). Langmuir cavitation and collapse are observed to occur for $2000 < x/\lambda_{\text{De}} < 4000$.

participating in LDI have weak Fourier spectral amplitudes. The ponderomotive beating of the obliquely propagating laser waves produces a standing-wave pattern, which manifests itself as density channels on the background plasma seen in the bottom panel of Fig. 127.1. Langmuir cavitation and collapse occur preferentially in these density channels and in sufficiently strongly driven cases, can lead to “kinking” of these initially straight channels, perhaps signaling that the channels will self-focus or filament in three-dimensional (3-D) simulations. Plots of the caviton correlation as a function of density and time (not shown) indicate that LW activity peaks at $n_e/n_c \sim 0.24$, where the forward TPD LW’s become degenerate and overlap for laser-propagation angles of $\pm 23^\circ$ and $T_{e0} = 2$ keV (Refs. 9–12). In addition to $C(x,t)$ shown in Fig. 127.1, which indicates that all Langmuir cavitation and collapse occur in the active region $2000 < x/\lambda_{De} < 4000$, one can perform a statistical analysis by defining (for the purposes of this study) a caviton as a spatial local maximum of $|E_{LW}(x,y)|^2$ that exceeds $10\times$ the average LW energy density in the active region. All local maxima identified as cavitons by this criterion are plotted as a caviton-distribution function versus the normalized LW energy density $|E_{LW}|^2/4\pi n_{e0}T_{e0}$. Interestingly, it is found that cavitons follow Gaussian statistics for all RPIC simulations under consideration at each given time. In addition, the heated-electron distribution is found to be bi-Maxwellian. As an example, caviton statistics and the heated-electron-distribution function, at $t = 13$ ps, for the simulation described in Fig. 127.1, are shown in Fig. 127.2. The average LW energy density in the active region is $\langle |E_{LW}|^2 \rangle / 4\pi n_{e0}T_{e0} \sim 0.05$, and cavitons are distributed according to $F(|E_{LW}|^2) \propto \exp(-|E_{LW}|^2/4\pi n_{e0}T_{e0}\epsilon)$, where $\epsilon \approx 0.135$. The v_y -averaged electron distribution shows a bi-Maxwellian distribution with a bulk temperature of $T_{\text{bulk}} \approx 1.1 T_{e0} = 2.2$ keV (slightly heated above T_{e0}) and a suprathermal

electron temperature $T_{\text{hot}} \approx 30 T_{e0} = 60$ keV. It is observed that T_{hot} depends on the strength of the laser drive and not on the kinetic energy associated with the phase velocity of the primary LW.

The electric-field intensity $|E(x,y)|^2$ is very spiky, with about 10^4 cavitons (by the above criterion) present in the active region at any given time after the system reaches saturation. Some of these cavitons can proceed to collapse and “burn out,” wherein all the electrostatic energy is given up to accelerated electrons. It has been argued that in 2-D, cavitons must gather a finite amount of electrostatic energy before collapse can occur, whereas in 3-D, this threshold energy is zero. In 3-D, collapse events are expected to be weaker but more numerous.¹⁴ Magnification of a spatial region where caviton activity is observed is shown in Fig. 127.3. Several stages of the nucleation–collapse–burnout caviton cycle are observed simultaneously. Frequency spectral diagnostics of the LW envelope fields were employed in corresponding ZAK simulations, which show significant LW energy for frequencies below the local electron-plasma frequency—an unambiguous signature of collapse.^{13,14} Finally, the time history of the suprathermal heat flux through simulation boundaries indicates that the simulation is slowly approaching a nonlinear saturated state with $\sim 1.5\%$ of the input laser fluence converted into suprathermal heat flux at 20 ps.

In summary, we have performed a number of RPIC simulations with varying laser fluences for the parameters listed above. Our simulations, spanning a wide range of laser fluences ($I_0/I_{\text{thres}} = 1$ to 4), indicate the following salient features, which are also qualitatively observed in Zakharov simulations¹² and quasi-linear Zakharov simulations.¹⁵ First, the ponderomotive beating of the crossed laser beams creates a standing wave

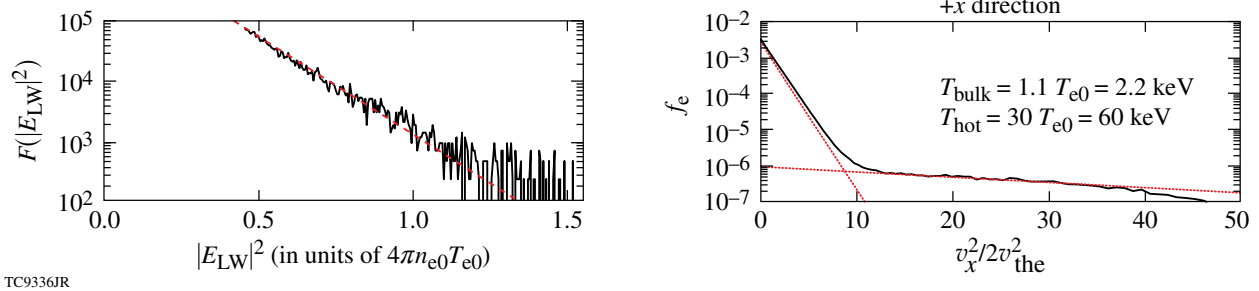
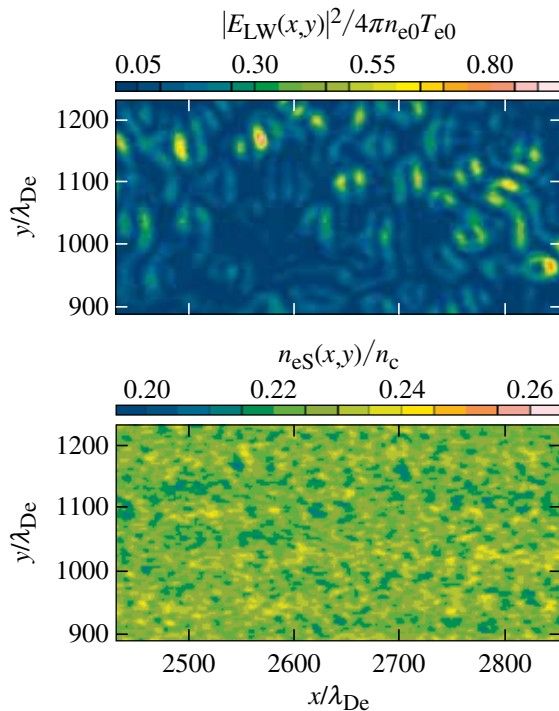


Figure 127.2

Caviton statistics and the heated-electron-distribution function at $t = 13$ ps. The spatial average LW energy density in the active region is $\langle |E_{LW}|^2 \rangle / 4\pi n_{e0}T_{e0} \sim 0.04$, and cavitons follow the distribution $F(|E_{LW}|^2) \propto \exp(-|E_{LW}|^2/4\pi n_{e0}T_{e0}\epsilon)$, where $\epsilon \approx 0.135$. The total number of cavitons $N = \int_{\epsilon_{\text{min}}}^{\infty} F(|E_{LW}|^2) d(|E_{LW}|^2)$. The v_y -averaged electron distribution shows a bi-Maxwellian distribution with a bulk temperature of $T_{\text{bulk}} \approx 1.1 T_{e0} = 2.2$ keV (slightly heated above the initial temperature) and a suprathermal electron temperature $T_{\text{hot}} \approx 30 T_{e0} = 60$ keV.



TC9337JR

Figure 127.3

Magnification of a spatial region where caviton activity is observed (marked by the boxes in the middle and bottom panels of Fig. 127.1). Several stages of nucleation and collapse are observed simultaneously.

pattern, manifested as density channels in which Langmuir cavitation and collapse preferentially occur. Second, Langmuir cavitation and collapse occur at early times ($t < 1$ ps), accompanied by suprathermal electron production and nonlinear saturation of TPD. These observations lead us to the preliminary conclusion that LDI, which is observed in the low-frequency density-fluctuation spectrum for stronger drive, plays a secondary role in the nonlinear saturation of TPD in the regimes studied here. (A more-complete understanding of the competition of cavitation, collapse, and LDI, along with their contribution to electron acceleration, warrants further study.) Third, cavitons are shown to follow Gaussian statistics, a general observation in both RPIC and ZAK simulations, regardless of drive strength (as long as the drives are sufficiently strong to cause Langmuir cavitation). The suprathermal electron-distribution function is observed in all cases to be bi-Maxwellian, with hot temperatures reaching 60 to 100 keV in our simulations. The suprathermal heat flux out of the simulation domain, normalized to the overlapped laser fluence, achieved values of 0.5% to 2% for the RPIC simulations considered here. Langmuir collapse and burnout provide the dissipation (into fast electrons) that stabilizes the system in saturation and drives the LW spectrum to the small dissipation scales at the “Landau cutoff.”

ACKNOWLEDGMENT

This research was supported by the U.S. Department of Energy, Office of Inertial Confinement Fusion under Cooperative Agreement No. DE-FC52-08NA28302, the University of Rochester, and the New York State Energy Research and Development Authority, and the National Nuclear Security Agency through its High-Energy-Density Laboratory Plasmas Grant No. DE-FG52-09NA29545. The support of DOE does not constitute an endorsement by DOE of the views expressed in this article.

REFERENCES

1. S. H. Glenzer *et al.*, Phys. Rev. Lett. **106**, 085004 (2011).
2. J. A. Delettrez, V. N. Goncharov, P. B. Radha, C. Stoeckl, A. V. Maximov, T. C. Sangster, J. A. Frenje, and D. Shvarts, Bull. Am. Phys. Soc. **53**, 248 (2008).
3. V. A. Smalyuk, D. Shvarts, R. Betti, J. A. Delettrez, D. H. Edgell, V. Yu. Glebov, V. N. Goncharov, R. L. McCrory, D. D. Meyerhofer, P. B. Radha, S. P. Regan, T. C. Sangster, W. Seka, S. Skupsky, C. Stoeckl, B. Yaakobi, J. A. Frenje, C. K. Li, R. D. Petrasso, and F. H. Séguin, Phys. Rev. Lett. **100**, 185005 (2008).
4. B. Yaakobi, C. Stoeckl, W. Seka, J. A. Delettrez, T. C. Sangster, and D. D. Meyerhofer, Phys. Plasmas **12**, 062703 (2005).
5. W. Seka, D. H. Edgell, J. F. Myatt, A. V. Maximov, R. W. Short, V. N. Goncharov, and H. A. Baldis, Phys. Plasmas **16**, 052701 (2009).
6. D. F. DuBois, D. A. Russell, and H. A. Rose, Phys. Rev. Lett. **74**, 3983 (1995).
7. D. A. Russell and D. F. DuBois, Phys. Rev. Lett. **86**, 428 (2001).
8. D. A. Russell, D. F. DuBois, and H. X. Vu, presented at the Workshop on SRS/SBS Saturation, Livermore, CA, 2–5 April 2002.
9. H. X. Vu, D. F. DuBois, D. A. Russell, and J. F. Myatt, Phys. Plasmas **17**, 072701 (2010).
10. R. W. Short, Bull. Am. Phys. Soc. **54**, 144 (2009).
11. J. F. Myatt, J. Zhang, J. A. Delettrez, A. V. Maximov, R. W. Short, W. Seka, D. H. Edgell, D. F. DuBois, D. A. Russell, and H. X. Vu, “The Dynamics of Hot-Electron Heating in Direct-Drive Implosion Experiments Due to the Two-Plasmon-Decay Instability,” submitted to Physics of Plasmas.
12. H. X. Vu, D. F. DuBois, J. F. Myatt, and D. A. Russell, “Kinetic Simulations of the Nonlinear Evolution of the Two-Plasmon-Decay Instability in an Inhomogeneous Plasma,” to be submitted to Physics of Plasmas.
13. D. F. DuBois, H. A. Rose, and D. A. Russell, Phys. Scr. **T63**, 16 (1996).
14. D. F. Dubois *et al.*, J. Geophys. Res. **98**, 17,543 (1993).
15. K. Y. Sanbonmatsu *et al.*, Phys. Plasmas **7**, 2824 (2000) and references therein.

Demonstration of a Closed-Loop Beam-Shaping System Based on the Phase-Only Carrier Method in High-Power Lasers

Beam-shaping applications in high-power laser systems have been presented in many different contexts such as the improvement of laser performance¹ or the manipulation of laser-target interactions.^{2,3} These applications commonly employ static apodizers or deformable mirrors. Spatial-light modulators (SLM's) are also popular beam-shaping devices. Because of their low damage threshold and small aperture, they have been used in laser front ends⁴ or inside laser cavities.⁵ The advantage of SLM beam shapers lies in programmability and high spatial resolution, allowing for extremely fine control of the laser-beam profile. This is an especially important feature for maximizing the performance of high-power lasers. Defects or damages sites in the compressor gratings⁶ or final optics assembly⁷ often limit laser operation to a lower energy level. At the National Ignition Facility^{8,9} efforts have been made to address this problem by introducing a programmable spot-shadowing system at an upstream image plane. An SLM-based beam-shaping system combined with closed-loop control has been recently demonstrated in a test-bed setup.^{10,11} We have implemented this system in a multiterawatt laser¹² and at the front end of OMEGA EP's long-pulse beamlines.¹³ This effort has revealed a few important issues that need to be addressed for applications in high-power laser systems. Among these, the problem of image distortion will be discussed here, followed by the problem of determining the damage threshold of an SLM device.

Previous work on adaptive beam shaping presented an algorithm based on direct linear mapping between the measured fluence and the command map of an SLM.¹¹ The motivation for direct mapping is to avoid characterizing the enormous number of influence functions associated with an SLM. A linear transformation is experimentally shown to be accurate enough for the imaging systems considered in high-power laser systems. Higher-order distortions such as barrel/pincushion distortions are negligible if the laser beams are image relayed with slow optics. On the other hand, image-distortion effects associated with the presence of tilted plates or wedges in the system are important for this application. As shown in Fig. 127.4, tilted plates/wedges introduce not only astigmatic image blurring¹⁴

but also image shear. Such elements, e.g., beam diagnostic pickoffs, thin-film polarizers, or amplifier slabs, are ubiquitous in high-power lasers. The image shear can be represented as a linear transformation as follows:

$$\begin{pmatrix} x' \\ y' \end{pmatrix} = \begin{pmatrix} 1 & \sigma \\ 0 & 1 \end{pmatrix} \begin{pmatrix} x \\ y \end{pmatrix},$$

where σ is a shear parameter. This linear transformation can be combined with other linear transformations such as translation, magnification, and rotation. As a result, the sheared image can be numerically corrected. The transformation parameters are found by comparing a known phase or amplitude pattern introduced on the SLM and the measured pattern at the diagnostic image by running an optimization routine.

The blurring is caused by the axial astigmatism in the imaging system; i.e., the foci at sagittal and tangential planes are at different locations. Numerical simulations show that the severity of the blurring in the case of parallel plates is proportional to the tilt angle and the thickness of the plate. The wedged plate introduces an additional dependence of the blurring on the wedge angle and the distance from the image plane. Since the blurring limits the resolution of the beam profile to be shaped, it is best to design the optical system to minimize the axial astigmatism. It is possible to significantly reduce the effect by

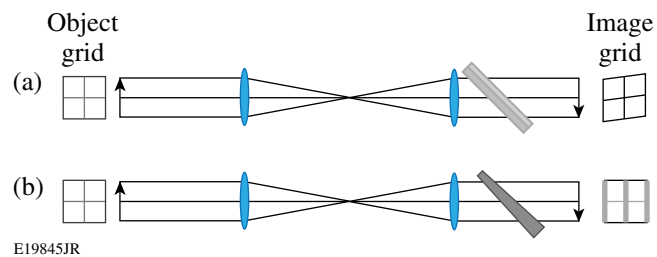


Figure 127.4 Arrangement of wedges and the effects on imaging. A rectangular grid is imaged by a 1-to-1 telescope, where a wedge is placed immediately behind the second lens. The affected image is shown on the right. (a) Image shear occurs when the wedge is placed vertically at an angle. (b) Image blurring occurs in one direction as indicated by the thicker vertical bars in the image grid.

using a compensator plate/wedge,¹⁵ for example, a compensator wedge with the opposite angle.

A schematic of the experimental layout in a multiterawatt system¹² is shown in Fig. 127.5. The laser system is based on optical parametric chirped-pulse amplification (OPCPA) followed by a glass amplifier and compressor chamber. The closed-loop SLM beam-shaping system was implemented using two near-field image feedbacks, one (WFS1 in Fig. 127.5) placed nearby the SLM device and the other (WFS2 in Fig. 127.5) placed at the end of the system before the target chamber. The OPCPA laser beam is image relayed through the glass amplifier to the compressor chamber by three imaging telescopes. There are additional image relays on the diagnostic lines for WFS1 and WFS2 (in the dashed boxes).

The OPCPA front end produces 200-mJ pulses at 5 Hz. Only 10% of full OPCPA energy was used for this experiment and the glass amplifier was turned off. The SLM is an electrically addressed [liquid-crystal-on-silicon (LCOS)], nematic-type liquid crystal made by Hamamatsu. The SLM has 600×792 points, whereas the wavefront sensors have 130×130 sampling points. The wavefront sensors also provide near-field images with the same sampling as wavefront. The case of producing a

flat-top-profile laser beam was first demonstrated with WFS1. The diagnostic imaging system for WFS1 has a wedged leaky mirror that initially caused large spatial registration errors because of the image blurring. A secondary wedge compensator was inserted to restore the image quality. The result of flat-beam shaping is shown in Fig. 127.6. Within the flat area, the peak-to-mode improved from 39% to 12% and the relative rms (root mean square) improved from 9% to 3%.

Closed-loop control with WFS2 proved to be more difficult than with WFS1 because of the axial astigmatism in the system. The astigmatism comes not so much from the amplifier slabs because it is actually minimized by the orthogonal configuration of the slabs on the second pass of the beam. Ray tracing suggests that the astigmatism comes primarily from the compressor gratings. Calculations show that a 20-cm-thick, 1.5° wedge is needed as a compensator, which is not easily available. Therefore, the resolution of the calculated command map on the SLM was intentionally blurred to match the system resolution, which is necessary to prevent the ripple problem of the closed-loop control shaping.¹¹ The fluence distribution improved from 44% to 25% in peak-to-mode as shown in Figs. 127.7(a) and 127.7(b).

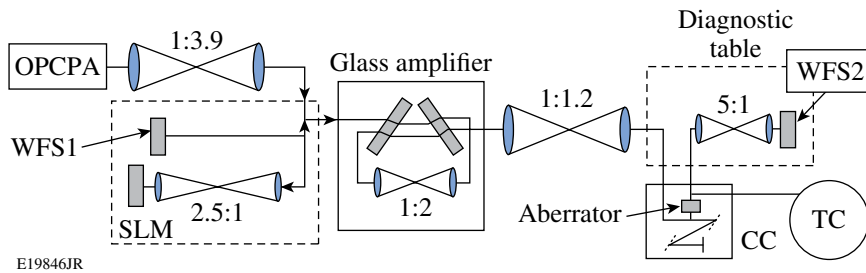


Figure 127.5
Experimental setup for demonstrating an SLM beam shaper in a multiterawatt laser system. CC: compressor chamber; TC: target chamber; WFS: wavefront sensor.

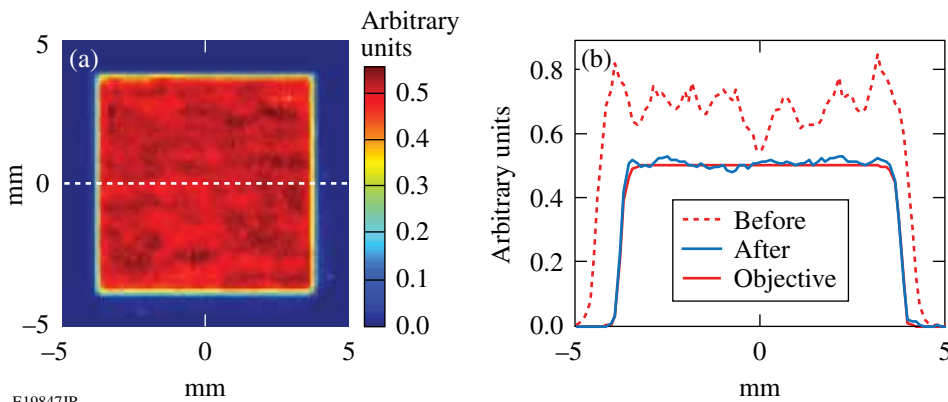
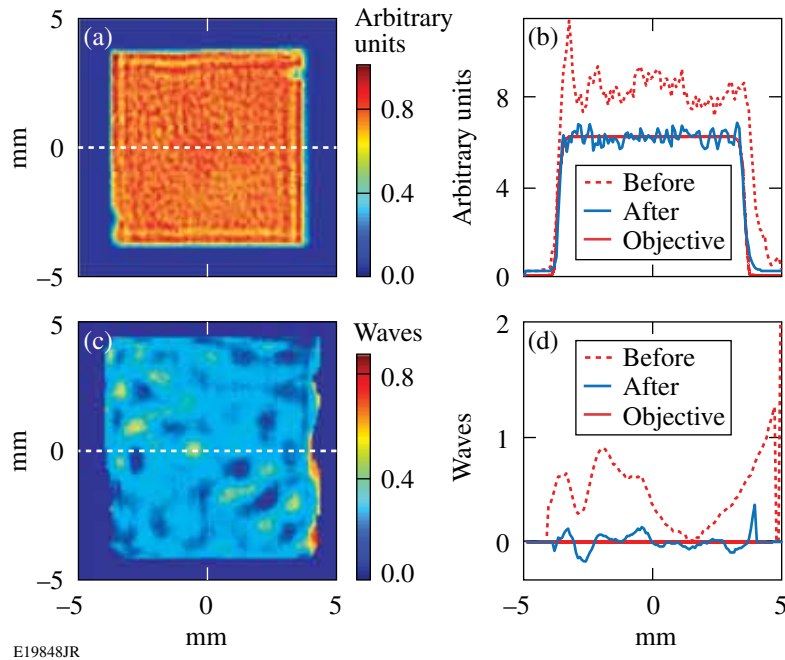


Figure 127.6
Flat-beam shaping with WFS1 (multi-terawatt system). (a) Fluence after shaping; (b) fluence lineouts.

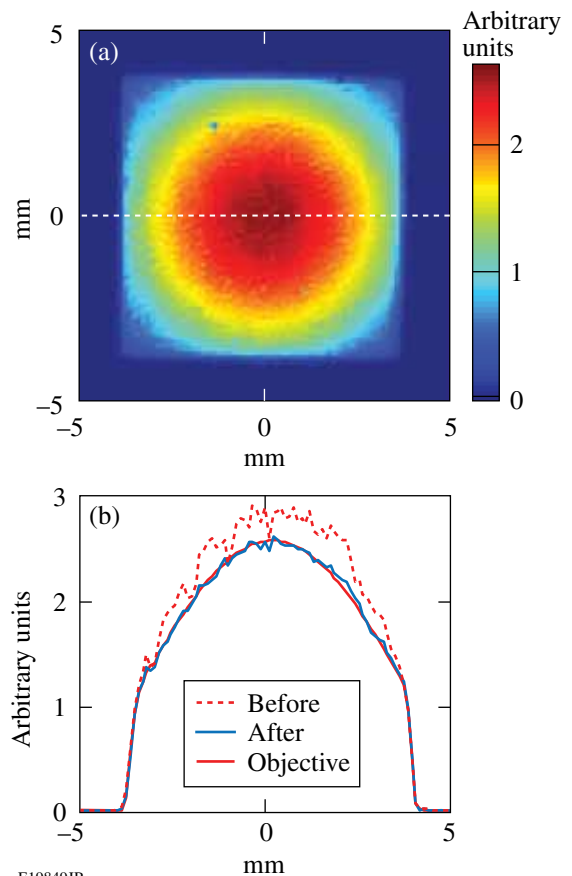


E19848JR

The capability of high-order wavefront correction was tested in WFS2 closed-loop operation. A static wavefront aberrator was manufactured by the magnetorheological finishing process¹² using the map described in Ref. 11. Physical constraints prevented the phase plate from being placed exactly at the image plane of the SLM; therefore, the condition for closed-loop control was not optimum. Nevertheless, the rms value of the wavefront improved from 0.375 waves down to 0.08 waves [Figs. 127.7(c) and 127.7(d)].

The same beam-shaping system has been implemented in the front end of the OMEGA EP long-pulse beamlines. The initial application is to provide intensity smoothing of a beam, which is parabolically shaped by a static apodizer. The parabolic beam shape is used to precompensate for rod-amplifier-gain nonuniformity.¹³ The test confirmed the effectiveness of the direct linear-mapping algorithm for intensity smoothing of a non-flat beam, as shown in Fig. 127.8. A comparable level of convergence error, 2% in relative rms, was achieved as in the OPCPA case. The image shear and rotation were numerically corrected.

Damage-threshold measurements over a small area ($\sim 500 \mu\text{m}$) of an SLM sample with a focused beam resulted in varying values (from 570 mJ/cm^2 to 2 J/cm^2 over ten sites). This suggests that the damage-initiation sites or defects are sparsely distributed over the sample area. The measurement procedure is based on increasing the incident energy by a small step and waiting for a damage spot to occur for minutes of



E19849JR

Figure 127.8
Parabolic beam shaping (OMEGA EP long-pulse front end). (a) Fluence after shaping; (b) fluence lineouts.

duration (a few thousand shots at 5 Hz). The energy is ramped up to the next level until damage is observed where the local fluence for the spot is estimated from the measured laser-beam profile. This procedure often takes several hours for a single site, so it is not practical to perform over hundreds of sites. We performed large-area (~ 5 -mm) damage tests on samples that would effectively enable one to perform hundreds of small-area damage tests in a single ramp-up procedure. The samples were illuminated by 5-Hz, 2.5-ns laser pulses with an $8\text{-mm} \times 8\text{-mm}$ square beam with a flattop profile. The laser pulses were generated from an optical-parametric conversion process at $1.053\text{-}\mu\text{m}$ wavelength. The laser energy on the sample was gradually increased, starting from 50 mJ to 100 mJ in 10-mJ steps. The duration of exposure at each step was 10 min or 3000 shots. The near-field image of the laser beam on the sample was measured every 10 s. The ramping and the short-term exposure continued until a damage site appeared on the near-field image. The local damage fluence at the damage site was calculated based on the separate incident-energy measurement and the calibrated near-field image. The calculated local fluences at the observed damaged sites of the three samples (two of them being under active condition) were 230, 235, and 267 mJ/cm^2 . The minimum of these values can be considered as the damage-threshold fluence. Considering the use area of the SLM to be $\sim 1\text{ cm}^2$ within a $12 \times 16\text{-mm}^2$ total area of the actual device, the total energy the SLM can handle is $\sim 230\text{ mJ}$. The safe energy level can be much lower than this, depending on the local beam modulation of the incident beam.

A successful closed-loop beam shaping was demonstrated in a multiterawatt laser and in an OMEGA EP long-pulse front end. The main issues of implementing an LCOS-SLM beam-shaping system in high-power laser systems have been discussed. It was demonstrated that the imaging-registration problems can be either numerically corrected or avoided by design. The damage threshold of SLM's can be measured by the method described here to ensure safe operations in high-power laser systems. One of the future challenges will be to develop a larger-area or a higher-damage-threshold SLM to accommodate higher-energy operation.

ACKNOWLEDGMENT

This work was supported by the U.S. Department of Energy Office of Inertial Confinement Fusion under Cooperative Agreement No. DE-FC52-08NA28302, the University of Rochester, and the New York State Energy Research and Development Authority. The support of DOE does not constitute an endorsement by DOE of the views expressed in this article.

REFERENCES

1. C. Dorrer, *Opt. Lett.* **34**, 2330 (2009).
2. B. Wattellier *et al.*, *J. Opt. Soc. Am. B* **20**, 1632 (2003).
3. O. Boyko *et al.*, *Opt. Commun.* **246**, 131 (2005).
4. N. Sanner *et al.*, in *Conference on Lasers and Electro-Optics* (Optical Society of America, Washington, DC, 2004), Vol. 1, Paper CTuP34.
5. J. Bourderionnet *et al.*, *Opt. Lett.* **26**, 1958 (2001).
6. J. Qiao, A. W. Schmid, L. J. Waxer, T. Nguyen, J. Bunkenburg, C. Kingsley, A. Kozlov, and D. Weiner, presented at the 2010 International Committee on Ultra-High Intensity Lasers Conference, Watkins Glen, NY, 26 September–1 October 2010 (Paper FO3).
7. A. Conder *et al.*, in *Laser-Induced Damage in Optical Materials: 2007*, edited by G. J. Exarhos *et al.* (SPIE, Bellingham, WA, 2007), Vol. 6720, p. 672010.
8. S.-W. Bahk, J. D. Zuegel, J. R. Fienup, C. C. Widmayer, and J. Heebner, *Appl. Opt.* **47**, 6586 (2008).
9. J. Heebner *et al.*, in *Laser-Induced Damage in Optical Materials: 2010*, edited by G. J. Exarhos *et al.* (SPIE, Bellingham, WA, 2010), Vol. 7842, p. 78421C.
10. V. Bagnoud and J. D. Zuegel, *Opt. Lett.* **29**, 295 (2004).
11. S.-W. Bahk, E. Fess, B. E. Kruschwitz, and J. D. Zuegel, *Opt. Express* **18**, 9151 (2010).
12. V. Bagnoud, M. J. Guardalben, J. Puth, J. D. Zuegel, T. Mooney, and P. Dumas, *Appl. Opt.* **44**, 282 (2005).
13. M. J. Guardalben and L. J. Waxer, in *High Power Lasers for Fusion Research*, edited by A. A. S. Awwal, A. M. Dunne, H. Azechi, and B. E. Kruschwitz (SPIE, Bellingham, WA, 2011), Vol. 7916, Paper 79160G.
14. R. Korniski and J. K. Lawson, in *International Optical Design Conference, 2002 OSA Technical Digest Series* (Optical Society of America, Washington, DC, 2002), Paper ITuD5.
15. J. W. Howard, *Appl. Opt.* **24**, 4265 (1985).

Temporal Contrast Degradation at the Focus of Ultrafast Pulses from High-Frequency Spectral Phase Modulation

Introduction

Ultrafast laser systems generate intensities at focus as high as 10^{22} W/cm² for a variety of relativistic and high-energy-density physics applications. Although several types of amplifiers are used, all systems use chirped-pulse amplification (CPA) to overcome limits caused by optical damage and nonlinearities.¹ CPA uses stretchers and compressors to modify the pulse's spectral phase, increasing its length and lowering the peak power within the amplifier chain. Stretchers and compressors typically rely on diffraction gratings to geometrically disperse the pulse into spectral components.² Imperfections at optical surfaces where the pulse is dispersed imprint directly onto the spectral phase. The group delay of a spectral component equals the derivative of its phase, and therefore high-frequency phase noise scatters energy before and after the main pulse.^{3–6} (This effect is directly analogous to the halo formed around the far field of a lens by high-frequency wavefront noise in the near field.⁷) Any portion scattered before the peak of the pulse that exceeds 10^{11} W/cm² is capable of ionizing solid targets. Therefore, care is needed when selecting stretchers and compressors to ensure they do not degrade the temporal contrast of the laser system, defined as the ratio of the peak of the pulse to the low-intensity pedestal.

This article presents a theoretical analysis of the impact of high-frequency spectral phase modulation on the temporal contrast of ultrafast pulses. A three-dimensional (3-D) treatment is used to extend the results of Ref. 8. The temporal contrast is evaluated in the focal plane, the target location for ultra-intense experiments. The spectral phase imprint in the near field of a spectrally dispersed beam produces space–time coupling in the far field or focal plane. The pedestal is swept across an area in the focal plane many times the size of the diffraction-limited spot. These phenomena raise questions about the validity of applying measurements made in the near field (the usual domain for high-dynamic-range cross-correlators) to the target plane.

A general model is used in the next section to propagate a spectrally dispersed beam through a noisy phase screen.

Expressions are derived for the average intensity of an ultrafast pulse in the near and far fields. In subsequent sections, closed-form results are obtained for Gaussian functional forms that show the impact on temporal contrast of the scale of optical surface modulation, the beam size, and the scale of geometric dispersion in the near field. Analytic results are compared to numeric simulations, and the numeric analysis is extended to include the usual Lorentzian functional form of the power spectral density of optical surfaces. Simulation results are presented for generic stretchers and compressors that show fundamentally different properties of the temporal contrast at the focal plane.

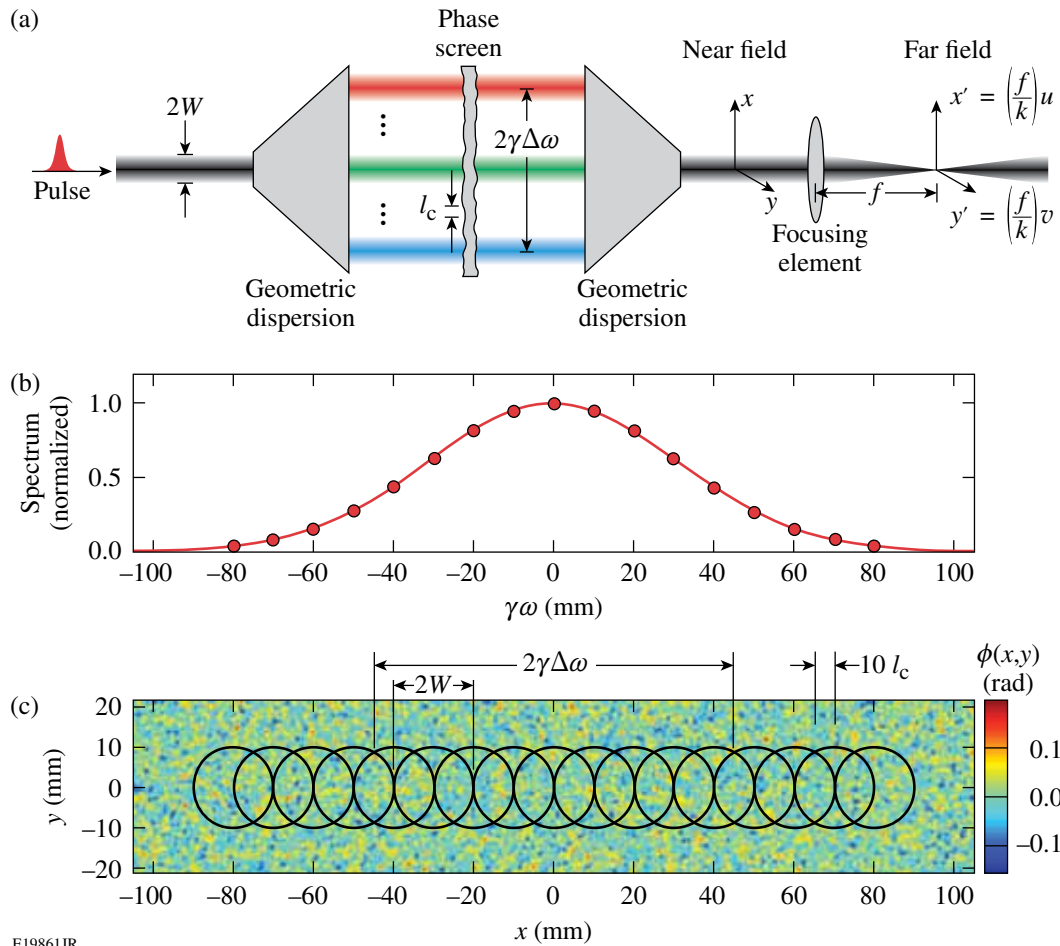
General Expressions for the Temporal Contrast in Near and Far Fields

1. Model

A general schematic of an optical device for spectral phase modification is shown in Fig. 127.9(a). A beam of optical pulses passes through a subsystem that spreads the spectral components using geometric dispersion. The phase of each spectral component is modified using phase screens or other optical systems before a second dispersive component is used to recombine them. Optical pulse stretchers and compressors are examples of this type of device. They modify the chirp of ultrafast pulses by adding or subtracting large, predominantly quadratic spectral phases. High-frequency imperfections in the surface quality of their optics produce unwanted phase modulation. In this article, such imperfections are modeled by adding noisy phase screens to otherwise ideal systems.

A focusing element located in the near field focuses the beam in the far-field plane. The near-field spatial coordinates are (x,y) . The far-field wave-vector components (u,v) are related to the spatial coordinates (x',y') by the focal length f and wave number $k = 2\pi/\lambda$ according to $u = kx'/f$. Figure 127.9(b) shows a Gaussian spectrum spread across the near field. The mapping of spectral components onto the x axis is assumed to be linear. The center of the beam x_0 and a given optical frequency ω are related by

$$x_0(\omega) = \gamma\omega, \quad (1)$$



EI9861JR

Figure 127.9

(a) Generic schematic of a system that imprints spectral phase noise on an optical pulse propagating with a finite beam size. The near-field spatial coordinates are (x, y) and the far-field wave-vector components are (u, v) . Three important scale lengths are (1) $\gamma\Delta\omega$, the spatial width of the dispersed spectrum; (2) W , the beam size; and (3) l_c , the correlation length of the phase noise. (b) Gaussian spectrum plotted against the near-field coordinate x ; $\gamma = 0.44$ mm/THz and $\Delta\omega = 100$ THz, corresponding to a 17-fs pulse width. (c) Simulated phase screen $\phi(x, y)$ and beam locations for optical frequencies marked in (b). Scale lengths are $W = 10$ mm, $l_c = 0.5$ mm, and $\gamma\Delta\omega = 44$ mm.

where γ is the spatio-spectral coefficient. The optical frequency ω is defined as the offset from a central frequency ω_0 , which was arbitrarily chosen to correspond to a central wavelength of 910 nm throughout this article.

Figure 127.9(c) shows a simulated realization of a random phase screen, $\phi(x, y)$. The circles denote the beam locations for the spectral components marked on Fig. 127.9(b). Three scale lengths are shown that are key to understanding the impact of phase noise on temporal contrast:

- $\gamma\Delta\omega$ – the optical bandwidth ($1/e$ half-width), scaled onto the near-field axis
- W – the beam size ($1/e$ intensity half-width)
- l_c – the correlation length of the phase noise

Here, l_c can be defined in terms of the correlation function

$$C(x, x', y, y') = \langle \phi(x, y) \phi^*(x', y') \rangle. \quad (2)$$

For a homogeneous, isotropic Gaussian phase screen, the correlation function is related to the correlation length by

$$C(\Delta x, \Delta y) = \sigma^2 \exp\left(-\frac{\Delta x^2 + \Delta y^2}{2l_c^2}\right), \quad (3)$$

where $\Delta x = x - x'$, $\Delta y = y - y'$, and σ is the rms (root mean square) phase of the screen in radians. Depending on the design of the device, the three scale lengths may differ by an order of magnitude or more.

2. Average Far-Field Intensity

In the spectral domain, the optical field of the pulse in the near field is given by

$$\tilde{E}(x, y, \omega) = \tilde{E}_0(x, y, \omega) e^{i\Phi(x, y, \omega)}, \quad (4)$$

where $\tilde{E}_0(x, y, \omega)$ is the input pulse. The spatio-spectral phase function $\Phi(x, y, \omega)$ is related to the phase screen using Eq. (1):

$$\Phi(x, y, \omega) = \phi(x - x_0, y) = \phi(x - \gamma\omega, y). \quad (5)$$

In the limit of small phase modulation ($\phi \ll 1$), the exponential in Eq. (4) is approximated to give

$$\tilde{E}(x, y, \omega) = \tilde{E}_0(x, y, \omega) [1 + i\phi(x - \gamma\omega, y)]. \quad (6)$$

The optical field in the time domain is obtained by a Fourier transform:

$$\begin{aligned} E(x, y, t) &= \int_{-\infty}^{\infty} d\omega \tilde{E}(x, y, \omega) e^{-i\omega t} \\ &= E_0(x, y, t) \\ &\quad + i \int_{-\infty}^{\infty} d\omega \tilde{E}_0(x, y, \omega) \phi(x - \gamma\omega, y) e^{-i\omega t}. \end{aligned} \quad (7)$$

In the far field of a focusing element, the optical field can be expressed in terms of wave-vector components (u, v) , as denoted in Fig. 127.9(a). The double Fourier transform of Eq. (7) gives

$$\begin{aligned} \check{E}(u, v, t) &= \int_{-\infty}^{\infty} \int_{-\infty}^{\infty} dx dy E(x, y, t) e^{-iux} e^{-ivy}, \\ &= \check{E}_0(u, v, t) + i \int_{-\infty}^{\infty} \int_{-\infty}^{\infty} \int_{-\infty}^{\infty} d\omega dx dy \\ &\quad \times \tilde{E}_0(x, y, \omega) \phi(x - \gamma\omega, y) e^{-i(\omega t + ux + vy)}. \end{aligned} \quad (8)$$

The intensity in the far field is $I(u, v, t) = |\check{E}(u, v, t)|^2$. Averaging over an ensemble of phase screens for which $\langle \phi(x, y) \rangle = 0$, the average intensity in the far field is

$$\begin{aligned} \langle I(u, v, t) \rangle &= I_0(u, v, t) + \int_{-\infty}^{\infty} \dots \int_{-\infty}^{\infty} d\omega d\omega' dx dx' dy dy' \\ &\quad \times \tilde{E}_0(x, y, \omega) \tilde{E}_0^*(x', y', \omega') \\ &\quad \times \langle \phi(x - \gamma\omega, y) \phi^*(x' - \gamma\omega', y') \rangle \\ &\quad \times e^{-i(\omega - \omega')t} e^{-i(x - x')u} e^{-i(y - y')v}. \end{aligned} \quad (9)$$

Using a coordinate transformation and completing four integrals [see **Appendix A** (p. 128)], the average far-field intensity can be written in terms of the power spectral density (PSD) of the phase screen:

$$\begin{aligned} \langle I(u, v, t) \rangle &= I_0(u, v, t) \\ &\quad + \int_{-\infty}^{\infty} \int_{-\infty}^{\infty} du' dv' I_0(u', v', t' + \gamma u - \gamma u') \\ &\quad \times \text{PSD}(u - u', v - v'). \end{aligned} \quad (10)$$

Equation (10) is an integral expression for the average far-field intensity given the PSD of the phase screens and I_0 , the far-field intensity without a phase screen. Further analysis is only possible if one assumes functional forms for the integrand.

3. Average Near-Field Intensity

An expression for the average intensity in the near field can be derived using a similar formalism. One starts with an expression similar to Eq. (9), but with all quantities defined in the near field, thereby eliminating the four integrals over the near-field coordinates:

$$\begin{aligned} \langle I(x, y, t) \rangle &= I_0(x, y, t) \\ &\quad + \int_{-\infty}^{\infty} \int_{-\infty}^{\infty} d\omega d\omega' \tilde{E}_0(x, y, \omega) \tilde{E}_0^*(x, y, \omega') \\ &\quad \times \langle \phi(x - \gamma\omega, y) \phi^*(x - \gamma\omega', y) \rangle e^{-i(\omega - \omega')t}. \end{aligned} \quad (11)$$

In this case, it is convenient to use a one-dimensional (1-D) correlation function where the near-field coordinates (x, y) are parameters:

$$C_{xy}(\Delta\omega) = \langle \phi(x - \gamma\omega, y) \phi^*(x - \gamma\omega', y) \rangle. \quad (12)$$

Performing the same coordinate transformation as outlined in **Appendix A** (p. 128), replacing the 1-D correlation function with its Fourier transform PSD_{xy} , and completing integrals of exponentials and a delta function give the following:

$$\langle I(x, y, t) \rangle = I_0(x, y, t) + \int_{-\infty}^{\infty} dt' I_0(x, y, t') \text{PSD}_{xy}(t - t'). \quad (13)$$

That is, the average near-field intensity has an additional term as a result of phase noise that is the convolution of the noise-free intensity and the 1-D power spectral density. This near-field result is similar to that derived in Ref. 8, but without the stated approximations.

The connection between the two-dimensional (2-D) and 1-D PSD functions, $\text{PSD}(u, v)$ and $\text{PSD}_{xy}(t)$, is derived in **Appendix B** (p. 129) and is

$$\text{PSD}_{xy}(t) = \frac{1}{\gamma} \int_{-\infty}^{\infty} dv \text{PSD}(t/\gamma, v). \quad (14)$$

That is, the 1-D temporal PSD is proportional to the integral of the 2-D spatial PSD over one spatial frequency axis after the other axis—the one that defines the plane of geometric dispersion—is replaced by the scaled time axis using $u = t/\gamma$.

Analytic Expressions Assuming Gaussian Functional Forms

It is instructive to consider the case where all quantities are Gaussians. That is, the 2-D PSD function of the phase screen has a Gaussian functional form, as well as the beam profile and the pulse shape. In this case, the integral expressions for the average intensity in the far field [Eq. (10)] and near field [Eq. (13)] can be reduced to closed-form analytic expressions. The PSD is the Fourier transform of Eq. (3):

$$\text{PSD}(u, v) = \frac{\sigma^2 l_c^2}{2\pi} \exp\left[-l_c^2(u^2 + v^2)/2\right]. \quad (15)$$

The noise-free intensity is

$$I_0(u, v, t) = I_P \exp(-\Delta\omega^2 t^2 - W^2 u^2 - W^2 v^2), \quad (16)$$

where I_P is the peak, on-axis intensity at $u = v = t = 0$. The pulse width τ_0 (defined as the half-width at the $1/e$ intensity) is equal to $1/\Delta\omega$. Similarly, the width of the focal spot, w_0 (defined as

the half-width at $1/e$ intensity), is equal to $1/W$. Substitution into Eq. (10) gives

$$\begin{aligned} \langle I(u, v, t) \rangle &= I_0(u, v, t) \\ &+ I_P \frac{\sigma^2 l_c^2}{2W} \left(l_c^2/2 + \gamma^2 \Delta\omega^2 + W^2 \right)^{-1/2} \\ &\times \exp\left[\frac{(\gamma\Delta\omega^2 t - W^2 u)^2}{l_c^2/2 + \gamma^2 \Delta\omega^2 + W^2} \right] \\ &\times \exp\left(-W^2 u^2 - l_c^2 v^2/2 - \Delta\omega^2 t^2 \right). \end{aligned} \quad (17)$$

The second term is the low-intensity pedestal that is produced by the phase screen. The magnitude of the pedestal scales with the variance of the phase, σ^2 . One limit that is often the case for stretchers and small-scale compressors is that the spatial spread of the spectrum across the phase screen ($\gamma\Delta\omega$) is much larger than both the input beam size (W) and the correlation length (l_c). Typical values for the three quantities are of the order of 100 mm, 1 mm, and 100 μm , respectively. Using this limit, the far-field intensity can be approximated as

$$\begin{aligned} \langle I(u, v, t) \rangle &= I_0(u, v, t) + I_P \frac{\sigma^2 l_c}{\sqrt{2} \gamma \Delta\omega} \left(\frac{l_c}{\sqrt{2} W} \right) \\ &\times \exp\left[-W^2 \left(u + \frac{t}{\gamma} \right)^2 - \frac{l_c^2 v^2}{2} - \frac{l_c^2 t^2}{2\gamma^2} \right]. \end{aligned} \quad (18)$$

The expression for the near-field intensity has a similar form, where I_P is the peak intensity in the near field:

$$\langle I(x, y, t) \rangle = I_0(x, y, t) + I_P(x, y) \frac{\sigma^2 l_c}{\sqrt{2} \gamma \Delta\omega} \exp\left(-\frac{l_c^2 t^2}{2\gamma^2} \right). \quad (19)$$

There are several important differences between these two expressions. First, the noise-dependent terms at the peak of the pulse differ by the factor $l_c/\sqrt{2}W$. Typically this factor is much less than unity. Therefore one could expect a much smaller on-axis, noise-dependent contribution in the vicinity of $t = 0$ in the far field than in the near field.

The second and more significant difference is the presence of the space–time coupling term in the exponent: $-W^2(u + t/\gamma)^2$. As a result, the maximum far-field intensity of the pedestal at a given time corresponds to a different transverse location in the far field. The location is determined from the equation

$u = -t/\gamma$. More general results, discussed below, support this conclusion. This space–time coupling is analogous to that reported in certain types of pulse shapers.⁹ In summary, these analytic results, although derived specifically for Gaussian functional forms, show that one should expect large differences between the temporal contrast in the near and far fields.

Comparison of Analytic Results and Numerical Simulations

The analytic expressions were tested against numerical simulations of spatially dispersed ultrafast pulses propagating through phase screens. Table 127.I shows default model parameters, unless explicitly specified. The 2-D PSD function was used to generate a random phase screen of Gaussian random numbers over the entire near-field plane in the dispersed region.¹⁰ An input beam was dispersed into spectral components that were incident on different sections of the phase screen, as shown in Fig. 127.9(c). Beams of each component

were modulated by the screen and then propagated to the far field using 2-D fast Fourier transforms (FFT's). Each spectral component was added coherently. The far-field intensity at each position (u,v,t) was calculated as the magnitude of the total field squared. To avoid noise from interpolation, the near-field and spectral sampling intervals were matched using the spatio-spectral coefficient so that $\delta x = \gamma \delta \omega$.

Figures 127.10–127.12 compare numerical simulations to the analytic results for Gaussian functional forms. The near-field average intensity in the x – t plane is shown in Fig. 127.10(a). The intensity is plotted on a logarithmic scale in dB relative to the peak. The narrow peak down the center around $t = 0$ is the intense, noise-free term $I_0(x,y,t)$ in Eq. (19). The low-intensity pedestal comes from the second, PSD-driven term. In Figs. 127.10(b)–127.10(d) numerical simulations for a single-phase screen realization and the analytic average are compared at three different x positions in the near field. While

Table 127.I: Default simulation parameters used in this article, unless explicitly specified.

Parameter	Symbol	Value	Parameter	Symbol	Value
Center wavelength	λ_0	910 nm	Time step	δt	8 fs
1/e pulse half-width	τ_0	10 fs	Number of time steps	N_T	2^{12}
Near-field beam size	W	1 mm	Near-field step	δx	84 μm
Spatiospectral coefficient	γ	0.44 mm/THz	Number of steps across beam	N_X	2^8
rms phase	σ	0.04 rad	Frequency step	$\delta \omega$	0.19 THz
Correlation length	l_c	100 μm	Phase screen dimensions	$x_{\text{max}}, y_{\text{max}}$	360×21 mm

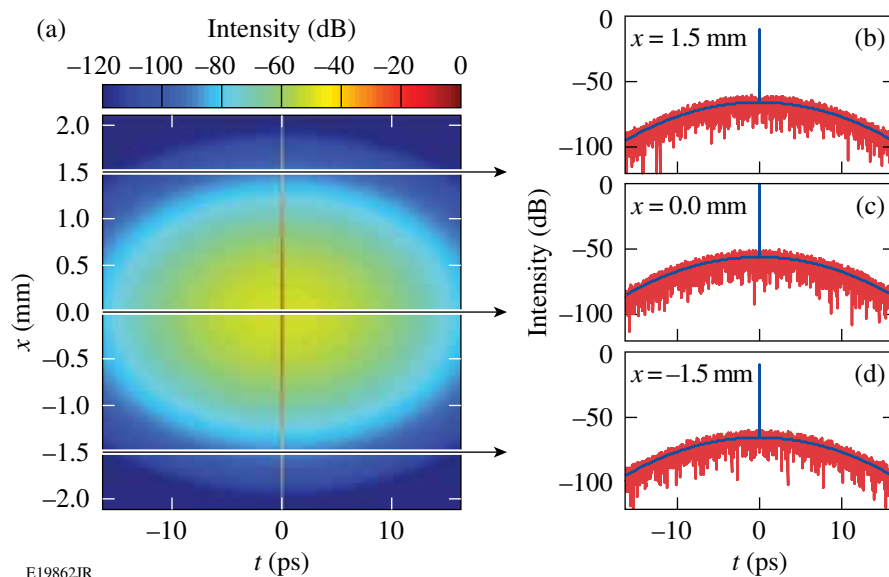


Figure 127.10

(a) Near-field average intensity in the x – t plane calculated using Eq. (19). The main pulse $I_0(x,y,t)$ is the red line at $t = 0$ ps. [(b),(c),(d)] Analytic (blue) and numeric (red) values of intensity calculated at different x values.

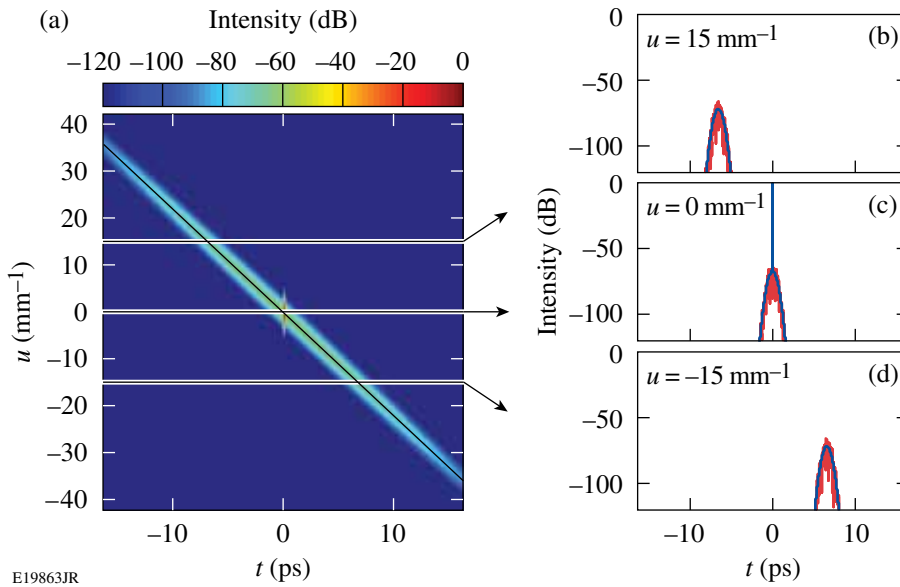


Figure 127.11

(a) Far-field average intensity in the u - t plane calculated using Eq. (18). Space-time coupling in the noise-dependent term follows the black line, $u = -t/\gamma$. [(b),(c),(d)] Analytic (blue) and numeric (red) values of intensity calculated at different u values.

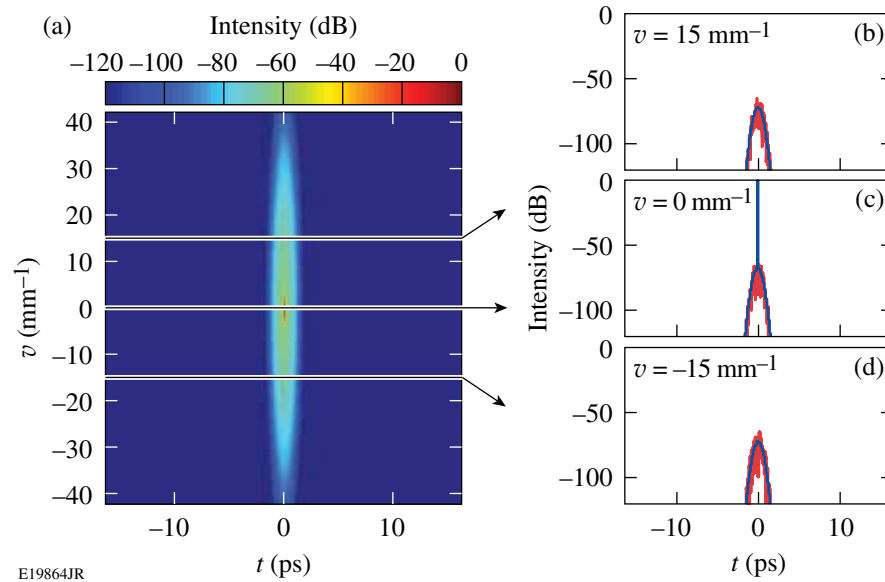


Figure 127.12

(a) Far-field average intensity in the v - t plane calculated using Eq. (17). [(b),(c),(d)] Analytic (blue) and numeric (red) values of intensity calculated at different v values.

the numerical results (red lines) have high-frequency structure, which is a consequence of using a single-phase screen realization, their overall profile follows the analytic results (blue lines).

Results calculated for the far field in the u - t plane, using Eq. (18), are shown in Fig. 127.11. The space-time coupling between u and t appears as a diagonal noise-dependent contribution to the intensity that follows $u = -t/\gamma$. As a consequence, the slices at different u positions show a temporal displacement of the noise-dependent term. In contrast, plots in the v - t plane (Fig. 127.12) do not show space-time coupling. The v axis is conjugate to the y axis, which is orthogonal to the plane of spectral dispersion.

The temporal narrowing on axis in the far field ($u = v = 0$) depends on W , the size of the beam in the near field. Figure 127.13 shows results for four values of W . The far-field intensity approaches the near-field result as the size of the beam is reduced from 3 to 0.1 mm. In this small-beam limit, each spectral component samples only a small portion of the screen, and the statistics become identical to the 1-D case for the near field. The beneficial effect of averaging the phase contributions over multiple correlation lengths no longer occurs, and the on-axis contrast is reduced.

The numeric results have high-frequency structure because they used a single realization of the phase screen. Averag-

ing over multiple pulses (each calculated using a different phase screen) increases the level of agreement between the numeric and analytic results in both the near and far fields (see Fig. 127.14).

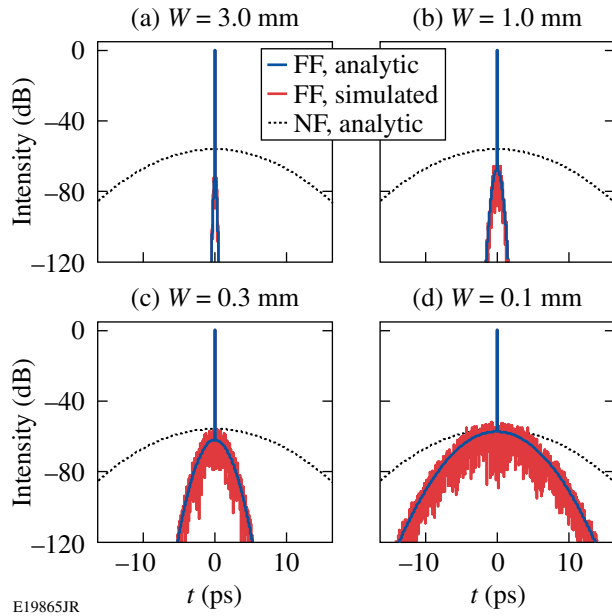


Figure 127.13

On-axis temporal intensities for Gaussian functional forms and a range of near-field beam sizes (W). The on-axis far-field contrast increases with the beam size.

In principle, there can be significant differences between temporal and ensemble averages for non-ergodic phenomena. Since a laser's stretcher or compressor typically uses static optics, an ensemble average over many phase screens is not relevant. Intensity averaging in time may occur, however, depending on the nature of the interaction with a target. The physical processes may not respond quickly enough to follow the high-frequency temporal modulation. In this case, the relevant quantity is the temporal average of the intensity over the response time of the interaction.

Figure 127.15 shows on-axis plots of the intensity in the near field and far field. The red line is a box-car average in time of the temporal intensity from a single realization of the phase screen. The black line is an ensemble average over pulses that were each calculated using an independent realization of the phase screen. The overall profiles are similar; therefore, one can treat intensity noise from phase screens in spectrally dispersed beams as an ergodic process.

The statistical nature of the intensity fluctuations at a given time may be relevant if the target interaction is nonlinear. In

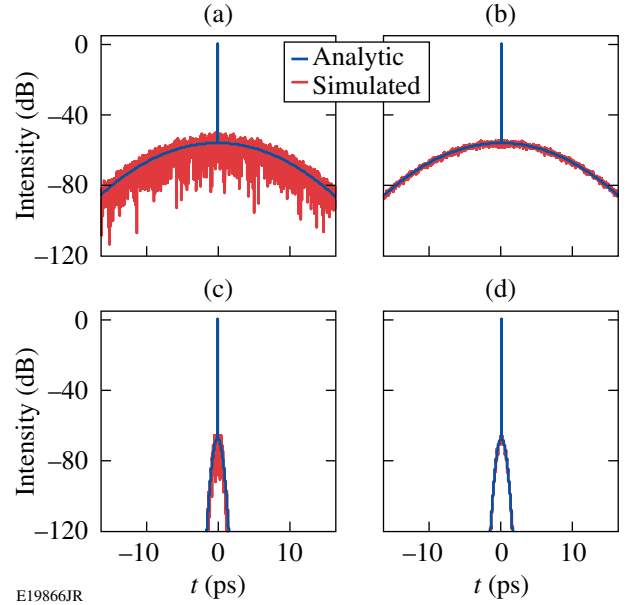


Figure 127.14

On-axis temporal intensities for Gaussian functional forms. Near-field results for (a) one phase screen and (b) an ensemble average of pulses for 25 phase screens. Far-field results for (c) one phase screen and (d) an ensemble average of pulses for 25 phase screens.

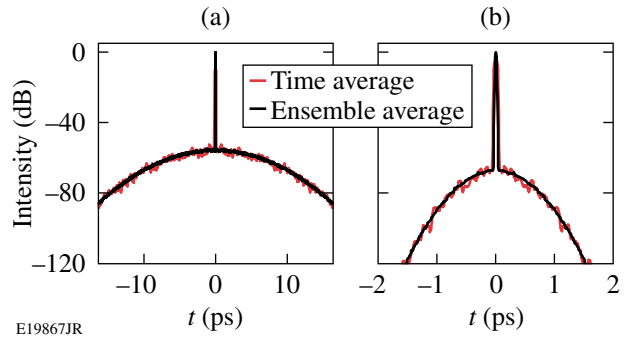


Figure 127.15

Average on-axis intensity calculated either by averaging in time (rectangular window, T) or over an ensemble of phase maps (N). (a) Near-field intensity: $T = 200$ fs, $N = 200$; (b) far-field intensity: $T = 40$ fs, $N = 200$.

general, the intensity-probability distribution for the coherent addition of two beams, one uniform and one statistically fluctuating with a uniform phase distribution $[0, 2\pi]$, is given by¹¹

$$p(I) = \frac{1}{\langle I \rangle} \exp\left(-r - \frac{I}{\langle I \rangle}\right) \mathbf{I}_0\left(2\sqrt{rI/\langle I \rangle}\right), \quad (20)$$

where \mathbf{I}_0 is the modified Bessel function of the first kind of order zero and $r = I_0/\langle I \rangle$. At times where the intensity of the noise-free pulse, I_0 , is much less than that of the pedestal, the parameter $r \ll 1$ and Eq. (19) may be approximated by

$$p(I) \approx \frac{1}{\langle I \rangle} \exp\left(-\frac{I}{\langle I \rangle}\right). \quad (21)$$

Figure 127.16 shows the probability density of the intensity in both the near and far fields at $t = 250$ fs, calculated using an ensemble of phase maps. The numeric results for 200 phase screens are in agreement with the probability calculated using Eq. (21), shown in red.

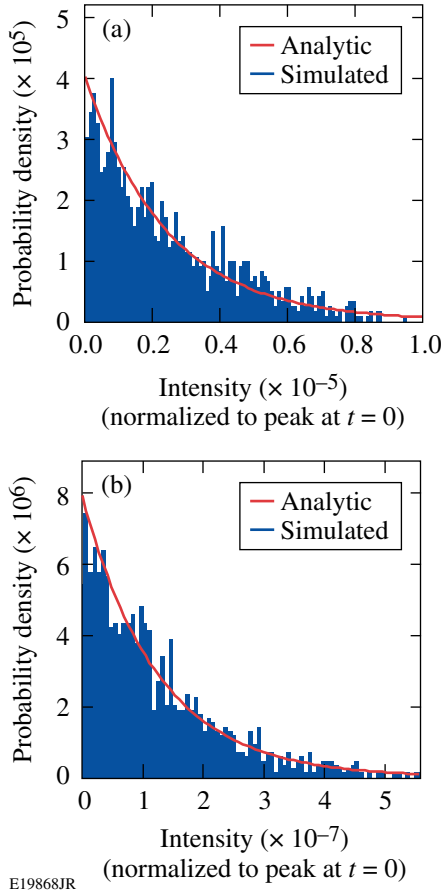


Figure 127.16
Intensity probability distributions at $t = 250$ fs for (a) the near field and (b) the far field.

Lorentzian PSD Functional Forms

Gaussian PSD's are convenient for obtaining closed-form analytic expressions that show the relative impact of the three main scale lengths: $\gamma\Delta\omega$, W , and l_c . In practice, however, optical surfaces do not have Gaussian PSD's. More common are PSD's with a Lorentzian functional form.¹²

$$\text{PSD}(u,v) = \frac{(S-1)\sigma^2 l_c^2}{2\pi(1+l_c^2 u^2 + l_c^2 v^2)^{(S+1)/2}}. \quad (22)$$

The parameter S is the asymptotic slope of the 1-D PSD function. Following Eq. (14), the 1-D PSD in the time domain is

$$\text{PSD}_{xy}(t) = \frac{\sigma^2 l_c \Gamma(S/2)}{\sqrt{\pi} \gamma \Gamma\left(\frac{S-1}{2}\right) \left(1 + l_c^2 t^2 / \gamma^2\right)^{S/2}}, \quad (23)$$

which scales as $1/t^S$ for large times ($t \gg \gamma/l_c$). Typical values of S are in the range of 1.5 to 1.6 (Ref. 12). Despite differences in the functional forms of the Lorentzian and Gaussian PSD's, Fig. 127.17 shows that the nature of the near- and far-field temporal intensities for Lorentzians is qualitatively similar except for a slower fall-off far from the peak.

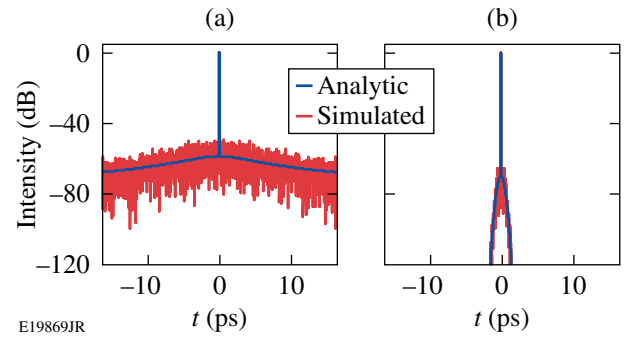


Figure 127.17
On-axis temporal intensity calculated in (a) near field and (b) far field for a Lorentzian PSD with $\sigma = 0.04$ radians, $l_c = 100 \mu\text{m}$, and $S = 1.55$.

Application of Results to Stretchers and Compressors

1. Systems with Multiple Elements

Pulse stretchers and compressors are commonly used in ultrafast CPA laser systems to raise the limits for damage and nonlinearity in their optical amplifiers. Pulses must pass through an even number of dispersing elements such as gratings or prisms to eliminate residual angular dispersion. Additional optical components may be required in portions of the system where the pulse is geometrically dispersed; therefore their surface quality will affect the pulse's temporal contrast. One example is the case of an Öffner stretcher.¹³ Here, two spherical mirrors are used to create an image of a diffraction grating at a "negative" distance from the object, resulting in net positive dispersion for the pulse. It has been shown that the surface quality of stretcher mirrors⁴ and gratings⁶ can have a significant impact on the temporal contrast of the pulse.

It is important, therefore, to be able to apply the preceding results, derived for a single phase screen, to systems with several phase screens. If the phase screens are practically

coincident or imaged onto each other, their phases are summed using the appropriate spatio-spectral coefficients, to get a total phase screen:

$$\Phi_{\text{total}}(x, y, \omega) = \sum_n \phi_n(x - \gamma_n \omega, y). \quad (24)$$

If the phase screens are uncorrelated, the correlation function for the total phase reduces to a sum of correlation functions:

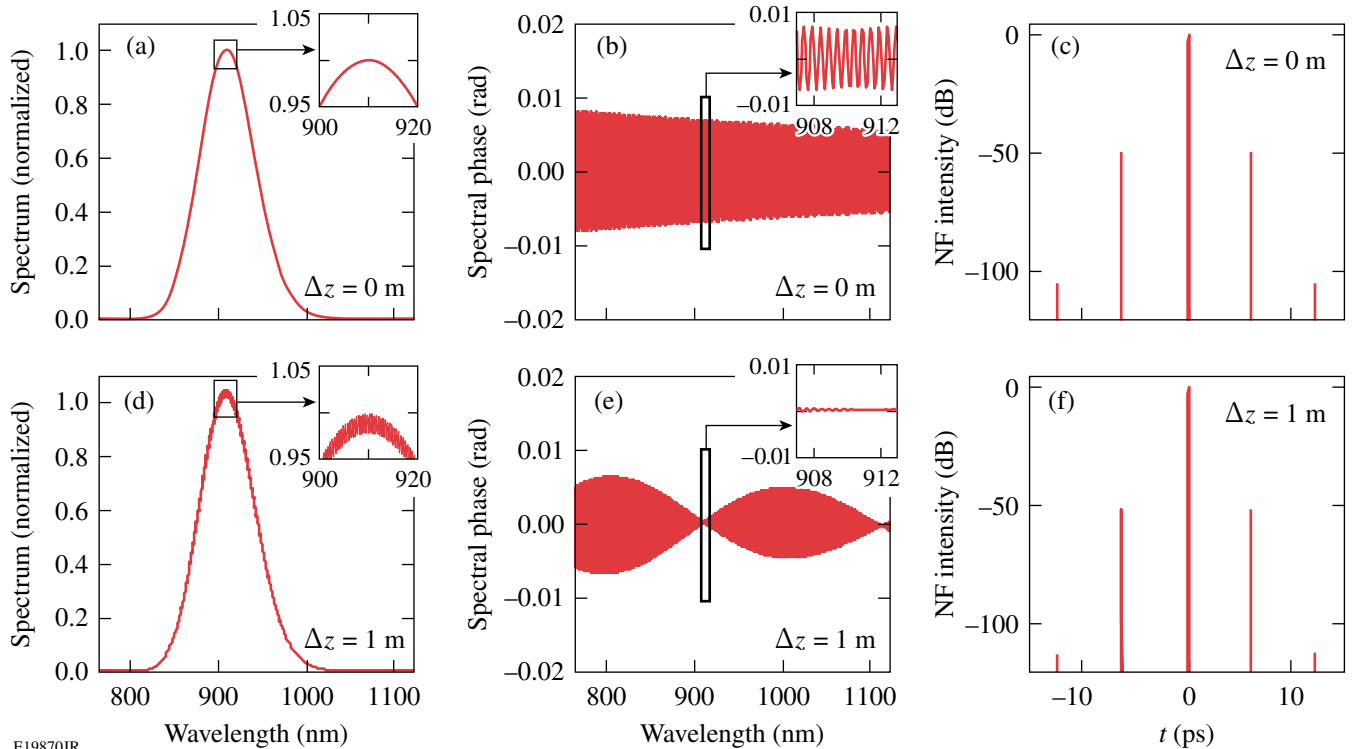
$$\langle \Phi_{\text{total}}(x, y, \omega) \Phi_{\text{total}}^*(x', y', \omega') \rangle = \sum_n C_n(\Delta x - \gamma_n \Delta \omega, \Delta y). \quad (25)$$

In the expressions for the average intensity in the near field or far field, the noise-dependent term becomes a sum over the PSD of each phase screen. For example, in the far field, the average intensity is

$$\begin{aligned} \langle I(u, v, t) \rangle &= I_0(u, v, t) \\ &+ \sum_n \int_{-\infty}^{\infty} \int_{-\infty}^{\infty} du' dv' I_0(u', v', t' + \gamma_n u - \gamma_n u') \\ &\times \text{PSD}_n(u - u', v - v'). \end{aligned} \quad (26)$$

Typically, however, the phase screens are not coincident or imaged onto each other. Significant distances of free propagation (of the order of a meter) are often required to obtain the desired amount of dispersion. In this case, propagation between the surfaces causes high-frequency phase modulation to be converted into amplitude modulation, and vice versa. The distance required for complete phase-to-amplitude conversion is derived from the Talbot effect and is equal to $\Delta x^2/2\lambda$, where Δx is the modulation period.^{14,15} The high-frequency modulation relevant to ultrafast pulse contrast may have periods as short as $100 \mu\text{m}$, for which the phase-to-amplitude conversion distance at $1 \mu\text{m}$ is only 5 mm.

A full description, analytical or numerical, that includes diffraction is complicated. Such an approach, however, is not required when estimating the overall impact on temporal contrast from a series of phase screens. Although near-field propagation changes the fine-scale structure, it has only a minor effect on the average intensity. This is because amplitude modulation degrades the temporal contrast in a way that is very similar to phase modulation. This is shown in Fig. 127.18, where



E19870JR

Figure 127.18

Near-field quantities after spectrally dispersed propagation through a sinusoidal phase screen with a modulation period and amplitude of $450 \mu\text{m}$ and 0.5 nm , respectively. (a) The spectrum, (b) spectral phase, and (c) temporal intensity immediately after the screen. [(d),(e),(f)] The same quantities after propagating a distance of 1 m. There is complete conversion of phase-to-amplitude modulation at the peak wavelength of 910 nm .

the near-field properties of a pulse (spectrum, spectral phase, and temporal intensity) are shown at two distances from a sinusoidal phase screen with a 450- μm period. The simulations show clear evidence of phase-to-amplitude conversion after propagation over 1 m. The resulting satellite pulses, however, are qualitatively similar in magnitude and temporal location.

This conclusion is reinforced in Fig. 127.19, which shows results from numeric simulations that included scalar Fresnel propagation between two Lorentzian phase screens. The distance between them was varied and the far-field intensity in the u - t plane was calculated. In one case, shown in Fig. 127.19(a), the two Lorentzian phase screens were coincident. In Fig. 127.19(b), the screens were separated by 1 m. Differences can be seen in the fine-scale structure, but the average far-field intensity is very similar, even though the separation between phase screens is orders of magnitude more than the coherence length, $l_c = 100 \mu\text{m}$, and the beam size, $W = 1 \text{ mm}$.

For the remainder of this article, therefore, diffraction is not included when estimating the nature of temporal contrast degradation for standard stretcher and compressor designs. Instead, the contributions from each phase screen are added according to Eq. (26).

2. Grating-Based Pulse Compressor and Öffner Stretcher

A schematic of a standard four-grating compressor is shown in Fig. 127.20(a). The gratings, G_1 and G_2 , in the first pair geometrically disperse the input pulse into its spectral components, which are recombined by the second pair. The group delay through the compressor for each component decreases approximately linearly with frequency, corresponding to negative dispersion.^{2,16} The magnitude of dispersion depends on the slant distances between the gratings in each pair, which are usually, but not always, matched.¹⁷ The compressor produces short pulses by compensating for the residual positive dispersion of the stretcher and amplifier glass.

Nonuniformity in the optical surfaces of G_2 and G_3 imprints onto the spectral phase of the pulse. The two gratings can be modeled as perfect elements plus additional phase screens. A retroreflector, placed at the AA' plane to halve the number of required gratings, can potentially degrade the temporal contrast and would be treated as a third phase screen.

A simulation of the output far-field intensity is shown in Fig. 127.20(b). The PSD parameters for the gratings were chosen arbitrarily according to Table 127.I. In this device, the

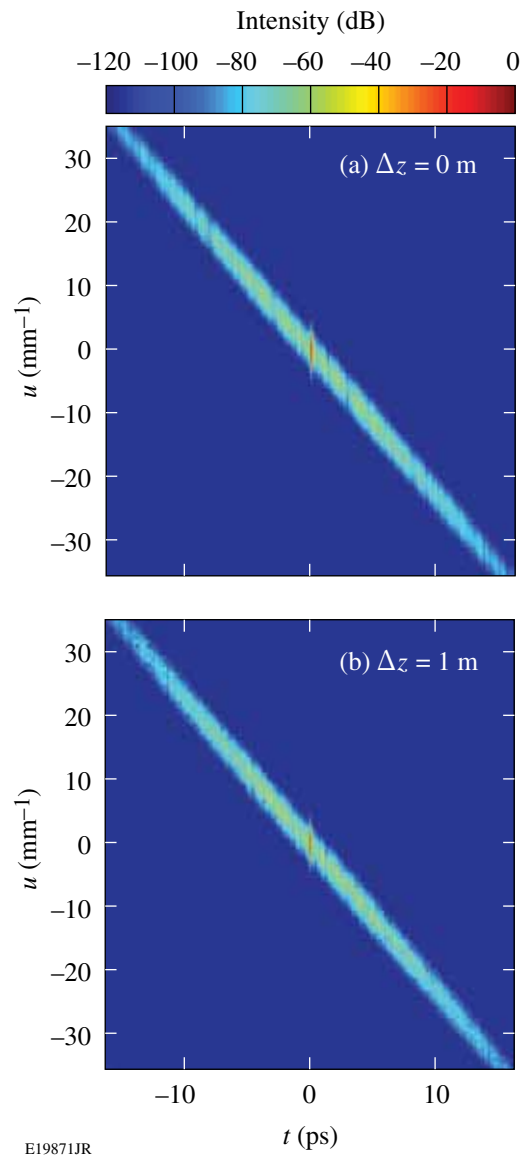
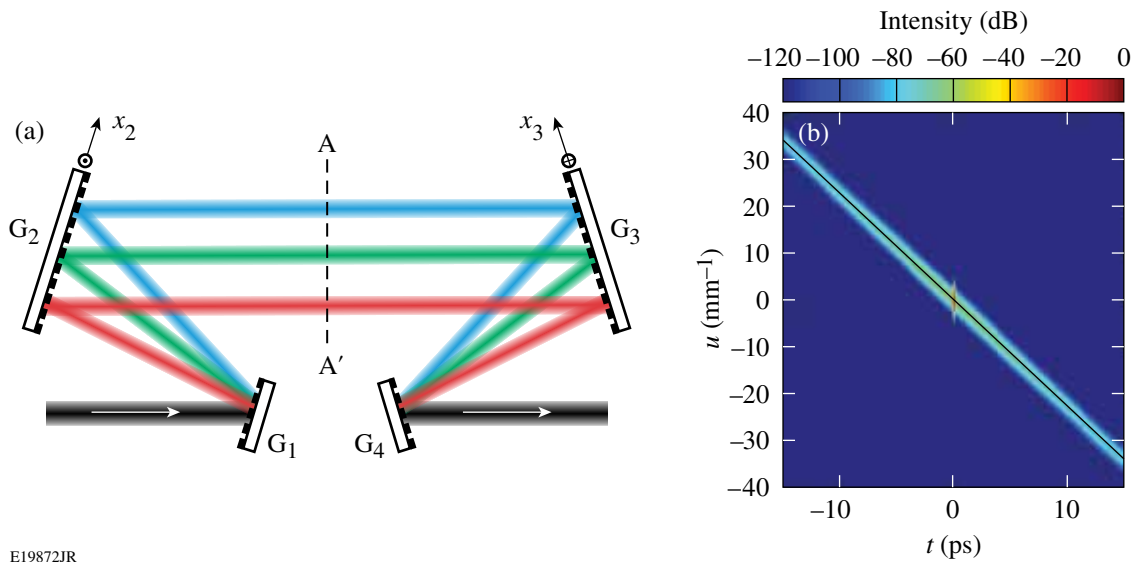


Figure 127.19

Far-field intensity calculated in the u - t plane for two phase screens. (a) Simulation results where phase screens were coincident, and (b) simulation results where phase screens were separated by $\Delta z = 1 \text{ m}$. Each spectral field after the first phase screens was propagated to the second using a scalar Fresnel propagation code. The details of the intensity structure between (a) and (b) are different, but any differences between the average profiles are insignificant.

two phase screens have the same spatio-spectral coefficient, $y = 0.44 \text{ mm/THz}$, and therefore the noise contributions from each grating follow the same line $u = -t/\gamma$.

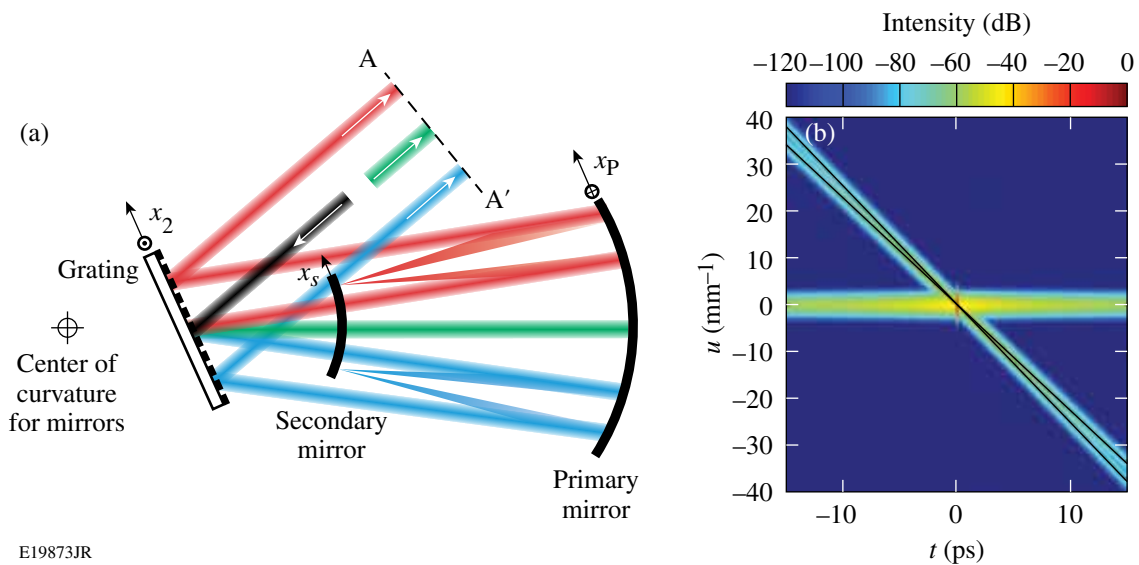
The far-field intensity distribution for an Öffner stretcher is qualitatively different (see Fig. 127.21). In this device, positive dispersion is obtained using a primary and secondary mir-



E19872JR

Figure 127.20

(a) Schematic of a four-grating compressor, showing the input and output beams (black) and three spectral components. Modulation on the surfaces of G_2 and G_3 produces spectral phase noise. A roof mirror can be used along the line AA' to retroreflect the beam, halving the required number of gratings. (b) Far-field average intensity calculated using Lorentzian PSD's in the $u-t$ plane at $t = 0$. G_2 and G_3 have the same spatio-spectral coefficient, $\gamma = 0.44$ mm/THz. The black line corresponds to $u = -t/\gamma$ and tracks the peak intensity from the PSD term.



E19873JR

Figure 127.21

(a) Schematic of an Öffner stretcher, showing the input beam (black) and three spectral components. (b) Far-field average intensity calculated using the same Lorentzian PSD for each optic in the $u-t$ plane at $t = 0$.

ror to form an image of a single grating, thereby achieving a negative separation distance.¹³ Modulation on the surfaces of the grating and primary and secondary mirrors produces spectral phase noise. A roof mirror (not shown) is typically used along the line AA' to retroreflect the beam at a different height back through the stretcher, eliminating spatial chirp. In

this simulation, the spatio-spectral coefficients γ are 0.44, 0.22, and 0.40 mm/THz for the primary mirror, secondary mirror, and grating, respectively.

The secondary mirror is located at a focal plane for each spectral component so, therefore, phase noise added to each

component is transferred directly to the system's far field. The resulting pedestal is centered on the main focal spot (at $u = v = 0$) and can be calculated using Eq. (13), but with spatial coordinates (x', y') replaced with angular coordinates (u, v) , where $u = kx/f$. The primary mirror and grating are located in the near-field planes, however, and therefore the pedestals that they produce are swept across the focal spot, as predicted by Eq. (10).

When identical PSD's are assumed for all optics, the secondary mirror has the largest impact on the contrast degradation. This is fundamentally different than on a compressor, where the surface quality of all optics in the spectrally dispersed planes affects the contrast equally.

Conclusions

A theoretical study was presented on the impact of high-frequency spectral phase modulation on the temporal contrast of ultrafast pulses. Expressions were derived for the intensity pedestal produced by optical surface roughness of components within pulse stretchers and compressors. The average intensity in the far field—the target location for ultra-intense experiments—was evaluated. Analytic closed-form expressions show that spectral phase imprint in the near field of a spectrally dispersed beam produces space–time coupling in the far field. As a result, the low-intensity pedestal that precedes the peak of the pulse sweeps across the target, covering an area many times the diffraction-limited spot size. Simulations of standard stretcher and compressor designs show fundamentally different forms of temporal contrast degradation at focus. These observations raise interesting questions about the nature of the target interaction when such impairments are present and about the validity of applying measurements made in the near field (the usual domain for high-dynamic-range cross-correlators¹⁸) to the target plane.

ACKNOWLEDGMENT

This work has been supported by the U.S. Department of Energy Office of Inertial Confinement Fusion under Cooperative Agreement No. DE-FC52-08NA28302, the University of Rochester, and the New York State Energy Research and Development Authority. The support of DOE does not constitute an endorsement by DOE of the views expressed in this article.

Appendix A

Equation (10) is obtained from Eq. (9) by first replacing variable pairs such as x and x' with X and Δx , where $X = x + x'$ and $\Delta x = x - x'$. The Jacobian of each transformation is 1/2. Equation (9) is then written as

$$\begin{aligned} \langle I(u, v, t) \rangle &= I_0(u, v, t) \\ &+ \frac{1}{2^3} \int_{-\infty}^{\infty} \dots \int_{-\infty}^{\infty} d\Omega d\Delta\omega dX d\Delta x dY d\Delta y \\ &\times \tilde{E}_0\left(\frac{X + \Delta x}{2}, \frac{Y + \Delta y}{2}, \frac{\Omega + \Delta\omega}{2}\right) \\ &\times \tilde{E}_0^*\left(\frac{X - \Delta x}{2}, \frac{Y - \Delta y}{2}, \frac{\Omega - \Delta\omega}{2}\right) \\ &\times C(\Delta x - \gamma\Delta\omega, \Delta y) e^{-i\Delta\omega t} e^{-i\Delta x u} e^{-i\Delta y v}, \end{aligned} \quad (27)$$

where the phase map has been assumed to be wide-sense stationary, so that

$$C(\Delta x, \Delta y) = \langle \phi(x, y) \phi^*(x', y') \rangle. \quad (28)$$

The integrals over Ω , X , and Y involve only the spectral near fields \tilde{E}_0 and not the correlation function. Replacing these fields with their temporal Fourier transforms adds integrals over t' and t'' to give a portion of the integrand of Eq. (27) that is

$$\begin{aligned} \int_{-\infty}^{\infty} \dots \int_{-\infty}^{\infty} d\Omega dX dY dt' dt'' E_0\left(\frac{X + \Delta x}{2}, \frac{Y + \Delta y}{2}, t'\right) \\ \times E_0^*\left(\frac{X - \Delta x}{2}, \frac{Y - \Delta y}{2}, t''\right) \\ \times e^{i\left(\frac{\Omega + \Delta\omega}{2}\right)t'} e^{-i\left(\frac{\Omega - \Delta\omega}{2}\right)t''}. \end{aligned} \quad (29)$$

Collecting exponential factors that depend only on Ω and completing the integral gives a Dirac delta function $2\delta(t' - t'')$. This allows one to evaluate the t'' integral, giving

$$\begin{aligned} 2 \int_{-\infty}^{\infty} \dots \int_{-\infty}^{\infty} dX dY dt' E_0\left(\frac{X + \Delta x}{2}, \frac{Y + \Delta y}{2}, t'\right) \\ \times E_0^*\left(\frac{X - \Delta x}{2}, \frac{Y - \Delta y}{2}, t'\right) e^{i\Delta\omega t'}. \end{aligned} \quad (30)$$

That is, each field in Eq. (27) is replaced by its temporal Fourier transform, the integral over Ω is replaced by an integral over its conjugate variable, and a phase factor of $2e^{i\Delta\omega t'}$ is added. Repeating this operation for the integrals over X and Y gives the following equivalent expression for Eq. (29):

$$2^3 \int_{-\infty}^{\infty} \dots \int_{-\infty}^{\infty} dt' du' dv' I_0(u', v', t') e^{i\Delta\omega t'} e^{i\Delta x u'} e^{i\Delta y v'}. \quad (31)$$

Equation (27) is therefore rewritten as

$$\begin{aligned} \langle I(u, v, t) \rangle &= I_0(u, v, t) \\ &+ \int_{-\infty}^{\infty} \dots \int_{-\infty}^{\infty} du' dv' dt' d\Delta\omega d\Delta x d\Delta y I_0(u', v', t') \\ &\times C(\Delta x - \gamma\Delta\omega, \Delta y) \\ &\times e^{-i\Delta\omega(t-t')} e^{-i\Delta x(u-u')} e^{-i\Delta y(v-v')}. \end{aligned} \quad (32)$$

The integrals over Δx and Δy are Fourier transforms of the correlation function, which is equal to the power spectral density of the phase screen and is defined as

$$\text{PSD}(u, v) = \int_{-\infty}^{\infty} d\Delta x d\Delta y C(\Delta x, \Delta y) e^{-i\Delta x u} e^{-i\Delta y v}, \quad (33)$$

The remaining integral over $\Delta\omega$ is evaluated to give the Dirac delta function $\delta(t - t' + \gamma u - \gamma v)$. This makes it possible to complete the integral over t' , which gives

$$\begin{aligned} \langle I(u, v, t) \rangle &= I_0(u, v, t) \\ &+ \int_{-\infty}^{\infty} \int_{-\infty}^{\infty} du' dv' I_0(u', v', t' + \gamma u - \gamma v) \\ &\times \text{PSD}(u - u', v - v'). \end{aligned} \quad (34)$$

Appendix B

Equation (14) is obtained by first integrating the 2-D PSD function over v , the axis normal to the plane of geometric dispersion:

$$\begin{aligned} &\int_{-\infty}^{\infty} \text{PSD}(u, v) dv \\ &= \int_{-\infty}^{\infty} \int_{-\infty}^{\infty} d\Delta x d\Delta y C(\Delta x, \Delta y) e^{-i\Delta x u} \left(\int_{-\infty}^{\infty} dv e^{-i\Delta y v} \right). \end{aligned} \quad (35)$$

The quantity in parentheses is equal to $\delta(\Delta y)$, making it possible for the integral over Δy to complete. Finally, by noting

that $C(-\gamma\Delta\omega, 0) = C_{xy}(\Delta\omega)$, making the substitutions $\Delta x = \gamma\Delta\omega$ and $u = t/\gamma$, and using the fact that

$$\text{PSD}_{xy}(t) = \int_{-\infty}^{\infty} d\Delta\omega C_{xy}(\Delta\omega) e^{-i\Delta\omega t},$$

one obtains the connection between the two PSD functions:

$$\int_{-\infty}^{\infty} dv \text{PSD}(t/\gamma, v) = \gamma \text{PSD}_{xy}(t). \quad (36)$$

REFERENCES

1. P. Maine *et al.*, IEEE J. Quantum Electron. **24**, 398 (1988).
2. E. B. Treacy, IEEE J. Quantum Electron. **QE-5**, 454 (1969).
3. A. Antonetti *et al.*, Appl. Phys. B **65**, 197 (1997).
4. V. Bagnoud and F. Salin, J. Opt. Soc. Am. B **16**, 188 (1999).
5. K.-H. Hong *et al.*, Appl. Phys. B **81**, 447 (2005).
6. C. Hooker *et al.*, Opt. Express **19**, 2193 (2011).
7. J. W. Goodman, *Statistical Optics*, Wiley Series in Pure and Applied Optics (Wiley, New York, 1985).
8. C. Dorrer and J. Bromage, Opt. Express **16**, 3058 (2008).
9. M. M. Wefers and K. A. Nelson, IEEE J. Quantum Electron. **32**, 161 (1996).
10. E. Sidick, in *Modeling Aspects in Optical Metrology II*, edited by H. Bosse, B. Bodermann, and R. M. Silver (SPIE, Bellingham, WA, 2009), Vol. 7390, p. 73900L.
11. J. C. Dainty, J. Opt. Soc. Am. **62**, 595 (1972).
12. E. L. Church, P. Z. Takacs, and T. A. Leonard, in *Scatter from Optical Components*, edited by J. C. Stover (SPIE, Bellingham, WA, 1990), Vol. 1165, pp. 136–150.
13. G. Chériaux *et al.*, Opt. Lett. **21**, 414 (1996).
14. H. F. Talbot, Lond. & Edin. Phil. Mag. & J. of Sci., Third Series **9**, 401 (1836).
15. P. Latimer and R. F. Crouse, Appl. Opt. **31**, 80 (1992).
16. I. Walmsley, L. Waxer, and C. Dorrer, Rev. Sci. Instrum. **72**, 1 (2001).
17. H. Huang and T. J. Kessler, Opt. Lett. **32**, 1854 (2007).
18. S. Luan *et al.*, Meas. Sci. Technol. **4**, 1426 (1993).

Highly Accurate Wavefront Reconstruction Algorithms Over Broad Spatial-Frequency Bandwidth

Introduction

Frequency-domain wavefront reconstruction methods are as old as the very early wavefront reconstructors.^{1,2} Freischlad placed this subject on solid ground.³ The rectangular map constraint of the conventional Fourier method has been removed in an iterative Gerchberg-type algorithm dealing with an arbitrary boundary shape.⁴ A series of recent papers by Poyneer discuss improvements on handling boundary conditions and applications in extreme adaptive optics.^{5,6} Similar principles have been applied in shearing interferometers.⁷ More serious attention has been paid to the accuracy of the reconstruction methods in Refs. 8–10. The works of Campos and Yaroslavsky presented a solution based on a band-limited integration technique in frequency domain. The two-dimensional (2-D) extension of the same method was not discussed. Complementary to their works, Bahk introduced a full 2-D wavefront reconstructor based on the band-limited derivative calculation.¹¹ Both approaches emphasize the frequency response of the reconstructed signals. The frequency response of wavefront reconstruction has been discussed earlier in the analysis of lateral-shearing interferometry.¹² Frequency-response characteristics of a reconstruction is important in focal-spot diagnostics for high-power lasers, where the focal spot is indirectly characterized using wavefront information reconstructed from Shack–Hartmann slopes data.¹³

This article develops a set of encompassing mathematical tools for wavefront reconstruction problems, where many additional benefits naturally arise, interconnecting the results of previous works. The benefits are exemplified by the development of two new wavefront reconstructors and the analytical derivation of noise-propagation coefficients of several well-known wavefront reconstructors.

This article is organized as follows: (1) The mathematical tools and symbols regarding band-limited derivative operations, which are needed for the analyses in the subsequent sections, are introduced. (2) A way to improve the accuracy of the finite-difference method is discussed in connection with wavefront reconstruction. The Simpson rule is adopted for developing a

new spatial-domain iterative reconstruction algorithm. The exact details of the algorithm and its frequency-domain property are described. (3) A band-limited reconstruction algorithm is extended to hexagonal geometry, which greatly enhances the flexibility of band-limited reconstructors. (4) Finally, the noise-propagation curve is analytically derived and compared with numerical simulations.

Band-Limited Derivative

The main results of band-limited derivative techniques in the context of wavefront reconstruction were summarized in Ref. 11. The full derivation of the results will be presented here for the sake of completeness. Additional new notations are introduced that will simplify the expressions in **Hexagonal Band-Limited Reconstructor** (p. 136).

The motivation for band-limited derivatives, especially for discrete samples, lies in the fact that it provides an analytical tool for converting back and forth between slope measurements and wavefront signal. We start by asking what the exact interpolation formula is for derivatives in discrete samples. According to sampling theorem, a band-limited signal can be exactly reconstructed at any point by convolving a sinc function with discrete samples. The derivative of a band-limited signal is obtained by directly differentiating the sinc function's convolution kernel that becomes a spherical Bessel function (j_1) (Ref. 14). The derivative interpolation expression at discrete points is

$$\begin{aligned} \frac{d\varphi}{dx} \Big|_{(x = m\Delta x)} &\equiv \varphi_x(m) \\ &= \frac{1}{\Delta x} \sum_{n=1}^{\infty} \pi j_1(n\pi) \left\{ \varphi[(m+n)\Delta x] - \varphi[(m-n)\Delta x] \right\}, \quad (1) \end{aligned}$$

where the spherical Bessel function evaluated at integer multiples of π is equivalent to

$$\pi j_1(n\pi) = \frac{(-1)^{n+1}}{n}, \quad n = 1, 2, \dots \quad (2)$$

The summation of the left-hand side of Eq. (1) for all sample points can be shown to be equal to zero by taking advantage of the expression on the right-hand side and using the periodicity condition of discrete samples:

$$\sum_{m=0}^{N-1} \frac{d\varphi}{dx} \Big|_{(x=m\Delta x)} = 0. \quad (3)$$

Equation (1) is easier to handle in frequency domain. Discrete Fourier transform (DFT) and Fourier series analysis lead to the following equivalent expression:

$$\overline{\varphi}_x(k) = i \frac{2\pi}{\Delta x} \mathfrak{S}(k) \tilde{\varphi}(k), \quad (4)$$

where the tilde notation means DFT of the symbol beneath it and $\mathfrak{S}(k)$ (sawtooth wave) is defined as

$$\mathfrak{S}(k) = \begin{cases} \text{for even } N \begin{cases} \frac{k}{N}, & k = 0, \dots, N/2 - 1 \\ 0, & k = N/2 \\ \frac{k}{N} - 1, & k = \frac{N}{2} + 1, \dots, N - 1 \end{cases} \\ \text{for odd } N \begin{cases} \frac{k}{N}, & k = 0, \dots, (N-1)/2 \\ \frac{k}{N} - 1, & k = (N+1)/2, \dots, N - 1 \end{cases} \end{cases} \quad (5)$$

Equation (4) provides a convenient way of calculating exact derivatives from band-limited signals. When the sampling points of a derivative signal are offset by a half-sampling space from the sampling points of the original signal, a slightly different form should be used:

$$\begin{aligned} \frac{d\varphi}{dx} \Big|_{(x=m\Delta x + \frac{1}{2}\Delta x)} &\equiv \varphi_{x,1/2}(m) \\ &= \frac{1}{\Delta x} \sum_{n=1}^{\infty} \pi j_1 \left(n\pi - \frac{1}{2}\pi \right) \\ &\quad \times \left\{ \varphi[(m+n)\Delta x] - \varphi[(m-n+1)\Delta x] \right\}, \end{aligned} \quad (6)$$

where the Bessel coefficients can be replaced again with an integral expression

$$\pi j_1 \left(n\pi - \frac{1}{2}\pi \right) = \frac{4}{\pi} \frac{(-1)^{n+1}}{(2n-1)^2}, \quad n = 1, 2, \dots \quad (7)$$

Employing a similar Fourier series analysis that leads to Eq. (4), the frequency-domain expression of Eq. (6) is reduced to

$$\overline{\varphi}_{x,1/2}(k) = i \frac{2\pi}{\Delta x} \exp\left(i \frac{\pi}{N} k\right) \mathfrak{T}(k) \tilde{\varphi}(k), \quad (8)$$

where $\mathfrak{T}(k)$ (triangular wave) is defined as

$$\mathfrak{T}(k) = \begin{cases} k/N, & k = 0, \dots, \left\lfloor \frac{N-1}{2} \right\rfloor \\ 1 - k/N, & k = \left\lfloor \frac{N-1}{2} \right\rfloor + 1, \dots, N-1 \end{cases} \quad (9)$$

We also need an interpolation formula for creating a signal shifted by half-sample spacing for Fried geometry:

$$\begin{aligned} \varphi(x) \Big|_{(x=m\Delta x + \frac{1}{2}\Delta x)} &\equiv \varphi_{1/2}(m) \\ &= \sum_{n=1}^{\infty} \text{sinc}\left(n - \frac{1}{2}\right) \left\{ \varphi[(m+n)\Delta x] - \varphi[(m-n+1)\Delta x] \right\}. \end{aligned} \quad (10)$$

The DFT of Eq. (10) is

$$\overline{\varphi}_{1/2}(k) = \exp\left(i \frac{\pi}{N} k\right) \mathfrak{R}(k) \tilde{\varphi}(k), \quad (11)$$

where $\mathfrak{R}(k)$ (rectangular wave) is

$$\mathfrak{R}(k) = \begin{cases} \text{for even } N \begin{cases} 1, & k = 0, \dots, N/2 - 1 \\ 0, & k = N/2 \\ -1, & k = N/2 + 1, \dots, N - 1 \end{cases} \\ \text{for odd } N \begin{cases} 1, & k = 0, \dots, (N-1)/2 \\ -1, & k = (N+1)/2, \dots, N - 1 \end{cases} \end{cases} \quad (12)$$

Therefore, the partial derivative in the x direction for Fried geometry in frequency domain is

$$\begin{aligned} \overline{\varphi}_{x,1/2,1/2}(p,q) \\ = i \frac{2\pi}{\Delta x} \exp\left[i \frac{\pi}{N} (p+q)\right] \mathfrak{T}(q) \mathfrak{R}(p) \tilde{\varphi}(p,q). \end{aligned} \quad (13)$$

Equation (13) has an additional degree of freedom (index p for the y direction) because the reconstructed sample point in the Fried geometry must first be shifted in the y direction by a half-sample size before applying the half-sample shifted-derivative operation in the x direction.

For consistency, we can verify that the sequential operations of half-pixel shift and derivative operation using $\mathbb{R}(k)$ and $\mathbb{S}(k)$ produce the same result as single operation of $\mathbb{T}(k)$, i.e., $\mathbb{T}(k) = \mathbb{R}(k)\mathbb{S}(k)$. This relation, however, does not hold for the value at $N/2$ for even N , where the left-hand side is 0.5, whereas the right-hand side is 0. To remove this paradox for an even number of samples, we choose to use $\mathbb{S}(N/2) = 0.5$ and $\mathbb{R}(N/2) = 1$ or $\mathbb{S}(N/2) = -0.5$ and $\mathbb{R}(N/2) = -1$. A similar choice was made in Ref. 9 for band-limited integration operators from a different perspective. *The redefinition of \mathbb{S} and \mathbb{R} at the midpoint is implied from hereon.* Using the new definition, the half-pixel operator used in the right-hand side of Eq. (11) can be alternatively expressed as

$$\exp\left(\pm \frac{\pi i}{N} k\right) \mathbb{R}(k) = \exp[\pm \pi i \mathbb{S}(k)]. \quad (14)$$

We can establish the connection from discrete to continuous variable derivative as follows: \mathbb{S} can be considered as a discrete angular frequency vector circularly shifted by $[N/2]$. If we define $k_x(p) = (2\pi/\Delta x)p$ for $p = 0, \dots, (N-1)$, then

$$\frac{2\pi}{\Delta x} \mathbb{S} = \overline{k_x}, \quad (15)$$

where the bar over k_x denotes a circular shift by $[N/2]$. Using Eq. (14), Eqs. (4), (8), and (11) can be alternatively expressed as

$$\overline{\varphi_x} = i \overline{k_x} \tilde{\varphi}, \quad (16)$$

$$\overline{\varphi_{x,1/2}} = i \overline{k_x} \exp\left(i \frac{\Delta x}{2} \overline{k_x}\right) \tilde{\varphi}, \quad (17)$$

$$\overline{\varphi_{1/2}} = \exp\left(i \frac{\Delta x}{2} \overline{k_x}\right) \tilde{\varphi}, \quad (18)$$

The $\overline{k_x}$ notation establishes the formal connection with continuous variable derivatives.

In many practical situations, the band-limited calculations may not produce exact results, depending on the nature of signals. The magnitudes of the Fourier coefficients of a linear function, for example, decrease as $1/(\text{spatial frequency})$, whereas Eq. (16) indicates that the coefficients of the derivative are multiplied by the spatial-frequency vector. Therefore, the highest spatial-frequency coefficient does not vanish, even if N approaches ∞ . Therefore, the linear terms are not band limited and need to be treated separately. Equations (16)–(18) form the basis of the following analysis.

Simpson Reconstructor

The analysis in the previous section suggests that an accurate derivative calculation at discrete samples requires the superposition sum of the whole set of samples. This can be done more conveniently in the frequency domain, which results in a band-limited reconstructor with unity frequency response.¹¹ On the other hand, it is still worthwhile to investigate an improved finite-difference scheme for purely spatial-domain operation. In finite-difference methods involving only a few points, a high degree of accuracy is preserved by distributing the finite difference over both the measured derivative samples (i.e., slopes) and the integrated samples. Denoting the wavefront estimate as $\hat{\varphi}$ and the measured slope as S , one can start from a general finite-difference expression such as

$$\sum_j a(j) \hat{\varphi}(i+j) = \sum_k b(k) S(i+k) \quad (19)$$

for 1-D problems. Coefficients a and b belong to a specific finite-difference scheme. For example, Southwell¹⁴ showed a reconstructor based on

$$\hat{\varphi}(i+1) - \hat{\varphi}(i) = \frac{\Delta x}{2} [S(i) + S(i+1)]. \quad (20)$$

The frequency response of the Southwell reconstructor is low at high spatial frequency. We enhance the frequency response using the Simpson rule, which is

$$\hat{\varphi}(i+1) - \hat{\varphi}(i-1) = \frac{\Delta x}{3} [S(i-1) + 4S(i) + S(i+1)]. \quad (21)$$

An iterative wavefront reconstruction based on this scheme will be developed in the next section.

1. Simpson Iterator

Casting the local 1-D Eq. (21) into a least squares form in 2-D, we obtain an error metric (ε) as

$$\begin{aligned} \varepsilon = \sum_{i,j} & \left\{ \frac{1}{2\Delta x} [\hat{\varphi}(i,j+1) - \hat{\varphi}(i,j-1)] \right. \\ & \left. - \frac{1}{6} [S_x(i,j+1) + 4S_x(i,j) + S_x(i,j-1)] \right\}^2 \\ & + \left\{ \frac{1}{2\Delta y} [\hat{\varphi}(i+1,j) - \hat{\varphi}(i-1,j)] \right. \\ & \left. - \frac{1}{6} [S_y(i+1,j) + 4S_y(i,j) + S_y(i-1,j)] \right\}^2. \quad (22) \end{aligned}$$

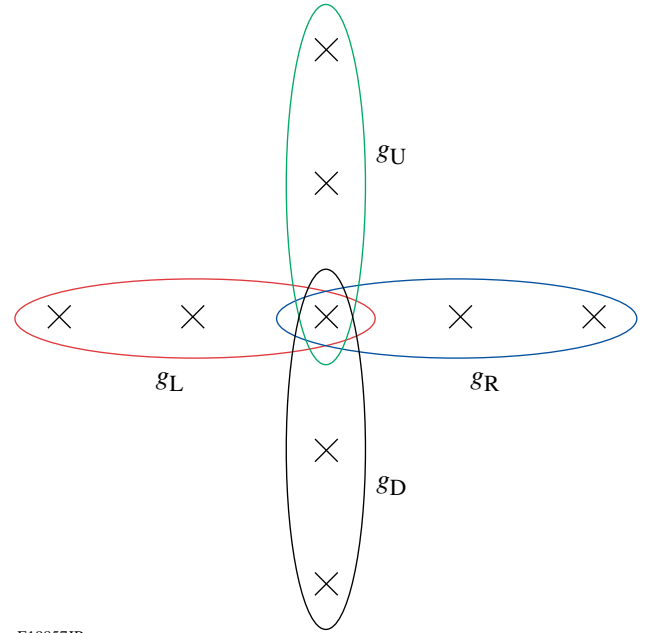
Δx and Δy are moved around to the $\hat{\phi}$ side so that squared terms are in units of slopes. This provides equal weight to the differences in x and y directions on the assumption that the magnitude of slopes is comparable in either direction.

The condition $\partial \varepsilon / \partial \hat{\phi}(i, j) = 0$ leads to an equation that can be used for the iterative algorithm. It is assumed that phase and slope points are embedded in an arbitrary region. The differentiation of the error metric results in four groups, which are indicated by different colors in Fig. 127.22. Each group can be used in the equation only when all of its elements exist. This strategy is realized by using g parameters as shown in the following:

SIMPSON:

$$\begin{aligned}
 & g_L [\hat{\phi}(i, j) - \hat{\phi}(i, j - 2)] + g_R [\hat{\phi}(i, j) - \hat{\phi}(i, j + 2)] \\
 & + g_U \left(\frac{\Delta x}{\Delta y} \right)^2 [\hat{\phi}(i, j) - \hat{\phi}(i - 2, j)] \\
 & + g_D \left(\frac{\Delta x}{\Delta y} \right)^2 [\hat{\phi}(i, j) - \hat{\phi}(i + 2, j)] \\
 = & g_L [S_x(i, j - 2) + 4S_x(i, j - 1) + S_x(i, j)] \frac{\Delta x}{3} \\
 & - g_R [S_x(i, j) + 4S_x(i, j + 1) + S_x(i, j + 2)] \frac{\Delta x}{3} \\
 & + g_U \left(\frac{\Delta x}{\Delta y} \right)^2 [S_y(i - 2, j) + 4S_y(i - 1, j) + S_y(i, j)] \frac{\Delta y}{3} \\
 & - g_D \left(\frac{\Delta x}{\Delta y} \right)^2 [S_y(i, j) + 4S_y(i + 1, j) + S_y(i + 2, j)] \frac{\Delta y}{3} \\
 \equiv & \Delta S(i, j). \tag{23}
 \end{aligned}$$

g_L , g_R , g_U , and g_D are flags with values 0 or 1, where L, R, U, and D indicate left, right, up, and down directions, respectively. They are 0's if the quantities in the parentheses next to them are incalculable or 1's otherwise. For example, g_L at the point (i, j) does not vanish only when the slopes' measurements exist at the additional points at $(i, j - 1)$ and $(i, j - 2)$. The scope of each flag is graphically indicated in Fig. 127.22. For comparison, the iterative equation for the Southwell reconstructor is written here using the same format.



E19857JR

Figure 127.22
Simpson iterator geometry.

SOUTHWELL:

$$\begin{aligned}
 & g_L [\hat{\phi}(i, j) - \hat{\phi}(i, j - 1)] + g_R [\hat{\phi}(i, j) - \hat{\phi}(i, j + 1)] \\
 & + g_U \left(\frac{\Delta x}{\Delta y} \right)^2 [\hat{\phi}(i, j) - \hat{\phi}(i - 1, j)] \\
 & + g_D \left(\frac{\Delta x}{\Delta y} \right)^2 [\hat{\phi}(i, j) - \hat{\phi}(i + 1, j)] \\
 = & g_L [S_x(i, j - 1) + S_x(i, j)] \frac{\Delta x}{2} \\
 & - g_R [S_x(i, j) + S_x(i, j + 1)] \frac{\Delta x}{2} \\
 & + g_U \left(\frac{\Delta x}{\Delta y} \right)^2 [S_y(i - 1, j) + S_y(i, j)] \frac{\Delta y}{2} \\
 & - g_D \left(\frac{\Delta x}{\Delta y} \right)^2 [S_y(i, j) + S_y(i + 1, j)] \frac{\Delta y}{2}. \tag{24}
 \end{aligned}$$

The same successive-over-relaxation technique¹⁵ can be applied to the Simpson iterative reconstructor:

$$\hat{\phi}^{(m+1)}(i, j) = \hat{\phi}^{(m)}(i, j) + \omega \left[\overline{\hat{\phi}^{(m)}}(i, j) - \hat{\phi}^{(m)}(i, j) \right], \tag{25}$$

where

$$\begin{aligned} & \overline{\hat{\phi}^{(m)}}(i,j) \\ &= \left[\overline{\hat{\phi}_0^{(m)}}(i,j) + \Delta S(i,j) \right] / (g_L + g_R + g'_U + g'_D), \end{aligned} \quad (26)$$

$$\begin{aligned} \overline{\hat{\phi}_0^{(m)}}(i,j) &= g_L \hat{\phi}^{(m)}(i,j-2) \\ &+ g_R \hat{\phi}^{(m)}(i,j+2) + g'_U \hat{\phi}^{(m)}(i-2,j) \\ &+ g'_D \hat{\phi}^{(m)}(i+2,j). \end{aligned} \quad (27)$$

Here, ω is the over-relaxation parameter; g' is $(\Delta x/\Delta y)^2 \cdot g$.

2. Frequency Response and Regularization

The frequency response of the Simpson reconstructor will be calculated following the method presented in Ref. 11. The sum of the squared error in the spatial domain in Eq. (22) is equivalent to the sum of the squared error of the Fourier-transformed component by the Parseval theorem:

$$\varepsilon = \frac{1}{N^2} \sum \left\{ \left| D_x \tilde{\phi} - A_x \tilde{S}_x \right|^2 + \left| D_y \tilde{\phi} - A_y \tilde{S}_y \right|^2 \right\}, \quad (28)$$

where

$$D_x = \frac{1}{2\Delta x} \left[\exp(i\bar{k}_x \Delta x) - \exp(-i\bar{k}_x \Delta x) \right] \equiv D_{x,\text{Simpson}} \quad (29)$$

and

$$A_x = \frac{1}{6} \left[\exp(i\bar{k}_x \Delta x) + 4 + \exp(-i\bar{k}_x \Delta x) \right] \equiv A_{x,\text{Simpson}}. \quad (30)$$

The solution for $\tilde{\phi}$ in Eq. (28) is

$$\tilde{\phi} = \frac{(D_x^* A_x \tilde{S}_x + D_y^* A_y \tilde{S}_y)}{|D_x|^2 + |D_y|^2}. \quad (31)$$

As $\tilde{S}_x = i\bar{k}_x \tilde{\phi}$ and $\tilde{S}_y = i\bar{k}_y \tilde{\phi}$, the frequency response H defined as the ratio of the reconstructed wavefront amplitude to the true wavefront amplitude associated with the measured slopes at a given spatial frequency point is

$$H = \frac{\tilde{\phi}}{\hat{\phi}} = \frac{(D_x^* A_x D_{x,0} + D_y^* A_y D_{y,0})}{|D_x|^2 + |D_y|^2}, \quad (32)$$

where new notations $D_{x,0}$ and $D_{y,0}$ were introduced in place of $i\bar{k}_x$ and $i\bar{k}_y$, respectively.

Applying the Simpson derivative and average operators [Eqs. (29) and (30)], we obtain

$$\begin{aligned} & H_{\text{Simpson}} \\ &= \frac{1}{3} \frac{\omega_x \sin \omega_x (2 + \cos \omega_x) + \omega_y \sin \omega_y (2 + \cos \omega_y)}{\sin^2 \omega_x + \sin^2 \omega_y}, \end{aligned} \quad (33)$$

where $\bar{k}_x \Delta x \equiv \omega_x = 2\pi f_x$ and $\bar{k}_y \Delta x \equiv \omega_y = 2\pi f_y$, f_x and f_y are normalized frequencies ranging from -0.5 to 0.5 . It is assumed $\Delta x = \Delta y$. The frequency response of H_{Simpson} has eight singularities on the four corners and side centers. Except for the region near the poles, the frequency response is nearly unity everywhere, which proves higher accuracy of the Simpson rule than the traditional reconstructors over all spectrums in wavefront reconstruction (refer to Fig. 1 of Ref. 11).

The singularities can be removed by introducing the following Phillips regularization term¹⁶ to the right-hand side of Eq. (22):

$$\begin{aligned} \varepsilon_{\text{reg}} &= \lambda \sum_{i,j} \left\{ \frac{1}{(2\Delta x)^2} \left[\hat{\phi}(i,j+1) - 2\hat{\phi}(i,j) + \hat{\phi}(i,j-1) \right]^2 \right. \\ &\quad \left. + \frac{1}{(2\Delta y)^2} \left[\hat{\phi}(i+1,j) - 2\hat{\phi}(i,j) + \hat{\phi}(i-1,j) \right]^2 \right\}. \end{aligned} \quad (34)$$

In the frequency domain, this transforms into

$$\varepsilon_{\text{reg}} = \lambda \frac{1}{N^2} \sum \left\{ \left| D_{x,\text{reg}} \tilde{\phi} \right|^2 + \left| D_{y,\text{reg}} \tilde{\phi} \right|^2 \right\}, \quad (35)$$

where

$$D_{x,\text{reg}} = \frac{2}{\Delta x} \sin^2 \left(\frac{\bar{k}_x \Delta x}{2} \right), \quad (36)$$

and similarly for $D_{y,\text{reg}}$.

The denominator of the Simpson frequency response will have an additional term of $\lambda \left(|D_{x,\text{reg}}|^2 + |D_{y,\text{reg}}|^2 \right)$ that removes the singularity. The regularized frequency response is

$$\begin{aligned} & H_{\text{Simpson}}(\lambda) \\ &= \frac{1}{3} \frac{\omega_x \sin \omega_x (2 + \cos \omega_x) + \omega_y \sin \omega_y (2 + \cos \omega_y)}{\sin^2 \omega_x + \sin^2 \omega_y + 4\lambda \left(\sin^4 \frac{1}{2} \omega_x + \sin^4 \frac{1}{2} \omega_y \right)}. \end{aligned} \quad (37)$$

The 1-D frequency response with the regularization term has a second peak near high spatial frequency for sufficiently small λ (<0.08) [Fig. 127.23(b)]. The free parameter λ can be fixed to a value such that the second peak is 1. The numerically determined value of λ for such a condition is 0.07489. This choice of λ gives only a 3% error in wavefront amplitude over 80% of the frequency range. Another choice can be $\lambda = 0.07026$, which balances the local maximum and minimum around 1. The second option reduces the maximum deviation below 2.2% within 85% of the spectral range. Figure 127.23(a) shows a 3-D view of the frequency response of the Simpson-rule reconstructor with $\lambda = 0.07489$. The 1-D response is shown in Fig. 127.23(b). The solid line was calculated from an analytic expression [Eq. (36)], whereas the circles are from numerical simulations. The numerical simulation consists of steps of generating slopes from sinusoid wavefronts at a given spatial frequency and of reconstructing the wavefront and comparing the ratio between the original and the reconstructed wavefront amplitude at that frequency. The reconstruction algorithm used in the simulation will be explained in detail in the following section. The result shows good agreement with the analytic curve.

3. Iterative Algorithm with Regularization Terms

The frequency-domain analysis does not give a detailed picture of how the successive-over-relaxation method can be applied in spatial-domain iteration, especially around the measurement boundary. Resolving the stationary condition with the

regularization term gives additional terms on the left-hand side of Eq. (23). These are fully written out using g flags:

$$\begin{aligned}
 & (2\Delta x)^2 \frac{\partial \varepsilon_{\text{reg}}}{\partial \hat{\phi}(i,j)} \\
 &= \lambda g_L [\hat{\phi}(i,j) - 2\hat{\phi}(i,j-1) + \hat{\phi}(i,j-2)] \\
 &+ \lambda g_R [\hat{\phi}(i,j+2) - 2\hat{\phi}(i,j+1) + \hat{\phi}(i,j)] \\
 &+ \lambda g'_U [\hat{\phi}(i,j) - 2\hat{\phi}(i-1,j) + \hat{\phi}(i-2,j)] \\
 &+ \lambda g'_D [\hat{\phi}(i+2,j) - 2\hat{\phi}(i+1,j) + \hat{\phi}(i,j)] \\
 &- 2\lambda g'_{LR} [\hat{\phi}(i,j+1) - 2\hat{\phi}(i,j) + \hat{\phi}(i,j-1)] \\
 &- 2\lambda g'_{UD} [\hat{\phi}(i+1,j) - 2\hat{\phi}(i,j) + \hat{\phi}(i-1,j)]. \quad (38)
 \end{aligned}$$

g_{LR} or g_{UD} is 1 only if two points exist to the right and left or up and down, respectively, and zero otherwise. The iteration formula (26) will be modified to

$$\bar{\phi}(i,j) = \frac{[\bar{\phi}_0(i,j) + \Delta S(i,j) + \lambda \Delta \hat{\phi}(i,j)]}{[(1 + \lambda)(g_L + g_R + g'_U + g'_D) + 4\lambda(g_{LR} + g'_{UD})]}, \quad (39)$$

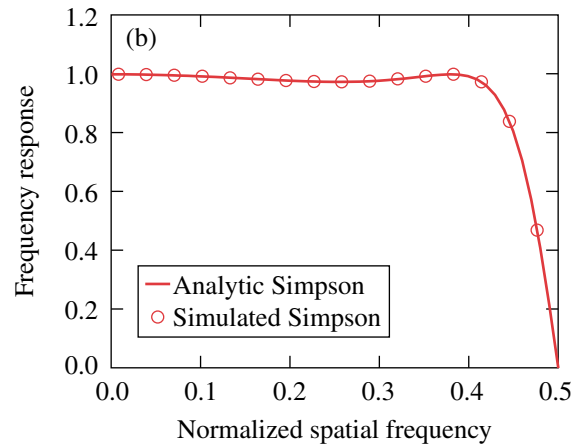
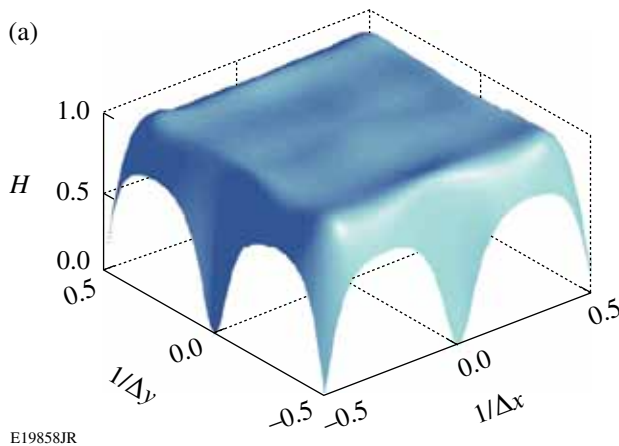


Figure 127.23

Frequency response of Simpson reconstructor with $\lambda = 0.07489$. (a) A 3-D view of the frequency response; (b) cross section along f_x axis. The solid line was calculated from the analytic expression; the circles are from simulations of Simpson iterator geometry.

where

$$\begin{aligned}
 \Delta\hat{\phi}(i,j) = & g_L [2\hat{\phi}(i,j-1) - \hat{\phi}(i,j-2)] \\
 & + g_R [2\hat{\phi}(i,j+1) - \hat{\phi}(i,j+2)] \\
 & + g'_U [2\hat{\phi}(i-1,j) - \hat{\phi}(i-2,j)] \\
 & + g'_D [2\hat{\phi}(i+1,j) - \hat{\phi}(i+2,j)] \\
 & + 2g_{LR} [\hat{\phi}(i,j+1) + \hat{\phi}(i,j-1)] \\
 & + 2g'_{UD} [\hat{\phi}(i+1,j) + \hat{\phi}(i-1,j)]. \quad (40)
 \end{aligned}$$

Hexagonal Band-Limited Reconstructor

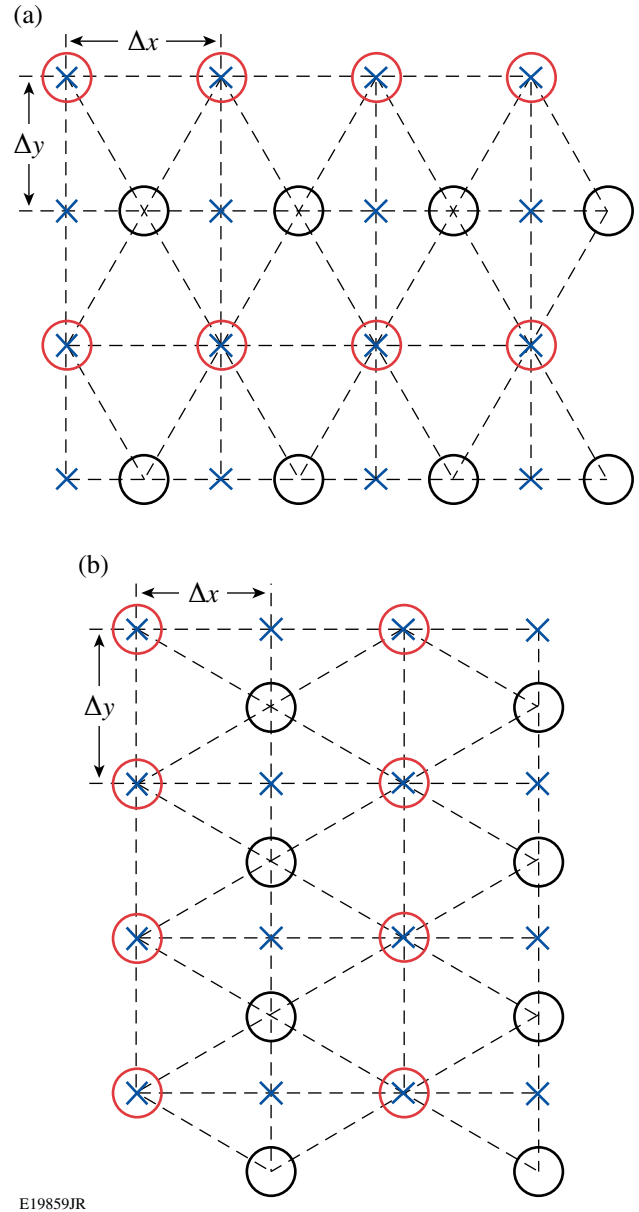
Band-limited reconstruction provides a unity frequency response over all spatial bandwidths. The band-limited reconstructor for the Southwell geometry was presented in Ref. 11. It was shown that band-limited derivative operators are also available for Hudgin and Fried geometries. Table 127.II summarizes the three operators depending on the geometry.

Table 127.II: Summary of band-limited derivative operators ($D_{x,0}$).

Geometry	$D_{x,0}$
Southwell	$i\bar{k}_x$
Hudgin	$i\bar{k}_x \exp[i\bar{k}_x(\Delta x/2)]$
Fried	$i\bar{k}_x \exp[i\bar{k}_x(\Delta x/2) + i\bar{k}_y(\Delta y/2)]$

Here we present band-limited reconstructors for hexagonal arrays. Hexagonal geometry may be well suited for adaptive optic systems for large telescopes with hexagonal mirror arrays (e.g., James Webb).¹⁷ Large deformable mirrors used in some laser fusion facilities (National Ignition Facility)¹⁸ also have hexagonal actuator patterns. The number density of lenslets is slightly higher in hexagonal geometry than square. Figure 127.24 shows two possible hexagonal arrays. In Fig. 127.24(a) the unit hexagon is lying on its facet, whereas in Fig. 127.24(b) the unit hexagon is standing on the apex. The circles indicate the measurement points and the \times 's are reconstruction points. In Fig. 127.24(a) geometry, the band-limited derivative calculation for the indicated square array involves first grouping the slopes measured at red- and black-circled positions. Marking them as index 1 and 2, respectively, the DFT's of slopes at the reconstruction points are

$$\widetilde{S}_x = \begin{bmatrix} \widetilde{S}_{1,x} + T_{\text{hex}} \circ \widetilde{S}_{2,x} \\ \widetilde{S}_{1,x} - T_{\text{hex}} \circ \widetilde{S}_{2,x} \end{bmatrix} \equiv \begin{bmatrix} \widetilde{S}_{x,I} \\ \widetilde{S}_{x,II} \end{bmatrix}. \quad (41)$$



E19859JR

Figure 127.24

(a) Prostrate hexagon array; (b) standing hexagon array.

T_{hex} is a matrix whose size is M by N (i.e., the size of either array 1 or array 2) and “ \circ ” denotes entry-wise matrix multiplication. The p th row and q th column element of T_{hex} is

$$T_{\text{hex}}(p,q) = \exp\left[-\frac{\pi i}{M}p - \pi i S(q)\right]. \quad (42)$$

The combined total array is therefore a vertical concatenation of the two matrices. On the other hand, the resulting total matrix for Fig. 127.24(b) geometry is a horizontal concatenation:

$$\begin{aligned}\widetilde{S}_x &= [\widetilde{S}_{1,x} + T_{\text{hex}} \circ \widetilde{S}_{2,x} \quad \widetilde{S}_{1,x} - T_{\text{hex}} \circ \widetilde{S}_{2,x}] \\ &\equiv [\widetilde{S}_{x,\text{I}} \quad \widetilde{S}_{x,\text{II}}].\end{aligned}\quad (43)$$

$$T_{\text{hex}}(p, q) = \exp\left[-\pi i \mathcal{S}(p) - \frac{\pi i}{N} q\right].\quad (44)$$

The same combination rule applies to y-slope measurements.

The above decomposition technique can be inverted such that each subgroup of the hexagonal array can also be expressed as the linear sum of blocks I and II of the rectangular array. This inversion is used only for wavefront points in the algorithm, which is

$$\widetilde{\varphi}_1 = \frac{1}{2}(\widetilde{\varphi}_1 + \widetilde{\varphi}_2),\quad (45)$$

$$\widetilde{\varphi}_2 = \frac{1}{2}T_{\text{hex}}^* \circ (\widetilde{\varphi}_1 + \widetilde{\varphi}_2).\quad (46)$$

Using the basic results obtained in **Band-Limited Derivative** (p. 130) and the DFT procedures for the hexagonal arrays in this section, the band-limited reconstruction algorithm for hexagonal slope arrays can be implemented as shown in the flowchart in Fig. 127.25.

Step 1 consists of fitting the slopes over low-order polynomials, e.g., third order, which will significantly reduce non-band-limited components of the wavefront. If the regions of interest are disconnected, the fitting must be performed per each region. Owing to the sum requirement [Eq. (3)], a column and row are appended to the edge of the measured slope matrices (groups 1 and 2 separately), which will satisfy the zero-sum conditions in the x and y directions.

Step 2 initializes the slopes with measured values. Steps 3–8 form a closed loop required for extrapolating slopes outside the non-rectangular region. The iteration is not required if the region is rectangular.

Slopes in groups 1 and 2 are separately Fourier transformed using Eqs. (40)–(43) in Step 3. In Step 4, wavefront matrices corresponding to each block (I or II) are reconstructed in the Fourier domain using the band-limited filter function, which is

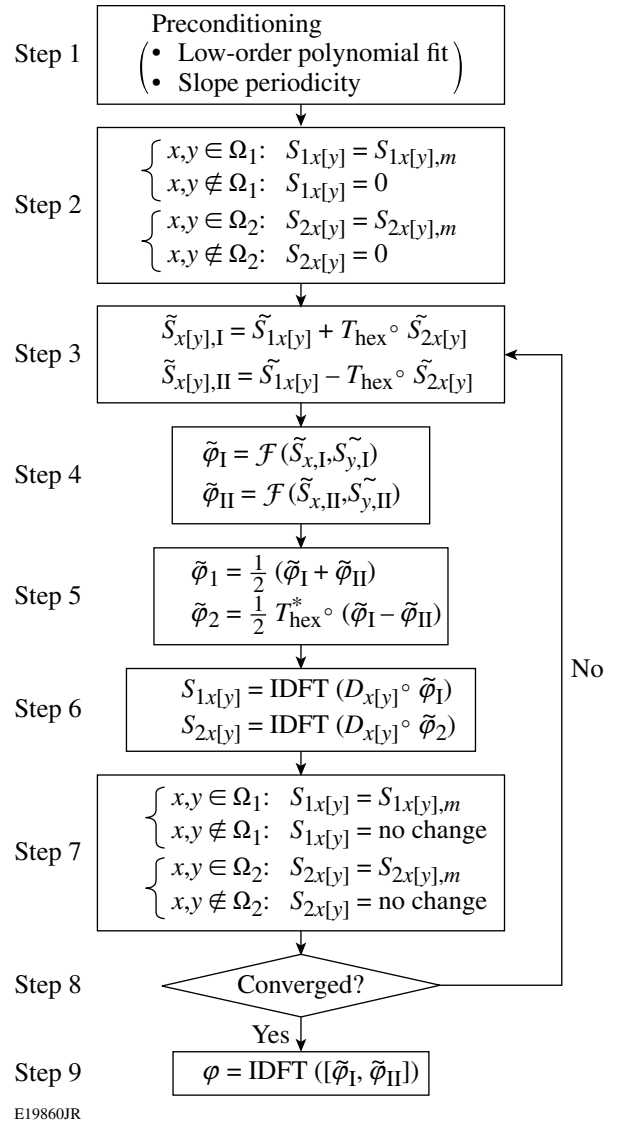


Figure 127.25

Flowchart of band-limited reconstruction for a hexagonal geometry. \mathcal{F} is the band-limited filter function [Eq. (46)]. The “ m ” subscript denotes the measured slopes. IDFT stands for inverse discrete Fourier transform. Ω_1 and Ω_2 are the regions where the slopes’ groups 1 and 2 data exist.

$$\begin{aligned}\mathcal{F}[\widetilde{S}_x(p, q), \widetilde{S}_y(p, q)] \\ = \frac{D_x^*(p, q)\widetilde{S}_x(p, q) + D_y^*(p, q)\widetilde{S}_y(p, q)}{|D_x(p, q)|^2 + |D_y(p, q)|^2},\end{aligned}\quad (47)$$

where the band-limited derivative operators D_x and D_y are defined as

$$D_x(p, q) = \frac{2\pi i}{\Delta x} \mathcal{S}(q), \quad (48)$$

$$D_y(p, q) = \frac{2\pi i}{(2\Delta y)} \mathcal{S}(p), \quad (49)$$

for a prostrate hexagon array and

$$D_x(p, q) = \frac{2\pi i}{(2\Delta x)} \mathcal{S}(q), \quad (50)$$

$$D_y(p, q) = \frac{2\pi i}{\Delta y} \mathcal{S}(p), \quad (51)$$

for a standing hexagon array.

Step 5 creates wavefront groups 1 and 2 by using Eqs. (51) and (52). In Steps 3 and 5, the correct T_{hex} must be used according to its geometry. In Step 6, derivative operators are applied to these temporary wavefront matrices to obtain slopes in groups 1 and 2, respectively. These new slopes are different from the measured slopes. We leave the values external to the boundary untouched while restoring the internal values to the original measured slopes. The difference between the measured slopes and the calculated slopes decreases over the course of iterations. Step 8 determines whether this difference is within tolerance. Once the convergence criterion is met, the wavefront matrices generated in Step 4 ($\overline{\varphi}_I, \overline{\varphi}_{II}$) are combined to form a single matrix by either vertical or horizontal concatenation, depending on the hexagon geometry and inverse Fourier transformed to the spatial domain to produce the final result in Step 9. Small terms in the imaginary part of the solution can be neglected.

The band-limited algorithms shown in Fig. 2 of Ref. 11 and Fig. 127.25 can be used together with a non-band-limited filter function, which enables one to conveniently switch between different algorithms. The reconstruction algorithms proposed here are not limited to a specific boundary shape.

Error Propagation

The wavefront reconstructors have traditionally been characterized with a so-called error propagation curve. This indicates the sensitivity of the noise in the reconstructed phase to the noise in the slopes measurements. Early numerical and theoretical works show that this sensitivity is a logarithmic function of the number of measurement points.^{1,2,15} Simulations confirm this. The noise-propagation coefficient will be calculated using discrete samples and frequency-domain filter functions. We limit the scope to the rectangular area.

Let σ_φ be the root mean square of the reconstructed phase φ . According to the Wiener-Khintchin theorem,

$$\sigma_\varphi^2 = \frac{1}{N_t} \sum \langle \Delta\varphi^2 \rangle = \frac{1}{N_t N^2} \sum \langle |\overline{\Delta\varphi}|^2 \rangle, \quad (52)$$

where $\langle \cdot \rangle$ denotes ensemble average of the quantity inside.

According to linear stochastic system theory, the power spectrum of input and output signals is related by the absolute square of the linear system function. In the case of wavefront reconstruction dictated by the linear response

$$\tilde{\varphi} = \frac{(D_x^* A_x \overline{\mathcal{S}}_x + D_y^* A_y \overline{\mathcal{S}}_y)}{|D_x|^2 + |D_y|^2 + \lambda(|D_{x,\text{reg}}|^2 + |D_{y,\text{reg}}|^2)}, \quad (53)$$

the corresponding stochastic response in power spectrum is

$$\begin{aligned} & \langle |\overline{\Delta\varphi}|^2 \rangle \\ &= \frac{(|D_x A_x \Delta \overline{\mathcal{S}}_x|^2 + |D_y A_y \Delta \overline{\mathcal{S}}_y|^2)}{[|D_x|^2 + |D_y|^2 + \lambda(|D_{x,\text{reg}}|^2 + |D_{y,\text{reg}}|^2)]^2}. \end{aligned} \quad (54)$$

Assuming that $\Delta \overline{\mathcal{S}}_x$ and $\Delta \overline{\mathcal{S}}_y$ are uncorrelated white noise with a variance of $\overline{\sigma}_S^2$ for each, and since $\sigma_S^2 = (1/N) \overline{\sigma}_S^2$, the noise-propagation coefficient is

$$\begin{aligned} \eta &= \frac{\sigma_\varphi^2}{h^2 \sigma_S^2} \\ &= \frac{1}{L^2} \sum_{k_x, k_y} \frac{(|D_x A_x|^2 + |D_y A_y|^2)}{[|D_x|^2 + |D_y|^2 + \lambda(|D_{x,\text{reg}}|^2 + |D_{y,\text{reg}}|^2)]^2}, \end{aligned} \quad (55)$$

where $\sigma_\varphi^2 = (1/N_t) \langle |\overline{\Delta\varphi}|^2 \rangle$, $h = \Delta x = \Delta y$, and L is the aperture size. This result is equivalent to Noll's¹⁹ in the case of band-limited operators.

Table 127.III summarizes finite-difference derivative/averaging operators for four geometries to be used with Eq. (55).

The right-hand side of Eq. (50) is inversely proportional to $|D_{x,0}|^2 + |D_{y,0}|^2$ for band-limited reconstruction and is difficult to visualize in linear scale. We define a “noise-response function (S_N)” with the inverse power dependence removed as follows:

$$S_N = \frac{(|D_{x,0}|^2 + |D_{y,0}|^2)(|D_x A_x|^2 + |D_y A_y|^2)}{\left[|D_x|^2 + |D_y|^2 + \lambda(|D_{x,\text{reg}}|^2 + |D_{y,\text{reg}}|^2)\right]^2}. \quad (56)$$

It can be shown by the Cauchy–Schwartz inequality that the noise response is always larger than or equal to the absolute frequency response squared,

$$|H|^2 \leq S_N. \quad (57)$$

The inequality [Eq. (52)] shows that the error propagation is intimately related to the frequency response of a reconstructor. The lower bound of η is

$$\sum_{k_x, k_y} \frac{|H|^2}{k_x^2 + k_y^2} \leq \sum_{k_x, k_y} \frac{S_N}{k_x^2 + k_y^2} = \eta. \quad (58)$$

From this, one can expect that the Southwell reconstructor will have the lowest lower bound and the Fried reconstructor the highest. It agrees with the result of Zou.²⁰

The analytic expression for η can be calculated and fit to a logarithmic curve, although the logarithm dependence is only approximate except for the band-limited reconstructors. The result is summarized in the second column of Table 127.IV. Singularity points were excluded in the summation over spatial-

frequency space. The third column shows the simulated η obtained by running actual reconstructors with zero slopes input with Gaussian noise. Two hundred realizations were performed at each N , where N^2 is the number of points. N was varied from 10 to 100 by 10. The logarithm fit over the averaged η is shown in the column. The multiplicative coefficients roughly agree with the analytic ones up to the second decimal point, but the additive constants from simulation are always estimated higher than the calculated ones. The offset is about 0.2771 on average. The discrepancy appears to come from the apparent inconsistency in assuming white noise in the slopes power spectrum and the use of band-limited derivative formalism. For example, the reconstructed wavefront from white spectrum noise always has some amount of low-order polynomial terms, which cannot be represented by Eq. (48). The constant offset 0.2771 therefore can be considered as the ratio of energy conversion from white noise to non-band-limited signals.

The legacy formulas of noise propagation for each reconstructor are also shown in the fourth column of Table 127.IV, quoted from the three authors' original publications.^{1,2,15} The quoted Southwell η is estimated only from the graph in the original paper since no explicit formula was given. Noll's calculation essentially corresponds to the band-limited case. Considering the fact that there is some ambiguity in the determination of the constant offset, at least the multiplicative coefficient of the Fried formula comes close to our analytic result; whereas there

Table 127.III: Summary of frequency-domain equivalents of the associated finite-difference schemes.

Finite-difference scheme	D_x	A_x
Southwell ¹⁴	$\frac{1}{\Delta x}[\exp(i\bar{k}_x \Delta x) - 1]$	$\frac{1}{2}[\exp(i\bar{k}_x \Delta x) + 1]$
Hudgin ²	$\frac{1}{\Delta x}[\exp(i\bar{k}_x \Delta x) - 1]$	1
Fried ¹	$\frac{1}{2\Delta x}[\exp(i\bar{k}_x \Delta x) - 1][\exp(i\bar{k}_y \Delta y) + 1]$	1
Simpson	$\frac{1}{2\Delta x}[\exp(i\bar{k}_x \Delta x) - \exp(-i\bar{k}_x \Delta x)]$	$\frac{1}{6}[\exp(i\bar{k}_x \Delta x) + 4 + \exp(-i\bar{k}_x \Delta x)]$

Table 127.IV: Summary of noise propagation.

Numerical Scheme	Calculated η	Simulated η	Quoted η
Southwell difference	$-0.1211 + 0.1591 \ln N$	$0.1356 + 0.1638 \ln N$	$-0.1237 + 0.3164 \ln N$
Hudgin difference	$0.0485 + 0.1592 \ln N$	$0.3456 + 0.1528 \ln N$	$0.561 + 0.103 \ln N$
Fried difference	$-0.0865 + 0.3202 \ln N$	—	$0.6558 + 0.3206 \ln N$
Band limited	$-0.0285 + 0.1594 \ln N$	$0.2449 + 0.1615 \ln N$	$0.1072 + 0.318 \ln N$
Simpson difference	$0.0314 + 0.1610 \ln N$	$0.3125 + 0.1647 \ln N$	—

is about a factor-of-2 difference in the Southwell and Noll's expression compared with ours. On the other hand, Hudgin's formula does not agree with our results. Fried's formula is based on a comparatively large number of N (≤ 39) compared with Southwell and Hudgin's calculations ($N \leq 20$).

Conclusion

We have presented derivations of band-limited derivative operators in the frequency domain. These are important tools for characterizing and improving the frequency response of wavefront reconstructors over broad bandwidth. Two new wavefront reconstructors were proposed utilizing these tools. The reconstructors were designed to be accurate up to high spatial frequency. The first one is based on the Simpson integration rule. The bandwidth of the frequency response of this reconstructor, after being regularized, is excellent up to 85% of the spatial frequency range. A successive-over-relaxation iterative solver was presented in detail, where the outermost samples are elegantly handled using g flags. The frequency-response behavior of the iterative solver agrees well with the predicted frequency-response curve. The second reconstructor is an extension of the band-limited reconstruction algorithm previously developed; the measurement points are on a hexagonal array instead of a rectangular array. A Fourier-domain iterative algorithm was proposed for two types of hexagonal arrays. As was previously pointed out in Ref. 11, the reconstruction process must be preconditioned with the low-order polynomial fit. The Simpson-rule-based algorithm works purely in the spatial domain; therefore, it is computationally less complex than band-limited algorithms, whereas the latter provides flexibility against any geometry change. Fourier-domain algorithms have a potential of boosting reduction speed with the help of digital-signal processors.

The new wavefront reconstructors are compared with the traditional reconstructors in terms of noise-propagation properties through a generalized noise-propagation expression. The analytically calculated noise-propagation coefficients are consistent with the numerical fit deduced from our own simulations. We did not find, however, universal agreement with the published results.

The broad-bandwidth wavefront reconstructors developed here are used in wavefront-reduction software to characterize focal spots of the OMEGA EP laser beams.¹³ The importance of the band-limited reconstructor was well illustrated in Ref. 21 for a closed-loop wavefront-shaping application. One may also find applications in the study of metrology and atmospheric turbulence.²²

ACKNOWLEDGMENT

This work was supported by the U.S. Department of Energy Office of Inertial Confinement Fusion under Cooperative Agreement No. DE-FC52-08NA28302, the University of Rochester, and the New York State Energy Research and Development Authority. The support of DOE does not constitute an endorsement by DOE of the views expressed in this article.

REFERENCES

1. D. L. Fried, *J. Opt. Soc. Am.* **67**, 370 (1977).
2. R. H. Hudgin, *J. Opt. Soc. Am.* **67**, 375 (1977).
3. K. R. Freischlad and C. L. Koliopoulos, *J. Opt. Soc. Am. A* **3**, 1852 (1986).
4. F. Roddier and C. Roddier, *Appl. Opt.* **30**, 1325 (1991).
5. L. A. Poyneer, D. T. Gavel, and J. M. Brase, *J. Opt. Soc. Am. A* **19**, 2100 (2002).
6. L. A. Poyneer and B. Macintosh, *J. Opt. Soc. Am. A* **21**, 810 (2004).
7. A. Dubra, C. Paterson, and C. Dainty, *Appl. Opt.* **43**, 1108 (2004).
8. C. Elster and I. Weingartner, in *X-Ray Mirrors, Crystals, and Multilayers II*, edited by A. K. Freund *et al.* (SPIE, Bellingham, WA, 2002), Vol. 4782, pp. 12–20.
9. J. Campos *et al.*, *Opt. Lett.* **27**, 1986 (2002).
10. L. Yaroslavsky, A. Moreno, and J. Campos, *Opt. Express* **13**, 2892 (2005).
11. S.-W. Bahk, *Opt. Lett.* **33**, 1321 (2008).
12. M. Servin, D. Malacara, and J. L. Marroquin, *Appl. Opt.* **35**, 4343 (1996).
13. J. Bromage, S.-W. Bahk, D. Irwin, J. Kwiatkowski, A. Pruyne, M. Millecchia, M. Moore, and J. D. Zuegel, *Opt. Express* **16**, 16,561 (2008).
14. R. Marks, II and M. W. Hall, *IEEE Trans. Audio, Speech, Lang. Process.* **29**, 872 (1981).
15. W. H. Southwell, *J. Opt. Soc. Am.* **70**, 998 (1980).
16. D. L. Phillips, *J. ACM* **9**, 84 (1962).
17. See <http://www.jwst.nasa.gov/>.
18. S. E. Winters, J. H. Chung, and S. A. Velinsky, *J. Dyn. Syst. Meas. Contr.* **124**, 297 (2002).
19. R. J. Noll, *J. Opt. Soc. Am.* **68**, 139 (1978).
20. W. Zou and J. P. Rolland, *J. Opt. Soc. Am. A* **23**, 2629 (2006).
21. S.-W. Bahk, E. Fess, B. E. Kruschwitz, and J. D. Zuegel, *Opt. Express* **18**, 9151 (2010).
22. T. W. Nicholls, G. D. Boreman, and J. C. Dainty, *Opt. Lett.* **20**, 2460 (1995).

Time-Resolved Optical Response of All-Oxide, $\text{YBa}_2\text{Cu}_3\text{O}_7/\text{La}_{0.7}\text{Sr}_{0.3}\text{MnO}_3$ Proximitized Bilayers

The interplay between superconductivity (S) and ferromagnetism (F) is one of the most intriguing and challenging fields of research in solid-state physics. The proximity effect at the interface between traditional, both metallic, S and F films has been widely investigated.¹ In comparison, properties of bilayers consisting of high-temperature superconducting cuprates and ferromagnetic manganites are much less understood, despite large research activities and substantial progress in the comprehension of the physics of the involved materials.^{2–4} The superconducting proximity effect at the S/F interface is governed by the short coherence length of the cuprate $\xi_0 \approx v_F/2\Delta$ and by the even shorter coherence length $\xi_m \approx v'_F/2E_b$ in manganites, where v_F and v'_F are the Fermi velocities in the S and F layers, respectively, Δ is the superconducting energy gap, and $E_b \approx 3$ eV is the manganite exchange energy.⁵ At the interface, a layer with a thickness of about ξ_0 within the superconductor is expected to show a depressed superconductivity that, in combination with extremely short ξ_m , suggests that Cooper pairs should not practically penetrate into the F layer. This simple consideration is, however, still subject to debate since an unexpected long-range proximity effect recently reported^{3,6,7} has been ascribed to the spin superconducting triplet-pairing at the F side of the bilayer in the presence of magnetic inhomogeneities or domain walls.^{6,8} Magnetic properties of the S/F interface, on the other hand, are governed by the short-length exchange field and associated to nonconventional ordering of Cu spins,⁴ while longer-range effects depend on the spin-diffusion mechanism.⁹ Finally, the establishment of the equilibrium chemical potential determines a charge transfer,² with screening length of the order of 1 to 2 nm, determining “dead layers” on both the S and F sides.

Cuprate/manganite oxide, nanostructured heterostructures are likely to have a high potential for applications. Beside a constantly growing field of spintronics, our research attention has been devoted to $\text{YBa}_2\text{Cu}_3\text{O}_7/\text{La}_{0.7}\text{Sr}_{0.3}\text{MnO}_3$ (YBCO/LSMO) hybrids as possible, artificially engineered, ultrafast optoelectronics devices.^{10,11} However, nonequilibrium properties of the S/F bilayers are far from being fully characterized

and understood. Time-resolved pump–probe ultrafast optical spectroscopy can provide a great deal of information on the dynamics of such complex structures.¹² In this article, we present the successful fabrication of epitaxial YBCO/LSMO nanobilayers and their subpicosecond pump–probe characterization in a temperature range below and above the superconducting critical temperature T_c .

Our YBCO/LSMO heterostructures were grown by pulsed-laser deposition on (001) SrTiO_3 substrates (with a single TiO_2 termination layer), in an O_2 atmosphere at 0.25-Mbar pressure, for deposition of both the first (YBCO) and the second (LSMO) layers. The growth process was performed at 800°C and was controlled *in situ* by the reflection high-energy electron diffraction (RHEED) method. The RHEED patterns demonstrated very high crystallinity of our bilayer structures at every step of the process.¹⁰ Cooling of the samples included a prolonged exposure to 200 Mbar of O_2 at 500°C, to promote full oxidation of YBCO through the LSMO capping. The resulting nanostructures had excellent structural and transport properties, with $\sim 0.3^\circ$ full-width-at-half-maximum rocking curves and sharp superconducting transition (T_{c0} up to 91.5 K, $\Delta T_c \sim 0.3$ K). From measurements of the conductivity's dependence on temperature, we could deduce that the Curie temperature T_c of LSMO largely exceeded room temperature, concluding that in our experiments, even under optical illumination, the LSMO film always remained in the ferromagnetic state. Our test samples consisted of a plain, 100-nm-thick YBCO film (a reference sample) and a sequence of 100-nm-thick YBCO layers capped with 10 and 35 nm of LSMO, respectively (named LY10 and LY35, respectively). The LSMO thicknesses guaranteed a partially transparent behavior at near-infrared wavelengths since, based on our conductivity data, the optical penetration depth was estimated to be

$$\delta \approx \sqrt{\frac{2\varepsilon_0 c^2}{\sigma_0 \omega}} \approx 100 \text{ nm}$$

at our lowest test temperatures.

The femtosecond pump–probe spectroscopy experiments were performed using a mode-locked Ti:sapphire laser, which produced 100-fs pulses at 810-nm wavelength and a 76-MHz repetition rate. The pump and probe beams were focused onto the sample, down to 30 μm in diameter, and cross polarized to eliminate the coherent artifact caused by the direct interference of the two beams. The pump-to-probe average power ratio was set at 10:1 with the pump power set at the 30-mW level (400 pJ of energy per pulse), in order to minimize optical heating and, simultaneously, ensure a good signal-to-noise ratio. The samples were mounted on a cold finger, inside a temperature-controlled, liquid-helium, continuous-flow optical cryostat, operating down to 4 K.

Typical recorded data of the relative optical-reflectivity change $\Delta R/R$ versus time delay are presented in Fig. 127.26. Figure 127.26(a) shows the $\Delta R/R(t)$ waveforms for the reference 100-nm-thick YBCO film, recorded at different temperatures.

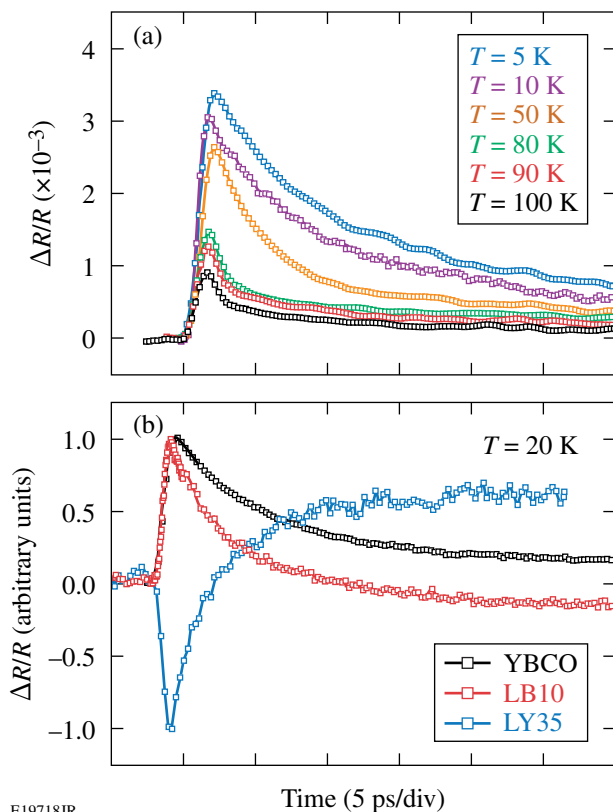
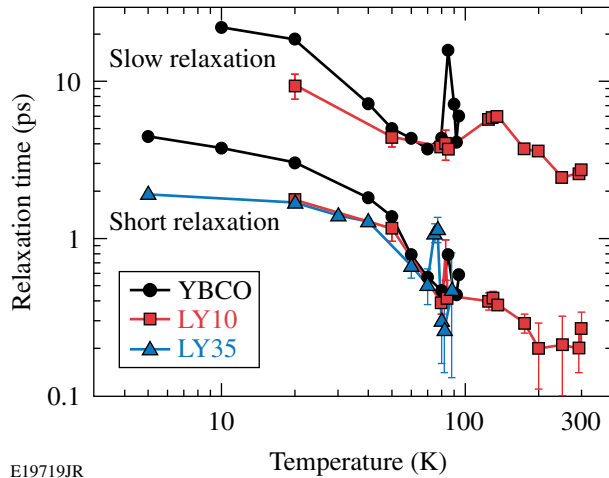


Figure 127.26 (a) The photoresponse $\Delta R/R$ transient versus delay time for a 100-nm-thick YBCO film at different temperatures. (b) The normalized $\Delta R/R$ waveforms versus delay time measured at 20 K for the reference YBCO film and the LY10 and LY35 S/F bilayers.

According to earlier studies on high- T_c materials,¹³ the amplitude of the $\Delta R/R$ signal grows below T_c , while, simultaneously, the recovery becomes progressively slower. This is consistent with other pump–probe studies performed under low-fluence excitations.^{13,14} Contrary to some earlier observations,^{15,16} our data are fitted by a simple linear recombination model, and weak, damped oscillations on top of the exponential decay might, tentatively, be ascribed to displaced excitation of coherent acoustic phonons.^{15,17} Overall, our observations for the pure YBCO film are in agreement with reported data^{14,18–20} and corroborate current interpretation that the slow dynamics below T_c (several tens of picoseconds) cannot be ascribed to the acoustic phonon bottleneck, in contrast with the case of low- T_c superconductors.²¹ In high- T_c materials, recombination of two quasiparticles into a Cooper pair by emission of an acoustic phonon is, in fact, forbidden because the quasiparticle's velocity is faster than the sound velocity²² and the Cooper-pair recombination reflects a complex kinematics involving both nodal and anti-nodal quasiparticles.^{18,19}

The $\Delta R/R$ transients collected at 20 K for two YBCO/LSMO bilayers (LY10 and LY35) and the YBCO reference sample are shown in Fig. 127.26(b). We observe that the thickness of the LSMO overlayer is critically important to the bilayer photoresponse. While the functional dependence of waveform LY10 follows that of the YBCO sample, although with reduced relaxation time, the LY35 curve is very different: it consists of a negative initial peak, followed by an extended relaxation tail, which crosses into the positive values of the $\Delta R/R$ dependence. The negative peak with a time constant ≤ 1 ps can be due to the presence of an additional relaxation mechanism related most likely to localized traps at the S/F interface²³ or multiple reflection from thin heterostructures.

During the course of our research, we have collected dozens of $\Delta R/R$ waveforms for all three samples in the temperature range from 4 K to 300 K, under nominally the same optical pump–probe conditions, and have fitted the data with bi-exponential functions containing two characteristic relaxation times. The latter was justified by the assumption that well above T_c , the system is simply governed by subpicosecond-in-duration, hot-electron cooling in our two materials, of which LSMO has a somewhat slower relaxation time, while below T_c , the fast relaxation process is related to the electron–phonon interaction and the slow one corresponds to the quasi-particle recombination. The results are summarized in Fig. 127.27, where we plot the fast and slow relaxation time dependences on temperature. First we note that below T_c , our YBCO/LSMO bilayers have relaxation times shorter than YBCO, in agreement with the



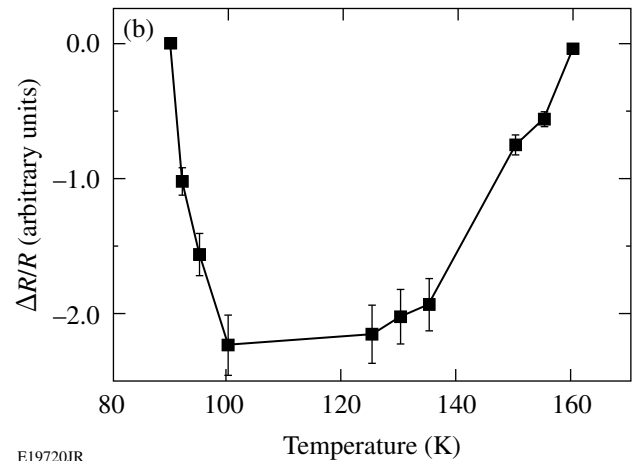
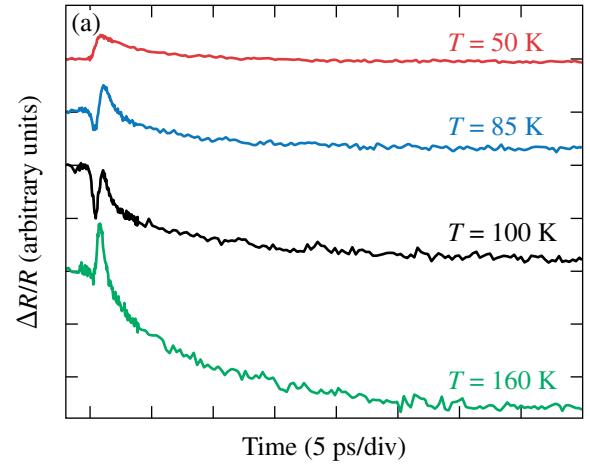
E19719JR

Figure 127.27

The characteristic, both short and slow, relaxation times extracted from the $\Delta R/R(t)$ plots for all our tested samples as a function of temperature.

YBCO/Au/NiCu case.¹⁰ We also observe the presence of sharp peaks in both the fast and slow (YBCO only) relaxation time dependences, which we believe correspond to the occurrence of a superconducting transition within the probed samples, reflecting the change in the quasi-particle dynamics caused by the electronic-specific heat jump.^{21,24} As expected, the T_c peak feature shifts slightly to lower temperatures for the thicker LSMO overlayers but, most interestingly, still remains well visible, contrary to metallic, S/F proximitized bilayers.²⁵ Finally, we note that the characteristic time constant of heat transfer from phonons to the spin-wave gas in LSMO below T_c (Ref. 26) is of the order of 30 ps; consequently, it is essentially out of scale in our measurements.

The active role of the S/F interface results in a clear difference between the dynamics of the bilayers and the mere superposition of behaviors of components films. This is well illustrated by LY10 data shown in Fig. 127.28. Figure 127.28(a) presents examples of the $\Delta R/R$ curves well below T_c , in the vicinity of T_c , and, finally, high above T_c . As mentioned above, in a range of temperature above T_c , we observe a sharp undershoot that precedes the positive $\Delta R/R$ peak. As demonstrated in Fig. 127.28(b), the undershoot quickly increases its magnitude at the superconducting transition, reaching the maximum value at ~ 100 K, remains roughly constant negative in the ~ 100 -K to 140-K range, and finally disappears at ~ 160 K. We stress that no undershoot has ever been observed in either pure LSMO or YBCO films. In our opinion, the undershoot reflects the presence of a few-nm-thick “dead layer” at the S/F interface, with degraded properties. This layer is a result of a charge



E19720JR

Figure 127.28

(a) Examples of photoresponse $\Delta R/R$ transients versus delay time for an LY10 sample at different temperatures. The waveforms are shifted in the y axis for clarity. (b) The magnitude of the $\Delta R/R$ negative peak (undershoot) versus temperature.

transfer from YBCO to LSMO that forms an underdoped YBCO region. The underdoped YBCO (e.g., an oxygen-poor compound) is well known to exhibit a sharp, negative $\Delta R/R$ transient.^{27,28} A similar behavior was also observed for underdoped $\text{Bi}_2\text{Sr}_2\text{CaCu}_2\text{O}_{8+y}$ single crystals.²⁹

The presence of both the depressed-superconductivity layer on the YBCO side and the degraded-magnetic layer on the LSMO side leads to another physical consideration. The quasi particles that are excited in bulk YBCO reach the interface in a characteristic time $d/v_F \approx 100$ fs, comparable with our optical excitation pulse. The quasi-particle injection into the LSMO layer is inhibited because a half metal cannot host free electrons with both spin orientations. Reciprocally, hot electrons from LSMO cannot directly enter the YBCO layer

because they possess only one spin orientation. Within the underdoped YBCO, however, the quasi particles experience a much faster recombination in Cooper pairs since this region acts as an energy trap (suppressed Δ region) that substantially shortens their relaxation process. The concept of excitations being trapped at the boundary between a superconductor and a half metal seems to be quite general and the subject certainly deserves further investigation, both experimental and theoretical. Our early results indicate, however, that this mechanism may efficiently enhance the speed of relaxation of an optically perturbed, nonequilibrium, high- T_c superconductor, capped by the ultrathin F layer.

In conclusion, we investigated the temperature dependence of the nonequilibrium dynamics of YBCO/LSMO nanostructured bilayers in the temperature range from 4 K to room temperature. Experiments have demonstrated the active role of the S/F interface, where the electronic charge transfer from $\text{La}_{0.7}\text{Sr}_{0.3}\text{MnO}_3$ to $\text{YBa}_2\text{Cu}_3\text{O}_7$ determines a thin layer with degraded properties. The LSMO/YBCO bilayers are characterized by quasi-particle relaxation times that are shorter than those of the pure YBCO film, opening a new route to their possible applications in the field of ultrafast superconducting optoelectronics.

ACKNOWLEDGMENT

The authors gratefully acknowledge M. Cuoco for fruitful discussion and D. Pan for assistance in early experiments. The work was partially supported by the European Union under the MAMA project (Napoli, Italy) and by the NSF ECCS under Grant No. 0824075 (University of Rochester, Rochester, NY, USA).

REFERENCES

1. E. A. Demler, G. B. Arnold, and M. R. Beasley, *Phys. Rev. B* **55**, 15174 (1997).
2. S. Yunoki *et al.*, *Phys. Rev. B* **76**, 064532 (2007).
3. V. Peña *et al.*, *Phys. Rev. B* **69**, 224502 (2004).
4. J. Chakhalian *et al.*, *Nat. Phys.* **2**, 244 (2006).
5. J. Y. T. Wei *et al.*, *J. Appl. Phys.* **83**, 7366 (1998).
6. I. Asulin *et al.*, *Phys. Rev. B* **74**, 092501 (2006).
7. T. Holden *et al.*, *Phys. Rev. B* **69**, 064505 (2004).
8. A. F. Volkov, F. S. Bergeret, and K. B. Efetov, *Phys. Rev. Lett.* **90**, 117006 (2003).
9. S. Soltan, J. Albrecht, and H.-U. Habermeier, *Phys. Rev. B* **70**, 144517 (2004).
10. G. P. Pepe, L. Parlato, N. Marrocco, V. Pagliarulo, G. Peluso, A. Barone, F. Tafuri, U. Scotti di Uccio, F. Miletto, M. Radovic, D. Pan, and R. Sobolewski, *Cryogenics* **49**, 660 (2009).
11. N. Marrocco, G. P. Pepe, A. Capretti, L. Parlato, V. Pagliarulo, G. Peluso, A. Barone, R. Cristiano, M. Ejrnaes, A. Casaburi, N. Kashiwazaki, T. Taino, H. Myoren, and R. Sobolewski, *Appl. Phys. Lett.* **97**, 092504 (2010).
12. X. Zou *et al.*, *Appl. Phys. Lett.* **97**, 141910 (2010).
13. M. L. Schneider, S. Rast, M. Onellion, J. Demsar, A. J. Taylor, Y. Glinka, N. H. Tolk, Y. H. Ren, G. Lüpke, A. Xu, Y. Klimov, R. Sobolewski, W. Si, X. H. Zeng, A. Soukiassian, X. X. Xi, M. Abrecht, D. Ariosa, D. Pavuna, A. Krapf, R. Manzke, J. O. Printz, M. S. Williamsen, K. E. Downum, P. GuptaSarma, and I. Bozovic, *Eur. Phys. J. B* **36**, 327 (2003).
14. N. Gedik *et al.*, *Science* **300**, 1410 (2003).
15. B. Mansart *et al.*, *J. Mod. Opt.* **57**, 959 (2010).
16. X. Li, Y. Xu, Š. Chromik, V. Štrbík, P. Odier, D. De Barros, and R. Sobolewski, *IEEE Trans. Appl. Supercond.* **15**, 622 (2005).
17. I. Bozovic, M. Schneider, Y. Xu, R. Sobolewski, Y. H. Ren, G. Lüpke, J. Demsar, A. J. Taylor, and M. Onellin, *Phys. Rev. B* **69**, 132503 (2004).
18. P. C. Howell, A. Rosch, and P. J. Hirschfeld, *Phys. Rev. Lett.* **92**, 037003 (2004).
19. C. W. Luo *et al.*, *J. Appl. Phys.* **102**, 033909 (2007).
20. X. Deng *et al.*, *Phys. Rev. B* **77**, 144528 (2008).
21. A. Rothwarf and B. N. Taylor, *Phys. Rev. Lett.* **19**, 27 (1967).
22. B. J. Feenstra *et al.*, *Phys. Rev. Lett.* **79**, 4890 (1997).
23. L. Vasiliu-Doloc *et al.*, *Phys. Rev. Lett.* **83**, 4393 (1999).
24. J. Demsar *et al.*, *Phys. Rev. Lett.* **82**, 4918 (1999).
25. T. Taneda, G. P. Pepe, L. Parlato, A. A. Golubov, and R. Sobolewski, *Phys. Rev. B* **75**, 174507 (2007).
26. R. D. Averitt and A. J. Taylor, *J. Phys. (USSR)* **14**, R1357 (2002).
27. L. Shi, T. Gong, X. Weng, Y. Kostoulas, R. Sobolewski, and P. M. Fauchet, *Appl. Phys. Lett.* **64**, 1150 (1994).
28. K. H. Wu *et al.*, *Chin. J. Phys.* **38**, 279 (2000).
29. Y. H. Liu *et al.*, *Phys. Rev. Lett.* **101**, 137003 (2008).

Hot-Spot Mix in Ignition-Scale Inertial Confinement Fusion Targets

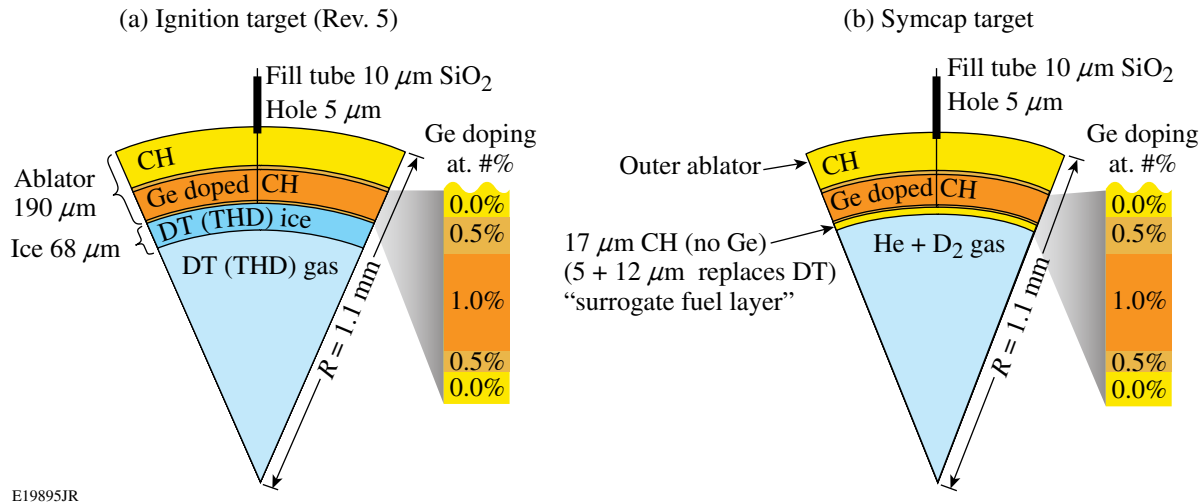
Inertial confinement fusion (ICF) depends on the formation of a central hot spot with sufficient temperature and areal density for ignition.^{1,2} Laser-driven hohlraums are used to accelerate targets via x-ray ablation^{1,2} at the 192-beam, 351-nm, 1.8-MJ National Ignition Facility (NIF).³ Shock-timing,^{4,5} implosion velocity,⁶ and symmetry^{7,8} experiments on the NIF are underway with ignition-scale targets^{5,9} to optimize the hot-spot formation. The concentric spherical layers of current NIF ignition targets consist of a plastic Ge-doped ablator surrounding a thin shell of cryogenic thermonuclear fuel (i.e., hydrogen isotopes), with fuel vapor filling the interior volume.¹⁰ Liquid deuterium–tritium (DT) is directed inside the ablator shell using a fill tube, and a DT-ice layer is formed using the beta-layering technique.¹¹ As the shell converges, it compresses the fuel vapor, forming a hot spot as it decelerates. The hot spot contains $\sim 20 \mu\text{g}$ of DT mass, which undergoes fusion reactions. As the DT-fusion alpha particles deposit their energy in the hot spot, the hot-spot temperature sharply rises, and a thermonuclear burn wave propagates out through the surrounding cold and dense DT fuel. Ignition is predicted to occur when the temperature and areal density of the hot spot reach a minimum of 5 keV and 0.3 mg/cm^2 , respectively.¹⁰

Radiative and conductive losses from the hot spot can be increased by hydrodynamic instabilities.¹⁰ The Richtmyer–Meshkov and Rayleigh–Taylor hydrodynamic instabilities seeded by high-mode ($50 < \ell < 200$) ablator-surface mass perturbations from intrinsic CH surface roughness, the fill tube, or microscopic dust particles are predicted to mix ablator material into the interior of the shell at the end of the acceleration phase and into the hot spot as it forms (i.e., hot-spot mix), producing Ge K-shell emission.¹² This article presents conclusive experimental evidence of hot-spot mix occurring in ignition-scale implosions, for the first time, and quantifies the amount of hot-spot mix mass. These experimental observations are important for ICF because there is a requirement for ignition, set from multidimensional radiation–hydrodynamic simulations, that the hot-spot mix mass be less than 75 ng (Ref. 10). The amount of hot-spot mix mass, estimated from the Ge K-shell line brightness using a detailed atomic physics

code,¹³ was found to be comparable to the 75-ng allowance for hot-spot mix. Predictions of a simple mix model¹⁴ based on linear growth of the measured surface-mass modulations are close to the experimental results. The strategy to control the amount of hot-spot mix involves reducing the capsule-surface mass perturbations and reducing the growth factors of the hydrodynamic instability¹² of the plastic ablator through dopant and laser pulse shape choices, or changing to another ablator material (e.g., Cu-doped Be).¹⁵

The amount of hot-spot mix mass in ignition-scale NIF implosions was diagnosed using x-ray spectroscopy.¹⁶ The ablator was doped with Ge to minimize preheat of the ablator closest to the DT ice caused by Au M-band emission from the hohlraum x-ray drive.¹⁷ A schematic of an ignition target highlighting the Ge-doped ablator surrounding the cryogenic-DT layer and DT vapor is shown in Fig. 128.1(a). The K-shell line emission from the ionized Ge that has penetrated into the hot spot provides an experimental signature of hot-spot mix.¹² If the Ge remains in the cold and dense ablator, the Ge ionization will be insufficient to create K-shell line radiation; therefore, the Ge K-shell line emission provides a direct diagnosis of Ge-doped plastic mixing with the hot spot.

The Ge emission from DT and tritium–hydrogen–deuterium (THD) cryogenic targets and gas-filled plastic-shell capsules, which replace the cryogenic fuel layer with a mass-equivalent CH layer^{7,8} [shown in Fig. 128.1(b)] was examined. The latter, called a symmetry capsule or symcap, is used to infer the symmetry of the hohlraum x-ray drive by measuring the spatial distribution of the x-ray emission from the hot spot around the time of peak compression under simpler noncryogenically layered conditions. Symcap targets have a D^3He (30:70) gas fill. Ignition targets have an equimolar mixture of D and T; however, tritium-rich layered targets with H and D were imploded to exploit the lower neutron yields for diagnostic purposes.¹⁰ The THD implosions are hydrodynamically equivalent to the DT implosions. As seen in Fig. 128.1, the ignition target had an outside diameter of 2.2 mm and an ablator thickness of $190 \mu\text{m}$. The radial distribution of the Ge-dopant atomic percentage



E19895JR

Figure 128.1

Schematic of (a) an ignition target and (b) a symcap target. The cryogenic fuel of the ignition target and the D^3He gas fill of the symcap are transported to the interior of the Ge-doped, plastic ablator using a fill tube. The radial distribution of the Ge atomic doping level in the plastic ablator is shown.

in the plastic ablator was varied to achieve a more-optimal Atwood number between the ablator and the fuel layer at peak shell velocity.¹⁰ In an ignition target the Ge-doped plastic layer is separated from the DT fuel by an undoped plastic layer of $5\text{-}\mu\text{m}$ thickness. In the symcap target, an extra inner $12\text{-}\mu\text{m}$ of plastic of equivalent mass replaces the DT fuel layer.

Bright spots in broadband, gated x-ray implosion images for photon energies greater than 8 keV indicate that hot-spot mix may be occurring in NIF implosions.¹⁸ These bright spots do not provide conclusive evidence, however, of ablator mixing into the hot spot nor do they allow for quantification of the mix mass since the bright spots depend on the plasma composition and conditions and on spatial variations in shell x-ray attenuation caused by regions of low shell areal density. Consequently, a hot-spot x-ray spectrometer (HSXRS) providing coverage in the $9.75\text{- to }13.1\text{-keV}$ range for analysis of the Ge K-shell emission was installed on the NIF.¹⁹ This time-integrated, one-dimensional (1-D) imaging spectrometer viewed the implosion capsule through the laser entrance hole within $\sim 2^\circ$ of the hohlraum symmetry axis. The HSXRS combines a $100\text{-}\mu\text{m}$ -wide slit aperture and a pentaerythritol (PET) Bragg crystal to record 1-D spectral images of the implosion core with a magnification of about 11, a spatial resolution in the target plane of approximately $100\text{ }\mu\text{m}$, and a spectral resolution of 12 eV (Ref. 19). Therefore, the implosion emission is spatially discriminated from the background hohlraum plasma emission in the time-integrated 1-D spectral images. Figure 128.2 shows

an x-ray spectrum measured on symcap implosion N110208 from this diagnostic (black curve), highlighting the spectral features resulting from cold Ge in the pusher (edge drop at 11 keV and fluorescent emission at 9.8 keV) and, most importantly, the emission from the highly ionized Ge in the hot-spot mix mass between 10 and 10.5 keV . He-like Ge is the highest charge state observed. This emission is the first direct evidence of ablator mix into the hot spot of ignition-scale targets. In Fig. 128.2 the x-ray continuum from the hot spot transmitted through the compressed shell is modeled (red curve) assuming the x-ray continuum and the shell optical thickness scale with photon energy ($h\nu$) as $e^{-h\nu/kT}$ and $h\nu^{-3}$, respectively. I_C , M_L , and M_{K+L} are the fitting constants and $h\nu_K$ is the Ge K-edge photon energy.

The Ge K-shell line emission in the $10\text{- to }10.5\text{-keV}$ range from the hot-spot mix mass is highlighted in Fig. 128.3(a) for symcap implosion N110208. As shown in Fig. 128.3(b) a similar spectrum is observed for DT implosion N110620. In these plots the hot-spot x-ray continuum was subtracted and a correction for pusher absorption was applied. This photon-energy range contains a rich spectrum of line emissions from Ge He-like resonance $1s^2-1s2p(1P)$ and intercombination $1s^2-1s2p(3P)$ transitions as well as from Ge B-like $1s^2(2s,2p)^3-1s2p(2s,2p)^3$, Ge Be-like $1s^2(2s,2p)^2-1s2p(2s,2p)^2$, and Ge Li-like $1s^2(2s,2p)^1-1s2p(2s,2p)^1$ satellite lines. The spectral envelope of the He_α + satellite feature is sensitive to variations in the electron temperature (T_e) and electron density (n_e) of the mix mass.²⁰

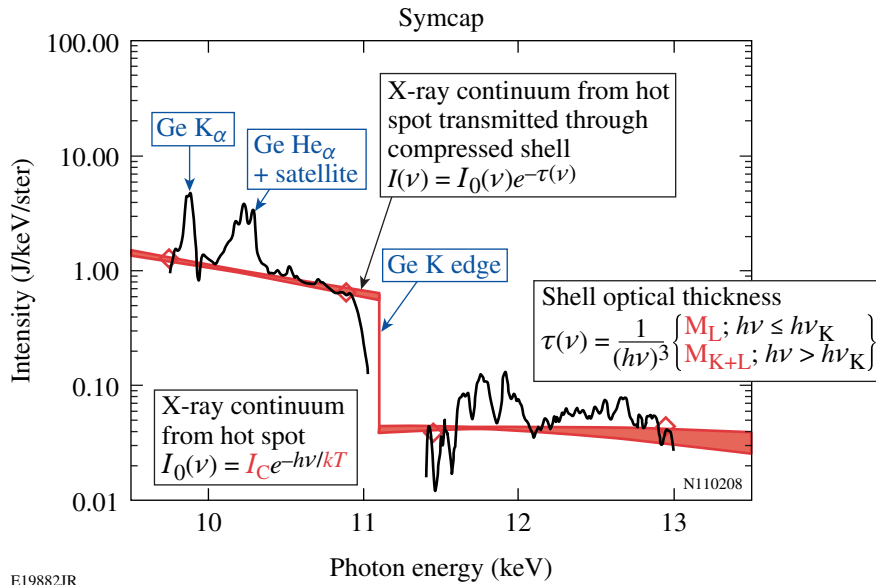
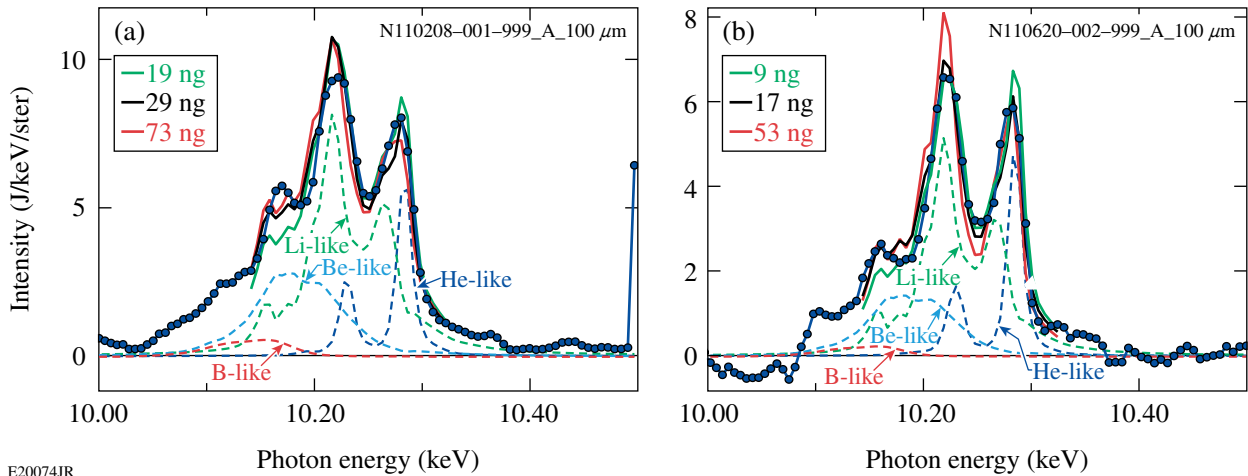


Figure 128.2

Spatially integrated and photometrically calibrated measured x-ray spectrum for symcap implosion N110208 showing Ge He α + satellite and Ge K α emissions and the Ge K edge (black curve). The x-ray continuum from the hot spot transmitted through the compressed shell is modeled (red curve) assuming the x-ray continuum and the shell optical thickness scale with photon energy ($h\nu$) as $e^{-h\nu/kT}$ and $h\nu^{-3}$, respectively. I_C , M_L , and M_{K+L} are the fitting constants and $h\nu_K$ is the Ge K-edge photon energy.

E19882JR



E20074JR

Figure 128.3

Measured Ge K-shell line emission in the 10- to 10.5-keV range from the hot-spot mix mass (blue circles) for (a) symcap implosion N110208 and (b) DT implosion N110620. Modeled spectra assuming uniform plasma conditions and based on least squares fitting are shown [best fit (black curve); 1σ spectral fits (red and green curves)]. Uniform plasma conditions determined from spectral fitting and inferred mix masses are given in Tables 128.I and 128.II. Dashed lines show contributions from He-like, Li-like, Be-like, and B-like charge states for the best fit.

The physical picture of the hot-spot mix is shown in Fig. 128.4. Most of the Ge remains in the compressed shell and absorbs x rays from the hot spot. Depending on the temperature of the shell, this absorption manifests as either Ge K α emission or Ge $1s-2p$ absorption features.²⁰ The ablator material mixed into the hot spot is ionized and emits Ge K-shell x rays. The mix mass is modeled as multiple identical independent spheres of CH ablator mass doped with 1% atomic Ge, each at the same single electron density and temperature, and with

areal densities of Ge-doped CH ($\rho R_{CH\ Ge}$) and Ge (ρR_{Ge}). A detailed atomic and radiation physics model¹³ is used to estimate the amount of mix mass from the Ge K-shell line spectrum as follows: The temperature- and density-dependent emissivity model gives the total emission per Ge mass within the Ge He α + satellite feature. The spectral fit includes self-absorption-coupled level kinetics, giving an estimate of the areal density of Ge in the mix-mass sphere. The Ne through H-like species are represented with detailed-configuration

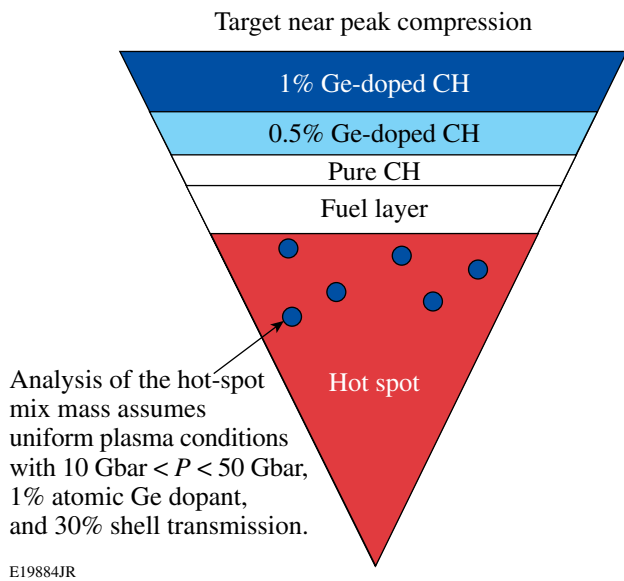


Figure 128.4
Schematic of mix mass in compressed target near peak compression.

accounting (DCA) including all single excitations through $n = 10$, all double excitations through $n = 3$, and splitting important resonance-line-emitting configurations. The Stark-broadening of the Ge line shapes was calculated using the MERL code,²¹ but it is not significant for $n_e < 10^{25} \text{ cm}^{-3}$. The calculated emergent intensity distribution is sensitive to variations in n_e , T_e , and ρR_{Ge} (Ref. 20). The measured spectra are compared with modeled spectra, including instrumental broadening effects for several thousand combinations of n_e , T_e , and ρR_{Ge} , and the best match is determined based on a least squares fit. The amount of mix mass is then determined from the inferred plasma conditions (n_e , T_e , and ρR_{Ge}) and the absolute brightness of the Ge He_α + satellite feature. From the inferred plasma conditions, each sphere of radius R has a CH Ge mass $M_{\text{CH Ge}} = 4\pi R^3 \rho_{\text{CH Ge}}/3$, where $R = \rho R_{\text{CH Ge}}/\rho_{\text{CH Ge}}$ is calculated using the inferred areal densities and electron density of the mix mass and assuming the average ionization is 3.75. The number of spheres the total mix mass are determined by comparing the brightness per sphere to the total measured brightness of the Ge He_α + satellite measurement.

An analysis of the hot-spot mix mass assumes uniform plasma conditions (n_e , T_e , and ρR_{Ge}), electron pressures between 10 and 50 Gbar, 1% atomic Ge dopant, and 30% shell transmission for the Ge He_α + satellite feature (per 1-D hydrodynamic simulations). The estimated shell transmission represents a lower limit for the experiment, leading to an upper limit of inferred mix mass. The two-dimensional (2-D) hydrodynamic simulations show that most of the hot-spot mix mass

originates from the shell layer doped with 1% atomic Ge.¹² The modeled spectra are shown in Fig. 128.3 with the black curve representing the best fit (i.e., minimum χ^2) and the red/green curves representing 1σ spectral fits. The latter define the upper and lower limits of the hot-spot mix mass. The dashed curves in Fig. 128.3 show the contributions to the spectrum from the He-like, Li-like, Be-like, and B-like charge states. Similar mix-mass observations were made on other symcap shots (as shown in Table 128.I) and on DT and THD implosions (as shown in Table 128.II). The mix-mass sphere diameter from the spectral analysis is micron scale, and the number of mix-mass spheres varies from hundreds to thousands, depending on the implosion.

The expected hot-spot mix mass for each capsule is independently estimated with a simple hot-spot mix-mass model that combines linear analysis of the perturbation growth with detailed 2-D hydrodynamic simulations following these steps:¹⁴ (1) transform the capsule-surface perturbation measurements into Legendre-mode space; (2) multiply the decomposed initial perturbations by linear growth factors, calculated for a final perturbation at the ice-ablator interface at peak shell velocity that resulted from a small initial bump on the outside of the ablator; (3) transform back to physical space; (4) find the volume of the ablator that is inside the ice for a DT or THD implosion or the inner CH for a symcap; and (5) multiply by the density calibrated with a detailed bump simulation ($\sim 10 \text{ g/cm}^3$), yielding an estimate of the hot-spot mix mass.¹⁴ The simple hot-spot mix model does not describe the detailed shape of perturbations, but it is calibrated against simulations with actual bump sizes and nonlinear perturbation growth. The hot-spot mix mass (i.e., CH doped with 1% atomic Ge) inferred from the x-ray spectroscopy is compared with the simple hot-spot mix-mass model in Fig. 128.5, and the model is close to the measured results. Most ignition-scale implosions have hot-spot mix mass below the 75-ng requirement for ignition. The experimentally inferred values of hot-spot mix mass in Fig. 128.5 represent a lower bound since the x-ray spectroscopy is only sensitive to the Ge hot-spot mix mass and inferring the CH mass requires an assumed doping level of Ge in the mix mass. Measurements of the mass remaining of ignition-scale targets are close to or slightly larger than predicted, but the implosion velocity is about 10% low.⁶ Higher levels of hot-spot mix mass may occur when higher laser powers and/or thinner shells are used to increase the peak implosion velocity to reach the ignition requirement of $350 \mu\text{m/ns}$ (Ref. 10).

In the future, hot-spot mix will be examined with Cu and Ge dopants located at different radial locations in the ablator to test

Table 128.I: Fitting parameters and hot-spot mix mass inferred for symcap implosions.

Shot	Mix n_e (10^{25} cm $^{-3}$)	Mix T_e (keV)	Mix ρR_{Ge} (mg/cm 2)	CH Ge mix mass (ng)
N101004	0.8 (+0.2, -0.5)	2.4 (+0.6, -0.3)	0.150 (-0, +0.25)	14 (-7, +30)
N110208	1.0 (+0, -0.5)	2.3 (+0.4, -0.3)	0.125 (+0.025, +0.1)	29 (-10, +44)
N110211	0.9 (+0.1, -0.4)	2.0 (+0.3, -0.2)	0.150 (-0, +0.125)	20 (-8, +24)
N110612	0.9 (+0.1, -0.5)	2.2 (+0.5, -0.5)	0.075 (+0.025, -0)	79 (-39, +300)

Table 128.II: Fitting parameters and hot-spot mix mass inferred for DT and THD implosions.

Shot	Mix n_e ($\times 10^{25}$ cm $^{-3}$)	Mix T_e (keV)	Mix ρR_{Ge} (mg/cm 2)	CH Ge mix mass (ng)	
N100929	0.4 (+0.6, +0.1)	1.7 (+0.2, -0.2)	0.075 (+0, -0)	74 (-48, +55)	
N110121	0.3 (+0.6, +0.1)	2.1 (+0.3, -0.5)	0.075 (+0, -0)	67 (-47, +110)	
N110201	1.0 (+0, -0.4)	1.6 (+0.8, -0.5)	0.2 (-0.1, +0.15)	15 (-12, +285)	
N110212	0.5 (+0.1, +0.1)	1.6 (+0.8, -0.5)	0.075 (-0, +0.15)	20 (-17, +265)	
N110603	0.4 (+0.6, +0)	1.9 (+0.6, -0.3)	0.075 (+0.025, -0)	18 (-14, +23)	THD
N110608	0.4 (+0.6, +0)	2.0 (+0.4, -0.3)	0.075 (+0, -0)	63 (-44, +65)	DT
N110615	0.9 (+0, -0.5)	2.2 (+1.0, -0.5)	0.075 (+0, -0)	15 (-10, +56)	
N110620	0.8 (+0.2, -0.5)	2.4 (+0.6, -0.3)	0.075 (+0, -0)	17 (-8, +36)	

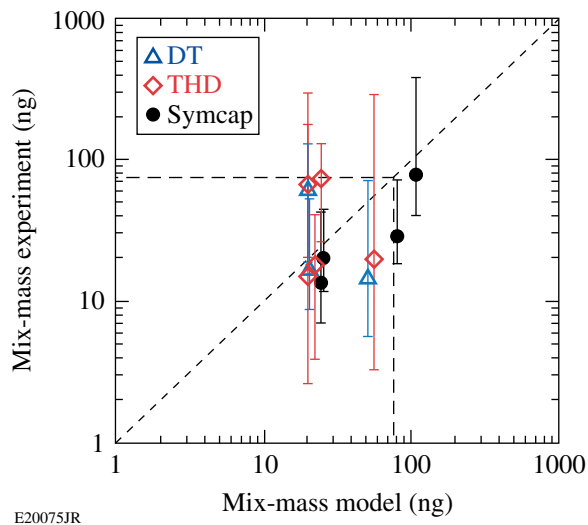


Figure 128.5

Comparison of hot-spot mix mass (i.e., CH doped with 1% atomic Ge) inferred from x-ray spectroscopy with a simple hot-spot mix-mass model that combines linear analysis of the perturbation growth with detailed 2-D hydrodynamic simulations.

assumptions of the origin of the hot-spot mix mass, and x-ray radiography of imposed surface perturbations will be studied to directly relate surface perturbations with the hot-spot mix mass inferred from the x-ray spectroscopy.¹²

Conclusive experimental evidence of the hot-spot mix predicted to occur in ignition-scale implosions as a result of the Richtmyer–Meshkov combined with Rayleigh–Taylor hydrodynamic instabilities¹² has been presented. The amount of hot-spot mix mass in NIF implosions inferred from x-ray spectroscopy is close to or below the 75-ng limit for ignition. These experimental observations are important for ICF because predictions from multidimensional hydrodynamic simulations show that hot-spot mix mass in excess of 75 ng could quench the temperature of the hot spot, reduce the thermonuclear fusion rate, and jeopardize the realization of ignition in the laboratory.¹⁰ Further efforts to control hot-spot mix by reducing the capsule surface-mass perturbations and reducing the growth factors of the hydrodynamic instability of the plastic ablator, or by changing to another ablator material [e.g., Cu-doped Be (Ref. 16)] are ongoing.

ACKNOWLEDGMENT

The authors acknowledge the excellent operation of the National Ignition Facility and helpful suggestions from M. H. Key. This work was supported by the U.S. Department of Energy Office of Inertial Confinement Fusion under Cooperative Agreement No. DE-FC52-08NA28302, the University of Rochester, and the New York State Energy Research and Development Authority. The support of DOE does not constitute an endorsement by DOE of the views expressed in this article.

REFERENCES

1. J. D. Lindl *et al.*, Phys. Plasmas **11**, 339 (2004).
2. S. H. Glenzer *et al.*, Science **327**, 1228 (2010).
3. G. H. Miller, E. I. Moses, and C. R. Wuest, Opt. Eng. **43**, 2841 (2004).
4. T. R. Boehly, D. H. Munro, P. M. Celliers, R. E. Olson, D. G. Hicks, V. N. Goncharov, G. W. Collins, H. F. Robey, S. X. Hu, J. A. Marozas, T. C. Sangster, O. L. Landen, and D. D. Meyerhofer, Phys. Plasmas **16**, 056302 (2009).
5. O. L. Landen, J. Edwards, S. W. Haan, H. F. Robey, J. Milovich, B. K. Spears, S. V. Weber, D. S. Clark, J. D. Lindl, B. J. MacGowan, E. I. Moses, J. Atherton, P. A. Amendt, T. R. Boehly, D. K. Bradley, D. G. Braun, D. A. Callahan, P. M. Celliers, G. W. Collins, E. L. Dewald, L. Divol, J. A. Frenje, S. H. Glenzer, A. Hamza, B. A. Hammel, D. G. Hicks, N. Hoffman, N. Izumi, O. S. Jones, J. D. Kilkenny, R. K. Kirkwood, J. L. Kline, G. A. Kyrala, M. M. Marinak, N. Meezan, D. D. Meyerhofer, P. Michel, D. H. Munro, R. E. Olson, A. Nikroo, S. P. Regan, L. J. Suter, C. A. Thomas, and D. C. Wilson, Phys. Plasmas **18**, 051002 (2011).
6. D. G. Hicks, presented at The Seventh International Conference on Inertial Fusion Sciences and Applications, Bordeaux-Lac, France, 12–16 September 2011.
7. P. Michel *et al.*, Phys. Plasmas **17**, 056305 (2010).
8. G. A. Kyrala *et al.*, Phys. Plasmas **18**, 056307 (2011).
9. M. J. Edwards, J. D. Lindl, B. K. Spears, S. V. Weber, L. J. Atherton, D. L. Bleuel, D. K. Bradley, D. A. Callahan, C. J. Cerjan, D. Clark, G. W. Collins, J. E. Fair, R. J. Fortner, S. H. Glenzer, S. W. Haan, B. A. Hammel, A. V. Hamza, S. P. Hatchett, N. Izumi, B. Jacoby, O. S. Jones, J. A. Koch, B. J. Koziowski, O. L. Landen, R. A. Lerche, B. J. MacGowan, A. J. MacKinnon, E. R. Mapoles, M. M. Marinak, M. Moran, E. I. Moses, D. H. Munro, D. H. Schneider, S. M. Sepke, D. A. Shaughnessy, P. T. Springer, R. Tommasini, L. Bernstein, W. Stoeffl, R. Betti, T. R. Boehly, T. C. Sangster, V. Yu. Glebov, P. W. McKenty, S. P. Regan, D. H. Edgell, J. P. Knauer, C. Stoeckl, D. R. Harding, S. Batha, G. Grim, H. W. Herrmann, G. Kyrala, M. Wilke, D. C. Wilson, J. Frenje, R. Petrasso, K. Moreno, H. Huang, K. C. Chen, E. Giraldez, J. D. Kilkenny, M. Mauldin, N. Hein, M. Hoppe, A. Nikroo, and R. J. Leeper, Phys. Plasmas **18**, 051003 (2011).
10. S. W. Haan, J. D. Lindl, D. A. Callahan, D. S. Clark, J. D. Salmonson, B. A. Hammel, L. J. Atherton, R. C. Cook, M. J. Edwards, S. Glenzer, A. V. Hamza, S. P. Hatchett, M. C. Herrmann, D. E. Hinkel, D. D. Ho, H. Huang, O. S. Jones, J. Kline, G. Kyrala, O. L. Landen, B. J. MacGowan, M. M. Marinak, D. D. Meyerhofer, J. L. Milovich, K. A. Moreno, E. I. Moses, D. H. Munro, A. Nikroo, R. E. Olson, K. Peterson, S. M. Pollaine, J. E. Ralph, H. F. Robey, B. K. Spears, P. T. Springer, L. J. Suter, C. A. Thomas, R. P. Town, R. Vesey, S. V. Weber, H. L. Wilkens, and D. C. Wilson, Phys. Plasmas **18**, 051001 (2011).
11. A. J. Martin, R. J. Simms, and R. B. Jacobs, J. Vac. Sci. Technol. A **6**, 1885 (1988); B. J. Koziowski *et al.*, Fusion Sci. Technol. **59**, 14 (2011).
12. B. A. Hammel *et al.*, High Energy Density Phys. **6**, 171 (2010); B. A. Hammel, H. A. Scott, S. P. Regan, C. Cerjan, D. S. Clark, M. J. Edwards, R. Epstein, S. H. Glenzer, S. W. Haan, N. Izumi, J. A. Koch, G. A. Kyrala, O. L. Landen, S. H. Langer, K. Peterson, V. A. Smalyuk, L. J. Suter, and D. C. Wilson, Phys. Plasmas **18**, 056310 (2011).
13. J. J. MacFarlane *et al.*, High Energy Density Phys. **3**, 181 (2007).
14. J. Ralph *et al.*, Bull. Am. Phys. Soc. **55**, 294 (2010).
15. P. A. Bradley and D. C. Wilson, Bull. Am. Phys. Soc. **41**, 1557 (1996); P. Bradley and D. C. Wilson, Phys. Plasmas **8**, 3724 (2001).
16. H. R. Griem, *Principles of Plasma Spectroscopy* (Cambridge University Press, Cambridge, England, 1997).
17. D. S. Clark *et al.*, Phys. Plasmas **17**, 052703 (2010).
18. G. A. Kyrala *et al.*, Rev. Sci. Instrum. **81**, 10E316 (2010).
19. S. P. Regan, B. A. Hammel, R. Prasad, L. J. Suter, P. Bell, M. Eckart, M. A. Barrios, D. K. Bradley, N. Izumi, J. D. Kilkenny, J. L. Kline, G. A. Kyrala, O. L. Landen, T. Ma, R. L. McCrory, D. D. Meyerhofer, T. C. Sangster, and H. Scott, "Hot-Spot X-Ray Spectrometer for the National Ignition Facility," to be submitted to Review of Scientific Instruments.
20. S. P. Regan, R. Epstein, B. A. Hammel, L. J. Suter, J. Ralph, H. Scott, M. A. Barrios, D. K. Bradley, D. A. Callahan, G. W. Collins, S. Dixit, M. J. Edwards, D. R. Farley, S. H. Glenzer, I. E. Golovkin, S. W. Haan, A. Hamza, D. G. Hicks, N. Izumi, J. D. Kilkenny, J. L. Kline, G. A. Kyrala, O. L. Landen, T. Ma, J. J. MacFarlane, A. J. MacKinnon, R. C. Mancini, F. J. Marshall, R. L. McCrory, N. B. Meezan, D. D. Meyerhofer, A. Nikroo, K. J. Peterson, T. C. Sangster, P. Springer, and R. P. J. Town, "Diagnosing Implosions at the National Ignition Facility with X-Ray Spectroscopy," to be published in the *AIP Proceedings on the 17th International Conference on Atomic Processes in Plasmas*.
21. R. C. Mancini *et al.*, Comput. Phys. Commun. **63**, 314 (1991).

Measurements of the Differential Cross Section for the Elastic n - ^3H and n - ^2H Scattering at 14.1 MeV by Using an Inertial Confinement Fusion Facility

The development of an accurate description of light-ion reactions is currently of great interest since it would provide valuable insights into low-energy nuclear reactions important to nuclear astrophysics. Radiative capture reactions, for example, occur in red giants at temperatures low enough that the reaction rates are too small to be directly measured in a laboratory. Extrapolation from measurements at higher energies is also suspect without a fundamental theory for computing these reactions. Fusion energy research also requires accurate cross sections for light-ion reactions to constrain models of inertial confinement fusion (ICF) experiments involving deuterium–tritium fuel. For instance, uncertainties in the differential cross section for the elastic n - ^3H scattering need to be $\sim 5\%$ to reliably infer a fuel areal density (ρR) from the yield ratio between scattered neutrons and primary 14.1-MeV neutrons, called down-scatter ratio (DSR),¹ produced in an ICF implosion. The determination of the ρR from the DSR value is essential for understanding how the fuel is assembled in an implosion and for ultimately guiding the community toward the demonstration of thermonuclear ignition and net energy gain² at the National Ignition Facility (NIF).³

Since the 1950s, the differential cross section for the elastic n - ^3H scattering at 14.1 MeV has been subject to both experimental and theoretical studies. Kootsey *et al.*⁴ measured the cross section at center-of-mass (CM) angles ranging from 55° to 165° , resulting in data with statistical uncertainties of $\sim 20\%$ and a systematic uncertainty of 11%. Shirato *et al.*⁵ and Debertain *et al.*⁶ measured the cross section in the CM angular range of 100° to 175° with an uncertainty varying from $\sim 10\%$ to $\sim 70\%$, and their results are in good agreement with each other, but up to a factor-of-2 smaller than the Kootsey data. Optical-model calculations conducted by DeVries *et al.*⁷ and by Sherif and Podmore⁸ reproduced the Shirato and Debertain data in this CM angular range. Additionally, Hale *et al.*⁹ conducted an R -matrix analysis of all experimental data sets, and the result from that analysis forms the basis of the current ENDF/B-VII evaluation¹⁰ of the differential cross section for the elastic n - ^3H scattering that can be found in nuclear databases. Although efforts have been made to quantify this fundamental cross section, significant discrepancies exist

between the different measurements and between measurements and models. However, a theoretical understanding of the $n + ^3\text{H}$ scattering based on first-principles calculations is within reach.¹¹ For example, *ab initio* variational calculations using a hyperspherical harmonics basis expansion performed with a modern nuclear Hamiltonian consisting of an accurate nucleon–nucleon (NN) potential and a three-nucleon interaction (NNN) provide a good description of the differential cross section for elastic $n + ^3\text{H}$ scattering at low energies.¹² This type of calculation is currently limited, however, to energies below the breakup threshold.

This article describes the first measurement of the differential cross section for the elastic n - ^3H scattering at 14.1 MeV by an ICF facility. It also describes a theoretical calculation¹³ of this cross section, which combines the *ab initio* no-core shell model¹⁴ with the resonating group method¹⁵ into a unified method (NCSM/RGM).¹⁶ Using this theoretical approach, an accurate assessment of the n - ^3H cross section can be made from precision data taken for the isobaric analogue p - ^3He reaction. In these experiments, carried out on the OMEGA laser,¹⁷ deuterium–tritium-gas-filled, thin-glass capsules were used. Each capsule, made of SiO_2 , had a diameter of about $850 \mu\text{m}$, a gas-fill pressure of about 20 atm, and a shell thickness of $3.5 \mu\text{m}$. The fuel–gas mixture was $48.2\% \pm 0.3\%$ deuterium, $48.8\% \pm 0.3\%$ tritium, 2.5% hydrogen, and 0.5% helium-3 from the tritium decay. These capsules were imploded by 60 laser beams that uniformly delivered 30 kJ to the capsule in a 1-ns square pulse. Since the laser energy is quickly absorbed by the glass, the outer part of the glass shell explodes outward while the remaining part moves inward. The imploding part of the shell acts as a piston and drives a shock through the deuterium–tritium fuel that heats the ions. The glass shell continues to move inward behind the shock front, isentropically compressing the post-shock region of the fuel and additionally heating the ions to thermonuclear temperatures. Each implosion, acting as both a 14.1-MeV neutron source and a deuterium–tritium target, produced a burn-averaged ion temperature of $8.5 \pm 0.5 \text{ keV}$ and neutron yield of about 4×10^{13} , which were measured with a neutron time-of-flight diagnostic.¹⁸ The energy spectra of

the emitted tritons and deuterons, elastically scattered by the 14.1-MeV neutrons, were measured simultaneously using a magnet-based charged-particle spectrometer (CPS)¹⁹ installed on the OMEGA chamber (Fig. 128.6). To cover the energy range of interest in this experiment, the detector plane of the CPS was comprised of two pieces of CR-39, which is a plastic polymer that is insensitive to γ rays and x rays produced in an implosion.¹⁹ Different particle track characteristics in CR-39 enables the CPS to make simultaneous measurements of the scattered deuterons (d') and tritons (t') with energies greater than ~ 3.7 MeV and ~ 2.5 MeV, respectively (the lower-energy

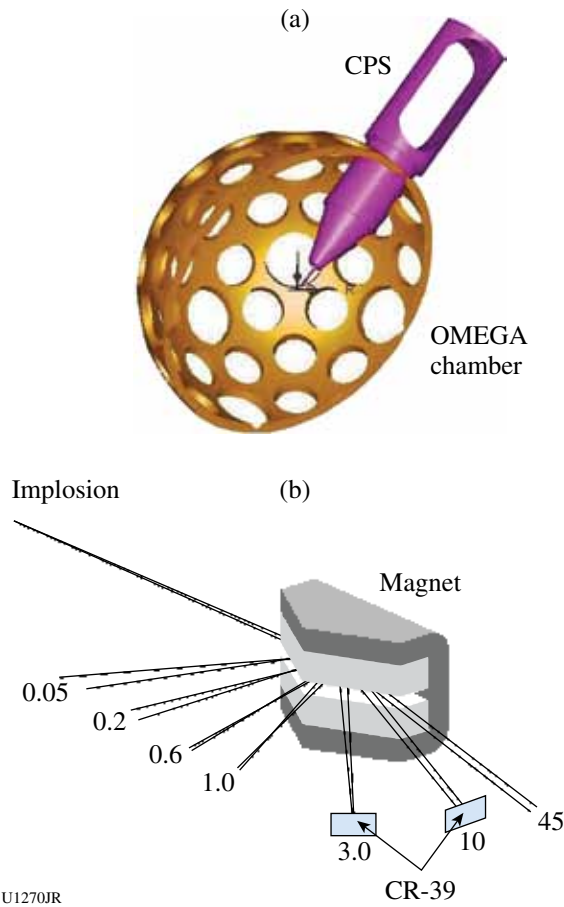


Figure 128.6

(a) The charged-particle spectrometer (CPS) on the OMEGA chamber simultaneously measures deuterons and tritons elastically scattered by 14.1-MeV neutrons and protons from d-d reactions in a deuterium-tritium-gas-filled, thin-glass capsule implosion. A bending magnet (gray) was used for momentum analysis. (b) Schematic drawing of the CPS, which uses a 2-mm-wide aperture in front of a 7.6-kG permanent magnet (Nd-Fe-B) for dispersion and high-resolution measurements of the charged particles. Two pieces of CR-39 were used to detect the dd protons and the elastically scattered deuterons and tritons. The energies are given in MeV for protons.

limits are set by the width and position of the CR-39 piece). The proton spectrum from d-d reactions was measured as well to check that the emitted charged particles were not subject to any significant energy losses in the plasma.

In Figs. 128.7(a)–128.7(c), d' and t' spectra measured simultaneously on three different OMEGA shots are shown. These spectra, which are background subtracted, were obtained by putting constraints on the diameter and darkness of the observed ion tracks in the CR-39 (the triton, deuteron, and background tracks have different characteristics that were used for the differentiation¹⁹). The remaining background that could not be rejected was characterized from regions on the CR-39, where the d' and t' signals cannot be detected. The error bars shown in the spectra are statistical uncertainties associated with the number of signal and background counts in each energy bin. The dd-proton spectrum measured for shot 31753 [Fig. 128.7(d)] displays an average energy that is similar to the birth energy of 3.05 MeV (temperature corrected), indicating that energy losses in the plasma are negligible. From

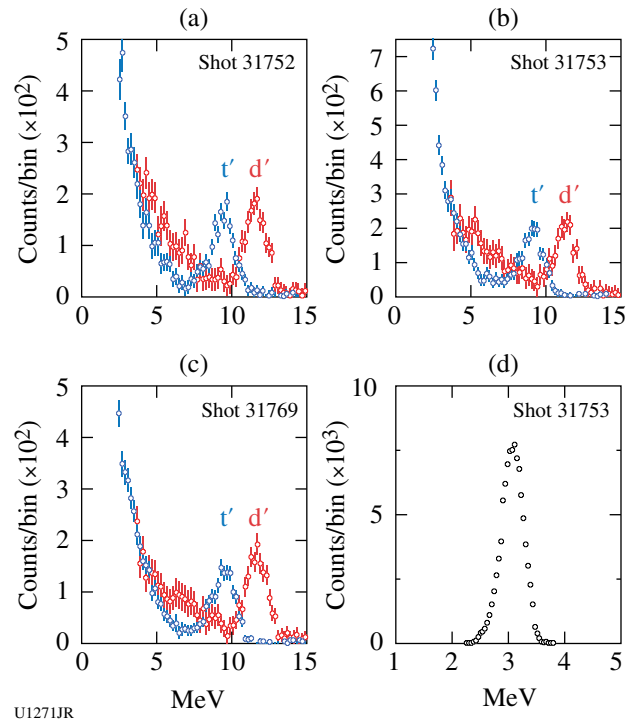


Figure 128.7

[(a)–(c)] The d' and t' spectra measured simultaneously on three different OMEGA shots. The broadening of these spectra is caused by the Doppler effect and CPS response. (d) The dd-proton spectrum measured for shot 31753 illustrates that the average energy is similar to the birth energy of 3.05 MeV (temperature corrected).

the measured d' and t' spectra, the differential cross section for the elastic $n\text{-}^3\text{H}$ and $n\text{-}^2\text{H}$ scattering was determined by deconvolving the CPS response²⁰ and the Doppler-broadened 14.1-MeV neutron spectrum.²¹ While determining the $n\text{-}^2\text{H}$ cross section, the effect of the deuterons from the $t(n,2n)d$ reaction was considered and accounted for. Here, it was assumed that the cross section for this reaction was 6 ± 4 mb, which covers the reported value in Ref. 22, or about $3\%\pm 2\%$ of the total deuteron spectrum in the range 3.7 to 7.3 MeV. Additionally, since the plasma had a burn-averaged ion temperature of 8.5 keV, a density of ~ 1 g/cm³, and a total areal density of ~ 2 to 3 mg/cm², energy-loss effects were insignificant and therefore not considered. From an energy-loss point of view, these plasma conditions correspond to a cold target with an areal density less than 0.3 mg/cm².

Figures 128.8(a) and 128.8(b) show the differential cross section for the elastic $n\text{-}^2\text{H}$ and $n\text{-}^3\text{H}$ scattering measured in this work. These cross sections, compared to the other data sets, are averages of the three measurements shown in Figs. 128.7(a)–128.7(c). The $n\text{-}^2\text{H}$ cross section determined for each shot was normalized to a Faddeev calculation that is accurate to about 1%, and that normalization factor, modified by the deuterium–tritium fuel ratio, was subsequently applied to the measured $n\text{-}^3\text{H}$ cross section for the same shot (the Faddeev calculation was obtained with the NNLO NN plus NNN chiral force of Ref. 23). As illustrated by Fig. 128.8(a), the angular variation of the measured $n\text{-}^2\text{H}$ elastic cross section is in good agreement with the Faddeev-calculated cross section, indicating that the background subtraction, characterization of the response function, and the effect of the Doppler broadening are accurate, and that the deconvolution process provides high-fidelity data. The uncertainties shown for the $n\text{-}^3\text{H}$ cross section [shown in Fig. 128.8(b) and Table 128.III] are based on the statistical uncertainty and the uncertainty associated with the normalization factor. Since the total $n\text{-}^2\text{H}$ elastic cross section and the deuterium–tritium-fuel ratio in these experiments have an uncertainty of 1.0% and 0.9%, respectively, the uncertainty in the normalization factor is estimated to be 1.4%. This results in a total uncertainty ranging from 4% to 7% in the CM-angle range of 60° to 80° , which is the most important range for diagnosing ICF implosions over which the $n\text{-}^3\text{H}$ cross section dominates the other ICF-relevant cross sections. This uncertainty should be contrasted to the total uncertainty larger than 20% for the Kootsey data, which is the only other data set in this angular range. Considering the uncertainties involved, the experimentally determined $n\text{-}^3\text{H}$ cross section compares well with the current ENDF/B-VII evaluated cross section, which is based on Hale’s R -matrix analysis of accurate $p\text{-}^3\text{He}$ data in

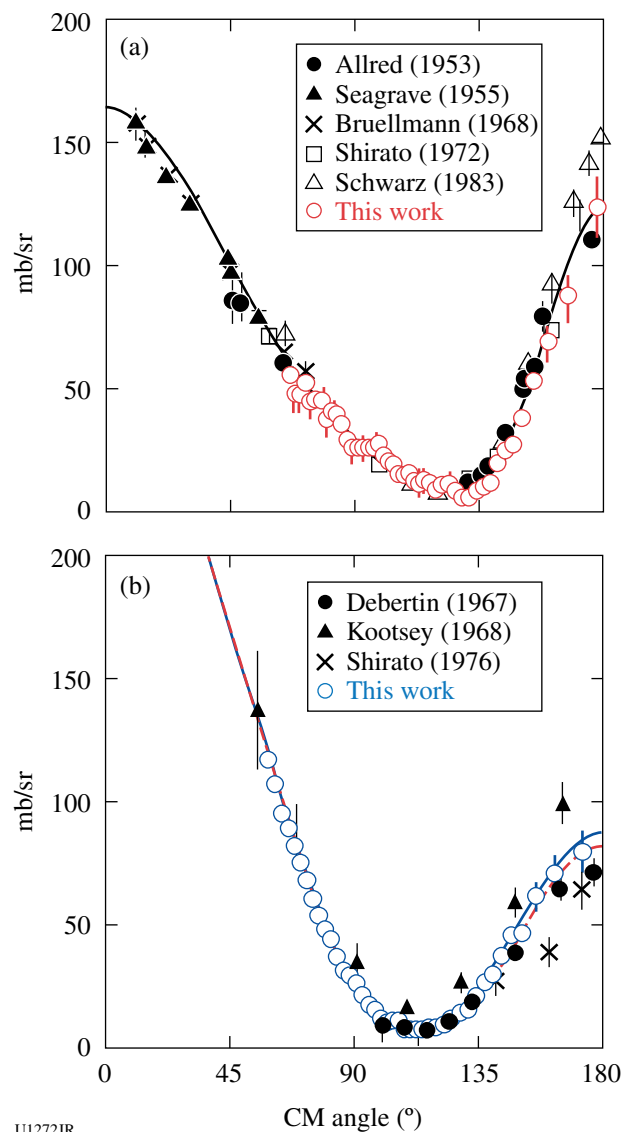


Figure 128.8
(a) Measured differential cross section for the elastic $n\text{-}^2\text{H}$ scattering, which has been normalized to a Faddeev calculation. (b) Measured and calculated differential cross section for the elastic $n\text{-}^3\text{H}$ scattering. The experimental data have been normalized with the deuterium–tritium fuel-ratio–modified normalization factor derived in (a). The blue solid curve represents an *ab initio* NCSM/RGM calculation; the red dashed curve represents an R -matrix-calculated $n\text{-}^3\text{H}$ cross section

a wide range of energies. The fit parameters obtained in that analysis were then adjusted to account for the Coulomb effects, as explained in Ref. 9, and subsequently applied to the $n\text{-}^3\text{H}$ reaction. The results from the R -matrix analysis are shown by the red dashed curve in Fig. 128.8(b). Another theoretical approach, described in detail in Ref. 16, was recently developed to evaluate the cross sections of light-ion reactions. This

Table 128.III: Measured and calculated differential cross section for the elastic n - ^3H scattering as a function of CM angle at 14.1 MeV. The NCSM/RGM calculation, which is corrected at forward angles as explained in the text, is considered to be accurate to about 5%.

CM angle (°)	Measured (mb/sr)	Error (mb/sr)	NCSM/RGM (mb/sr)
58.6	116.7	4.4	119.3
61.2	106.6	3.3	109.9
63.7	94.7	3.5	101.1
66.1	88.8	3.6	93.1
68.3	81.6	3.7	85.6
70.5	75.0	3.9	78.7
72.6	67.8	3.7	72.1
74.7	60.3	3.6	65.9
76.8	53.4	3.5	59.9
79.0	48.1	3.2	54.1
81.2	44.0	3.2	48.5
83.4	37.1	3.3	43.2
85.7	31.5	3.1	38.2
87.9	29.4	2.8	33.4
90.3	26.3	2.9	29.1
92.6	21.7	2.9	25.1
94.8	17.5	2.7	21.6
97.1	15.7	2.5	18.5
99.3	11.9	2.4	15.9
101.5	10.2	2.5	13.7
103.6	11.3	3.3	11.8
105.7	11.2	2.2	10.4
107.8	7.4	1.9	9.2
110.0	7.8	1.9	8.4
112.2	7.6	1.8	8.0
114.4	7.5	1.6	7.9
116.8	8.5	1.3	8.1
119.4	8.5	1.3	8.9
122.0	9.6	1.3	10.2
124.8	12.0	1.2	12.1
127.7	14.4	1.4	14.6
130.7	15.5	1.3	17.7
133.7	21.2	1.4	21.5
136.8	26.5	1.7	25.8
139.8	29.9	1.8	30.5
142.9	37.2	2.2	35.9
146.3	45.6	2.7	42.1
150.2	46.5	3.4	49.4
155.2	61.4	4.7	59.1
162.2	70.5	6.0	71.6
172.3	79.4	7.7	84.3

NCSM/RGM approach, unlike earlier *ab initio* approaches, allows one to calculate various nucleon–nucleus scattering processes for systems with $A > 4$, i.e., both on s - and p -shell nuclei.^{13,16} The present NCSM/RGM calculations for the n - ^3H and p - ^3He systems use a similarity-renormalization-group–evolved chiral N^3LO NN interaction that includes Coulomb and other isospin breaking terms.²⁴ A less-than-15% inaccuracy in these calculations at forward angles is introduced by limiting the model space to channel states with the three-nucleon system in its ground state. To quantify and correct for this inaccuracy, high-precision p - ^3He data²⁵ are compared to the corresponding NCSM/RGM results, and the obtained correction function is applied to the n - ^3H calculation. The result of this procedure, which is accurate to $\sim 5\%$, is illustrated by the blue solid curve in Fig. 128.8(b), which is also in good agreement with our experimental data, but differs from the R -matrix analysis by several percent in the backward-scattering angles of the outgoing neutron. Considering the estimated uncertainty of $\sim 5\%$ for the NCSM/RGM calculation, this discrepancy is, however, insignificant. Additional details of the n - ^3H and p - ^3He NCSM/RGM calculations are found in Ref. 13.

In summary, we report on the first measurements of the differential cross section for the elastic n - ^3H and n - ^2H scattering at 14.1 MeV by an ICF facility. The resulting n - ^3H data are of higher quality than achieved in previous accelerator experiments reported in the literature and accurate enough to reliably determine the fuel ρR from the yield ratio between scattered neutrons and primary 14.1-MeV neutrons produced in an ICF implosion. The experimental results obtained at CM angles ranging from 59° to 172° are in good agreement with a theory that is based on isospin-corrected *ab initio* calculations of the isobaric analogue $p + ^3\text{He}$ reaction. Both measured and calculated cross sections compare well with current ENDF/B-VII-evaluated cross section, which is based on Hale’s R -matrix analysis. A total n - ^3H elastic cross section of 941 ± 47 mb was calculated using the NCSM/RGM method.

ACKNOWLEDGMENT

The authors would like to thank Prof. Dr. Evgeny Epelbaum for providing Faddeev calculations of n - ^2H scattering at 14.1 MeV, which provided the basis for normalizing these experimental results. The work described here was supported in part by U.S. DOE (Grant No. DE-FG03-03SF22691), LLE (No. 412160-001G), LLNL (No. B504974), and General Atomics under DOE (DE-AC52-06NA27279).

REFERENCES

1. J. A. Frenje, D. T. Casey, C. K. Li, F. H. Séguin, R. D. Petrasso, V. Yu. Glebov, P. B. Radha, T. C. Sangster, D. D. Meyerhofer, S. P. Hatchett, S. W. Haan, C. J. Cerjan, O. L. Landen, K. A. Fletcher, and R. J. Leeper, *Phys. Plasmas* **17**, 056311 (2010).
2. B. K. Spears *et al.*, “Prediction of Ignition Implosion Performance Using Measurements of Low-Deuterium Surrogates,” to be published in *Physics of Plasmas*.
3. G. H. Miller, E. I. Moses, and C. R. Wuest, *Nucl. Fusion* **44**, S228 (2004).
4. J. M. Kootsey, *Nucl. Phys.* **A113**, 65 (1968).
5. S. Shirato *et al.*, *Nucl. Phys.* **A267**, 157 (1976).
6. K. Debertin, E. Roessle, and J. U. Schott, <http://www.nndc.bnl.gov/exfor/servlet/X4sGetSubent?reqx=3489&subID=21507002&plus=1>, Brookhaven National Laboratory, Upton, NY (1967).
7. R. M. Devries, J. L. Perrenoud, and I. Slaus, *Nucl. Phys.* **A188**, 449 (1972).
8. H. S. Sherif and B. S. Podmore, in *Few Particle Problems in Nuclear Interaction*, edited by I. Slaus *et al.* (North-Holland, Amsterdam, 1972), pp. 691–694.
9. G. M. Hale *et al.*, *Phys. Rev. C* **42**, 438 (1990).
10. M. B. Chadwick *et al.*, *Nuclear Data Sheets* **107**, 2931 (2006).
11. R. Lazauskas *et al.*, *Phys. Rev. C* **71**, 034004 (2005).
12. M. Viviani *et al.*, *Few-Body Syst.* **45**, 119 (2009).
13. P. Navrátil, S. Quaglioni, and R. Roth, *J. Phys., Conf. Ser.* **312**, 082002 (2011); P. Navrátil *et al.*, Lawrence Livermore National Laboratory, Livermore, CA, Report LLNL-TR-423504 (2010).
14. P. Navrátil, J. P. Vary, and B. R. Barrett, *Phys. Rev. Lett.* **84**, 5728 (2000); P. Navrátil, J. P. Vary, and B. R. Barrett, *Phys. Rev. C* **62**, 054311 (2000).
15. K. Wildermuth and Y. Tang, *A Unified Theory of the Nucleus, Clustering Phenomena in Nuclei* (Vieweg, Braunschweig, Germany, 1977).
16. S. Quaglioni and P. Navrátil, *Phys. Rev. Lett.* **101**, 092501 (2008); S. Quaglioni and P. Navrátil, *Phys. Rev. C* **79**, 044606 (2009).
17. T. R. Boehly, D. L. Brown, R. S. Craxton, R. L. Keck, J. P. Knauer, J. H. Kelly, T. J. Kessler, S. A. Kumpan, S. J. Loucks, S. A. Letzring, F. J. Marshall, R. L. McCrory, S. F. B. Morse, W. Seka, J. M. Soures, and C. P. Verdon, *Opt. Commun.* **133**, 495 (1997).
18. V. Yu. Glebov, C. Stoeckl, T. C. Sangster, S. Roberts, G. J. Schmid, R. A. Lerche, and M. J. Moran, *Rev. Sci. Instrum.* **75**, 3559 (2004).

19. F. H. Séguin, J. A. Frenje, C. K. Li, D. G. Hicks, S. Kurebayashi, J. R. Rygg, B.-E. Schwartz, R. D. Petrasso, S. Roberts, J. M. Soares, D. D. Meyerhofer, T. C. Sangster, J. P. Knauer, C. Sorce, V. Yu. Glebov, C. Stoeckl, T. W. Phillips, R. J. Leeper, K. Fletcher, and S. Padalino, *Rev. Sci. Instrum.* **74**, 975 (2003).
20. The CPS response is described by a 300- and 1,000-keV rectangular distribution at 5 and 10 MeV, respectively. For a 8.5-keV plasma, the Doppler-broadened DT-neutron spectrum is described by a Gaussian distribution with a width of 520 keV (FWHM; see Ref. 21).
21. H. Brysk, *Plasma Phys.* **15**, 611 (1973).
22. I. J. Thompson, *Comput. Phys. Rep.* **7**, 167 (1988).
23. E. Epelbaum *et al.*, *Phys. Rev. C* **66**, 064001 (2002).
24. S. K. Bogner, R. J. Furnstahl, and R. J. Perry, *Phys. Rev. C* **75**, 061001(R) (2007); D. R. Entem and R. Machleidt, *Phys. Rev. C* **68**, 041001(R) (2003).
25. R. L. Hutson *et al.*, *Physical Review C* **4**, 17 (1971).

Study of Rayleigh–Taylor Growth in Directly Driven Cryogenic-Deuterium Targets

Introduction

In inertial confinement fusion (ICF),^{1,2} a spherical capsule is uniformly irradiated to compress a target containing a deuterium–tritium (DT) ice shell, creating the hot-spot temperature and fuel-density conditions required to achieve ignition and significant thermonuclear energy gain. The growth of areal-density (ρR) perturbations resulting from Rayleigh–Taylor^{3,4} (RT) instability can compromise the target’s integrity, quenching the hot-spot formation prior to achieving thermonuclear ignition.^{1,2,5–23} In the linear regime, modulations grow exponentially with a growth rate given by²⁴

$$\gamma = \alpha \sqrt{kg/(1 + kL_m)} - \beta kV_a, \quad (1)$$

where α and β are constants, k is the wave number of the modulation, g is the acceleration of the target, L_m is the density scale length at the ablation front, and V_a is the ablation velocity. Prior to target acceleration, during shock transit, the ablative Richtmyer–Meshkov (RM) instability causes areal-density modulations to oscillate with an oscillation frequency of^{25,26}

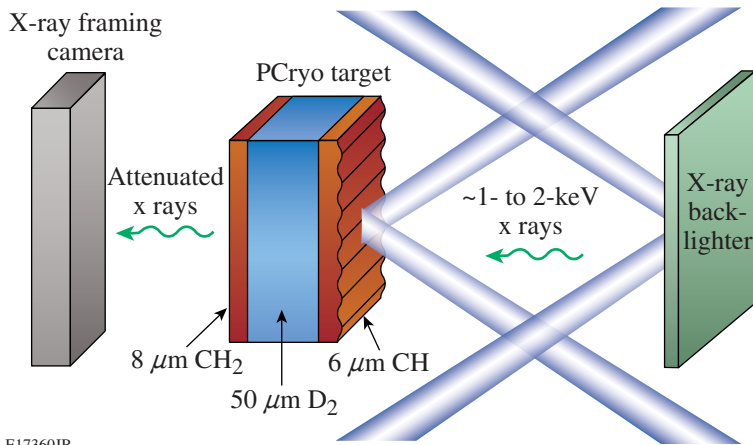
$$\omega = k\sqrt{V_b \cdot V_a}, \quad (2)$$

where V_b is the blowoff velocity. Direct-drive–ignition designs²⁷ use a thick cryogenic (cryo)-DT shell encased by a thin ($\sim 4\text{-}\mu\text{m}$) CH ablator to maximize the amount of fusion fuel contained in the compressed target at peak burn of the implosion.²⁸ As the thin CH layer is ablated, the implosion hydrodynamics become ablative in DT. Targets with DT ablators are predicted to be more robust to the RT instability than mass-equivalent CH ablators.²⁴ Reduced density in DT ablators compared to CH increases the ablation velocity, reducing the growth rate while also allowing for thicker ablators without compromising target acceleration and implosion velocity. The ablative stabilization constant β [Eq. (1)] is ~ 1.7 for CH and ~ 2.6 for DT, providing increased hydrodynamic stability for DT ablators.²⁴ The growth rate of the RT instability has been measured experimentally under a variety of target and drive conditions for room-temperature materials, such as CH, showing good agreement with theoretical predictions

and hydrodynamic simulations at drive intensities up to $\sim 5 \times 10^{14}$ W/cm² (Refs. 2,10,12,29,30). Areal-density modulations can be seeded by target defects created during manufacturing and/or nonuniformities in the target driver (laser imprinting). Significant mitigation of laser imprinting is achieved by the use of distributed phase plates (DPP’s)³¹ and smoothing by spectral dispersion (SSD).³² To design a target that is robust to RT instability and will achieve thermonuclear ignition, it is essential to understand the evolution of ρR modulations in cryo DT. This article presents the first experiments that verify hydrodynamic simulations of RT growth in cryo D₂ (hydrodynamically equivalent to DT) at conditions relevant to achieving direct-drive thermonuclear ignition with a mass preimposed initial condition. Previous experiments have been performed using intensity-imprinted initial modulations, although they could not be simulated because of software limitations.³³ The following sections describe the experimental design; present the experimental configuration and the experimental results; compare results with simulations; and present conclusions.

Experimental Design

Laser-driven RT experiments are typically performed in planar geometry using face-on x-ray radiography.^{12,12,29,30} A target with a known seed modulation (either preimposed or laser imprinted) is irradiated while a high-Z x-ray backlighter foil is used to image the modulation evolution. Figure 128.9 shows the basic face-on radiography configuration used in most direct-drive planar RT experiments. The drive target is irradiated with overlapping drive beams while x rays from a high-Z backlighter traverse the target and are measured on an x-ray framing camera with an imaging pinhole array.³⁴ X-ray radiography relies on the attenuation of backlighter x rays (typically greater than 1 keV because of the spectral response of the framing camera) by the drive target such that variations in the target’s areal density will be measured as variations in the optical depth of the radiograph. Measuring ρR modulation evolution in cryo D₂ presents two significant challenges to the typical face-on x-ray radiography scheme: D₂ has little x-ray attenuation at energies greater than 1 keV and a cryo-D₂ layer must be contained by a solid ambient material, typically plas-



E17360JR

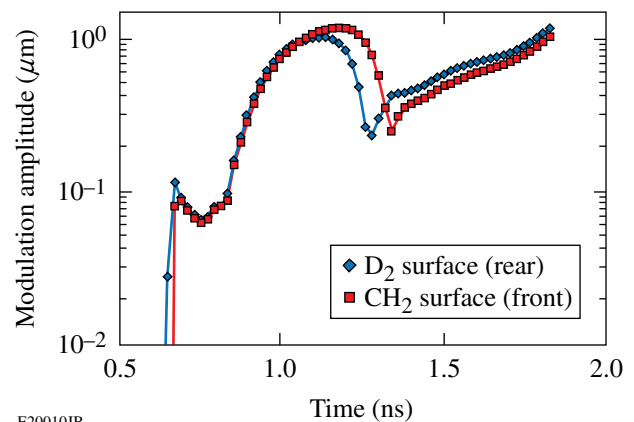
tic (CH). Lower-energy x rays required to directly radiograph the cryo D_2 would suffer from severe attenuation in the CH layer and increased background from the soft x rays produced by the CH plasma. Instead, the modulation evolution in D_2 is measured indirectly using modulation feedthrough³⁵ into the rear window of a planar cryo- D_2 target. A schematic of the planar cryo- D_2 target can be seen in Fig. 128.9. The target consists of a 50- μm -thick D_2 “sandwich” held in place by a 6- μm -thick front CH window and an 8- μm -thick rear CH_2 window mounted in a 2-mm-sq copper washer with an inner diameter of 1.5 mm. The front CH window is seeded with a 60- μm -wavelength sinusoidal modulation with an initial amplitude of 0.25 μm , and the entire assembly is mounted to a cryo finger that cools the target to ~ 20 K so a liquid- D_2 layer exists between the two plastic windows. As the target is driven, the front CH window is ablated away and the modulation evolution at the ablation front is governed by the ablative growth in D_2 . These D_2 modulations feed through to the rear CH_2 window of the target with the relationship

$$a_{CH_2}(k, t) = a_{D_2}(k, t) e^{-k \cdot d(t)}, \quad (3)$$

where α_{D_2} is the modulation amplitude at the D_2 ablation front, α_{CH_2} is the modulation amplitude at the rear CH_2 window, k is the modulation wave number, and $d(t)$ is the distance between the D_2 ablation front and the rear CH_2 window of the target. Equation (3) indicates that the modulation amplitude at the D_2 ablation front will always be greater than in the CH_2 window. *DRACO*³⁶ simulations indicate that the modulations in D_2 correlate well with the observed modulation on the rear CH_2 window. The modulation amplitude at the ablation surface in D_2 feeds through to the back D_2 surface and is governed by the same feedthrough relation as defined in Eq. (3). Figure 128.10 shows the simulated modulation amplitude evolution at the

Figure 128.9

Experimental configuration for face-on x-ray radiography. A planar cryogenic (PCryo) target with a sinusoidal seed areal-density modulation is driven by 12 OMEGA drive beams while a backlighter emits 1.3-keV x rays, which are imaged with a time-gated x-ray framing camera. The planar cryogenic drive target consists of a 50- μm , liquid- D_2 layer sandwiched between a 6- μm -thick front CH window and an 8- μm -thick rear CH_2 window. The entire assembly is held in a 2- μm -sq Cu washer with a 1.5-mm inner diameter (not pictured) and is cryogenically cooled to ~ 20 K. The front CH window is seeded with a 60- μm -wavelength sinusoidal modulation with an initial amplitude of 0.25 μm , which will imprint into the D_2 layer as the window is ablated by the drive beams.



E20010JR

Figure 128.10

Simulated rear-surface modulation for a 50- μm -thick liquid- D_2 target with a 6- μm -thick modulated front CH window and an 8- μm -thick rear CH_2 window driven by a 2-ns square pulse. The plot shows the modulation amplitude at the back D_2 surface (blue diamonds) and the modulation in the rear CH_2 window of the target (red squares), indicating that the CH_2 window modulation evolution is dominated by feedthrough from the D_2 ablation front.

back D_2 surface (blue diamonds) as well as the modulation in the rear CH_2 window (red squares) from *DRACO* for a target with a 50- μm -thick D_2 layer held in place by a 6- μm -thick front CH window and an 8- μm -thick rear CH_2 window with an initial front-surface modulation with an amplitude of 0.25 μm at a wavelength of 60 μm being driven by a 2-ns square pulse with an intensity of 4×10^{14} W/cm², showing good correlation between the D_2 and CH_2 layers.

Experimental Configuration

The target shown in Fig. 128.9 was irradiated by 12 overlapping UV beams from OMEGA with a spot diameter of ~ 750 μm using a 2-ns square pulse at a peak intensity of 4×10^{14} W/cm². The spatial profiles of the beams were smoothed

using SSD³² and DPP's.³¹ A uranium backlighter located 9 mm from the drive target was irradiated by ten UV beams with a spot diameter of 1 mm, creating x-ray radiographs on a time-gated x-ray framing camera³⁴ filtered with 1 μm of Al with an additional 3- μm -Al blast shield located 4.5 mm from the drive target to prevent preheating of the target by soft x rays. This configuration yielded a peak x-ray energy of ~ 1.3 keV to radiograph the front and rear plastic windows of the target. The framing camera captured eight radiographs with a temporal resolution of ~ 80 ps and a spatial resolution of ~ 10 μm . Data were extracted from five radiographs from 0.8 to 1.6 ns.

A Weiner filter was constructed to extract the signal from the noise from each individual image.³⁷ The true signal was reconstructed only from data with spatial frequencies near 16.6 mm^{-1} , corresponding to the 60- μm -wavelength seed modulation. For each image, the noise was approximated by the lineout perpendicular to the seed modulation. The noise for all of the images was compared to ensure that the noise spectrum was not changing significantly during the target drive, which would indicate true broadband modulation growth and not noise. Figure 128.11 shows a filtered 300- μm -sq radiograph taken at 1.25 ns into the drive.

The two-dimensional (2-D) hydrodynamics code *DRACO*³⁶ simulated the modulation evolution using flux-limited local electron transport, where the heat flux is taken as the smaller of the *Spitzer-Härm heat flux*³⁸ and the *flux-limited free-*

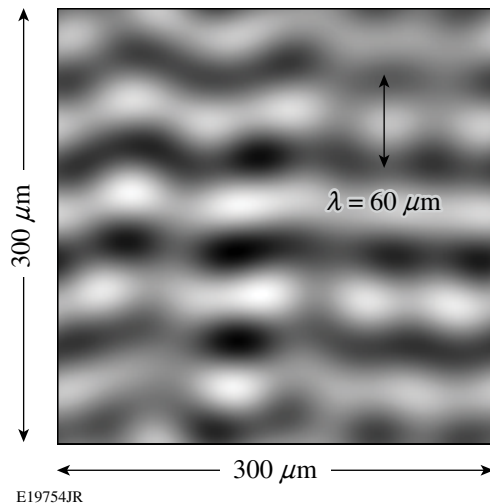


Figure 128.11
A Weiner-filtered, 300- μm -sq face-on radiograph for the planar-cryogenic- D_2 target in Fig. 128.9 driven by 12 drive beams with a 2-ns square pulse with a peak overlapped intensity of 4×10^{14} W/cm^2 taken at 1.25 ns. The 60- μm wavelength appears as horizontal fringes in the image.

streaming heat flux,³⁹ with a standard flux limiter of $f = 0.06$. The simulation used *SESAME 5263* (Ref. 40) for the equation of state (EOS) of the cryogenic- D_2 layer. Figure 128.12 shows the temperature and pressure profiles of the D_2 shock front from *DRACO*. The simulated shocked D_2 density reaches 3 to 4 \times the initial liquid- D_2 density (0.171 g/cc) with pressures ranging from 15 to 25 Mbar and temperatures from 20 to 30 eV during the shock transit into the D_2 liquid. Multiple shocks and rarefactions traverse the target prior to the onset of target acceleration caused by the multiple interfaces. At 0.8 ns, the D_2 layer achieves its peak pressure of 65 Mbar at a temperature of 50 eV because of the rarefaction wave heating from the rear CH_2 window. For these conditions, *SESAME 5263* is in good agreement with the first principles EOS (FPEOS) for D_2 calculated by S. X. Hu *et al.*⁴¹

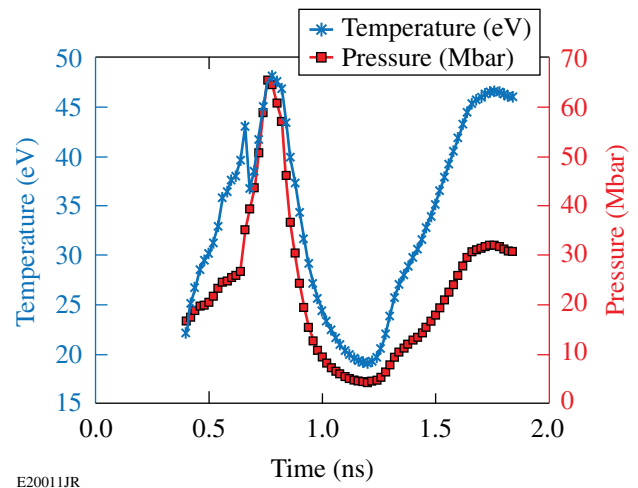


Figure 128.12
Simulated temperature (blue stars) and pressure (red squares) profiles of the D_2 shock front of the planar cryogenic target from *DRACO*. The shocked D_2 density reaches 3 to 4 \times the initial liquid- D_2 density (0.171 g/cc) with pressures ranging from 15 to 25 Mbar and temperatures from 20 to 30 eV during the shock transit into the D_2 liquid. At 0.8 ns, the D_2 layer achieves its peak pressure of 65 Mbar at a temperature of 50 eV as a result of the rarefaction wave heating from the rear CH_2 window.

Experimental Results

Figure 128.13 shows the measured modulation optical depth of the planar cryogenic target in Fig. 128.9 seeded with a 60- μm -wavelength preimposed mass modulation with an initial amplitude of 0.25 μm . The target was driven by a 2-ns square pulse with an intensity of 4×10^{14} W/cm^2 [Fig. 128.13(a)]. The measured modulation amplitude (blue diamonds) are overplotted with the prediction from the 2-D hydrodynamics simulation *DRACO* (red line) showing relatively good agreement [Fig. 128.13(b)]. The measurement and simulation include contributions from both the front and rear plastic windows of

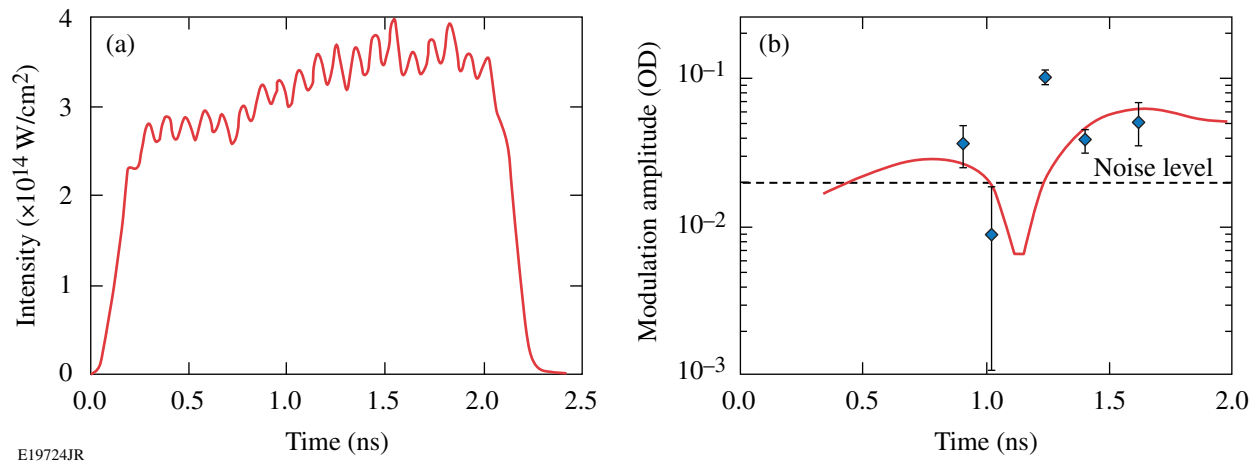


Figure 128.13

(a) The planar cryogenic target in Fig. 128.9 is driven by 12 overlapping drive beams with a 2-ns square pulse at a peak intensity of 4×10^{14} W/cm 2 . (b) The measured modulation amplitude is plotted (blue diamonds) as well as the prediction by *DRACO* using flux-limited thermal transport (red line) showing relatively good agreement.

the target up to ~ 1.2 ns, when the front window is ablated. The target acceleration begins at ~ 1.4 ns, so the modulation signal up to this time is dominated by the oscillating ablative RM instability,²⁵ observed as the large oscillating feature in the simulation. This characteristic of the ablative RM instability has been experimentally observed by U. Aglitskiy *et al.*^{42,43} and O. Gotchev *et al.*^{44,45} in pure-CH targets. After ~ 1.2 ns, simulation and measurements are dominated by the feedthrough modulations in the rear 8- μ m CH $_2$ window, which are related to the modulation at the D $_2$ ablation front by Eq. (3).

Discussion

The experiment demonstrates that *DRACO* closely reproduces the experiment using flux-limited local electron transport at an intensity of 4×10^{14} W/cm 2 . The large discrepancy between the experiment and simulation at the data point at 1.25 ns is likely the result of a difference between the experimental and simulated mass-ablation rates. Early in the drive ($t \ll 1.2$ ns), both the experimental and simulated optical depths include contributions from the front and rear plastic windows, while later in the drive ($t \gg 1.2$ ns) the front window is completely ablated, leaving only the rear window as the optical-depth contributor. In these regions, a small difference in ablation velocity between experiment and simulation could exist without disagreement in measured and simulated optical depths as a result of the slow growth observed in the target. Measurements taken as the front window is being completely ablated away ($t \sim 1.2$ ns) would show a larger discrepancy. In this case, if the simulated ablation velocity is greater than the experimental ablation velocity,

the measurement at 1.25 ns would include contributions from both the front and rear windows, while the simulation includes only the rear window, contributing to the difference between experiment and simulation for that data point. In the other temporal regions, the simulation reproduces the behavior of the modulation evolution in this complex target, indicating that the measured hydrodynamic stability characteristics of D $_2$ are close to those predicted through theory and simulation.

Signal levels can be increased by designing an experiment with a longer pulse duration, causing the modulation to grow to larger amplitudes or decreasing the distance between the D $_2$ ablation front and the rear CH $_2$ window of the target, while still keeping a thick-enough D $_2$ layer such that the hydrodynamics of D $_2$ are relevant to the measurement. Noise is dominated by x-ray photon statistics as a result of condensation on the windows of the target, resulting in large-scale features with low x-ray transmissions. This effect was significantly reduced by the use of a target shroud and selective image analysis, although it remains the dominate noise contributor.

An alternative radiography approach to that presented here is the use of charged particles or low-energy x rays to directly measure the modulation evolution at the D $_2$ ablation front as well as the front and rear plastic windows. Targets designed for this approach would use thinner plastic windows that would directly measure the modulation evolution in the D $_2$ layer, allowing for higher-confidence comparisons between experiment and simulation.

Conclusion

A direct-drive, RT experiment with a planar cryogenic-D₂ target was performed at the Omega Laser Facility. These are the first RT measurements in D₂ at conditions relevant to ICF using a mass-preimposed initial modulation. A planar cryogenic target was seeded with a 60- μ m-wavelength mass modulation and driven with a 2-ns square pulse with a peak intensity of 4×10^{14} W/cm² and radiographed using 1.3-keV x rays from a uranium backlighter. Experimental measurements showed reasonable agreement with the 2-D hydrodynamics code *DRACO*.

ACKNOWLEDGMENT

This work was supported by the U.S. DOE Office of Inertial Confinement Fusion under Cooperative Agreement No. DE-FC52-08NA28302, the University of Rochester, and the New York State Energy Research and Development Authority. The support of DOE does not constitute an endorsement by DOE of the views expressed in this article.

REFERENCES

1. S. Atzeni and J. Meyer-ter-Vehn, *The Physics of Inertial Fusion: Beam Plasma Interaction, Hydrodynamics, Hot Dense Matter*, International Series of Monographs on Physics (Clarendon Press, Oxford, 2004).
2. J. D. Lindl, *Inertial Confinement Fusion: The Quest for Ignition and Energy Gain Using Indirect Drive* (Springer-Verlag, New York, 1998).
3. Lord Rayleigh, Proc. London Math Soc. **XIV**, 170 (1883).
4. G. Taylor, Proc. R. Soc. London Ser. A **201**, 192 (1950).
5. S. E. Bodner, Phys. Rev. Lett. **33**, 761 (1974).
6. B. A. Remington *et al.*, Phys. Rev. Lett. **73**, 545 (1994).
7. S. G. Glendinning, S. N. Dixit, B. A. Hammel, D. H. Kalantar, M. H. Key, J. D. Kilkenny, J. P. Knauer, D. M. Pennington, B. A. Remington, R. J. Wallace, and S. V. Weber, Phys. Rev. Lett. **78**, 3318 (1997).
8. J. Grun *et al.*, Phys. Rev. Lett. **58**, 2672 (1987).
9. K. Shigemori *et al.*, Phys. Rev. Lett. **78**, 250 (1997).
10. H. Azechi *et al.*, Phys. Plasmas **4**, 4079 (1997).
11. C. J. Pawley *et al.*, Phys. Plasmas **6**, 565 (1999).
12. J. P. Knauer, R. Betti, D. K. Bradley, T. R. Boehly, T. J. B. Collins, V. N. Goncharov, P. W. McKenty, D. D. Meyerhofer, V. A. Smalyuk, C. P. Verdon, S. G. Glendinning, D. H. Kalantar, and R. G. Watt, Phys. Plasmas **7**, 338 (2000).
13. H. Azechi *et al.*, Phys. Rev. Lett. **98**, 045002 (2007).
14. V. A. Smalyuk, T. R. Boehly, D. K. Bradley, V. N. Goncharov, J. A. Delettrez, J. P. Knauer, D. D. Meyerhofer, D. Oron, and D. Shvarts, Phys. Rev. Lett. **81**, 5342 (1998).
15. M. M. Marinak *et al.*, Phys. Plasmas **5**, 1125 (1998).
16. V. A. Smalyuk, O. Sadot, J. A. Delettrez, D. D. Meyerhofer, S. P. Regan, and T. C. Sangster, Phys. Rev. Lett. **95**, 215001 (2005).
17. V. A. Smalyuk, O. Sadot, R. Betti, V. N. Goncharov, J. A. Delettrez, D. D. Meyerhofer, S. P. Regan, T. C. Sangster, and D. Shvarts, Phys. Plasmas **13**, 056312 (2006).
18. W. W. Hsing *et al.*, Phys. Plasmas **4**, 1832 (1997).
19. D. L. Tubbs, C. W. Barnes, J. B. Beck, N. M. Hoffman, J. A. Oertel, R. G. Watt, T. Boehly, D. Bradley, P. Jaanimagi, and J. Knauer, Phys. Plasmas **6**, 2095 (1999).
20. C. Chérifils *et al.*, Phys. Rev. Lett. **83**, 5507 (1999).
21. S. G. Glendinning *et al.*, Phys. Plasmas **7**, 2033 (2000).
22. V. A. Smalyuk, V. N. Goncharov, J. A. Delettrez, F. J. Marshall, D. D. Meyerhofer, S. P. Regan, and B. Yaakobi, Phys. Rev. Lett. **87**, 155002 (2001).
23. V. A. Smalyuk, S. B. Dumanis, F. J. Marshall, J. A. Delettrez, D. D. Meyerhofer, S. P. Regan, T. C. Sangster, B. Yaakobi, and J. A. Koch, Phys. Plasmas **10**, 830 (2003).
24. R. Betti, V. N. Goncharov, R. L. McCrory, and C. P. Verdon, Phys. Plasmas **5**, 1446 (1998).
25. V. N. Goncharov, Phys. Rev. Lett. **82**, 2091 (1999).
26. J. G. Wouchuk and K. Nishihara, Phys. Plasmas **3**, 3761 (1996).
27. P. W. McKenty, V. N. Goncharov, R. P. J. Town, S. Skupsky, R. Betti, and R. L. McCrory, Phys. Plasmas **8**, 2315 (2001).
28. C. P. Verdon, Bull. Am. Phys. Soc. **38**, 2010 (1993).
29. B. A. Remington *et al.*, Phys. Plasmas **22**, 241 (1995).
30. S. G. Glendinning, Bull. Am. Phys. Soc. **36**, 2375 (1991).
31. Y. Lin, T. J. Kessler, and G. N. Lawrence, Opt. Lett. **20**, 764 (1995).
32. S. Skupsky, R. W. Short, T. Kessler, R. S. Craxton, S. Letzring, and J. M. Soures, J. Appl. Phys. **66**, 3456 (1989).
33. V. Smalyuk, T. Boehly, and J. Knauer, Laboratory for Laser Energetics, private communication (2005).
34. D. G. Stearns *et al.*, Rev. Sci. Instrum. **57**, 2455 (1986).
35. R. Betti, V. Lobatchev, and R. L. McCrory, Phys. Rev. Lett. **81**, 5560 (1998).
36. P. B. Radha, T. J. B. Collins, J. A. Delettrez, Y. Elbaz, R. Epstein, V. Yu. Glebov, V. N. Goncharov, R. L. Keck, J. P. Knauer, J. A. Marozas, F. J. Marshall, R. L. McCrory, P. W. McKenty, D. D. Meyerhofer, S. P. Regan, T. C. Sangster, W. Seka, D. Shvarts, S. Skupsky, Y. Srebro, and C. Stoeckl, Phys. Plasmas **12**, 056307 (2005).
37. V. A. Smalyuk, T. R. Boehly, D. K. Bradley, J. P. Knauer, and D. D. Meyerhofer, Rev. Sci. Instrum. **70**, 647 (1999).

38. L. Spitzer, Jr. and R. Härm, *Phys. Rev.* **89**, 977 (1953).
39. R. C. Malone, R. L. McCrory, and R. L. Morse, *Phys. Rev. Lett.* **34**, 721 (1975).
40. S. P. Lyon and J. D. Johnson, Los Alamos National Laboratory, Los Alamos, NM, Report LA-UR-92-3407, NTIS Order No. DE85014241 (1992).
41. S. X. Hu, B. Militzer, V. N. Goncharov, and S. Skupsky, *Phys. Rev. Lett.* **104**, 235003 (2010).
42. Y. Aglitskiy *et al.*, *Phys. Rev. Lett.* **87**, 265001 (2001).
43. Y. Aglitskiy *et al.*, *Phys. Plasmas* **9**, 2264 (2002).
44. O. Gotchev, “Experiments on Dynamic Overpressure Stabilization of the Ablative Richtmyer–Meshkov Instability in ICF Targets,” Ph.D. thesis, University of Rochester, 2004.
45. V. N. Goncharov, O. V. Gotchev, R. L. McCrory, P. W. McKenty, D. D. Meyerhofer, T. C. Sangster, S. Skupsky, and C. Cherfils-Clérouin, *J. Phys. IV France* **133**, 123 (2006).

Highly Efficient Room-Temperature Yb:YAG Ceramic Laser and Regenerative Amplifier

Room-temperature, Yb-doped YAG ceramics are attractive materials for high-efficiency broadband lasers and scalable amplifiers.^{1–5} Their properties make them an excellent choice for high-energy, broadband, diode-pumped lasers and amplifiers.⁶ They have a reasonably large emission cross section ($2 \times 10^{-20} \text{ cm}^2$), a long upper-level lifetime ($>1 \text{ ms}$), a high saturation fluence, a small quantum defect (8.6%), and broadband absorption (18 nm) and emission ($>100 \text{ nm}$) spectra. Their hardness and fracture toughness are higher than for YAG crystals, high doping levels are possible (up to 20%), and active elements with large apertures (tens of centimeters) are available. In addition, they function as a quasi-three-level system at room temperature and a four-level system at liquid-nitrogen temperature, and they are polarization insensitive, enabling one to easily configure multipass amplifiers using polarization switching schemes.

A room-temperature diode-pumped Yb:YAG ceramic pulsed laser has been developed that produces 120 mJ at 1030 nm in free-running mode with a high optical efficiency (laser output power divided by diode pump power) of 51%. The laser (Fig. 128.14) has a folded, $\sim 280\text{-cm}$ linear resonator that is close to semiconcentric. The mode diameter in the active element is tuned by moving the 3-m concave end mirror along the resonator axis. Initially, the mode diameter was set

to $550 \mu\text{m}$ at the $1/e^2$ level. The $8 \times 8 \times 10\text{-mm}$, 7% Yb-doped YAG ceramic active element⁷ is wedged and AR coated for the pump and laser wavelengths. A 940-nm, 250-W-rated, fiber-coupled pump diode (Jenoptik JOLD-250-CPXF-2P2) (Ref. 8) is used in pulsed mode with a 1-ms pulse width at a 5-Hz repetition rate. The pump radiation is 1:1 re-imaged from a 0.4-mm fiber core into the active element. Approximately 235 mJ of pump-pulse energy is absorbed in the active element at the maximum 140-A diode-driver current.

A single-pass, small-signal gain of 160 has been measured at the maximum driver current. The laser output energy was maximized by optimizing the output-coupler reflectivity, using a set of flat mirrors with reflectivities from 10% to 90% with 10% steps. The optimum reflectivity has been found to be 50%, resulting in output energy in excess of 102 mJ.

Further optimization was accomplished by fine tuning the mode size inside the active element to achieve the highest-possible energy. A mode-diameter increase from $550 \mu\text{m}$ to $665 \mu\text{m}$ (when the pump-to-mode-diameter ratio is 0.6) led to an output-energy increase from 102 mJ to 120 mJ, corresponding to an optical-to-optical efficiency of 51%. The output energy of the laser as a function of absorbed pump energy is shown in

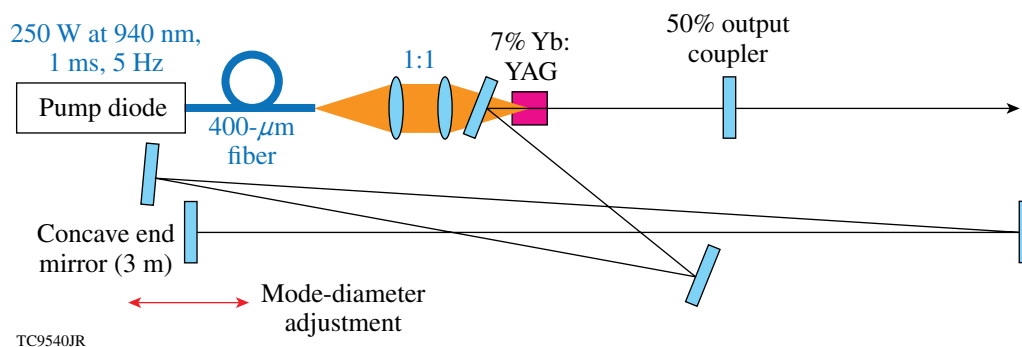


Figure 128.14
Block diagram of the Yb:YAG ceramic laser.

Fig. 128.15(a). Taking into account that contemporary pump laser diodes can provide an electrical-to-optical efficiency of up to 80%, a Yb:YAG ceramic laser can potentially achieve a wall-plug efficiency of >40%. The fine tuning of the mode diameter made it possible to achieve a slope efficiency of 78%, which is slightly higher than has been previously achieved in a room-temperature Yb:YAG ceramic laser.^{1,2} Figure 128.15(b) shows a good-quality output-beam profile with lineouts through the center that are approximately Gaussian.

The active element has also been demonstrated in a regenerative amplifier (regen) used to amplify 8-ns FWHM (full-width-at-half-maximum) square pulses (Fig. 128.16). Here optical damage was avoided by increasing the mode and pump-beam diameters. The pump fiber was re-imaged into the active element with a 50% expansion, producing a 600- μm pump spot. The regen mode diameter was optimized for maximum output energy with a pump-to-mode-diameter ratio of 0.62. The output energy was limited to 5 mJ because of intracavity polarizer

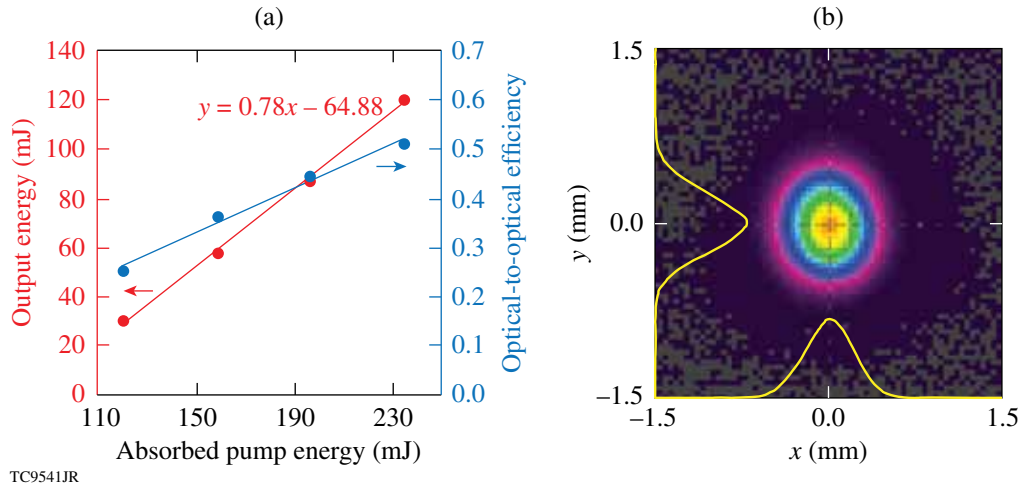


Figure 128.15

(a) Output energy and optical efficiency as functions of absorbed pump energy for the optimized Yb:YAG laser. (b) Near-field image of the laser output at maximum energy with one-dimensional (1-D) lineouts overlaid.

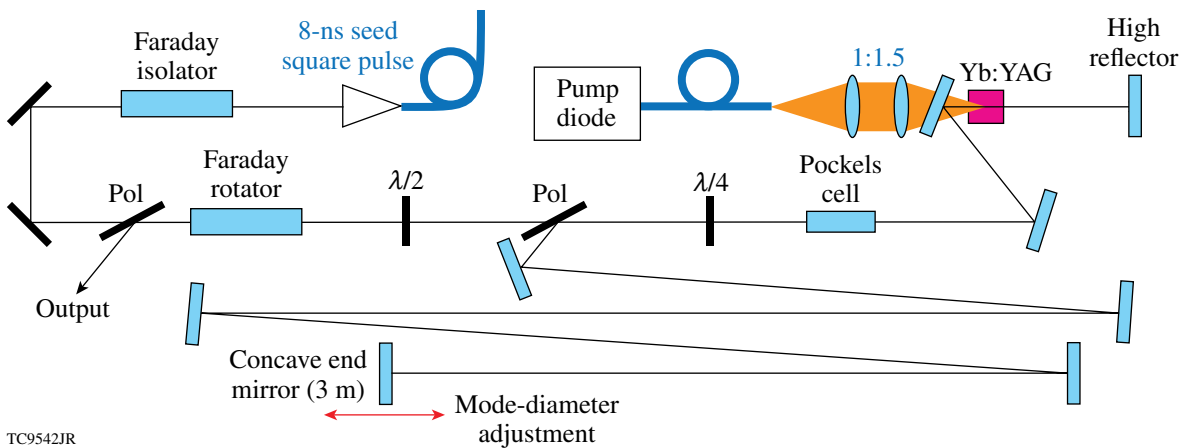


Figure 128.16

Yb:YAG ceramic regenerative amplifier. Pol: polarizer; $\lambda/2$: half-wave plate; $\lambda/4$: quarter-wave plate.

damage. The pump current was 80 A at this point, with the 140-A maximum current available indicating that more energy can be achieved from the regen with increased pump-volume diameter. The output-beam profile was of similar quality to that of the free-running laser and was close to TEM₀₀.

The pump-volume diameter was further increased to 670 μm with the mode diameter increased in proportion. Output energy of 14.5 mJ was produced at the 140-A maximum pump current [Fig. 128.17(a)]. The output energy variations decreased to ~0.2% rms as the output energy was increased, as a result of the increase of the gain/loss ratio.⁹ The number of round trips in the regen at this point is 4, with the regen functioning more as a multipass amplifier, where the beam profile is defined not by the resonator but by the radial-gain variations in the Yb:YAG.

The output profile was a fourth-order super-Gaussian, resulting from heavy gain saturation along the beam axis [Fig. 128.17(b)].

The broad bandwidth of the Yb:YAG makes this regen suitable for the amplification of stretched broadband pulses in chirped-pulse-amplification laser systems and also for systems that require bandwidth for SSD (smoothing by spectral dispersion).¹⁰

In conclusion, a room-temperature, diode-pumped pulsed Yb:YAG free-running laser with 78% slope efficiency has been demonstrated. It has been shown that fine tuning of the mode diameter to the diameter of the pumped volume is important to achieve maximum laser efficiency with a Gaussian-like beam profile. A regenerative Yb:YAG amplifier with maximum output energy of 14.5 mJ and a super-Gaussian beam profile has been built and tested.

ACKNOWLEDGMENT

This work was supported by the U.S. Department of Energy Office of Inertial Confinement Fusion under Cooperative Agreement No. DE-FC52-08NA28302, the University of Rochester, and the New York State Energy Research and Development Authority. The support of DOE does not constitute and endorsement by DOE of the views expressed in this article.

REFERENCES

1. S. Nakamura *et al.*, *Opt. Commun.* **281**, 4411 (2008).
2. B. Zhou *et al.*, *Opt. Lett.* **35**, 288 (2010).
3. A. Pirri *et al.*, *Opt. Express* **18**, 17,262 (2010).
4. S. T. Fredrich-Thornton *et al.*, in *Advanced Solid-State Photonics*, OSA Technical Digest Series (CD) (Optical Society of America, Washington, DC, 2008), Paper WB13.
5. S. Pearce *et al.*, *Opt. Commun.* **282**, 2199 (2009).
6. P. Lacovara *et al.*, *Opt. Lett.* **16**, 1089 (1991).
7. Baikowski International Corporation, Charlotte, NC, 28216-2385.
8. JENOPTIK Laser GmbH, 07745 Jena, Germany.
9. A. V. Okishev and J. D. Zuegel, *Appl. Opt.* **43**, 6180 (2004).
10. S. Skupsky, R. W. Short, T. Kessler, R. S. Craxton, S. Letzring, and J. M. Soures, *J. Appl. Phys.* **66**, 3456 (1989).

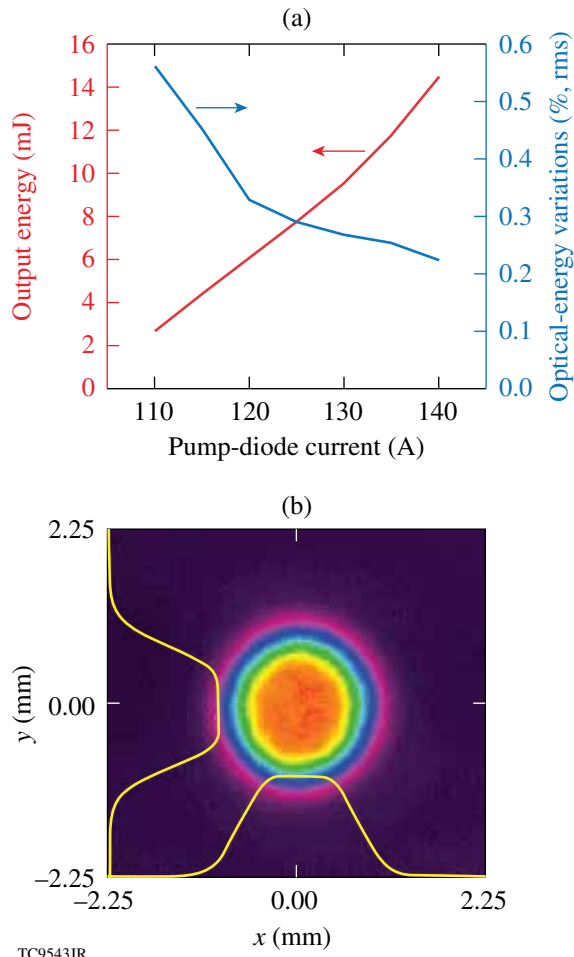


Figure 128.17 (a) Output energy and energy variations of the regen pumped with a 670-μm pump spot. (b) Near-field image of the output beam at maximum energy with 1-D lineouts overlaid.

LLE's Summer High School Research Program

During the summer of 2011, 16 students from Rochester-area high schools participated in the Laboratory for Laser Energetics' Summer High School Research Program. The goal of this program is to excite a group of high school students about careers in the areas of science and technology by exposing them to research in a state-of-the-art environment. Too often, students are exposed to "research" only through classroom laboratories, which have prescribed procedures and predictable results. In LLE's summer program, the students experience many of the trials, tribulations, and rewards of scientific research. By participating in research in a real environment, the students often become more excited about careers in science and technology. In addition, LLE gains from the contributions of the many highly talented students who are attracted to the program.

The students spent most of their time working on their individual research projects with members of LLE's technical staff. The projects were related to current research activities at LLE and covered a broad range of areas of interest including experimental systems and diagnostic development, computational modeling of implosion physics, chemistry, materials science, laser system development and diagnostics, and database development (see Table 128.IV).

The students attended weekly seminars on technical topics associated with LLE's research. Topics this year included laser physics, fusion, holography, nonlinear optics, atomic force microscopy, glass and glass fracture, and electronic paper. The students also received safety training, learned how to give scientific presentations, and were introduced to LLE's resources, especially the computational facilities.

The program culminated on 24 August with the "High School Student Summer Research Symposium," at which the

students presented the results of their research to an audience including parents, teachers, and LLE staff. The students' written reports will be made available on the LLE Website and bound into a permanent record of their work that can be cited in scientific publications.

Two hundred and eighty-one high school students have now participated in the program since it began in 1989. This year's students were selected from over 50 applicants.

At the symposium LLE presented its 15th annual William D. Ryan Inspirational Teacher Award to Mrs. Deborah Reynolds, a chemistry teacher at Brighton High School. This award is presented to a teacher who motivated one of the participants in LLE's Summer High School Research Program to study science, mathematics, or technology and includes a \$1000 cash prize. Teachers are nominated by alumni of the summer program. Mrs. Reynolds was nominated by Andrew Chun and Connie Jiang, participants in the 2010 program. Andrew described Mrs. Reynolds as "one of the few teachers who can take AP-level material and make it extremely easy for everyone in the class to understand...She makes learning fun and entertaining...She inspires her class through her kindness and unique ability to reach each of her individual students, in a special way that few teachers can, to want to learn more about science." For Connie, Mrs. Reynolds was "a truly inspirational teacher" who was "so outstanding because she was so thorough." Connie added, "She was kind, patient, organized and thorough, and taught me more about chemistry than I had ever thought to ask or know." Mrs. Reynolds was also enthusiastically recommended by Dr. Nancy Hackett, Brighton High School Principal, who attended the symposium. She said of Mrs. Reynolds, "She takes the students to the next level and she is passionate about chemistry. She always tries to improve herself professionally to keep her teaching at the cutting edge."

Table 128.IV: High School Students and Projects—Summer 2011.

Name	High School	Supervisor	Project Title
Brandon Avila	Allendale Columbia	R. W. Kidder	Optimizing LLE Information Operations Through Natural Language Processing
Andrew Boyce	McQuaid	W. T. Shmayda	Water-Stimulated Tritium Release from Metals
Matthew DeCross	Pittsford Sutherland	L. D. Lund	Automation of Vibration Measurement and Characterization of Cryogenic Deuterium–Tritium Target Motion
Avery Gnolek	Webster Thomas	K. L. Marshall	Photoaligned Liquid Crystal Wave Plate
Dana Gretton	Honeoye Falls Lima	R. G. Peck, E. Druszkiewicz	Design of a New Master-Timing Generator
Sean Hamlin	Fairport	R. Epstein	X-Ray Fluorescence as an Imploded-Shell Diagnostic
Felix Jin	Brighton	G. Fiksel	Characterization of Magnetic Coils for the Magneto-inertial Fusion Energy Delivery System
Jefferson Lee	Canandaigua Academy	W. T. Shmayda	Modeling Tritium Removal from Metal Surfaces
Kevin Mizes	Pittsford Sutherland	R. Boni, D. H. Froula, S. Ivancic	Two Techniques for Array Generation with Applications in Grid-Imaging Refractometry
Patricia Olson	Brighton	R. S. Craxton	Optimization of Beam Configurations for Shock-Ignition Experiments on the NIF and OMEGA
Sean Reid	Fairport	M. Burke, R. Boni, S. D. Jacobs	Surface Grinding and Polishing to Remove Etch-Induced Noise Pitting in CR-39 Samples
Madeline Rutan	Penfield	K. L. Marshall	Abrasion-Resistant Antireflection Sol-Gel Coatings
Michael Statt	School of the Arts	K. L. Marshall, C. Dorrer	Generation of Radially Polarized Beams Using Optically Patterned Liquid Crystals
Troy Thomas	Webster Thomas	B. E. Kruschwitz	Optical Time-Domain Reflectometry for the Transport Spatial Filter on the OMEGA Extended Performance Laser
Harrison Xiao	Pittsford Sutherland	P. A. Jaanimagi	Dynamic Defocusing in Streak Tubes
Andrew Zhao	Webster Thomas	R. Boni, D. H. Froula, S. Ivancic	Image Processing and Analysis of 4ω Grid-Image Refractometry Data

FY11 Laser Facility Report

During FY11, the Omega Laser Facility conducted 1348 target shots on OMEGA and 457 target shots on OMEGA EP for a total of 1805 target shots (see Tables 128.V and 128.VI). OMEGA averaged 10.3 target shots per operating day with availability and experimental effectiveness averages for FY11 were 93.3% and 96.1%, respectively.

OMEGA EP was operated extensively in FY11 for a variety of internal and external users. Of the 457 target shots, 401

Table 128.V: Omega Facility target shot summary for FY11.

Laboratory	Planned Number of Target Shots	Actual Number of Target Shots	NIC	Shots in Support of NIC	Non-NIC
LLE	335	389	0	375	14
LLNL	260	301	131	0	170
NLUF	155	203	0	0	203
LANL	170	195	45	0	150
LBS	155	170	0	0	170
CEA	40	50	0	0	50
AWE	20	23	0	0	23
U. Mich	20	17	0	0	17
Total	1155	1348	176	375	797

Table 128.VI: Omega EP Facility target shot summary for FY11.

Laboratory	Planned Number of Target Shots	Actual Number of Target Shots	NIC	Shots in Support of NIC	Non-NIC
LLE	174	192	0	192	0
LLNL	65	79	10	5	64
AWE	10	21	0	0	21
NLUF	60	57	0	0	57
LBS	65	74	0	0	74
LANL	25	28	0	0	28
CEA	5	6	0	0	6
Total	404	457	10	197	250

were shot in the OMEGA EP target chamber and 56 were joint shots in the OMEGA target chamber. OMEGA EP averaged 5.5 target shots per operating day with availability and experimental effectiveness averages for FY11 of 85.6% and 95.2%, respectively.

OMEGA EP Improved Energy Capabilities

Short-pulse (IR) and long-pulse (UV) energy on target has been increased. The UV energy was increased after the acquisition of improved optics. Lithographic-quality fused-silica substrates were finished using LLNL-developed protocols, LLNL-supported production controls, and the latest LLNL post-processing techniques for enhanced damage threshold (Acid Mitigation Process II). The extended UV energy operational envelope was made available after completion of a damage-testing laser shot campaign with the previous optics. UV energy on target was increased from 2.3 kJ per beam to 6.6 kJ at 10 ns, exceeding the 6.5-kJ system-design goal. Short-pulse IR energy was increased following the installation of improved damage-threshold gratings in the grating-compressor vessel. Additionally, a comprehensive short-pulse small-beam damage-testing program was conducted on multilayer dielectric coatings. The combination of new gratings and coating performance analysis resulted in an increase to the IR energy operational envelope for the short-pulse laser beams. IR energy on target for beamline 2 at 10 ps was increased from 1.0 kJ to 1.6 kJ, 60% of the 2.6 kJ design goal. Up-to-date limits to the energy on target are now summarized and available to all users through the Operations Website.

OMEGA EP 100-ps UV Temporal Pulse Shapes

At the request of users, the shortest UV pulse durations have been extended from the previous limit of 1 ns to 100 ps. Users are now able to request pulse shapes between 100 ps and 10 ns. The 100-ps pulse shapes have been utilized to produce short-duration x-ray pulses useful for a variety of target-physics campaigns, including backlighter platform development for the NIF. With this new functionality, the temporal co-timing of all four beamlines has been calibrated to <50 ps.

OMEGA EP Short-Pulse Focal-Spot Improvement Using a Static Wavefront Corrector

Static wavefront correction has been developed for OMEGA EP to correct high-order residual wavefront that is beyond the spatial resolution of the existing adaptive optics. A small-aperture phase corrector, manufactured by QED Technologies, using the magnetorheological finishing (MRF) process, has been added to the injection system to pre-compensate for repeatable high-order wavefront errors that arise in the beamlines. Following successful proof-of-principle demonstrations, these optics were implemented on both of the OMEGA EP short-pulse beamlines, providing an $\sim 2\times$ reduction in focal-spot extent at the output of the beamline during active wavefront correction. On amplified shots, target-plane focal-spots have met the specification of 80% of the energy in less than a $20\text{-}\mu\text{m}$ radius ($R_{80} < 20\ \mu\text{m}$). The $\sim 25\%$ improvement is realized on the first shots, although thermal distortion of the amplifier disks has led to focal-spot degradation after multiple shots have been taken on a day. Future revisions of the phase-corrector design will partially compensate for this effect. See Fig. 128.18 for representative focal-spot results. This work follows on the successful implementation of advanced phase-retrieval techniques developed in FY10 that allow for accurate characterization of the focal spot.

OMEGA EP Infrared Alignment Table and Beamline Injection Table Enhancement

The daily operation of the OMEGA EP laser has been improved with enhancements to the OMEGA EP infrared

alignment table (IRAT). This work improved the imaging accuracy from the laser source apodizer plane to the beamline input image plane. This improvement reduces modulation on critical optics in the OMEGA EP Laser System. Additional diagnostics were added to improve the injection energy measurements and centering of beams. All of these improvements have increased system operability and are primary contributors to an increase in shots per day from FY10 to FY11.

Improved OMEGA UV On-Target Predictions

Target implosions have been shown to slowly degrade the UV transmission, primarily on the final debris shield, causing a decrease in on-target energy relative to the diagnostic prediction. During FY11, the study of UV transmission has resulted in a better understanding of the loss mechanisms. The study found that the losses are dependent on target type, target composition, target quantity, number of beams used for each shot, and beam location in the tank. The results of this study and daily measurements of transmission on representative UV optics have been incorporated into a new on-target energy prediction that is reported to the principal investigator. The system average loss is predicted within $\pm 1\%$ accuracy, and the rms error is $< 2\%$.

Experimental Diagnostics

Diagnostic capabilities continue to evolve with the commissioning of 24 new diagnostic instruments on OMEGA and 9 new diagnostic instruments on OMEGA EP. These include a new spherical crystal x-ray imager, upgraded hard x-ray diode arrays, B-dot magnetic field probes, an electron spectrometer,

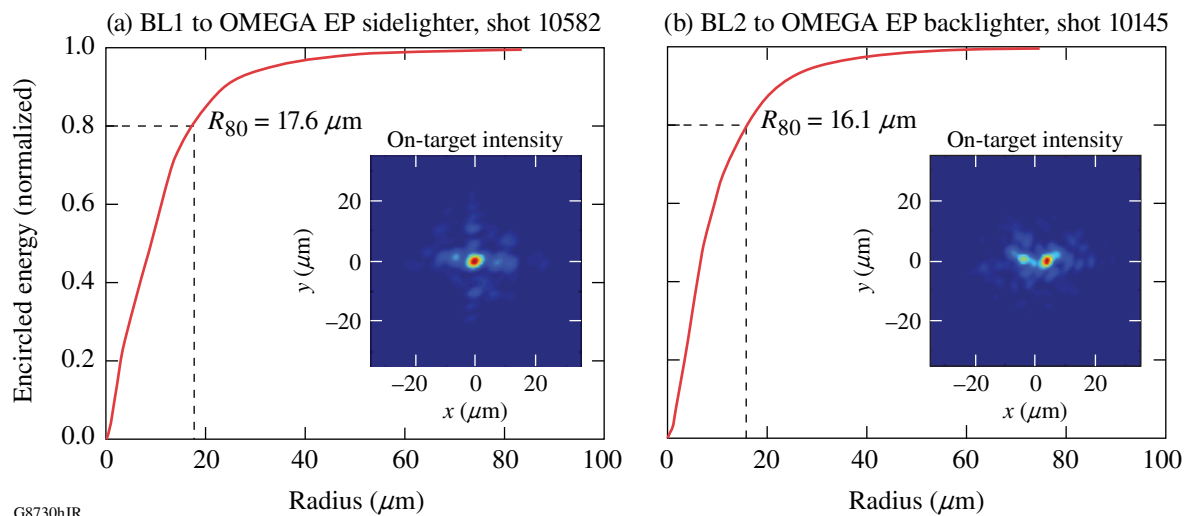


Figure 128.18

(a) Beam 1 (BL1) and (b) Beam 2 (BL2) focal-spot images from target shots with the static wavefront correctors installed.

and a new test platform for CVD-diamond neutron detectors. Many of these new instruments were developed by or in cooperation with other laboratories (including LLNL, LANL, CEA, Oxford University, Osaka University, and SNL).

Improvements to the online information systems available to our scientific users include availability of specification sheets and operating procedures for diagnostic instruments, as well as target chamber port assignment tables. Other facility improvements include commissioning of an additional image plate scanner and electromagnetic interference hardening of the target positioners on both OMEGA and OMEGA EP.

A number of safety improvements were implemented in the experimental area. These include the commissioning of filtered air flow hoods for servicing equipment that contains or is contaminated with beryllium, higher-resolution beryllium monitoring capability; and review and certification of heavy equipment lift procedures. Additionally, tracking beryllium survey data and radioactive material inventory has improved visibility to the operators and other stakeholders.

National Laser Users' Facility and External Users' Programs

Under the facility governance plan implemented in FY08 to formalize the scheduling of the Omega Laser Facility as an NNSA User Facility, Omega Facility shots are allocated by campaign. The majority (65%) of the FY11 target shots were allocated to the National Ignition Campaign (NIC) conducted by integrated teams from the national laboratories and LLE and to the high-energy-density campaigns conducted by teams led by scientists from the national laboratories.

In FY11, 27.6% of the facility shots were allocated to basic science experiments. Half of these were dedicated to university basic science under the National Laser Users' Facility (NLUF) Program, and the remaining shots were allotted to the Laboratory Basic Science (LBS) Program, comprising peer-reviewed basic science experiments conducted by the national laboratories and by LLE including the Fusion Science Center (FSC).

The Omega Facility is also being used for several campaigns by teams from the Commissariat à l'énergie atomique (CEA) of France, the Atomic Weapons Establishment (AWE) of the United Kingdom, and the Center for Radiative Shock Hydrodynamics (CRASH) of the University of Michigan.

The facility users during this year included 11 collaborative teams participating in the NLUF Program; 15 teams led by LLNL and LLE scientists participating in the LBS Program; many collaborative teams from the national laboratories and LLE conducting experiments for the NIC; investigators from LLNL and LANL conducting experiments for high-energy-density-physics programs; scientists and engineers from CEA and AWE, and scientists and students from CRASH.

In this section, we briefly review all the external user activity on OMEGA during FY11.

FY11 NLUF Program

FY11 was the first of a two-year period of performance for the NLUF projects approved for the FY11–FY12 funding and OMEGA shots. Eleven NLUF projects (see Table 128.VII) were allotted Omega Facility shot time and conducted a total

of 255 target shots at the facility. This work is summarized in this section.

Study of Fast-Electron Transport into Imploded High-Density Plasmas Using Cu-Doped CD-Shell Targets

Principal Investigators: F. N. Beg (University of California, San Diego) and M. S. Wei (General Atomics)

Co-investigators: R. B. Stephens (GA); H. Sawada (UCSD); W. Theobald, C. Stoeckl, J. A. Delettrez, and R. Betti (LLE); C. D. Chen, M. H. Key, P. K. Patel, and H. McLean (LLNL); and T. Yabuuchi and H. Habara (ILE)

Lead Graduate Student: L. C. Jarrott (UCSD)

Understanding fast-electron generation in the cone and their subsequent transport into hot, dense plasma is crucial to the success of the cone-guided fast-ignition scheme. The goal of the University of California, San Diego, NLUF project is to investigate the coupling efficiency and spatial distribution of fast-electron energy deposition in imploded CD shells attached to Au cone targets. To achieve this, a Cu dopant (at ~1% atomic number density of CD) is added to the CD shell (3/4 of the inner part of the shell), which allows for the characterization of fast-electron transport via fast-electron-induced, 8-keV Cu K-shell fluorescence radiation. The experiment consists of two parts: (1) characterization of background 8-keV x-ray emission generated from the compression (by the 20-kJ OMEGA beams) of a CD shell with and without Cu dopant and (2) characterization of fast-electron-produced Cu fluorescence emission from the compressed Cu-doped CD with an additional-kJ, 10-ps, high-intensity OMEGA EP beam timed and injected into the compressed core through the Au cone tip. The primary diagnostics were a narrowband spherical crystal imager (SCI) to image 8-keV x-ray emission and a zinc Von Hamos (ZVH) x-ray spectrometer tuned for Cu K-shell and ionic-line-emission yield measurement. Several other diagnostics including broadband x-ray imaging diagnostics such as pinhole cameras and Kirkpatrick–Baez (KB) microscopes, neutron time-of-flight detectors, and magnetic electron spectrometers (one multichannel spectrometer along the OMEGA EP beam axis and one single-channel spectrometer at the side) were employed.

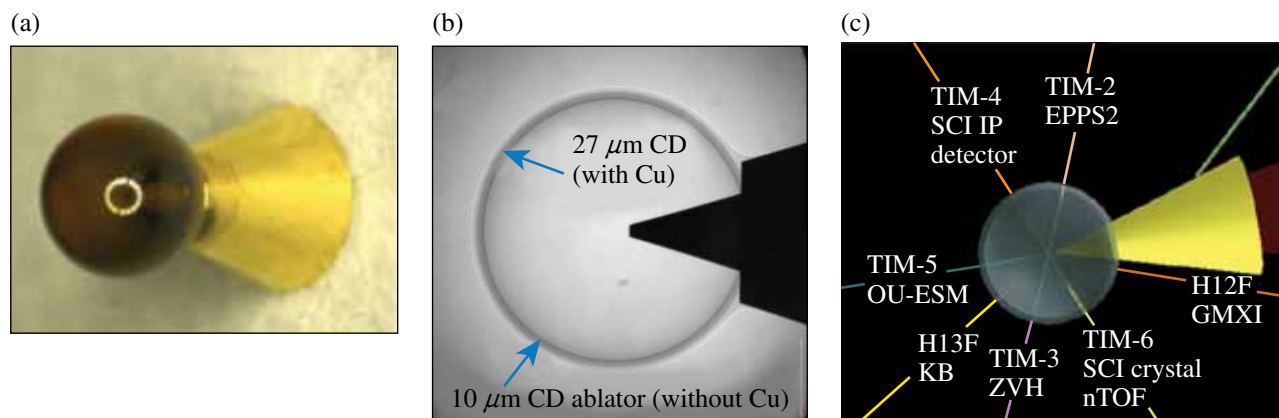
Table 128.VII: Approved FY11 and FY12 NLUF proposals.

Principal Investigator	Institution	Project Title
F. N. Beg	University of California, Berkeley	Systematic Study of Fast-Electron Transport in Imploded Plasmas
R. P. Drake	University of Michigan	Experimental Astrophysics on the OMEGA Laser
T. Duffy	Princeton University	Ramp Compression for Studying Equations of State, Phase Transitions, and Kinetics on OMEGA
R. Falcone	University of California, Berkeley	Detailed <i>In-Situ</i> Diagnostics of High-Z Shocks
P. Hartigan	Rice University	Clumpy Environments and Interacting Shock Waves: Realistic Laboratory Analogs of Astrophysical Flows
R. Jeanloz	University of California, Berkeley	Recreating Planetary Core Conditions on OMEGA
K. Krushelnick	University of Michigan	Intense Laser Interactions with Low-Density Plasma Using OMEGA EP
R. Mancini	University of Nevada, Reno	Investigation of Hydrodynamic Stability and Shock Dynamics in OMEGA Direct-Drive Implosions Using Spectrally Resolved Imaging
R. D. Petrasso	Massachusetts Institute of Technology	Charged-Particle Probing of Inertial Confinement Fusion Implosions and High-Energy-Density Plasmas
A. Spitkovsky	Princeton University	Collisionless Shocks in Laboratory High-Energy-Density Plasmas
R. Stephens	General Atomics	Investigation of Laser to Electron Energy Coupling Dependence on Laser Pulse Duration and Material Composition

Figure 128.19 shows pictures of the cone-in-shell target and experimental layout including ten-inch manipulator (TIM) and port locations for various diagnostics. In this experiment, 54 of the 60 OMEGA beams with low-adiabat pulse shape [LA24170P with smoothing by spectral dispersion (SSD) off] were used (18 to 20 kJ) to compress the shell, while the remaining six beams were used to destroy the target cone 5 ns after the short-pulse laser was fired in the cone. The 10-ps OMEGA EP backlight beam BL2 was used with a 3.65-ns delay at 10 ps, tight focus at the inner cone tip, and a minimum prepulse. The target consisted of a plastic (CD) shell with an outer diameter of 870 μm and a cone with an angle of 34° with 40- μm offset distance between the outer cone tip and the shell center. The CD shell consisted of a 10- μm pure-CD outer layer as the ablator and a 27- μm inner layer doped with Cu at 1% atomic number density of CD. The thickness of the cone tip was 15 μm , while the cone wall thickness was 10 μm .

In this experiment, the SCI was fielded for the first time on OMEGA. Figure 128.20 compares 8-keV x-ray emission recorded with the SCI in three different shots: (a) background x-ray emission from an OMEGA-only imploded cone-in-

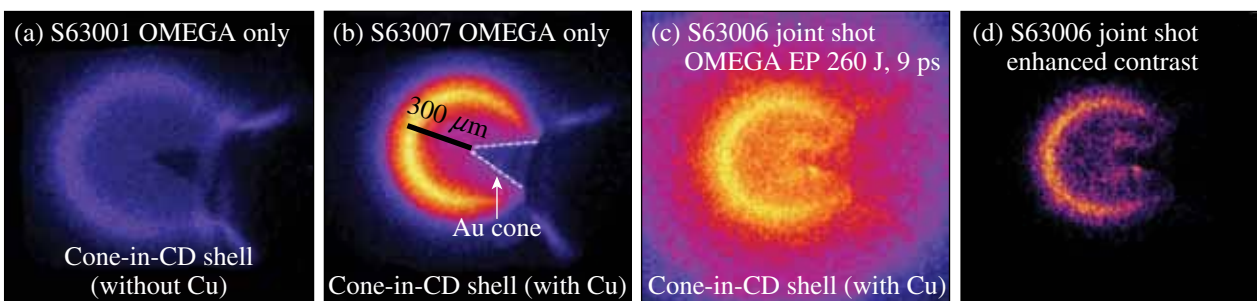
CD-shell target (without Cu dopant), (b) bremsstrahlung and fluorescence emission from an imploded cone-in-CD-shell target with Cu dopant, (c) bremsstrahlung and fluorescence emission from a joint shot of both OMEGA and OMEGA EP with OMEGA EP being fired at 300 J, and (d) enhanced contrast view of the image in (c). The Cu fluorescence emission in the OMEGA-only implosion shots with Cu-doped CD shells is due to the driver-beam-produced superthermal (tens of keV) electrons. The 8-keV x-ray image from the joint shot [as seen in Figs. 128.20(c) and 128.20(d)] shows emission from imploded plasmas just outside the cone tip area with features that were not observed in the OMEGA-only shots, which presumably is due to short-pulse, OMEGA EP beam-produced fast electrons. A detailed analysis of the data, taking into account opacity corrections, is underway. Cu K-shell and ionic line emission (not shown here) measured by the ZVH spectrometer showed extremely strong Cu He α line emission. Radiation-hydrodynamic modeling of the implosion suggested that this is caused by the direct heating by the implosion driver beams of the Cu-doped CD layer after completely ablating off the first 10- μm non-doped CD layer. A slightly thicker ablator will be used in the improved targets for future experiments.



U1359JR

Figure 128.19

(a) A Au cone-in-(Cu-doped) CD-shell target; (b) contact x-ray radiograph image of the target; and (c) experiment and diagnostics layout.



U1360JR

Figure 128.20

SCI-recorded, 8-keV x-ray images from (a) an OMEGA-only compression shot with cone-in-CD-shell target without Cu doping; (b) an OMEGA-only compression shot with cone-in-CD-shell target with Cu doping; (c) a joint shot with OMEGA EP beam energy of 260 J at 9 ps. Images shown in (a), (b), and (c) have the same spatial and color scales. (d) Image of (c) with enhanced contrast. Additional visible features indicate that fast electrons produced x rays outside the cone.

In summary, the NLUF fast-electron-transport experiment with a cone-in-shell (with Cu doping) target has been successfully performed on OMEGA with a comprehensive suite of x-ray, particle, and neutron diagnostics including the newly implemented monochromatic x-ray imager (SCI) and multichannel electron spectrometer. The platform for complex electron-transport physics experiments has been established and will be pursued for greater than kilojoule short-pulse-laser energies.

Experimental Astrophysics on the OMEGA Laser

Principal Investigator: R. P. Drake (University of Michigan)
 Co-investigators: B. Loupias and E. Falize (CEA); D. H. Froula, T. R. Boehly, and J. P. Knauer (LLE); J. Holloway, K. Powell, and C. C. Kuranz (University of Michigan); T. Plewa (Florida State University); and B. A. Remington, S. Ross, H.-S. Park, and S. H. Glenzer (LLNL)

The OMEGA laser makes it feasible to conduct experiments relevant to astrophysical phenomena because of the very high energy-density conditions it can create. This project explores the contribution of radiative shock waves to the evolving dynamics of binary star-accretion disk systems in which they reside. Radiative shock waves produce shocked matter so hot that it radiates away most of its thermal energy. This radiation causes variable structures to develop depending on the optical properties of the material on either side of the shock. To control these properties and understand the shock-front emission, we devised an experiment that accelerates a plasma flow into vacuum and then develops a radiative shock when the flow is impeded. We study the shock structure using x-ray radiography and its radiative flux with μ DMX, an x-ray diode spectrometer.

The experiments on the 60-beam OMEGA laser employ a laser configuration of 10 UV beams with a 1-ns square pulse. The laser beams are smoothed using the SSD technique and SG4 distributed phase plates. They are focused on a 10- μm plastic ablator whose opposite face is coated with 5 μm of Sn. The beams deposit a total energy of ~ 4.5 kJ, giving an average irradiance of $\sim 1.2 \times 10^{15}$ W/cm². This generates a laser ablation pressure of ~ 75 Mbar that initially drives a shock through the plastic and Sn, which is mounted on one side of an evacuated acrylic tube. After this ablative shock breaks out of the Sn into vacuum, the Sn plasma expands, cools, and accelerates down the target cylinder at an average velocity of ~ 150 km/s. About 4 mm from the laser-drive surface, the Sn ejecta impact a 100- μm -thick, cold Al foil. In response, a reverse shock develops in the flow and a forward shock is driven into the Al end wall. The traditional “upstream” velocity in the shocked system is defined by the Sn flow, which is fast enough that radiative effects play a significant role in the dynamics of the reverse shock. An additional five OMEGA laser beams irradiate a zinc foil on a backlit pinhole target for 1 ns, creating the x rays that image the reverse shock onto film and image plates. To investigate the effects of different flow velocities and oblique collisions, targets were also shot that had varied plastic-Sn thicknesses and tilted Al foils. Figure 128.21 shows an image from a single target, taken

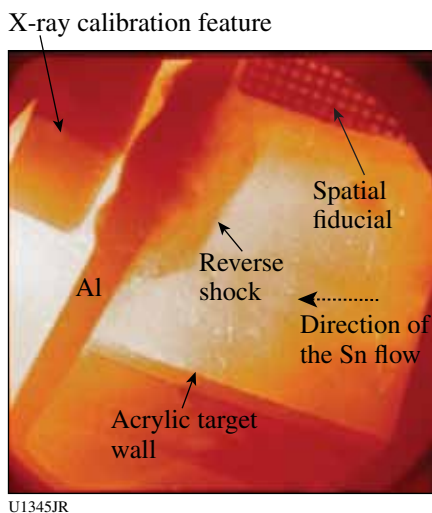


Figure 128.21

X-ray radiograph of a radiative reverse shock in Sn plasma. One can see the radiating shock, an acrylic tube wall, the spatial fiducial, and the x-ray calibration feature used in the experiment. The reverse shock, which forms in the incoming Sn flow, is to the right of the Al wall, where the laser drive is 4 mm away. As the unshocked Sn moves from right to left, it is not dense enough to resolve, while the reverse shock absorbs the diagnostic x rays, revealing its structure.

~ 29 ns after the drive laser pulse was turned off and a few nanoseconds after the collision. It has a 6- μm -thick plastic ablator coated with 4 μm of Sn and an Al wall $\sim 13^\circ$ off of normal to the tube axis.

Development of a Platform for Laser-Ramp Compression of Planetary Materials on OMEGA

Principal Investigator: T. S. Duffy (Princeton University)

Co-investigators: J. Wang (Princeton University); R. F. Smith, F. Coppari, J. H. Eggert, P. M. Celliers, D. Braun, and G. W. Collins (LLNL); and T. R. Boehly (LLE)

The goal of this project is to develop techniques for quasi-isentropic ramp compression of planetary materials. This work has important applications for understanding the structure and dynamics of the interiors of planets both within and outside our solar system. Ramp compression achieves high compression at relatively modest temperatures and can be used to extract quasi-isentropic equation-of-state data and study solid–solid phase transitions. Iron (Fe) and magnesium oxide (MgO) are geologically important materials each representative of one of the two major interior regions (core and mantle) of terrestrial planets. An experimental platform for ramp loading of Fe and MgO has been established and tested in experiments on OMEGA. Target packages consisted of stepped samples and a diamond ablator attached to a Au halfraum [Fig. 128.22(a)]. Each target had four steps that were approximately 5 to 7 μm thick. Composite laser pulses are used to drive a ramp-compression wave into the sample. Detection of the ramp wave’s arrival and its velocity at the free surface of each step was made using a velocity interferometer system for any reflector (VISAR). For MgO, we also carried out x-ray–diffraction experiments using the PXRDIIP (powder x-ray diffraction image plate) target. The target design consisted of a 5- to 10- μm -thick powder MgO sample sandwiched between a diamond ablator and window attached to a Ta pinhole [Fig. 128.22(b)]. Initial experimental results showed that we could successfully compress samples to above 4 Mbar and obtain x-ray–diffraction images of the compressed sample. By enhancing the sample diffraction signal and further reducing background in future experiments, we expect to obtain structural information on this material. Figure 128.23 shows examples of the input pulse, VISAR signal, and wave profiles obtained for a typical MgO ramp-compression experiment. Through the use of Lagrangian analysis on the measured wave profiles, stress–density states in MgO have been determined to pressures of 260 GPa. Figure 128.24 compares the ramp-compression curve to previous diamond-anvil-cell and shock-compression data. At high pressures, the compression curve softens and is similar to the extrapolated 300-K

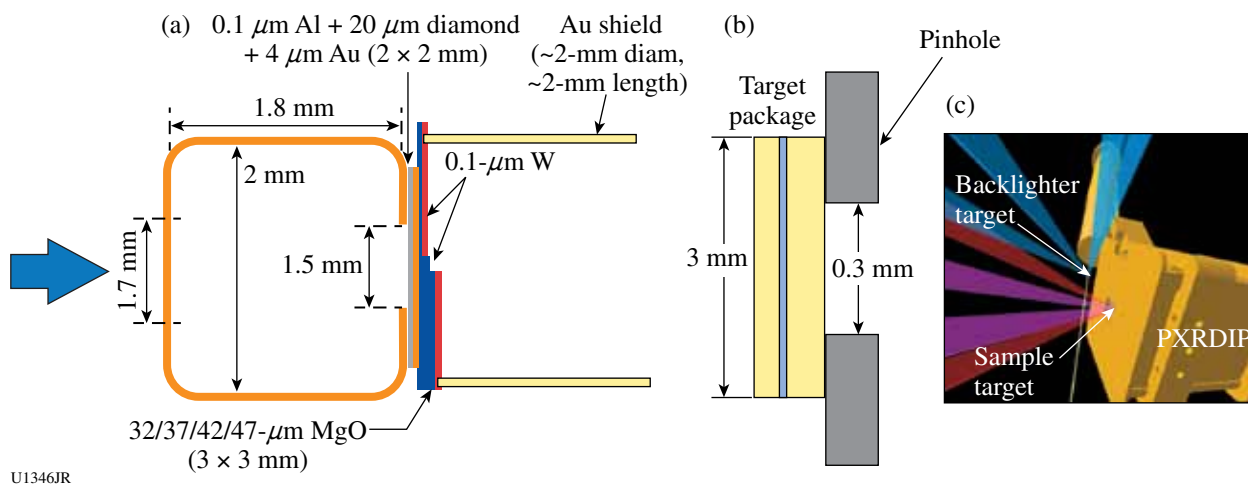


Figure 128.22

(a) Target package for the stepped MgO sample; (b) PXRDIIP setup and target package for the powder MgO sample.

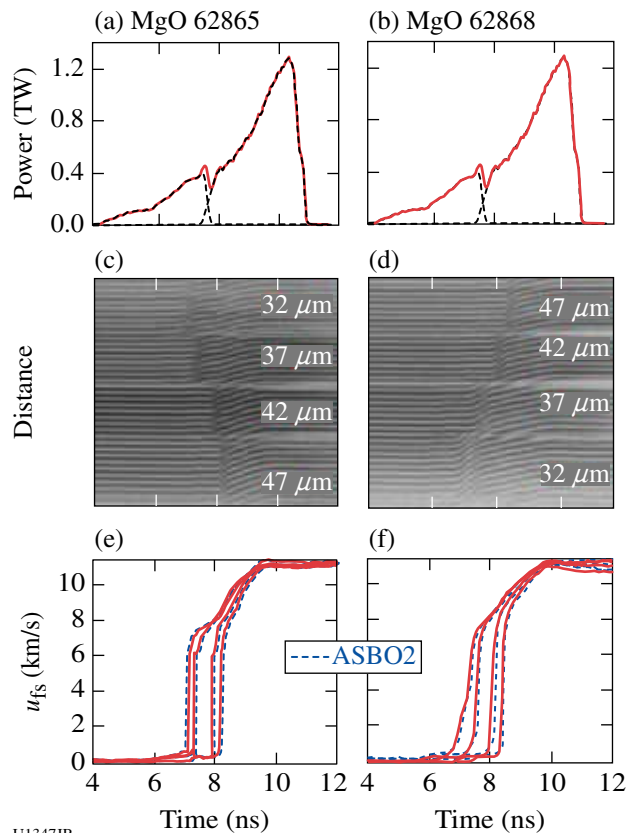


Figure 128.23

[(a),(b)] Laser pulse for two representative MgO shots (62865 and 62868). The dashed lines show the individual pulses and the solid line is the composition pulse shape. [(c),(d)] Line VISAR streak camera images from a ramp-compressed multisteped MgO target corresponding to (a) and (b), respectively. [(e),(f)] Extracted free-surface velocity profiles from (c) and (d) for both active shock breakouts (ASBO1 and ASBO2).

quasi-hydrostatic isotherm. Further experiments will focus on extending MgO ramp compression and x-ray diffraction to higher pressures and reducing experimental uncertainties. Further theoretical work will be devoted to the development of new analytical tools for analyzing ramp-compression data for materials undergoing time-dependent compression including treating the initial shock and phase transformation.

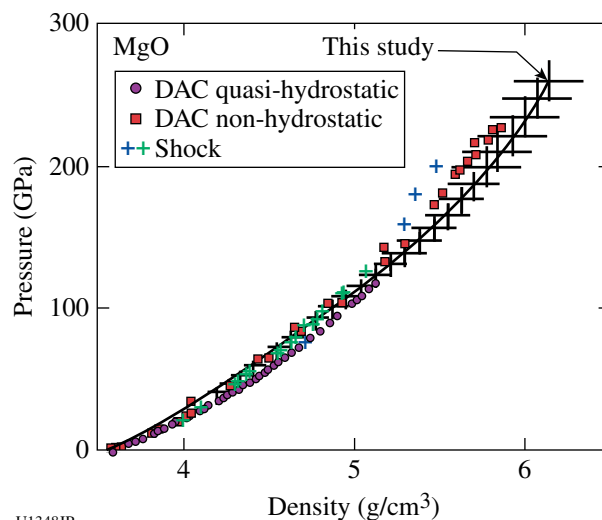


Figure 128.24

Comparison of stress versus density of MgO from the quasi-isentropic compression experiment (62868) to previous studies including diamond anvil cell (DAC) and shock data. The black curve with error bars is the quasi-isentrope from a representative MgO experiment.

Probing the Ion-Ion Structure Factor (S_{ii}) of Shocked Al Using 18-keV Angularly Resolved XRTS

Principal Investigator: R. Falcone (LBL)
 Co-investigators: T. Ma, A. Pak, H. J. Lee, T. Doeppner, C. Fortmann, L. Fletcher, O. L. Landen, and S. H. Glenzer (LLNL)

The goal of the HiZShk-11A experiment is to test dense-matter models on shocked Al using a Mo He_α (18-keV) backlighter to perform x-ray Thomson scattering on the 60-beam OMEGA laser. Simulations have shown significant differences in the static ion-ion (S_{ii}) structure feature of aluminum, depending on the theoretical model used, so these predicted differences were experimentally evaluated by measuring the scattering spectrum of shocked Al at a number of different scattering \mathbf{k} vectors.

The 125- μm Al targets were shock compressed to $>3\times$ solid density using nine beams with a total energy of 4.5 kJ in a stacked 1-ns configuration (Fig. 128.25). SG4 distributed phase plates were used to achieve a smooth 800- μm focal spot, yielding a total drive intensity of $3 \times 10^{14} \text{ W/cm}^2$ on the sample. Sixteen beams were incident on a thin Mo foil to generate Mo He_α x rays at 17.9 keV used to probe the compressed targets.

Initial analysis is very promising: the S_{tot} (Rayleigh + background fluctuations + Compton signals) shows an increasing relative intensity as we approach lower \mathbf{k} (smaller scattering angle). Work continues to extract the S_{ii} structure factor from the data.

PlanetCore 11A, 11B

Principal Investigator: R. Jeanloz (University of California, Berkeley)
 Co-investigators: J. H. Eggert, D. G. Hicks, P. M. Celliers, and G. W. Collins (LLNL); and T. R. Boehly (LLE)

Two half-day campaigns were carried out in FY11 under the Planetary Core NLUF Project: one in December 2010 (11A) and a second in March 2011 (11B). Both series focused on exploring the phase diagram of mixtures of 80% H_2 and 20% He. The primary goal of these studies was to look for evidence of He phase separation under hot, pressurized conditions. There are recent predictions of this effect,^{1,2} and its existence has ramifications for understanding the interior structure of the planet Saturn. Our previous studies had focused on He/ H_2 in a 50:50 ratio, using samples with initial pressures ranging from 1 kbar to 40 kbar that were then shock compressed to pressures ranging from 40 to 200 GPa. The measurements done with the ASBO/VISAR and streak optical pyrometer (SOP)

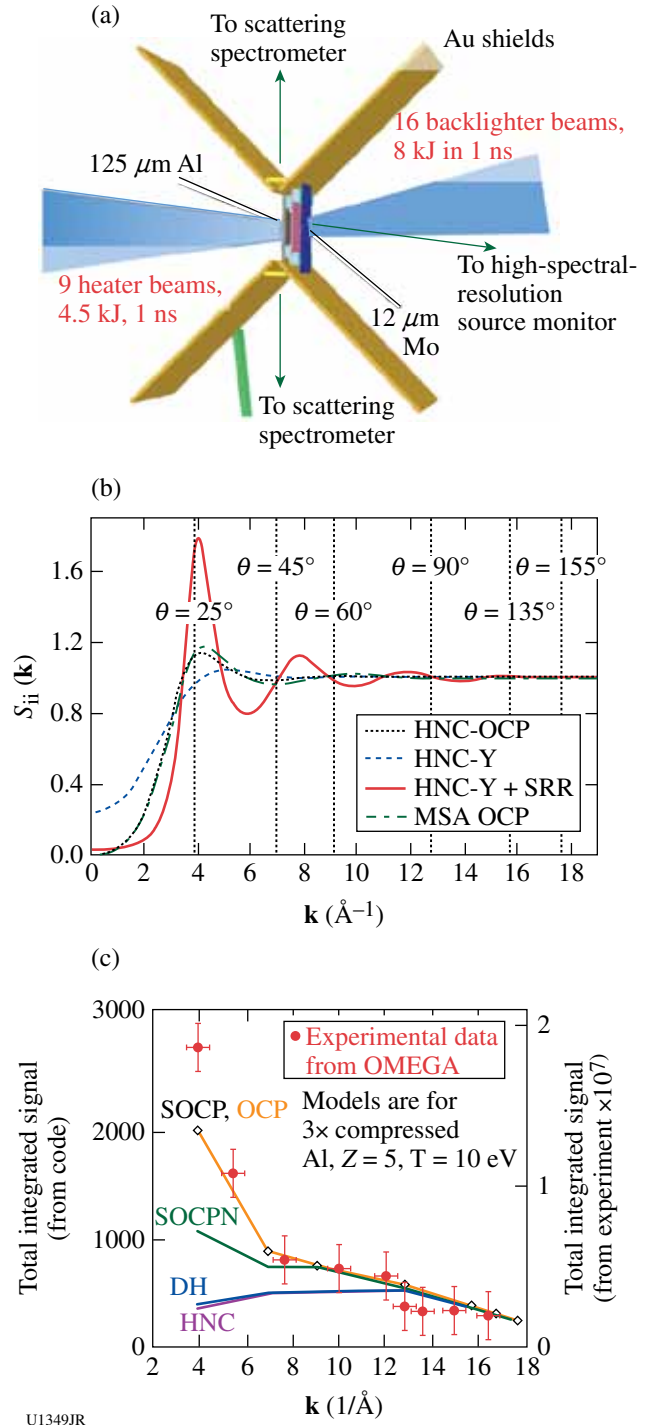


Figure 128.25 (a) The experimental setup for HiZShk-11A. (b) The S_{ii} of shocked Al oscillates as a function of scattering vector \mathbf{k} for several models, where the most interesting region to probe S_{ii} and validate models is around $\mathbf{k} = 4 \text{ \AA}^{-1}$. (c) Preliminary data analysis shows the total integrated signal of scattering data at varying \mathbf{k} follows the trends predicted by the screened-one-component plasma (SOCP) or one-component plasma (OCP) models.

diagnostics determined the pressure, density, internal energy, shock-front reflectivity, and shock-front temperature along each Hugoniot (Fig. 128.26). The results from those studies showed no evidence of phase separation over the full range of densities and temperatures that were explored, and it turns out that this is consistent with the recent predictions. Recent calculations suggested, however, that phase-separating states in the 80%:20% mixtures could be accessed experimentally under the pressure and temperature conditions that are achieved on OMEGA. Preliminary evaluation of the results from these latest campaigns may provide the first experimental evidence of phase separation in hot, pressurized H_2/He mixtures. Relative to the 50%:50% mixture case, the 80%:20% samples precompressed to near 40 kbar and shocked to the 100- to 200-GPa range showed a clear reduction of the shock temperatures. Such a temperature reduction is expected to arise as a consequence of the entropy of mixing in these samples: the phase separation (demixing) is expected to lead to a reduction in specific entropy and a corresponding reduction in shock temperatures. A third full-day campaign to extend and confirm these results was planned for August 2011 but had to be postponed into FY12 because of equipment problems. In addition to the mixture

experiments, we performed two shots with targets filled with H_2 and constructed with LiF anvils. A multipulse drive was used to test a multishock compression scheme for achieving cool, high-density states in the samples. The results from these experiments look promising but are too preliminary to reach conclusions about the technique. Further experiments with the multishock technique are planned for the future campaigns.

Investigation of Hydrodynamic Stability and Shock Dynamics in OMEGA Direct-Drive Implosions Using Spectrally Resolved Imaging

Principal Investigator: R. C. Mancini

(University of Nevada, Reno)

Co-investigators: R. Tommasini (LLNL);
and S. P. Regan, B. Yaakobi, V. Yu. Glebov,
W. Theobald, and J. A. Delettrez (LLE)

Arrays of spectrally resolved images recorded with the multimonoenergetic x-ray imager (MMI) instrument open up new opportunities for observation and diagnosis of high-energy-density plasmas with an unprecedented level of detail. The MMI instrument records the spectrally, spatially, and time-resolved x-ray signal from a tracer element added to the plasma by combining pinhole-array imaging with the dispersion of a Bragg multilayer mirror, and the time-resolution provided by a framing camera detector. In this project, we apply spectrally resolved imaging to investigate the hydrodynamic stability and shock dynamics of low-adiabat direct-drive implosions on OMEGA. In low-adiabat implosions, a nearly isentropic compression is launched by a shaped laser pulse drive that starts from a low intensity, gradually leading to a high intensity. By minimizing preheat, higher compressions are achieved in low-adiabat implosions compared to high-adiabat implosions, therefore making fundamental studies on the stability of low-adiabat implosions relevant to high-energy-density plasma hydrodynamics and inertial confinement fusion. Furthermore, benchmarking and testing of hydrodynamic codes with data from well-characterized low-adiabat implosions are important since these codes are also used to model and design low-adiabat cryogenic implosions and advanced ignition concepts.

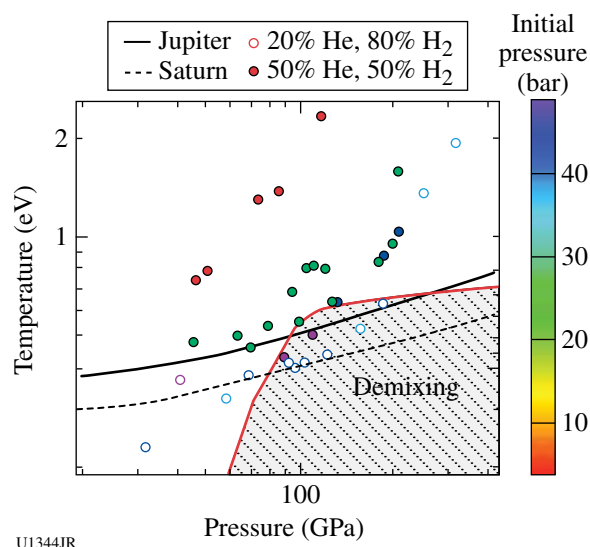
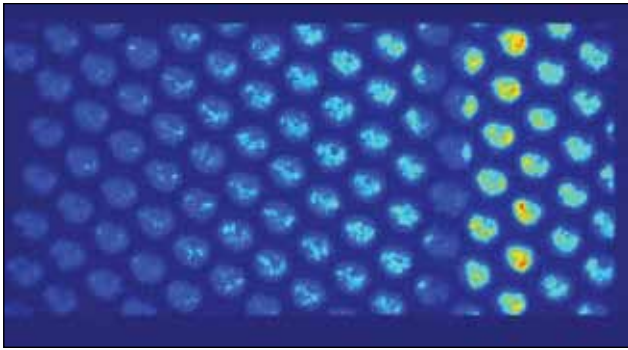


Figure 128.26

Phase diagram of precompressed shock states achieved on OMEGA for 50% H_2 :50% He mixtures (filled circles) and 80% H_2 :20% He (open circles). Symbol colors are associated with the sample initial pressure indicated by the color bar at left. The predicted demixing region for the 80% H_2 :20% He mixture is shown by the shaded zone with a red boundary. Black curves indicate the planetary isentropes for Jupiter (solid) and Saturn (dashed). The Hugoniot temperatures for the 80% H_2 :20% He case are reduced compared to the 50% H_2 :50% He mixture at similar pressures, suggesting that the 80% H_2 :20% He mixture may be undergoing phase separation under these conditions.

Figure 128.27 shows an array of about 100 gated, spectrally resolved images of the implosion core recorded with an MMI instrument in OMEGA shot 60933. This experiment was driven by a low-adiabat ($\alpha \sim 2$) laser pulse with approximately 21 kJ of UV laser energy on target. The target was a plastic shell of 27- μm wall thickness, filled with 20 atm of deuterium. It also had a 0.5- μm -thick plastic tracer layer doped with Ti at the 6% (atomic) level placed on the inner surface of the plastic shell.



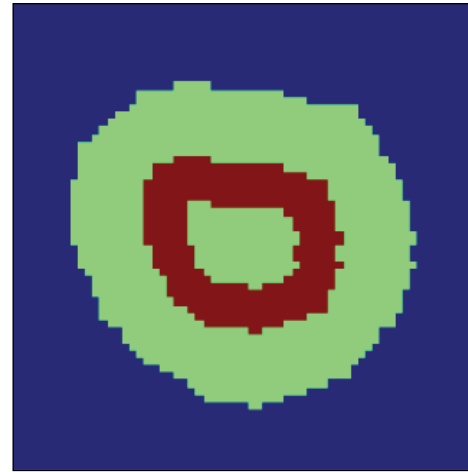
U1423JR

Figure 128.27

An array of gated, spectrally resolved images recorded in OMEGA shot 60933. The horizontal axis is a photon-energy axis spanning the spectral range from 3500 eV to 5000 eV. Therefore, each image is characteristic of a slightly different photon-energy range.

The MMI instrument recorded the x-ray signal of this spectroscopic tracer. We note that while the vertical and horizontal axes of the image data in Fig. 128.27 are spatial-resolution axes, the horizontal axis is also a spectral-resolution axis. Therefore, each one of the images shown in Fig. 128.27 is characteristic of a slightly different photon-energy range.³ The bright features observed in the image data correspond to the titanium He_α and Ly_α line emissions at 4750 eV and 4979 eV, respectively. The low-intensity or dark features observed to the left (i.e., low-energy side) of these features are due to absorption in $n = 1$ to 2 line transitions in L-shell titanium ions.

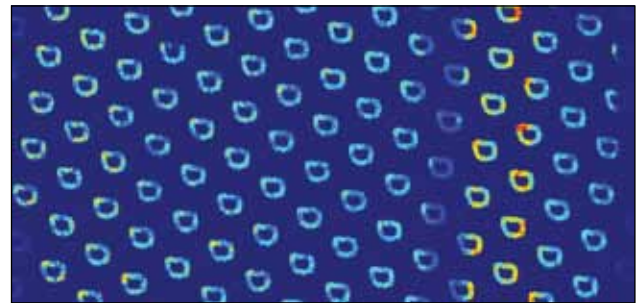
Processing the array of spectrally resolved images yields broad- and narrowband images as well as spatially integrated and spatially resolved line spectra. In particular, the latter provides critical information for a quantitative analysis of the spatial structure and details of the implosion core plasma.³ In this connection, Fig. 128.28 illustrates an image mask employed to extract a spatially resolved spectrum from the data shown in Fig. 128.27. A broadband image defines the shape and spatial extension of the projection of the implosion core on the image plane, and a region within it defines the domain of integration that characterizes the spatially resolved spectrum (see Fig. 128.28). In object space, this domain corresponds to the volume defined by the intersection of the implosion core with a cylindrical shell of cross section given by the region within the image. By applying this mask to the spectrally resolved images in Fig. 128.27, an array of spectrally resolved image regions can be obtained; this array is displayed in Fig. 128.29. Finally, by integrating one photon energy at a time, the intensity distribution of the spatially resolved spectrum can be obtained; this result is displayed in Fig. 128.30.



U1350JR

Figure 128.28

Illustration of an image mask employed to extract a spatially resolved spectrum. The green area represents a broadband image obtained from the data shown in Fig. 128.27; the red area is the domain of integration associated with the spatially resolved spectrum.

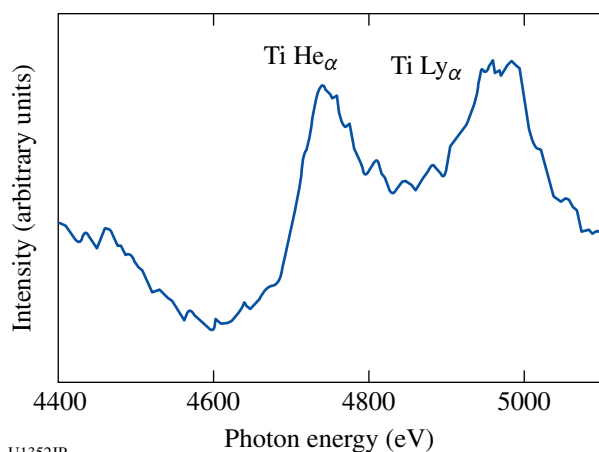


U1351JR

Figure 128.29

An array of spectrally resolved image regions based on the data of Fig. 128.27 and the mask displayed in Fig. 128.28.

The spatially resolved spectrum shown in Fig. 128.30 displays simultaneously line emission and absorption over a range of titanium ions from F- to H-like charge states. This suggests that the titanium tracer, initially located only on the inner surface of the shell, has spread in space and can later be found in low-temperature as well as high-temperature regions of the implosion core; i.e., close to the periphery as well as the central regions of the core. Quantitative analysis of narrowband images and spatially resolved spectra at the collapse of the implosion using a detailed atomic and radiation physics model for titanium yields information about the distribution of tracer and mixing in the implosion core, which, in turn, depend on the hydrodynamic stability of the implosion. Alternatively, measurements at earlier times permit one to investigate the tracer's state and spatial distribution at the time when the shock breaks into the core.



U1352JR

Figure 128.30

Spatially resolved spectrum based on the mask displayed in Fig. 128.28 and the array of image regions shown in Fig. 128.29. The titanium He_α and Ly_α line emissions correspond to the bright features observed in the data displayed in Fig. 128.27. The low-intensity darker features to the left of these bright features in Fig. 128.27 correspond to the absorption part of the spectrum.

Proton Radiography of Direct- and Indirect-Drive ICF and HEDP Plasmas and the First Basic Nuclear Physics Measurements in an ICF Plasma

Principal Investigators: R. D. Petrasso and C. K. Li
(Massachusetts Institute of Technology)

Co-investigators: F. H. Séguin and J. A. Frenje (MIT);
T. C. Sangster, V. Yu. Glebov, and D. D. Meyerhofer (LLE);
and D. P. McNabb (LLNL)

MIT's NLUF work in FY11 included a wide range of experiments applying MIT-developed proton radiography methods to the study of high-energy-density physics (HEDP) and inertial confinement fusion (ICF) plasmas; it also included a completely new and groundbreaking class of experiments utilizing MIT- and LLE-developed spectrometry methods to study basic nuclear physics at an ICF facility. Our NLUF experiments also provided unique research opportunities in HEDP for eight MIT graduate students, who will use resultant data in major parts of their theses, and for several undergraduates.

During the present and previous NLUF programs, we have used the MIT-developed method of monoenergetic, charged-particle radiography⁴ in new types of studies of electromagnetic fields and plasmas in HEDP and in ICF physics. These projects, undertaken at the Omega Laser Facility,^{5,6} were performed because of their importance to the future of ICF, HEDP, and the physics of fields generated by laser-plasma interactions. Topics studied include the imaging, identification, and measurement of electric and magnetic fields in laser-generated

plasmas; reconnection of MG magnetic fields in high- β plasmas; self-generated electromagnetic fields in ICF implosions; the dynamics of ICF capsule implosions; electromagnetic fields in laser-driven hohlraums; and the development of a proton backlighter using short-pulse beams from OMEGA EP. The work has already resulted in nine publications in *Science*^{7,8} and *Physical Review Letters*,^{9–15} in addition to many other papers, invited talks, and contributed talks at conferences, including three papers submitted this year.^{16–18} The work has successfully addressed basic physics issues and issues directly relevant to the future success of ignition experiments at the NIF.

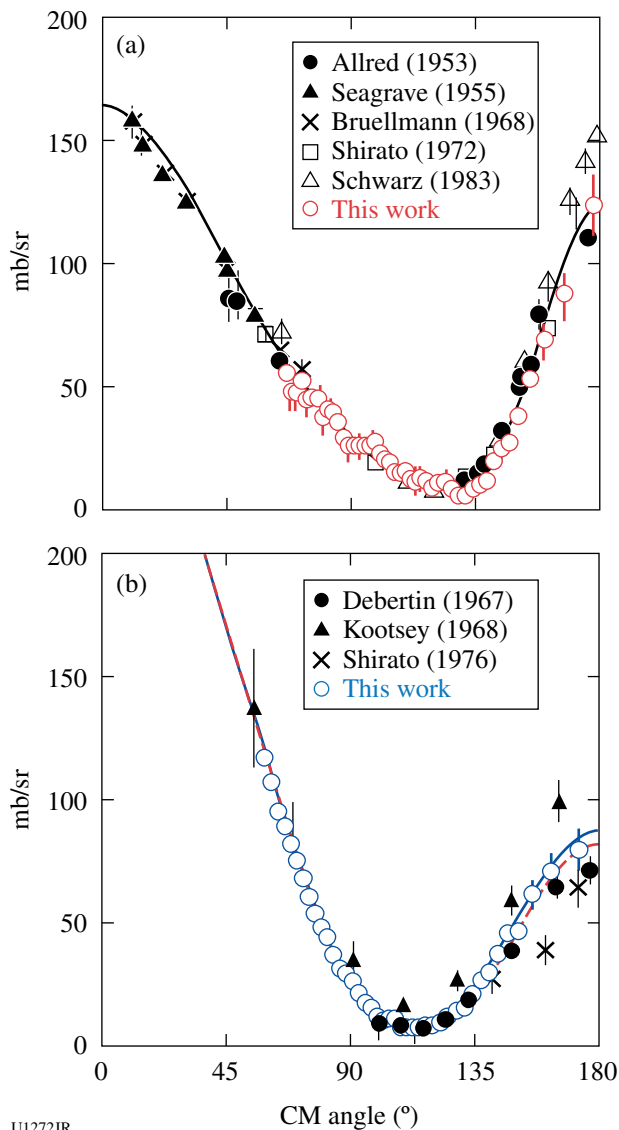
As described in Ref. 19 and illustrated in Figs. 128.31 and 128.32, we performed the first basic nuclear physics experiment in the context of an ICF facility, measuring the differential cross section for elastic neutron-triton ($n\text{-}^3\text{H}$) and neutron-deuteron ($n\text{-}^2\text{H}$) scattering at 14.1 MeV on OMEGA using the MIT-developed, magnet-based charged-particle spectrometer CPS-2 (Ref. 20). In these experiments, which were carried out by simultaneously measuring elastically scattered ^3H and ^2H ions from a DT (deuterium-tritium)-gas-filled inertial confinement fusion capsule implosion, the differential cross section for the elastic $n\text{-}^3\text{H}$ scattering was obtained with significantly higher



U1353JR

Figure 128.31

The CPS-2 charged-particle spectrometer during installation on the OMEGA target chamber. The cone-shaped end contains the entry aperture, while the cylindrical section contains a 7.6-kG magnet and CR-39 nuclear track detectors. In the experiment described here, CPS-2 was used to simultaneously measure energy spectra of deuterons and tritons elastically scattered by 14.1-MeV neutrons, and protons from d-d reactions in a DT (deuterium-tritium)-gas-filled thin-glass capsule implosion.



U1272JR

Figure 128.32 (From Ref. 19) (a) Measured differential cross section for the elastic $n\text{-}^2\text{H}$ scattering, which has been normalized to a Faddeev calculation. (b) Measured and calculated differential cross section for the elastic $n\text{-}^3\text{H}$ scattering. The experimental data have been normalized with the deuterium–tritium fuel-ratio–modified normalization factor derived in (a). The blue solid curve represents an *ab initio* NCSM/RGM calculation and the red dashed curve represents an *R*-matrix calculated $n\text{-}^3\text{H}$ cross section.

accuracy than achieved in previous accelerator experiments. The results compare well with calculations that combine the resonating group method with an *ab initio* no-core shell model, which demonstrate that recent advances in *ab initio* theory can provide an accurate description of light-ion reactions. This work is ushering in a new and exciting field of research—Plasma Nuclear Science—blending the separate disciplines of plasma and nuclear physics.

Collisionless Shocks in Laboratory High-Energy-Density Plasmas

Principal Investigator: A. Spitkovsky (Princeton)
 Co-investigators: L. Gargat  (Princeton); H.-S. Park, B. A. Remington, S. M. Pollaine, and D. Ryutov (LLNL); J. P. Knauer, G. Fiksel, and R. Betti (LLE); K. Sakawa, T. Ide, T. Kato, Y. Kurimatsu, T. Morita, and H. Takabe (Osaka University); G. Gregori and T. Bell (Oxford); F. Miniati (ETH Sci-Tech University); M. Koenig and A. Ravasio (Ecole Polytechnique); and E. Liang (Rice University)

This NLUF program studies the creation of collisionless shocks in counter-propagating laser-produced plasmas. Collisionless shocks are of great importance in astrophysical and space plasmas and occur when the mean free path to Coulomb collisions is large compared to the size of the shock transition.^{21–30} The shock is then mediated by the collective plasma effects from the interaction between plasma particles and the self-generated electromagnetic fields. Collisionless plasma conditions can now be created on the OMEGA and OMEGA EP lasers, where the laser-driven plasmas propagate at speeds of ~ 1000 km/s and densities of $\sim 10^{18}$ to 10^{19} cm^{-3} . The experiments in this program collide two streams of high-speed plasma and study the formation of shocks as a function of an externally applied magnetic field that is generated by a set of Helmholtz coils at the interaction region. The theoretical expectation is that at low external fields, the shock is mediated by the filamentation (Weibel) instability, while at higher fields, magnetic reflection of ions will form the shock. These regimes are representative of the conditions encountered in a range of astrophysical environments, including supernova remnant shocks and solar wind shocks. These experiments on OMEGA and OMEGA EP test these shock-formation mechanisms and address the open questions of astrophysical collisionless shock physics, such as the presence of particle acceleration and the mechanisms of magnetic-field amplification in shocks.

In FY11 we completed an extensive set of particle-in-cell and radiation–hydrodynamics simulations to converge on the design of the experiment. We determined the minimal interaction length necessary to achieve filamentation-mediated shocks and predicted the field strengths needed to transition the shock into the magnetized regime. In close collaboration with LLE (G. Fiksel’s group), a set of Helmholtz coils capable of generating 1-T magnetic fields was designed and fabricated. Also, proton radiography and Thomson-scattering diagnostics were fielded and tested in related experiments by Principal Investigator H.-S. Park (AstroPlasmas-11A, EPColPlasmas-11B, ColPlasmas-11C, EPColPlasmas-11D). These efforts

culminated in a joint-shot day on 3 August. In this experiment, we used OMEGA to initiate two ablated plasma flows from CH foils. The OMEGA EP laser was used to provide a short pulse for proton radiography of the interaction region. Helmholtz coils were triggered to provide an external magnetic field in the experiment. Thomson scattering was used to monitor plasma conditions (see Fig. 128.33). This was one of the most-complicated experimental setups at LLE, and we are extremely pleased that the experiment worked without major problems and thankful to the facility for the extensive preparatory work required of the staff. We performed eight shots, with four OMEGA-only shots and four joint shots. On the experimental side we learned that the basic experimental setup is sound, and both the magneto-inertial fusion energy delivery system (MIFEDS) and Thomson-scattering diagnostics can survive the electromagnetic pulse (EMP) monitor from the short-pulse laser. On the science side, we studied the difference in the radiography signal between one and two beams and obtained the first evidence for filamentation in the crossing beams (Fig. 128.34). These proton radiography data demonstrate the development of magnetic fields expected from the Weibel instability, suggesting that the collisionless shock mediation mechanism is possible even in the weak magnetic fields. The experiment also produced data with MIFEDS fields, and the differences in the Thomson-scattering data

and radiography are currently being analyzed. We developed a suite of post-processing diagnostics for the particle-in-cell (PIC) simulation code that allows us to calculate Thomson and radiography signals based on the full distribution function from the simulations. Preliminary analysis of the data and PIC simulations indicates that the next experiment in this program in FY12 will require stronger magnetic fields. The design work on increasing the MIFEDS fields is currently underway.

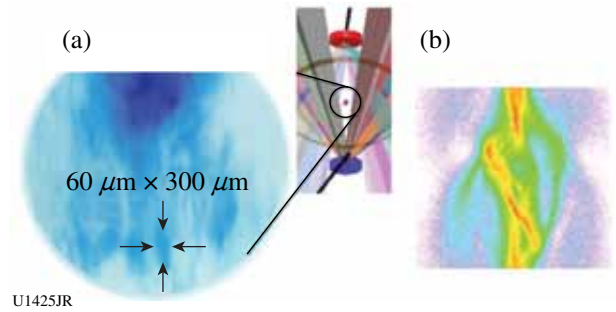


Figure 128.34
 (a) Thomson parabola (TPIE) data showing high-energy protons up to nearly 70 MeV from OMEGA EP using 1 ps and ~400 J of laser energy; color indicates ion density, highest (red) to lowest (blue). (b) TPIE data showing carbon species up to 30 MeV in energy using 10 ps and 1000 J of laser energy; color scale indicates density (in arbitrary units), highest (dark blue) to lowest (white).

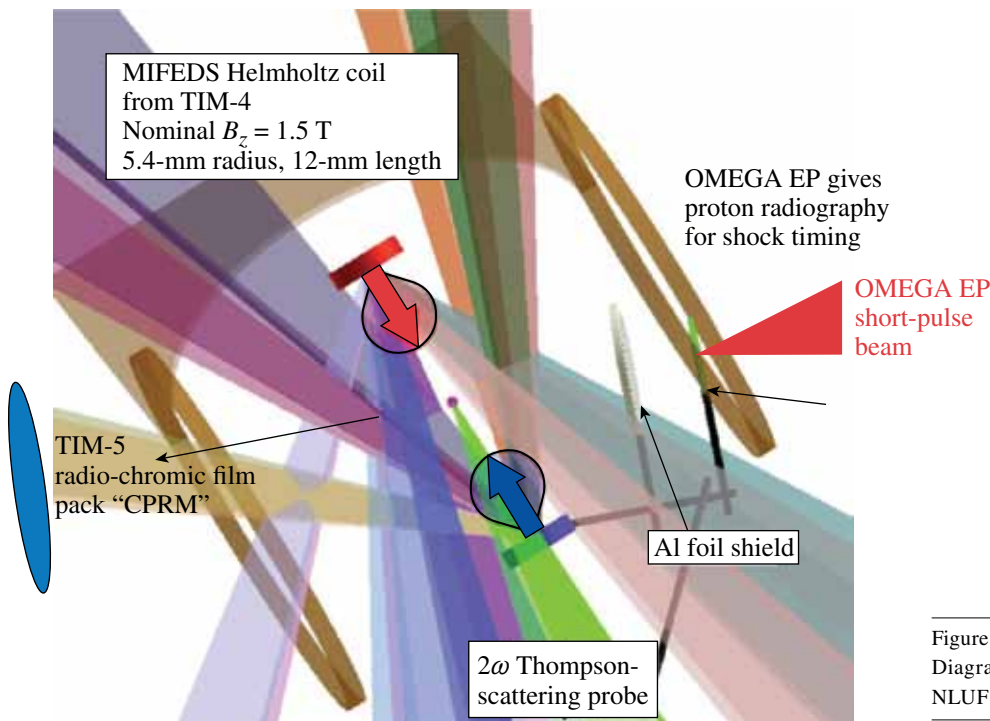


Figure 128.33
 Diagram of the experimental setup for NLUF ClessShk-11A.

U1424JR

Dependence of Laser-Energy Coupling on Target Material and Laser Pulse Length

Principal Investigators: M. S. Wei and R. B. Stephens (General Atomics)

Co-investigators: F. N. Beg and H. Sawada (UCSD); C. D. Chen, H. McLean, and P. K. Patel (LLNL); and W. Theobald and C. Stoeckl (LLE)

Lead graduate student: A. Sorokovikova (UCSD)

Efficient conversion of laser energy to hot electrons and their subsequent energy transport to the compressed fuel are extremely important for the success of fast ignition to reduce the energy required for ignition. Energy coupling is controlled by the nature of the plasma (i.e., density profile, ionization, etc.) at the laser-plasma interface and the dynamic response of the transport material, which evolve with time, and therefore are dependent on the laser pulse length. Previous experiments³¹ performed on the Titan laser (0.7-ps pulse length, 150 J) at LLNL showed that 10- μm , high-Z material in the multilayer planar solid target suppresses fast-electron angular spread and reduces the forward-going fast-electron flux. The goal of the General Atomics NLUF project is to further investigate target material effects on fast-electron transport and extend such a study to 10-ps time scale at high intensity using the OMEGA EP laser. The project consists of two steps: (1) characterization of fast-electron generation and transport through different transport materials at 1 ps with 300-J energy to compare with the Titan experiments; and (2) extend such a study to 10 ps with 1.5-kJ energy. In FY11, we performed experiments on OMEGA EP using the high-intensity, short-pulse backlighter beam (BL2) with the multilayer planar-foil targets.

Figure 128.35 shows the schematics of the target and experimental setup at the Omega Laser Facility. High-intensity, short-pulse OMEGA EP backlighter beams (300 J at 1 ps or 1500 J at 10 ps) were tightly focused onto the front surface of the multilayer planar-foil target with approximately 80% of laser energy in a 50- to 60- μm focal spot. The mm-square-sized multilayer target consists of a front-surface Al layer (4 μm) over a thin transport layer ($\sim 10 \mu\text{m}$) of various Z materials (Au, Mo, and Al), an Al spacer (75 μm), and a Cu tracer layer (12 μm) followed by a 20- μm -thick Al layer. The multilayer target had a 1-mm-thick, 5 \times 5-mm²-wide conductive CH back layer to minimize electron refluxing. Fast electrons were characterized by two primary diagnostics: a spherical crystal imager (SCI) to measure the spatial distribution of fast-electron-induced 8-keV fluorescence radiation in the Cu trace layer and a zinc Von Hamos (ZVH) x-ray spectrometer tuned to measure the

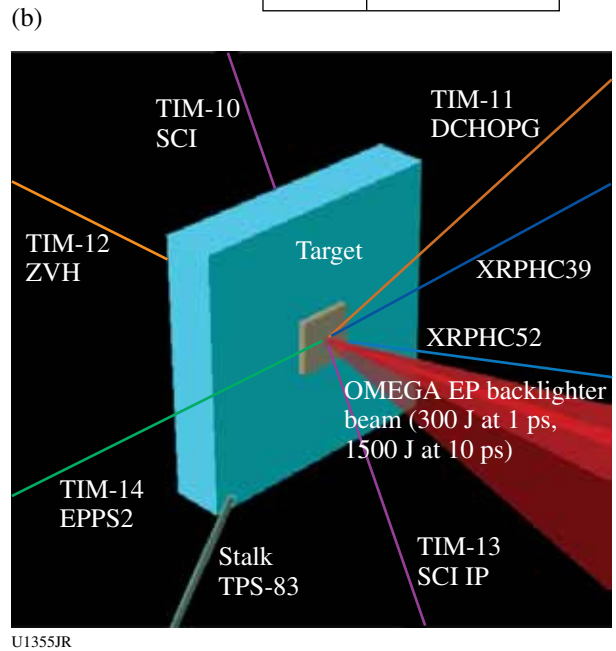
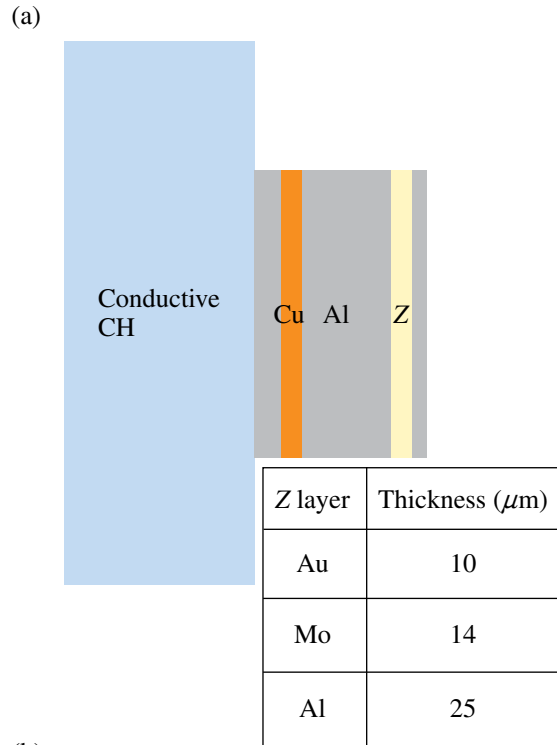


Figure 128.35 Schematic of the (a) multilayer planar-foil target and (b) experimental setup.

absolute Cu K_{α} yield. The Cu K_{α} emission is proportional to the fast-electron flux in this single-pass target.

In the 1-ps OMEGA EP laser-interaction experiment, we observed a smaller Cu K_{α} fluorescence spot with the high-Z Au

transport target compared to the Al transport target with good reproducibility. As shown in Fig. 128.36, the measured Cu K_{α} spot for the Au case is $R_{50} \sim 70 \mu\text{m}$ in radius (R_{50} is the radius of the spot counting all the pixels with a signal greater than or equal to the peak value) and $93 \mu\text{m}$ for the Al target case, which is consistent with the previous Titan results. Collisional particle-in-cell (PIC) modeling, including dynamic ionization and radiation cooling, suggests that strong resistive magnetic fields inside the high-Z transport target collimate fast electrons and reduce the forward-going fast-electron angular spread.³²

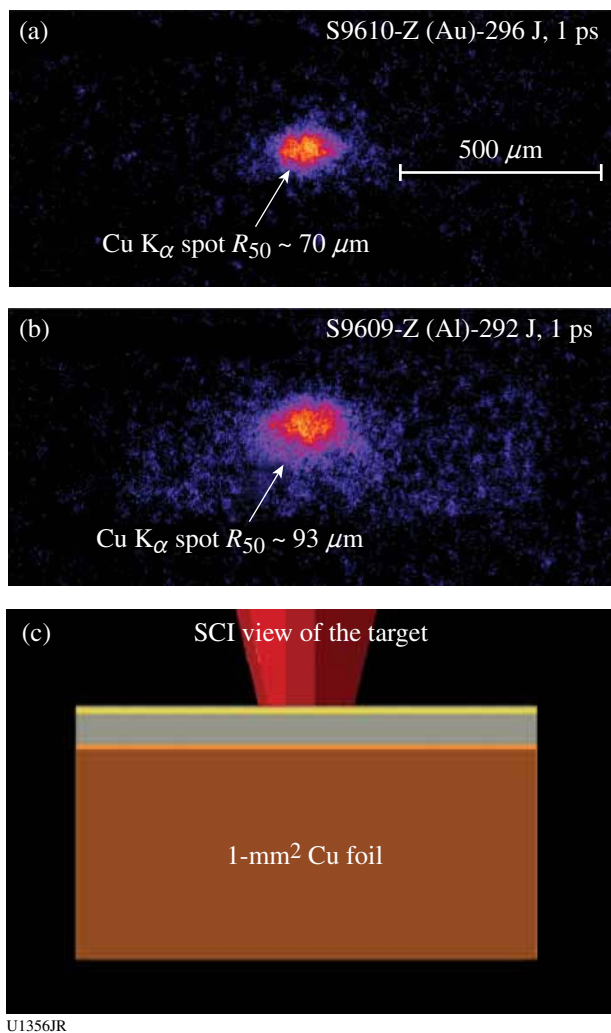


Figure 128.36
SCI recorded Cu K_{α} radiation spots in a 1-ps interaction experiment: (a) with a Z = Al transport target; (b) with a Z = Au transport target; and (c) SCI diagnostic view of the target. Images (a) and (b) have the same color and spatial scales. A smaller K_{α} spot is observed in Z = Au transport targets.

Experiments with a 10-ps, 1500-J OMEGA EP pulse showed a large shot-to-shot variation however. The behavior of laser-produced fast electrons and their transport as evidenced in the observed K_{α} spots was very different compared to the experiments with 1 ps as shown above. Figure 128.37 shows the SCI-recorded Cu K_{α} images with 9- to 10-ps pulses from three different types of Z-transport targets. It is evident in this case that there are pronounced filamentary structures [Figs. 128.37(a) and 128.37(b)] and irregular shapes [as shown in Fig. 128.37(d)] in the fluorescence spot. With identical Al

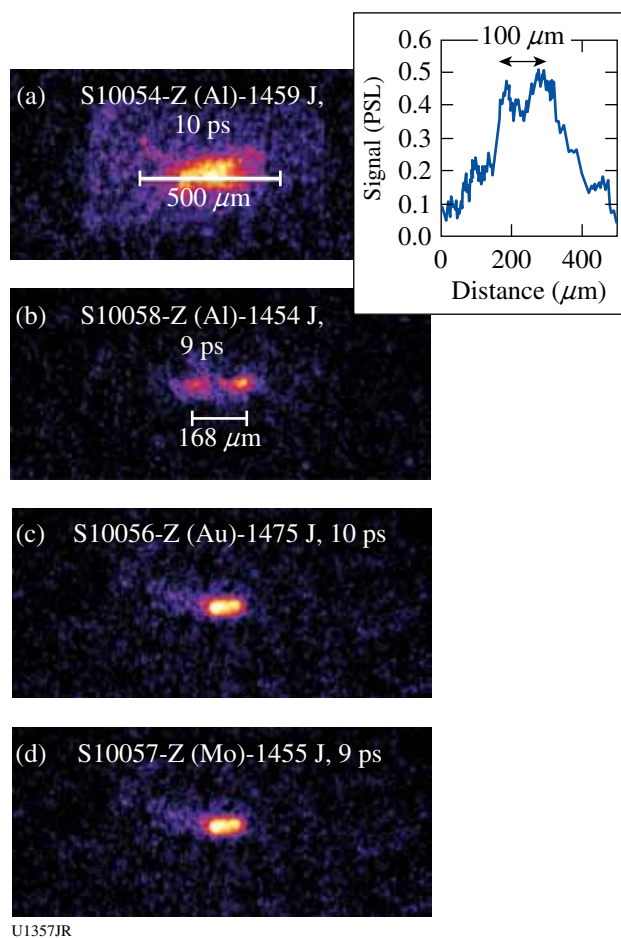


Figure 128.37
SCI-recorded Cu K_{α} radiation spots in a 10-ps interaction experiment: (a) and (b) with Z = Al transport target [lineout of (a) is shown in the inset]; (c) with Z = Au transport target and (d) with Z = Mo transport target. Images have the same color and spatial scales. Filamentary structures and irregular shapes of fast-electron beams can be clearly seen with a large shot-to-shot variation.

targets, two to three filaments were observed with a separation distance of $\sim 100 \mu\text{m}$, which suggests the growth of widely separated stable filaments after a few picoseconds, either in the laser-plasma interaction region or inside the solid target. PIC modeling is underway to study high-intensity laser-plasma interaction (LPI) and fast-electron transport in a 10-ps time scale. Further experimental investigation with similar targets to compare 1-ps versus 10-ps LPI and fast-electron transport will be performed in the coming year with additional hard x-ray spectrometers, together with SCI and ZVH, to fully characterize the fast-electron source and transport phenomena.

Low-Density Plasma Interactions

Principal Investigators: L. Willingale, C. Zulick, A. Maksimchuk, and K. Krushelnick (University of Michigan); P. M. Nilson, R. S. Craxton, C. Stoeckl, and T. C. Sangster (LLE); H. Chen (LLNL); J. Cobble (LANL); and P. A. Norreys and R. Scott (RAL)

The interaction of a high-power, short-duration laser pulse with underdense plasma has been investigated to study laser propagation, channel formation, filamentation, and particle acceleration. To generate an underdense CH target, a long-pulse beam (2.5 ns, $\sim 1200 \text{ J}$ in an $800\text{-}\mu\text{m}$ -diam focal spot) is used to create a plasma plume from a foil target. The main interaction beam is then focused into the plasma plume, with the laser propagating parallel to the target surface so that it sees an approximately Gaussian density profile (2-D *SAGE* modeling estimates a width of $650 \mu\text{m}$ with a peak density of around either $5 \times 10^{19} \text{ W/cm}^2$ or $1.5 \times 10^{20} \text{ W/cm}^2$ depending on the height above the target surface). The channel electromagnetic fields have been imaged simultaneously using a proton probe generated by the second short-pulse beam, which can observe laser filamentation, channel self-correction, and channel-wall instabilities.³³ In addition to the channel imaging, particle spectra are measured with magnetic spectrometers.

The laser pulse length, laser energy, and plasma density are varied to investigate the effect of each parameter. Figure 128.38 shows the electron spectra measured in the direction of laser propagation for different laser pulse lengths, with the labels indicating the laser pulse length, laser power, and peak plasma density. For comparison, the spectra from a 9 ps with 30 TW shot onto a solid 50- μm -thick copper target are shown. Large numbers of electrons are accelerated to high energy during the underdense interaction, many more and to a higher energy than for a solid target. Shot-to-shot variation for similar parameters

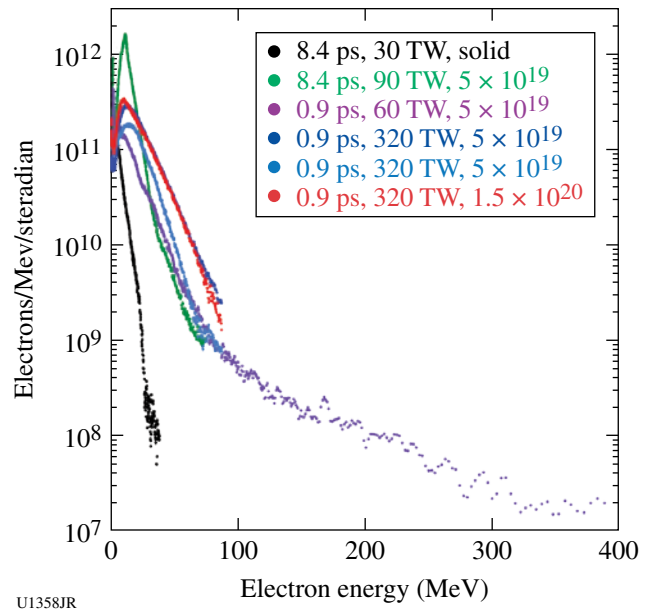


Figure 128.38
Electron spectra for various pulse lengths, powers, and peak plasma densities (labels indicate laser pulse length, laser power, and target density).

may be due to the laser filamentation causing a number of channels within which electrons could be accelerated. The possible acceleration mechanisms are currently under investigation using PIC simulations.

FY11 Laboratory Basic Science Programs

In early 2011, LLE issued a solicitation for LBS proposals to be conducted in FY12. A total of 41 proposals requesting a total of 87.5 shot days of Omega Facility shot time were submitted. An independent review committee comprised of Prof. Farhat Beg (University of California, San Diego), Dr. Robert Heeter (LLNL), Prof. Karl Krushelnick (University of Michigan), Dr. Carolyn Kuranz (University of Michigan), Dr. Paul Keiter (LANL), Prof. Roberto Mancini (University of Nevada, Reno), Dr. Rick Olson (SNL), Prof. Charlie Freeman (State University of New York–Geneseo), Dr. Frederick Marshall (LLE), and Dr. John Soures (Committee Chair, non-voting) reviewed the proposals and recommended that 15 proposals receive 28 shot days at the Omega Laser Facility in FY12. Table 128.VIII lists the successful LBS proposals.

Fifteen LBS projects were allotted Omega Facility shot time and conducted a total of 303 target shots at the facility in FY11. The FY11 LBS research is summarized in this section.

Table 128.VIII: Approved FY12 LBS proposals.

Principal Investigator	Affiliation	Project Title
P. M. Celliers	LLNL	Measurement of the Viscosity of Shock-Compressed Fluids: Studies of Water and Silica
H. Chen	LLNL	Exploring Pair Plasma and Its Applications Using OMEGA EP and OMEGA Lasers
G. Fiksel	LLE	Magnetic Field Compression in Spherical Implosions on OMEGA
G. Fiksel	LLE	Magnetic Reconnection in High Energy Density Plasmas in the Presence of an External Magnetic Field
O. A. Hurricane	LLNL	Measurements of Linear, Nonlinear, and Turbulent-Mixing Regimes in Kelvin–Helmholtz Instability in the Subsonic Regime
A. L. Kritcher	LLNL	Nuclear-Atomic-Plasma Interactions in Laser-Produced Plasmas
B. R. Maddox	LLNL	Dislocations and Twinning at High Pressure and Strain Rate on BCC Metals
D. P. McNabb	LLNL	Thermonuclear Reactions in Stellar Plasmas and High Resolution Measurements of Three-Body Breakup in Isobaric Analogue Reactions
H.-S. Park	LLNL	Astrophysical Collisionless Shock Generation by Laser-Driven Laboratory Experiments on OMEGA and OMEGA EP
P. K. Patel	LLNL	Compton Radiography of Cone-in-Shell Implosions for Fast Ignition
S. P. Regan	LLE	Probing Shocked Liquid H, H/He, CH ₄ , N ₂ , and NH ₃ with Inelastic X-Ray Scattering and Shock Velocity Measurements: Toward the Equation-of-State of Planetary Interiors
J. R. Rygg	LLNL	Extreme Chemistry: Molecular Fluids at Mbar Pressure
V. A. Smalyuk	LLNL	Measurements of Ablative Richtmyer–Meshkov Instability in Nonlinear Regime
C. Stoeckl	LLE	Spectroscopy of Neutrons Generated Through Nuclear Reactions with Light Ions in Short-Pulse Laser Interaction Experiments
W. Theobald	LLE	Integrated Fast-Ignition Experiments

Exploring Pair Plasma and Its Applications Using OMEGA EP

Principal Investigator: H. Chen (LLNL)
 Co-investigators: L. Willingale (University of Michigan); C. Stoeckl, D. D. Meyerhofer, J. F. Myatt, and P. M. Nilson (LLE); J. Park and R. Tommasini (LLNL); W. Wilks, L. Divol, and P. Michel (LLNL); and J. Seeley (NRL)

In FY11, an LLNL/LLE/NRL team performed a Laboratory Basic Science experiment on the OMEGA EP Laser System to study positron production during high-intensity laser interactions with high-Z targets. This experiment was a follow-up to those of April 2009 and August 2010. In the previous experiments, a record number of positrons was produced using the 1-kJ, 10-ps OMEGA EP backlighter interacting with a 1-mm-thick Au target.³⁴ It was deduced that a non-neutral pair plasma was made in those shots.³⁵ In FY11, thanks to the facility improvements, the laser energy was extended to 1400 J for the backlighter beam. The FY11 experiments had two main objectives: to measure the energy scaling of the positron generation and to measure angular divergence of the electron–positron jets. The preliminary results are shown in Figs. 128.39 and 128.40

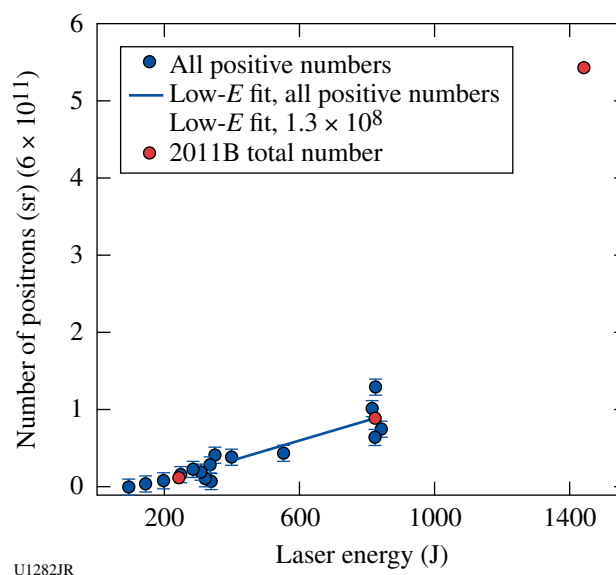
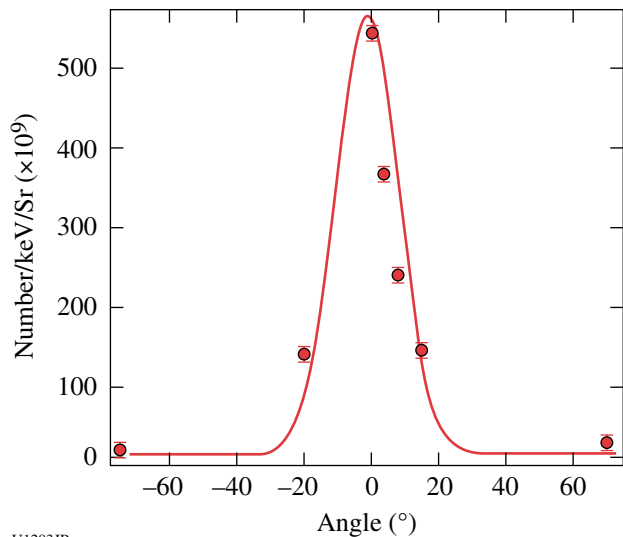


Figure 128.39
 Positron number as a function of laser energy. Red dots are from FY11 OMEGA EP experiments. Blue dots are all previous data.



U1283JR

Figure 128.40 Angular divergence of the positron jet measured from FY11 OMEGA EP experiments. (The red dots are measured points and the solid line is a fit to the data.)

for the energy scaling and angular divergence, respectively. A faster increase in positron number was observed once the laser energy exceeded 1 kJ. The electron–positron jet has a very narrow angular divergence of about 6° to 7°. On these shots, the gamma-crystal spectrometer (with an energy coverage between 40 to 700 keV) that was modified to reduce the background radiation was further tested. Annihilation of electron–positron radiation was not observed, perhaps because of low efficiency of the crystal as well as the detector.

Positron research has extended over diverse fields from particle physics and astrophysics to medical applications. This often requires the production of large numbers of positrons on a short time scale, which has been difficult to supply. The

new OMEGA EP results could alter the direction of the quest of establishing a laser-produced positron source for research in these fields.

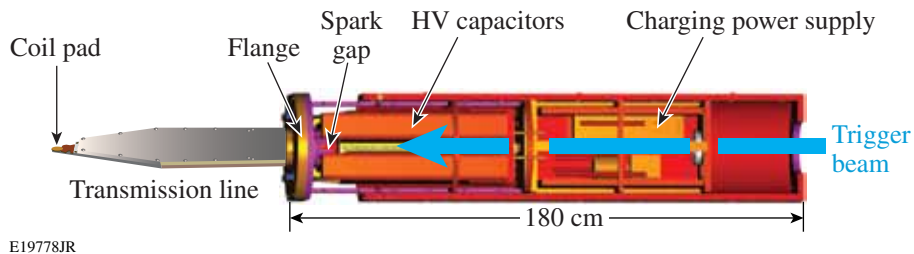
Fusion-Yield Enhancement in Magnetized Laser-Driven Implosions

Principal Investigator: G. Fiksel (LLE)

Co-investigators: M. Hohenberger, J. P. Knauer, and P.-Y. Chang (LLE); K. S. Anderson, R. Betti, and J. R. Davies (FSC/LLE); and F. H. Séguin (MIT/PSFC)

Exploring the magnetization of inertial confinement fusion (ICF) targets is beneficial for both fusion and astrophysical high-energy-density (HED) applications. Magnetization of an ICF hot spot suppresses the electron heat conduction perpendicular to the magnetic field, which increases the plasma temperature, decreases the compression velocity required for ignition, and increases the fusion gain.³⁶ Because of a high plasma density at the center of a typical ICF target, a magnetic field of the order of tens of megagauss is required to magnetize the electrons. Such large fields can be produced only by compression of an existing seed field.

LLE has been pursuing laser-driven compression as a novel method for reaching super-high magnetic field strengths. Using an LLE-built seed magnetic field generator (MIFEDS),³⁷ the generation of high magnetic fields (up to 40 MG) and subsequent fusion enhancement in magnetized spherical implosions have been demonstrated. The MIFEDS device is shown in Fig. 128.41. The device's vacuum enclosure contains a high-voltage charging power supply, capacitors, a spark-gap switch, and control circuits. The device stores up to 150 J and delivers a short high-voltage pulse of <10-ns duration to a coil via a transmission line.



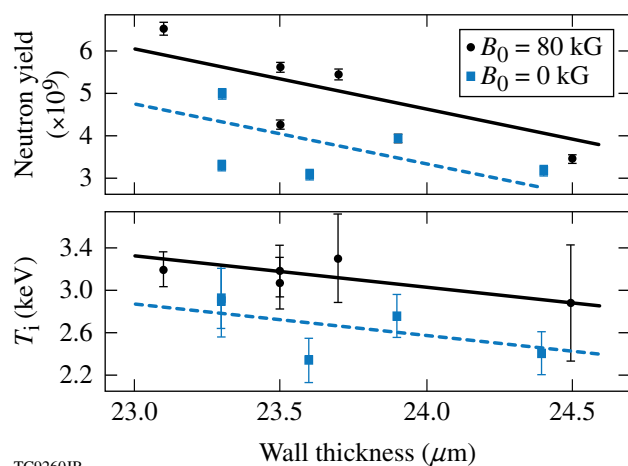
E19778JR

Figure 128.41

A schematic view of MIFEDS. The device's vacuum enclosure contains a high-voltage charging power supply, capacitors, a laser-triggered spark-gap switch, and control circuits. The transmission line is attached via a vacuum feedthrough flange. Tens-of-kilogauss magnetic fields can be generated by discharging MIFEDS through a coil attached to the coil pad at the end of the transmission line.

The applied magnetic field's effect on the fusion yield was studied for implosions in spherical geometry.³⁸ In these experiments, spherical CH targets with a 430- μm radius were imploded using 40 beams of the OMEGA laser delivering a total of 18 kJ at an average intensity of $\sim 7 \times 10^{14} \text{ W/cm}^2$. The capsules were filled with room-temperature D_2 gas at pressures from 3 to 10 atm. Figure 128.42 demonstrates the fusion enhancement in magnetized targets. For shots where the magnetic seed field was applied, the neutron yield is enhanced by $\sim 30\%$ and the ion temperature by $\sim 15\%$.

For astrophysical and HEDP applications, MIFEDS has already been used in studies of collisionless shock formation in colliding magnetized plasmas. Future plans include the use of a strong magnetic field to collimate a stream of energetic electrons in a fast-ignition experiment and to apply MIFEDS to astrophysical problems, such as magnetic reconnection in stellar media and momentum transport of incoming matter in accretion disks.



TC9260JR

Figure 128.42

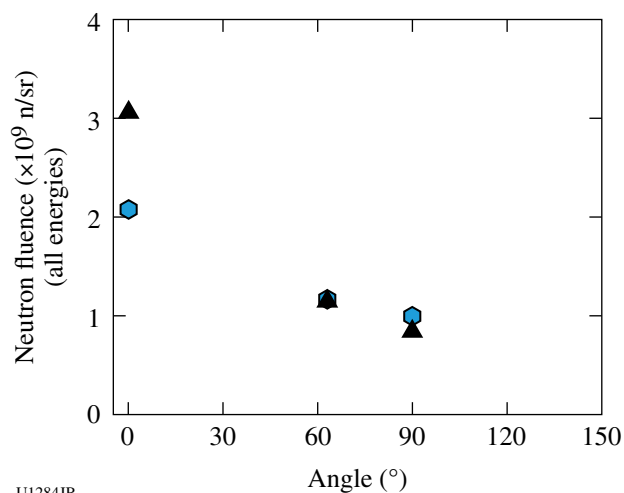
Experimental neutron yield and ion temperature plotted against target wall thickness. A clear enhancement of the magnetized implosions at $B_{\text{seed}} = 80 \text{ kG}$ (red) compared to the $B_{\text{seed}} = 0$ case (blue) is observed. The lines are fits to the data using multiple linear regression.

Short-Pulse Neutron Production on OMEGA EP

Principal Investigators: D. P. Higginson and J. M. McNaney (LLNL); J. Cobble (LANL); and J. A. Frenje (MIT/PSFC)

We have preformed the first-ever measurement of 1-kJ-class, short-pulse-laser-produced neutrons on OMEGA EP. In this experiment, protons and deuterons were accelerated into a LiF slab. These ions produced high-energy neutrons ($>10 \text{ MeV}$) through the ${}^7\text{Li}(d,xn){}^8\text{Be}$ reaction ($Q = 15 \text{ MeV}$), as well as

lower-energy neutrons ($\sim 2.5 \text{ MeV}$) through the ${}^7\text{Li}(p,n){}^7\text{Be}$ reaction ($Q = -1.6 \text{ MeV}$). Spectrally integrated yields of $3 \times 10^9 \text{ n/sr}$ were observed in the forward direction, which is a significant increase over previously observed yields of $8 \times 10^8 \text{ n/sr}$ observed on the Titan laser (Fig. 128.43). The yield of neutrons with energies above 10 MeV was $1 \times 10^8 \text{ n/sr}$, which was diagnosed using $\text{Cu}(n,2n)$ activation. This experiment also used neutron time-of-flight (nTOF) spectroscopy. The use of nTOF diagnostics is extremely challenging in the short-pulse laser-matter environment because of the high x-ray background created by the laser interaction. We were able to get a relatively clean signal, however, through a careful design of this diagnostic by LLE scientists (Fig. 128.44). In addition to the observation of spectrally and spatially resolved neutron measurements, we have also diagnosed the incident proton and deuteron beams. Knowledge of the incident ion beams means that we will be able to model the entire system in a well-constrained and consistent manner.



UI284JR

Figure 128.43

Angularly resolved neutron fluence, which is spectrally integrated, as measured with CR-39 detectors, from two different shots with the same nominal laser parameters.

Charged-Particle Stopping Power in Warm, Dense Plasmas

Principal Investigators: S. X. Hu (LLE) and C. K. Li (MIT)

Measuring the stopping power of charged particles in plasmas is of particular interests for ICF. Warm, dense plasmas (of a few-electron-volts temperature and denser than solid), which extensively exist in the universe, make up a new type of matter that can be created in laboratories, for example, by laser-driven shocks and magnetically driven flyer impacts. Such warm, dense matter can readily provide access to strongly coupled

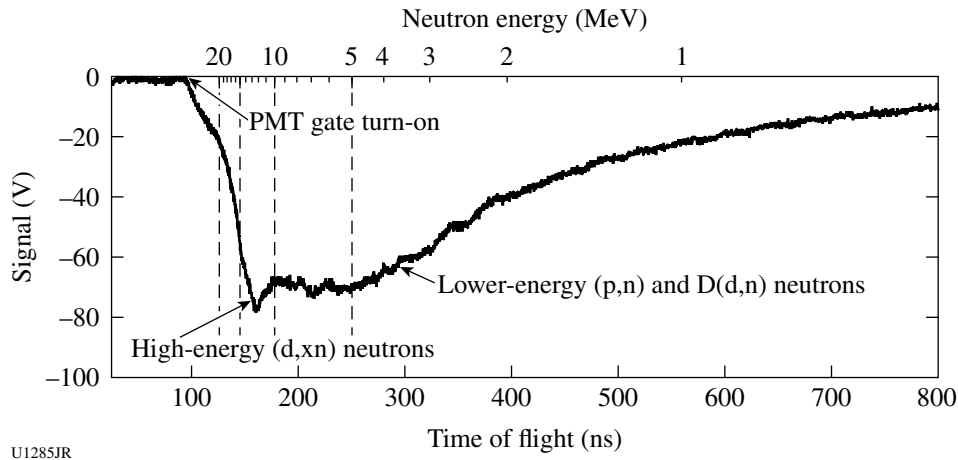
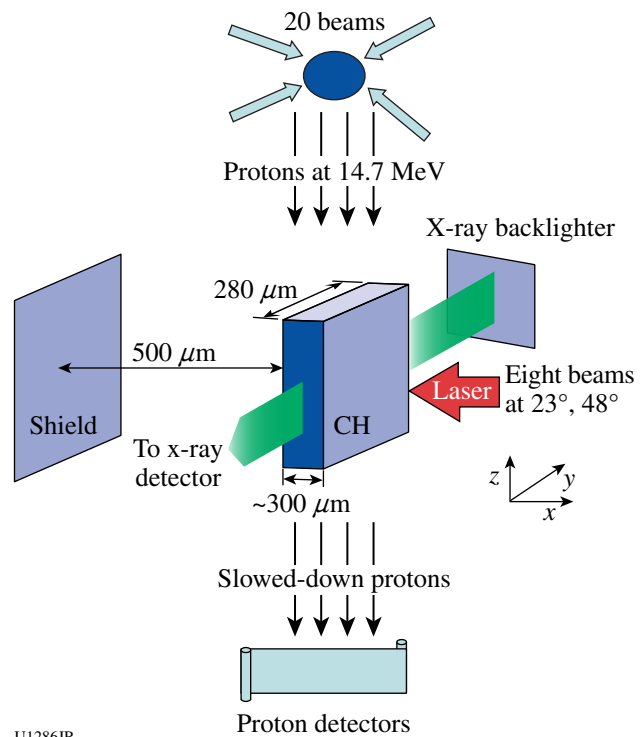


Figure 128.44

Scope traces from neutron time-of-flight spectrometers when shooting a CD₂ foil with ions incident onto a LiF slab. The signal begins with the photomultiplier tube around 100 ns. The first bump is from high-energy neutrons and the following signal is from ⁷Li(p,n) and D(d,n) neutrons.

and degenerate plasma conditions. The stopping power in such nonideal warm, dense plasmas is still unknown in contrast to the well-studied classical plasma conditions. Investigations of charged-particle stopping power in warm, dense plasmas not only advance the basic understanding of properties of such exotic matter but also find important applications in ICF, e.g., alpha particles stopping in compressed DT shells is critical to initiate the “burn-wave” propagation for ignition. There have been many theoretical predictions in the past decades that have shown an observable reduction in stopping power caused by the coupling and quantum degeneracy effects. There have been no experiments so far, however, that verify such theoretical calculations.

In the LBS experiment carried out in May 2011, we built a platform to measure charged-particle stopping power in laser-shocked plastic (CH) plasmas at the Omega Laser Facility. Using 20 OMEGA beams to drive glass-shell capsules filled with D₂ gas (6 atm) and ³He gas (12 atm), monoenergetic protons with kinetic energies of 14.7 MeV were generated. These protons slowed down passing through the laser-shocked CH plasmas, and their energy spectra were recorded using both a wedged-range-filter spectrometer and track diameter on a CR-39 imaging detector. The CH plasmas were created by eight OMEGA beams staggered in time with a total driving duration of ~4 ns. The plasma conditions were simultaneously characterized by a side-on x-ray radiograph with a V-backlighter, as shown in Fig. 128.45. The laser intensity on target varied from ~10¹⁴ W/cm² to ~5 × 10¹³ W/cm². The CH-foil targets



U1286JR

Figure 128.45

The schematic diagram of the experimental setup.

varied in size from 300 μm × 300 μm × 300 μm to 500 μm × 500 μm × 300 μm. A total of eight shots were taken during this one-day campaign.

The typical proton spectra from these experiments are shown in Fig. 128.46. The highest peak represents the initial protons without any slowdown, while the down-shifted peaks correspond to the slowdown protons. In Fig. 128.46(a), the small-sized target $[(300 \mu\text{m})^3]$ was used and the areal density (ρL) of the undriven CH target sampled by protons is estimated to be $\sim 30 \text{ mg/cm}^2$. This amount of ρL gives $\sim 1\text{-MeV}$ energy loss, which is in agreement with what is observed in Fig. 128.46(a). For the larger targets $(500 \times 500 \times 300 \mu\text{m}^3)$, Fig. 128.46(b) shows the proton spectrum in which the slowdown proton peak moves further to $\sim 13 \text{ MeV}$ as a result of the ρL increase. Although detailed analyses of experiments are under way, these primary results indicate that the platform may be useful for future studies of the charged-particle stopping power in laser-shocked warm, dense plasmas. Some improvements to enhance the proton yield and enlarge the solid angles of acceptance can be optimized for future campaigns.

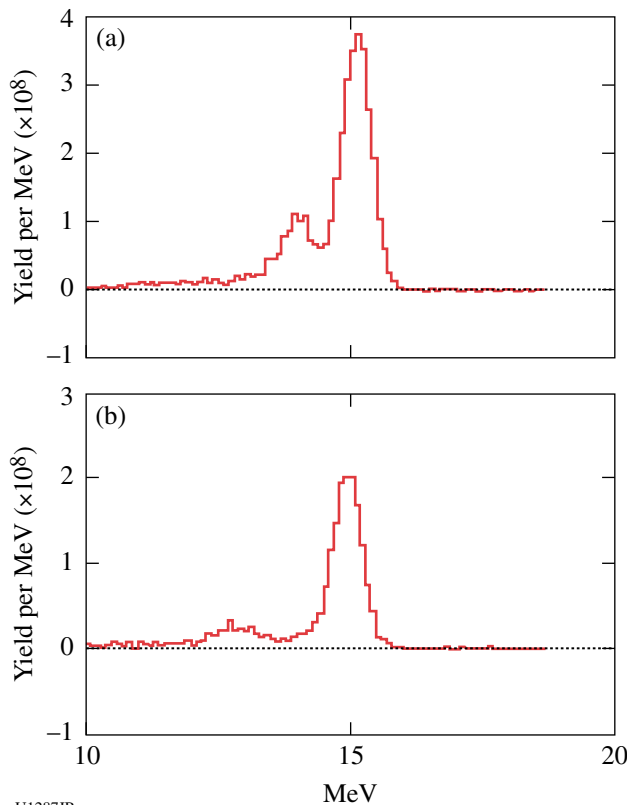


Figure 128.46
The typical proton spectra from the charged-particle stopping experiments.

Measurements of Linear, Nonlinear, and Turbulent-Mixing Regimes in Kelvin–Helmholtz Instability in the Subsonic Flow Regime

Principal Investigators: O. A. Hurricane and V. A. Smalyuk
Co-investigators: H.-S. Park and B. A. Remington (LLNL); and R. P. Drake (University of Michigan)

A Kelvin–Helmholtz (KH) growth experiment was performed on the OMEGA laser using a platform successfully developed in earlier OMEGA experiments.^{39–41} Figure 128.47 shows the target schematic, which consists of a plastic ablator and a shock tube. In the shock tube the interface between the low-density foam and the high-density plastic was either flat or had preimposed sinusoidal modulation at a wavelength of $400 \mu\text{m}$ and an amplitude of $30 \mu\text{m}$, as in previous experiments. The central part of the plastic target contained a layer of I-doped CH (CHI) to increase the contrast to 5-keV backlighter x rays. The ablator of the target was directly driven with laser light, producing a strong shock that propagated through the target. The shock produced a velocity gradient at the interface between the foam and plastic. This velocity difference

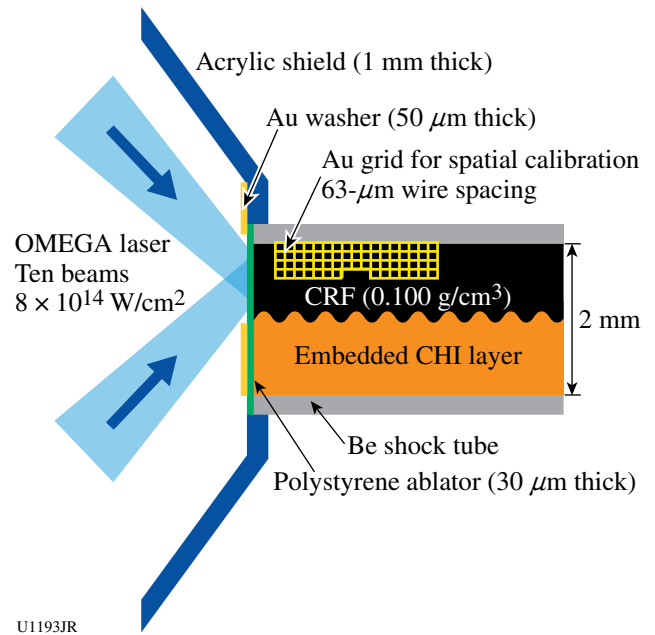


Figure 128.47
Experimental configuration. The interface between lower-density carbon-resorcinol foam (CRF) and higher-density I-doped plastic was either flat or had a preimposed 2-D modulation with wavelength of $400 \mu\text{m}$, as in previous experiments. The surface roughness at the interface had rms amplitude of 100 nm . The density of CRF foam was 100 mg/cc .

between two materials resulted in the KH growth of the surface modulations. The density of foam was 100 mg/cc. Previous experiments detected a mixing layer that developed from 3-D, short-scale modulations growing in addition to preimposed 2-D, 400- μm -wavelength modulations. New experiments were performed with flat CH-foam interfaces. These were aimed at measuring 3-D turbulent mixing since in previous experiments the growth of large 400- μm -wavelength modulations could have modified the growth of 3-D, short-scale modulations.

Figure 128.48 shows experimental data. Figures 128.48(a) and 128.48(b) present flat-interface data at 35 ns and 75 ns, respectively. Figure 128.48(c) shows data with 2-D preimposed modulation at 75 ns, taken to confirm the evolution measured in previous experiments. The shock traveled from left to right, so the modulations at the left part of the image had more time to grow than the modulations at the right part. The light color in

the image corresponded to foam material, while the dark color corresponded to plastic. A mixing layer developed behind the shock front, as expected, since the Reynolds number was high in this experiment, $Re \sim 1 \times 10^6$. The mix width was about $\sim 60 \mu\text{m}$ at $\sim 700 \mu\text{m}$ behind the shock front, inferred from the measured image at 35 ns, close to mix-model predictions. Growth of 2-D, preimposed modulations [Fig. 128.48(c)] was similar to previous experiments, confirming the repeatability of the drive. In addition, growth of 3-D modulations at the Be tube-foam interfaces was also detected, as shown in both 75-ns images. These experimental data are used to develop and validate mix models that are based on post-processing of hydrodynamic simulations currently in progress.

Self-Generated Electromagnetic Fields in Directly Driven ICF Implosions Using Proton Radiography

Principal Investigators: I. V. Igumenshev (LLE); and C. K. Li and A. Zylstra (PSFC-MIT)

Self-generated electromagnetic fields from surface perturbations and electric fields at ablation surfaces in directly driven implosion targets have been observed and quantified using proton radiography. The surface perturbations were induced by stalk mounts, 10- μm Cu wires, and glue spots. Numerical simulations show good agreement with experimental proton images and predict magnetic fields up to $\sim 5 \text{ MG}$. Proton images allow one to detect the position of the spherical ablation front during the initial stages of implosions.

The experiments were performed with backlighters in the form of foils driven by short-pulse petawatt laser beams from OMEGA EP.⁶ This type of backlighter, which has been used on other lasers,⁴² should have a smaller source size, a shorter duration, and a potentially higher proton energy than what have been achieved with imploding-pusher backlighters,⁹ but with the disadvantages of a much broader spectrum and nonisotropic (strongly forward peaked) emission in both fluence and energy. However, higher spatial resolution obtainable with a smaller source and higher proton energy are useful as well for imaging ICF implosions with higher areal densities than can be studied with 15-MeV protons from exploding pushers and with less proton scattering. The higher proton fluences' broad spectra of these foil backlighters necessitate the use of a different imaging detector; a combination of radiochromic films is used.⁴²

The proton source is used to obtain information about imploding ICF capsules that is complementary to the information we are obtaining using exploding-pusher backlighters (see Fig. 128.49). The advantage of this approach over the

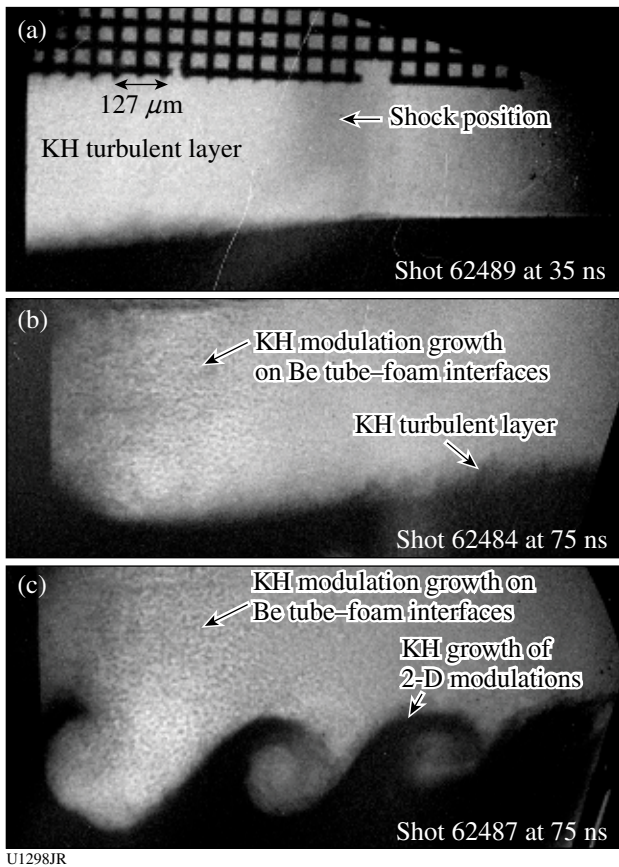


Figure 128.48 X-ray radiographs of KH growth with flat CHI-foam interface were taken at (a) 35 ns, at (b) 75 ns, and with interface having a 2-D modulation at (c) at 75 ns. The areas on the right-hand side of the images experienced less KH growth than those on the left-hand side.

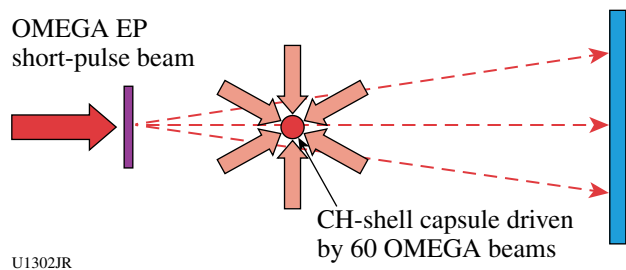


Figure 128.49
Schematic illustration of the experimental setup for imaging an imploding, CH-shell capsule in the OMEGA chamber with protons from a foil backlighter driven by a short-pulse OMEGA EP beam.

exploding-pusher-backlighter approach is that it does not use any beams from OMEGA, meaning that it would be possible to image implosions driven by all 60 OMEGA beams. The experiment employs 860- μm -diam plastic capsules with 20- μm wall thickness. The capsule filling does not play a role in this experiment because the proton radiographs were always taken during the laser pulse, when the compression of the capsule is not significant. The implosions were driven by a 1-ns square pulse with a total laser energy ~ 30 kJ.

Self-generated electromagnetic fields have been developed from perturbations induced by a stalk-mounted, on-surface, 10- μm -diam Cu wire going around half an implosion capsule and a 50- μm -diam glue spot. Figures 128.50(a)–128.50(d) show proton images taken at ~ 200 , 600, 600, and 300 ps, respectively. The capsule center is projected in the center of each image. The ablation front at the capsule's outer surface is clearly distinguished in Figs. 128.50(a) and 128.50(d) as light circles in proton fluence. These fronts that appear on the images are caused by deflection of the protons by electric fields developed at the ablation and critical surfaces. All figures show features at the bottom that correspond to the stalk mount. One can follow the evolution of electromagnetic fields around the stalk in Figs. 128.50(a), 128.50(d), and 128.50(b) [or Fig. 128.50(c), which shows features very similar to those from the stalk in Fig. 128.50(b)].

Figures 128.50(a)–128.50(c) show targets with the Cu wire. The two images in Figs. 128.50(a) and 128.50(b) show the cases where the wire is located on the side of the target toward the proton source. It is clear that developed magnetic fields deflect protons in such a way that proton trajectories going on both sides of the wire are mostly diverged, forming light strips in the proton fluence. Figure 128.50(c) shows the case where the wire is located on the opposite side of the target with respect to

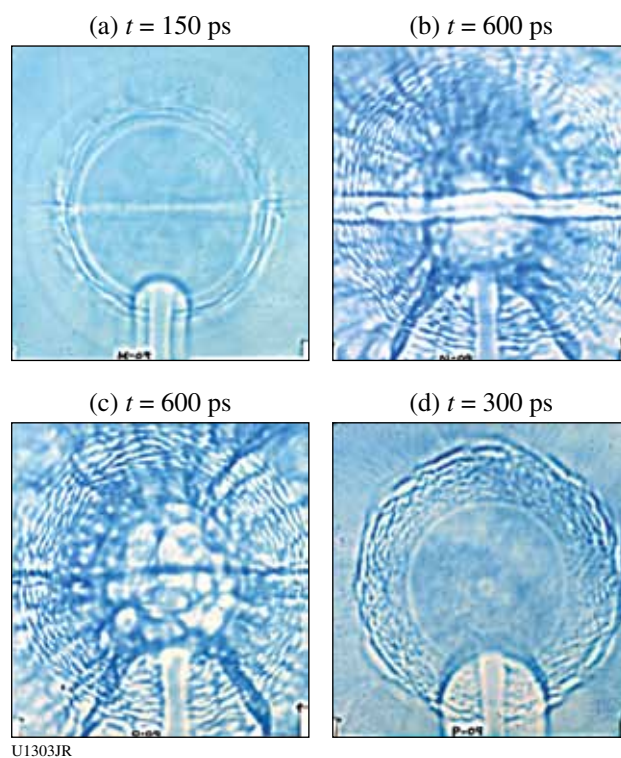


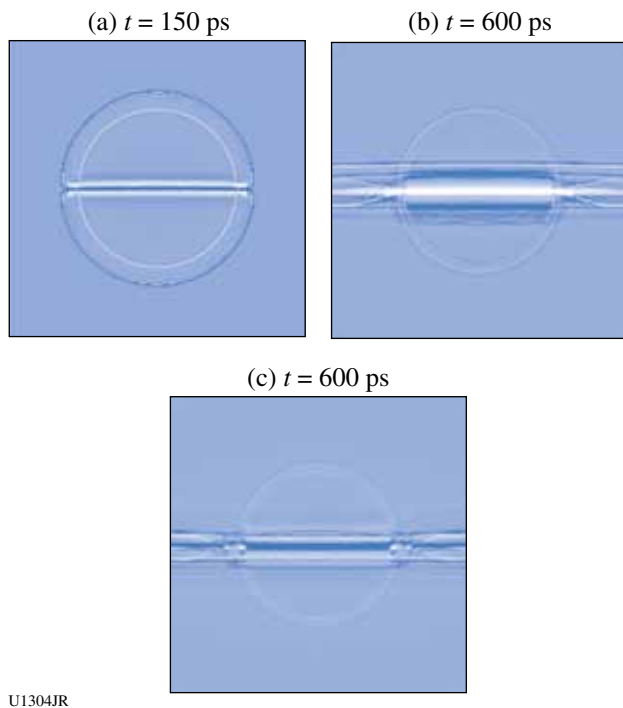
Figure 128.50
Proton images of implosion plastic-shell targets with different surface perturbations. The images show variations of proton fluence that result from the deflection of proton trajectories caused by the interaction with electromagnetic fields. Implosions in (a)–(c) show targets with Cu wire; (a) and (b) correspond to the case where the wire is located on the side of the target toward the proton source and (c), where the wire is on the opposite side of the target. (d) shows the target with a glue spot, which is located on the side of the target toward the proton source.

the proton source. In the latter case the proton rays are mostly converged toward the wire, forming a dark strip in the proton fluence. This is because the protons interact with magnetic fields of similar structure as in the case of Fig. 128.50(b), but the fields here have opposing polarity and opposing signs of the proton deflection angles.

Figure 128.50(d) shows a target at the glue spot, which is located on the target surface toward the proton source. There is a small light circle in the proton fluence located in the center of the image that is clearly associated with the glue spot. Magnetic fields that develop around the glue spot affect proton trajectories in a way that is similar to the fields in the case of the Cu wire in Figs. 128.50(a) and 128.50(b): the trajectories are deflected outward from the glue spot, forming a small light area at the projected location of the glue spot.

Figures 128.51(a)–128.51(c) show preliminary simulation results for the experimental conditions corresponding to Figs. 128.50(a)–128.50(c), respectively, but without modeling the effects of stalk mounts. The horizontal line features are produced by the Cu wires. The simulations show horizontal light strips in the proton fluence in Figs. 128.51(a) and 128.51(b), similar to the experimental results in Figs. 128.50(a) and 128.50(b) where the wire is located on the side of the target facing the proton source. The simulations shown in Fig. 128.51(c) correspond to the case where the wire is located on the opposing side of the target with respect to the proton source. Magnetic fields around the wire cause the proton trajectories to converge toward the wire, resulting in the horizontal dark strip in the proton fluence, which is similar to the dark strip seen in Fig. 128.50(c).

The circular features in Figs. 128.51(a)–128.51(c) are caused by electric fields developed at the ablation and critical surfaces (the light circles in all three images) and at the outer plasma front [the dark outer circle in Fig. 128.51(a)]. All these features can be associated with the corresponding circular features in



U1304JR

Figure 128.51

Simulated proton fluence for the experimental conditions of implosion targets with a Cu wire shown in Figs. 128.50(a)–128.50(c). The images were simulated employing a proton ray-trace code that initiates proton trajectories from a point source. This code uses distributions of electromagnetic fields obtained using 2-D DRACO simulations.⁴³

experimental images [Figs. 128.50(a)–128.50(c)]. Simulations of the magnetohydrodynamic effects and proton images of the stalk mount and glue spot are in progress.

Capsule Adiabats Measurement with X-Ray Thomson Scattering

Principal Investigator: A. Kritcher (LLNL)

Co-investigators: T. Doeppner, O. L. Landen, and S. H. Glenzer (LLNL)

The first simultaneous measurements of electron densities and temperatures of spherically convergent matter via spectrally resolved x-ray Thomson scattering have been performed at the Omega Laser Facility. In these experiments, we infer in-flight adiabats of 1.6 to 2, approaching the desired adiabat of 1.5 for implosions driven by shaped laser pulses (see Fig. 128.52). While Thomson scattering has previously been applied to planar shock systems, here we employed high-energy x rays at ~ 9 keV to characterize matter densities of $n_e > 10^{24}$ cm⁻³ obtained in spherically convergent geometries. Our signal-to-noise ratios (SNR's) of ~ 200 obtained at these densities indicate the ability for single-shot characterization of imploding targets to result in a 20% error bar on electron density and temperature if both parameters are simultaneously determined. Measurement of the temperature and density enables us to infer the time-resolved CH and Be capsule adiabats, which can be used to test low-adiabat laser pulse shaping and models that predict shock timing for spherically convergent targets.

Probing microscopic plasma properties results in both elastic and inelastic scattering features. The intensity of the elastic scattering is sensitive to the static structure factor of the material. The Compton feature provides a direct measure of the electron-velocity distribution. For these weakly degenerate plasmas, the velocity distribution is a hybrid of a Thomas–Fermi ($T_e = 0$) and a Boltzmann distribution ($T_e \gg T_F$). The width of the inelastic Compton feature is sensitive to the Fermi temperature T_F , which is only dependent on electron density, and the shape of the red wing is sensitive to electron temperature T_e (Ref. 44). Therefore, the temperature and density are simultaneously determined from first principles by accurately measuring the Compton feature width and shape (see Fig. 128.52).

These experiments complete a series of campaigns to develop a platform that enables us to measure electron temperature and density from imploding Be and CH capsules. These results have been summarized and published in peer-reviewed journals.^{44,45}

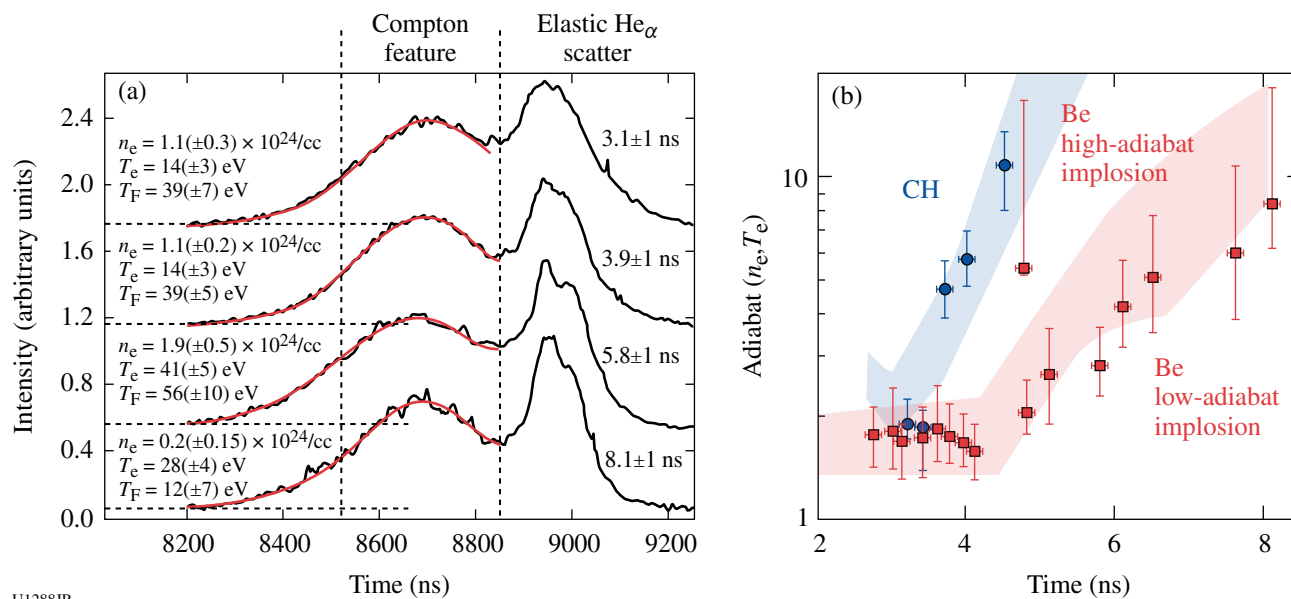


Figure 128.52

(a) Measured (black) and best fits (red) to the Compton feature of the scattered x-ray spectra from Be implosions at various times, yielding n_e and T_e . (b) Adibat plotted as function of time for compressed Be and CH ablaters. Also plotted are 1-D radiation–hydrodynamic calculations.

Astrophysical Collisionless Shock Generation in Laser-Driven Experiments

Principal Investigator: H.-S. Park, S. Ross, and N. Kugland (LLNL)

Co-investigators: A. Spitkovsky (Princeton); Y. Sakawa (Osaka University); G. Gregori (Oxford University); M. Koenig (LULI); D. H. Froula (LLE); R. P. Drake (University of Michigan); and R. Presura (University of Nevada, Reno)

This LBS program studies astrophysical collisionless shocks with counter-streaming plasmas from high-power lasers. Collisions of high-Mach-number flows occur frequently in astrophysics, and the resulting shock waves are responsible for the properties of many astrophysical phenomena, such as supernova remnants, gamma-ray bursts, and jets from active galactic nuclei. Because of the low density of astrophysical plasmas, the mean free path of Coulomb collisions is typically very large. Therefore, most shock waves in astrophysics are “collisionless” since they form as a result of plasma instabilities and self-generated magnetic fields. Laboratory experiments at the laser facilities can achieve the conditions necessary for the formation of collisionless shocks and will provide a unique avenue for studying the nonlinear physics of collisionless shock waves. We are performing a series of experiments on the OMEGA and OMEGA EP lasers, with the goal of generating collisionless shock conditions by the collision of two high-

speed plasma flows resulting from laser ablation of solid targets using $\sim 10^{16}$ W/cm² laser irradiation. The experiments will aim to answer several questions of relevance to collisionless shock physics: the importance of the electromagnetic-filamentation (Weibel) instabilities in shock formation, the self-generation of magnetic fields in shocks, the influence of external magnetic fields on shock formation, and the signatures of particle acceleration in shocks. Our first experiments studied the plasma state from a single foil and from double foils whose flows collide “head on,” using Thomson-scattering (TS) diagnostics. Our data showed a flow velocity at 10^8 cm/s and an electron density of 10^{19} cm⁻³, where the Coulomb mean free path was much larger than the interaction system size. Simulations of our experimental conditions show that weak Weibel-mediated current filamentation and magnetic-field generation were likely starting to occur. This report presents the results from these first OMEGA experiments.

Our first OMEGA experiments [AstroPlasmas-11A (10 December 2010) and ColPlasmas-11C (1 June 2011)] concentrated on measuring and understanding the plasma conditions created by the OMEGA lasers on single- and double-foil configurations. Thomson scattering was used to characterize the plasma created by ten heater-drive beams incident on a CH foil. Our two shot days produced high-quality data spanning two different laser intensities, three different probe times, single-versus double-foil geometry, and different flow directions.

The heater-drive beams deliver 5 kJ of energy in a 1-ns square pulse shape. The target geometry is shown in Fig. 128.53. A probe beam of 0.53- μm wavelength (labeled “ 2ω probe” in the figures) is pointed 4 mm from the foil surface. The TS probe

volume was $100\ \mu\text{m} \times 100\ \mu\text{m} \times 60\ \mu\text{m}$. We measured the flow plasma conditions along both the flow direction and the transverse directions. Both shot days produced excellent-quality TS data; an example is shown in Fig. 128.54 for a single foil.

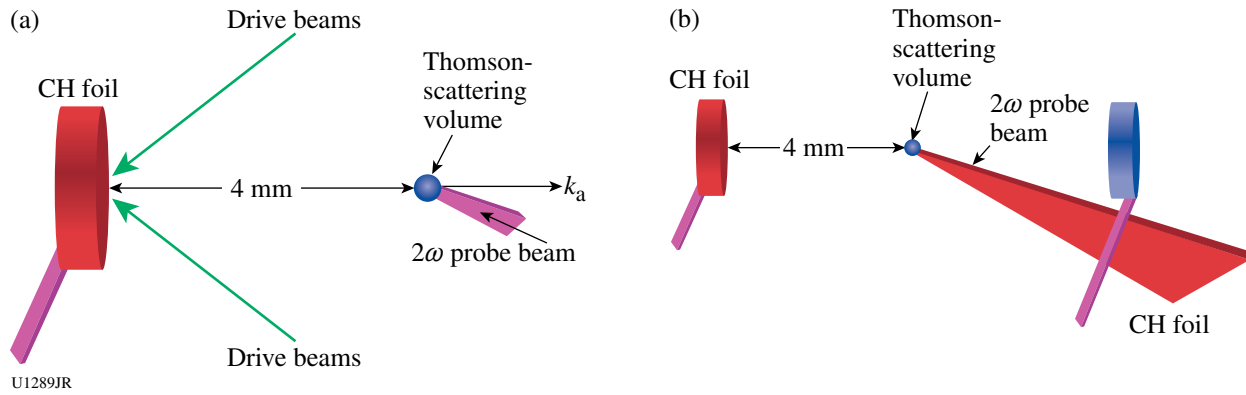
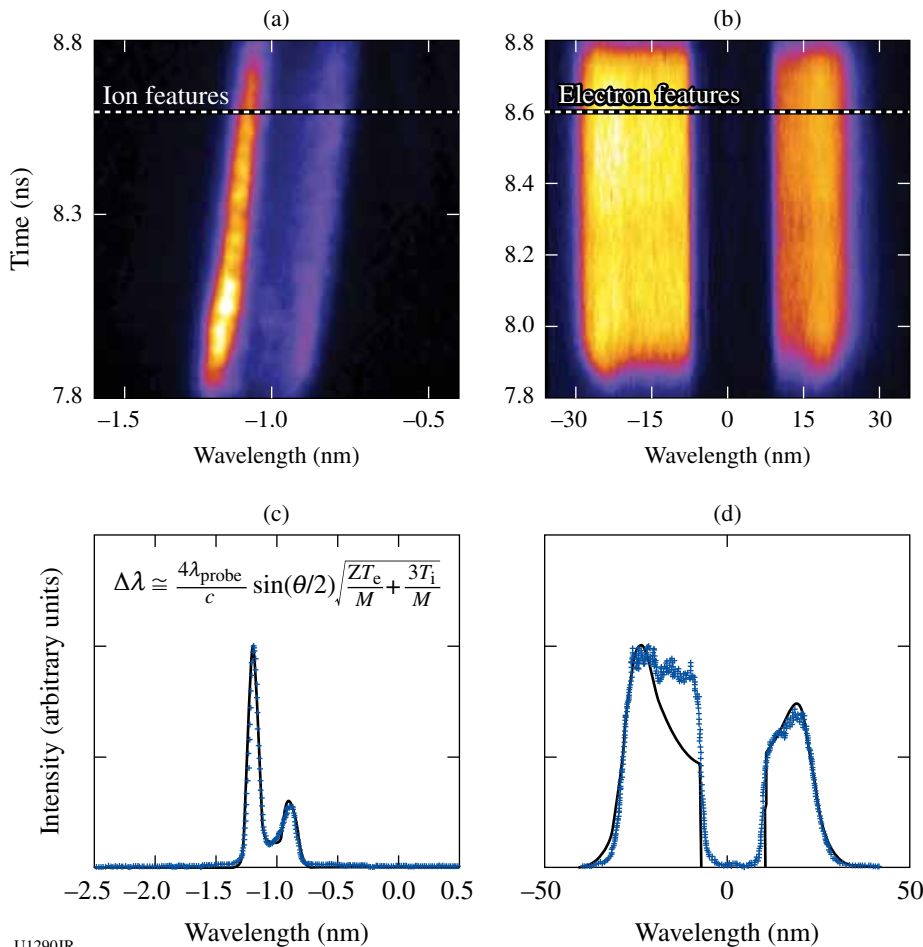


Figure 128.53
 Geometry used for astrophysical collisionless shock experiment of June 2011 for the (a) single- and (b) double-foil cases. The laser intensity on the target was $8 \times 10^{15}\ \text{W/cm}^2$.



$T_e = 170\ \text{eV}$
 $T_i = 26\ \text{eV}$
 $n_e = 3.1 \times 10^{18}\ \text{cm}^{-3}$
 $v_{\text{flow}} = 5.7 \times 10^7\ \text{cm/s}$
 $u_{\text{drift}} = 1.2 \times 10^8\ \text{cm/s}$

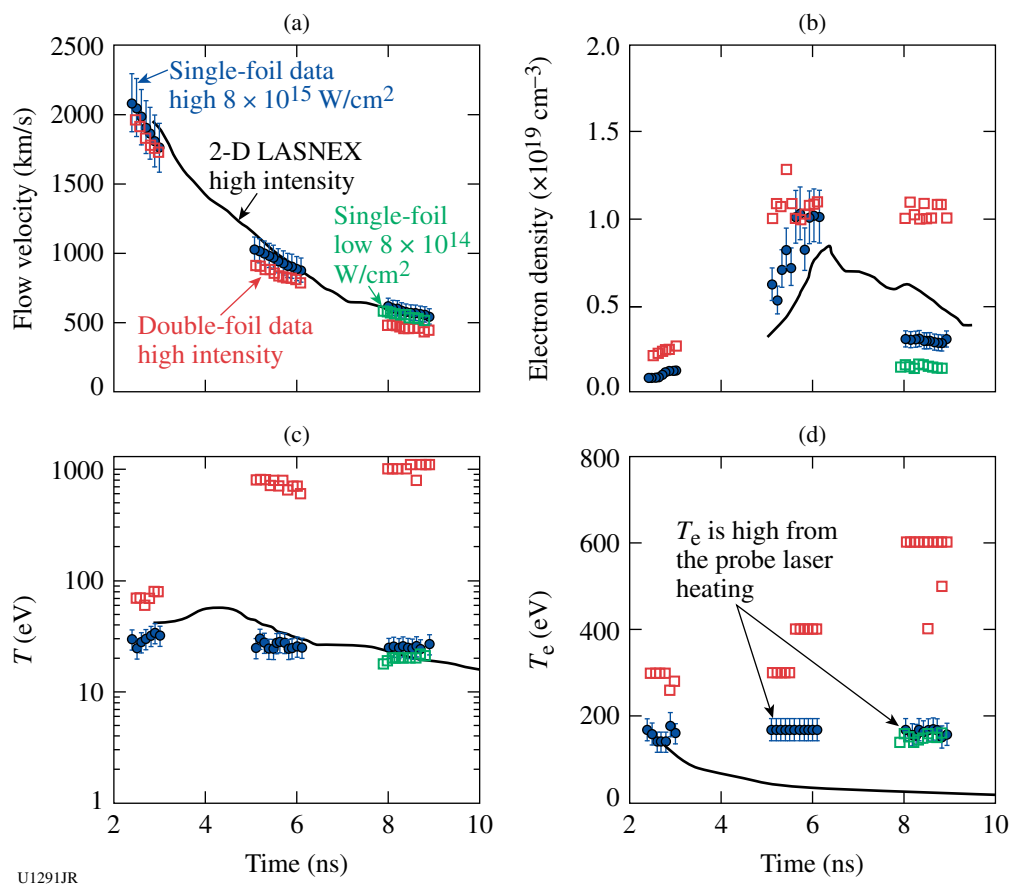
Figure 128.54
 An example of Thomson-scattering data and fitting for a single-foil shot. (a) Ion features; (b) electron features; (c) ion features' data and fitting; and (d) electron features' data and fitting. A time slice of the ion and electron features is simultaneously fitted to produce T_e , T_i , n_e , v_{flow} , and u_{drift} parameters.

The measured plasma characteristics from different shots covering a 2- to 9-ns time interval and single and double foils are compiled in Fig. 128.55. The flow velocity, electron density, ion temperature, and electron temperature are shown. Different-color data points represent different experimental conditions of single-foil shots (blue), double-foil shots (red), and single foil with 10 \times -lower drive laser intensity (green). The data are compared to 2-D LASNEX hydrodynamic simulations (for the single-foil case) in solid black curves. There is good agreement between the measured and simulated bulk plasma flow velocity over all three time intervals. The measured electron density shows a sharp increase between 5.0 and 6.0 ns, which is also present in the simulations, indicating that the bulk of plasma arrives at this time. This is consistent with flow arrival at the 4-mm location of the plasma flow with a velocity of $\sim 10^3$ km/s. The measured electron temperature is significantly higher than the simulations. We attribute this to reheating the

plasma by the TS probe beam. The measured ion temperature is consistent with 2-D simulations. An electron temperature of 170 eV is assumed in this time interval because of a lack of electron feature data.

The double-foil data also showed very interesting results. The difference between the single-foil versus the double-foil data for the ion feature is very striking. Compared to the single-foil flow, the ion temperature and electron density are considerably higher. Another interesting observation is that the flow velocity is reduced systematically for the double-foil flows, indicating interaction between the two flows late in time.

Our first OMEGA EP experiments [EPCoIPlasmas-11B (26 April 2011) and EPCoIPlasmas-11D (30 August 2011)] concentrated on developing proton deflectometry and proton radiography diagnostics to understand electric and magnetic fields

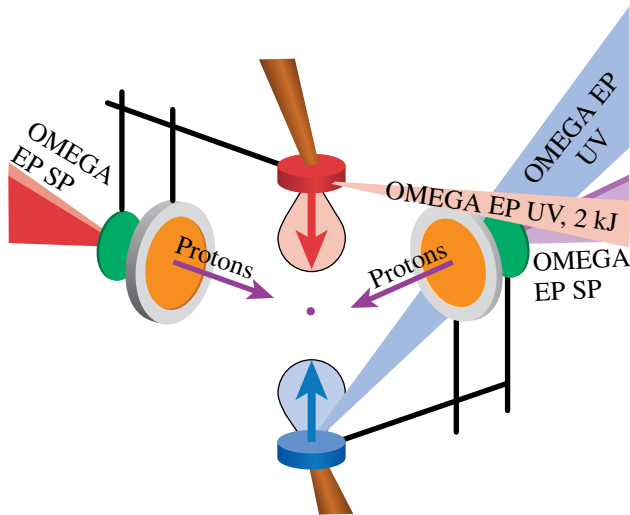


U1291JR

Figure 128.55

Measured plasma parameters from a single-foil flow versus a 2-D hydrodynamics simulation. The high measured electron temperature, compared to that simulated, is likely caused by the probe beam heating. Blue points are single-foil data with laser intensities of 8×10^{15} W/cm²; green are single-foil data with laser intensities of 8×10^{14} W/cm²; red are double-foil data with 8×10^{15} W/cm² on each foil; the black line is the 2-D LASNEX simulation for the single foil with 8×10^{15} W/cm².

generated by the interpenetrating plasmas. The experimental setup is shown in Fig. 128.56. Two long-pulse UV beams drive the CH₂ targets with 2200 J in a 3-ns square pulse. The laser-generated high-velocity plasma flow moves upward and downward, and the entire region between the two targets was probed by two short-pulse-laser-generated proton beams. Since it is known that the long-pulse-driven plasmas can interrupt proton generation, a careful shield design was necessary. Our experiment on 30 August 2011 was successful in generating an interesting time sequence of proton radiography images as shown in Fig. 128.57. There are three different features in these radiographs: (1) large bubble-like features; (2) very fine striation features only at 2 to 5 ns; and (3) two planar disk-like features. We postulate that they may result from laser-ablative Rayleigh–Taylor instabilities, magnetohydrodynamic instabilities, and electrostatic field generation from the hot-plasma expansion and temperature gradient, respectively. We are currently working on the data interpretation and analysis using analytic models, radiation–hydrodynamics simulations, and particle-in-cell simulations.

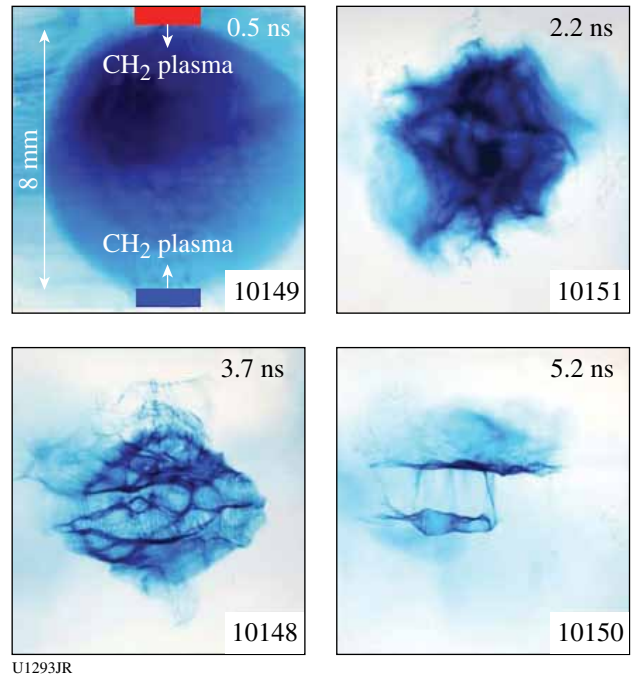


U1292JR

Figure 128.56

OMEGA EP experimental setup. Two UV long-pulse beams illuminate the CH₂ targets creating high-velocity plasma flows. The short-pulse-generated protons are used to radiograph the flowing plasmas.

This LBS project has resulted in the formation of a large international team called the ACSEL (Astrophysical Collisionless Shock Experiments with Lasers) collaboration. ACSEL has key members from LLNL (H.-S. Park); Princeton (A. Spitkovsky); Osaka University (Y. Sakawa); Oxford University (G. Gregori); LULI (M. Koenig); LLE (D. H. Froula); University of Michigan (R. P. Drake); University of Nevada, Reno (R. Presura); and their team members. The results have



U1293JR

Figure 128.57

Proton-radiography images of the interpenetrating plasmas from the astrophysical collisionless shock experiments of August 2011. The analyses of interpretation of different features using both plasma theories and PIC simulations are in progress.

been presented at many conferences, one paper has been submitted, and many papers are in preparation.^{21,25–30,46}

Electron-Source Characterization for Cone-Guided Fast Ignition

Principal Investigators: P. K. Patel (LLNL) and H. Sawada (University of California, San Diego)

Co-investigators: C. D. Chen, H. S. McLean, and M. H. Key (LLNL); F. N. Beg (University of California, San Diego); R. B. Stephens (General Atomics); and W. Theobald and C. Stoeckl (LLE)

In cone-guided fast ignition (FI), the directionality of laser-generated relativistic electrons escaping from a cone is one of the critical parameters that determine the required ignition laser energy of a FI point design. We have used cone-foil targets to investigate the angular spread of the forward-going electrons by measuring the 2-D profile of Cu K_α x-ray emission with an OMEGA EP spherical crystal imager (SCI). Figure 128.58(a) shows an overview of the experiment. The fast electrons were generated at a cone tip with the OMEGA EP backlighter beam at 300 J in a 1-ps or at 1500 J in a 10-ps pulse duration and transported through a 10-μm-thick Al or Au cone tip. A frac-

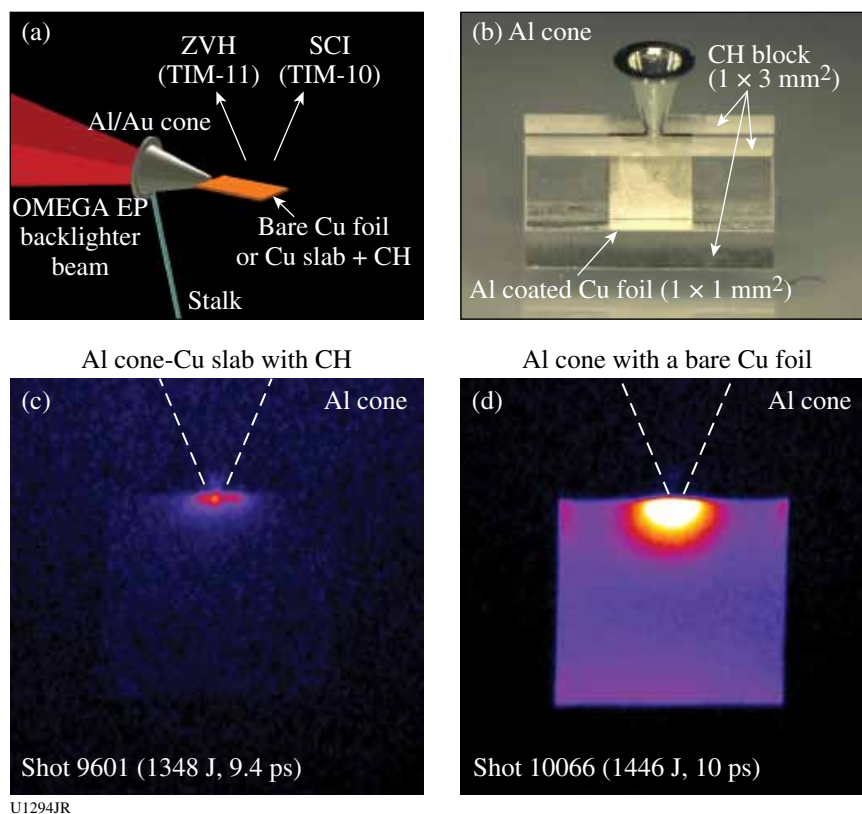


Figure 128.58

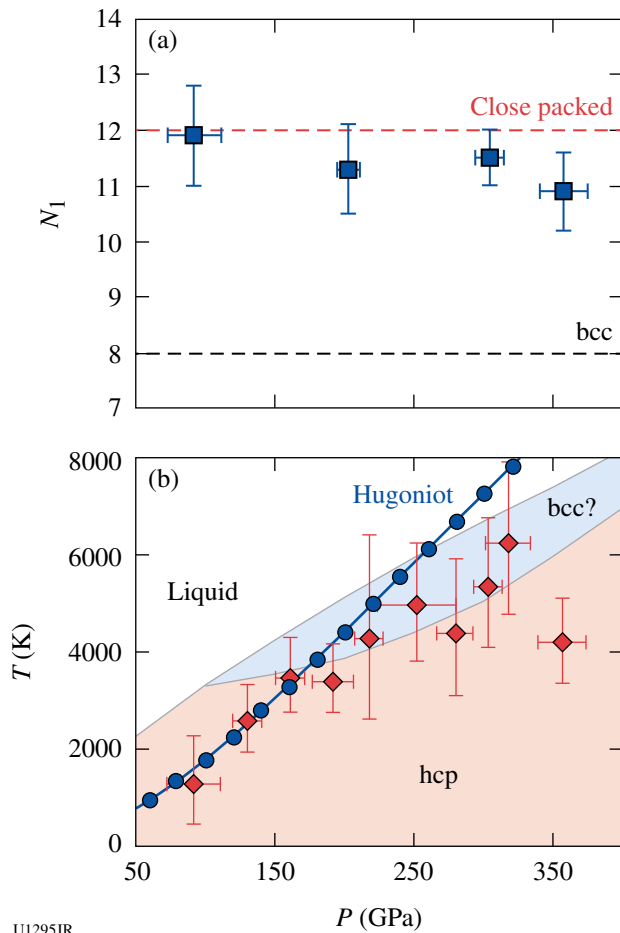
(a) Experimental overview and (b) a photograph of an Al cone–Cu slab target. In the bottom row, measured K_{α} images of (c) Al cone–Cu slab with CH target (shot 9601) and (d) Al cone–bare Cu foil target (shot 10066) at 1500 J in the 10-ps pulse in the same color scale.

tion of the electrons that escaped from the cone were measured in either (1) an aluminum-coated Cu foil surrounded by CH blocks or (2) a bare Cu foil. For both cases, the Cu foil was $1 \times 1 \text{ mm}^2$ and $40 \text{ }\mu\text{m}$ thick. As shown in Fig. 128.58(b), the Cu slab consisted of the Cu foil coated with $20\text{-}\mu\text{m}$ -thick aluminum on both sides and $500\text{-}\mu\text{m}$ -thick CH blocks ($1 \times 3 \text{ mm}^2$) surrounding it to prevent electron refluxing. The dimensions of the Al and Au cones were identical with a $65\text{-}\mu\text{m}$ wall thickness and $30\text{-}\mu\text{m}$ inner tip diameter. The Cu K_{α} emission was recorded with the OMEGA EP SCI at 27° and an absolutely calibrated ZVH crystal spectrometer at 41° from the foil normal. Figures 128.58(c) and 128.58(d) show the 2-D monochromatic images of a Cu slab with CH blocks (shot 9601) and a bare Cu foil (shot 10066) attached to the Al cones for 10-ps shots. In the nonrefluxing Cu slab target, the total K_{α} yield was reduced by a factor of ~ 7 , and the sharper falloff of the emission profile along the laser axis was observed compared to the bare Cu foil. The absolute K_{α} yield and 2-D K_{α} emission profile will be modeled with a hybrid PIC code, *LSP*, to infer the electron divergence, electron energy distribution, and laser-to-electron conversion efficiency.

EXAFS Measurements of Iron at Earth's Inner Core Conditions

Principal Investigators: Y. Ping, D. G. Hicks, D. E. Fratanduono, F. Coppari, S. Hammel, J. H. Eggert, J. R. Rygg, R. F. Smith, and G. W. Collins (LLNL); and B. Yaakobi and T. R. Boehly (LLE)

Iron is the most-abundant element at Earth's core. Its properties under extreme conditions are critical for understanding phenomena in geophysics, geochemistry, and seismology. By means of dynamically compressing a thin iron sample sandwiched between diamond anvils with multiple shocks, we achieved off-Hugoniot states of iron at pressures up to 3.5 Mbar and temperatures of $\sim 5000 \text{ K}$, which is the expected condition at Earth's inner solid core. Measurements of extended x-ray absorption fine structure (EXAFS) have been performed with a broadband x-ray backlighter created by a spherical implosion. The results indicate that iron is not at bcc phase under these conditions, which is contradictory to recent simulation results (Fig. 128.59).



U1295JR

Figure 128.59

(a) The coordination number of the first shell obtained from EXAFS data as a function of pressure, showing that our data are consistent with the close-packed structure but inconsistent with the bcc lattice. (b) The temperature obtained from the Debye–Waller factor in EXAFS data versus pressure. The data are all consistent with the hcp phase, even inside the proposed bcc regime (Ref. 47).

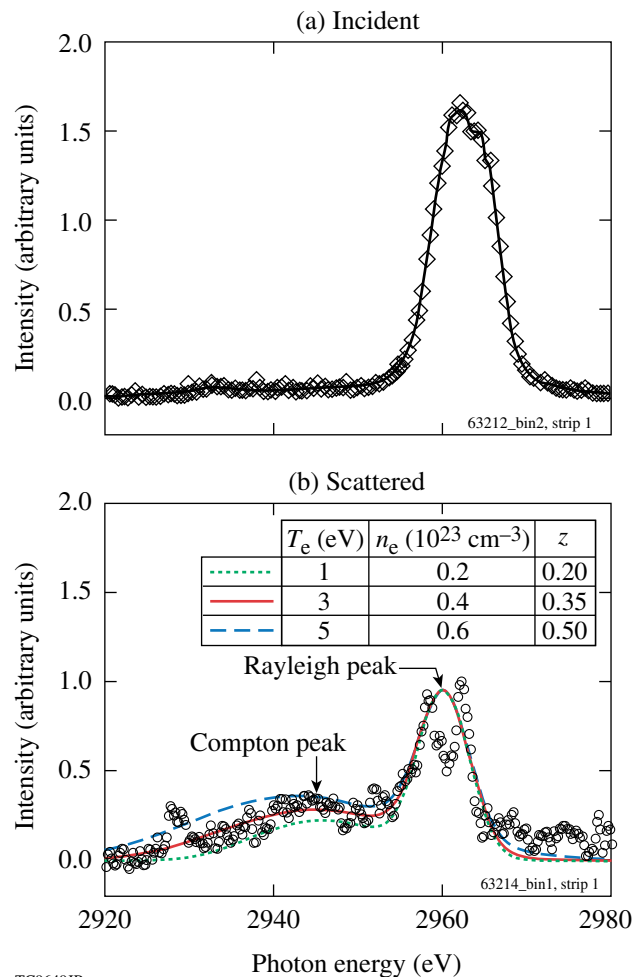
Diagnosing P , ρ , n_e , T_e , and Z of H , H/He , CH_4 , and NH_3 Warm, Dense Matter Using Inelastic X-Ray Scattering and Shock-Velocity Measurements: Toward the Equation of State of Planetary Interiors

Principal Investigator: S. P. Regan (LLE)

Co-investigators: T. R. Boehly, S. X. Hu, D. D. Meyerhofer, P. B. Radha, and T. C. Sangster (LLE); K. Falk, G. Gregori, and C. D. Murphy (University of Oxford); B. Crowley (AWE); T. Doeppner, S. H. Glenzer, and O. L. Landen (LLNL); and D. O. Gericke and J. Vorberger (Warwick University)

An experimental platform has been developed on OMEGA to study inelastic x-ray scattering from shocked deuterium and nitrogen. This work was performed in collaboration with Oxford University, Warwick University, and Lawrence Liver-

more National Laboratory. In the past decade, developments in laser-produced plasma sources and detector efficiencies have resulted in inelastic x-ray scattering becoming a powerful diagnostic providing electron temperature (T_e), electron density (n_e), and ionization (Z) for critical equation-of-state measurements in ICF and planetary science research.^{48–52} Laser-ablation-driven shock waves are launched into planar liquid-deuterium targets, creating warm, dense matter with conditions similar to those of an imploding ICF shell during the shock-propagation and acceleration phases. X rays from a backlighter target are scattered off the shocked deuterium. The incident spectrum of the Cl Ly_α emission is shown in Fig. 128.60(a) and the scattered spectrum is shown in Fig. 128.60(b). The incident spectrum is measured by irradiating a parylene D foil target on a separate



TC9649JR

Figure 128.60

Spectra of (a) Cl Ly_α emission incident on shocked liquid deuterium and (b) Cl Ly_α emission scattered from shocked liquid deuterium on a different scale. The colored curves in (b) are predictions of the x-ray scattering (XRS) code, indicating that $T_e = 3 \pm 2$ eV, $Z \sim 0.35 \pm 0.15$, and $n_e = 0.4 \pm 0.2 \times 10^{23} \text{ cm}^{-3}$.

laser shot. The scattered spectrum has a strong Rayleigh peak around 2960 eV and a Compton-downshifted feature. Splitting of the Cl Ly_α emission is observed in the scattered spectrum, but not in the incident spectrum, because of differences in the amount of source broadening in each measurement (i.e., the backlighter plasma is bigger than the scattering volume).

Scattered x-ray spectra were calculated using the x-ray scattering *XRS*⁵³ code for various values of the plasma conditions. Three examples that bracket the experimental data are shown in Fig. 128.60(b). The fit allows one to estimate mean values in the D_2 plasma of $\bar{T}_e = 3 \pm 2$ eV, $\bar{n}_e = 0.4 \pm 0.2 \times 10^{23} \text{ cm}^{-3}$, and $\bar{Z} = 0.35 \pm 0.15$. These values are consistent with the 2-D *DRACO*⁵⁴ simulations, recognizing that a large part of the Thomson-scattering signal comes from unshocked deuterium. Improvements to the experimental design are planned to provide a smaller, more-homogeneous scattering region with less unshocked deuterium. The elastic (Rayleigh) feature is well fitted by assuming a ion-ion structure factor S_{ii} of unity, indicating weak correlations in the deuterium plasma, which is consistent with predictions from density-functional-theory molecular-dynamics simulations using the VASP package.^{55,56} The *XRS* prediction does not include the fine-structure splitting observed in the measured spectrum. These are the first experimental observations of noncollective, inelastic x-ray scattering from shocked liquid deuterium. This work represents an important step toward measuring all the thermodynamic variables needed for equation-of-state research [pressure (P), mass density (ρ), electron density (n_e), electron temperature (T_e), and ionization (Z)]. Future work will combine inelastic x-ray scattering observations with shock-velocity measurements and extend to other materials like nitrogen.

Measurements of Ablative Richtmyer–Meshkov Instability in the Nonlinear Regime

Principal Investigator: V. A. Smalyuk (LLNL)
 Co-investigators: B. A. Remington, H.-S. Park,
 and K. Raman (LLNL); A. Casner and L. Masse (CEA);
 I. V. Igumenshchev (LLE); and D. Shvarts and Y. Elbaz
 (NRCN, Beer Sheva, Israel)

Figure 128.61 shows a schematic of an experimental setup for nonlinear Richtmyer–Meshkov (RM) and Rayleigh–Taylor (RT) instability experiments on OMEGA EP. Planar 15-, 30-, and 50- μm -thick CH targets were driven with one UV beam using a 6-ns square pulse shape, a total energy of ~ 4 kJ, and a laser intensity of $\sim 8 \times 10^{13} \text{ W/cm}^2$. Initial target modulations were imposed by laser imprinting of the perturbations in the drive beam during the first ~ 100 ps of the drive. The growth of

the target modulations was measured with x-ray radiography using uranium (~ 1.3 -keV), samarium (~ 1.8 -keV), and tantalum (~ 2.2 -keV) backlighters and a framing camera with 10- μm spatial resolution and 80-ps temporal resolution. The backlighter targets were driven with a 2-ns square pulse shape at an intensity of $\sim 3 \times 10^{14} \text{ W/cm}^2$ using three UV beams. Figure 128.62 shows examples of measured images at 1.1 ns (near the end of

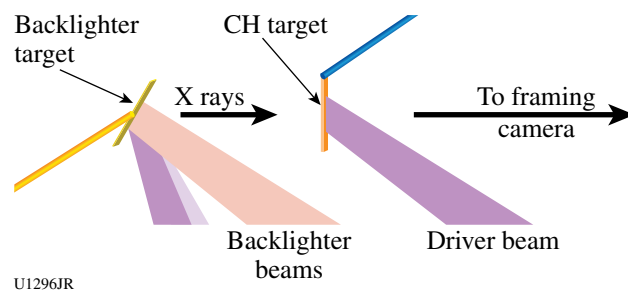


Figure 128.61
 Experimental setup.

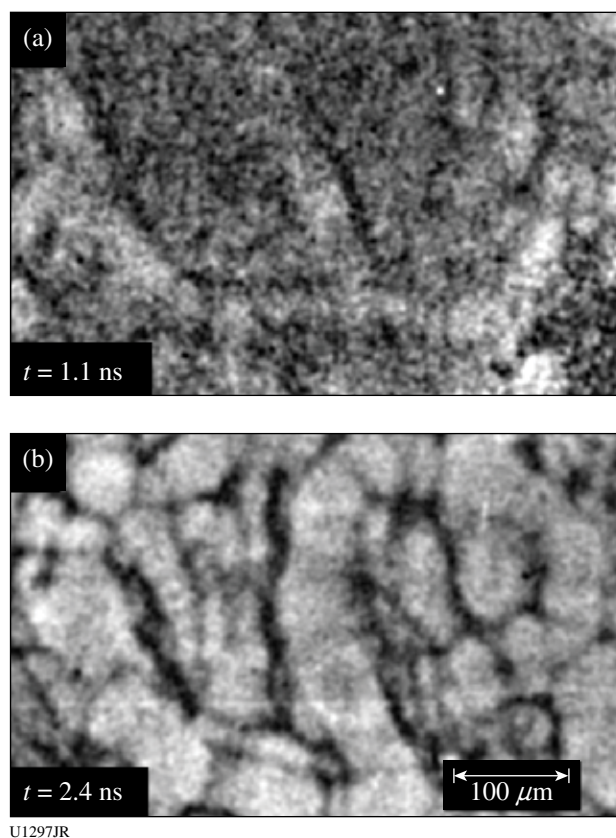


Figure 128.62
 X-ray images of 3-D broadband modulations (a) at the end of the Richtmyer–Meshkov instability growth phase and (b) during the Rayleigh–Taylor instability growth phase measured in 30- μm -thick CH targets.

the RM phase) and 2.4 ns (during the RT phase) taken with a 30- μm -thick CH foil and samarium backlighter. Evolution of 3-D broadband modulations was observed in the RM phase for all target types during a shock-transit time before the beginning of acceleration and subsequent RT growth. Thicker targets had larger modulations at the end of the RM phase owing to the longer time for instability development. This provided larger initial modulations in thicker targets for subsequent RT growth. Therefore, this experiment provided data not only on the RM growth of 3-D broadband modulations, but also the dependence of RT growth on initial conditions. Modulation images in the RT phase show developed bubble-spike structures, typical features of nonlinear RT growth. These experiments, therefore, also provided information about nonlinear high-mode generation from known modulations. These experimental data are now being analyzed.

Measurement of Nucleation and Growth of the Fe $\alpha \rightarrow \epsilon$ Phase Transformation

Principal Investigators: R. Smith, P. M. Celliers, and D. Erskine (LLNL)

The goal of this project is to combine for the first time the recently developed 2-D imaging OMEGA high-resolution velocimeter⁵⁷ (OHRV) with the 1-D line VISAR (ASBO) to determine the time dependence and mechanisms associated with nucleation and growth of the $\alpha \rightarrow \epsilon$ phase transformation in dynamically compressed Fe.

The target design consists of a Au halfraum, a 12% Br/CH reservoir, a vacuum gap, and 50 μm of Fe coated onto a sapphire window (Fig. 128.63). Twenty beams (2-ns square, P6-axis, 300- μm phase plates) from the OMEGA laser were focused onto the inner walls of an Au halfraum generating a near-blackbody source of x rays with a characteristic radiation temperature of

~ 120 eV. As x rays ablate material from the Br/CH foil, a shock wave is launched into the material.

As the ablatively driven shock reaches the back surface of the reservoir, the 12% Br-CH unloads across the ~ 0.3 -mm vacuum gap, piles up against the front surface of the Fe target, and launches a ramp-compression wave into the sample with a peak longitudinal stress of ~ 50 GPa. As the Fe sample is dynamically compressed, it undergoes different states of deformation: 1-D elastic, 3-D plastic, and a solid-solid phase transformation from α (bcc) to ϵ (hcp) phase.

Each stage of compression of the Fe sample results in a change in the sound speed, which modifies the initially smoothly monotonic ramp wave during transit through the sample and is recorded as a structured particle-velocity history, $U_p(t)$, on the line-VISAR diagnostic (ASBO) (Fig. 128.64).

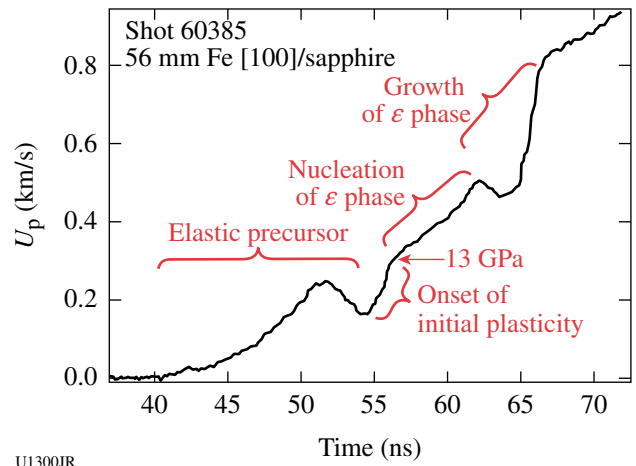


Figure 128.64 Particle velocity versus time for a ramp-compressed Fe/sapphire target as recorded on the 1-D line VISAR (ASBO).

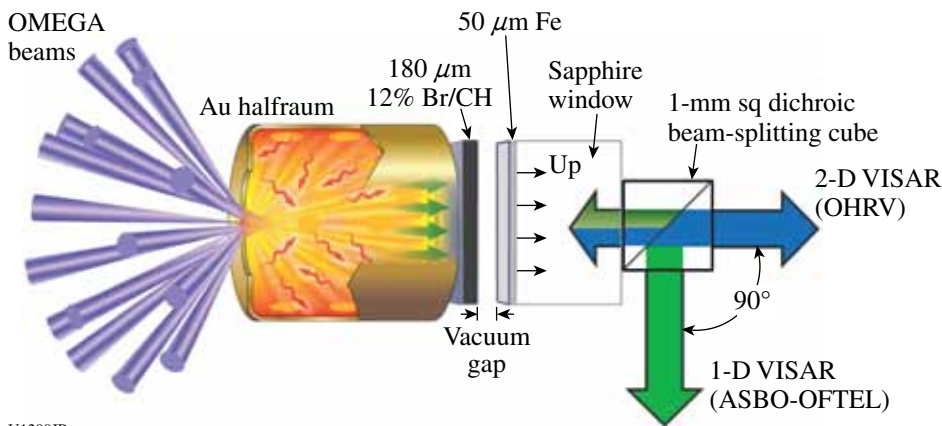


Figure 128.63 Target geometry for a combined 1-D/2-D VISAR diagnosis of a ramp-compressed Fe target.

Snapshots of the 2-D velocity map at the Fe–sapphire interface with the OHRV at velocities close to the velocity pull-back feature on the line VISAR reveal the kinetics associated with the nucleation and growth of the emerging ε phase.

Progress in the Shock-Ignition Inertial Confinement Fusion Concept

Principal Investigators: W. Theobald, R. Nora, K. S. Anderson, R. Betti,* R. S. Craxton, J. A. Delettrez, V. Yu. Glebov, M. Hohenberger, O. V. Gotchev, F. J. Marshall, R. L. McCrory,* D. D. Meyerhofer,* T. C. Sangster, W. Seka, C. Stoeckl, and B. Yaakobi (LLE) (*also Departments of Mechanical Engineering and Physics); A. Casner (CEA); J. A. Frenje (MIT); X. Ribeyre, M. Lafon, and G. Schurtz (Centre Lasers Intenses et Applications, University of Bordeaux, France); and L. J. Perkins and V. A. Smalyuk (LLNL)

Shock ignition is a two-step inertial confinement fusion concept in which a strong shock wave is launched by an intensity spike at the end of the laser pulse to ignite the compressed core.⁵⁸ Parametric plasma instabilities⁵⁹ such as stimulated Brillouin scattering (SBS), stimulated Raman scattering (SRS), and two-plasmon-decay (TPD) instability are of concern for laser intensities in the range of $\sim 3 \times 10^{15}$ to $\sim 10^{16}$ W/cm². The instabilities increase the back-reflection of the laser light from the target, degrading the laser-energy coupling to the capsule. They increase the fraction of the laser energy transferred to suprathermal electrons—a potential source of preheat that could reduce the final core compression. Whether or not these are harmful depends on the hot-electron temperature and the amount of laser energy that is transferred into hot electrons at high laser intensities.⁶⁰ The objective of this work is to study the coupling of laser energy from high-intensity beams into a spherically imploding capsule and the laser–plasma instabilities at shock-ignition–relevant laser intensities.

The targets were 34- to 36- μm -thick, 430- μm -outer-radius, deuterated plastic shells coated outside with a 0.1- μm layer of aluminium and filled with D₂ gas with a pressure of ~ 25 atm. The capsules were imploded using 40 of the 60 OMEGA beams with a low-adiabat pulse shape with ~ 13.6 kJ of UV laser energy and phase plates. The beams were repointed to achieve improved illumination uniformity. The blue curve in Fig. 128.65(a) shows the drive-pulse shape. A late shock was driven by the remaining 20 beams with an ~ 600 -ps FWHM square-pulse shape (red curve) without phase plates. The intensity was varied by shifting the focus of the 20 beams relative

to the shell's center. Figure 128.65(b) shows a schematic for intermediate spike intensity. The foci of the 20 spike beams did not overlap at the critical density for most lens positions. The experimental observables are the neutron yield,⁶¹ the backscattered laser energy,⁶² the hard x-ray signal,⁶³ and the neutron-rate–averaged areal density.²⁰ The hard x-ray signals were measured with four channels (>20 , >40 , >60 , and >80 keV) (Ref. 63). Areal densities (ρR) were inferred from secondary proton spectra.²⁰

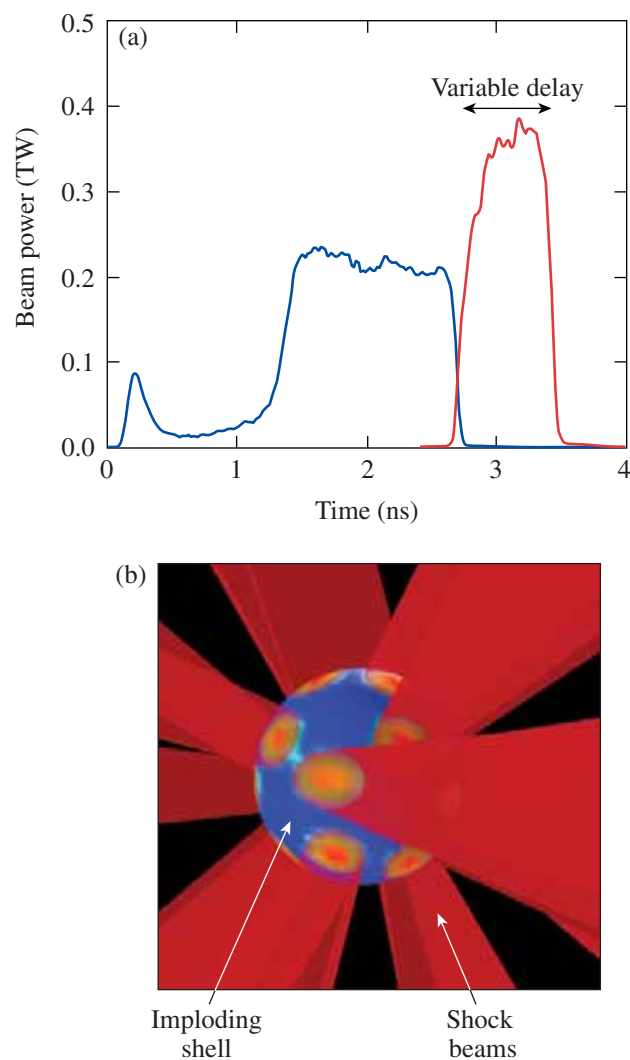


Figure 128.65

(a) The drive-pulse shape (blue) for the 40 beams and the high-intensity pulse (red) for the 20 spike beams. Beam delay and spike intensity were varied. (b) The 20 delayed spike beams were tightly focused onto the critical-density surface, where plasma instabilities led to the generation of energetic electrons and laser backscattering.

Two-dimensional hydrodynamic simulations with the code CHIC⁶⁴ are consistent with the measured areal density (see Fig. 128.66). The solid curve is from the 2-D simulation and the dashed line is from a 1-D simulation. The experimental values are noted by solid circles. The simulation values are higher because they represent the areal density at peak neutron production, whereas the experimental values are averaged over the observed neutron-production rate.

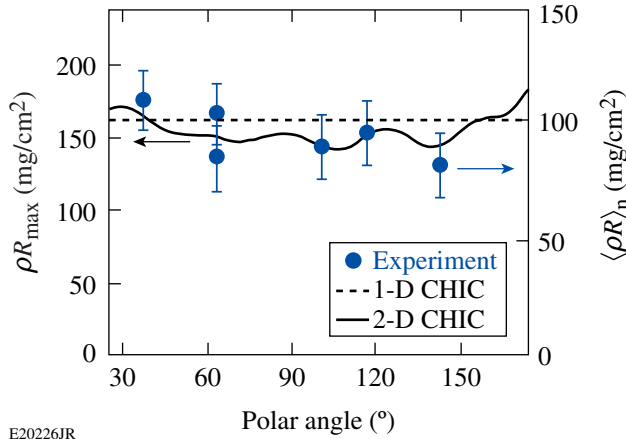


Figure 128.66 Simulated (curves) and measured areal density (circles) as functions of the polar angle. The dashed line is from a 1-D simulation and the solid curve from a 2-D hydrodynamic simulation with the code CHIC.⁵⁸

The effect on the (a) measured and (b) simulated neutron yields is shown in Fig. 128.67 for various spike-onset times. The different symbols represent various focus conditions. Implosions with only 40 drive beams (i.e., no spike beams) produced $\sim 1.5 \times 10^9$ neutrons [solid line in Fig. 128.67(a)]. Adding the 20 spike beams enhanced the yield by a factor of up to 2.3, with a trend of lower yields at later times. There is no significant dependence on intensity with the total energy kept constant. A similar trend is observed in the predicted neutron yield [Fig. 128.67(b)]. The enhancement in the simulation is up to a factor of ~ 3.5 when adding the spike beams because of the extra energy delivered to the target. The yield-over-clean ratio, defined as the measured to predicted neutron number, is about 3% to 5%.

The hard x-ray detector provides information on the hot-electron number and temperature. The hot-electron temperature was determined by fitting estimated values from the convolution of an exponentially decaying hard x-ray spectrum with the sensitivity of the different channels to the measurements in the four channels.⁶³ The inferred temperature was 45 ± 5 keV for all

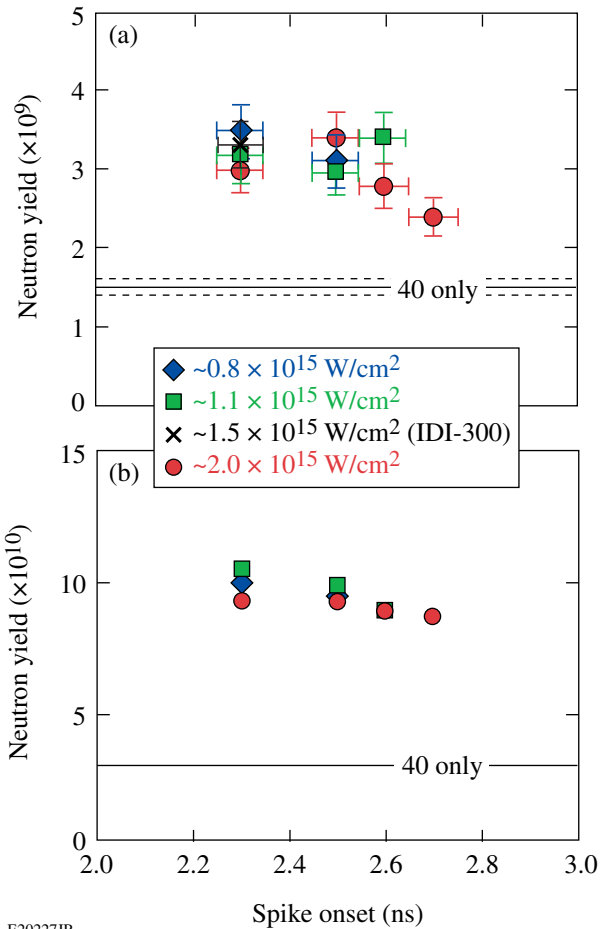
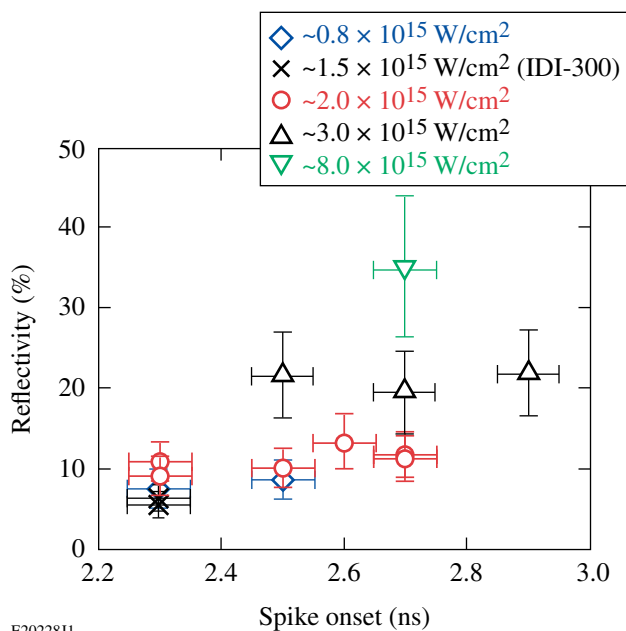


Figure 128.67 (a) Measured and (b) 1-D-simulated neutron yields in 40 + 20-beam implosions for various spike onset times and spike intensities.

shots without phase plates, independent of laser intensity. A low hot-electron temperature is beneficial for shock ignition since these electrons are stopped in a thin outer layer of the imploding target, augmenting the strong hydrodynamic shock. The plasma reflectivity was measured for various laser intensities. Figure 128.68 shows the measured fraction of laser backscatter energy of one shock beam for various laser intensities as a function of the spike onset. No significant variation is observed with spike onset. The reflectivity increases from $\sim 8\%$ at $\sim 0.8 \times 10^{15}$ W/cm² to $\sim 35\%$ at $\sim 8 \times 10^{15}$ W/cm². The simultaneously measured back-reflection through a neighboring drive-beam port remained constant at the level of implosions without the 20 spike beams for all beam delays and lens positions. This shows that the light from the spike beams was scattered back in a narrow cone and that there was no significant spill over into adjacent ports.



E20228J1

Figure 128.68

Percentage of the laser light reflected back into the solid angle of the focusing lens for various intensities and delay times.

FY11 LLNL OMEGA Experimental Programs

In FY11, LLNL conducted several campaigns on the OMEGA and OMEGA EP Laser Systems, as well as campaigns that used the OMEGA and OMEGA EP beams jointly. Overall, LLNL led 301 target shots involving OMEGA and 81 target shots involving OMEGA EP (not including LLNL-led shots under the LBS program). Approximately 35% of the shots (126 OMEGA shots, 10 OMEGA EP shots) supported the National Ignition Campaign (NIC). The remainder were dedicated to experiments for high-energy-density (HED) physics (168 OMEGA shots, 72 OMEGA EP shots).

Objectives of the LLNL-led NIC campaigns at OMEGA included the following:

- Characterization of long-pulse, high-resolution, laser-produced backlighters
- 4ω Thomson scattering
- Neutron-induced backgrounds for ARIANE
- Thermal-conductivity measurements at a heated CH/Be interface by refraction-enhanced x-ray radiography
- 18-keV x-ray Thomson scattering of shock-compressed beryllium and aluminum
- High-resolution measurements of velocity nonuniformities created by microscopic perturbations in NIF ablator materials

- X-ray Thomson scattering of shock-compressed beryllium on OMEGA EP
- Pb Hohlraums
- Surrogate mix targets with dual backlighting

The LLNL-led HED campaigns covered four main areas of research:

1. Material dynamics and equation of state
 - a. Kr Hugoniot measurements to 730 GPa
 - b. Ramped compression of different materials
 - c. Tin melt
 - d. Powder x-ray-diffraction measurements of solid Fe and Ta to 570 GPa
 - e. Hohlraum diffraction
 - f. Equation of state for foams
 - g. Gigabar equation of state
 - h. Double pulse
 - i. Dynamic and lattice diffraction
 - j. Tantalum Rayleigh-Taylor experiments
 - k. ICEDrive-11A/ICEHohl-11A
 - l. Strength diffraction
2. High-temperature plasma opacity
 - a. High-temperature plasma opacity experiments on OMEGA and OMEGA EP
3. Hydrodynamics
 - a. Short-pulse, UV backlighting development for the NIF
 - b. Backlighting experiments on OMEGA
4. X-ray source development and application
 - a. Iron K-shell x-ray source development
 - b. Solar-cell electrostatic discharge

This work was performed under the auspices of the U.S. Department of Energy by Lawrence Livermore National Laboratory under Contract DE-AC52-07NA27344.

National Ignition Campaign Experiments

Characterization of Long-Pulse, High-Resolution-Laser-Produced Backlighters

Principal Investigator: R. Tommasini

In FY10 we characterized short-pulse bremsstrahlung backlighters produced by 10-ps, 1ω laser pulses from the OMEGA EP laser. Using these pulses, we successfully dem-

onstrated Compton radiography of direct-drive implosions of spherical-shell and cone-in shell targets. The cone-in-shell targets are of interest for fast ignition.

In FY11 we characterized long-pulse Bremsstrahlung backlighters produced by 100-ps, 3ω laser pulses from the OMEGA laser. These x-ray sources are of interest for the earliest implementation of Compton radiography on the NIF.⁶⁵ The backlighters were produced by overlapping up to 18 100-ps, 3ω OMEGA laser beams with a total power ~ 8 TW to match or exceed single NIF 3ω quad intensities onto 300- μm -long, 10- μm -diam Au microwires.

The conversion efficiency of the backlighters, into 70- to 200-keV x rays, was measured using an annular step-wedged filter hosted in the custom-built Compton radiography snout (CRS). Figure 128.69 shows a comparison of the conversion from 1ω , 10-ps- (dots) and 3ω , 100-ps- (squares) laser-produced, 10- μm -diam Au backlighters. This target gives conversion efficiencies between 1×10^{-5} and 3×10^{-5} , in the available intensity range 3×10^{16} to 1×10^{17} W/cm². As observed, these conversion efficiencies are typically a factor of 7 to 10 less than for planar-foil targets and consistent with the ratio of wire area to laser-spot area. They are also $\approx 7\times$ less than for 1ω sources at the same intensity, ascribed to the $I\lambda^2$ dependence of hot-electron production. Such efficiencies at 3ω should be sufficient to measure fuel areal densities and radii to 7% accuracy at 20- μm spatial scales on the NIF and to observe 20% fuel areal density and shape nonuniformities up to mode 4.

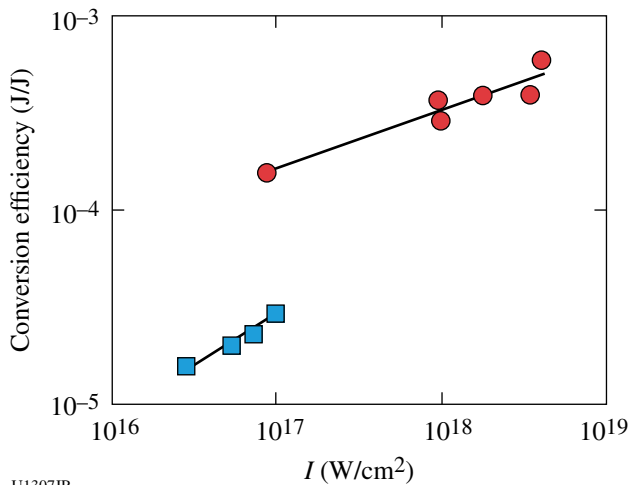


Figure 128.69 Conversion efficiency as a function of laser intensity into 70- to 200-keV x rays from 1ω , 10-ps (dots) and 3ω , 100-ps (squares) laser-produced, 10- μm -diam Au backlighters.

The source size of the 3ω backlighters was measured by fitting experimental radiographic transmission lineouts of tungsten-carbide spheres to simulated radiographs for Gaussian-shaped sources using the spectra measured by the CRS step wedge. This method resulted in typical Gaussian FWHM source sizes of $(11 \pm 2) \mu\text{m}$, in all cases close to the diameter of the Au wires. The pulse durations were inferred from an x-ray streak camera measuring the emission from Au in the spectral region above 3 keV to be 100 ± 5 ps.

4ω Thomson Scattering

Principal Investigator: S. Ross

The 4ω Thomson-scattering measurements were made from foil (shown in Fig. 128.70) and hohlraum targets to determine plasma conditions. Figure 128.71 shows the measurement of Thomson scattering from the ion-acoustic wave (ion feature) and the electron-plasma wave (electron feature) resonances using a 4ω probe beam from a CH-foil target. From the scattered spectra, the electron density, temperature, plasma flow velocity, and ion temperature are measured.

Measurements from foil targets produced excellent data. Hohlraum targets proved more difficult because of the complex target geometry, which produced increased background and

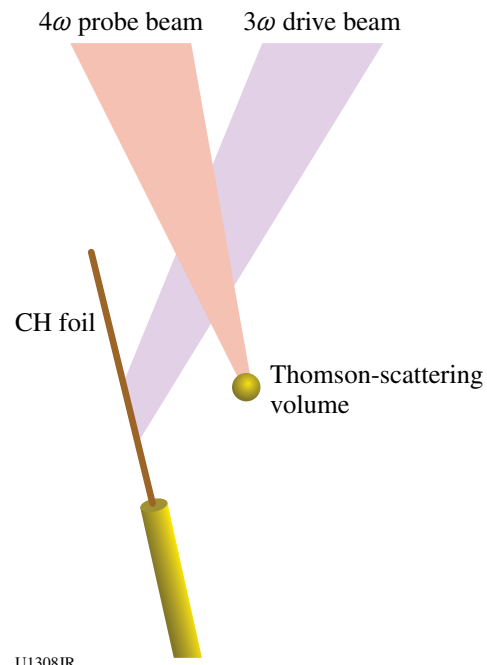
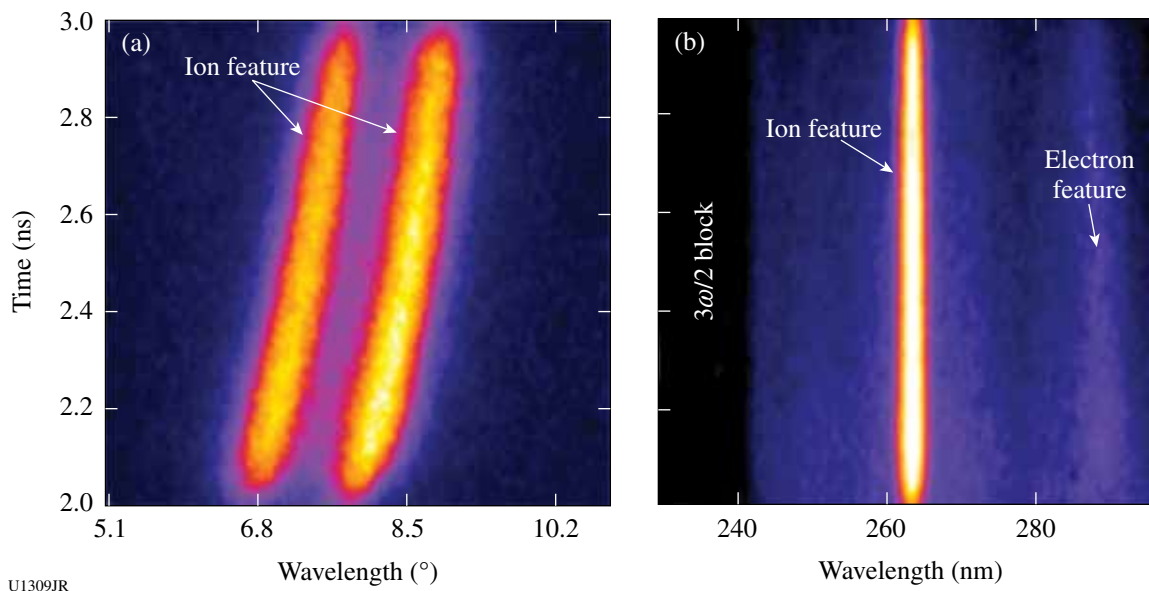


Figure 128.70 The foil-target configuration.



U1309JR

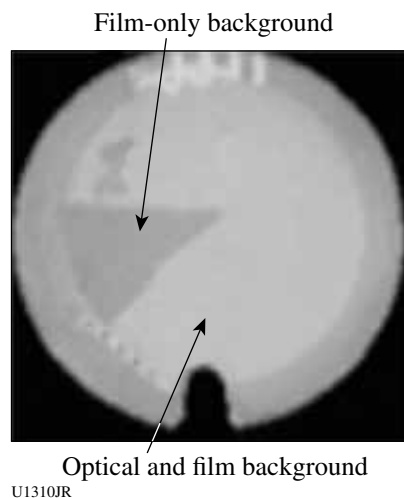
Figure 128.71
Streaked Thomson-scattering data from the resonances of (a) an ion-acoustic wave and (b) an electron-plasma wave.

inhibited probe-beam propagation. The Thomson-scattering diagnostic was activated successfully, and the measurements made from foil and hohlraum targets will be used to improve experimental and diagnostic design for upcoming experiments planned for FY12.

Neutron-Induced Backgrounds for ARIANE

Principal Investigator: V. A. Smalyuk

X-ray imaging instruments will operate in a harsh ionizing radiation background environment on implosion experiments at the NIF. These backgrounds consist of mostly neutrons and gamma rays produced by inelastic scattering of neutrons. The experiment was designed to measure these backgrounds generated in some of the components of x-ray framing cameras used in the ARIANE imaging system: phosphors, fiber-optic plates, and T-MAX 3200 film. The experiment consisted of six implosions with 1.5-mm-outer-diam, 4- μ m-thick glass shells filled with 5 atm of DT gas, driven with 60 OMEGA beams with a total UV energy of ~ 28 kJ. Measured DT neutron yields were in the range from $\sim 3 \times 10^{13}$ to $\sim 4 \times 10^{13}$. Fiber-optic plate samples were coated with five different phosphors (P-11, P-20, P-43, P-46, and P-47) and placed in the OMEGA target chamber at ~ 21 and ~ 42 cm from target chamber center. Neutron-induced background signals were detected on T-MAX 3200 film. Figure 128.72 shows an example of the film data, with measured backgrounds in P-43 phosphor, fiber-optic plate, and film (lighter area) and with film only (darker area). Figure 128.73(a)



U1310JR

Figure 128.72
Measured optical backgrounds in P-43 phosphor, fiber-optic plate, and film (lighter area); and with film only (darker area).

shows the background intensity as a function of DT neutron exposure measured in P-43 phosphor, fiber-optic plate, and film (diamonds with exponential fitting shown with a solid curve) and in film only (triangles with exponential fitting shown by a dashed curve). Figure 128.73(b) shows background intensity in a fiber-optic plate with a film (diamonds) and in film only (triangles). Measured total backgrounds in samples with P-11, P-46, and P-47 phosphors were similar, with $\sim 50\%$ generated in film, $\sim 20\%$ in fiber-optic plates, and $\sim 30\%$ in phosphors. The

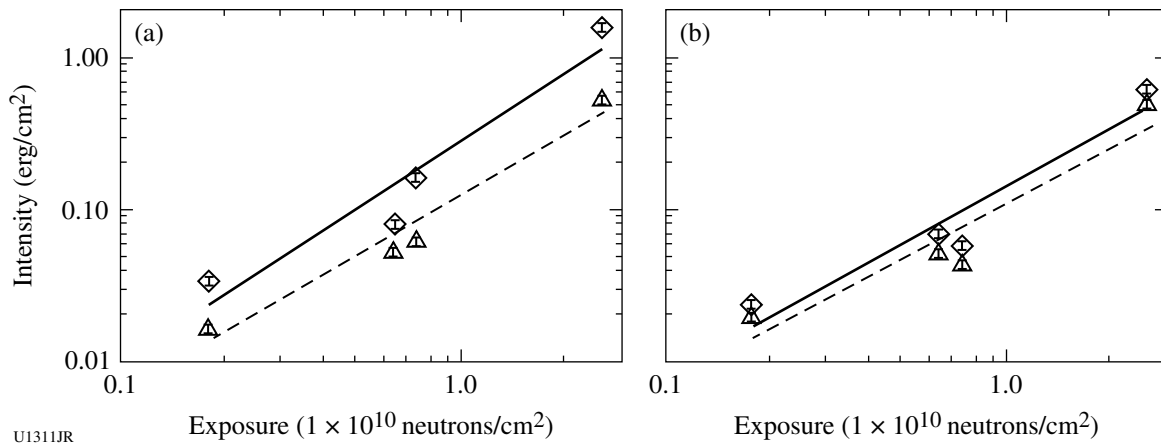


Figure 128.73

(a) Background intensity as a function of DT neutron exposure measured in P-43 phosphor, fiber-optic plate, and film (diamonds with exponential fitting shown with a solid curve); and in film only (triangles with exponential fitting shown with a dashed curve). (b) Backgrounds in fiber-optic plate with a film (diamonds), and in film only (triangles)

total backgrounds generated in both P-20 and P-43 phosphors were about a factor of 1.5 larger than in samples with P-11, P-46, and P-47 phosphors. Based on these measurements, the maximum peak signal is predicted to be about $5\times$ higher than the background for an ARIANE framing camera using P-11 phosphor and film for NIF shots with DT yields of 4×10^{16} . Such a background will be manageable when measuring the shape of the implosion core.

Thermal-Conductivity Measurements at a Heated CH/Be Interface by Refraction-Enhanced X-Ray Radiography

Principal Investigator: Y. Ping

A new series of campaigns are aimed at thermal conductivity measurements at the CH/Be interface under conditions relevant to the NIC target design, where the Be is a surrogate for DT. A novel technique, refraction-enhanced slit projection x-ray radiography, was successfully implemented to measure the evolution of the density profile at a cylindrical CH/Be interface, which was isochorically heated by Ag, L-band, 3-keV radiation. High-quality radiographs enabled us to determine the density gradient near the CH/Be interface from the fringe contrast with $2\text{-}\mu\text{m}$ -level accuracy, from which the thermal conductivity will be inferred (Fig. 128.74). In addition to the expected density evolution caused by thermal conduction, counter-propagating shock and rarefaction waves were also observed and their velocities were measured simultaneously. The multiple observables with the same diagnostic will strongly constrain the equation of state (EOS) of CH/Be and the temperatures after heating. A technical paper based on this

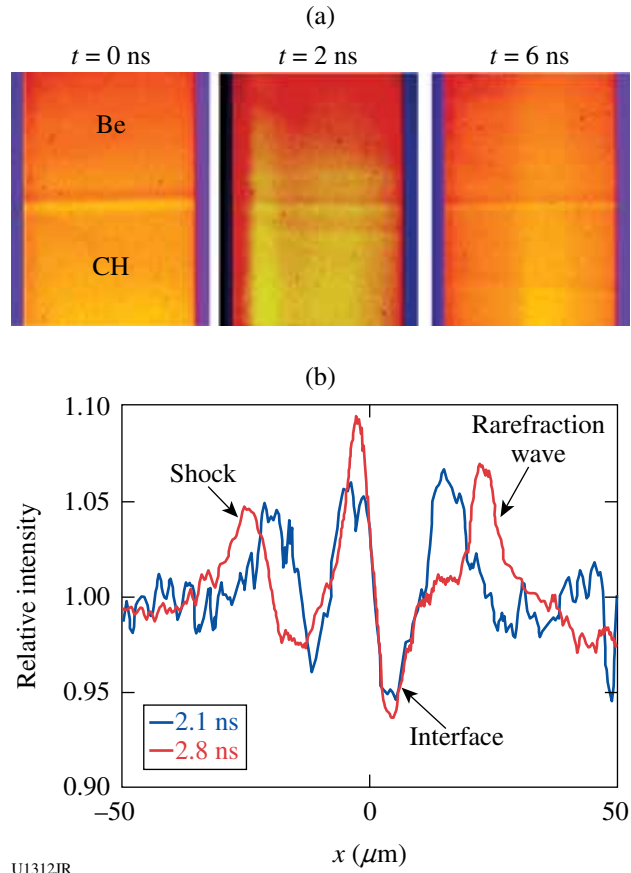


Figure 128.74

(a) 5.4-keV radiographs at $t = 0, 2,$ and 6 ns. (b) Lineouts of two frames taken in one shot, showing the shock wave and rarefaction wave counter-propagating from the interface.

campaign has been published,⁶⁶ and data are being analyzed to benchmark the transport models in NIC design codes. In FY12 this experimental design will be extended to include cryogenic cells for measuring thermal conductivity of D₂, which is critical for assessing hydro-instability margins during ICF implosions.

18-keV X-Ray Thomson Scattering of Shock-Compressed Beryllium and Aluminum

Principal Investigator: T. Ma

The accurate characterization of material properties under extreme conditions is an important issue for understanding high-energy-density states of matter. We performed two experiments on OMEGA in FY11 in which spectrally resolved x-ray Thomson scattering at 18 keV was used to determine the electron density and temperature of shocked Be and Al. Targets of 125- μ m solid beryllium and aluminum were shock compressed to high density ($>3\times$ solid density) using nine beams with a total energy of 4.5 kJ in a stacked 1-ns or 3-ns configuration. SG4 distributed phase plates were used to achieve a smooth 800- μ m focal spot, yielding a total drive intensity of 3×10^{14} W/cm² on the sample.

The materials were probed in the noncollective scattering regime using Mo 2-1 line radiation x rays at ~ 17.9 keV. In the first portion of the campaign (BeXRTS-11A), the scattering angle was held constant at 90°, while scattering was performed on undriven and driven Be and Al.

In the case of beryllium scattering, both the driven and undriven cases showed, as expected, depressed elastic scattering attributed to the fact that the ionization potential of Be electrons is less than the Compton energy ≈ 600 eV. Fits to the ratio of elastic to inelastic peaks for the undriven data gave a Z of ~ 1.5 to 2 [see Fig. 128.75(b)], in agreement with Ref. 67. In the case of Al, the unshifted Rayleigh scattering increased when driving the Al sample, attributed to increased disorder in the heated lattice [see Fig. 128.75(c)]. It was found that the ratio of the elastic to inelastic scattering features in the shocked Al were very sensitive to the ionization potential of the L-shell electrons (when Compton energy $>$ ionization potential of L-shell electrons, these electrons contribute in the same way as free electrons, and only the two K-shell electrons will Rayleigh scatter).

For the last series (BeXRTS-11B), Mo 2-1 line radiation was again employed as an x-ray probe while the scattering angle was varied from 25° to 155° (Compton energy from 60 eV to 1.2 keV). This allowed us to assess the sensitivity to continuum

lowering and measure the angularly resolved strength of the static structure factor. Experimental data were found to corroborate the code predictions: at smaller scattering angles, the Compton feature was merged into the Rayleigh, while the relative strength of the inelastic feature grows at a higher scattering angle.

High-Resolution Measurements of Velocity Nonuniformities Created by Microscopic Perturbations in NIF Ablator Materials

Principal Investigator: P. M. Celliers

This campaign focused on three aspects of NIF ablaters: (1) continue the survey of NIF Rev5 Ge-doped CH samples (seven shots), (2) continue the survey of diamond samples near the melt curve (two shots), and (3) perform the first test measurements of double-shocked diamond samples (two shots). For the CH samples we also tested a simplified target design in which the shock was transmitted from the ablator directly into the fused-silica window instead of the polymethylmethacrylate (PMMA) layer that was used in previous designs. The results showed that the shock-front reflectivity in the fused-silica window is too low to produce high-quality data, so future designs will continue to use the PMMA layer to capture the shock-front nonuniformities. The two single-shock experiments on diamond samples were designed to probe into the shock-melt region (about 600 GPa), and the results confirmed that partial shock melting produced much smoother shock fronts than lower-amplitude shocks that do not melt the sample. Finally, the two shots on double-shocked diamond were performed to test the drive and measure timing information in preparation for a more-extensive future series. On the first shot, the second-shock overtake was clearly observed (Fig. 128.76); however, the probe was synchronized too early to capture the second-shock overtake event. For the second shot, the probe was adjusted to capture the data just after the second shock overtook the first. On this shot we recorded the first data on shock-front perturbations from double-shocked diamond. This information will be used to design a more-comprehensive future campaign to assess diamond ablaters up to the second shock level.

X-Ray Thomson Scattering of Shock-Compressed Beryllium on OMEGA EP

Principal Investigator: A. Pak

This year, two shot days with a total of ten laser shots were used to study laser-shock-compressed beryllium using noncollective x-ray Thomson scattering (XRTS) on OMEGA EP. The primary goal of the first series of this campaign (EPXRTS-11A)

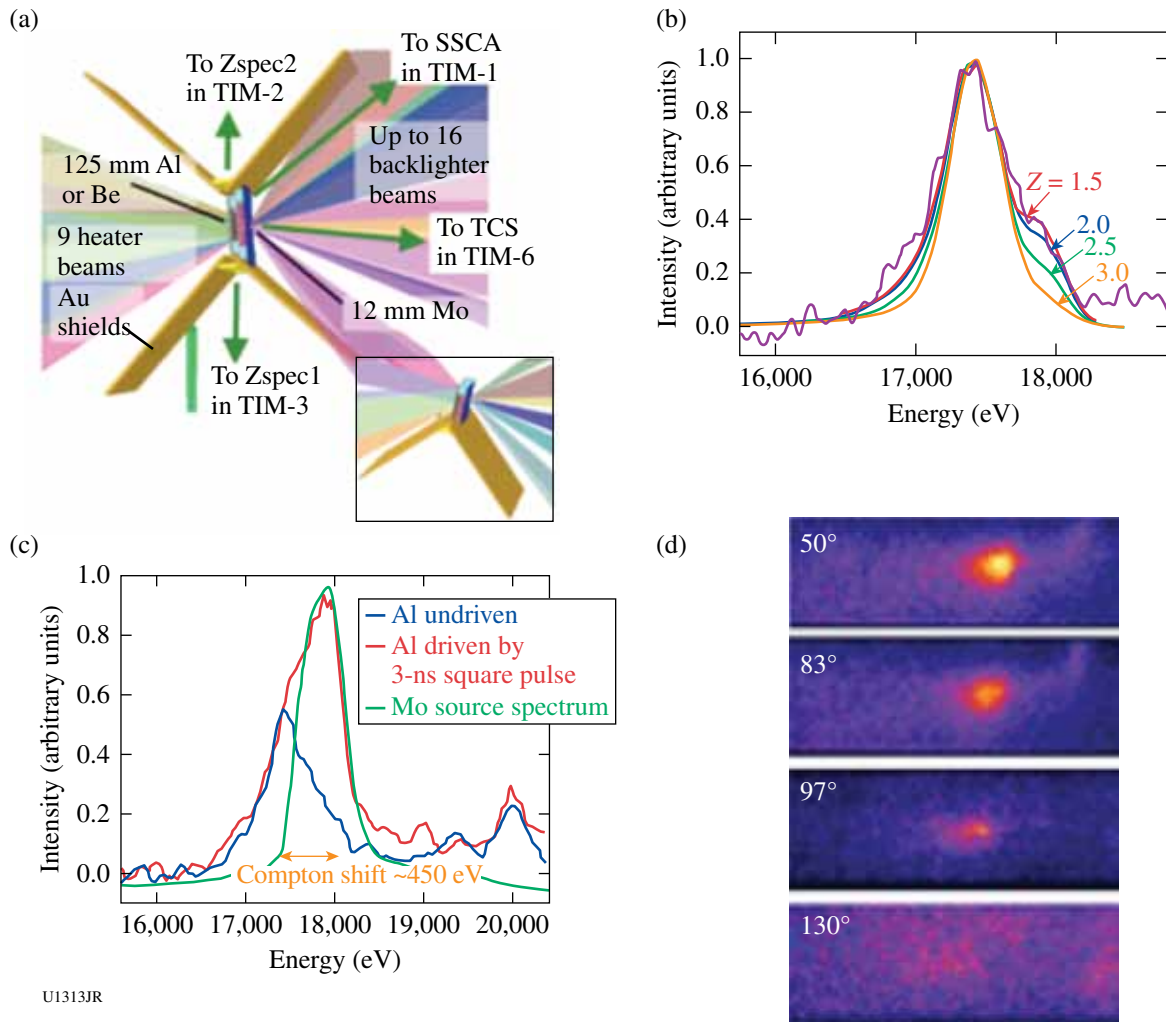
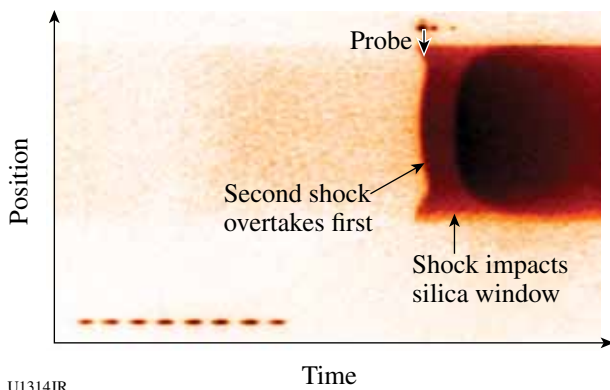


Figure 128.75

(a) The experimental configuration for BeXRTS-11B. Inset shows the single-wing, 90° configuration used in BeXRTS-11A. (b) Fits to the undriven beryllium scattering versus Z . (c) Comparison of source spectrum (green), undriven Al (blue), and driven Al (red) scattered spectra. (d) Al scattering versus increasing scattering angle (scattering k).

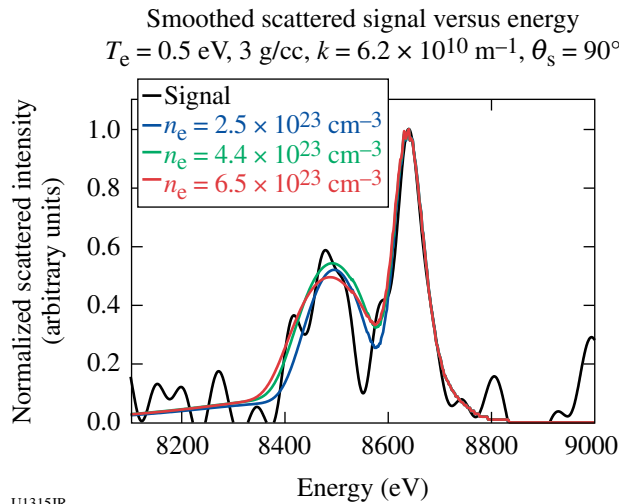


U1314JR

Figure 128.76

Streak record showing the second shock overtake and OHRV (OMEGA high-resolution velocimeter) probe timing for a two-shock drive applied to a noncrystalline diamond ablator sample.

was to develop a suitable experimental platform to study laser-shock-compressed matter with XRTS. Four laser shots were taken to test two scattering targets and two drive conditions. Only one of the scattering targets produced a scattering signal (shown in Fig. 128.77). The goal of the second shot day (EPXRTS-11B) was to use noncollective XRTS at two scattering angles to measure the change in the temperature of the shocked beryllium as the laser's drive-pulse shape was changed from a super-Gaussian shape to a ramped-adiabatic shape. Again four shots with two scattering targets were taken, but a clean scattered spectrum was not measured from this campaign. It is thought that a change in laser-beam configuration prevented the successful scattering target from EPXRTS-11A from producing a scattered signal. The second scattering target, which was modified to reach smaller scattered angles, allowed



U1315JR

Figure 128.77
Measured scattered signal from EPXRTS-11A (black) versus scattered energy. Here Zn-K α x rays at 8.64 keV elastically and inelastically scatter through a Be target that has been shocked by a laser with an $I_0 \approx 1 \times 10^{13}$ W/cm 2 . Three theoretical scattered spectra are plotted versus energy as a function of density, at a fixed temperature and scattering angle.

for unscattered x rays to reach the detector, preventing a clean scattered signal from being measured.

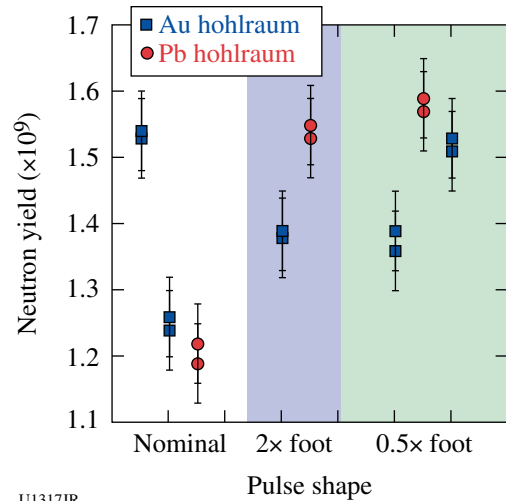
Pb Hohltraums

Principal Investigator: S. Ross

A comparison of Pb and Au hohlraums shows very similar performance for three shaped laser pulses. The point design for laser inertial fusion energy (LIFE) targets relies on Pb as the primary hohlraum material. Lead and gold hohlraums are pre-

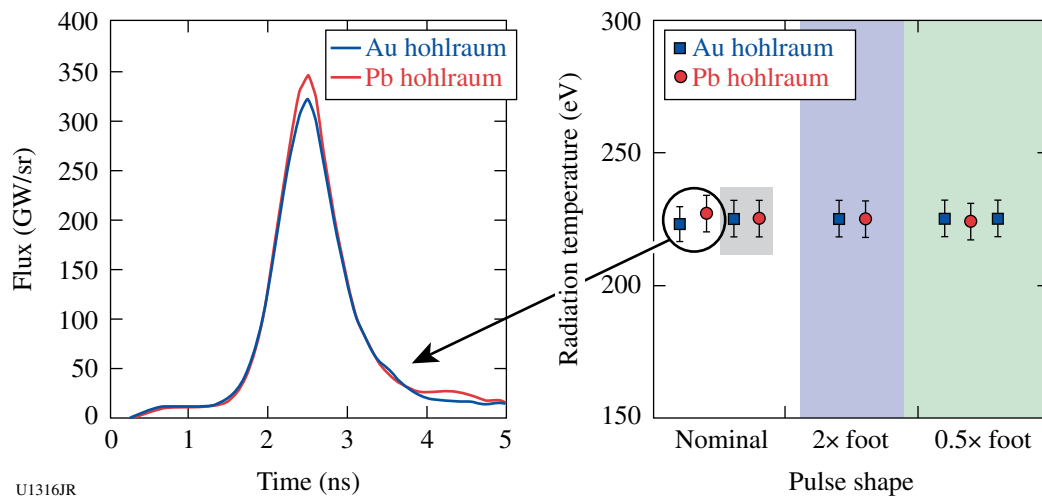
dicted to have similar performance and are the first measurements to validate those predictions. The hohlraum performance was measured using Dante to determine the hohlraum radiation temperature (Fig. 128.78) and a full-aperture backscatter station (FABS) to measure the backscattered energy. Both diagnostics show no measurable difference between Pb and Au.

Neutron yield (shown in Fig. 128.79) was also used to assess hohlraum performance, and again Pb and Au hohlraums produced very similar results. These experiments are a successful first step in validating Pb as a viable hohlraum material for a LIFE point-design target.



U1317JR

Figure 128.79
The neutron yield is compared for three pulse shapes for the Au and Pb hohlraums.



U1316JR

Figure 128.78
Time-resolved Dante flux and peak radiation temperature for Pb versus Au hohlraums.

Surrogate Mix Targets with Dual Backlighting

Principal Investigator: D. Farley

On 13 January 2010 a half day was devoted to OMEGA experiments to test two-color radiography of surrogate mix samples as a means of assessing both density and concentration. The backlighters and surrogate-mix materials were paired so that the backlighter resonance line energies straddled the K edge of one material, while both energies stayed either below or above the K edge of the other material. One type of surrogate mix target used Cu and Ge thin foils mounted on a CH block, which was backlit separately by Cu (8.4 keV), Ge (9.6 keV), or Zn (9.0 keV) backlighter materials (see Fig. 128.80). This type of surrogate-mix target simulates dopant levels at peak velocity for Ge- and Cu-doped plastic capsules. The other type of surrogate-mix target consisted of Si and Ge foils mounted on the same-sized block of CH to simulate Si and Ge dopants in a CH capsule, paired with Cu and Zr backlighters. Since Zr helium-like emission peaks at ~ 16.4 keV, it should transmit through Si-doped CH slightly better than Ge-doped CH with no noticeable transmission difference in the overlapped Si/Ge foil region, but there should be an observable change in transmission in the Si/Ge (or Cu/Ge) 100- μm overlapped region for the 8.4-keV Cu backlighter emission. Therefore, comparison of the transmission profiles of the two backlighters would provide an indication of mix width; however, the Zr laser-to-x-ray conversion efficiency will be quite low.

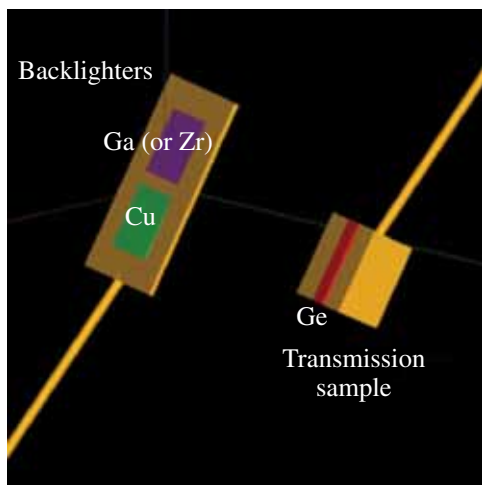


Figure 128.80

Setup of the experiment showing dual backlighters and mix target [Si or Cu on back side of transmission sample (not shown)]. The mix foils overlap ~ 100 μm when viewed face-on by camera.

C. Reverdin and F. Girard from CEA assisted in these experiments by providing diagnostic support for their CEA x-ray crystal spectrometer (XCCS), which had the spectral range to cover the Zr emission up to ~ 17 keV. A collection of spectra from the XCCS spectrometer is shown in Fig. 128.81. From this spectral result, the Zr conversion efficiency was estimated at 0.04%, at least $10\times$ lower than for Cu. The transmission profile for the Cu backlighter through the simulated mix sample was as expected. Further work is needed to determine the best dopant-backlighter pairing, but clearly we would have preferred a lower Z such as As or Se, if feasible.

High-Energy-Density Experiments**1. Material Dynamics and Equation of State****Kr Hugoniot Measurements to 730 GPa**

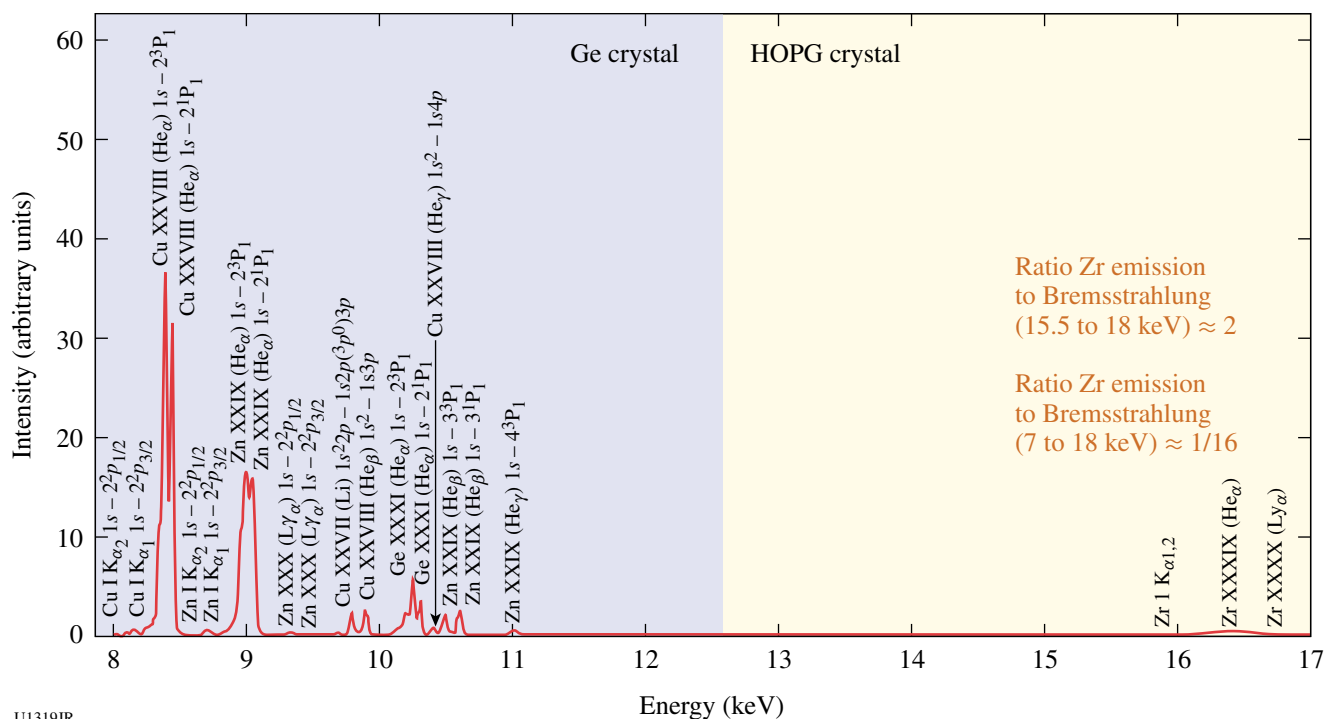
Principal Investigator: J. R. Rygg

Experimental measurement of the Kr Hugoniot was extended up to 730 GPa by launching shocks into Kr samples precompressed in diamond anvil cells to ~ 0.5 GPa (see Fig. 128.82). VISAR (velocity interferometer system for any reflector) and SOP (streaked optical pyrometer) measurements of the Kr shock front in comparison to concomitant measurements in quartz were used to infer pressure, density, reflectance, and temperature of shocked Kr. In addition, Hugoniot measurements on solid CO_2 precompressed to 1.0 GPa were compared to previous liquid CO_2 measurements to infer Grüneisen Γ of 0.5 and isochoric specific heat of 4.0 kJ/atom for CO_2 , T of 4.5 g/cc , 4 eV.

Ramped Compression of Different Materials

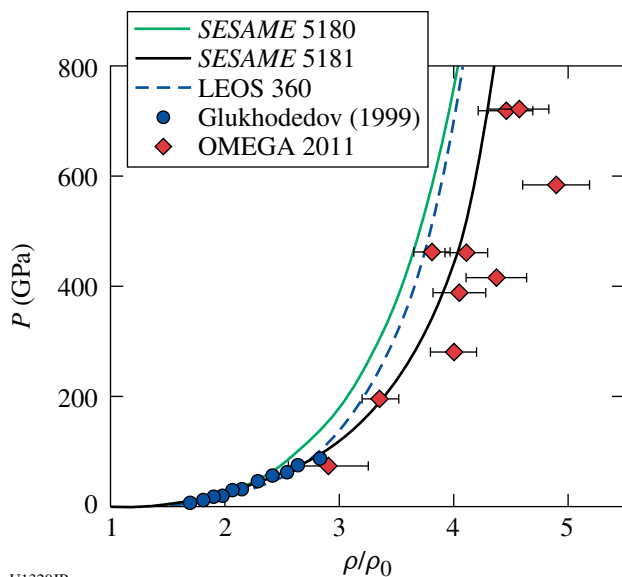
Principal Investigator: R. Smith

The goal of this experiment (RampComp-11A) was to measure the stress-density response of a nanodiamond step target through an indirect-drive ramp-compression technique. As shown in the inset of Fig. 128.83, the target geometry consists of an Au hohlraum with a multistep diamond sample attached to the back. The target was aligned on the H7-H14 axis on OMEGA. Fifteen beams with 300- μm elliptical phase plates inserted into the beamlines were focused onto the inner walls of the hohlraum. We used a 3.5-ns ramp-laser profile (RM3502) to generate a time-dependent x-ray temperature, which translates into a ramped longitudinal stress wave propagating through the stepped diamond (30/35/40/45- μm) target. The primary diagnostic was the ASBO (active shock breakout) (VISAR), which records the free-surface velocity as a function of time, $u_{fs}(t)$, for each step. Following a Lagrangian sound speed analysis the stress-density response is calculated from the $u_{fs}(t)$ record



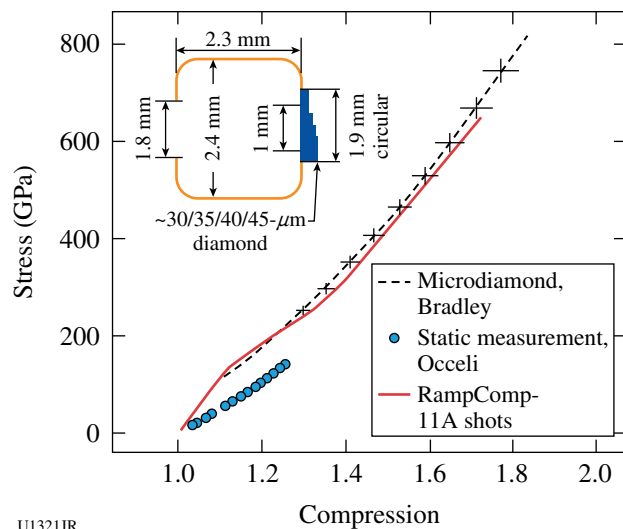
U1319JR

Figure 128.81 Collected spectra from TwoColorBL experiment backlighters, scaled by laser energy that was applied to each foil material. CEA XCCS spectrometer was used.



U1320JR

Figure 128.82 Previous experimental measurements of the Kr Hugoniot (blue dots) reached 87 GPa. In FY11, the OMEGA laser was used to extend the range to 730 GPa (red diamonds). The Kr shock pressure and density were inferred by shock-velocity measurements impedance matched to a quartz standard.



U1321JR

Figure 128.83 Stress-density response of a 200-nm-grain-size nanodiamond sample (red curve). This is an average of seven shots from the RampComp-11A series. Also shown are previous ramp compression data from Bradley⁶⁸ on micrograin diamond and static measurements from Occelli.⁶⁹ Shown as an insert is the target geometry for the RampComp-11A shot series.

and shown as the red curve in Fig. 128.83. Also shown are previously reported ramp-compression data of Bradley⁶⁸ on micrograin data and statically compressed data of Occelli.⁶⁹

The goal of the second day of this experiment (RampComp-11B) shots was to measure the stress–density response of a Ta step target through an indirect-drive ramp-compression technique. As shown in the inset of Fig. 128.84, the target geometry consists of a Au hohlraum with a multistep Ta sample (with 20- μm diamond ablator) attached to the back. The target was aligned on the H7–H14 axis on OMEGA. Fifteen beams with 300- μm elliptical phase plates inserted into the beamlines were focused onto the inner walls of the hohlraum. We used a 3.5-ns ramp-laser profile (RM3501) to generate a time-dependent x-ray temperature, which translates into a time-dependent ablation of a 20- μm diamond ablator. This results in a ramp longitudinal stress wave propagating through the stepped Ta (6/8/10/12- μm) target. ASBO (VISAR) records the $u_{fs}(t)$ for each step (Fig. 128.84). On the RampComp-11B series, we conducted seven shots in a half day. Using a Lagrangian sound-speed analysis technique,⁶⁸ we can extract the stress–density response of Ta to 3 Mbar. These data are currently being prepared for publication.

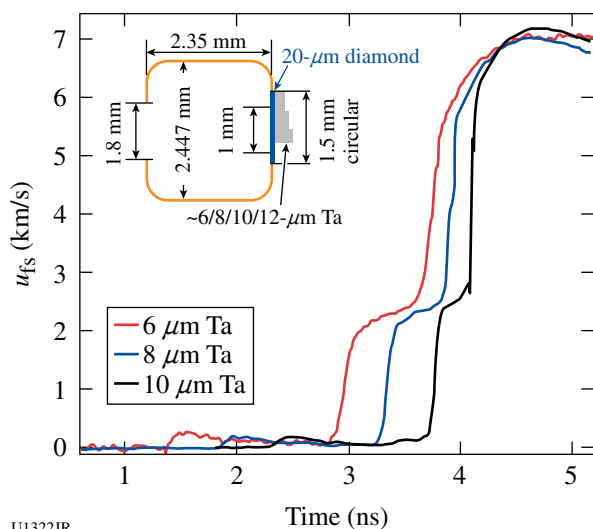


Figure 128.84

Free-surface velocity versus time, $u_{fs}(t)$, for three different thicknesses of Ta. The low-velocity precursors are a result of laser glint of hohlraum walls being absorbed at the diamond/Ta interface. The ramped plateau initiated at ~ 2 km/s is from the transmitted diamond elastic wave

The goal of the third shot day (RampComp-11C) was to measure the stress–density response of Fe through an indirect-drive ramp compression technique. The target geometry con-

sists of a Au hohlraum with a multistep diamond sample attached to the back. The target was aligned on the H7–H14 axis on OMEGA. Fifteen beams with 300- μm elliptical phase plates inserted into the beamlines were focused onto the inner walls of the hohlraum. We used a composite laser pulse shape with six beams in the RR1901 pulse shape to launch a 70-GPa shock into the sample followed 2 ns later by nine beams with the RM4002 pulse shape to ramp compress to ~ 300 GPa. The time-dependent laser power results in a time-dependent longitudinal stress wave propagating through the Fe. Following a Lagrangian sound speed analysis,⁶⁸ the stress–density response is calculated from the $u_{fs}(t)$ record and shown as the red curve in Fig. 128.85. Also shown are previously reported shock-compression and static measurements from Dewaele⁷⁰ and Dubrovinsky.⁷¹

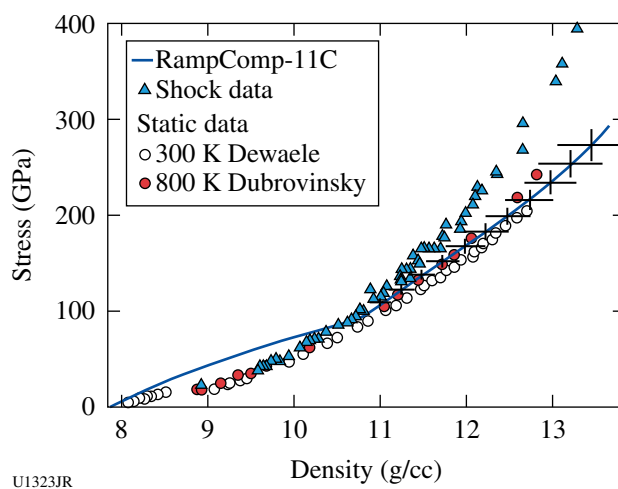


Figure 128.85

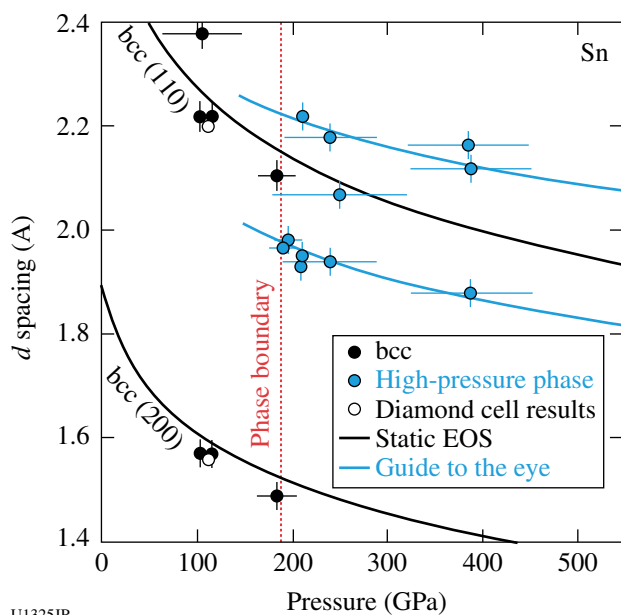
Stress–density response of Fe (blue curve). This is an average of six shots from the RampComp-11C series. Also shown are previous shock-compression data and static measurements from Dewaele⁷⁰ and Dubrovinsky.⁷¹

Tin Melt

Principal Investigators: J. M. McNaney and A. Lazicki

During the April 2011 tin-melt campaign, we shocked and/or ramp compressed tin prepared in diamond–tin–diamond or diamond–tin–LiF sandwiched targets, while measuring particle velocities, powder x-ray diffraction, and temperature using the VISAR, powder x-ray diffraction image plate (PXRDIP), and SOP diagnostics. One purpose of the campaign was to probe for high-pressure solid crystalline phases using pure ramp compression in order to extend the solid equation of state to higher pressure, and to look for new phase transitions. We were able to exceed 200 GPa on multiple shots, and we see a shift

in the dominant diffraction peak and the appearance of new features, indicating a phase transition (Fig. 128.86, compared with known diamond anvil cell results⁷²). The second purpose of the campaign was to begin exploration of the tin melting curve by creating a pulse shape that would shock-melt tin followed by a ramp compression back across the melting curve, measuring x-ray diffraction at the end of the ramp to confirm recrystallization. We succeeded in generating a shock followed by a ramp to the desired pressures and observed a plateau in the velocity profile consistent with a phase transition such as recrystallization (Fig. 128.87). We also observed x-ray diffraction features that appeared crystalline, indicating that the phase boundary back to the solid had been crossed within the time scale of the experiment. Work is ongoing to verify these observations and to explore the solid to higher pressures and the melting curve to higher temperatures.



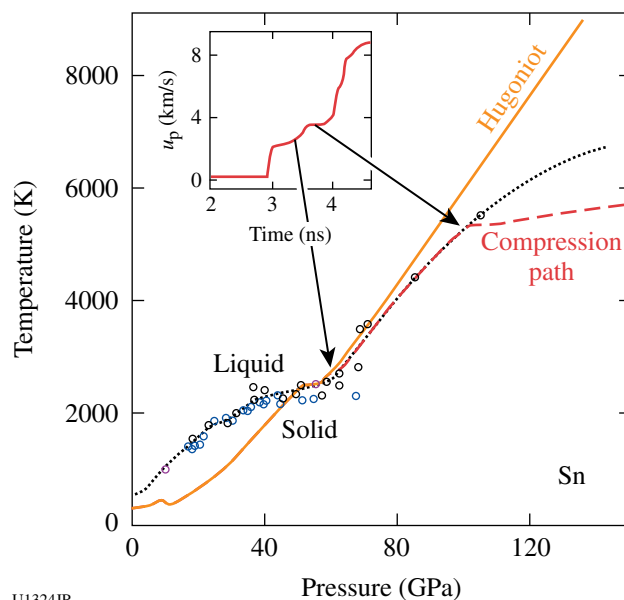
U1325JR

Figure 128.86
Pressure-induced shift in d spacing of different peaks of tin compared to static diamond anvil cell results.

Powder X-Ray-Diffraction Measurements of Solid Fe and Ta to 570 GPa

Principal Investigators: J. R. Rygg and J. Hawreliak

The OMEGA powder x-ray-diffraction platform was further refined in FY11 to obtain diffraction results on solid samples at pressures above Hugoniot melt, including the first detection of the highest solid-solid phase transition to date (to our knowledge) (see Fig. 128.88). Fe and Ta samples were sandwiched between a diamond pusher and window and ramp-compressed



U1324JR

Figure 128.87
Melting curve of Sn with suggested compression path corresponding to observed velocity profile (shown in inset).

to high pressure and density using up to six beams. VISAR velocity measurements were used to infer the pressure history in the sample, and the 8.37-keV Cu-He α x-ray source, driven by ten beams, was timed to coincide with the peak pressure. The diffraction signal is collimated through a 300- μ m-diam aperture and captured on image plate detectors. Density is inferred from the diffraction data by assuming a crystal structure, then verifying self-consistency with a best fit to density. Fe diffraction measurements were consistent with the hexagonal close packing (hcp) phase up to 570 GPa, and an extra peak observed in Ta above 340 GPa is consistent with a phase transition from the body-centered-cubic (bcc)-to- ω phase.

Hohlraum Diffraction

Principal Investigator: J. Hawreliak

In-situ x-ray diffraction (XRD) provides a unique measurement of atomic arrangement that helps us determine the materials' lattice structure and phase, which are key components to understanding a material's equation of state. Many scientific and programmatic objectives will use XRD as a means of understanding the high-pressure state. The current materials platform on the NIF will use a hohlraum drive to load the sample. Our current diffraction techniques may not be compatible with a hohlraum drive or other planned high-pressure materials experiments on the NIF and OMEGA. The objective of this experiment (HohlDiff 11A) is to test an energy-dispersive dif-

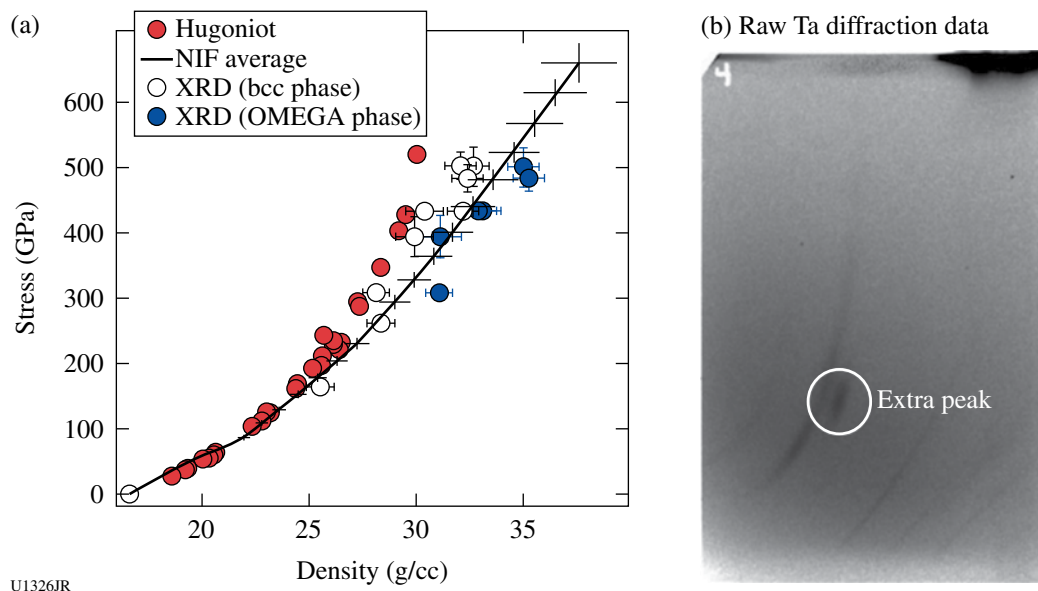


Figure 128.88

(a) Stress density of tantalum, where x-ray-diffraction (XRD) points assume either the ambient bcc phase or ω phase. (b) The appearance of an additional Ta peak for pressures above 340 GPa is consistent with a transition to the ω phase predicted by Burakovski.⁷³ To the best of our knowledge, this is the highest-pressure solid-solid phase transition observed to date.

fraction technique on the OMEGA EP Laser System, which may be compatible with a hohlraum drive.

The energy-dispersive diffraction technique uses a fixed experimental geometry, with a broadband x-ray source. The relative angle between the x-ray source and detector fixes the angle θ in the Bragg equation $\lambda = 2d \sin \theta$. Then peaks in the scattered energy will correspond to lattice plane spacing d . This technique has the advantage that the detector can be remote from the sample and x-ray source, and because the energy spectrum of the drive can be measured separately, it can be spectrally separated from the diffraction signal. We used the L- and M-shell emission from a cocktail backlighter source to generate a quasi-broadband x-ray spectrum and used the single-photon-counting diagnostic on the OMEGA EP Laser System as our energy dispersive detector.

Figure 128.89 shows the energy-corrected scattering data from the experiment. The black line is the backlighter when there is no target sample. The low-energy signal suggests we need to better isolate the region viewed by the detector. The remaining three traces are different shots using different backlighter energies and filtering on the detector. There is a very strong peak at ~ 6.4 keV, which is most likely caused by the fluorescence of the iron target sample. There are weaker peaks that begin to fall into the signal to noise, which are consistent with x-ray diffraction. We can use these results from the current

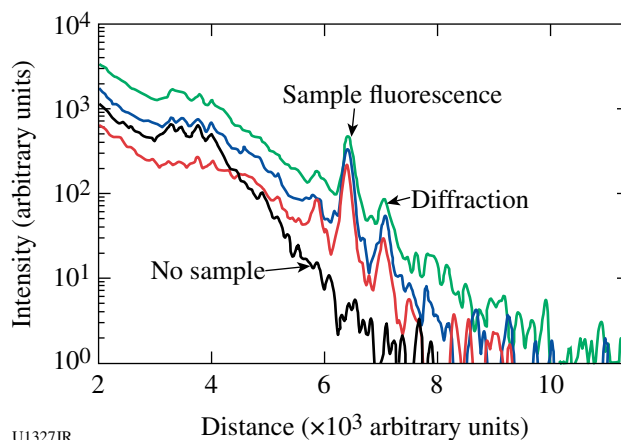


Figure 128.89

The energy-corrected single-photon-counting data from the experiment. The black line is the backlighter when there is no target sample.

configuration to determine a better experimental configuration that will yield higher diffracted photons on the detector.

Equation of State for Foam

Principal Investigator: J. Hawreliak

Low-density foams are currently being used and will continue to be used as materials in complex integrated experiments to model astrophysical phenomena, particularly for the formation and growth of density-driven hydrodynamic

instabilities. The shock response of the low-density foam is very important to the modeling, developing, and interpretation of these experiments. While velocimetry techniques have been used to measure the shock speed in transparent foams, there is a programmatic and scientific need to get a Hugoniot equation of state in opaque carbon-based foams. To do this, we will use *in-situ* radiography to measure the shock speed and shock density along with the Hugoniot conservation relations to determine the EOS.

The experiment used 16 beams to generate a Ti K-shell backlighter and four stacked beams to generate an ~ 10 -ns drive. When the shock propagated 10 ns into the target, we recorded multiple radiographs over 1 ns using an x-ray framing camera. Figure 128.90(a) is a VISRAD representation of the experiment.

Unfortunately, because of the hot temperatures, we were only able to get two shots, but the data shown in Fig. 128.90(b) are of excellent quality. The data are currently being analyzed but a first calculation of the shock speed is ~ 20 km/s.

Gigabar Equation of State

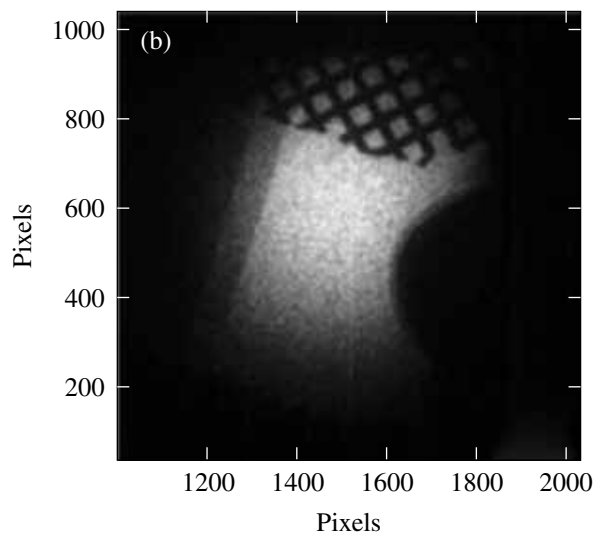
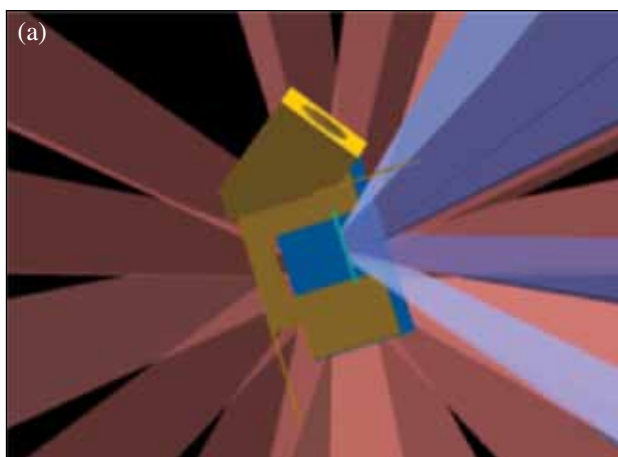
Principal Investigator: J. Hawreliak

The HEDP regime is where the energy density of a system is comparable to the binding energy density of a hydrogen

molecule, i.e., ~ 1 Mbar. We can define an atomic unit of pressure in the same fashion as the ground-state energy density of a hydrogen atom, which is ~ 300 Mbar. As we approach the atomic unit of pressure, we would begin to expect the core and inner shell electrons to be perturbed by the applied pressure. This will lead to novel chemistry and interesting science at high pressures. To achieve these high pressures, we used a convergent spherical geometry. Unlike a planar target, the applied shock pressure increases in strength as it approaches the center.

The experiments performed on the OMEGA laser used 40 beams on the P6–P7 axis in a hohlraum to indirectly drive a converging shock into a spherical capsule of polyacrylamide (PAM). Two backlighters were used to investigate the shock wave in the solid capsule. A gated framing camera on the P6–P7 axis was used to capture images, while an x-ray streak camera recorded a time-resolved radiograph on the axis of the capsule. Figure 128.91(a) shows a VISRAD view of the target configuration. In this configuration we can measure the equation of state by getting two points on the Hugoniot, the shock speed from the time-resolved measurement, and the density from the radiograph.

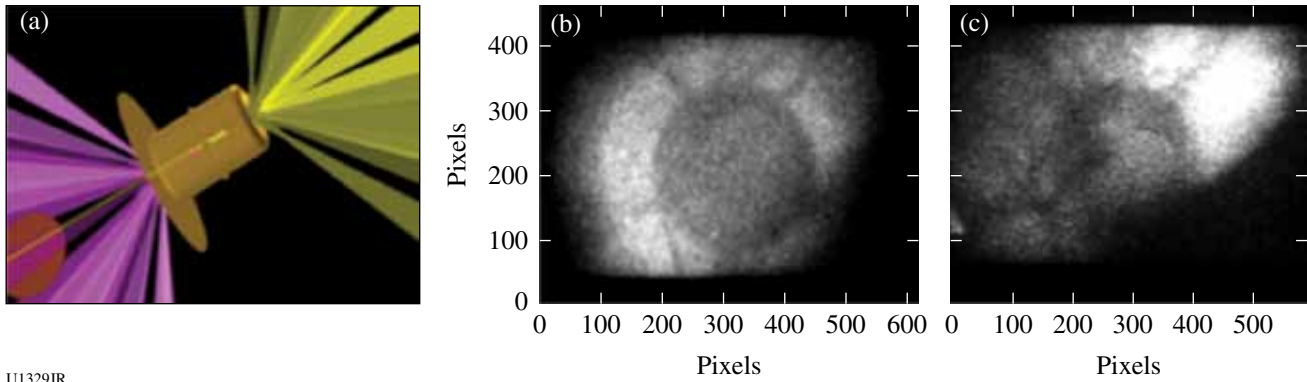
Figure 128.91(b) shows radiograph images of the shock wave in the capsule at two different times. These images were taken after the drive beams were turned off because of the x-ray signal from the hohlraum overwhelming the radiograph



U1328JR

Figure 128.90

(a) A VISRAD model of the experiment from a TIM-4 view; (b) a radiograph taken using an XRFC on TIM-4.



U1329JR

Figure 128.91
 (a) A VISRAD model of the experiment, (b) a radiograph of the capsule, and (c) radiograph 1 ns later.

signal. We see clear evidence of the shock wave propagating into the capsule, so while analysis is ongoing, we estimate the shock speed to be 80 km/s.

Double Pulse

Principal Investigators: B. R. Maddox and A. Comley

The goals of this campaign were to measure the sensitivity and the modulation transfer function (MTF) of the x-ray framing camera at 8 keV and 22 keV and to measure the conversion efficiency of a Cu microflag x-ray source using a 100-ps UV pulse. To measure the sensitivity of the x-ray framing camera (XRFC), we used Cu and Ag backlighters and placed filters in front of both the HERIE detector (on TIM-13) and the XRFC (on TIM-10). The filters consisted of a Ta mask and sets of filter steps placed over holes machined into the Ta mask. For the Cu shots, the filters were Cu and Al steps, and for the Ag shots, the filters were Ag and Ta steps with an additional Mo/Pd Ross pair. For the resolution tests, targets consisted of double-ended Au resolution grids aimed at TIM-13 and TIM-10, which were backlit using 5- μ m-thick Cu and Ag microflags. After a slow start and an issue with one of the Target Viewing System shutters, we were able to obtain high-quality data on all shots, resulting in data that will be used to calculate the sensitivity and resolution of the XRFC at 8 and 22 keV. Figure 128.92 shows a sample image from shot 10050 of the Au grid projected onto a single-strip XRFC using a 22-keV Ag backlighter. We also obtained very good conversion efficiency data using the single-photon-counting (SPC) camera for the 100-ps UV pulse, finding that the conversion efficiency (CE) at 8 keV was only a factor of 2 \times lower than that using a 1-ns UV pulse, with CE = 3.5 \times 10⁻³ for the 100-ps UV pulse.



U1330JR

Figure 128.92
 Radiograph collected on a single-strip XRFC of a Au grid backlit using a 5- μ m-thick Ag microflag.

Lattice Dynamics and Dynamic Diffraction

Principal Investigator: B. R. Maddox

The goal of these campaigns was to develop Bragg diffraction using a petawatt backlighter and to study single-crystal Mo shock compressed along the [111] direction using angle-dispersive Bragg diffraction. These campaigns produced a significant improvement in the quality of Bragg diffraction obtained using a petawatt backlighter, primarily because of the high-quality surface polish conducted at LLNL to remove a thick layer of damage from the rough manufacture polish

and also a new improved beam block design. Bragg diffraction requires one to block the x rays directly from the x-ray source while letting the diffracted x-rays pass. In these experiments the backlighter was a 250- μm -diam, 12- μm -thick Mo foil driven by the OMEGA EP backlighter beam, defocused to 200 μm and using a 100-ps pulse length. The new beam block design is specially shaped to avoid exposed corners, which can produce strong self-emission. The new design is also much closer to the x-ray source, effectively blocking all of the direct x rays while allowing one to use the Target Viewing Systems (xTVS and yTVS) for positioning. A representative diffraction image is shown in Fig. 128.93. Observed in this image are the diffraction lines from the shocked lattice and the unshocked lattice in front of the shock wave. The strong lines are diffraction 17-keV Mo K_{α} x rays while the faint lines are diffracted K_{β} x rays. Data spanning all three campaigns resulted in shock-compressed Mo data from 10 GPa to 40 GPa. A transition from elastic compression to plastic flow was observed at ~ 15 GPa. The diffraction data have been analyzed to extract the yield stress and the von Mises stress. We also observed plastic relaxation times $\ll 1$ ns above 15 GPa. These results are currently being prepared for publication.

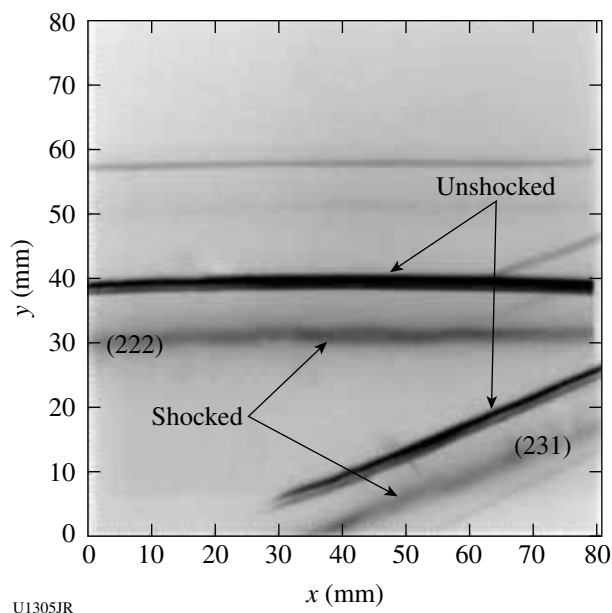


Figure 128.93
Laue diffraction pattern obtained from a single-crystal Ta shock along the [001] direction using a 20.6-J, 1-ns-long UV laser drive.

Tantalum Rayleigh–Taylor Experiments (ICETaRT)

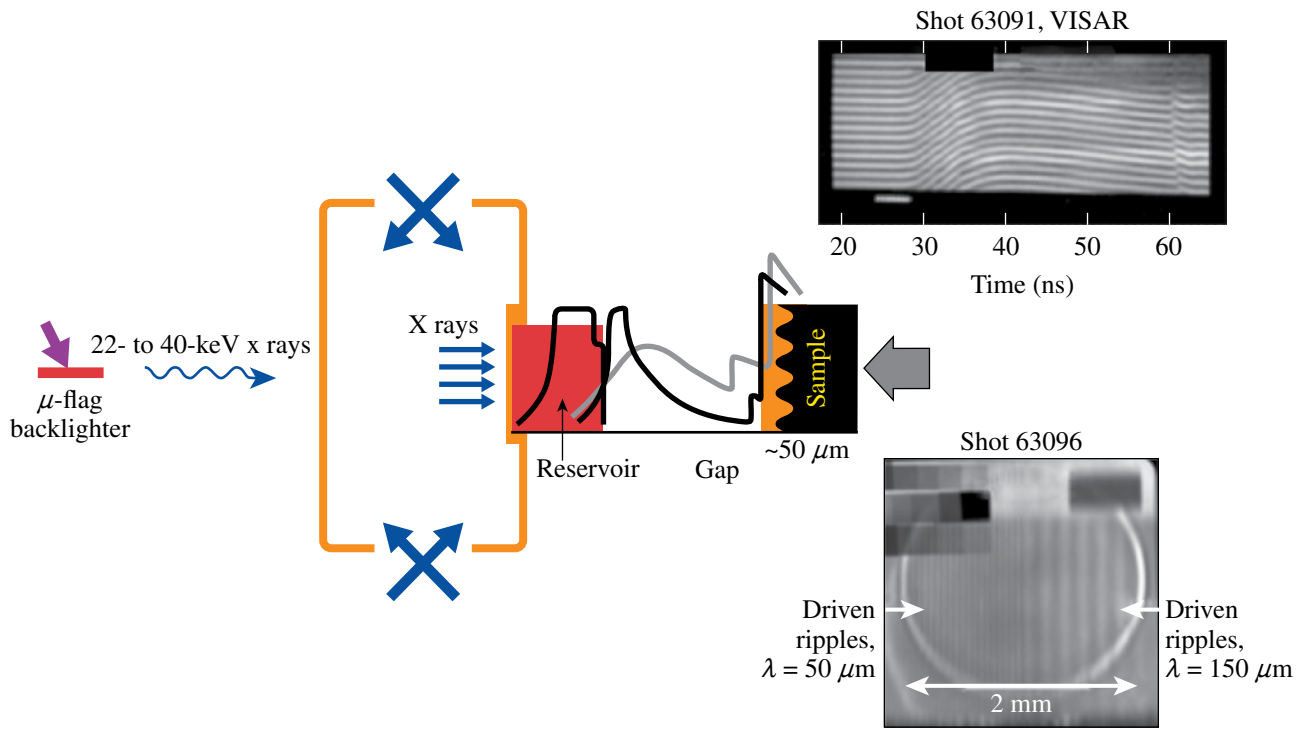
Principal Investigator: H.-S. Park

The goal of the ICETaRT campaigns is to measure dynamic properties of solid-state tantalum (Ta) under high pressures (>1 Mbar) and high strain rates (10^6 to 10^8 s^{-1}). We achieve quasi-isentropic high-pressure conditions by using a unique reservoir–gap–sample configuration, where the sample materials stay well below the melting temperature while they are plastically deforming under high pressure, as shown in Fig. 128.94. This year's campaign studied tantalum material strength properties under these conditions by measuring the growth attributable to the Rayleigh–Taylor (RT) instability in accelerated samples containing a preimposed sinusoidal ripple. We obtained two types of data from each set: drive measurement using the VISAR and face-on radiography using the 20-keV Ag K_{α} backlighter via the OMEGA EP short-pulse laser. We have obtained a series of successful radiographs over these campaigns. The radiometrics of the Ta stepped data are carefully analyzed to derive the $\rho\Delta Z$ of the ripple growth. The growth factor GF is then defined to be

$$GF = \frac{(\rho\Delta Z)_{\text{driven}}}{(\rho_0\Delta Z_0)_{\text{undriven}} \cdot \text{MTF}}, \quad (1)$$

where ρ_0 and ΔZ_0 are initial density and ripple amplitude, respectively, from the pre-shot metrology and MTF is the modulation transfer function measured by the knife edge. Figure 128.95 shows the ripple growth factor as a function of time from the 50- μm -wavelength samples. The simulation results from various material-strength models are also plotted in Fig. 128.95. Note that only the multiscale model fits the data well, which attempts to connect atomistic level behavior to the continuum-level plastic flow using density functional theory, molecular dynamics, dislocation dynamics, and continuum simulations to calculate yield strength. The details of this model are described in Ref. 74.

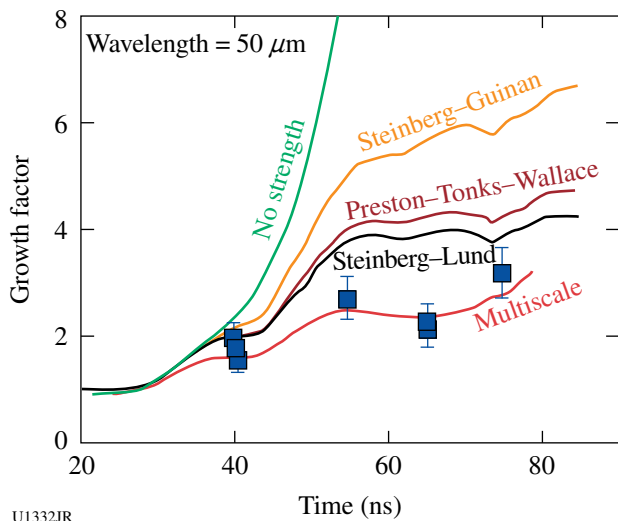
Flow stress is the stress that is needed for the metal material to flow plastically at a given loading condition and state. The inferred average flow stress using the multiscale model, averaged over the sample with e^{-kz} weighting (where $k = 2\pi/\lambda$ and z is the depth into the foil), is ~ 60 kbar, which is $\sim 8\times$ higher than the Ta ambient flow stress of 7.7 kbar. We find that the flow



U1331JR

Figure 128.94

ICETaRT experiment configuration for an OMEGA/OMEGA EP joint shot. We take two types of data on each set: drive data using the VISAR and face-on radiography using the OMEGA EP-generated high-energy backlighter.



U1332JR

Figure 128.95

Ta Rayleigh-Taylor growth factors as a function of time. The data points are noted as the blue squares. Various material-strength model predictions are plotted.

stress is largest when the strain rate is the largest, indicating that the strain-rate hardening is a dominant factor. From the pressure-dependent shear modulus calculation, the pressure hardening is about a factor of 2, with the remaining factor of 4 because of strain-rate hardening. This result has been submitted and accepted for publication.⁷⁵

The FY11 campaign also completed a study of the Ta grain-size effect on the strength under high-pressure and high-strain-rate conditions. While there are many strength measurements of Hall-Petch grain size scale at ambient conditions,⁷⁶ neither previous theory nor experimental measurements under high-pressure dynamic conditions exist. We fabricated three different types of targets that have average grain sizes of 92 μm, 15 μm, and 0.25 μm as shown in Fig. 128.96(a). The face-on radiography data are analyzed in a similar fashion as described above, and the normalized growth factor versus the average grain size is plotted in Fig 128.96(b). The conventional understanding is that the yield strength is stronger with smaller grain sizes known as the Hall-Petch effect and is formulated by $\sigma \sim \sigma_0 + kD^{-1/2}$, where σ is the yield strength, D is the average

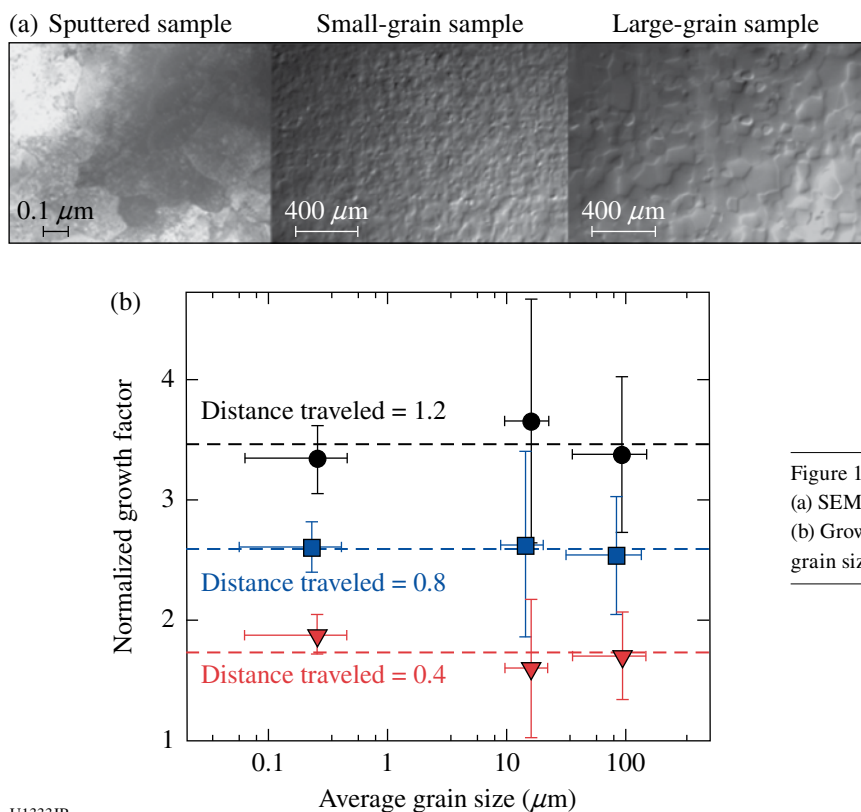


Figure 128.96

(a) SEM and TEM pictures of the different Ta grain-size samples. (b) Growth factor, a measure of material strength, as a function of grain size. No obvious Hall–Petch effect is observed.

U1333JR

grain-size diameter, and σ_0 and k are characteristic coefficients for different materials. This relation is known to hold for many materials. This is because the dislocations, whose mobility quantifies the strength, are pinned against the grain boundary, restricting their mobility. We consider two postulations of why we see no Hall–Petch effect: (1) In our experiment, the dislocations have not moved to the grain boundaries at our times scale of <100 ns; and (2) the work hardening is a dominant factor rather than the grain-size hardening. Our experimental results will be submitted for publication in *Nature Materials*.

ICEDrive-11A/ICEHohl-11A

Principal Investigators: M. May and A. Comley

The ICEDrive-11A and ICEHohl-11A campaigns were conducted at the Omega Laser Facility as part of the ramped-drive platform development required for the tantalum-strength Rayleigh–Taylor experiment on the NIF. Both half-day campaigns were fielded on the same day and used the 2.5-scale indirect-drive platform developed in the ICETaRT series of experiments, with slight variations in the drive package designed to address various issues as described below.

The ICEDrive-11A target packages are shown in Fig. 128.97. The hohlraum drive is incident on the beryllium ablator shown

in the figure. The BrCH (and foam layers if applicable) constitute the reservoir that releases across the gap, thereby generating a ramped pressure wave at the tantalum layer. The ramp drive is characterized using VISAR and SOP. The ICEDrive-11A experiments were designed to test VISAR measurement handoff from thin ($100\text{-}\mu\text{m}$) LiF to thick (1-mm) quartz at pressures of >2 Mbar (a key component of the NIF 5-Mbar drive target designs), test two-layer reservoir foam repeatability, provide further experience with diagnosing the drive through a releasing LiF reservoir, and provide a reference drive shot for the ICEHohl-11A experiments later in the day.

All six target shots returned good data from primary diagnostics VISAR, Dante, and SOP. The peak drive T_r measured from Dante is currently higher than previous campaigns by 3 to 8 eV. The drive (deviating in the opposite direction), as measured by VISAR, is lower by $\sim 15\%$.

The ICEHohl-11A target packages are shown in Fig. 128.98. The ICEHohl-11A experiments had two objectives. First, in the tantalum strength Rayleigh–Taylor experiment (ICETaRT), a plastic (CH_2) heat shield was placed over the front of the tantalum sample to insulate it from the heating effects of the unloading reservoir. The ability of CH_2 to act as a thermal insulator to the stagnating plasma in a planar geometry was

Type D1	Type D2	Type D3
NIF T_c/T_{melt} match	>2-Mb ramp High Pressure on Qz	Reference plasma drive
Be, 25 μm 12.5% BrCH, 50 μm 500-mg/cc CRF, 50 μm 500-mg/cc CRF, 100 μm 400- μm gap Ta, 10 μm LiF 100 μm LiF 1000 μm	Be, 25 μm 12.5% BrCH, 50 μm 500-mg/cc CRF, 50 μm 500-mg/cc CRF, 100 μm 400- μm gap Ta, 10 μm LiF 100 μm Qz 500 μm AR coating important Quartz is in the z direction (001)	Be, 25 μm 12.5% BrCH, 200 μm 400- μm gap 150 \pm 25- μm gap between Ta layers Ta, 50 μm Ta, 10 μm LiF 1000 μm
Quantity 2	Quantity 2	Quantity 2

U1334JR

Figure 128.97
ICEDrive-11A target packages.

Type H1	Type H2	Type H3
One vacuum hohlraum One gas-filled hohlraum	Gas-filled hohlraum	Vacuum hohlraum
Be, 25 μm 12.5% BrCH, 200 μm 400- μm gap Ta, 50 μm Ta, 10 μm LiF 1000 μm	Be, 25 μm 12.5% BrCH, 200 μm 400- μm gap CH ₂ , 15 μm Ta, 10 μm LiF 1000 μm	Be, 25 μm 12.5% BrCH, 200 μm 400- μm gap CH ₂ , T1 CH ₂ , T2 LiF 1000 μm Ti flash coating
Quantity 2 SRF 32912, 33584	Quantity 2 SRF 33585, 33586	Quantity 1 each SRF 33561(H3A), 33583(H3B)

	T1/T2
H3A	15/20 μm
H3B	5/10 μm

U1335JR

Figure 128.98
ICEHohl-11A target packages.

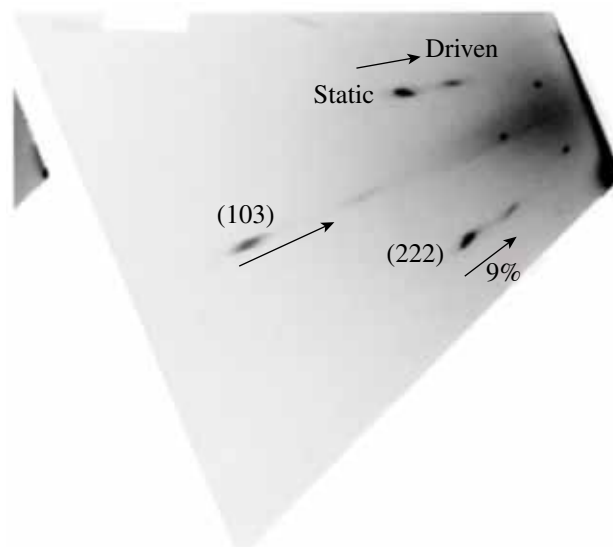
demonstrated (H3 target in Fig. 128.98) using streaked optical pyrometry. No thermal burnthrough was observed, in agreement with tabular electron-conductivity values.

The second objective was to test the performance of gas-filled hohlraums, particularly with the goal of mitigating late-time shock formation caused by hohlraum stagnation and late-time Tr effects. We tested three neopentane-filled hohlraums, with nominal gas pressures of 26, 129, and 180 Torr. It was found that the timing of the late-time shock could be influenced by the choice of gas fill. With increasing gas-fill pressure, the late-time shock was observed to arrive earlier: the shock time measured relative to the start of the initial ramp for the 180-Torr case was seen to shift ~ 4 ns earlier compared to the 129-Torr case.

Strength Diffraction

Principal Investigator: B. R. Maddox

The goals of this campaign were to study single-crystal Ta shocked along [001] using Laue diffraction and to measure the broadband x-ray output of a 1-ns UV pulse-driven foil source to that of a 44-beam imploded CH shell source using the dual-crystal spectrometer (DCS). This campaign was also used to test a new Ta crystal target construction scheme to keep the $5\text{-}\mu\text{m}$ -thick Ta single crystals as strain-free as possible. Laue diffraction was obtained using the broadband x-ray diffraction (BBXRD) diagnostic on TIM-4. Dante was used to time the capsule implosion for precise timing between the Ta crystal drive and the x-ray bang time. The results show that the new target construction scheme using a $10\text{-}\mu\text{m}$ n-HDC ablator glued to a Ta crystal with a $40\text{-}\mu\text{m}$ -thick u-HDC tamper effectively kept the Ta crystal from warping and produced high-quality static and shocked-diffraction patterns. Figure 128.99 shows a sample diffraction pattern from one of the image plates of the BBXRD from a Ta sample driven using 20.6 J in 1 ns. Diffraction spots from the shock-compressed lattice and the unshocked lattice ahead of the shock wave are evident in the image. This particular image corresponds to a 9% difference between the longitudinal and lateral strains. High-quality data were also obtained on the broadband spectrum of a Mo-foil backlighter driven by four UV beams at maximum energy with 1-ns pulse lengths, overlapped in space and time onto a 1-mm-diam, $12.5\text{-}\mu\text{m}$ -thick Mo foil. The results showed that the broadband emission of the Mo foil in the 10- to 20-keV range was $\sim 10\times$ lower than that from the imploded CH-shell backlighter. Subsequent campaigns will continue to use the CH shell as the broadband x-ray source for Laue diffraction.



U1336JR

Figure 128.99

Laue diffraction pattern obtained from a single-crystal Ta shock along the [001] direction using 20.6-J, 1-ns-long UV laser drive.

2. High-Temperature Plasma Opacity

High-Temperature Plasma Opacity Experiments on OMEGA and OMEGA EP

Principal Investigators: R. F. Heeter, S. Chen, G. V. Brown, and R. E. Marrs

LLNL opacity research in FY11 had four main directions: First, the MBOP-11 campaign followed up on physics questions from the very successful 2009–2010 Ti opacity shots, where the observed Ti continuum opacity and 1 to 3 line opacity regions did not match code expectations. The new data using thinner samples extended this data by a factor of 4 in sample ρL , pushing the K-shell absorption technique to its optically thin limit. As shown in Fig. 128.100, spectral absorption line positions from charge states consistent with $\sim 120\text{-eV}$ LTE sample temperatures are observed, now with 40% transmission. The new data continue to match the codes quite well, and detailed comparisons are in progress for the continuum and line-gap opacities, where disagreements with older data remain.

The second campaign, NEAHiZ-11, resumed previous work on the non-LTE x-ray emission properties of hot gold plasmas as found in hohlraums at the laser-driven “hot spots.” Shots performed in late FY11 extended earlier work to $2\times$ lower intensity (material temperature) and the data are now being compared with simulations.

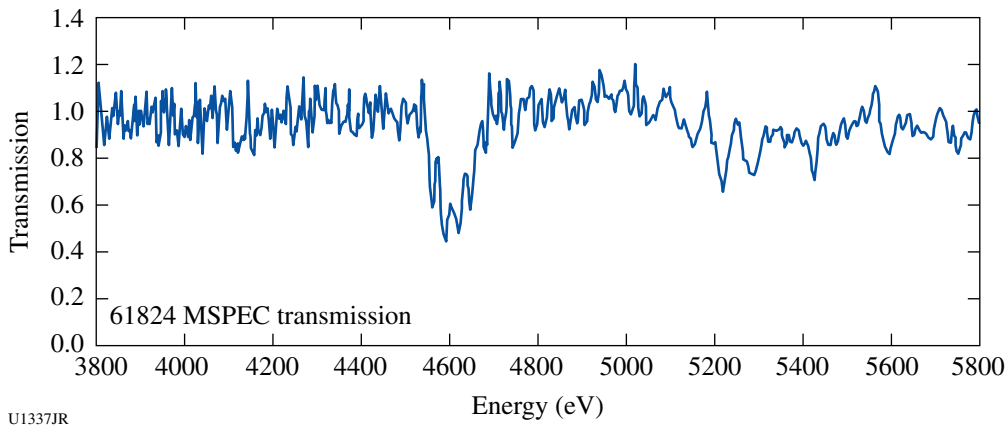


Figure 128.100

A Ti K-shell transmission spectrum with a 0.17- μm Ti sample. Foil expanded to 70 μm from initial 0.17 μm . Sample thickness was reduced 4 \times from earlier experiments, bringing K-shell features to >40% transmission. Ionization features for F, O, N, and C-like Ti indicate a temperature of 120 eV.

NEAHiZ-11 also supported a third line of inquiry to improve the signal/noise of gated opacity measurements. As part of the non-LTE measurements, the relative sensitivity of XRFC1 [50-ps pulse-forming module (PFM)] was compared with XRFC4 [new microchannel plate (MCP), 400-ps PFM]; the latter showed roughly 300 \times greater sensitivity for x rays from 250 to 1800 eV, using nearly identical snout setup and target views. The noise in both measurements is similar (therefore, not photon limited) and subsequent investigations established a signal/noise limit of 20:1 for film-based gated x-ray imaging with 60- to 100- μm spatial resolution. This ratio is limited by the film itself and not the scanner or XRFC components. The ratio may be increased by averaging over wider sections of film, or perhaps by modifying the film-developing process.

The fourth research direction was the EPOp-11 series, which successfully developed a novel short-pulse “absorption-emission” opacity platform on OMEGA EP. The initial goal was to cross-check short-pulse heated opacity measurements against similar long-pulse data (Fig. 128.101). Absorption experiments at higher densities and temperatures are possible but maintaining LTE conditions is difficult. In the FY11 experiments, the OMEGA EP sidelighter beam delivered 250 to 900 J in 100 ps with a broad focus to heat Al/Ti/Al₂O₃ opacity samples at 10¹⁵ to 10¹⁶ W/cm² intensities. The OMEGA EP backlighter beam, delayed by 200 to 300 ps, delivered 800 to 1500 J in 10 ps near best focus, driving a broadband 3- to 6-keV backlighter whose x rays probed the hot, expanded opacity sample. Figure 128.100 shows K-shell x-ray absorption from L-shell Ti ions (F, O, and C-like Ti) at $T > 100$ eV. The inferred tempera-

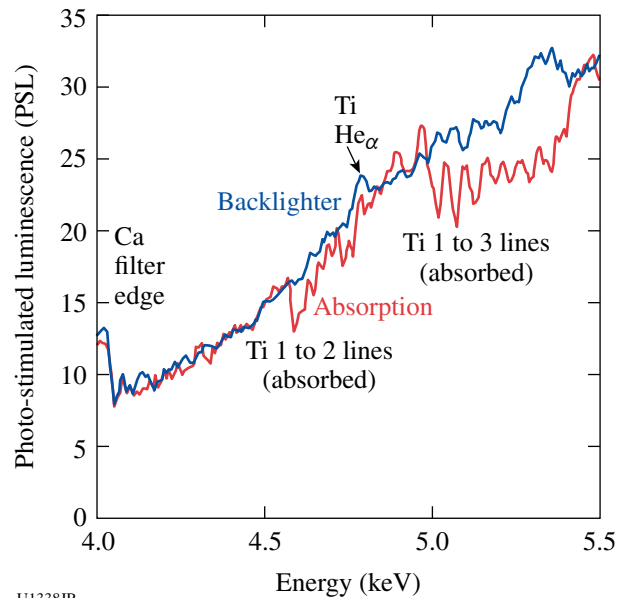


Figure 128.101

First Ti K-shell absorption spectrum from OMEGA EP opacity experiments. Similar charge states are seen in the OMEGA EP experiment as in the OMEGA experiment.

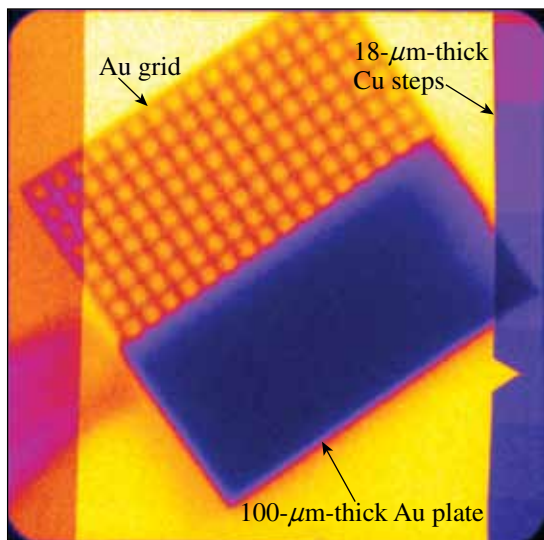
ture is below the ~ 1000 -eV temperatures predicted by the 1-D hydrocodes *HELIOS* and *HYDRA*. Imaging in the transverse direction shows an expansion of ~ 50 μm (density of ~ 0.05 g/cc) at the time of this measurement. A separate line of sight enabled us to take space- and energy-resolved sample emission spectra in the 250- to 1600-eV spectral band, which shows similar levels of expansion and ionization.

3. Hydrodynamics

Short-Pulse, UV Backlighting Development for the NIF

Principal Investigator: V. A. Smalyuk

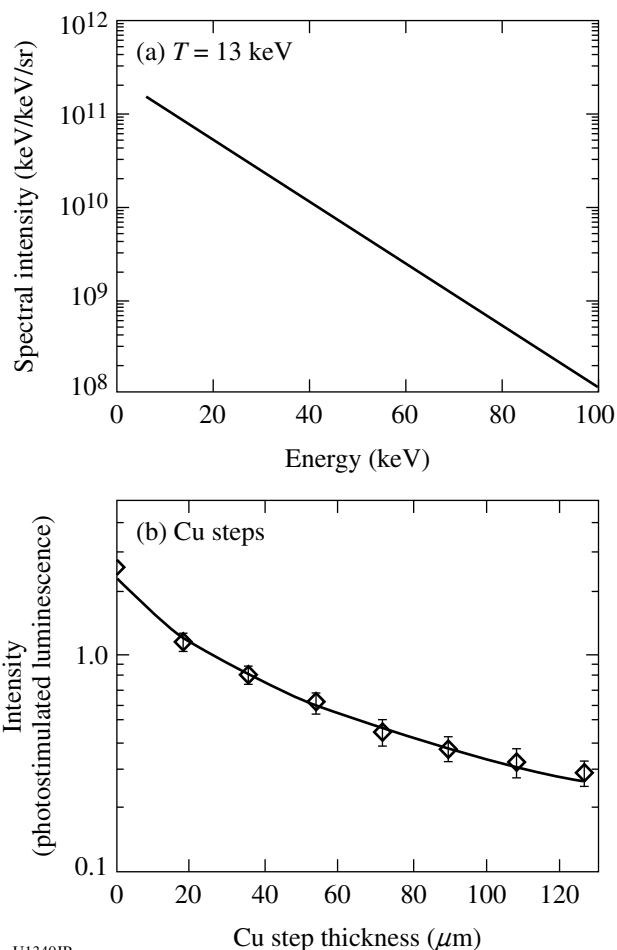
High-energy-density complex hydrodynamics experiments on the NIF require short-pulse–backlighting capability. Experiments on the OMEGA EP laser tested the short-pulse, UV beam backlighting concept for the NIF. Four OMEGA EP beams were focused onto 10- μm -thick Ag wires, mounted on $300 \times 300\text{-}\mu\text{m}$ -sq, 10- μm -thick polyimide foils to mimic illumination conditions of one quad on the NIF. The total laser energy was $\sim 400\text{ J}$ with an $\sim 100\text{-ps}$ Gaussian pulse shape and a peak laser intensity of $\sim 3 \times 10^{16}\text{ W/cm}^2$. Beam mistiming was $< 50\text{-ps}$ rms and mispointing was $< 50\text{-}\mu\text{m}$ rms. Results were compared with $\sim 1.2\text{-kJ}$ short-pulse ($\sim 100\text{-ps}$) IR beam backlighting with the same Ag-wire targets, driven at an intensity of $\sim 1 \times 10^{17}\text{ W/cm}^2$. Figure 128.102 shows a measured image of the target created with Ag-wire backlighting on an image plate using the high-energy radiographic imager (HERIE) diagnostic located 50 cm from target chamber center on OMEGA EP. It consists of the Au grid used to determine magnification, a 100- μm -thick Au plate used to determine resolution, and seven Cu steps with 18- μm thickness between adjacent steps used to determine contrast and sensitivity. Areas inside and outside of the Au plate were also used to measure noise. Figure 128.103(a) shows an inferred backlighter spectrum, determined by fitting measured intensity at different Cu steps [shown as diamonds in Fig. 128.103(b)].



U1339JR

Figure 128.102

X-ray radiograph of the target consisting of an Au grid, a 100- μm -thick Au plate, and seven 17- μm -thick Cu steps.



U1340JR

Figure 128.103

(a) Inferred backlighter spectrum, determined by fitting measured intensity in Cu steps, shown in (b) with diamonds. The thick solid line shows a fit to the data assuming an exponential spectrum with temperature of $13 \pm 2\text{ keV}$, presented in (a).

The solid line in Fig. 128.103(a) shows a fit to the data, assuming an exponential backlighter x-ray spectrum with a temperature of $13 \pm 2\text{ keV}$. The inferred temperature was $\sim 100\times$ lower than in experiments with a short-pulse IR beam, while the signal intensity in areas outside the Cu steps (about 2 photostimulated luminescence (PSL)) was decreased by $\sim 100\times$. The $\sim 20\text{-}\mu\text{m}$ spatial resolution was similar to IR-beam experiments, while noise was $\sim 2\times$ higher. The short-pulse UV backlighting might be feasible for complex hydrodynamics experiments on the NIF if hohlraum x-ray backgrounds (generated by mostly hot electrons from Raman laser–plasma instability) do not exceed $\sim 10\text{ PSL}$ on the image plate at 50 cm from the NIF target chamber center. The first complex hydrodynamics experiments on the NIF will measure and mitigate, if necessary, these backgrounds before radiography experiments. The next

campaign on OMEGA EP will be devoted to maximizing the x-ray backlighter signal by scanning a temporal advance of one of the beams with respect to other drive beams.

Backlighting Experiments on OMEGA

Principal Investigator: V. A. Smalyuk

Backlighting experiments were performed on the OMEGA Laser System to study the symmetry of foam balls illuminated with hohlraum x rays. Backlighter targets were driven either with short-pulse IR beams in joint OMEGA EP experiments, or with UV beams in OMEGA-only experiments. In a joint OMEGA EP configuration, 10- μm -thick Ag wires, mounted on $300 \times 300\text{-}\mu\text{m}$ -sq, 10- μm -thick polyimide foils were irradiated with an $\sim 1.2\text{-kJ}$ short-pulse ($\sim 100\text{-ps}$) IR beam at a laser intensity of $\sim 1 \times 10^{17} \text{ W/cm}^2$. X-ray radiographs of targets were measured on image plates using the HERIE diagnostic placed $\sim 50 \text{ cm}$ from target chamber center with a magnification of ~ 50 . In the OMEGA-only configuration, six OMEGA beams irradiated Ni point-projection backlighter at a laser intensity of $\sim 1 \times 10^{16} \text{ W/cm}^2$. Time-resolved (with $\sim 80\text{-ps}$ temporal resolution) x-ray radiographs of targets were measured on a framing camera with a magnification of ~ 20 . Experiments were very successful, producing high-quality radiographs that set up a baseline for future complex hydrodynamics experiments at the NIF.

4. X-Ray Source Development and Applications

Iron K-Shell X-Ray Source Development

Principal Investigator: K. Fournier

The X-Ray Source Development team, in collaboration with the Defense Threat Reduction Agency and researchers from the French CEA, conducted two campaigns in FY11 that developed and optimized two very different iron K-shell $\sim 6.7\text{-keV}$ x-ray sources. The two sources that were studied were ultralow-density iron-oxide aerogel materials ($\text{FeOOHCl}_{0.38}$) and stainless-steel-lined (SS-304) cavities (see Fig. 128.104). The density of the aerogel targets ranged from 3 to 16 mg/cm^3 , which resulted in laser-created plasma-radiation sources with densities between 10% to 50% of OMEGA's critical density. The critical measurements included x-ray spectral output from the sources, x-ray images of the volume heating of the target plasma, and streaked images of laser heating in the targets. Side-by-side images of the heated aerogel and foil-lined cavity targets are shown in Fig. 128.104. Results so far show that the aerogel material at 6 mg/cm^3 produced the highest-fluence, 6.7-keV output at $43.1 \pm 9.4 \text{ J/sr}$, which is a 2.9% laser-to-x-ray

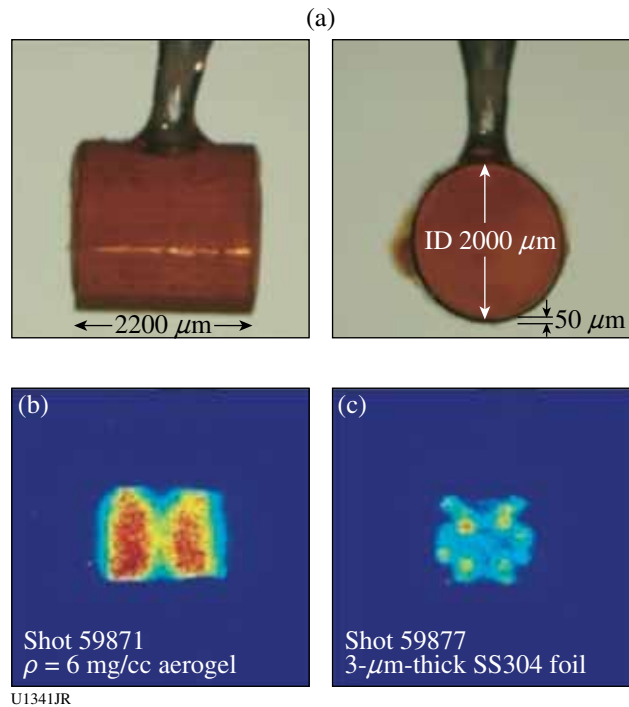


Figure 128.104

(a) Side-on and face-on views of a 12-mg/cm^3 iron-oxide aerogel target for Fe K-shell-11A shots, (b) x-ray framing camera (XRFC) image at 6.7-keV x-ray energy of a 6-mg/cm^3 aerogel target at $t = 1.0 \text{ ns}$, and (c) XRFC image at 6.7-keV x-ray energy of a 3-mm -thick steel-lined cavity at 0.8 ns . The Fe K-shell emission from the aerogel target is much brighter than from the foil-cavity target.

conversion. The Fe K-shell yield (6 to 8 keV) of the aerogel targets for three different densities is shown in Fig. 128.105. When measured over all x-ray energies, the targets yielded $\approx 850 \text{ J/sr}$ and $\approx 1220 \text{ J/sr}$ for aerogel and steel-lined cavities, respectively. These targets show promise for reproducible, high-flux, high-fluence x-ray sources to be used in NIF experiments in FY12 and beyond.

Solar Cell Electrostatic Discharge

Principal Investigator: K. Fournier

The X-Ray Source Development team, in collaboration with the Naval Research Laboratory and the Defense Threat Reduction Agency, has begun researching whether we can use the OMEGA target chamber as a test environment for investigating electrostatic discharge phenomena in solar-cell technology. Our initial steps in this process are to characterize the charged-particle flux (both electrons and ions) created by our laser-driven x-ray source before moving on to more-sophisticated tests of biased solar cells and solar-cell arrays. Our first experiments conducted on 14 September 2011 involved the fielding of arrays

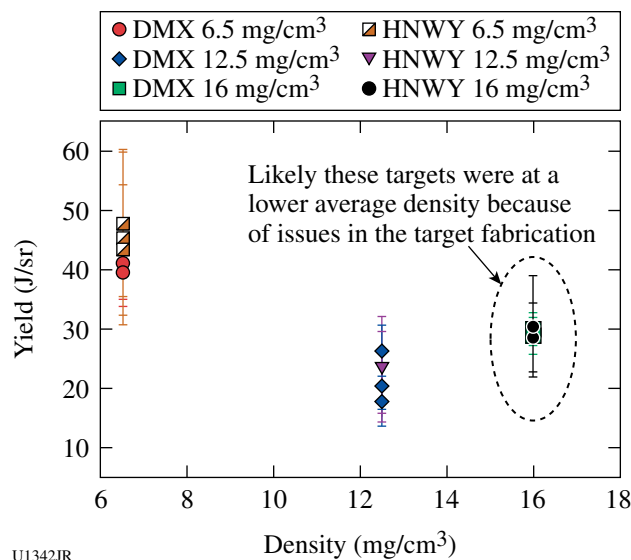


Figure 128.105
Measured Fe K-shell yields in the energy range of 6 to 8 keV for iron-oxide aerogel targets of different densities. The measurements were taken with the CEA diagnostic DMX and the LLNL diagnostic HENWAY; the two diagnostics show excellent agreement.

of Langmuir probes in TIM's that looked at the open face of our x-ray source targets and looked orthogonally to the target's axis. The two lines of sight provided quantitative measurements of x-ray-driven signals on a nanosecond time scale and electron and ion signals on the microsecond time scale. A photograph of one of our probe arrays is shown in Fig. 128.106. The Langmuir probe diagnostic is a new diagnostic created by modifying the x-ray source application (XRSA) cassette that we have used on many previous radiation-effects experiments. We will return to the development of this platform in FY12 with arrays with a greater number of probes on each shot that will allow us to map out the voltage-current curve for the passing ion and electron



U1343JR

fluxes and, ultimately, an investigation of the response of a solar-cell array operating under bias to x-ray loading.

FY11 LANL Experimental Programs—Overview

In FY11, Los Alamos National Laboratory (LANL) executed 223 total shots: 195 on the OMEGA Laser System and 28 on the OMEGA EP Laser System. LANL experiments contributed to the National Ignition Campaign in the following ways:

- Measured the x-ray ablative Richtmyer–Meshkov growth of isolated defects on plastic ablators
- Studied branching ratios in DT-fusion plasmas
- Measured the shape of the DT-fusion gamma-ray spectrum
- Continued neutron-imaging development for the NIF

HED campaigns included

- Study of shear and reshock-driven turbulent mixing
- Backlit defect implosion experiments to study the effect of trench defect
- Measuring the effect of capsule asymmetries on neutron yield and ion temperature
- Platform development for dense plasmas and warm, dense matter equation of state
- Measurement of a supersonic radiation wave
- Energetic ion generation for dynamic defect studies

CHaRM: The CHaRM campaign had two outstanding shot days in FY11 where the shock speed and bump's areal-density evolution were measured for multiple bump sizes and target conditions. Existing defects (bumps or divots) on ICF capsules can cause jetting of high-Z material into the hot spot during an implosion, an undesirable consequence of late-stage RT growth. The ablative Richtmyer–Meshkov (aRM) growth sets

Figure 128.106
An XRSA cassette fitted with two sets of Langmuir probes ready for delivery to the TIM for positioning in the OMEGA laser chamber. The probes measure electron- and ion-particle fluxes passing by their location following laser-irradiation of the x-ray source target at TCC.

the initial conditions for subsequent RT, so the aRM must be understood and controlled to optimize late-time capsule stability. The ablation process of aRM stabilizes the early-stage growth and is even predicted to decrease the amplitude of the initial perturbation. Ignition attempts will consider tailored driving pulse shapes designed to minimize the perturbation amplitude at the onset of RT. Experiments conducted at the Omega Laser Facility are being used to determine the time at which bump amplitudes approach zero for specified target conditions (electron temperature, density).

Nine to fifteen laser beams from OMEGA were used to create a moderate-temperature (70-eV) radiation environment inside a gold halfraum ablating and driving the aRM growth of a 2-D array of Gaussian-shaped bumps (see Fig. 128.107). On-axis, area-backlighting x-ray radiography measured the bump's areal density at different times following the driving laser pulse by recording the transmission of the 2.8-keV Cl He α line (from saran) through the bumped target with an x-ray framing camera. Summing over all of the identical bumps in the array from the raw radiograph allowed us to construct a composite bump with improved statistics. Averaging lineouts extracted around the azimuth of the composite bump improved statistics even further, resulting in an optical depth radial position bump profile that is converted to areal density using a known calibration on each shot. The areal density at bump center for various times is then compared to simulations of the target geometry.

Before 1-to-1 comparisons can be made, target conditions must be measured independently so that simulations can be tuned to match target conditions in the experiments. This is

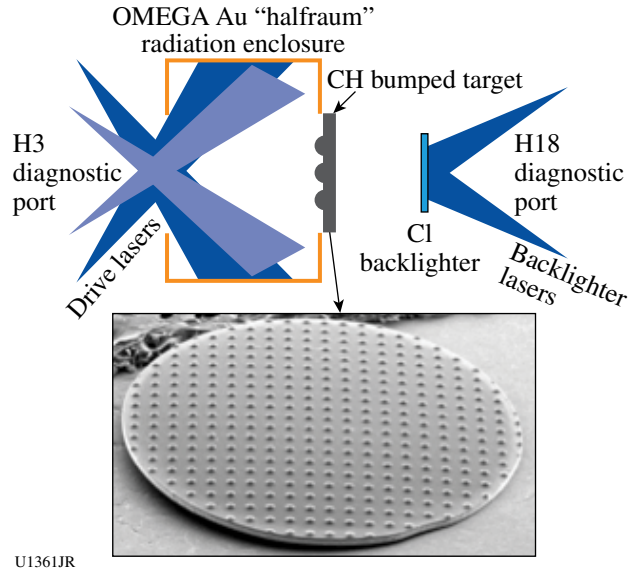


Figure 128.107
Experimental setup for CHaRM.

accomplished by measuring shock speed using the ASBO diagnostic under identical drive conditions as the bump-growth experiments.

A shot day in December 2010 focused on the early-time behavior of bump compression and rippled shock formation, which occur just before conventional aRM sets in. These experiments used 2-ns drive pulses in a halfraum, heating it to ~65 eV and driving an ~12.5- $\mu\text{m}/\text{ns}$ shock in the plastic ablator as measured by ASBO. The bump's areal density (Fig. 128.108) showed a 2.5 \times increase along the bump (initially, 12- μm -tall,

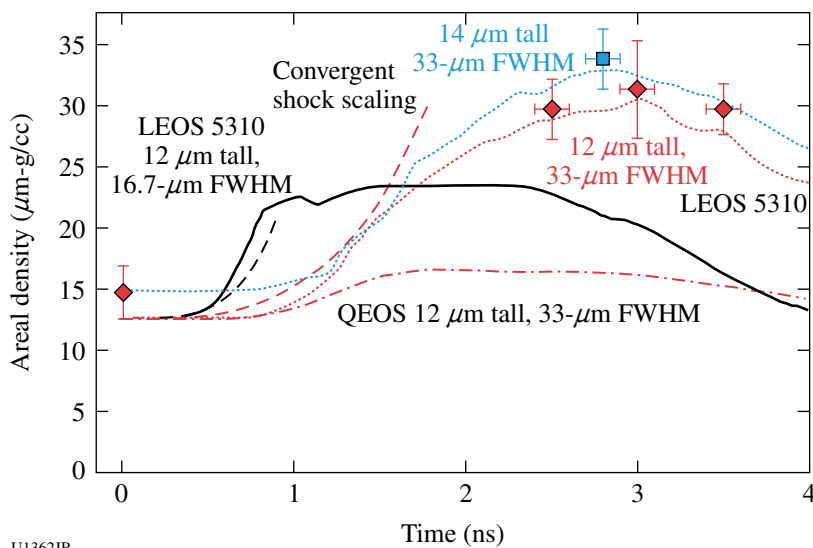


Figure 128.108
Early-time data and simulations using a 2-ns drive.

U1362JR

33- μm FWHM) axis at 3 ns after the start of the drive pulse. This initial increase in areal density is due to lateral compression of the bump as a converging shock propagates through it, raising the density on-axis. Simulations using the LEOS 5310 model showed good agreement with data; however, the QEOS model predicted 6 \times lower growth than measured owing to its lower compressibility. Results from this shot day were published in *Physics of Plasmas*.⁷⁷

The goal of the April 2011 shot day was to extend the drive pulse to observe bump behavior well into an established aRM stage. These experiments used 2.5-ns pulse durations stacked end-to-end in clusters 2 and 3 so that the effective pulse width was ~ 5 ns into the halfraum. Shock speed was measured using a slightly hotter halfraum than in the December experiment (~ 70 eV), resulting in a 15- $\mu\text{m}/\text{ns}$ shock velocity closer to the current NIC foot level, as shown in Fig. 128.109.

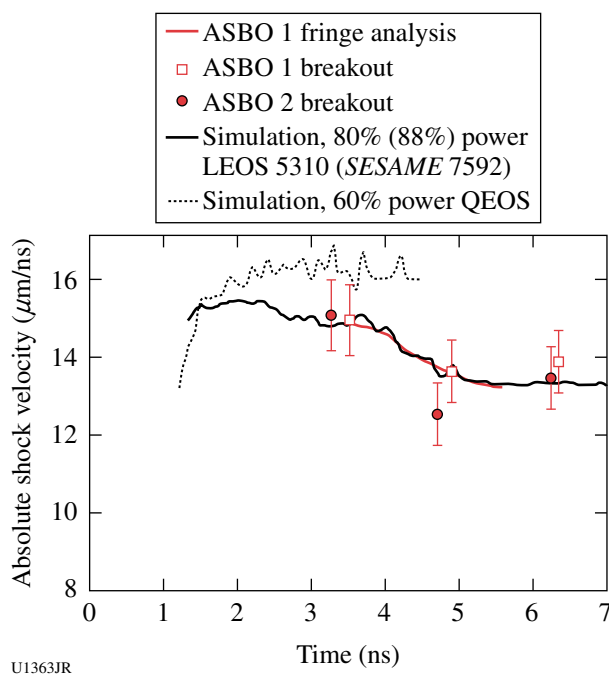


Figure 128.109 Shock-speed data and simulations for an extended 5-ns drive.

The evolution of two sets of bumps, one 6.5 μm tall, 44- μm FWHM, and one 10 μm tall, 34- μm FWHM, was measured out to 6 ns (Fig. 128.110). Similar early-time growth was observed, but evidence of aRM oscillations was not observed in experiments or matched simulations. The cause of this is a lack of sufficiently high spatial-frequency modes that are most effective in changing bump shape in the wide Gaussian bumps that were used. For x-ray-driven aRM, the mode oscillation frequency is much lower than the laser driven (by $\sim 7\times$),

so much more time is needed to witness bump oscillation if bumps are $>20\text{-}\mu\text{m}$ FWHM. These results were presented in an oral session at the International Conference on Inertial Fusion Sciences and Applications.⁷⁸ Experiments in FY12 will strive to measure oscillations in narrower ($\sim 17\text{-}\mu\text{m}$ FWHM) bumps.

ColShock/Shear: The colliding-shock experiments study the evolution of a shocked layer that evolves to a turbulent state and is then shocked a second time. A pre-shot radiograph of a typical target is shown in Fig. 128.111. A shock is launched on

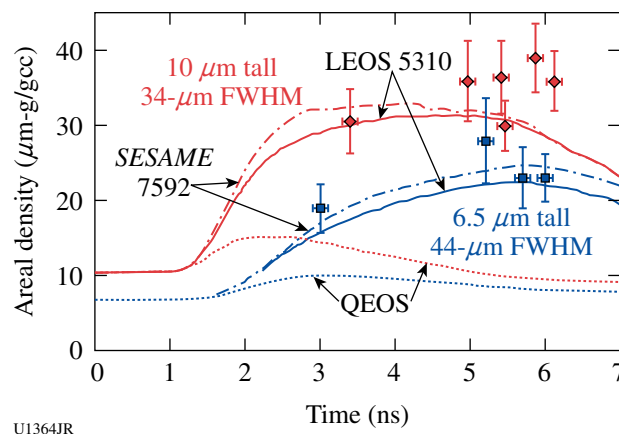


Figure 128.110 Measured and simulated bump evolution using an extended 5-ns drive.

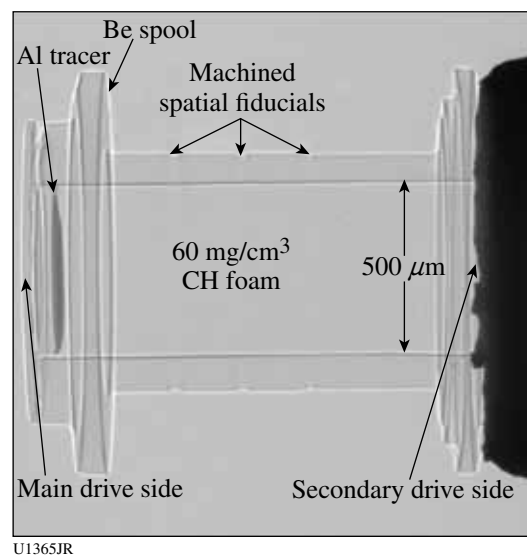
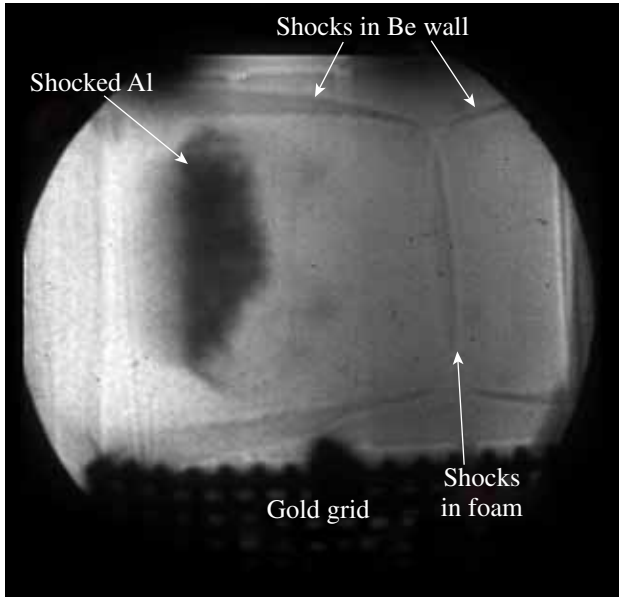


Figure 128.111 A pre-shot radiograph of the colliding-shock target. The main shock is launched from the left-hand side, and 5 ns later the second shock is launched from the right-hand side. Radiographs are obtained from two directions that measure the hydrodynamic evolution of the experiment at different times.

the left-hand side. The shock interacts with an Al tracer layer, which evolves toward a turbulent state over the course of the experiment. A second shock is launched from the right-hand side, which propagates toward the Al layer. The hydrodynamic evolution of the system, including the evolution of the Al layer and the positions of the shocks in both the CH foam and the Be walls, is measured. The x-ray radiograph in Fig. 128.112 taken just after the two counter-propagating shocks interacted.



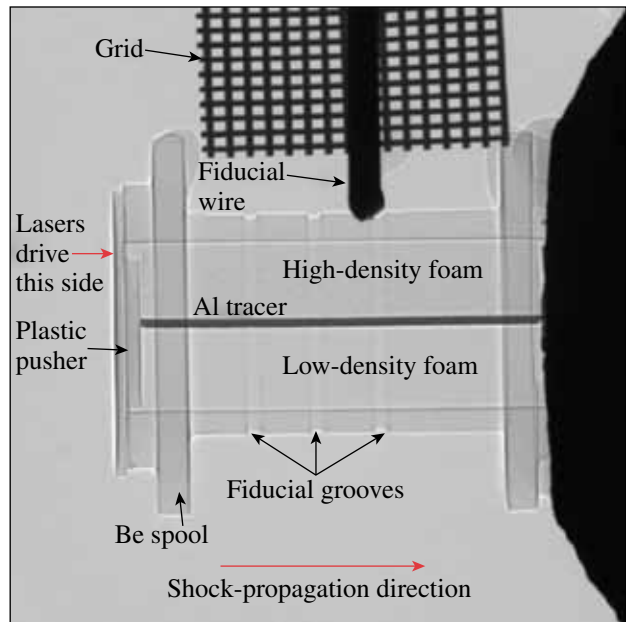
U1366JR

Figure 128.112
Radiograph of a colliding-shock target roughly 8 ns after the initial shock was launched. At this time the counter-propagating shocks have just interacted.

The goal of the Shear experiment is to study mix associated with large deformations or shear. The goal of this experimental campaign is to provide data to further constrain the Besnard–Harlow–Rauenzahn code (BHR),⁷⁹ the mix model implemented in the *RAGE* radiation–hydrodynamics code.

A pre-shot radiograph of a typical target is shown in Fig. 128.113. A shock is launched on the left-hand side. The shock propagates through the two different density foams. The shear is caused by the different shock speeds. The hydrodynamic evolution of the system, including the evolution of the Al layer and the positions of the shocks in both the CH foam and the Be walls, is measured with x-ray radiography (see Fig. 128.114).

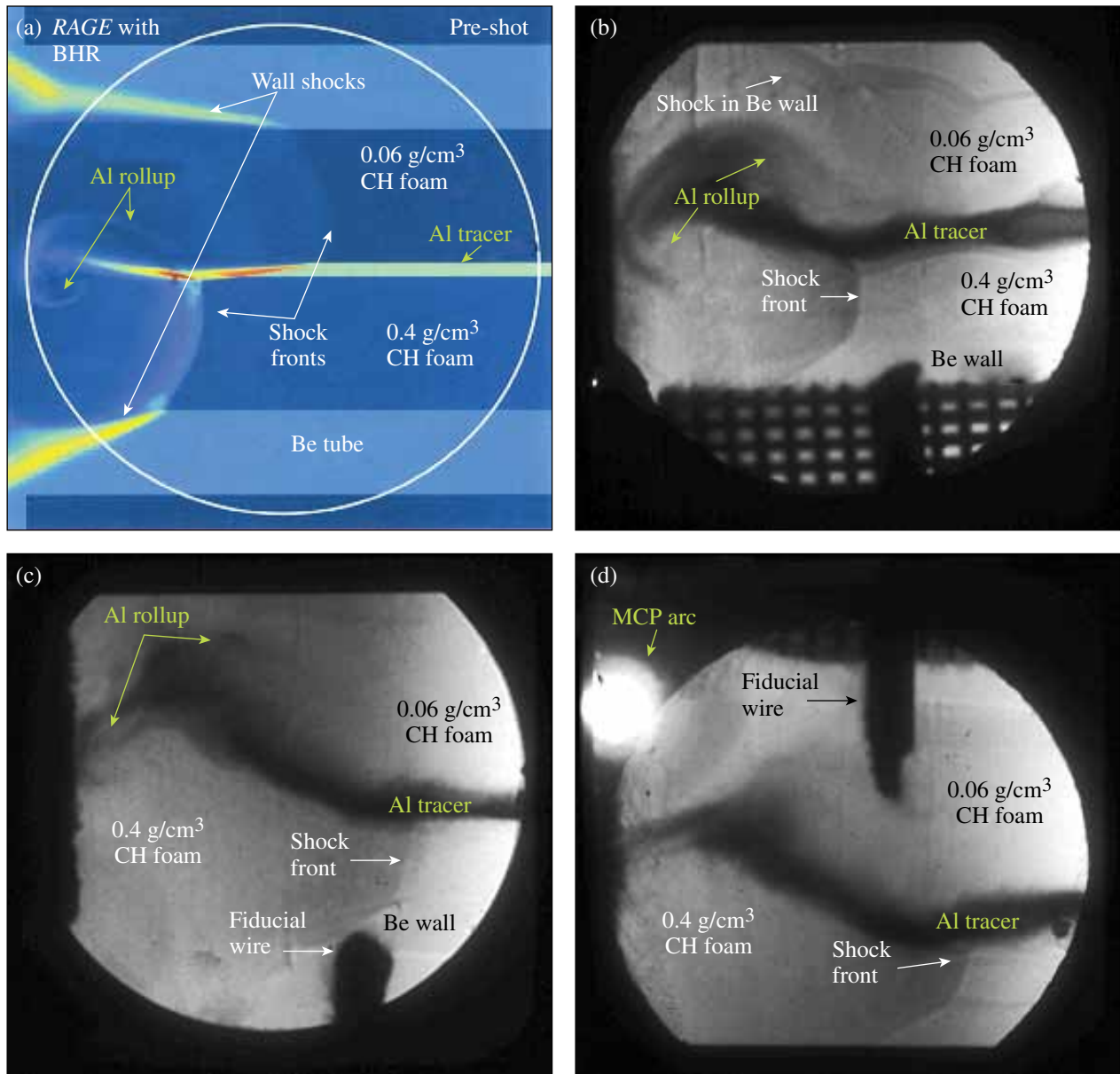
DTRatio (DTRat): On 25 May 2011, LANL's ICF Gamma-Ray Physics Team led the DT-Ratio Campaign on OMEGA, with external collaborators from AWE, NSTec, LLNL, LLE,



U1367JR

Figure 128.113
A pre-shot radiograph of the Shear target. The shock is launched from the left-hand side. Radiographs are obtained that measure the hydrodynamic evolution of the experiment at different times.

and MIT. The primary experimental objective was to cross-calibrate the fusion branching ratios of DT gamma/neutron against the better-known D³He gamma/proton. Three types of targets were fielded: six D³He (D₂ ~ 6 atm, ³He ~ 12 atm) in glass shells, three DT (50:50) in plastic shells, and two D₂ (15 atm) in glass shells. Three Cherenkov detectors (GCD1, GCD2, and GRH) were successfully operated at the same time. Since the branching ratio study requires accurate diagnosis of multiple fusion products, this study required close collaboration with LLE and MIT. In particular, MIT employed seven proton diagnostics: the proton temporal diagnostics, three wedge range filters, two charged-particle spectrometers; and the magnetic recoil spectrometer, with which they measured spatially averaged proton yield to within 5% accuracy. Figure 128.115 shows preliminary experimental data obtained by GCD-1. The top blue curves show D–³He gamma signals divided by proton yield data (proportional to D–³He gamma/proton branching ratio). The red curve shows D–T gamma signals divided by neutron yield (proportional to D–T gamma/neutron branching ratio). Since the primary D³He (E_g = 16.66 MeV) and DT (E_g = 16.75 MeV) gamma rays have almost the same energy, it is not necessary to determine the absolute efficiency of the gamma detector. Initial data show that the DT branching ratio is significantly smaller than the D³He branching ratio (DT/D³He ~ 0.41), which is in very good agreement with last year's campaign (DT/D³He ~ 0.42).



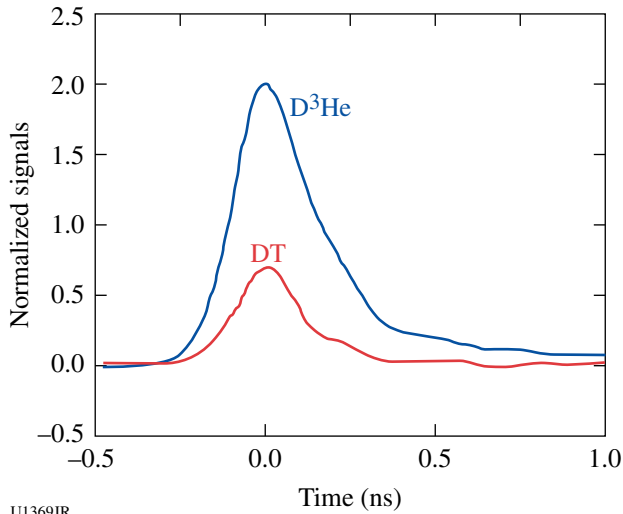
U1368JR

Figure 128.114

(a) Simulation result at 8.25 ns showing the density of the experimental system; (b) x-ray radiograph of the experiment at 8.25 ns. Preliminary comparisons show a number of qualitative similarities; (c) x-ray radiograph of the experiment at 12 ns; and (d) x-ray radiograph of the experiment at 14 ns.

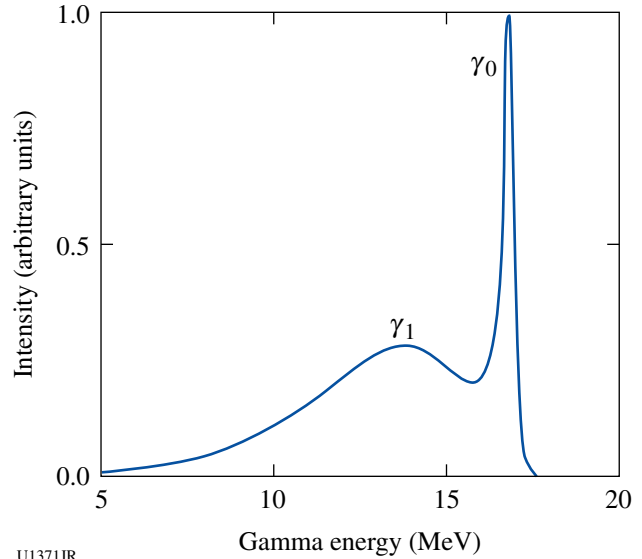
Gamma Reaction History (GRH): In addition to the dedicated DTRat shot day, the ICF Gamma-Ray Physics Team, led by LANL, participated in ten shot days on OMEGA. Through extensive energy thresholding experiments using GCD-1 and GRH across these shot days, the team examined the shape of the DT fusion gamma-ray spectrum. The data in Fig. 128.116 clearly indicate that the DT reaction spectrum consists of more than just a single line at 16.75 MeV, corresponding to de-excitation of the $^5\text{He}^*$ nucleus to the ground state. DT fusion gamma rays resulting from the transition of $^5\text{He}^*$ down to the

first excited state must also contribute significantly to the spectrum. Figure 128.117 shows the spectrum that is most consistent with the experimental data and modified spectra of the mirror nucleus ($^5\text{Li}^*$) resulting from D^3He fusion extrapolated to the ^5He system by quantum-mechanical *R*-matrix calculations. Using this new spectrum, a total $t(d,g)^5\text{He}/t(d,n)^4\text{He}$ branching ratio of $(2.7 \pm 0.7) \times 10^{-5}$ has been measured at the Omega Laser Facility. These measurements show that the DT branching ratio at ICF conditions is 2 to 3× less than that of previous measurements at particle accelerator facilities. In a practical sense,



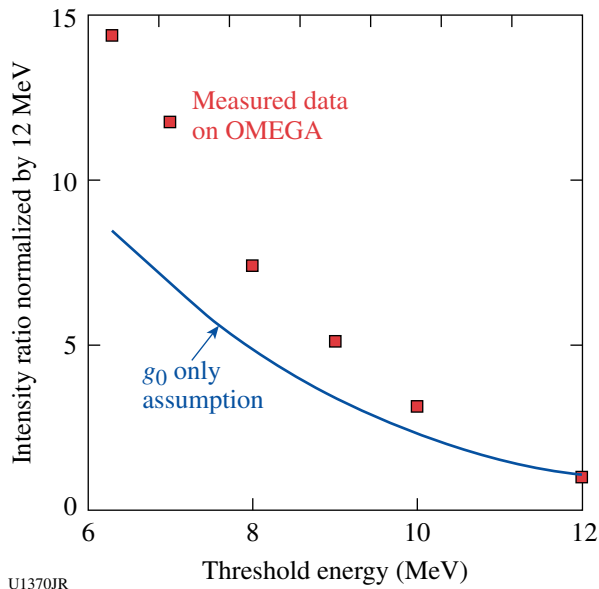
U1369JR

Figure 128.115
2011 DTRat campaign data. The blue curves show $D-^3\text{He}$ fusion gamma signal normalized by MIT's proton yield. The red curve shows the DT fusion gamma signal normalized by LLE's neutron yield.



U1371JR

Figure 128.117
Resulting DT fusion gamma-ray spectrum consisting of γ_0 at 16.75 MeV ($^5\text{He}^*$ transition to ground state) and γ_1 at ~ 14 MeV ($^5\text{He}^*$ transition to first excited state).



U1370JR

Figure 128.116
Ratio of GCD intensities as a function of threshold energy (MeV), normalized to 12-MeV threshold intensity. The red squares are experimental data. The blue curve was obtained by folding 16.75-MeV single-peak spectra with detector responses of GCD simulated by the *ACCEPT* code.

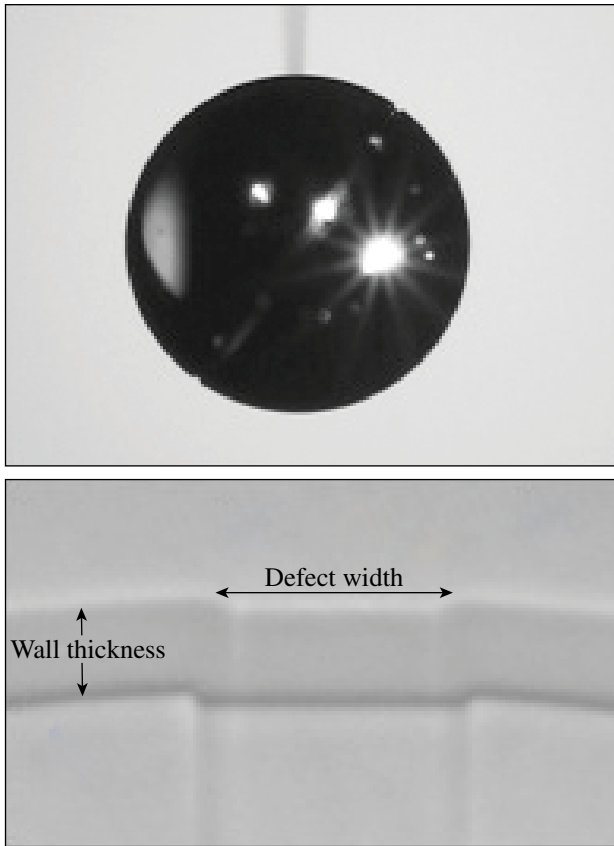
precise measurement of the branching ratio $t(d,\gamma)^5\text{He}$ relative to $t(d,n)^4\text{He}$ is important in order to diagnose gamma-ray yields from which to infer parameters such as target areal density and resultant fusion yield of cryogenically layered implosions at the NIF. The experimentally measured DT spectrum and recent DT branching ratio measured on OMEGA have been applied to

improve GRH responses and data analysis for the NIF. In addition, the team continued plastic and glass capsule ρR diagnostic efforts on OMEGA and extended the diagnostic concept to the NIF to provide a capsule implosion ρR parameter.

Defect Implosion Experiments (DIME): Direct-drive experiments on OMEGA have been performed to prototype eventual NIF-ignition applications campaigns. Experimental results are tied to simulations that will lead to better designs for those experiments. Spherical implosion targets with equatorial defects have been irradiated with polar drive—a requirement at the NIF. Collected data reveal implosion symmetry, neutron yield, and temperature and density profiles of the capsules with and without the defect. We have also modeled and measured the zeroth-order hydrodynamics. The testing of hydrodynamic codes provides a guide to accurately plan for polar-drive-ignition studies on the NIF platform. Target-design details are shown in Fig. 128.118. The equator is defined with respect to the polar drive as in Fig. 128.119.

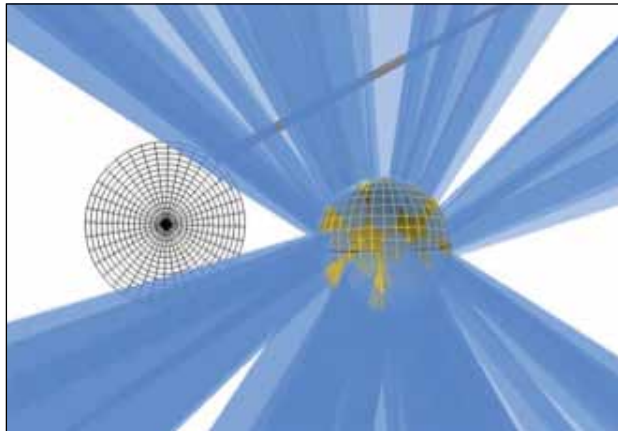
The laser drive for all shots included 40 beams for the nominal LLE polar drive (PD) plus 11 or 12 beams for pumping the saran backlighter. The capsule drive was ~ 17.5 kJ in a 1-ns, square-topped pulse.

As part of the capsule design, most targets have a 2- μm -thick Ti impurity layer (1% by atom) placed either at the inner wall of the target shell or 3 μm inboard of the inner wall. This



U1372JR

Figure 128.118
 (a) Photograph of an 870- μm -diam CH capsule. (b) Detail of the trench defect. Nominal wall thickness is 15 to 17 μm ; the trench is $\sim 28 \mu\text{m}$ wide and 5 to 8 μm deep.



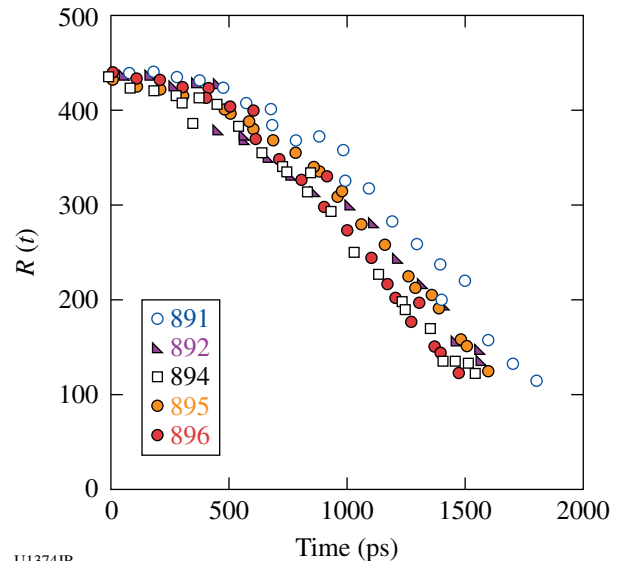
U1373JR

Figure 128.119
 A defect target is shown with polar drive. A backlighter foil to the left was used for x-ray radiography. The capsule drive beams are reduced in footprint size to enable one to clearly view the defect target (Visrad model).

is employed as a mix diagnostic for these ablation-driven implosion targets. We also shot thin-walled (8- μm) shells, so-called exploding-pusher targets, and, as a result of these experiments, have moved away from this choice.

Initially scheduled for two shot days this year, DIME benefited from three days, the last two coincident with the forced evacuation of Los Alamos by the state-record Las Conchas wild fire. Targets from another campaign were sequestered in the closed laboratory. Because we had extra DIME targets, we were able to use them during the extra day of shots. In fact, General Atomics (GA) personnel at LLE provided “last-minute” backlighter foils because the DIME backlighters were also locked up in New Mexico for the week prior to the laser shots. As usual, the expertise and professionalism of LLE and GA staff was very efficient and helpful in obtaining laser/target data under trying circumstances. DIME obtained a total of 28 laser shots during these two days plus another 11 shots during a campaign earlier in the year.

For the zeroth-order hydro, we measured bang time and implosion velocity with a gated, x-ray imager. Probing at 2.8 keV, we found that the capsules for the most part were relatively spherical, excepting the final assembly of defect targets. Defining R as the radius of the absorbing material left in the ablator, we plot the time-dependent R in Fig. 128.120. Not shown in Fig. 128.120 is the brightest emission radius of the capsules, for which the absorption feature is no longer visible.



U1374JR

Figure 128.120
 Zeroth-order hydrodynamics: capsule radius as a function of time for various shots. The slowest target (891) was a perfect capsule.

In this case, we measure the full width at half maximum as the operational radius. It is uniformly $40 \pm 10 \mu\text{m}$ for the entire period that it is visible (from 1.4 to 1.8 ns), and it is independent of the presence of a defect.

The pathology of the defect capsules is shown in Fig. 128.121. The features suggest a possibility of measuring mix in an ICF capsule under such circumstances, which is why we used the Ti tracer layer in these targets. There are more comments on this later.

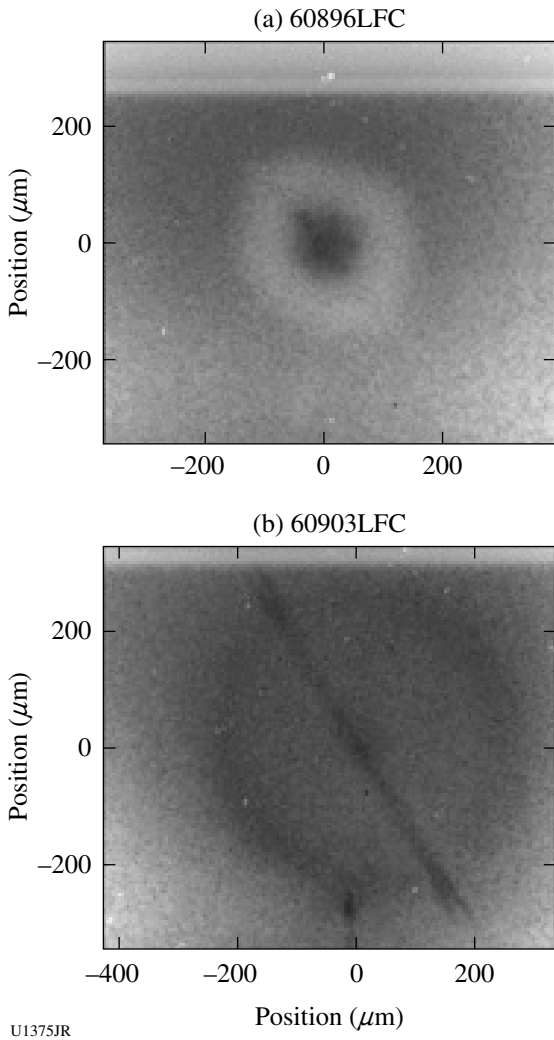


Figure 128.121
 (a) The thickening of the thick-walled ablator near peak compression of a defect capsule is very obvious. Note the Lengendre modes associated with the core. (b) A thin-walled capsule earlier in the discharge shows defect detail more dramatically than for the ablative case. The data come from the 80-ps gated x-ray framing camera LFC.

The bang time is measured by two other diagnostics: the SSCA x-ray streak camera and the neutron temporal history diagnostic. These are consistent with, and more accurate than, the x-ray framing camera data. The streak data are especially illuminating. We see in Fig. 128.122 a sample streaked spectrum showing bremsstrahlung from the laser drive and during the final compression (note the consistency of the time with the framing camera). This spectrum shows He-like Ti lighting up before the bang time, indicative of the ablator burning through to the Ti before the laser is turned off at ~ 1 ns. Figure 128.123

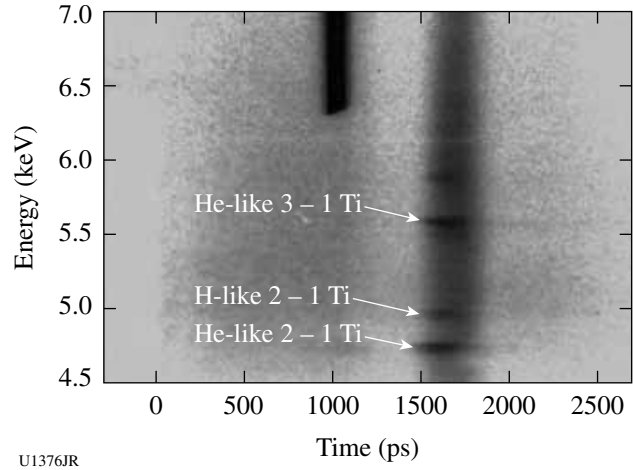


Figure 128.122
 X-ray streak record of a defect implosion. The continuum rises up at $t = 0$ with the laser pulse and reaches a maximum at 1 ns. The capsule implosion stagnates from 1.5 to ~ 1.8 ns. Note the 4.75-keV Ti emission during the laser pulse. The intense dark region at the top ($t \sim 1$ ns) is x-ray shinethrough that lights up the phosphor screen directly and has nothing to do with electrons accelerated from the photocathode in the streak tube.

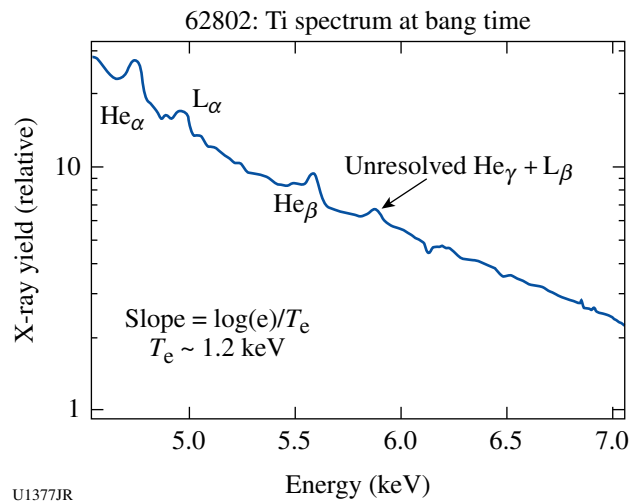


Figure 128.123
 Corrected lineout of spectrum at bang time for a defect target.

shows a lineout of the Ti spectrum after corrections are made for filter transmission, crystal reflectivity, and the sensitivity of the CsI photocathode in the streak tube. From this spectrum, we may estimate the electron temperature from the slope of the continuum.

These target shots are instructive in considering the use of these capsules as a mix platform. The idea is that Ti near the inner surface of the ablator shell will light up spectroscopically when the material is heated by the hot gas during stagnation. This is *prima facie* evidence of mix. The appearance of emission before stagnation shows that either the CH wall has burned through prior to stagnation (which would be a bad thing) or that the defect is responsible for the direct laser heating of Ti. This emission is reduced once the laser is extinguished at ~1 ns. Perfect capsules (no defect) show no Ti emission before stagnation. We note that for thinner layers of CH on top of the impurity layer, the Ti will light up and emit; this has already been used to calibrate capsule design codes for experiments on the NIF.

Neutron yield is a measure of the effect of a perturbation on capsule performance. We have accumulated data for a selection of perturbations: perfect capsules versus defect capsules, with/without a Ti impurity layer, with/without a second impurity layer of V, and a perfect Ti target with a NIF-style gas-fill tube. The yield performance is summarized in Fig. 128.124. All deviations from an undoped CH target reduce yield.

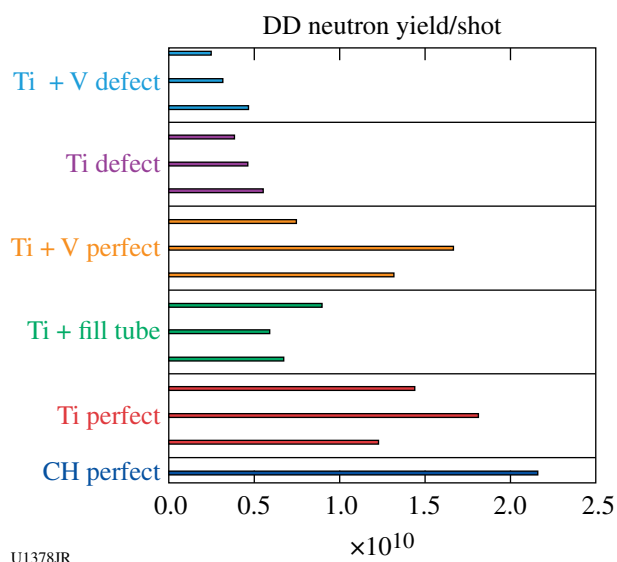


Figure 128.124 Results of neutron-yield measurements for different targets.

Asymmetric Burn Experiments (ABEX): The purpose of the ABEX project is to develop an experimental HED platform to study the impact on the performance of fusion burn caused by hydrodynamic issues related to asymmetrically driven ICF systems. The ABEX capsules were successfully fabricated and 12 successful shots were conducted at the Omega Laser Facility on 5 April 2011. All primary diagnostics obtained data, including neutron yield from both primary D–D and secondary D–T reactions, burn-weighted ion temperature, time-dependent neutron-production rate, time-resolved and time-integrated x-ray pinhole imaging, spatially integrated time-resolved x-ray spectra in the 4- to 7-keV band, and measurements of laser-scattered light.

The initial experiments on OMEGA had two objectives: (1) to successfully manufacture the perturbed targets and determine what manufacturing issues needed to be addressed for future target construction, and (2) to map out the performance versus perturbation-amplitude space for the next experimental series. These goals were met. Specifically, we developed the manufacturing technique to produce capsules that contained a P-8 asymmetry in the radius of the capsule. An image demonstrating this is shown in Fig. 128.125.

In addition to the development of the manufacturing technique, we measured the D–D neutron yield as a function of perturbation amplitude and obtained x-ray images of these capsules at times near the peak compression. In Fig. 128.126, we show a set of images that have an equatorial view of the capsules and demonstrate the asymmetric shape of the capsules at this time. In Fig. 128.127, we show the measured yield as a

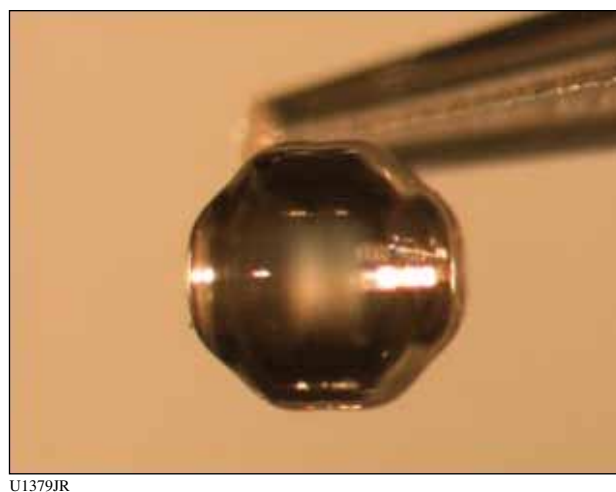


Figure 128.125 Photograph of a machined polyacrylamide (PAMS) mandrel with ±10-mm amplitude perturbation. The axis of symmetry is horizontal in this photograph.

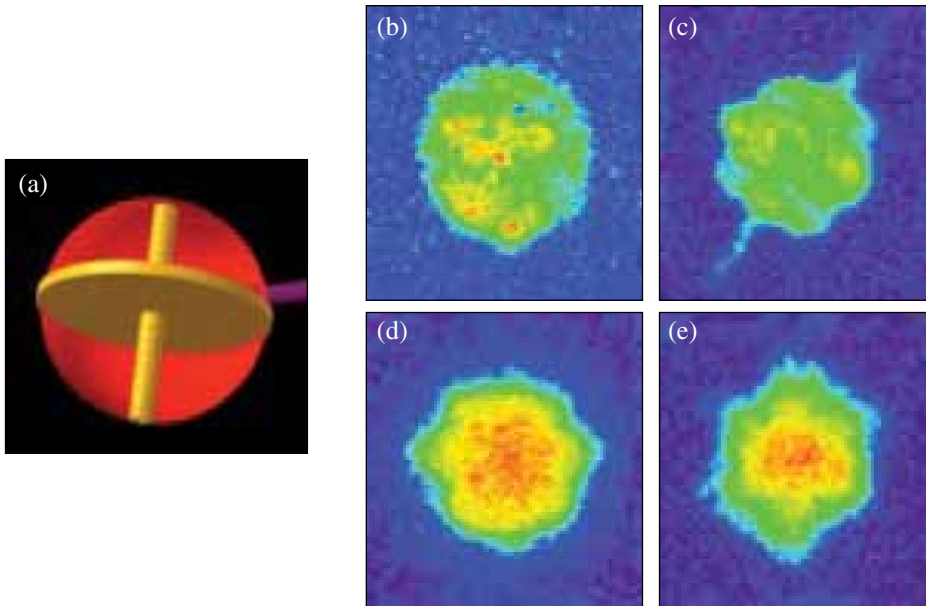
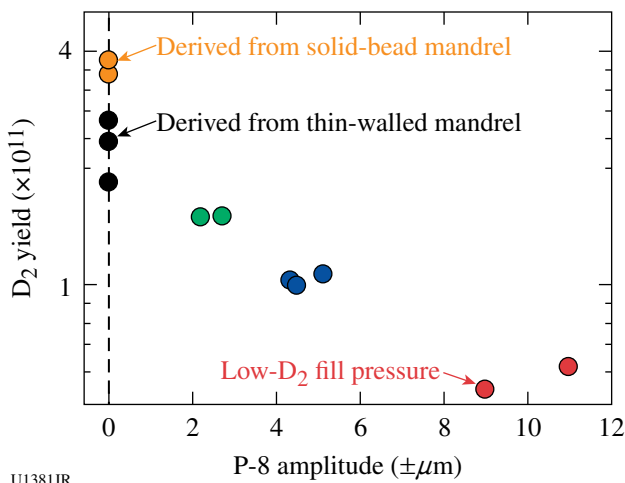


Figure 128.126

Sample images from the time-resolved x-ray pinhole camera in TIM-2 (XRFC1), which had an approximately equatorial view of the target. This camera had a 1-mil copper filter, which primarily passes x rays in the 5- to 9-keV band. Image (a) shows a view of the target from a VisRad model. Images (b) and (d) are from the same shot with a P-8 of ± 2.5 mm at (b) 1.35 ns and (d) 1.50 ns, where the bang time was 1.64 ns. Images (c) and (e) are from a different shot with a P-8 of ± 10 mm at (c) 1.33 ns and (e) 1.51 ns, where the bang time was 1.63 ns.

U1380JR



U1381JR

Figure 128.127

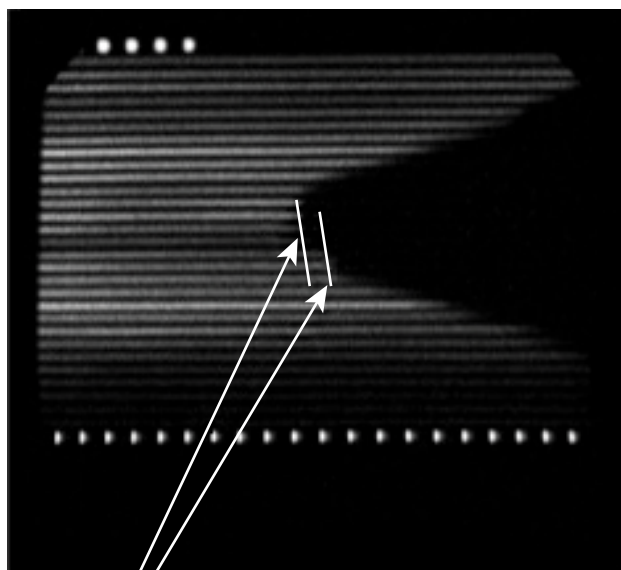
Measured primary D-D neutron yield as a function of the P-8 perturbation amplitude for all the targets, including those derived from thin-walled mandrels.

function of perturbation amplitude. These results have helped further develop this experimental platform, and this effort will continue with two shot days in FY12.

Warm, Dense Matter Equation of State (DPEOS): The purpose of the DPEOS project is to measure the equation of state (EOS) of material in the warm, dense matter regime. Currently, we are developing an experimental platform to accomplish this at the Omega Laser Facility. Our experimental platform uses the OMEGA laser to drive a very strong shock into an

aluminum sample. The shock is then released into 0.2 g/cm^3 aerogel foam, which is used as a pressure standard. A shock-breakout measurement is used to determine the shock velocity and pressure in the foam. We have also developed an imaging x-ray Thomson spectrometer to measure Compton-scattered x rays from the released aluminum sample. This information can be used to determine the temperature and density of the released aluminum, providing the necessary measurements to determine the EOS.

Our experimental plan for FY11 was to test and measure the shock and release conditions produced in the aluminum sample, finish the design and construction of the imaging x-ray Thomson spectrometer, get it approved for use on OMEGA, and obtain the first EOS measurements on warm, dense matter (WDM) aluminum. We were successful in the first goal, completing a total of 21 shots in two days on OMEGA, and completed our design for the spectrometer, but because of issues with materials used in the spectrometer, we were not able to obtain permission for its use on OMEGA. We expect this problem to be remedied for our shots in FY12. The accomplishments included verification of the shock conditions in the experimental design and the resolution of many issues related to the x-ray scattering measurements to be carried out in the future. An example of the data we obtained is shown in Fig. 128.128. This figure contains the VISAR signal and the shock-breakout measurement that demonstrates a release pressure near 5 Mbar. Other measurements demonstrate that we have an effective x-ray backlighter for the scattering measure-



U1382JR

Figure 128.128

Shock-breakout measurement from the ASBO diagnostic. The arrows point to shock-breakout occurrence at two different positions from a stepped target. The measurements indicate a shock velocity of 5.7×10^6 cm/s, corresponding to a pressure of ~ 540 GPa.

ments and that our x-ray background signal is relatively low. One shot day is planned for FY12 and we expect to obtain our first measurements with the spectrometer on that day.

NIF-5: The NIF-5 campaign had three shot days during FY11: 10 February, 7 July, and 29 September 2011. The 7 July date was cancelled because of the Las Conchas fire. The remaining two shot days were used to study the effect of wall albedo on supersonic radiation flow. We obtained very good data return on both days, with a much-improved signal level and timing calibration on our second shot day.

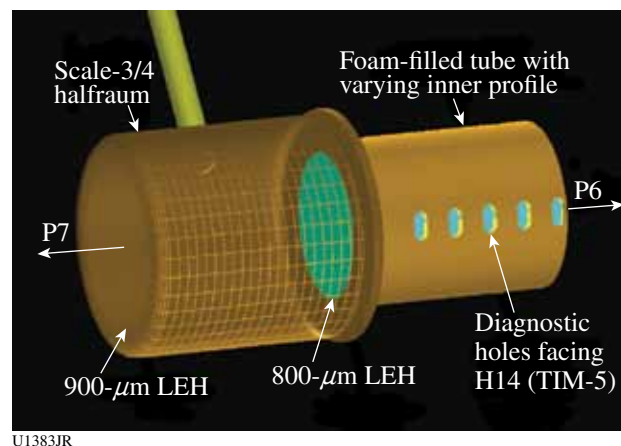
The purpose of the 10 February shots on OMEGA was to study the effect of wall albedo on supersonic radiation flow down a gold tube filled with low-density SiO_2 foam. We modified the wall albedo of the gold tube by varying its inner profile. While our original intent was to maintain a constant inner surface area to isolate the effect of the profile, this was not possible without other modifications that would also modify the problem [such as the rear entrance hole (REH) diameter, foam volume, etc.).

An experimental campaign on OMEGA EP explored the conversion efficiency of CsI backlighters as a function of the backlighter material size using a 40-ps laser pulse. The results from this campaign provided valuable data now being used to

evaluate possibilities for future NIF campaigns. The 29 September OMEGA shot day was a continuation of the campaign begun on 10 February. With this series of shots, we hoped to obtain enough data to wrap up our investigation. We modified the wall albedo of the gold tube by varying its inner profile, although in this case we limited ourselves to only two different profiles. We also maintained a constant inner surface area and foam mass to isolate the effect of the inner profile. We achieved this by varying the length of the cylinder of one type to match the surface area of the other, while lowering the foam density so that the total foam mass of both types of cylinders also matched. We did this for two foam densities. We maintained an identical radiation source for both: the halfraum, laser entrance hole (LEH), and REH were the same for all cases. The data obtained on both shot days are used to validate our codes.

An overview of the target is shown in Fig. 128.129. The halfraum and cylinder were mounted along the P6–P7 axis ($\theta = 63.44^\circ$, $\varphi = 342^\circ$), with the LEH facing P7. The radiation coming from the halfraum heats the foam; we then observe the self-emission of the heated foam from two orthogonal diagnostic axes. Imaging of the holes on the side of the cylinder was conducted from H14, while imaging of the radiation breakout from the end of the cylinder from P6.

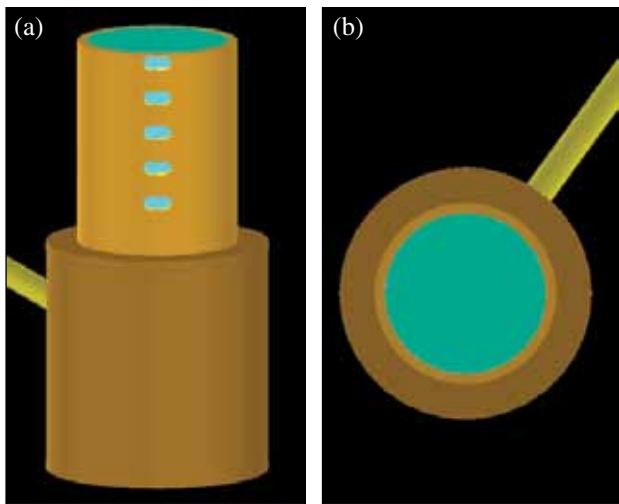
The side view was measured using the SSCA streak camera with the SXI $6.6\times$ snout. The camera was rotated 60° cw, so that the row of diagnostic holes was perpendicular to the streak direction. The view, after rotation, is shown in Fig. 128.130(a). Two fiducial beams were aimed at points along the row of



U1383JR

Figure 128.129

Halfraum target with cylinder is mounted along the P6–P7 axis, with LEH facing P7. Diagnostic holes face H14 and the back end faces P6. (Short-cylinder target type is shown.)



U1384JR

Figure 128.130
Diagnostic views for SSCA/SXI6.6x from (a) H14/TIM-5 and (b) XRFC3/SXR4x from P6/TIM-4. (Short-cylinder target type is shown.)

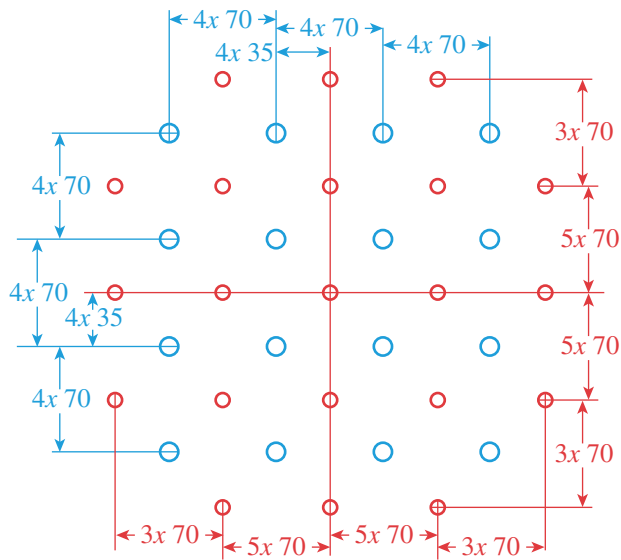
holes (within view of our vertical imaging slit) to provide a time fiducial on the streak record. One was aimed at a point below the bottom-most (first) hole and fired late (~ 1.5 ns) to mitigate its effect on the data. The second beam was fired later to provide an accurate calibration of the streak time/distance on film. Since the fall time of the x-ray emission from the fiducial beam spots do not accurately reflect the laser beam's fall time, we use the time between the two fiducial rise times for our calibration. Unfortunately, this means the second fiducial is aimed at a point in between the third and fourth holes of the long cylinder targets. The second fiducial was timed late to minimize any effect it may have on the data. The end-on view was recorded using XRFC3 with the SXR-4X diagnostic snout. This diagnostic consists of three independently filtered channels, two of which include a mirror and filter combination, measured at four different times. The third one is a direct view with a 25-mm-thick Be filter. We fielded practically identical setups on the mirror and filter combination channels, resulting in eight images, each at a different time. The view from this diagnostic is shown in Fig. 128.130(b).

In addition to our primary goal, we also used four shots of our second shot day to obtain the x-ray spectrum of SbI_3 —a different backlighter material being considered as a replacement for CsI for our NIF-5 spectroscopy absorption diagnostic. We obtained enough data to allow us to make this determination and analysis is underway.

We met all of our campaign goals for both shot days. On 10 February we obtained 13 shots with good data on all of the

primary diagnostics. Even though SXI had not been used in years, it produced data on every shot and also recorded an accurate timing fiducial along with the data. On 29 September, 14 shots were taken with returned data on all the primary diagnostics.

Neutron Imaging: During April 2011, successful neutron source images were obtained at the Omega Laser Facility, using the NIF Version 2 neutron-imaging pinhole. These images represent a significant milestone for the project. This pinhole was designed to provide higher-resolution images and to cover a larger effective field of view at the target plane than previous versions of this diagnostic by addressing pointing uncertainties in the NIF alignment system. The pointing tolerance at the NIF for individual pinholes is $\sim 100 \mu\text{rad}$, so by constructing an array of “mispointed” pinholes, the effective field of view may be increased. The pointing locations for the NIF Version 2 pinhole are illustrated in Fig. 128.131. Each pinhole points about $35 \mu\text{m}$ away from its nearest neighbor.



U1385JR

Figure 128.131
Pointing of the 37 NIF Version 2 pinholes at the target plane.

Figure 128.132 shows the front face of the NIF Version 2 pinhole, engineered by V. Fatherley of P-24 and fabricated by D. Schmidt and F. Garcia of MST-7. The dark squares on the gold background are the openings for each individual pinhole.

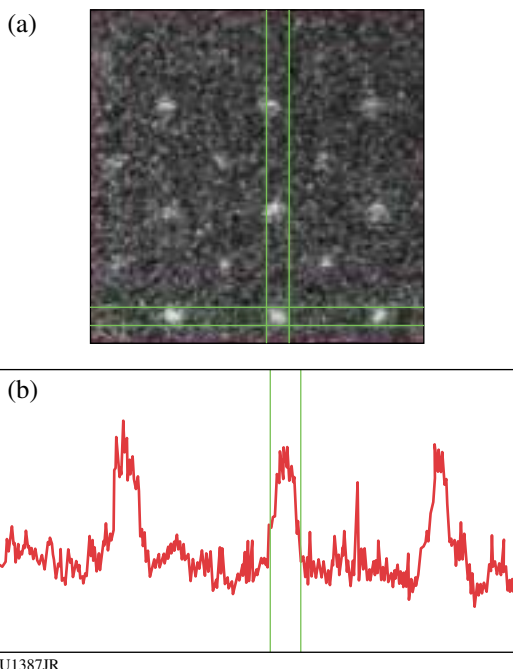
Figure 128.133 shows a sample of the data collected on the OMEGA laser on 14 April 2011. The image in Fig. 128.133(a) is from a direct-drive implosion of a CH capsule producing 2×10^{13} neutrons using the OMEGA laser. Clearly present



U1386JR

Figure 128.132

Image of the NIF Version 2 pinholes at the end of the 20-cm-long aperture body.



U1387JR

Figure 128.133

Shot 61898 on the OMEGA laser. (a) Clear images of the individual pinholes are present, and (b) the column-averaged lineout shows their relative signal to noise.

are images from both the small and large pinholes within the aperture array. Because of the size of the imaging floor on OMEGA, not all the pinhole images would fit within the camera. Figure 128.133(b) shows the column-averaged lineout

within the green box drawn on the image. From this data it is clear that the Version 2 pinhole works as an imaging array and can be brought to the NIF for further testing and use in imaging experiments.

In addition to this success, the team successfully fielded a new camera system that collected images from the start of the campaign. Furthermore late-time modifications to the pinhole mounting hardware that significantly reduced uncertainties in the pinhole pointing were also implemented.

OMEGA EP Ions: Los Alamos experimental team members have completed a new round of experiments on the OMEGA EP Laser System to test laser-generated ion beams at $10\times$ higher energy than similar lasers such as LANL's own Trident Laser System (which operates at around 100 J).

The objective of this work is to develop laser-driven carbon ion beams for ICF studies. To do this, new tools were developed to study the focusing characteristics of these ion beams. Consistent production of multi-MeV ion beams was demonstrated, using a kilojoule of short-pulse laser energy with a conversion efficiency of several percent, and proton beams of nearly 70 MeV, the highest energies seen on the OMEGA EP laser, and near the world record in energy were achieved (see Fig. 128.134).

Ion beams are produced when an energetic and ultra-intense laser interacts with a thin solid target at relativistic intensities. The interaction produces large currents (MA) of electrons coursing through the target. The currents produce extreme electric fields on the rear surface of the order of teravolts per meter (TV/m), which in turn accelerate the ions into an MeV beam of roughly 10^{14} to 10^{15} ions in a picosecond (10^{-12} s). When focused, this beam has the potential of delivering tens of joules of energy into a spot of the order of tens of microns.

Using a combination of experiments on the LANL Trident Laser Facility and OMEGA EP, the team demonstrated the non-ballistic focusing nature of the ions from hemi-shelled targets. This was the topic of a recent invited talk and article given at the American Physical Society Division of Plasma Physics's annual meeting in Chicago in November 2010.⁸⁰

This work has led to a new design for a focusing target, the "cusped hemi," which is a modified hemi-shell target with multiple radii of curvature to optimize the ion focusing and conversion efficiency (Figs. 128.135 and 128.136). These cusped hemis are made from $10\text{-}\mu\text{m}$ -thick diamond using

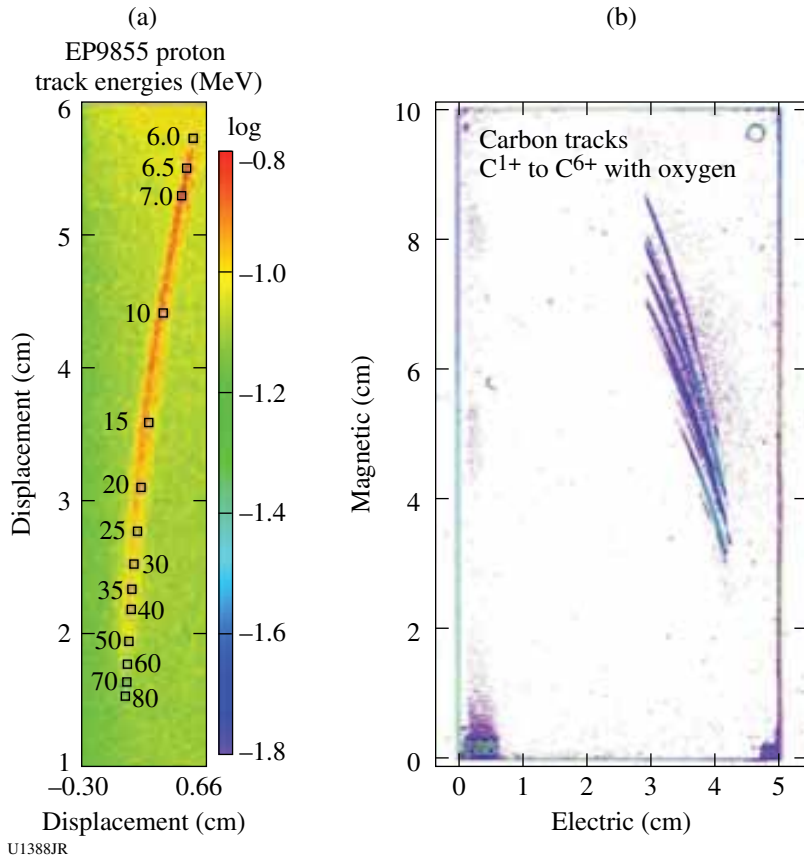


Figure 128.134

Thomson parabola (TPIE) data showing (a) high-energy protons up to nearly 70 MeV from OMEGA EP using 1 ps and ~400 J of laser energy and (b) carbon species up to 30 MeV in energy using 10 ps and 1000 J of laser energy.

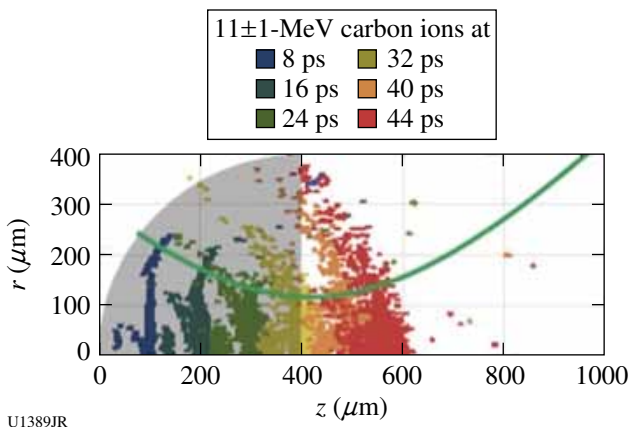


Figure 128.135

Simulated spatiotemporal data from the *LSP* code showing 11-MeV ions in a 1-MeV band for different time steps (colors) born on the hemi-shell's inner surface (gray) accelerated to the right and the ensemble trajectory as the green curve overlay.

chemical vapor deposition. The latest campaign on OMEGA EP (July 2011) tested these novel targets, the preliminary results of which indicate that they have outperformed their progenitors.

FY11 AWE OMEGA EP and OMEGA Experimental Programs

In FY11, AWE led six shot days on the OMEGA and OMEGA EP lasers. This work encompassed the development of MeV x-ray sources (one day in jointly funded collaboration with CEA) and 22- to 52-keV x-ray backlighters (three days in collaboration with LLNL, of which one was LLNL funded), a Laue x-ray diffraction study of the dynamics of shocked tantalum crystals (one day), and capsule implosions in asymmetrically driven hohlraums (one day).

MeV X-Ray Sources on OMEGA EP

Principal Investigators: R. Edwards and C. Aedy (AWE); C. Courtois, J. Gazave, O. Landoas, and O. Peyssonneaux (CEA); and C. Stoeckl (LLE)

High-intensity ($I\lambda^2 > 10^{19} \text{ W/cm}^2 \mu\text{m}^2$) laser-plasma experiments have been used for several years to study the generation of energetic particles such as electrons, positrons, and protons. When energetic electrons propagate in a high-Z solid target located behind the interaction area, they produce a high-energy (>MeV) Bremsstrahlung emission source of potential interest

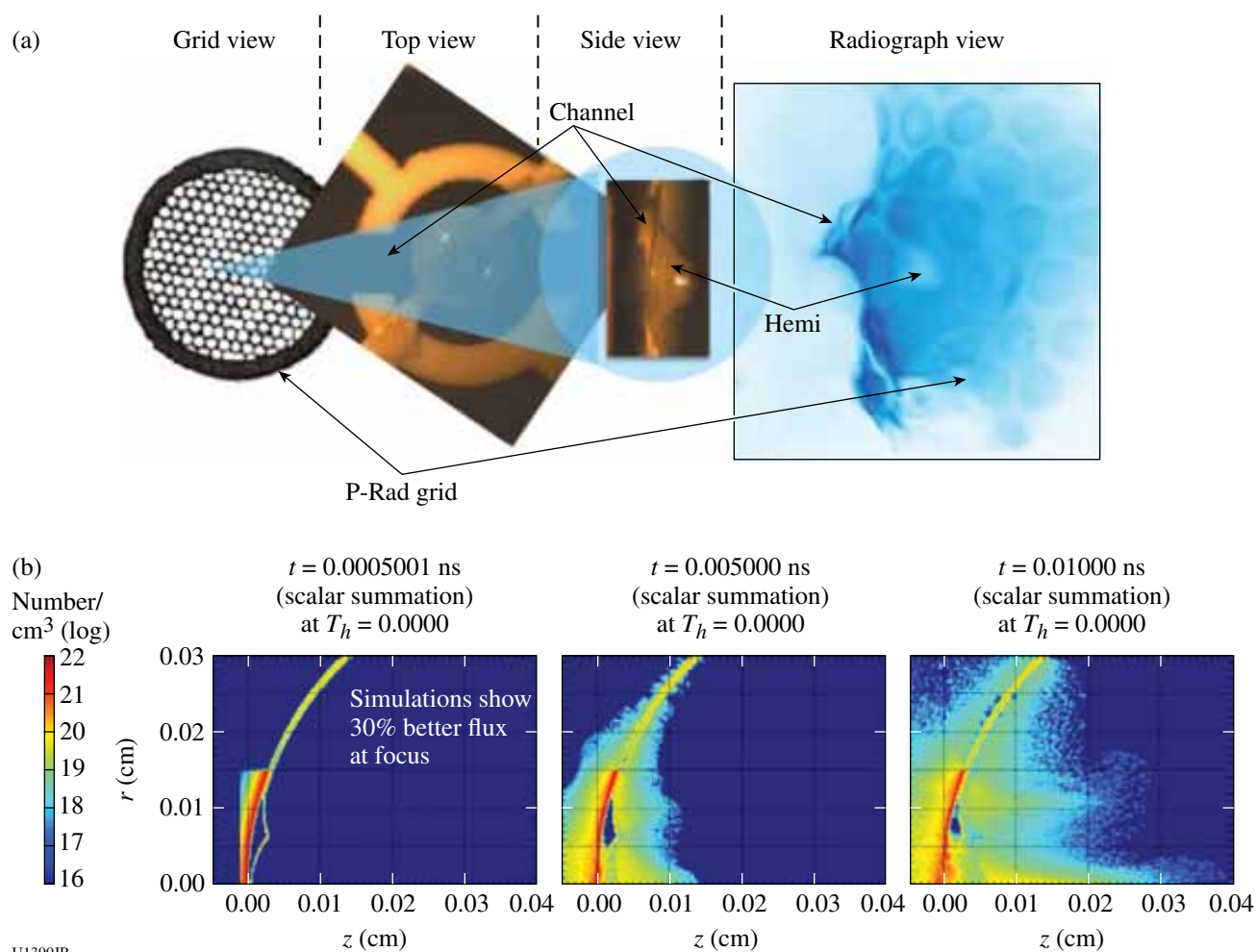


Figure 128.136

(a) Proton radiograph (P-Rad) of a cusped hemi (far right) starts with the radiography beam passing through a hexagonal grid (far left), and then the cusped-hemi target assembly (center, top, and side views) to create an image of the hemi target on a radiochromic film (RCF) stack with the grid superimposed (far right). The image in the RCF is formed from the cross-linking of a polymer dye in the active layer of the film caused by the energy deposited by the proton beam. The resulting image can then be deconvolved to measure the electric field strengths of the accelerating and preplasma fields formed by a second laser interacting with the hemi-apex, and used to refine the focusing design. (b) Simulations show a 30% increase in the flux of carbon ions at the focus of the cusped-hemi design compared to a traditional hemi-shell target. Left axis on the plots are r (cm), the radial dimension of the simulation in cm, and bottom axes are z , the length in cm; color scale indicates the carbon-ion density number/cm³ (log) from blue (10^{15}) to red (10^{22}) for three separate time steps, just as the laser interacts, then 4.5 ps later, and 5 ps after that, using a 10-ps pulse duration.

in nuclear-activation, radiation-effects, and radiation-safety studies. Laser-produced, multi-MeV x-ray sources are also of significant interest for radiography applications since intense, short-duration (picosecond) lasers can be focused to a micron-scale focal spot, which potentially gives access to high temporal and spatial resolution x-ray sources.

The present experiment is the third of this type performed on OMEGA EP by AWE in collaboration with CEA. The MeV x-ray source is produced by focusing a short-duration laser

pulse (the “backlighter”) onto a 2-mm-thick, 2-mm-diam tantalum cylinder target coated at its front surface with a 10- μ m-thick layer of plastic. In the present experiment, with the use of new gratings in the compressor, the backlighter energy on target increased to 1.5 kJ in 10 ps, which is significantly higher than was delivered (\sim 1 kJ) during previous AWE/CEA campaigns on OMEGA EP. For one of the shots, a nanosecond-duration heating beam (250 J, 1 ns with phase-plate smoothing) was used to produce a preformed plasma that was intended to increase the short-pulse energy absorption.

The x-ray source size is estimated from radiography of a resolution grid [Fig. 128.137(a)] and an “image-quality indicator” (IQI) test object. The lower-energy part of the x-ray spectrum is inferred from the radiography of a “Tower of Hanoi” [Fig. 128.137(b)] filter stack and filtered dosimeters. The high-energy (>10-MeV) component of the x-ray spectrum is studied from $^{63}\text{Cu}(\lambda, n)^{62}\text{Cu}$ and $^{12}\text{C}(\gamma, n)^{11}\text{C}$ photonuclear reaction measurements.

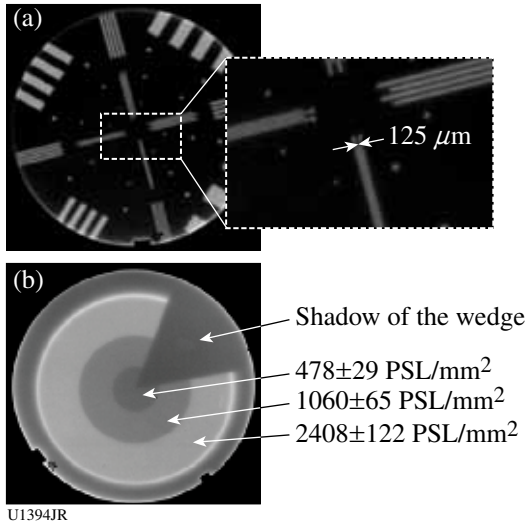


Figure 128.137
(a) Radiographic images of the resolution grid, with detail shown and (b) the Tower of Hanoi test object.

Figures 128.137(a) and 128.137(b) show, respectively, the radiography image of a 15-mm-thick tungsten resolution grid and the tungsten Tower of Hanoi object. Figure 128.137(a) demonstrates that a 125-μm-wide slot can be easily solved by the radiography source, implying that the x-ray source is relatively small (of the order of a few hundred microns). This is in agreement with previous data where the x-ray source size was inferred using a penumbral imaging technique. Figure 128.138 shows data from the IQI test object ($\rho R = 90 \text{ g/cm}^2$).

When the backlighter beam is used without the heating beam, the estimated x-ray temperature is around 3 MeV and an x-ray dose of up to 5 rad in air is measured at 1 m from the source. When both beams are used, the x-ray dose is a factor of 2 lower. This confirms previous data obtained on OMEGA EP, where x-ray emission is consistently lower when the long pulse is used (to create a preformed plasma) in combination with the short pulse. The future 4ω laser probe could be used to investigate this point by establishing the density profile of the preformed plasma with which the short pulse later interacts.

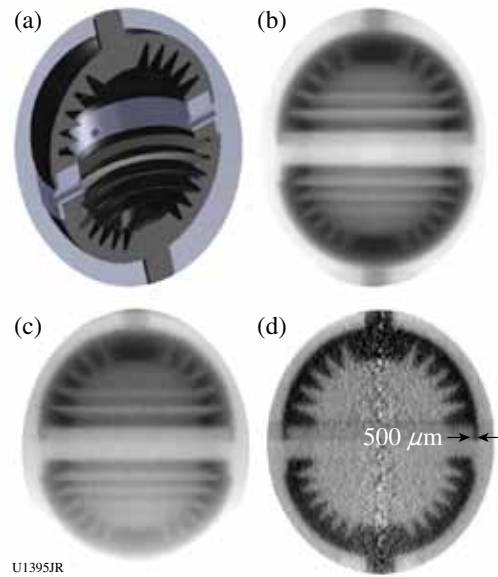


Figure 128.138
(a) CAD section view of the image-quality indicator (IQI) test object. Radiography images of the IQI through (b) 28-g/cm² and (c) 61-g/cm² tungsten equivalent. (d) Density map obtained from (c) after tomography.

High-Resolution 22- to 52-keV Backlighter Sources with Applications for X-Ray Radiography

Principal Investigators: K. Vaughan, A. Moore, K. Wallace, D. Gate, S. McAlpin and R. M. Stevenson (AWE); and V. A. Smalyuk, S. G. Glendinning, B. R. Maddox, H.-S. Park, and C. Sorce (LLNL)

AWE successfully led three shot days (TinMan-11A, HEERD-11A, and TinMan-11B) to investigate x-ray-backlighter microwire targets in the 22- to 52-keV region, in collaboration with LLNL.

Many HED experiments, in particular those investigating ICF applications, require x-ray diagnostic capabilities providing enough photons in a single event to probe HED targets with sufficient contrast and resolution. In light of this, much work has been undertaken to address the development of x-ray probes in the 20- to 100-keV energy range and spatial resolution of less than 20 μm (Refs. 81–84).

The OMEGA EP short-pulse beam was used to irradiate silver, samarium, and ytterbium microwire targets, delivering 22-, 40-, and 52-keV K_{α} x rays, respectively. The microwire targets, produced by the AWE Target Fabrication group, consisted of 10-μm × 10-μm × 300-μm wire of the K_{α} -generating material, supported by a 300-μm × 300-μm × 6-μm CH sub-

strate and held by a 6- μm -diam carbon fiber. To characterize the source size and demonstrate 2-D resolution, a secondary grid target was positioned 10 mm from target chamber center in the direction of the primary radiography diagnostic. Details of the microwire and grid targets are shown in Fig. 128.139.

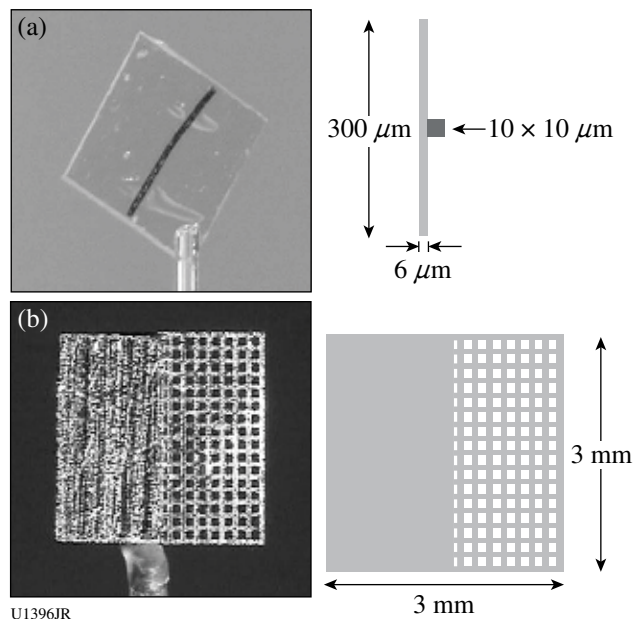


Figure 128.139

Microwire and grid targets. (a) The microwire target shown is a silver microwire supported by a thin CH flag. Other microwire targets fabricated from samarium and ytterbium were also supported by thin CH flags. (b) The grid target shown consists of a solid gold foil and a gold grid. The striations apparent on the foil part of the target are a result of the manufacturing process and are not a feature of the material.

Data were recorded using the transmission crystal spectrometer (TCS) and the high-energy radiography imager for OMEGA EP (HERIE) mounted on diametrically opposed ports of the target chamber (TIM-10 and TIM-13), each with an end-on view of the microwire target. The microwire targets were irradiated at a range of irradiances, incorporating changes in the laser parameters including focal spot size (85 μm to 200 μm), pulse duration (10 ps and 100 ps), and beam energy (100 J to 850 J), to investigate the K_{α} yield over a large parameter space.

Excellent experimental data were obtained for all microwire targets. Figure 128.140 shows a radiograph of the grid target backlit by a samarium microwire. A simple analytical line-spread function analysis of the images indicates that high resolution ($<20 \mu\text{m}$) was achieved in two dimensions.

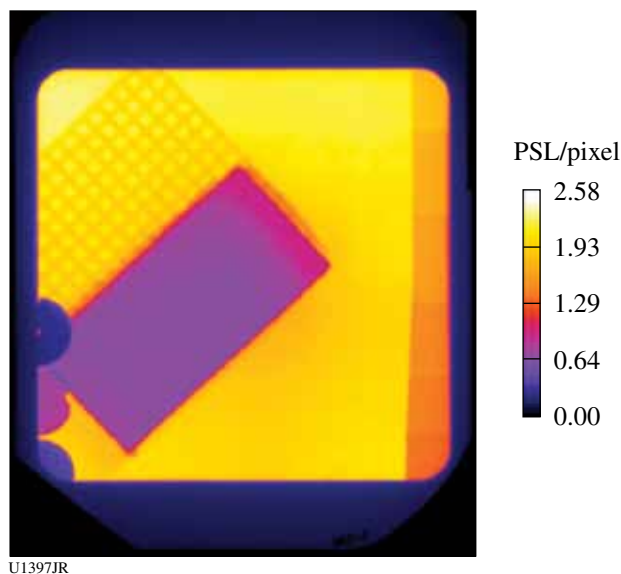


Figure 128.140

A typical radiograph collected by the HERIE diagnostic using a samarium microwire irradiated at $6 \times 10^{17} \text{ W/cm}^2$. Signal strength is shown in units of PSL/pixel. A copper step wedge ranging in thickness from 36 μm to 126 μm (top to bottom) is shown along the right-hand side of the radiograph. In the lower left-hand corner are three tantalum disks of thicknesses 750 μm , 75 μm , and 250 μm (top to bottom), respectively.

Future work on backlighter development continues with strong collaboration between AWE and LLNL.

Laue X-Ray Diffraction Studies of Crystal-Lattice Dynamics

Principal Investigators: A. Comley, J. M. Foster, S. Rothman, N. Park, P. A. Rosen, N. Bazin, and D. Gate (AWE); M. Suggit, A. Higginbotham, and J. Wark (Oxford); and B. R. Maddox, B. A. Remington, H.-S. Park, S. Prisbrey, and A. Elsholz (LLNL)

In the ShkLaue-11A campaign, we further developed our broadband x-ray (“white-light”) Laue diffraction platform designed to probe the lattice dynamics of single-crystal [100] tantalum under shock-loaded conditions, building on our initial study in StrDiff-11A (see LLNL programs section).

In the experiment, an implosion capsule backlighter (980- μm outer diameter with a 10- μm -thick CH wall) driven by 44 OMEGA beams (each beam delivered 500 J of energy in a 1-ns square pulse and SG4 phase plates were used) was employed to generate a smooth, broadband spectrum of x rays to produce the white-light diffraction pattern, recorded using

the LLNL broadband x-ray diffraction diagnostic (BBXRD). A single beam (10 to 40 J in a 1-ns square pulse, with an SG8 phase plate) was used to drive a shock in the tantalum crystal via a 10- μm -thick diamond ablator. The 5- μm -thick tantalum crystal was of [100] orientation.

We obtained an excellent data set that revealed a clear trend of increasing lattice strain anisotropy with a drive pressure in the 1- to 2-Mbar range, controlled in the experiment by varying the laser energy on the crystal target package (Fig. 128.141). VISAR was used to infer the pressure in the sample.

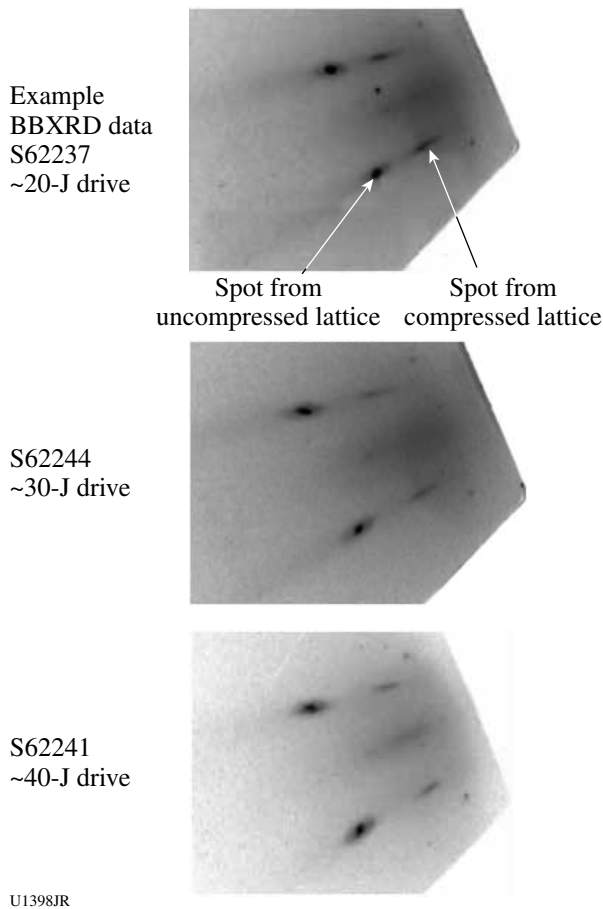


Figure 128.141
Raw BBXRD data showing how diffraction pattern varies with laser-drive energy on the tantalum crystal target package. Each pattern contains characteristic spots, each of which can be attributed to either the shocked or unshocked regions in the crystal, and to specific crystallographic lattice planes. Increasing laser drive energy (and pressure) results in increased spatial separation between the shocked and unshocked spots, indicative of increasing strain anisotropy in the lattice.

Asymmetrically Driven Hohlräume

Principal Investigators: J. M. Foster and S. McAlpin (AWE)

AWE carried out one day of OMEGA experiments (Hohl-Dyn-11A) to conclude a study of capsule implosions in asymmetrically driven hohlraums.

In previous work,^{85,86} a tailored angular and temporal asymmetry of radiation drive was achieved by several means: asymmetry of laser-beam energy and timing, asymmetry of capsule position and hohlraum wall material (albedo), and by introducing an annular restriction of diameter (baffle) within one part of the hohlraum. In these experiments, a 1.6-mm-diam, 2.7-mm-long hohlraum was heated by up to 30 beams of the OMEGA laser. X-ray backlighting of a thin-wall glass capsule (600- μm -diam, 3.5- μm -thick wall, 30- μm CH ablator) or silica aerogel sphere (600- μm -diam, 300- mg cm^{-3} density) provided the primary diagnostic of the angular distribution of radiation drive near the center of the hohlraum. The hydrodynamics was diagnosed using an area x-ray backlighting source together with a 16-image pinhole camera and four-strip-gated MCP detector.

In the most recent experiments, the same experimental platform of the hohlraum and thin-shell capsule was used, but x-ray point-projection backlighting was employed to obtain a single image of greater spatial resolution than had been formerly obtained. The point-projection backlighting technique has the additional advantage of highlighting (by virtue of x-ray refraction, the so-called “phase-contrast” enhancement effect) steep density gradients in the imploding capsule. Thin-shell capsules with walls of uniform thickness and walls that incorporate a shallow equatorial-groove defect were used, and a subset of the asymmetric hohlraum geometries used in the earlier (area-backlit experiments) provided the radiation drive. Excellent experimental data (Fig. 128.142) were obtained, demonstrating the sensitivity of the point-projection-imaging technique for this type of experiment. The data are being used to constrain 2-D hydrocode simulations.

FY11 CEA Experiments at the Omega Laser Facility

CEA Vulnerability Diagnostics on OMEGA: Vulnerability is a key point for the design of plasma diagnostics. Some diagnostics operating on megajoule class lasers require the integration of optical components with electronic devices. The Omega Laser Facility is a fundamental tool for studying the behavior of these elements under irradiation as the DT shot campaigns reproduce the perturbing source expected at early times on the NIF and LMJ. The aim is to maintain in opera-

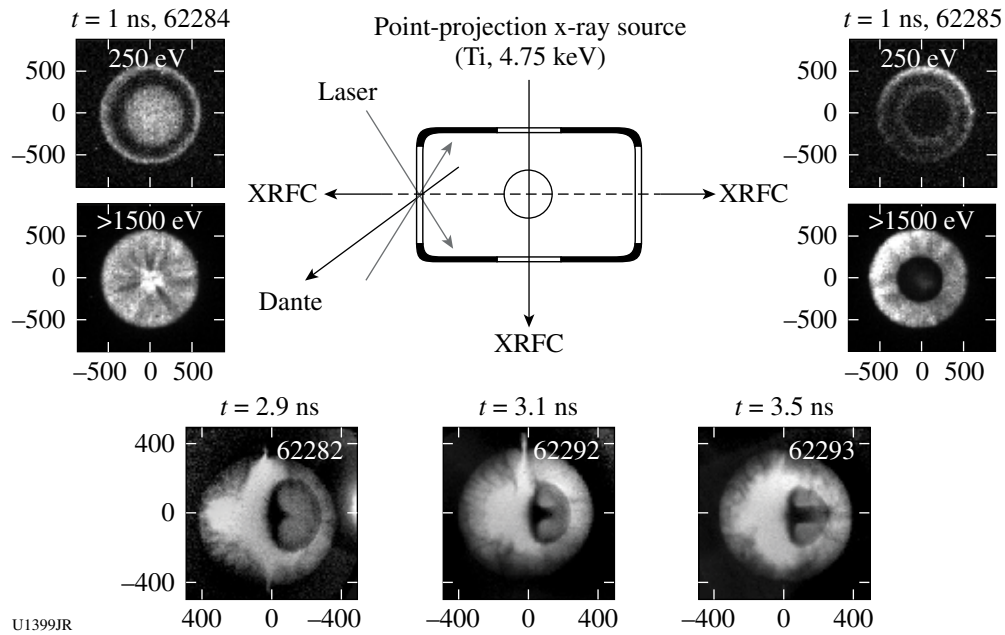


Figure 128.142

The asymmetrically imploded capsule is diagnosed using x-ray framing cameras (XRFC's) viewing along the hohlraum axis and by point-projection imaging viewing orthogonal to the hohlraum axis. The axial views record self-emission from the capsule and hohlraum (which serves as a backlighter for the capsule in one direction) at early time. The orthogonal, point-projection imaging view records details of the asymmetric implosion, with phase-contrast enhancement of the steep density gradient at the glass/ablator interface. Structure around the perimeter of the closing diagnostic hole is also revealed with high spatial resolution ($10\ \mu\text{m}$).

tion the diagnostic and preserve its nominal performance for neutron yields of $\sim 10^{17}$.

During the 8 March 2011 shot campaign, the amount of parasitic light generated by standard optical glasses and fiber bundles was quantified using a set of photomultipliers installed inside the Target Bay at 5 m from TCC (Fig. 128.143). Glasses presented different behavior in terms of the amount of emitted light and decay time (Fig. 128.144). As a result of such studies, glasses

that are prone to scintillators have been identified and their use must be minimized on the NIF/LMF diagnostic systems.

In addition to these characterizations, the vulnerability of an active pixel sensor (APS) based on a complementary metal oxide semiconductor (CMOS) has been studied. The objectives consisted of the evaluation of the durability of the APS in such a radiative environment, measurement of the APS recovery [Fig. 128.145(b)], and the radiation-induced charge generation

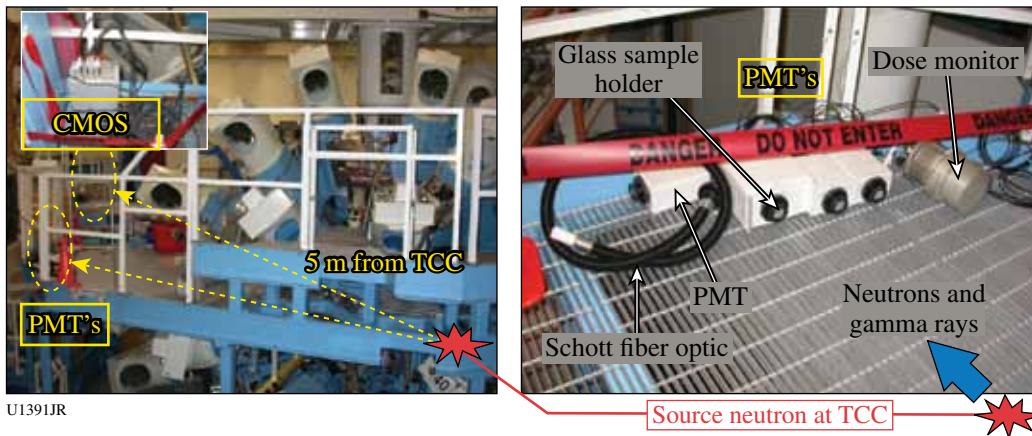
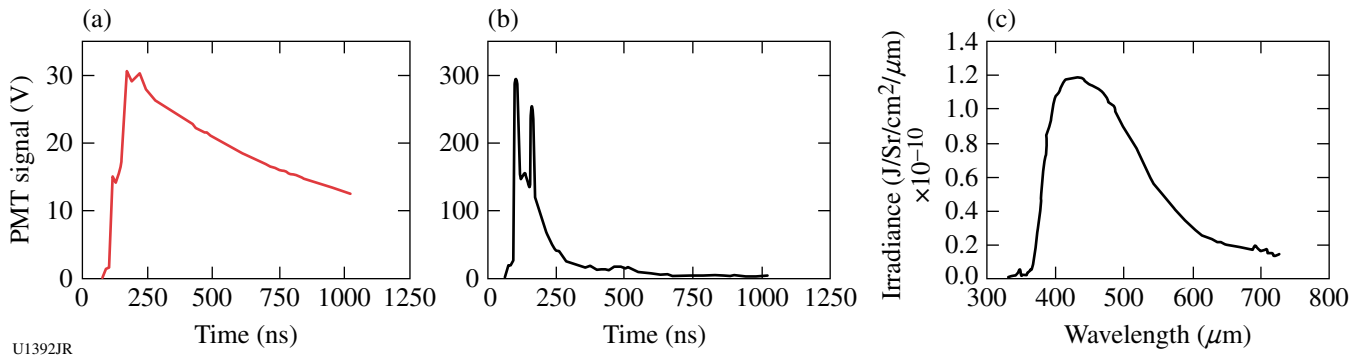
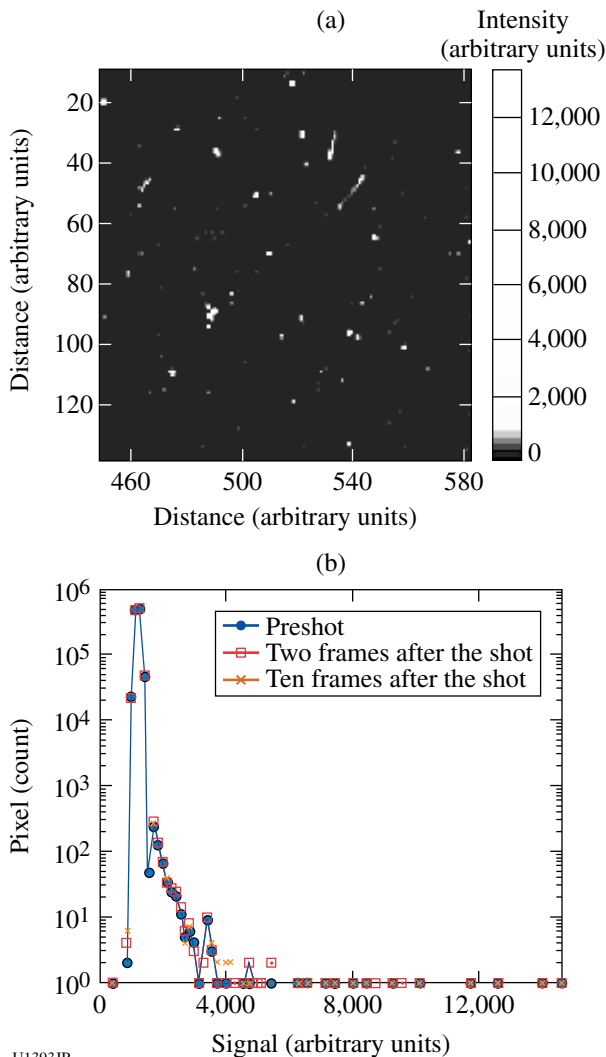


Figure 128.143
Experimental setup.



U1392JR

Figure 128.144
Typical behavior observed on OMEGA for (a) CaF2 and [(b) and (c)] Schott optical fibers bundle.



U1393JR

Figure 128.145
Typical image recording obtained with (a) APS and (b) kinetic of APS recovery.

by the mixed neutrons/gamma rays pulse [Fig. 128.145(a)]. The collected charge distribution inside the image sensor has been successfully measured: the APS remains functional after a DT shot and induced charges inside the pixel are removed. No permanent change in the dark-current distribution has been observed after irradiation.

CEA Neutron Imaging on OMEGA: Over the past ten years, CEA developed the LMJ neutron-imaging diagnostic (NIS) on OMEGA using penumbral or annular coded aperture techniques.⁸⁷⁻⁹⁰ The previous optimized NIS system provided a 20- μm spatial resolution in the source plane and a very good signal-to-noise ratio (SNR). Both the penumbral and the annular imaging techniques were developed successfully, and the annular (ring) technique seems the most promising way to achieve higher-resolution images with a good SNR. Nevertheless, the annular imaging technique is very sensitive to misalignment ($<50\ \mu\text{m}$ in a 200- μm field of view) compared to the penumbral aperture.^{91,92} The use of the annular aperture required the retraction/insertion of the TIM. The alignment technique was not accurate enough, so a new aperture manipulator was designed to increase rigidity and to allow one to change apertures online without retracting the TIM (cf., Fig. 128.146). A new lighting system, embedded in the aperture manipulator tritium protection, now allows one to align the diagnostic even if the opposite port is not available to use a backlighting technique. Penumbral and annular apertures are positioned on the same axis in a pre-alignment phase. The final alignment accuracy was also improved by using a cross-hair target at the target chamber center (TCC).

Apertures were placed at 26 cm and the large neutron camera (scaled for LMJ) at 13 m from TCC (magnification = 50). As in the previous campaigns, alignment was performed

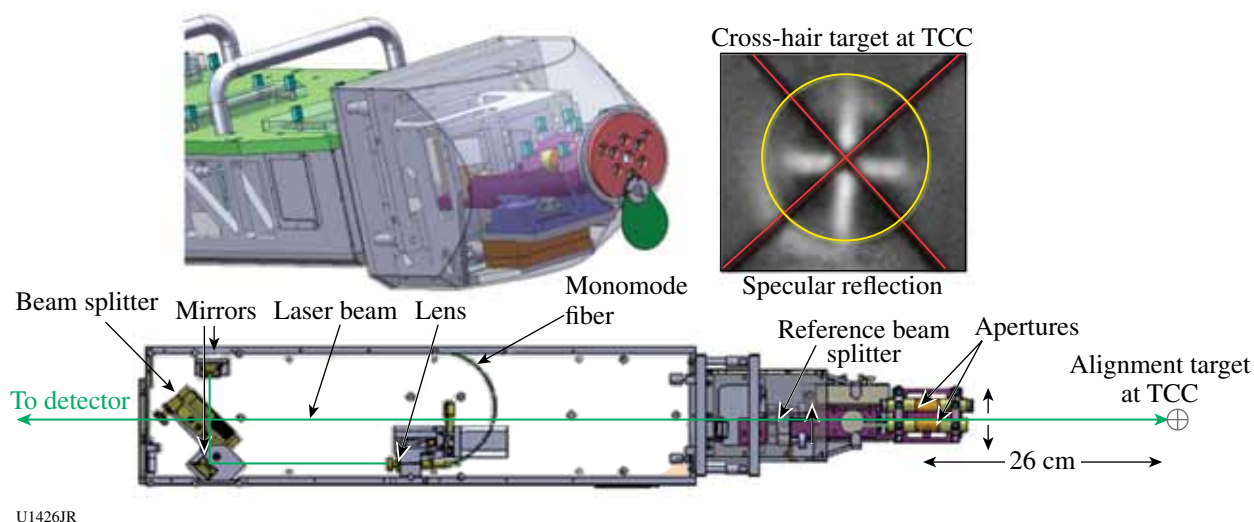


Figure 128.146

New aperture manipulator design allowing for the placement online of either a penumbral or annular aperture at 26 cm from TCC. The image shows the cross-hair target placed at TCC aligned on the axis defined by the telescope reticule placed at 8 m from TCC.

using the penumbral aperture. First images were obtained with the penumbral aperture and the diagnostic was aligned on the first shot. The aperture change was made between shot 61416 and shot 61419. The penumbral and annular images analysis shows a position difference in the image plane of only $144\ \mu\text{m}$ (2 pixels). This corresponds to an aperture relative misalignment of only $3\ \mu\text{m}$ in the source plane. During the entire shot day, alignment settings were not modified. Spherical, prolate, and oblate 14-MeV neutron core images were obtained by varying the laser-energy balance and compared to x-ray images from the LLE GMXI diagnostic in the 4- to 7-keV range (cf., Fig. 128.147). The neutron image SNR is in the 30 to 50 range and the system resolution is $\sim 16\ \mu\text{m}$.

First shot alignment is a crucial issue for megajoule-class lasers with a long line of sight (40 m for LMJ), and it was demonstrated again this year. The new alignment system and method now allow us to use both penumbral and annular apertures.

FY11 Center for Radiative Shock Hydrodynamics—Experiments

The Center for Radiative Shock Hydrodynamics (CRASH) is a scientific computing center where part of the Center's effort is to predict experimental data and quantify uncertainty in experimental data. CRASH is part of the Predictive Science Academic Alliance Program (PSAAP). The main experiment

that CRASH models is a radiative-shock experiment. In this system the radiative flux is so large that radiative effects must be considered when modeling the system since they affect the shock dynamics. The CRASH code is a 3-D Eulerian radiation-hydrodynamics code based on an adaptive, massively parallel magnetohydrodynamics code. Experiments for this year focused on obtaining early-time data of a radiative-shock system.

Figure 128.148(a) shows a radiograph of a radiative shock at 4.5 ns after the start of the laser drive. This image was taken with a four-strip x-ray framing camera using the area radiography technique. In this experiment, ten OMEGA laser beams are used with a 380-J/beam in a 1-ns square pulse to irradiate a 20- μm Be disk. SG8 distributed phase plates (DPP's) and the smoothing by spectral dispersion (SSD) technique at maximum modulation smooth the laser beams, which launch a shock into the Be disk. The shock breaks out of the disk and into nominally 1.1 atm of Xe gas. The shock moves rapidly (over $\sim 150\ \mu\text{m}/\text{ns}$ initially) and becomes so hot that radiative effects become important in the system. As the shock moves down the tube, it sweeps up more Xe and becomes a dense Xe layer with an entrained Xe flow behind the shock. This is evident in late-time data that we previously obtained and are shown in Figs. 128.148(b) and 128.148(c), which show a radiative shock observed at 13 and 26 ns, respectively.

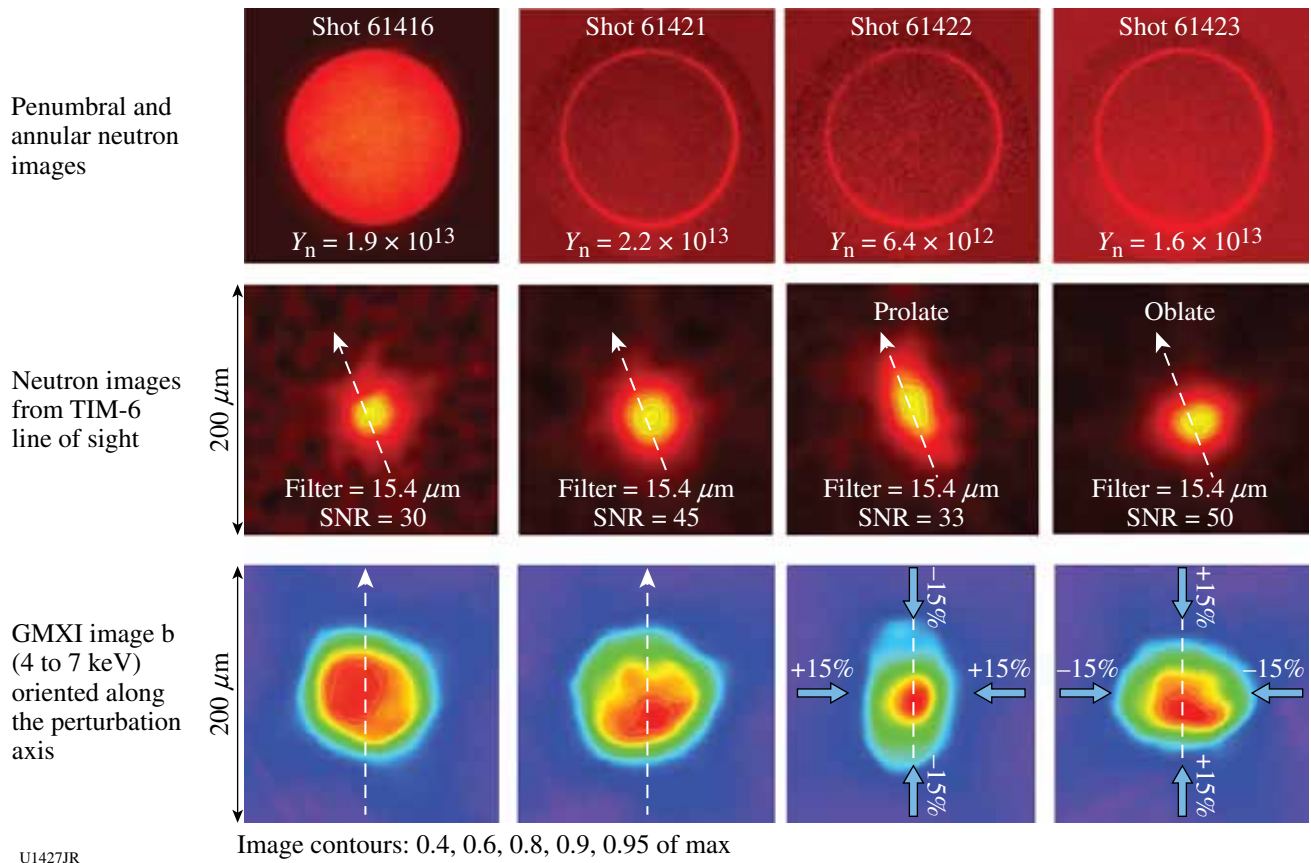


Figure 128.147

Neutron and LLE x-ray images obtained during spherical, oblate, and prolate implosions. The dashed white arrows show the perturbation axis on neutron and x-ray images.

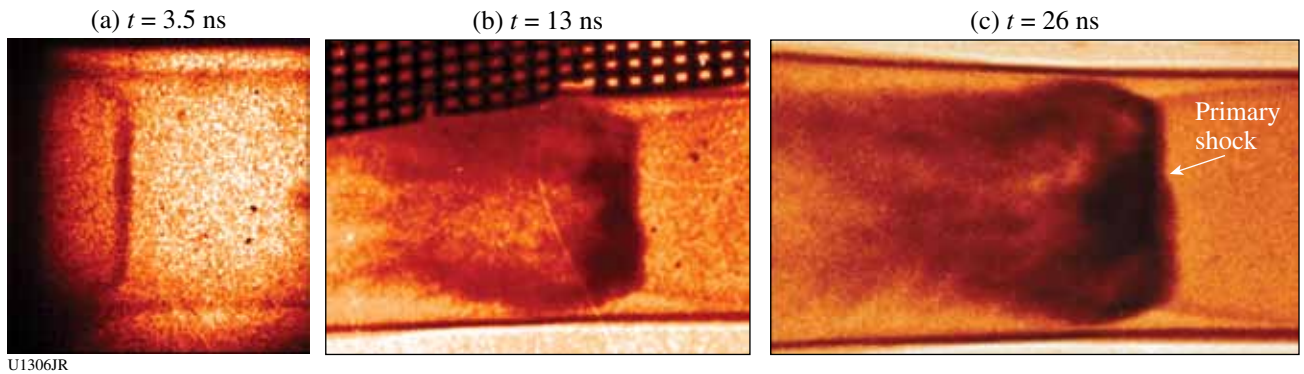


Figure 128.148

X-ray radiographs of a radiative shock experiment at (a) 3.5 ns, (b) 13 ns, and (c) 26 ns. As the shock moves down the Xe-filled tube, it accumulates more Xe.

REFERENCES

1. M. A. Morales *et al.*, Proc. Natl. Acad. Sci. **106**, 1324 (2009).
2. W. Lorenzen, B. Holst, and R. Redmer, Phys. Rev. Lett. **102**, 115701 (2009).
3. T. Nagayama, R. C. Mancini, R. Florido, R. Tommasini, J. A. Koch, J. A. Delettrez, S. P. Regan, and V. A. Smalyuk, J. Appl. Phys. **109**, 093303 (2011).
4. C. K. Li, F. H. Séguin, J. A. Frenje, J. R. Rygg, R. D. Petrasso, R. P. J. Town, P. A. Amendt, S. P. Hatchett, O. L. Landen, A. J. Mackinnon, P. K. Patel, V. Smalyuk, J. P. Knauer, T. C. Sangster, and C. Stoeckl, Rev. Sci. Instrum. **77**, 10E725 (2006).
5. T. R. Boehly, D. L. Brown, R. S. Craxton, R. L. Keck, J. P. Knauer, J. H. Kelly, T. J. Kessler, S. A. Kumpan, S. J. Loucks, S. A. Letzring, F. J. Marshall, R. L. McCrory, S. F. B. Morse, W. Seka, J. M. Soures, and C. P. Verdon, Opt. Commun. **133**, 495 (1997).
6. L. J. Waxer, D. N. Maywar, J. H. Kelly, T. J. Kessler, B. E. Kruschwitz, S. J. Loucks, R. L. McCrory, D. D. Meyerhofer, S. F. B. Morse, C. Stoeckl, and J. D. Zuegel, Opt. Photonics News **16**, 30 (2005).
7. J. R. Rygg, F. H. Séguin, C. K. Li, J. A. Frenje, M. J.-E. Manuel, R. D. Petrasso, R. Betti, J. A. Delettrez, O. V. Gotchev, J. P. Knauer, D. D. Meyerhofer, F. J. Marshall, C. Stoeckl, and W. Theobald, Science **319**, 1223 (2008).
8. C. K. Li, F. H. Séguin, J. A. Frenje, M. Rosenberg, R. D. Petrasso, P. A. Amendt, J. A. Koch, O. L. Landen, H. S. Park, H. F. Robey, R. P. J. Town, A. Casner, F. Philippe, R. Betti, J. P. Knauer, D. D. Meyerhofer, C. A. Back, J. D. Kilkenny, and A. Nikroo, Science **327**, 1231 (2010).
9. C. K. Li, F. H. Séguin, J. A. Frenje, J. R. Rygg, R. D. Petrasso, R. P. J. Town, P. A. Amendt, S. P. Hatchett, O. L. Landen, A. J. Mackinnon, P. K. Patel, V. A. Smalyuk, T. C. Sangster, and J. P. Knauer, Phys. Rev. Lett. **97**, 135003 (2006).
10. C. K. Li, F. H. Séguin, J. A. Frenje, J. R. Rygg, R. D. Petrasso, R. P. J. Town, P. A. Amendt, S. P. Hatchett, O. L. Landen, A. J. Mackinnon, P. K. Patel, M. Tabak, J. P. Knauer, T. C. Sangster, and V. A. Smalyuk, Phys. Rev. Lett. **99**, 015001 (2007).
11. C. K. Li, F. H. Séguin, J. A. Frenje, J. R. Rygg, R. D. Petrasso, R. P. J. Town, O. L. Landen, J. P. Knauer, and V. A. Smalyuk, Phys. Rev. Lett. **99**, 055001 (2007).
12. C. K. Li, F. H. Séguin, J. R. Rygg, J. A. Frenje, M. Manuel, R. D. Petrasso, R. Betti, J. Delettrez, J. P. Knauer, F. Marshall, D. D. Meyerhofer, D. Shvarts, V. A. Smalyuk, C. Stoeckl, O. L. Landen, R. P. J. Town, C. A. Back, and J. D. Kilkenny, Phys. Rev. Lett. **100**, 225001 (2008).
13. C. K. Li, F. H. Séguin, J. A. Frenje, R. D. Petrasso, P. A. Amendt, R. P. J. Town, O. L. Landen, J. R. Rygg, R. Betti, J. P. Knauer, D. D. Meyerhofer, J. M. Soures, C. A. Back, J. D. Kilkenny, and A. Nikroo, Phys. Rev. Lett. **102**, 205001 (2009).
14. R. D. Petrasso, C. K. Li, F. H. Séguin, J. R. Rygg, J. A. Frenje, R. Betti, J. P. Knauer, D. D. Meyerhofer, P. A. Amendt, D. H. Froula, O. L. Landen, P. K. Patel, J. S. Ross, and R. P. J. Town, Phys. Rev. Lett. **103**, 085001 (2009).
15. O. V. Gotchev, P. Y. Chang, J. P. Knauer, D. D. Meyerhofer, O. Polomarov, J. Frenje, C. K. Li, M. J.-E. Manuel, R. D. Petrasso, J. R. Rygg, F. H. Séguin, and R. Betti, Phys. Rev. Lett. **103**, 215004 (2009).
16. C. K. Li, F. H. Séguin, J. H. Frenje, M. J. Rosenberg, H. G. Rinderknecht, A. B. Zylstra, R. D. Petrasso, P. A. Amendt, O. L. Landen, A. J. Mackinnon, R. P. J. Town, S. C. Wilks, R. Betti, D. D. Meyerhofer, J. M. Soures, J. Hund, J. D. Kilkenny, and A. Nikroo, "Impeding Hohlraum Plasma Stagnation in Inertial Confinement Fusion," to be published in Physical Review Letters.
17. F. H. Séguin, C. K. Li, M. J.-E. Manuel, H. G. Rinderknecht, N. Sinenian, J. A. Frenje, J. R. Rygg, D. G. Hicks, R. D. Petrasso, J. Delettrez, R. Betti, F. J. Marshall, and V. A. Smalyuk, "Time Evolution of Filamentation and Self-Generated Fields in the Coronae of Directly Driven ICF Capsules," to be published in Physics of Plasmas.
18. A. B. Zylstra *et al.*, "Measurements of Hohlraum-Produced Fast Ions," submitted to Physics of Plasmas.
19. J. A. Frenje, C. K. Li, F. H. Séguin, D. T. Casey, R. D. Petrasso, D. P. McNabb, P. Navratil, S. Quaglioni, T. C. Sangster, V. Yu. Glebov, and D. D. Meyerhofer, Phys. Rev. Lett. **107**, 122502 (2011).
20. F. H. Séguin, J. A. Frenje, C. K. Li, D. G. Hicks, S. Kurebayashi, J. R. Rygg, B.-E. Schwartz, R. D. Petrasso, S. Roberts, J. M. Soures, D. D. Meyerhofer, T. C. Sangster, J. P. Knauer, C. Sorce, V. Yu. Glebov, C. Stoeckl, T. W. Phillips, R. J. Leeper, K. Fletcher, and S. Padalino, Rev. Sci. Instrum. **74**, 975 (2003).
21. H.-S. Park, D. D. Ryutov, J. S. Ross, N. L. Kugland, S. H. Glenzer, C. Plechaty, S. M. Pollaine, B. A. Remington, A. Spitkovsky, L. Gargaté, G. Gregori, A. Bell, C. Murphy, Y. Sakawa, Y. Kuramitsu, T. Morita, H. Takabe, D. H. Froula, G. Fiksel, F. Miniati, M. Koenig, A. Ravasio, A. Pelka, E. Liang, N. Woolsey, C. C. Kuranz, R. P. Drake, and M. J. Grosskopf, "Studying Astrophysical Collisionless Shocks with Counterstreaming Plasmas from High Power Lasers," to be published in High Energy Density Physics.
22. A. Spitkovsky, Bull. Am. Phys. Soc. **56**, Paper B6.00001 (2011).
23. A. Spitkovsky, presented at the Twenty-Second International Conference on Numerical Simulation of Plasmas, Long Branch, NJ, 7–9 September 2011.
24. A. Spitkovsky, presented at the Center for Magnetic Self-Organization (CMSO) General Meeting, Durham, NH, 17–20 October 2011.
25. H.-S. Park, presented at ICHED (International Conference on High Energy Density Physics), Lisbon, Portugal, 17–20 May 2011.
26. H.-S. Park, presented at the 7th International Conference on Inertial Fusion Sciences and Applications, Bordeaux, France, 12–16 September 2011.
27. Y. Sakawa, presented at The Seventh International Conference on Inertial Fusion Sciences and Applications, Bordeaux-Lac, France, 12–16 September 2011.
28. J. Ross, Bull. Am. Phys. Soc. **56**, 282 (2011).
29. L. Gargaté, A. Spitkovsky, H.-S. Park, N. L. Kugland, J. S. Ross, B. A. Remington, S. M. Pollaine, D. D. Ryutov, G. Gregori, Y. Sakawa,

- Y. Kuramitsu, H. Takabe, D. H. Froula, G. Fiksel, F. Miniati, M. Koenig, A. Ravasio, N. Woolsey, and M. Grosskopf, presented at the Interrelationship Between Plasma Experiments in Laboratory and Space, Whistler, Canada, 10–15 July 2011.
30. M. Grosskopf, presented at the 11th International Workshop on the Interrelationship Between Plasma Experiments in the Laboratory and in Space (IPELS), Whistler, Canada, 10–15 July 2011.
 31. M. Wei, presented at the 38th European Physical Society Conference on Plasma Physics, Strasbourg, France, 27 June–1 July 2011.
 32. R. Mishra, presented at the 7th International Conference on Inertial Fusion Sciences and Applications, Bordeaux, France, 12–16 September 2011.
 33. L. Willingale, P. M. Nilson, A. G. R. Thomas, J. Cobble, R. S. Craxton, A. Maksimchuk, P. A. Norreys, T. C. Sangster, R. H. H. Scott, C. Stoeckl, C. Zulick, and K. Krushelnick, *Phys. Rev. Lett.* **106**, 105002 (2011).
 34. H. Chen, S. C. Wilks, D. D. Meyerhofer, J. Bonlie, C. D. Chen, S. N. Chen, C. Courtois, L. Elbersen, G. Gregori, W. Krueer, O. Landoas, J. Mithen, J. Myatt, C. D. Murphy, P. Nilson, D. Price, M. Schneider, R. Shepherd, C. Stoeckl, M. Tabak, R. Tommasini, and P. Beiersdorfer, *Phys. Rev. Lett.* **105**, 015003 (2010).
 35. H. Chen, D. D. Meyerhofer, S. C. Wilks, R. Cauble, F. Dollar, K. Falk, G. Gregori, A. Hazi, E. I. Moses, C. D. Murphy, J. Myatt, J. Park, J. Seely, R. Shepherd, A. Spitkovsky, C. Stoeckl, C. I. Szabo, R. Tommasini, C. Zulick, and P. Beiersdorfer, *High Energy Density Phys.* **7**, 225 (2011).
 36. R. Betti, K. Anderson, T. R. Boehly, T. J. B. Collins, R. S. Craxton, J. A. Delettrez, D. H. Edgell, R. Epstein, V. Yu. Glebov, V. N. Goncharov, D. R. Harding, R. L. Keck, J. H. Kelly, J. P. Knauer, S. J. Loucks, J. A. Marozas, F. J. Marshall, A. V. Maximov, D. N. Maywar, R. L. McCrory, P. W. McKenty, D. D. Meyerhofer, J. Myatt, P. B. Radha, S. P. Regan, C. Ren, T. C. Sangster, W. Seka, S. Skupsky, A. A. Solodov, V. A. Smalyuk, J. M. Soures, C. Stoeckl, W. Theobald, B. Yaakobi, C. Zhou, J. D. Zuegel, J. A. Frenje, C. K. Li, R. D. Petrasso, and F. H. Séguin, *Plasma Phys. Control. Fusion* **48**, B153 (2006).
 37. O. V. Gotchev, J. P. Knauer, P. Y. Chang, N. W. Jang, M. J. Shoup III, D. D. Meyerhofer, and R. Betti, *Rev. Sci. Instrum.* **80**, 043504 (2009).
 38. P. Y. Chang, G. Fiksel, M. Hohenberger, J. P. Knauer, R. Betti, F. J. Marshall, D. D. Meyerhofer, F. H. Séguin, and R. D. Petrasso, *Phys. Rev. Lett.* **107**, 035006 (2011).
 39. O. A. Hurricane, *High Energy Density Phys.* **4**, 97 (2008).
 40. E. C. Harding *et al.*, *Phys. Rev. Lett.* **103**, 045005 (2009).
 41. O. A. Hurricane *et al.*, *Phys. Plasmas* **16**, 056305 (2009).
 42. M. Borghesi *et al.*, *Rev. Sci. Instrum.* **74**, 1688 (2003).
 43. I. V. Igumenshchev, F. J. Marshall, J. A. Marozas, V. A. Smalyuk, R. Epstein, V. N. Goncharov, T. J. B. Collins, T. C. Sangster, and S. Skupsky, *Phys. Plasmas* **16**, 082701 (2009).
 44. A. L. Kritcher *et al.*, *Phys. Rev. Lett.* **107**, 015002 (2011).
 45. A. L. Kritcher *et al.*, *High Energy Density Phys.* **7**, 271 (2011).
 46. D. D. Ryutov *et al.*, *Phys. Plasmas* **18**, 104504 (2011).
 47. A. B. Belonoshko, R. Ahuja, and B. Johansson, *Nature* **424**, 1032 (2003).
 48. S. H. Glenzer, *Rev. Mod. Phys.* **81**, 1625 (2009).
 49. S. H. Glenzer *et al.*, *Phys. Rev. Lett.* **90**, 175002 (2003).
 50. G. Gregori *et al.*, *Phys. Rev. E* **67**, 026412 (2003).
 51. H. Sawada, S. P. Regan, D. D. Meyerhofer, I. V. Igumenshchev, V. N. Goncharov, T. R. Boehly, R. Epstein, T. C. Sangster, V. A. Smalyuk, B. Yaakobi, G. Gregori, S. H. Glenzer, and O. L. Landen, *Phys. Plasmas* **14**, 122703 (2007).
 52. S. H. Glenzer *et al.*, *Phys. Rev. Lett.* **98**, 065002 (2007).
 53. G. Gregori *et al.*, *High Energy Density Phys.* **3**, 99 (2007).
 54. P. B. Radha, V. N. Goncharov, T. J. B. Collins, J. A. Delettrez, Y. Elbaz, V. Yu. Glebov, R. L. Keck, D. E. Keller, J. P. Knauer, J. A. Marozas, F. J. Marshall, P. W. McKenty, D. D. Meyerhofer, S. P. Regan, T. C. Sangster, D. Shvarts, S. Skupsky, Y. Srebro, R. P. J. Town, and C. Stoeckl, *Phys. Plasmas* **12**, 032702 (2005).
 55. G. Kresse and J. Furthmüller, *Phys. Rev. B* **54**, 11169 (1996).
 56. J. Vorberger *et al.*, *Phys. Rev. B* **75**, 024206 (2007).
 57. P. M. Celliers, D. J. Erskine, C. M. Sorce, D. G. Braun, O. L. Landen, and G. W. Collins, *Rev. Sci. Instrum.* **81**, 035101 (2010).
 58. R. Betti, C. D. Zhou, K. S. Anderson, L. J. Perkins, W. Theobald, and A. A. Solodov, *Phys. Rev. Lett.* **98**, 155001 (2007).
 59. W. L. Krueer, *The Physics of Laser–Plasma Interactions*, *Frontiers in Physics*, Vol. 73, edited by D. Pines (Addison-Wesley, Redwood City, CA, 1988).
 60. R. Betti, W. Theobald, C. D. Zhou, K. S. Anderson, P. W. McKenty, S. Skupsky, D. Shvarts, V. N. Goncharov, J. A. Delettrez, P. B. Radha, T. C. Sangster, C. Stoeckl, and D. D. Meyerhofer, *J. Phys., Conf. Ser.* **112**, 022024 (2008).
 61. V. Yu. Glebov, D. D. Meyerhofer, C. Stoeckl, and J. D. Zuegel, *Rev. Sci. Instrum.* **72**, 824 (2001).
 62. W. Seka, D. H. Edgell, J. P. Knauer, J. F. Myatt, A. V. Maximov, R. W. Short, T. C. Sangster, C. Stoeckl, R. E. Bahr, R. S. Craxton, J. A. Delettrez, V. N. Goncharov, I. V. Igumenshchev, and D. Shvarts, *Phys. Plasmas* **15**, 056312 (2008).
 63. C. Stoeckl, V. Yu. Glebov, D. D. Meyerhofer, W. Seka, B. Yaakobi, R. P. J. Town, and J. D. Zuegel, *Rev. Sci. Instrum.* **72**, 1197 (2001).
 64. X. Ribeyre *et al.*, *Plasma Phys. Control. Fusion* **50**, 025007 (2008).
 65. R. Tommasini, S. P. Hatchett, D. S. Hey, C. Iglesias, N. Izumi, J. A. Koch, O. L. Landen, A. J. MacKinnon, C. Sorce, J. A. Delettrez, V. Yu. Glebov, T. C. Sangster, and C. Stoeckl, *Phys. Plasmas* **18**, 056309 (2011).
 66. Y. Ping *et al.*, *J. Instrum.* **6**, P09004 (2011).

67. H. J. Lee, P. Neumayer, J. Castor, T. Döppner, R. W. Falcone, C. Fortmann, B. A. Hammel, A. L. Kritcher, O. L. Landen, R. W. Lee, D. D. Meyerhofer, D. H. Munro, R. Redmer, S. P. Regan, S. Weber, and S. H. Glenzer, *Phys. Rev. Lett.* **102**, 115001 (2009).
68. D. K. Bradley *et al.*, *Phys. Rev. Lett.* **102**, 075503 (2009).
69. F. Occelli, P. Loubeyre, and R. LeToullec, *Nat. Mater.* **2**, 151 (2003).
70. A. Dewaele *et al.*, *Phys. Rev. Lett.* **97**, 215504 (2006).
71. L. S. Dubrovinsky *et al.*, *Phys. Rev. Lett.* **84**, 1720 (2000).
72. S. Desgreniers, Y. K. Vohra, and A. L. Ruoff, *Phys. Rev. B* **39**, 10,359 (1989).
73. L. Burakovsky, D. L. Preston, and R. R. Silbar, *Phys. Rev. B* **61**, 15,011 (2000).
74. N. R. Barton *et al.*, *J. Appl. Phys.* **109**, 073501 (2011).
75. H.-S. Park *et al.*, "Experimental Results of Ta Material Strength at High Pressure and High Strain Rate," to be published in AIP for the SCCM proceedings.
76. H.-S. Park *et al.*, "Tantalum Material Strength Dependence on Grain Sizes at 100 GPa Pressure and 107 s^{-1} Strain Rates," in preparation.
77. E. N. Loomis, D. Braun, S. H. Batha, C. Sorce, and O. L. Landen, *Phys. Plasmas* **18**, 092702 (2011).
78. E. N. Loomis, presented at the 7th International Conference on Inertial Fusion Sciences and Applications, Bordeaux, France, 12–16 September 2011.
79. A. Banerjee, R. A. Gore, and M. J. Andrews, *Phys. Rev. E* **82**, 046309 (2010).
80. D. T. Offermann *et al.*, *Phys. Plasmas* **18**, 056713 (2011).
81. H.-S. Park, D. M. Chambers, H.-K. Chung, R. J. Clarke, R. Eagleton, E. Giraldez, T. Goldsack, R. Heathcote, N. Izumi, M. H. Key, J. A. King, J. A. Koch, O. L. Landen, A. Nikroo, P. K. Patel, D. F. Price, B. A. Remington, H. F. Robey, R. A. Snavely, D. A. Steinman, R. B. Stephens, C. Stoeckl, M. Storm, M. Tabak, W. Theobald, R. P. J. Town, J. E. Wickersham, and B. B. Zhang, *Phys. Plasmas* **13**, 056309 (2006).
82. H.-S. Park *et al.*, *Phys. Plasmas* **15**, 072705 (2008).
83. E. Brambrink, H. G. Wei, B. Barbrel, P. Audebert, A. Benuzzi-Mounaix, T. Boehly, T. Endo, C. Gregory, T. Kimura, R. Kodama, N. Ozaki, H. S. Park, M. Rabec le Gloahec, and M. Koenig, *Phys. Plasmas* **16**, 033101 (2009).
84. B. R. Maddox *et al.*, *Phys. Plasmas* **18**, 056709 (2011).
85. K. Vaughn, S. McAlpin, J. M. Foster, R. M. Stevenson, S. G. Glendinning, and C. Sorce, *Phys. Plasmas* **17**, 056316 (2010).
86. *LLE 2009 Annual Report, October 2008–September 2009*, Laboratory for Laser Energetics, University of Rochester, Rochester, NY, LLE Document No. DOE/NA/28302-923 (January 2010); *LLE 2010 Annual Report, October 2009–September 2010*, Laboratory for Laser Energetics, University of Rochester, Rochester, NY, LLE Document No. DOE/NA/28302-985 (January 2011).
87. L. Disdier, A. Rouyer, D. C. Wilson, A. Fedotoff, C. Stoeckl, J. L. Bourgade, V. Yu. Glebov, J.-P. Garçonnet, and W. Seka, *Nucl. Instrum. Methods Phys. Res. A* **489**, 496 (2002).
88. L. Disdier, A. Rouyer, A. Fedotoff, J.-L. Bourgade, F. J. Marshall, V. Yu. Glebov, and C. Stoeckl, *Rev. Sci. Instrum.* **74**, 1832 (2003).
89. L. Disdier, R. A. Lerche, J. L. Bourgade, and V. Yu. Glebov, *Rev. Sci. Instrum.* **75**, 2134 (2004).
90. A. Rouyer, *Rev. Sci. Instrum.* **74**, 1234 (2003).
91. L. Disdier, A. Rouyer, I. Lantuéjoul, O. Landoas, J. L. Bourgade, T. C. Sangster, V. Yu. Glebov, and R. A. Lerche, *Phys. Plasmas* **13**, 056317 (2006).
92. I. Thfoin, O. Landoas, T. Caillaud, L. Disdier, M. Vincent, J.-L. Bourgade, B. Rossé, T. C. Sangster, V. Yu. Glebov, G. Pien, and W. Armstrong, *Rev. Sci. Instrum.* **81**, 033503 (2010).

The Third Omega Laser Facility Users' Group Workshop

Introduction

A capacity gathering of 115 researchers from 25 universities and laboratories and 9 countries met at the Laboratory for Laser Energetics (LLE) for the third Omega Laser Facility Users' Group (OLUG) workshop. The purpose of the three-day workshop was to facilitate communication and exchanges among individual Omega Laser Facility users and between users and the LLE management; to present ongoing and proposed research; to encourage research opportunities and collaborations that could be undertaken at the Omega Laser Facility and in a complementary fashion at other facilities (such as the NIF or LULI); to provide an opportunity for students, postdoctoral fellows, and young researchers to present their

research in an informal setting; and to provide LLE management with feedback from the users about ways to improve the Facility and future experimental campaigns. The interactions were wide-ranging and lively, as can be seen in photographs shown in this article.

The Omega Laser Facility Users consist of 266 members from 32 universities and 23 centers and national laboratories; their names and affiliations can be found at www.lle.rochester.edu/media/about/documents/OLUGMEMBERS.pdf. OLUG is by far the largest users' group in the world in the field of high-energy-density (HED) physics, and it is certainly one of the most active.



U1400JR

Figure 128.149

A capacity gathering of 115 researchers from 25 universities and laboratories around the world participated in this year's workshop. The users' group itself has 266 members from 32 universities and 23 laboratories, making it by far the largest such high-energy-density-physics group in the world. The Omega Facility is now a member of the National Users' Facility Organization, which in turn promotes science education and outreach throughout the nation. The next annual Omega Laser Facility Users' Workshop will occur on 25–27 April 2012.

The first two mornings of the workshop comprised 13 science and Facility presentations. The Facility talks proved especially useful for those unfamiliar with the art and complexities of performing experiments on OMEGA. But since the Facility is constantly changing and improving, even experienced users significantly benefited from these updates. The overview science talks, given by leading world authorities, described the breadth and excitement of HED science undertaken at the Omega Laser Facility. The next section of this article contains a summary of the range of presentations and activities.

About 50 students and postdoctoral fellows, 44 of whom were supported by travel grants from NNSA, attended the workshop and presented 37 of the 57 contributed poster and oral presentations. The content of their presentations ranged from target fabrication to simulating aspects of supernovae; the presentations generated spirited discussions, probing questions, and friendly suggestions. In addition, 20 contributed presentations were made by professional scientists and academics.

An important function of the workshop was to develop a set of **Findings and Recommendations** (p. 253) to help set future priorities for the Omega Laser Facility.

These findings were grouped into four areas: 60-beam OMEGA, OMEGA EP, general Facility improvements, and the accessibility of OMEGA operational information. These categories comprise a report given to Omega Facility management (highlights to follow). LLE management is currently using these recommendations as a guide for making decisions about Omega Laser Facility operations, priorities, and future changes.

One highlight of the workshop was the panel of students and postdoctoral fellows who discussed their experiences at the Omega Laser Facility and presented their thoughts and recommendations on Facility improvements. Wide-ranging and engaging discussions were sparked by this forum, which resulted in the student/postdoctoral report.

Another important event was a job fair designed to bring students together with potential future employers and to discuss career opportunities that exist at national laboratories, in private industry, and at universities.

Finally, one of the important decisions made at the workshop was the scheduling of the next one. It will be held at LLE on 25–27 April 2012. Meetings of the Users' Group and interested



U1401JR

Figure 128.150

About 50 students and postdoctoral fellows, 44 of whom received travel assistance from an NNSA grant, attended and made 37 presentations. Travel assistance has already been arranged for the next annual workshop. The workshop places tremendous emphasis on the participation of young researchers.

members of the HED community are formulating plans for this fourth workshop. In addition, an annual meeting, in which the status of the **Findings and Recommendations** (p. 253) will be updated, will occur during the fall APS/DPP Conference.

The Presentations

A diverse set of 70 talks and posters were presented over a three-day period. In morning sessions, invited talks on the Facility and science were given. The invited science talks focused on several important topics, including HED plasmas in general, laboratory astrophysics, ignition in inertial confinement fusion (ICF), the physics of shock and fast ignition, and future experiments on OMEGA and the NIF.

The Omega Facility talks presented important details and developments on the status and performance of OMEGA/ OMEGA EP from pulse shaping and duration to beam smoothing; the qualification process for interfacing new experiments;

the present, and soon-to-be operating, set of diagnostics; and the critical role of targets, from design, to procurement, to full characterization, to fielding, and finally shooting.

In addition to the 13 invited presentations, 57 contributed posters and talks covered a wide spectrum of work on OMEGA from target fabrication to fast-ignition experiments to basic and novel nuclear physics experiments. Work was also presented on opportunities for taking physics platforms developed on OMEGA to other facilities that are both larger (the NIF) and smaller (Jupiter, Trident, and LULI, as examples). The invited and contributed presentations formed much of the basis for the discussions that resulted in the **Findings and Recommendations** (p. 253) for the Omega Facilities; topics and chairpersons for each are presented herein.

The photographs provide a representative sampling of the workshop's talks, interactions, and ambience.



U1403JR

Figure 128.151

In the plenary sessions, 13 authorities spoke about the science and opportunities of HED physics and described the evolving capabilities of the Omega Laser Facility needed to reach new science frontiers. Here LLE Director Dr. Robert L. McCrory, a strong supporter of OLUG since its inception, welcomes the users and talks about the evolving capabilities of the Facility that keep it at the cutting edge of research.

The 13 Findings and Recommendations of the OMEGA 2011 Users' Workshop (reports and presentations can be found on-line at www.lle.rochester.edu/about/OLUG11_workshop/index.php):

1. Tammy Ma, Chair, LLNL. *Findings and Recommendations of the Student/Postdoc Panel.*
2. Louise Willingale, Chair, University of Michigan. *Bringing OMEGA EP Performance up to Full Specification, and 4 ω Probe Utilization.*



U1404JR

Figure 128.152
University of Rochester astrophysicist Adam Frank gave a stellar talk on instabilities and clumping processes in jets and in astrophysical and laboratory settings.



U1405JR

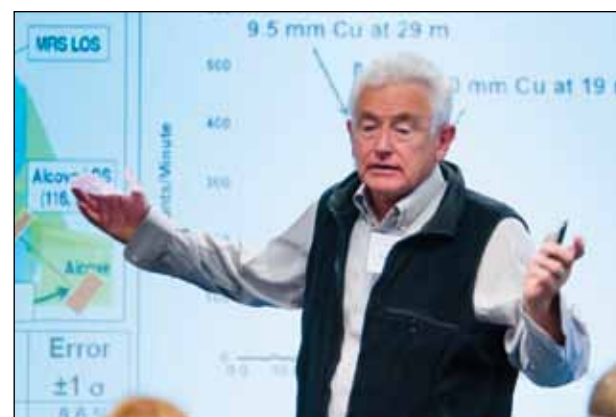
Figure 128.153
University of New Hampshire (UNH) theorist Will Fox talked about theoretical aspects of 3-D reconnection in laboratory and astrophysical settings. UNH is one of 32 universities who are members of the OMEGA Users' group. University researchers, 107 in number, comprise the largest component of OLUG's 266 members.

3. Mingsheng Wei, Chair, GA. *Long-Pulse Operations of OMEGA EP.*
4. Carolyn Kuranz, Chair, University of Michigan. *Independent Operations of the Three Legs of OMEGA 60.*



U1406JR

Figure 128.154
Nuclear physicist Dennis McNabb of LLNL described new and exciting opportunities in plasma nuclear science that are emerging on OMEGA and the NIF. Several contributed workshop talks, as well as Facility recommendations, focused on this nascent frontier field, whose origins directly derive from recent OMEGA Users' experiments. Subsequent to the workshop, a joint MIT, LLNL, and LLE press conference (www.web.mit.edu/press/2011/omega-laser.html) announced the results of the first basic nuclear physics experiments obtained in ICF. Many more such experiments are either already underway or are being actively planned on OMEGA.



U1407JR

Figure 128.155
Joe Kilkenny of General Atomics talked about the importance and pervasiveness of moving diagnostics and experimental platforms from OMEGA to the NIF. Many critical diagnostics at the NIF, such as the magnetic recoil (neutron) spectrometer, were first developed and used on OMEGA before being duplicated and deployed on the NIF.

5. Dustin Froula, Chair, LLE. *Work to Develop a Simulation Capability for the OMEGA External Users.*
6. Peter Norreys, Chair, Rutherford Appleton Laboratory. *Dual Foci for the Omega 60 Facility.*
7. Dennis McNabb (LLNL) and Johan Frenje (MIT), Chairs. *Developing Implosion Capabilities on OMEGA with*

Arbitrary Fuel Mixtures of Tritium for Advancing Plasma Nuclear Science.

8. Alex Zylstra, Chair, MIT. *An Ultra-Low-Charged-Particle Spectrometer for Studying Nucleo-Synthesis Reactions in OMEGA Implosions.*
9. Nareg Sinenian (MIT) and Jim Cobble (LANL), Chairs. *Utilization of Thomson Parabola on OMEGA for Characterizing Implosion Ion-Loss Channels and for Studying Nucleo-Synthesis Reactions in OMEGA Implosions.*



U1408JR

Figure 128.156

Sam Morse, the Omega Facility Director, talked about changes in the Facility and LLE's implementation of OLUG'S Findings and Recommendations. Sam leads the Facility's cognizant, approachable engineers and managers who are constantly working to facilitate and improve users' experiments. A very strong and cordial relationship exists between the users and the LLE management team, and extensive discussions occur throughout the year between OLUG and the management regarding OLUG's Findings and Recommendations.



U1410JR

Figure 128.158

Two poster sessions presented an opportunity for informal discussions about OMEGA experiments and their connections to important work at other HED facilities, especially the NIF.



U1409JR

Figure 128.157

Don Cook, NNSA's Deputy Administrator for Defense Programs, talked to the OMEGA Users about NNSA's perspective on HED science on OMEGA and on the value they place on the users' work and research.



U1412JR

Figure 128.159

The workshop provided many opportunities for informal interactions and discussions and for sowing the seeds of new experimental and theoretical efforts.



U1411JR

Figure 128.160

Thirty-seven posters and contributed talks were given by students and post-doctoral fellows.



U1413JR

Figure 128.161

The student–postdoc panel, chaired by LLNL’s Tammy Ma, led an engaging discussion about issues that young researchers face in performing experiments on OMEGA. This panel formulated their own Findings and Recommendations that became part of the workshop proceedings.



U1415JR

Figure 128.162

Thirteen different Findings and Recommendations for the Facility were extensively discussed by User leads and Chairs (shown here from top to bottom are Maria Gatu-Johnson from MIT; Hye-Sook Park from LLNL; and Carolyn Kuranz from University of Michigan). Women physicists have an extremely strong presence at every level of OLUG, from the Executive Committee to the chairs of the major OLUG committees on Findings and Recommendations.

10. Hans Herrmann, Chair, LANL. *Gamma-Ray Spectrometry for Plasma Nuclear Science and Implosion Physics.*

11. Maria Gatu-Johnson, Chair, MIT. *A Low-Energy Neutron Spectrometer for Plasma Nuclear Science and Implosion Physics.*

12. Gennady Fiksel, Chair, LLE. *Developing Magnetic Inertial Fusion Platforms for Basic Science and Implosion Physics.*

13. Hye-Sook Park, Chair, LLNL. *Cu-K α Crystal Imaging on OMEGA EP for HED Physics.*



U1416JR

Figure 128.163

Tours of OMEGA and OMEGA EP were a critical component of the workshop and greatly appreciated by users new and old. Here LLE engineer Steve Stagnitto is shown in the OMEGA viewing gallery talking with workshop attendees about the intricacies and challenges of organizing a successful experimental program.



U1418JR

Figure 128.165

The workshop banquet was enjoyed by all and offered a wonderful opportunity for good cheer and good food. The making of lifelong colleagues and friends is one of the lasting results of the Users' workshop. Good friends make for good science!



U1417JR

Figure 128.164

Physicist Ray Leeper discussed career opportunities in research at Sandia National Laboratory, Lawrence Livermore National Laboratory and Los Alamos National Laboratory also presented overviews of laboratory research opportunities. These talks presented a unique opportunity for young researchers to learn about research not only on OMEGA, but at the other major facilities, at Universities, and in the private sector.

Questions Addressed in the General Workshop Sessions:

What new avenues of research should we be pursuing on the Omega/Omega EP Laser Facilities?

What Facility improvements, large or small, can improve current research and help us pursue science at the cutting edge?

How can the administrative organization and the infrastructure at LLE better support ongoing and groundbreaking research?

What additional platforms/experiments/diagnostics might advantageously be built and coordinated, e.g., between OMEGA and the NIF, and/or between OMEGA and Trident or Jupiter?

The OMEGA Laser Users' Meeting was held at the APS/DPP conference in Utah on 15 November 2011. The next OMEGA Laser Users' Workshop will be held at LLE on 25–27 April 2012.

ACKNOWLEDGMENT

This OMEGA Users' Workshop is made possible in part by the generous support of the National Nuclear Security Administration for travel expenses of students and postdocs; by the Office of Fusion Energy Sciences for support of general workshop costs; by General Atomics; by the Fusion Science Center; by the MIT/Plasma Science and Fusion Center; and by the Laboratory for Laser Energetics for the use and availability of critical resources and support. In addition, OLUG thanks the LLE management for their responsiveness to our Findings and Recommendations. For capturing through his lens the workshop ambiance, OLUG thanks Eugene Kowaluk. R. D. Petrasso is the editor for this Proceeding.

Publications and Conference Presentations

Publications

- S.-W. Bahk, “Highly Accurate Wavefront Reconstruction Algorithms over Broad Spatial-Frequency Bandwidth,” *Opt. Express* **19**, 18,997 (2011).
- T. R. Boehly, V. N. Goncharov, W. Seka, M. A. Barrios, P. M. Celliers, D. G. Hicks, G. W. Collins, S. X. Hu, J. A. Marozas, and D. D. Meyerhofer, “Velocity and Timing of Multiple Spherically Converging Shock Waves in Deuterium,” *Phys. Rev. Lett.* **106**, 195005 (2011).
- T. R. Boehly, V. N. Goncharov, W. Seka, S. X. Hu, J. A. Marozas, D. D. Meyerhofer, P. M. Celliers, D. G. Hicks, M. A. Barrios, D. Fratanduono, and G. W. Collins, “Multiple Spherically Converging Shock Waves in Liquid Deuterium,” *Phys. Plasmas* **18**, 092706 (2011).
- J. Bromage, J. M. Fini, C. Dorrer, and J. D. Zuegel, “Characterization and Optimization of Yb-Doped Photonic-Crystal Fiber Rod Amplifiers Using Spatially Resolved Spectral Interferometry,” *Appl. Opt.* **50**, 2001 (2011).
- J. Bromage, J. Rothhardt, S. Hädrich, C. Dorrer, C. Jocher, S. Demmler, J. Limpert, A. Tünnermann, and J. D. Zuegel, “Analysis and Suppression of Parasitic Processes in Non-collinear Optical Parametric Amplifiers,” *Opt. Express* **19**, 16,797 (2011).
- P. Y. Chang, G. Fiksel, M. Hohenberger, J. P. Knauer, R. Betti, F. J. Marshall, D. D. Meyerhofer, F. H. Séguin, and R. D. Petrasso, “Fusion Yield Enhancement in Magnetized Laser-Driven Implosions,” *Phys. Rev. Lett.* **107**, 035006 (2011).
- B. Ciftcioglu, J. Zhang, R. Sobolewski, and H. Wu, “An 850-nm Normal-Incidence Germanium Metal–Semiconductor–Metal Photodetector With 13-GHz Bandwidth and 8- μ A Dark Current,” *IEEE Photon. Technol. Lett.* **22**, 1850 (2010).
- A. S. Cross, J. P. Knauer, A. Mycielski, D. Kochanowska, M. Wiktowska-Baran, R. Jakieła, J. Domagała, Y. Cui, R. B. James, and R. Sobolewski, “(Cd,Mn)Te Detectors for Characterization of X-Ray Emissions Generated During Laser-Driven Fusion Experiments,” *Nucl. Instrum. Methods Phys. Res. A* **624**, 649 (2010).
- W. R. Donaldson, D. N. Maywar, J. H. Kelly, and R. E. Bahr, “Measurement of the Self-Phase Modulation-Induced Bandwidth in a 30 kJ Class Laser Amplifier Chain,” *J. Opt. Soc. Am. B* **28**, 445 (2011).
- D. E. Fratanduono, T. R. Boehly, M. A. Barrios, D. D. Meyerhofer, J. H. Eggert, R. F. Smith, D. G. Hicks, P. M. Celliers, D. G. Braun, and G. W. Collins, “Refractive Index of Lithium Fluoride Ramp Compressed to 800 GPa,” *J. Appl. Phys.* **109**, 123521 (2011).
- C. G. Freeman, G. Fiksel, C. Stoeckl, N. Sinenian, M. J. Canfield, G. B. Graeper, A. T. Lombardo, C. R. Stillman, S. J. Padalino, C. Mileham, T. C. Sangster, and J. A. Frenje, “Calibration of a Thomson Parabola Ion Spectrometer and Fujifilm Imaging Plate Detectors for Protons, Deuterons, and Alpha Particles,” *Rev. Sci. Instrum.* **82**, 073301 (2011).
- D. H. Froula, S. H. Glenzer, N. C. Luhmann, and J. Sheffield, *Plasma Scattering of Electromagnetic Radiation: Theory and Measurement Techniques* (Elsevier, Burlington, MA, 2011).
- M. C. Ghilea, D. D. Meyerhofer, and T. C. Sangster, “A Freon-Filled Bubble Chamber for Neutron Detection in Inertial Confinement Fusion Experiments,” *Rev. Sci. Instrum.* **82**, 033305 (2011).
- M. C. Ghilea, D. D. Meyerhofer, and T. C. Sangster, “Neutron-Induced Nucleation Inside Bubble Chambers Using Freon 115 as the Active Medium,” *Nucl. Instrum. Methods Phys. Res. A* **648**, 210 (2011).
- V. Yu. Glebov, T. C. Sangster, C. Stoeckl, J. P. Knauer, W. Theobald, K. L. Marshall, M. J. Shoup III, T. Buczek,

- M. Cruz, T. Duffy, M. Romanofsky, M. Fox, A. Pruyne, M. J. Moran, R. A. Lerche, J. McNaney, J. D. Kilkenny, M. J. Eckart, D. Schneider, D. Munro, W. Stoeffl, R. A. Zacharias, J. J. Haslam, T. Clancy, M. Yeoman, D. Warwas, C. J. Horsfield, J.-L. Bourgade, O. Landoas, L. Disdier, G. A. Chandler, and R. J. Leeper, "The National Ignition Facility Neutron Time-of-Flight System and Its Initial Performance," *Rev. Sci. Instrum.* **81**, 10D325 (2010) (invited).
- E. Głowacki, K. L. Marshall, C. W. Tang, and N. S. Sariciftci, "Doping of Organic Semiconductors Induced by Lithium Fluoride/Aluminum Electrodes Studied by Electron Spin Resonance and Infrared Reflection-Absorption Spectroscopy," *Appl. Phys. Lett.* **99**, 043305 (2011).
- M. J. Guardalben and L. J. Waxer, "Improvements to Long-Pulse System Performance and Operational Efficiency on OMEGA EP," in *High Power Lasers for Fusion Research*, edited by A. A. S. Awwal, A. M. Dunne, H. Azechi, and B. E. Kruschwitz (SPIE, Bellingham, WA, 2011), Vol. 7916, Paper 79160G.
- S. X. Hu, "Attosecond Timing the Ultrafast Charge-Transfer Process in Atomic Collisions," *Phys. Rev. A* **83**, 041401(R) (2011).
- S. X. Hu, V. N. Goncharov, P. B. Radha, J. A. Marozas, S. Skupsky, T. R. Boehly, T. C. Sangster, D. D. Meyerhofer, and R. L. McCrory, "Two-Dimensional Simulations of the Neutron-Yield in Cryogenic Deuterium-Tritium Implosions on OMEGA," *Phys. Plasmas* **17**, 102706 (2010).
- I. V. Igumenshchev, D. H. Edgell, V. N. Goncharov, J. A. Delettrez, A. V. Maximov, J. F. Myatt, W. Seka, A. Shvydky, S. Skupsky, and C. Stoeckl, "Crossed-Beam Energy Transfer in Implosion Experiments on OMEGA," *Phys. Plasmas* **17**, 122708 (2010).
- S. D. Jacobs, "MRF with Adjustable pH," in *Optical Fabrication, Testing, and Metrology IV*, edited by A. Duparré (SPIE, Bellingham, WA, 2011), Vol. 8169, Paper 816902.
- V. Kaushal, I. Iñiguez-de-la-Torre, H. Irie, G. Guarino, W. R. Donaldson, P. Ampadu, R. Sobolewski, and M. Margala, "A Study of Geometry Effects on the Performance of Ballistic Deflection Transistors," *IEEE Trans. Nanotech.* **9**, 723 (2010).
- G. Li, R. Yan, C. Ren, J. Tonge, and W. B. Mori, "Three-Dimensional Particle-in-Cell Simulations of Laser Channeling in Fast Ignition," *Phys. Plasmas* **18**, 042703 (2011).
- F. J. Marshall, T. DeHaas, and V. Yu. Glebov, "Charge-Injection-Device Performance in the High-Energy-Neutron Environment of Laser-Fusion Experiments," *Rev. Sci. Instrum.* **81**, 10E503 (2010).
- K. L. Marshall, S. K.-H. Wei, M. Vargas, K. Wegman, C. Dorrer, P. Leung, J. Boule III, Z. Zhao, and S. H. Chen, "Liquid Crystal Beam-Shaping Devices Employing Patterned Photoalignment Layers for High-Peak-Power Laser Applications," in *Liquid Crystals XV*, edited by I. C. Khoo (SPIE, Bellingham, WA, 2011), Vol. 8114, Paper 81140P.
- D. D. Meyerhofer, R. L. McCrory, R. Betti, T. R. Boehly, D. T. Casey, T. J. B. Collins, R. S. Craxton, J. A. Delettrez, D. H. Edgell, R. Epstein, K. A. Fletcher, J. A. Frenje, V. Yu. Glebov, V. N. Goncharov, D. R. Harding, S. X. Hu, I. V. Igumenshchev, J. P. Knauer, C. K. Li, J. A. Marozas, F. J. Marshall, P. W. McKenty, P. M. Nilson, S. P. Padalino, R. D. Petrasso, P. B. Radha, S. P. Regan, T. C. Sangster, F. H. Séguin, W. Seka, R. W. Short, D. Shvarts, S. Skupsky, J. M. Soures, C. Stoeckl, W. Theobald, and B. Yaakobi, "High-Performance Inertial Confinement Fusion Target Implosions on OMEGA," *Nucl. Fusion* **51**, 053010 (2011).
- C. Miao, R. Shen, M. Wang, S. N. Shafrir, H. Yang, and S. D. Jacobs, "Rheology of Aqueous Magnetorheological Fluid Using Dual Oxide-Coated Carbonyl Iron Particles," *J. Am. Ceram. Soc.* **94**, 2386 (2011).
- M. Mikulics, P. Kordoš, D. Gregušová, R. Adam, M. Kočan, S. Wu, J. Zhang, R. Sobolewski, D. Grützmacher, and M. Marso, "Monolithic Integration of Ultrafast Photodetector and MESFET in the GaN Material System," *IEEE Photonics Technol. Lett.* **23**, 1189 (2011).
- P. M. Nilson, A. A. Solodov, J. F. Myatt, W. Theobald, P. A. Jaanimagi, L. Gao, C. Stoeckl, R. S. Craxton, J. A. Delettrez, B. Yaakobi, J. D. Zuegel, B. E. Kruschwitz, C. Dorrer, J. H. Kelly, K. U. Akli, P. K. Patel, A. J. Mackinnon, R. Betti, T. C. Sangster, and D. D. Meyerhofer, "Scaling Hot-Electron Generation to High-Power, Kilojoule-Class Laser-Solid Interactions," *Phys. Rev. Lett.* **105**, 235001 (2010).

- P. M. Nilson, A. A. Solodov, J. F. Myatt, W. Theobald, P. A. Jaanimagi, L. Gao, C. Stoeckl, R. S. Craxton, J. A. Delettrez, B. Yaakobi, J. D. Zuegel, B. E. Kruschwitz, C. Dorrer, J. H. Kelly, K. U. Akli, P. K. Patel, A. J. Mackinnon, R. Betti, T. C. Sangster, and D. D. Meyerhofer, "Scaling Hot-Electron Generation to Long-Pulse, High-Intensity Laser-Solid Interactions," *Phys. Plasmas* **18**, 056703 (2011).
- P. M. Nilson, W. Theobald, C. Mileham, C. Stoeckl, J. F. Myatt, J. A. Delettrez, J. MacFarlane, I. A. Begishev, J. D. Zuegel, R. Betti, T. C. Sangster, and D. D. Meyerhofer, "Target-Heating Effects on the $K_{\alpha_{1,2}}$ -Emission Spectrum from Solid Targets Heated by Laser-Generated Hot Electrons," *Phys. Plasmas* **18**, 042702 (2011).
- R. Nora and R. Betti, "One-Dimensional Planar Hydrodynamic Theory of Shock Ignition," *Phys. Plasmas* **18**, 082710 (2011).
- A. V. Okishev, "Characterization of Highly Stable Mid-IR, GaSb-Based Laser Diodes," *Opt. Express* **19**, 9863 (2011).
- J. B. Oliver, P. Kupinski, A. L. Rigatti, A. W. Schmid, J. C. Lambropoulos, S. Papernov, A. Kozlov, J. Spaulding, D. Sadowski, Z. R. Chrzan, R. D. Hand, D. R. Gibson, I. Brinkley, and F. Placido, "Large-Aperture Plasma-Assisted Deposition of Inertial Confinement Fusion Laser Coatings," *Appl. Opt.* **50**, C19 (2011).
- S. Papernov, A. Tait, W. Bittle, A. W. Schmid, J. B. Oliver, and P. Kupinski, "Near-Ultraviolet Absorption and Nanosecond-Pulse-Laser Damage in HfO_2 Monolayers Studied by Submicrometer-Resolution Photothermal Heterodyne Imaging and Atomic Force Microscopy," *J. Appl. Phys.* **109**, 113106 (2011).
- S. Papernov, A. Tait, W. Bittle, A. W. Schmid, J. B. Oliver, and P. Kupinski, "Submicrometer-Resolution Mapping of Ultraweak 355-nm Absorption in HfO_2 Monolayers Using Photothermal Heterodyne Imaging," in *Laser-Induced Damage in Optical Materials: 2010*, edited by G. J. Exarhos, V. E. Gruzdev, J. A. Menapace, D. Ristau, and M. J. Soileau (SPIE, Bellingham, WA, 2010), Vol. 7842, Paper 78420A.
- B. B. Pollock, C. E. Clayton, J. E. Ralph, F. Albert, A. Davidson, L. Divol, C. Filip, S. H. Glenzer, K. Herpoldt, W. Lu, K. A. Marsh, J. Meinecke, W. B. Mori, A. Pak, T. C. Rensink, J. S. Ross, J. Shaw, G. R. Tynan, C. Joshi, and D. H. Froula, "Demonstration of a Narrow Energy Spread, ~ 0.5 GeV Electron Beam from a Two-Stage Laser Wakefield Accelerator," *Phys. Rev. Lett.* **107**, 045001 (2011).
- P. B. Radha, R. Betti, T. R. Boehly, J. A. Delettrez, D. H. Edgell, V. N. Goncharov, I. V. Igumenshchev, J. P. Knauer, J. A. Marozas, F. J. Marshall, R. L. McCrory, D. D. Meyerhofer, S. P. Regan, T. C. Sangster, W. Seka, S. Skupsky, A. A. Solodov, C. Stoeckl, W. Theobald, J. A. Frenje, D. T. Casey, C. K. Li, and R. D. Petrasso, "Inertial Confinement Fusion Using the OMEGA Laser System," *IEEE Trans. Plasma Sci.* **39**, 1007 (2011).
- P. B. Radha, C. Stoeckl, V. N. Goncharov, J. A. Delettrez, D. H. Edgell, J. A. Frenje, I. V. Igumenshchev, J. P. Knauer, J. A. Marozas, R. L. McCrory, D. D. Meyerhofer, R. D. Petrasso, S. P. Regan, T. C. Sangster, W. Seka, and S. Skupsky, "Triple-Picket Warm Plastic-Shell Implosions on OMEGA," *Phys. Plasmas* **18**, 012705 (2011).
- S. P. Regan, H. Sawada, V. N. Goncharov, D. Li, P. B. Radha, R. Epstein, J. A. Delettrez, S. X. Hu, V. A. Smalyuk, B. Yaakobi, T. R. Boehly, T. C. Sangster, D. D. Meyerhofer, R. L. McCrory, and R. C. Mancini, "Spectroscopic Observations of Fermi-Degenerate Aluminum Compressed and Heated to Four Times Solid Density and 20 eV," *High Energy Density Phys.* **7**, 259 (2011).
- J. E. Schoenly, W. D. Seka, and P. Rechmann, "Near-Ultraviolet Removal Rates for Subgingival Dental Calculus at Different Irradiation Angles," *J. Biomed. Opt.* **16**, 071404 (2011).
- J. M. Soures, "Opportunities for Inertial Fusion and High-Energy-Density Physics Research at the National Laser Users' Facility," in *High Power Lasers for Fusion Research*, edited by A. A. S. Awwal, A. M. Dunne, H. Azechi, and B. E. Kruschwitz (SPIE, Bellingham, WA, 2011), Vol. 7916, Paper 791603.
- C. Stoeckl, M. Cruz, V. Yu. Glebov, J. P. Knauer, R. Lauck, K. Marshall, C. Mileham, T. C. Sangster, and W. Theobald, "A Gated Liquid-Scintillator-Based Neutron Detector for Fast-Ignitor Experiments and Down-Scattered Neutron Measurements," *Rev. Sci. Instrum.* **81**, 10D302 (2010).
- W. Theobald, V. Ovchinnikov, S. Ivancic, B. Eichman, P. M. Nilson, J. A. Delettrez, R. Yan, G. Li, F. J. Marshall, D. D. Meyerhofer, J. F. Myatt, C. Ren, T. C. Sangster, C. Stoeckl,

J. D. Zuegel, L. Van Woerkom, R. R. Freeman, K. U. Akli, E. Giraldez, and R. B. Stephens, "High-Intensity Laser-Plasma Interaction with Wedge-Shaped-Cavity Targets," *Phys. Plasmas* **17**, 103101 (2010).

W. Theobald, A. A. Solodov, C. Stoeckl, K. S. Anderson, R. Betti, T. R. Boehly, R. S. Craxton, J. A. Delettrez, C. Dorrer, J. A. Frenje, V. Yu. Glebov, H. Habara, K. A. Tanaka, J. P. Knauer, F. J. Marshall, K. L. Marshall, D. D. Meyerhofer, P. M. Nilson, P. K. Patel, H. Chen, T. C. Sangster, W. Seka, N. Sinenian, T. Ma, F. N. Beg, E. Giraldez, and R. B. Stephens, "Initial Cone-in-Shell Fast-Ignition Experiments on OMEGA," *Phys. Plasmas* **18**, 056305 (2011).

W. Wang, T. B. Jones, and D. R. Harding, "On-Chip Double Emulsion Droplet Assembly Using Electrowetting-on-Dielectric and Dielectrophoresis," *Fusion Sci. Technol.* **59**, 240 (2011).

S. K. H. Wei and S. H. Chen, "Spatially Resolved Lasers Using a Glassy Cholesteric Liquid Crystal Film with Lateral Pitch Gradient," *Appl. Phys. Lett.* **98**, 111112 (2011).

S. K.-H. Wei, L. Zeng, K. L. Marshall, and S. H. Chen, "Room-Temperature Processing of π -Conjugated Oligomers into Uniaxially Oriented Monodomain Films on Coumarin-Based Photoalignment Layers," *J. Polym. Sci. B, Polym. Phys.* **49**, 725 (2011).

R. Xin and J. D. Zuegel, "Amplifying Nanosecond Optical Pulses at 1053 nm with an All-Fiber Regenerative Amplifier," *Opt. Lett.* **36**, 2605 (2011).

B. Xu and S. X. Hu, "Effects of Electron-Ion Temperature Equilibration on Inertial Confinement Fusion Implosions," *Phys. Rev. E* **84**, 016408 (2011).

J.-H. Yang and R. S. Craxton, "An Empirical Model of Collective Electrostatic Effects for Laser-Beam Channeling in Long-Scale-Length Relativistic Plasmas," *Phys. Plasmas* **18**, 082703 (2011).

OMEGA External Users' Publications

H. Chen, D. D. Meyerhofer, S. C. Wilks, R. Cauble, F. Dollar, K. Falk, G. Gregori, A. Hazi, E. I. Moses, C. D. Murphy, J. Myatt, J. Park, J. Seely, R. Shepherd, A. Spitkovsky, C. Stoeckl, C. I. Szabo, R. Tommasini, C. Zwick, and P. Beiersdorfer, "Towards Laboratory Produced Relativistic Electron-Positron Pair Plasmas," *High Energy Density Phys.* **7**, 225 (2011).

C. Courtois, R. Edwards, A. Compant La Fontaine, C. Aedy, M. Barbotin, S. Bazzoli, L. Biddle, D. Brebion, J. L. Bourgade, D. Drew, M. Fox, M. Gardner, J. Gazave, J. M. Lagrange, O. Landoas, L. Le Dain, E. Lefebvre, D. Mastroianni, N. Pichoff, G. Pien, M. Ramsay, A. Simons, N. Sircombe, C. Stoeckl, and K. Thorp, "High-Resolution Multi-MeV X-Ray Radiography Using Relativistic Laser-Solid Interaction," *Phys. Plasmas* **18**, 023101 (2011).

M. J. Edwards, J. D. Lindl, B. K. Spears, S. V. Weber, L. J. Atherton, D. L. Bleuel, D. K. Bradley, D. A. Callahan, C. J. Cerjan, D. Clark, G. W. Collins, J. E. Fair, R. J. Fortner, S. H. Glenzer, S. W. Haan, B. A. Hammel, A. V. Hamza, S. P. Hatchett, N. Izumi, B. Jacoby, O. S. Jones, J. A. Koch, B. J. Kozioziemski, O. L. Landen, R. Lerche, B. J. MacGowan, A. J. MacKinnon, E. R. Mapoles, M. M. Marinak, M. Moran, E. I. Moses, D. H. Munro, D. H. Schneider, S. M. Sepke, D. A. Shaughnessy, P. T.

Springer, R. Tommasini, L. Bernstein, W. Stoeffl, R. Betti, T. R. Boehly, T. C. Sangster, V. Yu. Glebov, P. W. McKenty, S. P. Regan, D. H. Edgell, J. P. Knauer, C. Stoeckl, D. R. Harding, S. Batha, G. Grim, H. W. Herrmann, G. Kyrala, M. Wilke, D. C. Wilson, J. Frenje, R. Petrasso, K. Moreno, H. Huang, K. C. Chen, E. Giraldez, J. D. Kilkenny, M. Mauldin, N. Hein, M. Hoppe, A. Nikroo, and R. J. Leeper, "The Experimental Plan for Cryogenic Layered Target Implosions on the National Ignition Facility—The Inertial Confinement Approach to Fusion," *Phys. Plasmas* **18**, 051003 (2011).

R. Florido, R. C. Mancini, T. Nagayama, R. Tommasini, J. A. Delettrez, S. P. Regan, and B. Yaakobi, "Measurements of Core and Compressed-Shell Temperature and Density Conditions in Thick-Wall Target Implosions at the OMEGA Laser Facility," *Phys. Rev. E* **83**, 066408 (2011).

S. W. Haan, J. D. Lindl, D. A. Callahan, D. S. Clark, J. D. Salmonson, B. A. Hammel, L. J. Atherton, R. C. Cook, M. J. Edwards, S. Glenzer, A. V. Hamza, S. P. Hatchett, M. C. Herrmann, D. E. Hinkel, D. D. Ho, H. Huang, O. S. Jones, J. Kline, G. Kyrala, O. L. Landen, B. J. MacGowan, M. M. Marinak, D. D. Meyerhofer, J. L. Milovich, K. A. Moreno, E. I. Moses, D. H. Munro, A. Nikroo, R. E. Olson, K. Peterson,

- S. M. Pollaine, J. E. Ralph, H. F. Robey, B. K. Spears, P. T. Springer, L. J. Suter, C. A. Thomas, R. P. Town, R. Vesey, S. V. Weber, H. L. Wilkens, and D. C. Wilson, "Point Design Targets, Specifications, and Requirements for the 2010 Ignition Campaign on the National Ignition Facility," *Phys. Plasmas* **18**, 051001 (2011).
- B. A. Hammel, H. A. Scott, S. P. Regan, C. Cerjan, D. S. Clark, M. J. Edwards, R. Epstein, S. H. Glenzer, S. W. Haan, N. Izumi, J. A. Koch, G. A. Kyrala, O. L. Landen, S. H. Langer, K. Peterson, V. A. Smalyuk, L. J. Suter, and D. C. Wilson, "Diagnosing and Controlling Mix in National Ignition Facility Implosion Experiments," *Phys. Plasmas* **18**, 056310 (2011) (invited).
- K. Hendrix and J. Oliver, "Optical Interference Coatings Design Contest 2010: Solar Absorber and Fabry–Perot Etalon," *Appl. Opt.* **50**, C286 (2011).
- D. G. Hicks, B. K. Spears, D. G. Braun, R. E. Olson, C. M. Sorce, P. M. Celliers, G. W. Collins, and O. L. Landen, "Convergent Ablator Performance Measurements," *Phys. Plasmas* **17**, 102703 (2010).
- N. Izumi, C. Hagmann, G. Stone, D. Hey, S. Glenn, A. Conder, A. Teruya, C. Sorce, R. Tommasini, W. Stoeffl, P. Springer, O. L. Landen, H. W. Herrmann, G. A. Kyrala, R. Bahukutumbi, V. Y. Glebov, T. C. Sangster, M. Eckart, A. J. Mackinnon, J. A. Koch, D. K. Bradley, and P. Bell, "Experimental Study of Neutron Induced Background Noise on Gated X-Ray Framing Cameras," *Rev. Sci. Instrum.* **81**, 10E515 (2010).
- J. L. Kline, K. Widmann, A. Warrick, R. E. Olson, C. A. Thomas, A. S. Moore, L. J. Suter, O. L. Landen, D. Callahan, S. Azevedo, J. Liebman, S. H. Glenzer, A. Conder, S. N. Dixit, P. Torres III, V. Tran, E. L. Dewald, J. Kamperschroer, L. J. Atherton, R. Beeler, Jr., L. Berzins, J. Celeste, C. Haynam, W. Hsing, D. Larson, B. J. MacGowan, D. Hinkel, D. Kalantar, R. Kauffman, J. Kilkenny, N. Meezan, M. D. Rosen, M. Schneider, E. A. Williams, S. Vernon, R. J. Wallace, B. Van Wonterghem, and B. K. Young, "The First Measurements of Soft X-Ray Flux from Ignition Scale *Hohlraums* at the National Ignition Facility Using DANTE," *Rev. Sci. Instrum.* **81**, 10E321 (2010) (invited).
- G. A. Kyrala, S. Dixit, S. Glenzer, D. Kalantar, D. Bradley, N. Izumi, N. Meezan, O. L. Landen, D. Callahan, S. V. Weber, J. P. Holder, S. Glenn, M. J. Edwards, P. Bell, J. Kimbrough, J. Koch, R. Prasad, L. Suter, J. L. Kline, and J. Kilkenny, "Measuring Symmetry of Implosions in Cryogenic *Hohlraums* at the NIF Using Gated X-Ray Detectors," *Rev. Sci. Instrum.* **81**, 10E316 (2010) (invited).
- O. L. Landen, J. Edwards, S. W. Haan, H. F. Robey, J. Milovich, B. K. Spears, S. V. Weber, D. S. Clark, J. D. Lindl, B. J. MacGowan, E. I. Moses, J. Atherton, P. A. Amendt, T. R. Boehly, D. K. Bradley, D. G. Braun, D. A. Callahan, P. M. Celliers, G. W. Collins, E. L. Dewald, L. Divol, J. A. Frenje, S. H. Glenzer, A. Hamza, B. A. Hammel, D. G. Hicks, N. Hoffman, N. Izumi, O. S. Jones, J. D. Kilkenny, R. K. Kirkwood, J. L. Kline, G. A. Kyrala, M. M. Marinak, N. Meezan, D. D. Meyerhofer, P. Michel, D. H. Munro, R. E. Olson, A. Nikroo, S. P. Regan, L. J. Suter, C. A. Thomas, and D. C. Wilson, "Capsule Implosion Optimization During the Indirect-Drive National Ignition Campaign," *Phys. Plasmas* **18**, 051002 (2011).
- R. A. Lerche, V. Yu. Glebov, M. J. Moran, J. M. McNaney, J. D. Kilkenny, M. J. Eckart, R. A. Zacharias, J. J. Haslam, T. Clancy, M. F. Yeoman, D. P. Warwas, T. C. Sangster, C. Stoeckl, J. P. Knauer, and C. J. Horsfield, "National Ignition Facility Neutron Time-of-Flight Measurements," *Rev. Sci. Instrum.* **81**, 10D319 (2010) (invited).
- C. K. Li, F. H. Séguin, J. A. Frenje, M. Rosenberg, A. B. Zylstra, R. D. Petrasso, P. A. Amendt, J. A. Koch, O. L. Landen, H. S. Park, H. F. Robey, R. P. J. Town, A. Casner, F. Philippe, R. Betti, J. P. Knauer, D. D. Meyerhofer, C. A. Back, J. D. Kilkenny, and A. Nikroo, "Diagnosing Indirect-Drive Inertial-Confinement-Fusion Implosions with Charged Particles," *Plasma Phys. Control. Fusion* **52**, 124027 (2010).
- A. G. MacPhee, D. H. Edgell, E. J. Bond, D. K. Bradley, C. G. Brown, S. R. Burns, J. R. Celeste, C. J. Cerjan, M. J. Eckart, V. Y. Glebov, S. H. Glenzer, D. S. Hey, O. S. Jones, J. D. Kilkenny, J. R. Kimbrough, O. L. Landen, A. J. Mackinnon, N. B. Meezan, J. M. Parker, and R. M. Sweeney, "A Diamond Detector for X-Ray Bang-Time Measurement at the National Ignition Facility," *J. Inst.* **6**, P02009 (2011).
- J. D. Moody, P. Datte, K. Krauter, E. Bond, P. A. Michel, S. H. Glenzer, L. Divol, C. Niemann, L. Suter, N. Meezan, B. J. MacGowan, R. Hibbard, R. London, J. Kilkenny, R. Wallace, J. L. Kline, K. Knittel, G. Frieders, B. Golick, G. Ross, K. Widmann, J. Jackson, S. Vernon, and T. Clancy, "Backscatter Measurements for NIF Ignition Targets," *Rev. Sci. Instrum.* **81**, 10D921 (2010) (invited).

T. Nagayama, R. C. Mancini, R. Florido, R. Tommasini, J. A. Koch, J. A. Delettrez, S. P. Regan, and V. A. Smalyuk, "Processing of Spectrally Resolved X-Ray Images of Inertial Confinement Fusion Implosion Cores Recorded with Multimono-chromatic X-Ray Imagers," *J. Appl. Phys.* **109**, 093303 (2011).

J. S. Ross, S. H. Glenzer, J. P. Palastro, B. B. Pollock, D. Price, G. R. Tynan, and D. H. Froula, "Thomson-Scattering Measurements in the Collective and Noncollective Regimes in Laser-Produced Plasmas," *Rev. Sci. Instrum.* **81**, 10D523 (2010) (invited).

J. F. Seely, C. I. Szabo, U. Feldman, L. T. Hudson, A. Henins, P. Audebert, and E. Brambrink, "Hard X-Ray Transmission Crystal Spectrometer at the OMEGA-EP Laser Facility," *Rev. Sci. Instrum.* **81**, 10E301 (2010).

L. Steponaviciene, J. Sulcas, A. Jukna, G. Jung, V. Plausinaitiene, A. Abrutis, A. Maneikis, M. Gong, and R. Sobolewski, "Investigation of Vortex Density in Laser-Written Π -Shaped Channel of YBCO Bridge by Means of I - V Dependences," *Acta Phys. Pol. A* **119**, 180 (2011).

J. Sulcas, L. Steponaviciene, A. Jukna, G. Jung, V. Plausinaitiene, A. Abrutis, M. Gong, and R. Sobolewski, "Current Distribution

in Y-Ba-Cu-O Superconducting Microbridges Containing Π -Shaped Channel for Easy Vortex Motion," *Acta Phys. Pol. A* **119**, 183 (2011).

R. Tommasini, S. P. Hatchett, D. S. Hey, C. Iglesias, N. Izumi, J. A. Koch, O. L. Landen, A. J. MacKinnon, C. Sorce, J. A. Delettrez, V. Yu. Glebov, T. C. Sangster, and C. Stoeckl, "Development of Compton Radiography of Inertial Confinement Fusion Implosions," *Phys. Plasmas* **18**, 056309 (2011) (invited).

L. Willingale, P. M. Nilson, A. G. R. Thomas, S. S. Bulanov, A. Maksimchuk, W. Nazarov, T. C. Sangster, C. Stoeckl, and K. Krushelnick, "High-Power, Kilojoule Laser Interactions with Near-Critical Density Plasma," *Phys. Plasmas* **18**, 056706 (2011) (invited).

L. Willingale, P. M. Nilson, A. G. R. Thomas, J. Cobble, R. S. Craxton, A. Maksimchuk, P. A. Norreys, T. C. Sangster, R. H. H. Scott, C. Stoeckl, C. Zulick, and K. Krushelnick, "High-Power, Kilojoule Class Laser Channeling in Millimeter-Scale Underdense Plasma," *Phys. Rev. Lett.* **106**, 105002 (2011).

Conference Presentations

S. P. Regan, R. Epstein, T. C. Sangster, D. D. Meyerhofer, B. A. Hammel, H. A. Scott, D. K. Bradley, D. Callahan, M. J. Edwards, M. J. Eckart, S. H. Glenzer, J. D. Kilkenny, O. L. Landen, N. B. Meezan, R. Prasad, V. A. Smalyuk, L. J. Suter, and R. C. Mancini, "Hydrodynamic Mix Experiments for NIF Implosions Based on Spectroscopic Observations of K-Shell Emission," 14th International Workshop on Radiative Properties of Hot Dense Matter, Marbella, Spain, 4–8 October 2010.

D. D. Meyerhofer, R. L. McCrory, R. Betti, T. R. Boehly, D. T. Casey, T. J. B. Collins, R. S. Craxton, J. A. Delettrez, D. H. Edgell, R. Epstein, K. A. Fletcher, J. A. Frenje, V. Yu. Glebov, V. N. Goncharov, D. R. Harding, S. X. Hu, I. V. Igumenshchev, J. P. Knauer, C. K. Li, J. A. Marozas, F. J. Marshall, P. W. McKenty, P. M. Nilson, S. P. Padalino, R. D. Petrasso, P. B. Radha, S. P. Regan, T. C. Sangster, F. H. Séguin, W. Seka,

R. W. Short, D. Shvarts, S. Skupsky, J. M. Soures, C. Stoeckl, W. Theobald, and B. Yaakobi, "High-Performance Inertial Confinement Fusion Target Implosions on OMEGA," 23rd IAEA Fusion Energy Conference, Daejeon, Korea, 11–16 October 2010.

W. Theobald, A. A. Solodov, C. Stoeckl, K. S. Anderson, R. Betti, T. R. Boehly, R. S. Craxton, J. A. Delettrez, J. A. Frenje, V. Yu. Glebov, H. Habara, F. J. Marshall, K. A. Tanaka, K. L. Marshall, D. D. Meyerhofer, P. M. Nilson, P. K. Patel, H. Chen, T. C. Sangster, W. Seka, N. Sinenian, F. Beg, and R. B. Stephens, "Fast-Ignition Integrated Experiments on OMEGA," 11th International Workshop on Fast Ignition of Fusion Targets, Shanghai, China, 17–21 October 2010.

J. H. Kelly and T. Z. Kosc, "Modeling the OMEGA Laser System at the University of Rochester Using Miró," 5th Miró User Meeting, Haut Carré, Talence, France, 18–19 October 2010.

W. Theobald, A. A. Solodov, C. Stoeckl, K. S. Anderson, R. Betti, T. R. Boehly, R. S. Craxton, J. A. Delettrez, J. A. Frenje, V. Yu. Glebov, H. Habara, K. A. Tanaka, F. J. Marshall, K. L. Marshall, D. D. Meyerhofer, P. M. Nilson, P. K. Patel, H. Chen, T. C. Sangster, W. Seka, N. Sinenian, F. Beg, and R. B. Stephens, "Fast-Ignition Research at LLE," Japan–U.S. Ignitor and High Energy Density Physics Workshop, Osaka, Japan, 23–24 October 2010.

The following presentations were made at Frontiers in Optics, Rochester, NY, 24–28 October 2010:

L. Ji, W. R. Donaldson, and T. Y. Hsiang, "The Stability of the Active Mode-Locked Erbium-Doped Fiber Laser and Its Application in a Novel Electro-Optic Sampling System."

T. J. Kessler, H. Huang, J. B. Oliver, A. L. Rigatti, S. D. Jacobs, A. W. Schmid, and A. Kozlov, "Grating Development for High-Peak-Power CPA Laser Systems."

J. P. Leidner and J. R. Marciante, "Non-Adiabatically Tapered Multimode Interference Coupler for High-Power Single-Mode Semiconductor Lasers."

D. D. Meyerhofer, V. N. Goncharov, R. Betti, T. R. Boehly, T. J. B. Collins, R. S. Craxton, J. A. Delettrez, D. H. Edgell, R. Epstein, V. Yu. Glebov, D. R. Harding, S. X. Hu, I. V. Igumenshchev, J. P. Knauer, S. J. Loucks, J. A. Marozas, F. J. Marshall, R. L. McCrory, P. W. McKenty, P. M. Nilson, P. B. Radha, S. P. Regan, T. C. Sangster, W. Seka, R. W. Short, D. Shvarts, S. Skupsky, V. A. Smalyuk, J. M. Soures, C. Stoeckl, W. Theobald, B. Yaakobi, J. A. Frenje, D. T. Casey, C. K. Li, R. D. Petrasso, F. H. Séguin, S. P. Padalino, and K. A. Fletcher, "Inertial Confinement Fusion Research at the Laboratory for Laser Energetics."

J. Qiao, A. Kalb, T. Nguyen, D. Canning, and J. Price, "Development and Operation of Large-Aperture Tiled-Grating Compressors for High-Energy, Petawatt-Class Laser Systems."

J. E. Schoenly, W. Seka, and P. Rechmann, "Selective Near-UV Laser Ablation of Subgingival Dental Calculus at a 20° Irradiation Angle."

The following presentations were made at the 9th International Conference on Tritium Science and Technology, Nara, Japan, 24–29 October 2010:

J. E. Fair and W. T. Shmayda, "A Model for Removal of Surface-Bound Tritium Using Humid Air."

W. T. Shmayda and J. E. Fair, "Tritium Outgassing from Contaminated Metal Surfaces."

W. T. Shmayda, D. R. Harding, S. J. Brereton, and F. Javier, "Tritium Inertial Fusion: Extrapolation to Ignition Machines."

The following presentations were made at the 52nd Annual Meeting of the APS Division of Plasma Physics, Chicago, IL, 8–12 November 2010:

K. S. Anderson, R. Betti, R. S. Craxton, R. Nora, and L. J. Perkins, "A Plastic-Ablator Cryogenic Shock-Ignition Design for the NIF."

M. A. Barrios, D. E. Fratanduono, T. R. Boehly, D. D. Meyerhofer, D. G. Hicks, P. M. Celliers, and J. H. Eggert, "Precision Measurements of the Equation of State (EOS) of GDP Ablator Materials at ~1 to 10 Mbar Using Laser-Driven Shock Waves."

T. R. Boehly, M. A. Barrios, D. E. Fratanduono, V. N. Goncharov, S. X. Hu, T. J. B. Collins, J. A. Marozas, T. C. Sangster, D. D. Meyerhofer, P. M. Celliers, H. F. Robey, D. G. Hicks, J. H. Eggert, G. W. Collins, and R. Smith, "Shock-Timing Measurements in ICF Targets Filled with Cryogenic Deuterium."

D. T. Casey, J. A. Frenje, F. H. Séguin, M. Manuel, N. Sinenian, R. D. Petrasso, V. Yu. Glebov, P. B. Radha, T. C. Sangster, D. D. Meyerhofer, D. McNabb, A. Miles, P. Navratil, and S. Quaglioni, "Measurements of Down-Scattered and TT-Neutron Spectra Using the Magnetic Recoil Spectrometer (MRS) on OMEGA."

P. Y. Chang, G. Fiksel, M. Hohenberger, J. P. Knauer, R. Nora, R. Betti, F. H. Séguin, C. K. Li, M.-J. E. Manuel, and R. D. Petrasso, “Magnetized Spherical Implosions on the OMEGA Laser.”

T. J. B. Collins, J. A. Marozas, S. Skupsky, P. W. McKenty, V. N. Goncharov, P. B. Radha, A. Shvydky, and M. M. Marinak, “Preparing for Polar Drive at the National Ignition Facility.”

R. S. Craxton, L. Tucker, T. Mo, K. S. Anderson, R. Betti, L. J. Perkins, G. P. Schurtz, X. Ribeyre, and A. Casner, “A 96/96-Beam Polar-Drive Configuration for Shock Ignition on the NIF.”

J. A. Delettrez, S. X. Hu, and A. Shvydky, “Numerical Investigation of the Effect of Two-Plasmon-Decay Preheat in Planar Rayleigh–Taylor Experiments.”

D. H. Edgell, J. Magoon, T. C. Sangster, M. J. Shoup III, F. J. Marshall, C. Stoeckl, A. G. MacPhee, S. Burns, J. Celeste, M. J. Eckart, J. D. Kilkenny, J. Kimbrough, J. Parker, and T. Thomas, “South-Pole Bang-Time X-Ray Diagnostic for the NIF.”

R. Epstein, S. P. Regan, F. J. Marshall, J. A. Delettrez, V. N. Goncharov, S. X. Hu, P. W. McKenty, G. Liu, D. D. Meyerhofer, P. B. Radha, T. C. Sangster, C. Stoeckl, W. Theobald, R. Tommasini, N. Landen, and A. J. MacKinnon, “Hard X-Ray Compton Radiography of Cryogenic Implosions on OMEGA.”

G. Fiksel, R. Jungquist, C. Mileham, P. M. Nilson, W. Theobald, and C. Stoeckl, “Development of a Spherical Crystal X-Ray-Imaging Diagnostic for OMEGA and OMEGA EP.”

D. E. Fratanduono, M. A. Barrios, T. R. Boehly, D. D. Meyerhofer, J. H. Eggert, R. Smith, D. G. Hicks, P. M. Celliers, and G. W. Collins, “The Refractive Index and Transparency of Lithium Fluoride Compressed to 800 GPa.”

J. A. Frenje, D. T. Casey, C. K. Li, F. H. Séguin, R. D. Petrasso, R. Bionta, C. Cerjan, M. Eckart, S. W. Haan, S. P. Hatchett, H. Kather, J. D. Kilkenny, O. L. Landen, A. J. MacKinnon, M. J. Moran, J. R. Rygg, V. Yu. Glebov, T. C. Sangster, D. D. Meyerhofer, K. Fletcher, and R. Leeper, “First Measurements of the Absolute Neutron Spectrum Using the Magnetic Recoil Spectrometer (MRS) at the NIF.”

D. H. Froula, V. N. Goncharov, S. X. Hu, J. F. Myatt, J. S. Ross, L. Divol, and S. H. Glenzer, “Ion-Acoustic Wave Instability from Laser-Driven Return Currents.”

L. Gao, P. M. Nilson, W. Theobald, C. Stoeckl, C. Dorrer, T. C. Sangster, D. D. Meyerhofer, L. Willingale, and K. M. Krushelnick, “Measurements of Proton Generation with Intense, Kilojoule Laser Pulses on OMEGA EP.”

V. Yu. Glebov, J. P. Knauer, T. C. Sangster, C. Stoeckl, E. J. Bond, J. A. Caggiano, T. J. Clancy, M. J. Eckart, J. D. Kilkenny, R. A. Lerche, J. McNaney, M. J. Moran, and D. H. Munro, “Neutron Time-of-Flight Diagnostic Performance During the National Ignition Facility’s 2010 Campaign.”

V. N. Goncharov, “Low-Adiabatic, High-Compression Cryogenic Deuterium–Tritium Implosions on OMEGA” (invited).

M. Hohenberger, W. Theobald, S. X. Hu, K. S. Anderson, D. D. Meyerhofer, C. Stoeckl, T. R. Boehly, D. E. Fratanduono, R. Betti, A. Casner, X. Ribeyre, and G. Schurtz, “Shock-Ignition Studies on OMEGA.”

S. X. Hu, V. N. Goncharov, T. R. Boehly, S. Skupsky, T. C. Sangster, D. D. Meyerhofer, and R. L. McCrory, “The Equation-of-State Dependence of Nonuniformity Growth in Cryogenic-DT Implosions on OMEGA.”

I. V. Igumenshchev, V. N. Goncharov, P. M. Nilson, T. C. Sangster, C. K. Li, R. D. Petrasso, and M. G. Haines, “Study of Self-Generated Magnetic Fields in Implosion Experiments on OMEGA.”

M. Manuel, C. K. Li, F. H. Séguin, J. A. Frenje, D. T. Casey, N. Sinenian, R. D. Petrasso, R. Betti, V. A. Smalyuk, J. Hager, and R. P. J. Town, “Using Proton Radiography to Measure Rayleigh–Taylor-Induced Magnetic Fields.”

J. A. Marozas, T. J. B. Collins, and J. D. Zuegel, “Smoothing by Spectral Dispersion (SSD) for Multiple-Picket Pulses on OMEGA and the NIF.”

F. J. Marshall, V. Yu. Glebov, P. W. McKenty, P. B. Radha, and A. Shvydky, “NIF-Relevant, Polar-Drive Irradiation Tests on OMEGA.”

- A. V. Maximov, J. F. Myatt, R. W. Short, W. Seka, and R. Yan, “Two-Plasmon-Decay Instability and Stimulated Brillouin Scattering in Direct-Drive ICF Plasmas.”
- P. W. McKenty, R. S. Craxton, F. J. Marshall, A. Shvydsky, R. Epstein, A. M. Cok, J. A. Marozas, T. J. B. Collins, S. Skupsky, C. Stoeckl, T. C. Sangster, M. J. Bonino, R. T. Janezik, D. R. Harding, W. T. Shmayda, S. F. B. Morse, D. D. Meyerhofer, R. L. McCrory, A. Nikroo, J. D. Kilkenny, M. L. Hoppe, J. Fooks, A. J. MacKinnon, R. J. Wallace, D. K. Bradley, and G. A. Kyrala, “Evaluation of the First Polar-Drive, DT-Gas-Filled Target Implosions on the NIF.”
- D. D. Meyerhofer, S.-W. Bahk, J. Bromage, C. Dorrer, J. H. Kelly, B. E. Kruschwitz, S. J. Loucks, R. L. McCrory, S. F. B. Morse, J. Qiao, C. Stoeckl, and L. J. Waxer, “Status of the OMEGA EP Laser System.”
- J. F. Myatt, J. A. Delettrez, A. V. Maximov, R. W. Short, D. H. Edgell, W. Seka, D. F. Dubois, D. A. Russell, and H. X. Vu, “Two-Plasmon-Decay Preheat Calculations for OMEGA and Ignition-Scale Direct-Drive Inertial Confinement Fusion.”
- P. M. Nilson, A. A. Solodov, J. F. Myatt, W. Theobald, P. A. Jaanimagi, L. Gao, C. Stoeckl, R. S. Craxton, J. A. Delettrez, J. D. Zuegel, B. E. Kruschwitz, C. Dorrer, J. H. Kelly, K. U. Akli, P. K. Patel, A. J. MacKinnon, R. Betti, T. C. Sangster, and D. D. Meyerhofer, “Scaling Hot-Electron Generation to Long-Pulse, High-Intensity Laser–Solid Interactions” (invited).
- R. Nora, R. Betti, K. S. Anderson, P. Y. Chang, and M. Hohenberger, “One-Dimensional Hydrodynamic Theory of Shock Ignition.”
- P. B. Radha, C. Stoeckl, J. P. Knauer, V. N. Goncharov, I. V. Igumenshchev, R. L. McCrory, D. D. Meyerhofer, T. C. Sangster, S. Skupsky, J. A. Frenje, and R. D. Petrasso, “The Effect of Nonuniformity Growth on Direct-Drive Plastic-Shell Implosions on the OMEGA Laser.”
- S. P. Regan, R. Epstein, T. C. Sangster, D. D. Meyerhofer, B. A. Hammel, H. A. Scott, D. K. Bradley, D. Callahan, M. J. Edwards, M. J. Eckart, S. H. Glenzer, J. D. Kilkenny, O. L. Landen, N. B. Meezan, R. Prasad, V. A. Smalyuk, and L. J. Suter, “Spectroscopic Observations of Ablator Mass Mixed into the Hot Spot of NIF Implosions.”
- H. Rinderknecht, “A CVD Diamond-Based Proton-Bang-Time Detector for OMEGA and the NIF.”
- M. Rosenberg, “Yield and Ion-Temperature Measurements in Exploding Pusher Experiments on OMEGA and the NIF.”
- T. C. Sangster, V. N. Goncharov, R. Betti, T. R. Boehly, J. A. Delettrez, D. H. Edgell, V. Yu. Glebov, S. X. Hu, J. P. Knauer, F. J. Marshall, R. L. McCrory, P. W. McKenty, D. D. Meyerhofer, P. B. Radha, S. P. Regan, S. Seka, S. Skupsky, C. Stoeckl, B. Yaakobi, J. A. Frenje, and D. T. Casey, “Areal Density and Ion-Temperature Measurements in Cryogenic-DT Implosions on OMEGA.”
- W. Seka, D. H. Froula, D. H. Edgell, R. E. Bahr, J. F. Myatt, J. A. Delettrez, R. S. Craxton, S. X. Hu, A. V. Maximov, and R. W. Short, “Competitive Laser–Plasma Interaction Processes Near Quarter Critical Relevant to Direct-Drive ICF.”
- R. W. Short, “Angular Dependence of Two-Plasmon Decay in Multibeam Direct-Drive Irradiation Geometries.”
- A. Shvydsky, P. W. McKenty, F. J. Marshall, R. S. Craxton, J. A. Marozas, R. Epstein, S. Skupsky, and R. L. McCrory, “Numerical Investigation of NIF Diagnostic Commissioning Experiments on OMEGA.”
- N. Sinenian, J. A. Frenje, R. D. Petrasso, F. H. Séguin, C. K. Li, W. Theobald, and C. Stoeckl, “Observation of Fast Protons in Recent Electron Fast-Ignition Experiments on OMEGA.”
- A. A. Solodov, R. Betti, K. S. Anderson, J. F. Myatt, W. Theobald, and C. Stoeckl, “Controlling the Divergence of Laser-Generated Fast Electrons Through Resistivity Gradients in Fast-Ignition Targets.”
- C. Stoeckl, D. H. Edgell, C. Forrest, V. Yu. Glebov, J. P. Knauer, and T. C. Sangster, “Monte Carlo Simulations of Neutron Scattering in Current-Mode Neutron Time-of-Flight Detectors.”
- W. Theobald, A. A. Solodov, C. Stoeckl, K. S. Anderson, R. Betti, T. R. Boehly, R. S. Craxton, J. A. Delettrez, C. Dorrer, J. A. Frenje, V. Yu. Glebov, H. Habara, K. A. Tanaka, J. P. Knauer, F. J. Marshall, K. L. Marshall, D. D. Meyerhofer, P. M. Nilson, P. K. Patel, H. Chen, T. C. Sangster, W. Seka, N. Sinenian, T. Ma, F. N. Beg, E. Giraldez, and R. B. Stephens, “Initial Cone-in-Shell Target Fast-Ignition Experiments on OMEGA” (invited).
- R. Yan, A. V. Maximov, and C. Ren, “Saturation of Two-Plasmon-Decay and Ion-Density Fluctuations.”

D. D. Meyerhofer, K. S. Anderson, S.-W. Bahk, R. Betti, T. R. Boehly, J. Bromage, R. S. Craxton, C. Dorrer, J. A. Delettez, L. Gao, V. Yu. Glebov, P. A. Jaanimagi, J. H. Kelly, B. E. Kruschwitz, S. J. Loucks, F. J. Marshall, K. L. Marshall, R. L. McCrory, S. F. B. Morse, J. F. Myatt, P. M. Nilson, J. Qiao, T. C. Sangster, W. Seka, A. A. Solodov, C. Stoeckl, L. J. Waxer, W. Theobald, B. Yaakobi, J. D. Zuegel, J. A. Frenje, N. Sinenian, H. Habara, K. A. Tanaka, A. J. MacKinnon, H. Chen, P. K. Patel, F. N. Beg, T. Ma, K. U. Akli, R. B. Stephens, L. Willingale, and K. M. Krushelnick, "Initial Experiments on the OMEGA EP High-Energy Petawatt Laser System," International Symposium on Chirped Pulse Amplification, Quebec City, Canada, 17–21 November 2010.

D. R. Harding, T. B. Jones, Z. Bei, W. Wang, S. H. Chen, R. Q. Gram, M. Moynihan, and G. Randall, "Microfluidic Methods for Producing Millimeter-Size Fuel Capsules for Inertial Fusion," 2010 Materials Research Society Fall Meeting, Boston, MA, 29 November–3 December 2010.

J. M. Soures and R. L. McCrory, "The University of Rochester's Laboratory for Laser Energetics' Role in Inertial Fusion Energy Development," 31st Fusion Power Associates Annual Meeting and Symposium, Washington, DC, 1–2 December 2010.

The following presentations were made at LASE—SPIE Photonics West, San Francisco, CA, 22–27 January 2011:

M. J. Guardalben and L. J. Waxer, "Improvements to Long-Pulse System Performance and Operational Efficiency on OMEGA EP."

J. M. Soures, "Opportunities for Inertial Fusion and High-Energy-Density Physics Research at the National Laser Users' Facility."

J. D. Zuegel and J. Bromage, "Lasers at the University of Rochester's Laboratory for Laser Energetics: Laser Fusion to

Ultra-Intense Lasers," ETH-Hönggerberg Seminar, Zurich, Switzerland, 10 February 2011.

The following presentations were made at Advanced Solid-State Photonics, Istanbul, Turkey, 13–16 February 2011:

J. Bromage, C. Dorrer, and J. D. Zuegel, "Temporal Contrast Measurements of a Noncollinear Optical Parametric Amplifier Seeded by White-Light Continuum."

R. Xin and J. D. Zuegel, "All-Fiber Regenerative Amplifier for Nanosecond Optical Pulses at 1053 nm."

J. D. Zuegel, M. J. Shoup III, J. H. Kelly, and C. Frederickson, "Novel Actively Cooled Split-Disk Nd:Glass Laser Amplifier for High-Energy Applications with Improved Repetition Rate."

P. M. Nilson, R. Betti, J. A. Delettez, L. Gao, P. A. Jaanimagi, J. F. Myatt, T. C. Sangster, A. A. Solodov, C. Stoeckl, W. Theobald, B. Yaakobi, J. D. Zuegel, A. J. MacKinnon, and P. K. Patel, "Hot-Electron Lifetime Measurements," Fusion Science Center for Extreme States of Matter 10th Meeting, Rochester, NY, 7 March 2011.

The following presentations were made at the International Workshop on ICF Shock Ignition, Rochester, NY, 8–10 March 2011:

K. S. Anderson, R. Betti, P. W. McKenty, T. J. B. Collins, R. S. Craxton, R. Nora, A. A. Solodov, and L. J. Perkins, "Shock Ignition with Plastic-Ablator Cryogenic Shells on the NIF."

K. S. Anderson, W. Theobald, C. Stoeckl, R. Betti, R. S. Craxton, J. A. Delettez, O. V. Gotchev, V. Yu. Glebov, V. N. Goncharov, F. J. Marshall, D. N. Maywar, R. L. McCrory, D. D. Meyerhofer, R. Nora, P. B. Radha, W. Seka, T. C. Sangster, V. A. Smalyuk, B. Yaakobi, C. D. Zhou, J. A. Frenje, C. K. Li, F. H. Séguin, R. D. Petrasso, L. J. Perkins, M. Lafon, X. Ribeyre, G. Schurtz, A. Casner "60-Beam Shock-Ignition OMEGA Experiments and Simulations."

R. Betti, "An Overview of Shock Ignition."

T. J. B. Collins, J. A. Marozas, A. Shvydky, R. S. Craxton, and P. W. McKenty, "Polar-Drive Hot-Spot Ignition on the NIF."

R. S. Craxton, P. W. McKenty, E. Bond, S. LePape, A. J. MacKinnon, P. A. Michel, and J. D. Moody, "Three-Dimensional Distributions of Deposited Energy and Scattered Light in NIF 'Exploding-Pusher' Polar-Drive Experiments."

R. S. Craxton, L. Tucker, T. Mo, K. S. Anderson, R. Betti, L. J. Perkins, G. P. Schurtz, X. Ribeyre, and A. Casner, "Three-Dimensional Design of a 96-Beam NIF Target to Test the Compression Phase of Shock Ignition."

T. J. Kessler, "Phase and Polarization Plates for NIF Polar Drive."

J. A. Marozas, "Picket Pulses with 1-D Multi-FM Smoothing by Spectral Dispersion (SSD) for the NIF Drive."

F. J. Marshall, P. B. Radha, and A. Shvydky, "Backlighting of OMEGA Polar-Drive Experiments."

P. W. McKenty, R. S. Craxton, F. J. Marshall, A. Shvydky, R. Epstein, A. M. Cok, J. A. Marozas, T. J. B. Collins, S. Skupsky, C. Stoeckl, T. C. Sangster, M. J. Bonino, R. Janezic, D. R. Harding, W. T. Shmayda, S. F. B. Morse, D. D. Meyerhofer, R. L. McCrory, A. Nikroo, J. D. Kilkenny, M. L. Hoppe, J. Fooks, A. J. MacKinnon, S. LePape, R. J. Wallace, D. K. Bradley, and G. A. Kyrala, "Results of Polar-Drive, Exploding-Pusher Shots on the NIF."

P. B. Radha, F. J. Marshall, R. S. Craxton, and A. Shvydky, "Results from Polar-Drive OMEGA Experiments."

A. Shvydky, P. W. McKenty, F. J. Marshall, R. S. Craxton, J. A. Marozas, R. Epstein, S. Skupsky, and R. L. McCrory, "Numerical Investigation of NIF Diagnostic Commissioning Experiments on OMEGA."

W. Theobald, M. Hohenberger, R. Nora, K. S. Anderson, R. Betti, T. R. Boehly, D. E. Fratanduono, J. A. Frenje, S. X. Hu, D. D. Meyerhofer, T. C. Sangster, W. Seka, C. Stoeckl, B. Yaakobi, A. Casner, X. Ribeyre, and G. Schurtz, "Shock-Ignition Experiments on OMEGA."

J. D. Zuegel, "Demonstrating Polar-Drive Smoothing Technology for the NIF on OMEGA EP"

J. E. Schoenly, W. Seka, and P. Rechmann, "Fluence Dependency of the 400-nm Ablation Rates of Supra- and Subgingival Dental Calculus," American Society of Laser Medicine and Surgery 2011 Annual Conference, Grapevine, TX, 30 March–3 April 2011.

The following presentations were made at the Omega Laser Facility Users Group Workshop, Rochester, NY, 27–29 April 2011:

D. H. Froula, M. Bedzyk, R. Boni, R. Brown, R. S. Craxton, T. Duffy, F. Ehrne, S. Ivancic, R. Jungquist, J. Puth, W. Seka, M. J. Shoup, III, C. Stoeckl, W. Theobald, D. Weiner, and N. Kugland "The OMEGA EP 4ω Probe and Associated Plasma Diagnostics."

V. N. Goncharov, "Tuning Low-Adiabatic Cryogenic Implosions on OMEGA."

B. E. Kruschwitz, "Static Wavefront Correction on OMEGA EP"

P. W. McKenty, K. S. Anderson, R. Nora, C. Stoeckl, W. Theobald, J. Bates, A. Schmitt, M. Lafon, X. Ribeyre, G. Schurtz, S. Weber, V. Tykhonchuk, S. Atzeni, J. Perkins, and O. Klimov, "Overview of the Current Status of Shock Ignition."

S. F. B. Morse, "Omega Facility Update: Progress on OLUG Recommendations."

G. Pien, "OMEGA Experimental Operations 2011 OLUG Status Report."

The following presentations were made at CLEO 2011, Baltimore, MD, 1–6 May 2011:

C. Dorrer, "Characterization of a High-Contrast Front-End Prototype for the Omega EP Laser Facility."

C. Dorrer, A. Consentino, and D. Irwin, "Direct Estimation of the Intensity Contrast of High-Energy Laser Pulses."

A. V. Okishev, "A Highly Efficient Diode-Pumped Pulsed Laser Based on Room-Temperature Yb:YAG Ceramics."

R. Xin and J. D. Zuegel, "Amplification to the Period-Doubling Limit in an All-Fiber Regenerative Amplifier for High-Intensity Laser Systems."

The following presentations were made at Siemens PLM Connection, Las Vegas, NV, 2–5 May 2011:

C. Robillard, "The Engineer's Notebook."

T. Smith, "TDM to Teamcenter Meta Data Migration Strategy."

The following presentations were made at the Third International Conference on High Energy Density Physics, Lisbon, Portugal, 17–20 May 2011:

T. R. Boehly, "The Velocity and Timing of Multiple Spherically Converging Shock Waves in Liquid Deuterium."

G. Fiksel, P.-Y. Chang, M. Hohenberger, J. P. Knauer, R. Betti, F. J. Marshall, D. D. Meyerhofer, F. H. Séguin, and R. D. Petrasso, "Fusion-Yield Enhancement in Magnetized Laser-Driven Implosions."

S. P. Regan, R. Epstein, B. Hammel, L. J. Suter, J. Ralph, H. Scott, M. A. Barrios, D. K. Bradley, D. A. Callahan, G. W. Collins, S. Dixit, M. J. Edwards, D. R. Farley, S. H. Glenzer, I. E. Golovkin, S. W. Haan, A. Hamza, D. G. Hicks, N. Izumi, J. D. Kilkenny, J. L. Kline, G. A. Kyrala, O. L. Landen, T. Ma, J. J. MacFarlane, R. C. Mancini, R. L. McCrory, N. B. Meezan, D. D. Meyerhofer, A. Nikroo, K. J. Peterson, T. C. Sangster, P. Springer, and R. P. J. Town, "National Ignition Facility (NIF) Implosions: Hydrodynamic Mixing Experiments."

The following presentations were made at the NAS/NAE Committee on the Prospects for IFE Systems, Rochester, NY, 17 June 2011:

V. N. Goncharov, "Modeling of Cryogenic Implosions on OMEGA is Approaching Precision Required for Ignition."

T. J. Kessler, "Diffractive Optics Technology for ICF."

R. L. McCrory, "Laser-Driven Inertial Fusion Energy: Direct-Drive Targets Overview."

J. B. Oliver and A. L. Rigatti, "High-Damage Threshold Coating for ICF Laser Applications."

J. M. Soures, "The Omega Facility is Operated as a User Facility and has Produced the World's Largest ICF Physics and High-Energy-Density-Science Database."

W. Theobald, "Shock-Ignition and Fast-Ignition Research at LLE."

J. D. Zuegel, "New Laser Technologies for OMEGA EP."

The following presentations were made at the 41st Annual Anomalous Absorption Conference, San Diego, CA, 19–24 June 2011:

S. F. DuBois, D. A. Russell, H. X. Vu, and J. F. Myatt, "Strong Langmuir Turbulence in the Nonlinear Saturation of Parametric Instabilities Driven by Coherent Electromagnetic Waves."

D. H. Edgell, I. V. Igumenshchev, W. Seka, J. F. Myatt, V. N. Goncharov, R. S. Craxton, J. A. Delettrez, A. V. Maximov, R. W. Short, P. W. McKenty, "Crossed-Beam Energy Transfer in Polar Direct-Drive Implosions."

D. H. Froula, D. H. Edgell, I. V. Igumenshchev, P. B. Radha, and V. N. Goncharov, "Thomson Scattering Study of the Coronal Plasma Conditions in Direct-Drive Implosions."

S. X. Hu, D. H. Edgell, D. H. Froula, V. N. Goncharov, W. Seka, S. Skupsky, and B. Yaakobi, "Simulations and Analyses of Long-Scale-Length Plasma Experiments on the Omega EP Laser Facility."

A. V. Maximov, J. F. Myatt, R. W. Short, I. V. Igumenshchev, D. H. Edgell, and W. Seka, "Modeling of Energy Transfer Between Spatially Incoherent Crossing Laser Beams."

J. F. Myatt, J. Zhang, A. V. Maximov, R. W. Short, D. F. DuBois, D. A. Russell, and H. X. Vu, "Evaluation of a Quasilinear Model for the Two-Plasmon-Decay Instability in Inhomogeneous Plasmas."

W. Seka, I. V. Igumenshchev, D. H. Froula, D. H. Edgell, J. F. Myatt, V. N. Goncharov, R. W. Short, and A. V. Maximov, "Reducing the Cross-Beam Energy Transfer in Direct-Drive Implosion Targets Through Laser-Irradiation Control."

R. W. Short and J. F. Myatt, "Convective Multibeam Two-Plasmon Decay for Beam Configurations Relevant to Polar Direct Drive."

A. A. Solodov, R. Betti, K. S. Anderson, J. F. Myatt, W. Theobald, and C. Stoeckl, "Controlling the Divergence of Laser-Generated Fast Electrons Through Resistivity Gradients in Fast-Ignition Targets."

H. X. Vu, D. F. DuBois, J. F. Myatt, and D. A. Russell, "Langmuir Turbulence and Suprathermal Electron Production from the Two-Plasmon Decay Instability Driven by Crossed Laser Beams in an Inhomogeneous Plasma."

R. Yan, A. V. Maximov, C. Ren, and F. S. Tsung, "Energetic Electron Generation in Two-Plasmon-Decay Instabilities in Direct-Drive Inertial Confinement Fusion."

J. P. Knauer, V. Yu. Glebov, C. Stoeckl, T. C. Sangster, D. D. Meyerhofer, J. A. Caggiano, M. J. Moran, R. Hatarik, J. M. McNaney, S. Friedrich, E. J. Bond, M. J. Eckart, S. J. Padalino, and J. D. Kilkenny, "Neutron Time-of-Flight Measurements

on the National Ignition Facility," 38th IEEE International Conference on Plasma Science, Chicago, IL, 26–30 June 2011.

T. R. Boehly, V. N. Goncharov, M. A. Barrios, D. E. Fratanduono, S. X. Hu, T. J. B. Collins, J. A. Marozas, T. C. Sangster, D. D. Meyerhofer, P. M. Celliers, H. F. Robey, D. G. Hicks, and G. W. Collins, "Shock-Timing Measurements in ICF Targets Filled with Cryogenic Deuterium," 2011 APS Shock Compression of Condensed Matter, Chicago, IL, 26 June–1 July 2011.

The following presentations were made at the NAS/NAE ICF Targets Panel, Rochester, NY, 6–8 July 2011:

D. H. Froula, "Laser-Plasma Interaction in Direct-Drive Implosions."

R. L. McCrory, "Overview of LLE's ICF Program."

D. D. Meyerhofer, "Facilitating NIF Polar Drive."

D. D. Meyerhofer, "Shock and Fast Ignition."

P. B. Radha, "Polar-Drive Target Design."

T. C. Sangster, "Direct-Drive Progress on OMEGA."

M. J. Grosskopf, R. P. Drake, C. C. Kuranz, E. M. Rutter, H. S. Park, N. Kugland, S. Pollaine, S. Ross, B. A. Remington, D. Ryutov, A. Spikovsky, L. Gargate, G. Gregori, A. Bell, C. Murphy, Y. Sakawa, Y. Kuramitsu, H. Takabe, D. Froula, G. Fiksel, F. Miniati, M. Koenig, A. Ravasio, E. Liang, and N. Woolsey, "Hydrodynamic Simulation of Laboratory Astrophysics Experiments Generating Collisionless Shocks with Intense Lasers," Interrelationship Between Plasma Experiments in Laboratory and Space, Whistler, Canada, 10–15 July 2011.

D. D. Meyerhofer, "Diagnostics for High-Energy-Density Physics," HEDP Summer School, San Diego, CA, 10–16 July 2011.

P. W. McKenty, "ICF Research at the Laboratory for Laser Energetics: The Path to Polar-Drive Ignition," JOWOG 37, Aldermaston, United Kingdom, 11–15 July 2011.

S. P. Regan, R. Epstein, B. A. Hammel, L. J. Suter, J. Ralph, H. Scott, M. A. Barrios, D. K. Bradley, D. A. Callahan, G. W. Collins, S. Dixit, M. J. Edwards, D. R. Farley, S. H. Glenzer, I. E. Golovkin, S. W. Haan, A. Hamza, D. G. Hicks, N. Izumi, J. D. Kilkenny, J. L. Kline, G. A. Kyrala, O. L. Landen, T. Ma, J. J. MacFarlane, A. J. MacKinnon, R. C. Mancini, F. J. Marshall, R. L. McCrory, N. B. Meezan, D. D. Meyerhofer, A. Nikroo, K. J. Peterson, T. C. Sangster, P. Springer, and R. P. J. Town, "Diagnosing Implosions at the National Ignition Facility with X-Ray Spectroscopy," 17th International Conference on Atomic Processes and Plasmas, Belfast, Ireland, 19–22 July 2011.

K. L. Marshall, S. K.-H. Wei, M. Vargas, K. Wegman, C. Dorrer, P. Leung, J. Boule III, Z. Zhao, and S. H. Chen, "Liquid Crystal Beam-Shaping Devices Employing Patterned Photoalignment Layers for High-Peak-Power Laser Applications," SPIE Optics and Photonics, Liquid Crystals XV, San Diego, CA, 21–25 August 2011.

S. D. Jacobs, "MRF with Adjustable pH," Optical Fabrication, Testing and Metrology IV, Marseille, France, 5–8 September 2011.

The following presentations were made at the 7th International Conference on Inertial Fusion Sciences and Applications, Bordeaux, France, 12–16 September 2011:

R. L. McCrory, D. D. Meyerhofer, R. Betti, T. R. Boehly, T. J. B. Collins, R. S. Craxton, J. A. Delettrez, D. H. Edgell, R. Epstein, D. H. Froula, V. Yu. Glebov, V. N. Goncharov, D. R. Harding, S. X. Hu, I. V. Igumenshchev, J. P. Knauer, S. J. Loucks, J. A. Marozas, F. J. Marshall, P. W. McKenty, T. Michel, P. M. Nilson, P. B. Radha, S. P. Regan, T. C. Sangster, W. Seka, R. W. Short,

D. Shvarts, S. Skupsky, V. A. Smalyuk, J. M. Soures, C. Stoeckl, W. Theobald, B. Yaakobi, J. A. Frenje, D. T. Casey, C. K. Li, R. D. Petrasso, F. H. Séguin, S. P. Padalino, K. A. Fletcher, P. M. Celliers, G. W. Collins, and H. F. Robey, "Progress in Direct-Drive Inertial Confinement Fusion."

P. W. McKenty, T. J. B. Collins, J. A. Marozas, T. J. Kessler, J. D. Zuegel, M. J. Shoup III, R. S. Craxton, F. J. Marshall, A. Shvydky, S. Skupsky, V. N. Goncharov, P. B. Radha, R. Epstein, T. C. Sangster, D. D. Meyerhofer, R. L. McCrory, J. D. Kilkenny, A. Nikroo, M. L. Hoppe, M. M. Marinak, A. J. MacKinnon, M. J. Schmitt, P. A. Bradley, G. R. Magelssen, and T. J. Murphy, "Preparing for Polar-Drive Ignition on the NIF."

H.-S. Park, N. Kugland, S. Ross, B. Remington, S. Pollaine, D. Ryutov, A. Spitkovsky, L. Gargate, G. Gregori, A. Bell, C. Murphy, Y. Sakawa, Y. Kuramitsu, H. Takabe, D. Froula, G. Fiksel, F. Miniati, M. Koenig, A. Ravasio, E. Liang, N. Woolsey, and M. Grosskopf, "Collisionless Shocks in Laser Driven Laboratory High Energy Density Plasmas."

P. B. Radha, F. J. Marshall, T. R. Boehly, T. J. B. Collins, R. S. Craxton, D. H. Edgell, R. Epstein, J. A. Frenje, V. N. Goncharov, J. A. Marozas, R. L. McCrory, P. W. McKenty, D. D. Meyerhofer, R. D. Petrasso, T. C. Sangster, A. Shvydky, and S. Skupsky, "Polar Drive on OMEGA."

S. P. Regan, R. Epstein, B. A. Hammel, L. J. Suter, J. Ralph, H. Scott, M. A. Barrios, D. K. Bradley, D. Callahan, C. Cerjan, G. W. Collins, S. N. Dixit, J. Edwards, D. R. Farley, S. Glenn, S. H. Glenzer, I. E. Golovkin, S. W. Haan, A. Hamza, D. G. Hicks, N. Izumi, J. D. Kilkenny, J. L. Kline, G. A. Kyrala, O. L. Landen, T. Ma, J. J. MacFarlane, R. C. Mancini, R. L. McCrory, N. B. Meezan, D. D. Meyerhofer, A. Nikroo, K. J. Peterson, T. C. Sangster, P. Springer, and R. P. J. Town, "Diagnosing Implosions at the National Ignition Facility with X-Ray Spectroscopy."

A. Richard, V. Allouche, E. Alozy, F. Aubard, S. Bazzoli, T. Beck, J. Baggio, J. L. Bourgade, J. Y. Boutin, M. Briat, S. Brygoo, T. Caillaud, C. Cherfils, C. Chollet, P. Combis, S. Darbon, D. Dennetière, J. L. Desmeuzes, A. Duval, J. Fariat, J. Favier, S. Gary, J. Gazave, S. Girard, V. Glebov, J. C. Gomme, D. Gontier, O. Henry, S. Huevlan, H. P. Jacquet, J. P. Jadaud, O. Landoas, P. Llavador, B. Marchet, R. Marmoret, R. Maroni, I. Masclet-Gobin, D. D. Meyerhofer, J. P. Le Breton, G. Oudot, S. Perez, G. Pien, J. Raimbourg, C. Reverdin, P. Romary, R. Rosch, B. Rosse, A. Rousseau, D. Rubin de Cervens, T. C. Sangster, C. Schoech, P. Semécurbe, G. Souillé, P. Stemmler,

C. Stoeckl, I. Thfoin, C. Trosseille, P. Troussel, J. L. Ulmer, L. Videau, B. Villette, R. Wrobel, and C. Zuber, "Diagnosis Development for Plasma Experiments on LMJ."

T. C. Sangster, E. J. Bond, J. A. Caggiano, D. T. Casey, M. J. Eckart, J. A. Frenje, S. Friedrich, M. Gatu-Johnson, V. Yu. Glebov, E. P. Hartouni, R. Hatarik, S. P. Hatchett, H. W. Herrmann, C. J. Horsfield, M. Hutton, J. D. Kilkenny, J. P. Knauer, R. A. Lerche, J. McNaney, M. J. Moran, D. H. Munro, S. J. Padalino, P. K. Patel, D. Schneider, and C. Stoeckl, "High-Accuracy Ion-Temperature and Areal-Density Measurements with the NIF nTOF Suite."

W. Theobald, A. Casner, R. Nora, X. Ribeyre, K. S. Anderson, R. Betti, R. S. Craxton, J. A. Delettrez, J. A. Frenje, V. Yu. Glebov, O. V. Gotchev, M. Hohenberger, M. Lafon, F. J. Marshall, R. L. McCrory, D. D. Meyerhofer, L. J. Perkins, T. C. Sangster, G. Schurtz, W. Seka, V. A. Smalyuk, C. Stoeckl, and B. Yaakobi, "Progress in the Shock-Ignition Inertial Confinement Fusion Concept."

J. D. Zuegel, C. Dorrer, I. A. Begishev, R. Cuffney, T. J. B. Collins, E. Hill, J. H. Kelly, B. E. Kruschwitz, J. A. Marozas, P. W. McKenty, A. V. Okishev, R. G. Roides, D. F. Browning, G. V. Erbert, and M. W. Bowers, "Polar-Drive Beam Smoothing for Direct-Drive Ignition on the National Ignition Facility."

D. H. Froula, "Laser-Plasma Interactions in Direct-Drive Implosions," Assessment of Inertial Confinement Fusion Targets, Washington, DC, 20–21 September 2011.

The following presentations were made at Ultrafast Optics 2011, Monterey, CA, 26–30 September 2011:

J. Bromage, C. Dorrer, and R. K. Jungquist, "Temporal Contrast Degradation at the Focus of Ultrafast Pulses from High-Frequency Spectral Phase Modulation."

J. Bromage, M. Millecchia, J. Bunkenburg, R. K. Jungquist, C. Dorrer, and J. D. Zuegel, "A Cylindrical Öffner Stretcher Design for Reduced Chromatic Aberrations and Improved Temporal Contrast in Ultrafast Laser Systems."

C. Dorrer, "Interferometric Techniques for Optical-Pulse Characterization."

J. Qiao, P. A. Jaanimagi, R. Boni, J. Bromage, and E. Hill, "Measuring Short Pulse Using a High-Speed Streak Camera on Kilojoule, Petawatt-Class Laser Systems."

R. Xin and J. D. Zuegel, "All-Fiber Directly Chirped Laser Source (DCLS) for Chirped-Pulse Amplification."

